



2021

Development of Small Molecule Inhibitors of Therapeutic Target Enzymes: Paths to Discover Novel Antimicrobials

Thahani Shifna Habeeb Mohammad

Follow this and additional works at: https://ecommons.luc.edu/luc_diss

 Part of the [Chemistry Commons](#)

Recommended Citation

Habeeb Mohammad, Thahani Shifna, "Development of Small Molecule Inhibitors of Therapeutic Target Enzymes: Paths to Discover Novel Antimicrobials" (2021). *Dissertations*. 3888.

https://ecommons.luc.edu/luc_diss/3888

This Dissertation is brought to you for free and open access by the Theses and Dissertations at Loyola eCommons. It has been accepted for inclusion in Dissertations by an authorized administrator of Loyola eCommons. For more information, please contact ecommons@luc.edu.



This work is licensed under a [Creative Commons Attribution-NonCommercial-No Derivative Works 3.0 License](#).
Copyright © 2021 Thahani Shifna Habeeb Mohammad

LOYOLA UNIVERSITY CHICAGO

DEVELOPMENT OF SMALL MOLECULE INHIBITORS OF THERAPEUTIC TARGET ENZYMES:
PATHS TO DISCOVER NOVEL ANTIMICROBIALS

A DISSERTATION SUBMITTED TO
THE FACULTY OF THE GRADUATE SCHOOL
IN CANDIDACY FOR THE DEGREE OF
DOCTOR OF PHILOSOPHY

PROGRAM IN CHEMISTRY

BY

THAHANI HABEEB MOHAMMAD

CHICAGO, IL

AUGUST 2021

Copyright by Thahani Habeeb Mohammad, 2021
All rights reserved.

ACKNOWLEDGEMENTS

I would like to thank everyone who played a role in my personal and professional development upon completing this dissertation. Words cannot express the gratitude felt toward my advisor Dr. Daniel Becker: for his mentorship, guidance, and endless support during my time at Loyola University Chicago. His passion and knowledge in Medicinal Chemistry continue to inspire me to adopt interdisciplinary research methods and shaped my career trajectory. I would like to thank my dissertation committee members for providing feedback on my writing and guiding me in the right direction with my research projects. I would also like to extend my gratitude to Dr. Ken Olsen for providing me resources and suggestions in performing biochemical assays as part of the DapE project. I thank all the staff and faculty members of the Department of Chemistry and Biochemistry at Loyola University Chicago who assisted in my graduate research.

To my friends and colleagues, Thomas DiPuma (TJ), Sebastian, Zachary, and Emma, I thank you for always being on my side, for your support and laughs when I needed them the most. I will always cherish the joyous moments and memories we shared. I also would like to express my gratitude to my colleagues, Cory, Marlon, and Tahirah, for helping me set the course of my research projects during my first year at Loyola. Finally, I am grateful to the undergraduate researchers for the assistance provided to my work.

I would like to especially acknowledge my parents for their support and encouragement to follow the path of science. Their sacrifices and efforts kept me going during difficult times and strengthened my determination never to give up. I am eternally grateful to my husband Ayoob for his unconditional love and emotional support throughout my graduate studies. Finally, to my siblings, Zakiya and Feroz, and my extended family, I thank you for rejoicing every step of this long journey with me and being virtually present to show the love and support even though a great distance separates us.

To my parents, Habeeb Mohammad Abdul Cader and Inul Suadha Aboosalih

TABLE OF CONTENTS

ACKNOWLEDGEMENTS	iii
LIST OF TABLES	x
LIST OF FIGURES	xi
LIST OF SCHEMES	xvi
LIST OF EQUATIONS	xix
LIST OF ABBREVIATIONS	xx
ABSTRACT	xxiv
CHAPTER ONE: THE THREAT OF ANTIBIOTIC RESISTANT BACTERIAL INFECTIONS	1
CHAPTER TWO: SYNTHETIC STRATEGIES TO ACCESS <i>N</i> -FUNCTIONALIZED α -AMINOCYCLOBUTANONES AND CYCLOBUTANONES AS REVERSIBLE COVALENT INHIBITORS	5
Introduction	5
Electrophilic Covalent Reactive Groups in Drug Discovery	7
Historic Overview	8
Mechanistic Characteristics and Kinetics of Covalent Inhibitors	10
Cyclobutanones as Covalent Inhibitors	12
Synthetic Strategies in the Preparation of <i>N</i> -Functionalized 2-Aminocyclobutanones	15
Background and Previous Work	15
Attempted Synthetic Methods to Make Enantiopure 2-Aminocyclobutanone	17
A New Synthetic Route to Make Protected 2-Aminocyclobutanone as a Modular Transition State Synthon	22
Optimization of the Hydrogenolysis Reaction Conditions	23
Preparation of <i>N</i> -Functionalized 2-Aminocyclobutanone Library	25
Solvent Dependency of Hydration Equilibria of <i>N</i> -Functionalized 2-Aminocyclobutanones	29
Conclusion	30
Experimental	32
Methods and Materials	32
Attempted Enzymatic Hydrolysis of Benzyl(2-oxocyclobutyl)carbamate (2)	33
General Procedure for Alpha-Benzamide Cyclobutanones	35
General Procedure for <i>N</i> -Heterocyclic Benzamide Cyclobutanones	43
General Procedure for Sulfonamide Cyclobutanones (11b and 11b)	48
X-ray Crystallography Method	52

CHAPTER THREE: INHIBITION AND MOLECULAR DYNAMICS OF BACTERIAL ENZYME <i>N</i> -SUCCINYL-L,L-2,6-DIAMINOPIMELIC ACID DESSUCINYLAASE	54
DapE as a Novel Antibiotic Target	55
X-ray Crystal Structures and Conformational Changes of DapE Enzymes during Catalysis	57
Active Site Architecture of DapE Enzymes	59
A High-Resolution X-ray Crystal Structure of DapE	62
Inhibition of DapE by Sulfate	63
Targeted Molecular Dynamics	67
New Insights into DapE Catalytic Mechanism	69
Synthesis of DapE Substrate Analogs as Potential Inhibitors and Biochemical Tools	71
Development of Ninhydrin Inhibition Assay for DapE	71
Previous Work on Substrate Analogs for Ninhydrin Assay	72
Synthesis of <i>N</i> ⁶ -methyl-L,L-SDAP (15b)	75
Thioamide Analogs of DapE Substrates	77
Synthesis of the <i>N</i> ⁶ -methyl-L,L-SDAP Thioamide Analog	80
Synthetic Strategies and Inhibitory Potencies of DapE Inhibitors	84
Synthesis and Docking of Difluoromethyl Sulfonamides Inhibitors of DapE	86
Design, Synthesis, and Docking of Tetrazole- and Pyrazole-based DapE Inhibitors	90
Inhibitory Potencies of Cyclobutanone Inhibitors of DapE	99
Dose-Response Curves of Cyclobutanone Inhibitors and Observed Hill Coefficients	105
Conclusion	107
Experimental	110
General Procedure for Synthesis of <i>N</i> -(Difluoromethyl)-sulfonamide DapE Inhibitors (32 and 34)	112
DapE Enzyme Inhibition by Sulfate: IC ₅₀ Determination	114
DapE Enzyme Inhibition: IC ₅₀ Determinations	116
Molecular Docking Protocol	116
 CHAPTER FOUR: DESIGN AND SYNTHESIS OF INHIBITORS TARGETING DRUGGABLE ENZYMES OF SARS-COV-2 THROUGH COMPUTER-AIDED DRUG DESIGN	 119
Introduction	119
Coronaviruses	119
Development of Therapeutic Agents against SARS-CoV-2	121
Computer-aided Drug Design and Target Identification	122
Method Outline	123
Target Identification	124
Rational Design of Cyclobutanone Analogs Driven by Computer-Aided Drug Design and Structure-Activity Relationship	130
Preliminary Virtual Screening of the Cyclobutanone Library	131
Rational Design of Peptidomimetic 2-Aminocyclobutanone Helicase Inhibitors	135
Synthesis of Helicase Inhibitors	138

Lead Optimization and Rational Design of Main Protease Inhibitors	143
Synthesis of Benzimidazole-Based Main Protease Inhibitors	145
Antiviral Assay	147
Conclusion	150
Experimental	152
General Procedure for the Synthesis of <i>N</i> -Aryl Sulfonamide-Amino Acid Analogues 47a-d	152
General Procedure for the Synthesis of Amino Acid Cyclobutanone Analogues 48a-c	153
Synthesis of Cbz-Amino Acid Cyclobutanone Analogues 54a-d	161
<i>In silico</i> Methods	169
 CHAPTER FIVE: CHARACTERIZATION OF PA3944 GCN5-RELATED <i>N</i> -ACETYL TRANSFERASE BACTERIAL ENZYME	174
Introduction	174
X-ray Crystal Structures of GNATs	175
Design and Syntheses of Biochemical Tools Useful in Crystallization and Kinetic Studies of GNAT Enzyme	176
Design and Synthesis of Small Molecule Biochemical Tools Targeting PA3944	178
PA3944 Acetylates NANMO and Polymyxin B with Similar Catalytic Efficiencies	188
Kinetics, Mutagenesis, and Molecular Docking Experiments in Elucidating the Chemical Mechanism of GNAT PA3944	190
General Chemical Mechanism of GNATs	190
Significance of Serine148 for GNAT PA3944 Catalytic Activity	192
Substrate-Specific Catalytic Efficiency of PA3944 E102A Mutant	192
Substrate-Dependent Kinetic Mechanism of GNAT PA3944	195
Molecular Docking of NANMO with PA3944 WT and E102A Structures	198
Serine as a Nucleophile in GNAT Enzymatic Reactions: A New Paradigm for GNAT Chemical Mechanisms	203
Molecular Docking of Polymyxin B Substrate Analogues	206
Conclusion	209
Experimental	211
Synthesis of Aspartame Substrate Analogues (61-63)	211
Synthesis of Polymyxin B Substrate Analogues	213
Molecular Docking Protocol for GNAT Substrates	221
 APPENDIX A: SUPPLEMENTAL DATA FOR CHAPTER TWO	222
 APPENDIX B: SUPPLEMENTAL DATA FOR CHAPTER THREE	276
 APPENDIX C: SUPPLEMENTAL DATA FOR CHAPTER FOUR	289
 APPENDIX D: SUPPLEMENTAL DATA FOR CHAPTER FIVE	337

BIBLIOGRAPHY	350
VITA	369

LIST OF TABLES

Table 1. Dehydrants Screening for the Hydrogenolysis and Acetalization of 2-aminocyclobutanone	24
Table 2. Kinetic Parameters for <i>HiDapE</i> with <i>N</i> -Methyl-L,L-SDAP as the Substrate	66
Table 3. Preliminary inhibition data and percent yields for selected tetrazole and pyrazole analogs	96
Table 4. Inhibition of DapE by α -benzamide- and α -sulfonamide-cyclobutanones	101
Table 5. Inhibition of DapE by peptidomimetic cyclobutanones	103
Table 6. Docking parameters and calculated energies of amino acid-derived cyclobutanone hits against SARS-CoV-2 helicase	137
Table 7. Percent cell survival of SARS-CoV-2 inhibitors obtained via a cell survival assay	149
Table 8. PA3944 wild-type and mutant kinetics parameters toward NANMO and polymyxin B	190

LIST OF FIGURES

- Figure 1. (A) Mechanism of action for the inhibition of bacterial peptidoglycan layer synthesis by β -lactam antibiotics. Fragments of glycan strands are represented by chains of pentagons representing *N*-acetyl glucosamine (NAG) and *N*-acetyl muramic acid (NAM). (B) Inactivation of β -lactam antibiotics (penicillin) by β -lactamase enzyme through hydrolysis of the β -lactam ring. The core structure of penicillin analogous to *N*-Acyl-*N*-Alanyl-D-Alanine is highlighted in red. Copyright: Tulane University, School of Medicine, TMedWeb, 2015 7
- Figure 2. Historic advancement of approved covalent drugs. Covalent warheads are highlighted in pink. Thiophene is a pre-electrophile that undergoes oxidation to the CRG, the thiol/sulfenic acid 9
- Figure 3. Binding modes and kinetic parameters of (a) conventional non-covalent inhibitors and (b) covalent inhibitors. E represents the enzyme, and the inhibitor is denoted as I 10
- Figure 4. Core structures of clinically used antibiotics with β -lactam ring shown in blue and a general cyclobutanone analog of monobactam with cyclobutanone shown in red where the nitrogen atom of the β -lactam ring is replaced with a methylene (CH₂) group 13
- Figure 5. Binding mode of β -lactam analog of cyclobutanone to metallo- β -lactamase SPM-1 as observed in crystallography. (A) Cyclobutanone analog (yellow) bound to the SPM-1 active site. (B) Interactions of cyclobutanone analog with SPM-1. Distances between the cyclobutanone (cyan) and the SPM-1 active site are in magenta. Distances between active site atoms are in blue. The red sphere represents the bridging water molecule or hydroxide. Distances are given in Å. (C) Open cyclobutanone inhibitor-bound carboxylesterase (FTT258) binding pocket is shown. Inhibitor is shown (brown) as a ball and stick model. The chemical structure of the cyclobutanone analog is highlighted in the box 15
- Figure 6. (A) HPLC and (B) proton NMR of compound 12 highlighting the shoulder peak of potential hydrate and absence of hydrate peaks in the NMR 31
- Figure 7. Lysine and *m*-DAP biosynthesis via bacterial succinylase pathway 56

Figure 8. (A) Open conformation of <i>NmDapE</i> enzyme [PDB ID: 5UEJ], (B) Closed conformation of <i>HiDapE</i> products-bound structure [PDB ID: 5VO3]. Catalytic and dimerization domains of the homodimer are colored in green and orange	58
Figure 9. Architecture of di-zinc active sites of (A) <i>HiDapE</i> enzyme and (B) <i>NmDapE</i> with 1.3 Å resolution (PDB ID: 5UEJ)	59
Figure 10. (A) Succinic acid (cyan) and L-diaminopimelic acid (yellow) binding regions are highlighted to show the individual binding pockets (A) Interacting amino acid side chains. Zinc ions are shown as black spheres	60
Figure 11. (A) The position of His194.B (orange) is shown in the open conformation of <i>HiDapE</i> . (B) Structure of proposed oxyanion hole constitute with His194.B and a Zn ion in the <i>HiDapE</i> closed conformation	62
Figure 12. Key Coulombic interactions of (A) the terminal substrate derived carboxylates of the products in <i>HiDapE</i> (PDB ID: 5VO3) with Arg178 and Arg258 and (B) the two bound sulfate ions in the open conformation of <i>NmDapE</i> (PDB ID: 5UEJ) with the corresponding arginine residues, Arg179 and Arg259, respectively	64
Figure 13. <i>HiDapE</i> saturation curves with varying substrate and sulfate concentrations	66
Figure 14. (A) DapE at 0 and 12.5 ns showing the conformational change in the catalytic domains moving toward the dimerization domains with force applied to both subunits. The dimer at time zero is colored cyan, and the dimer at 12.5 ns is colored red (chain A) and blue (chain B). (B) Same as panel A but at 40 ns. (C) Same as panel A but viewed so that the rotation of the catalytic domain relative to the dimerization domain can be seen easily. No rotation occurred during the first 12.5 ns of the TMD simulation. (D) Same as panel C but at 40 ns. The large rotation of the catalytic domain relative to the initial structure can be seen	70
Figure 15. <i>N</i> ⁶ -Methyl (29b), <i>N</i> ⁶ , <i>N</i> ⁶ -dimethyl (29c), and <i>N</i> ⁶ -acetylated (29d) substrate analogs of L,L-SDAP (29a)	73
Figure 16. Docked and modeled (A) native substrate L,L-SDAP, (B) <i>N</i> ⁶ -methyl-L,L-SDAP and, (C) <i>N</i> ⁶ , <i>N</i> ⁶ -dimethyl-L,L-SDAP in the DapE active site. The diaminopimelate moiety is shown in yellow, and the succinate in turquoise. The catalytic domain of Subunit A is colored in green, and the dimerization domain of Subunit B is colored orange	74
Figure 17. (A) The resonance structures of thioamide. (B) Thioamide reactive centers and (C) structure of ethionamide	79

Figure 18. DapE hit compounds with calculated physicochemical properties	85
Figure 19. SAR functional group derivatizations of difluoromethyl sulfonamide series	87
Figure 20. Docked (A) <i>o</i> -OCH ₃ difluoromethyl sulfonamide (46) and (B) <i>p</i> -OCH ₃ analog (48) into DapE di-zinc active site	89
Figure 21. Plausible point derivatization of tetrazole and pyrazole derived DapE inhibitors	91
Figure 22. Docked (A) (<i>S</i>)-enantiomer is interacting with the zinc atoms (grey spheres) in the active site. (B) The (<i>R</i>)-enantiomer is bound to an allosteric site. The zinc atoms of DapE active site are highlighted as purple spheres	92
Figure 23. Hit-derived pyrazole bound to DapE active site through favorable interactions with active site residues	93
Figure 24. Schematic roadmap of the <i>N</i> -functionalized 2-aminocyclobutanone library screening against the seven SARS-CoV-2 target proteins. 3D protein models from the Protein Data Banks and other sources were optimized and relaxed by MD simulations. Active sites of the minimized structures were then mapped, and a GLIDE Grid was generated for a high-throughput virtual screening. The top 10% of the candidates were then subjected to high accuracy SP and XP dockings. The resultant top 10% were further refined in subsequence secondary rescoring (GBSA). Our method was validated via MD simulations of the highest scoring lead molecules specific to each target pool	124
Figure 25. The SARS-CoV-2 life cycle highlighting HTVS target proteins. Replicase translates the viral genomic RNA to synthesize pp1a and pp1ab, two replicase polyproteins (4). These polyproteins are proteolytically cleaved by two proteases, PLpro and 3CLpro, producing 16 nonstructural proteins (5). Viral Helicase is responsible for accelerating the required folding in viral replication (7). RdRp catalyzes the template synthesis of RNA genome that is critical in viral-host cell replication. ExoN is a viral exoribonuclease. Both 2'-O-MT (8) and ExoN are critical for coronaviruses to escape the recognition of viral RNA by the host immune system (9). NandoU is suggested to suppress the host cell immune response	125
Figure 26. Rational design of (A) cyclobutanone analog of TPCK by replacing the α -chloro ketone covalent warhead with a cyclobutanone ring and (B) cyclobutanone analogs via functional group derivatization including Cbz, natural and unnatural amino acids, and cyclobutanone isosteres from Ts-D-Phe cyclobutanone hydrate (HT-virtual screening original hit)	131

Figure 27. Docking images showing binding interactions of (A) Ts-D-Phe cyclobutanone (48b) in the ATP binding site where cyclobutanone hydrate is hydrogen bonded to His290, (B) benzimidazole cyclobutanone 10t in the Mpro active site with residues highlighting the proximal positioning of cyclobutanone ring to the catalytic Cysteine 145, (C) bicyclic thiourea 14 in the RdRp active site, and (D) 4-fluoro benzene sulfonamide cyclobutanone 11b bound to the PLPro active site and the residues interacting are highlighted	134
Figure 28. Rational design of benzimidazole-based main protease inhibitors	145
Figure 29. Acceptor substrates for PA4794, PA3944, and PA2271 GNATs identified via a broad-substrate screening assay	177
Figure 30. (A) Formation of bisubstrate 1 between CoA and α -haloacetyl NPACGK analog via enzyme-mediated alkylation of CoA. (B) X-ray induced radical-mediated addition of CoA to the alkene analog of NPACGK forming bisubstrate 2	178
Figure 31. Structures of NANMO and BAMOC designed as small-molecule analogs of polymyxin B. The Dab moiety is highlighted in red	181
Figure 32. Substrate saturation curves of PA3944 WT and E102A mutant toward polymyxin B and NANMO. The concentration of acceptor substrate was varied while AcCoA was held constant at 0.5 mM. Curves in black correspond to polymyxin B as the substrate and curves in red correspond to NANMO as substrate. WT is shown as solid squares for polymyxin B and open squares for NANMO, E102A is shown as black stars for polymyxin B and red stars for NANMO. (A) Substrate saturation curves. (B) Normalized data from substrate saturation curves	189
Figure 33. Comparison of PA3944 WT, PA3944 E102A, and PA4794 crystal structures and active sites. (A) WT PA3944 structure (cyan; PDB ID 6EDV). CoA is shown with white sticks and key active site residues are shown with cyan sticks. The gray bubble highlights the region of the active site where a general acid residue would typically be located. (B) WT PA3944 E102A crystal structure (green; PDB ID 7KPP). CoA is shown with white sticks and key active site residues are shown with green sticks. (C) PA4794 crystal structure (pink; PDB ID 5VDB). The ligand was removed for clarity and key active site residues are shown with pink sticks. The gray bubble highlights the region of the active site where a general acid residue would typically be located. (D) Overlay of PA3944 WT and E102A structures. The box highlights the F89 residue, which changes conformation when E102 is mutated to alanine	194
Figure 34. Hybrid ping-pong model with two components: a ping-pong path and a sequential path. E is enzyme, EX is acetylated enzyme, A is AcCoA, B is acceptor	

substrate (polymyxin B or NANMO), P is CoA, and Q is acetylated acceptor product. The hybrid model allows free enzyme to bind AcCoA or acceptor substrate at the same time. If it binds AcCoA first, the enzyme becomes acetylated and the ping-pong path is used, whereas if acceptor substrate binds first the acetyl group of AcCoA can be transferred directly to acceptor substrate using the sequential path 196

Figure 35. Ligand interaction maps for eight different conditions of NANMO docked into the PA3944 WT and E102A crystal structures. A single pose with the lowest binding energy for each of the eight experiments was selected. WT poses are numbered 1-4 and E102A are numbered 5-8. Ligands used for docking and modified residues (acetylated S148) are noted in each diagram. Purple circles are polar residues, green circles are hydrophobic residues, purple circles with red border are acidic polar residues, purple circles with blue border are basic polar residues. Ligand atoms highlighted in blue are exposed to solvent 199

Figure 36. Eight poses of NANMO docked with WT and E102A PA3944. Key residues are shown with sticks and the PA3944 protein is shown as ribbons. The acceptor site of the enzyme is shown with gray mesh and NANMO is in spheres with red as oxygen, blue as nitrogen, white as hydrogen and gray as carbon atoms. CoA is shown as gray sticks. NANMO does not occupy the entire acceptor site and adopts a variety of conformations 200

Figure 37. Frequency of WT PA3944 acceptor site interactions with NANMO during docking studies. All ligand interaction maps across all docking experiments with NANMO pointed toward the donor site were compiled and were analyzed to determine residues that most frequently interacted with NANMO. Residues were colored based on frequency (gradient from purple for high frequency to gray for low frequency) on the surface of the acceptor site. AcCoA is shown as sticks 204

Figure 38. The proposed chemical mechanism for PA3944 using both ping-pong and sequential components of the hybrid mechanism. In the ping-pong component, (A) S148 acts as a nucleophile and is acetylated during the enzymatic reaction and then (B) deprotonated NANMO is acetylated by the acyl enzyme. In the sequential component, (C) direct enzyme-mediated acetylation of NANMO by AcCoA occurs 206

Figure 39. Substrates docked with PA3944 (PDB ID: 6EDV) in complex with AcCoA. All substrates are bound to the acceptor binding pocket where the terminal Dab amine moieties of (A) NANMO, (B) BAMOC, (C) BABOC, (D) 3,4-BABOC, and (E) FABOC placed in a close proximity to the acetyl group of the AcCoA shown in cyan. Key interactions with residues and the distance between the terminal amine and the carbonyl carbon of AcCoA are visualized. Protein is shown as a gray ribbon and the ligands colored in magenta 208

LIST OF SCHEMES

Scheme 1. <i>N</i> -Functionalized cyclobutanones as inhibitors of serine hydrolases and proteases and metalloenzymes	12
Scheme 2. Synthesis of benzyl(2-oxocyclobutyl) carbamate (2)	17
Scheme 3. Attempted synthesis (<i>R</i>)-1-phenylethyl (2-oxocyclobutyl)carbamate (3) and acid catalyzed elimination reaction producing vinylbenzene (4)	18
Scheme 4. Attempted enzymatic resolution of racemic benzyl(2-oxocyclobutyl) carbamate	20
Scheme 5. Synthesis of 2,2-dimethoxycyclobutan-1-amine hydrochloride (9) via one-pot acetalization/debenzylation from carbamate 2	25
Scheme 6. Synthesis of cyclobutanone analogs from compound 9 and aromatic carboxylic acids via T3P coupling/hydrolysis reactions	26
Scheme 7. Synthesis of α -sulfonamide (11) and α -benzamide cyclobutanones (12) from compound 9 via base catalyzed coupling/hydrolysis reactions	27
Scheme 8. Synthesis of bicyclic thiourea 14 from compound 9 via acetal 13 and the ORTEP structure of 9	28
Scheme 9. Hydrolysis of L,L-SDAP to succinate and DAP by DapE	57
Scheme 10. Asymmetric synthesis of <i>N</i> ⁶ -methyl-L,L-SDAP substrate analog 23	76
Scheme 11. Attempted thionation of benzyl ester protected succinate amide 24 using LR	82
Scheme 12. Synthesis of <i>N</i> ⁶ -methyl-L,L-SDAP thioamide analog (28)	83
Scheme 13. Synthesis of <i>N</i> -difluoromethyl sulfoamides 32 and 34	90
Scheme 14. Synthesis of phenyl tetrazole thio-linked DapE inhibitors	94

Scheme 15. Synthesis of (A) phenyl pyrazole thione 40 and (B) phenyl pyrazole thio-linked DapE inhibitors	95
Scheme 16. Attempted synthetic routes in preparation of hit-derived tetrazole analogs 46	97
Scheme 17. Synthesis of tosyl-amino acid cyclobutanone analogs 48 using 2-aminocyclobutanone synthon 9. Prospective cyclobutanone analogs are also shown (48d-g)	139
Scheme 18. Synthesis of 4-(OCH ₃)-benzenesulfonamide-D-valine cyclobutanone (48h)	140
Scheme 19. Synthesis of Ts-L-tyrosine cyclobutanone analog 48d in progress	141
Scheme 20. Synthesis of cyclobutanone isostere compounds 51 and 52	141
Scheme 21. Synthesis of Cbz-amino acid cyclobutanone analogs 54a-d. Prospective analogs are listed as 54e-g	143
Scheme 22. Synthesis of benzimidazole analogs 55 and 56	145
Scheme 23. Synthesis of benzimidazole acrylamide analog 57 from acryloyl chloride	146
Scheme 24. Synthesis of α -chloro benzimidazole analog 58	147
Scheme 25. Synthesis of benzimidazole 2-chloronicotinamide 59 and 4-bromo pyridine benzimidazole analog 60	147
Scheme 26. Synthesis of internal alkene analogs of aspartame (A) <i>N</i> -maleyl-L-phenylalanine methyl ester (61), <i>N</i> -fumaryl-L-phenylalanine methyl ester (62), and (B) <i>N</i> -fumaryl-L-phenylalanine (63) targeting PA3944	179
Scheme 27. Synthesis of <i>N</i> -(2-aminoethyl)- <i>N</i> -methyloctanamide (NANMO, 64) and α -chloro analog of NANMO (65)	182
Scheme 28. Attempted synthesis of benzyl (S)-(4-amino-1-(methylamino)-1-oxobutan-2-yl)carbamate (BAMOC, 69) via a tosylate intermediate (67)	184
Scheme 29. Attempted synthesis of BAMOC (69). Mitsunobu conditions explored and the possible acid catalyzed hydrolysis of di-(Boc) protection group of compound 70	185

Scheme 30. BABOC (73) synthesis via Dess-Martin oxidation/reductive amination route	186
Scheme 31. Synthesis of BABOC (73) and FABOC (75) from globally protected L-2,4-Dab	187
Scheme 32. Synthesis of 3,4-BABOC (78) from N_{β} -Cbz- N_{γ} -Boc-L-3,4-Dab	188

LIST OF EQUATIONS

Equation 1. $\Delta G = E_{\text{complex}}(\text{minimized}) - (E_{\text{ligand}}(\text{minimized}) + E_{\text{receptor}}(\text{minimized}))$

172

LIST OF ABBREVIATIONS

2'-O-MT	2'-O-Methyltransferase
3CLpro	3-Chymotrypsin-Like Protease
ACE	Angiotensin-converting-enzyme
acetyl-CoA	Acetyl coenzyme A
ACN	Acetonitrile
ATP	Adenosine triphosphate
Au	Absorbance units
Bn	benzyl
Boc	tert-butyloxycarbonyl
Bzh	benzhydryl
CADD	Computer-aided drug design
Cbz	Carboxybenzyl
CCDC	Cambridge Crystallographic Data Centre
CDC	Centers for Disease Control and Prevention
CDCl ₃	Deuterated chloroform
CoVs	Coronaviruses
CRG	covalent reactive groups
Cs ₂ CO ₃	Cesium carbonate

DAP	L,L-diaminopimelate
DapE	<i>N</i> -succinyl-L,L-diaminopimelic acid desuccinylase
DCM	Dichloromethane
DKR	Dynamic kinetic resolution
DMF	Dimethylformamide
DMSO	Dimethyl sulfoxide
EA	Ethyl acetate
EDCI	1-Ethyl-3-(3-dimethylaminopropyl)carbodiimide
Et ₂ O	Diethyl ether
Et ₃ N	Triethylamine
ExoN	Exoribonuclease
FDA	Food and Drug Administration
GNAT	Gcn5-related <i>N</i> -acetyltransferase
HCl	Hydrochloric acid
HEPES	2-[4-(2-hydroxyethyl)piperizin-1-yl]ethanesulfonic acid
<i>HiDapE</i>	<i>Haemophilus influenzae N</i> -succinyl-diaminopimelic acid desuccinylase enzyme
HTS	High-throughput screening
HMDO	Hexamethyldisiloxane
HOBt	Hydroxybenzotriazole
HPLC	High-performance liquid chromatography
HTVS	High-throughput virtual screening
kDa	kilodalton

K_i	Inhibitory constant
k_{inact}	Rate of inactivation
KR	Kinetic resolution
L,L-SDAP	<i>N</i> -succinyl-L,L-diaminopimelic acid
LR	Lawesson's reagent
MBLs	metallo- β -lactamases
<i>m</i> -DAP	<i>meso</i> -diaminopimelate
MDR	Multiple drug resistance
MeOH	Methanol
MERS-CoV	Middle East respiratory syndrome coronavirus
MgSO ₄	Magnesium sulfate
MnO ₂	Manganese dioxide
MOE	Molecular Operating Environment
M ^{pro}	Main Protease
Na ₂ CO ₃	Sodium carbonate
Na ₂ SO ₄	Sodium sulfate
NaHCO ₃	Sodium bicarbonate
NDM-1	New Delhi metallo- β -lactamase-1
NendoU	Nonstructural uridylate-specific endoribonuclease
<i>NmDapE</i>	<i>Neisseria meningitidis</i> <i>N</i> -succinyl-diaminopimelic acid desuccinylase enzyme
NMR	Nuclear magnetic resonance

Nsp	Nonstructural protein
P ₂ S ₅	Phosphorus pentasulfide
PDB	Protein Data Bank
Pet. Ether	Petroleum ether
PLpro	Papain-Like Protease
RdRp	RNA-directed RNA polymerase
RT	Room temperature
SAR	Structure-activity relationship
SARS-CoV-2	Severe Acute Respiratory Syndrome Coronavirus 2
T3P	Propylphosphonic anhydride
TFA	Trifluoroacetic acid
TLC	Thin layer chromatography
TMD	Targeted Molecular Dynamics
TMS	Tetramethylsilane
TOF	Time-of-Flight
UPEC	UroPathogenic <i>Escherichia coli</i>
UPLC	Ultra performance liquid chromatography
UTIs	Urinary tract infections
UV	Ultra-violet
WHO	World Health Organization

ABSTRACT

The rising antimicrobial resistance to antibiotics is a major global problem, which has been exacerbated by the inappropriate use of antibiotics. The effectiveness of frequently prescribed penicillin derivatives and β -lactamase inhibitors are compromised by the evolution of bacterial β -lactamases and antibiotic-resistant bacteria. Consequently, the design and synthesis of small-molecule inhibitors of identified novel antibiotic targets is an urgent unmet medical need. We previously demonstrated that *N*-functionalized α -aminocyclobutanones can act as peptidomimetic enzyme inhibitors, including inhibition of a key esterase in *Francisella Tularensis*. The carbonyl of a cyclobutanone is electrophilic due to ring strain, therefore, cyclobutanone derivatives can serve as transition state inhibitors of serine- and metallo- β -lactamases, serine proteases, and other metalloenzymes, including DapE. The bacterial enzyme *N*-succinyl-L,L-diaminopimelic acid desuccinylase (DapE) is a novel antimicrobial target and a key enzyme in the bacterial lysine biosynthetic pathway. DapE catalyzes the hydrolysis of *N*-succinyl-L,L-diaminopimelic acid (L,L-SDAP) to succinate, and L,L-diaminopimelic acid (L,L-DAP), and the products of this reaction are critical precursors of bacterial cell wall synthesis. Due to the absence of the lysine biosynthetic pathway in mammals, inhibitors of DapE should be free of mechanism-based toxicity in humans, which makes DapE a promising antibiotic drug target. I have developed an efficient

synthetic route to make 2-aminocyclobutanone derivatives via a modular synthon and employed this methodology to synthesize a library of *N*-functionalized 2-aminocyclobutanone derivatives. The cyclobutanone library was tested against DapE using our ninhydrin assay, and a number of these analogs showed promising inhibition of DapE with IC₅₀s less than 100 μM. This library has also provided inhibitors of the coronavirus main protease (3CLpro) and helicase and demonstrated efficacy against SARS-CoV-2 *in vitro*. Following up on other DapE inhibitors that were identified through a high-throughput screen, *N*-aryl *N*-difluoromethyl sulfonamides and tetrazole-based inhibitors have been synthesized, and the inhibitory potencies against DapE have been established.

In a collaborative project, we focus on improving the structural and functional annotations of uncharacterized bacterial Gcn5-related *N*-acetyltransferase (GNAT) PA3944 from *Pseudomonas aeruginosa*. To determine the key residues that are critical in enzymatic activity and to identify functionally relevant acceptor substrates of PA3944, we designed and synthesized small-molecule substrate analogs of previously identified polymyxin B, including NANMO. The *in vitro* and docking studies demonstrated that NANMO can act as an acceptor substrate in a similar capacity to polymyxin B. Thus, GNAT PA3944 was characterized utilizing NANMO as a substrate. Based on the crystal structures, kinetic data, and *in silico* simulations, we demonstrated that PA3944 adopts a substrate-dependent hybrid ping-pong kinetic mechanism and a chemical mechanism for the ping-pong component of GNAT PA3944 has been proposed.

CHAPTER ONE

THE THREAT OF ANTIBIOTIC RESISTANT BACTERIAL INFECTIONS

The rising antibacterial resistance to antibiotics is a major global problem¹ that has been exacerbated by inappropriate use of antibiotics. In 2019, Centers for Disease Control and Prevention (CDC) reported that each year 2.8 million Americans acquire serious infections caused by antibiotic-resistant bacteria, and 35,000 deaths occurred as a result. In 2020, the World Health Organization (WHO) declared antimicrobial resistance as one of the top ten global health crises. Even though the statistics are discouraging, with the responsible use of antibiotics and through proper infection prevention programs, the mortality and the rate of rising antibiotic resistance could be mitigated. More importantly, a steady pipeline of new antibiotics is required to keep pace with evolving drug resistant pathogenic bacteria.

β -Lactams—a class of antibiotics to which penicillin belongs—were the first among antibiotics to be investigated and described in literature² and still are the most prescribed. The serendipitous discovery of penicillin in 1928 and the introduction of penicillin as a therapeutic agent in 1940 set the stage for modern day antibiotic therapies that save millions of lives each year. However, in 1941, a year after the introduction of penicillin as a therapeutic agent, four penicillin-resistant staphylococci strains were isolated from patients during treatment of localized infections.³

Presently, about 70% of the bacteria that cause infections in hospitals are resistant to at least one of the drugs most commonly used for treatment. An alarming increase in drug resistant bacteria that cause community acquired infections has also been documented, especially in staphylococci and pneumococci (*Streptococcus pneumoniae*), which are prevalent causes of disease and mortality.⁴ Studies have shown that drug resistant bacteria can pass genes that are responsible for drug resistance not only between bacterial strains but even between species. Antibiotic-resistance genes of staphylococci are carried on plasmids and are exchanged with bacillus, streptococcus, enterococcus, and even with UroPathogenic *Escherichia coli* (UPEC).^{5,6} The growing multiple drug resistance (MDR) among *E. coli* is alarming because *Escherichia coli* is the most common organism that causes about 150 million cases of urinary tract infections (UTIs) worldwide annually that alone add a yearly health care cost of 6 billion dollars.⁷

In recent years, several clinical studies revealed that MDR identified in ESKAPE pathogens as a threat that requires immediate and coordinated global attention. ESKAPE the acronym, represents six nosocomial pathogens including *Enterococcus faecium*, *Staphylococcus aureus*, *Klebsiella pneumoniae*, *Acinetobacter baumannii*, *Pseudomonas aeruginosa*, and *Enterobacter* species. The most significant MDR occurs in Methicillin/oxacillin-resistant *Staphylococcus aureus* (MRSA), Vancomycin-resistant enterococci (VRE), extended-spectrum beta-lactamases (ESBLs) (which are resistant to cephalosporins and monobactams), and penicillin-resistant *Streptococcus pneumoniae* (PRSP).⁴ As reported by the World Health Organization in 2020, infections caused multi-

drug resistant bacteria (“superbugs”) are increasingly difficult or almost impossible to treat with existing antibiotics. Statistics obtained via Global Antimicrobial Resistance and Use Surveillance System (GLASS) in 2020 indicated a substantial change in the resistance against ciprofloxacin, an antibiotic commonly used to treat urinary tract infections. Resistance against ciprofloxacin increased from 8.4% to 92.9% for *Escherichia coli* and from 4.1% to 79.4% for *Klebsiella pneumoniae*. *K. pneumoniae* is a common intestinal bacterium and is the major cause of hospital-acquired infections including pneumonia, bloodstream infections, and infections in newborns and intensive-care unit patients.

Despite the fact that there is an urgent unmet medical need for novel antimicrobials, there is still a huge gap to fill and keep the continuity of the antimicrobial pipeline through innovative pathways and through developing antibiotics against identified novel therapeutic targets. Drug development requires tremendous efforts in scientific research with its own challenges, and the risk of failure is high. Typically, it could take at least 8 to 10 years for a new drug to complete the journey from initial discovery to the marketplace.⁸ The average research and development cost of each successful drug is estimated to be 2.6 billion dollars.⁹

As of 2019, 32 out of 50 antibiotics in the development pipeline target WHO priority pathogens, including Ampicillin-resistant *Haemophilus influenzae* and carbapenem-resistant *Pseudomonas aeruginosa*.¹⁰ Approximately 1 in 4 drugs in the pipeline represents a novel drug class or a new mechanism of action. None of these are potentially active against Gram-negative ESKAPE pathogens or WHO critical threat pathogens. It is inevitable

that the infectious pathogens will continue to evolve and develop resistance to antibiotics; therefore, a sustainable supply of novel antimicrobial to the pipeline is crucial. Developing novel antibiotics that belong to new classes and/or with a new mechanism of action is critical and urgent, with significantly less contribution from major pharmaceutical companies to the field.¹¹

Our research lab joins the global effort in combating the drug resistant infectious pathogens and focuses on developing novel antimicrobials against previously identified therapeutically important bacterial enzymes, including *N*-succinyl-L,L-diaminopimelic acid desuccinylase (DapE), New Delhi metallo- β -lactamase-1 (NDM-1), and selected Gcn5-related *N*-acetyltransferase (GNAT).

CHAPTER TWO

SYNTHETIC STRATEGIES TO ACCESS

N-FUNCTIONALIZED α -AMINOCYCLOBUTANONES AND

CYCLOBUTANONES AS REVERSIBLE COVALENT INHIBITORS

Introduction

Cyclobutanones are important scaffolds as both synthetic targets and intermediates¹² with applications in both synthetic organic chemistry and medicinal chemistry. Cyclobutanone moieties are also found in a number of natural products such as the monoterpene chrysanthenone isolated from the flowers of *Chrysanthemum sinense* and found in two diterpenes, acetylcoriacenone and isoacetylcoriacenone isolated from the brown sea-alga *Pachydictyon coriaceum*.^{13, 14} The four-membered ring endows cyclobutanones with a degree of conformational rigidity while the strain inherent in the ring makes the ketone carbonyl more electrophilic than an unstrained ketone. Cyclobutanones provide a convenient four-carbon ring motif in which each carbon center of the ring can be potentially functionalized. α -Aminocyclobutanones can serve as peptidomimetic small molecule motifs that are the most common substituted cyclobutanones explored and are reported to show inhibitory potencies against drug target enzymes including β -lactamases, serine proteases, and esterases.

β -Lactam antibiotics including penicillin and cephalosporins are bactericidal, which kill bacteria¹⁵ by inhibiting the synthesis of the peptidoglycan layer of bacterial cell walls. The peptidoglycan layer is critical for cell wall structural integrity, as it is the outermost and primary component of the wall in both Gram-positive and Gram-negative bacteria. The final transpeptidation in the peptidoglycan/murein synthesis is catalyzed by D,D-transpeptidases, which are penicillin-binding proteins (PBPs) and are subject to inhibition.¹⁶ The β -lactam antibiotics act as substrate analogs, binding to the active site of PBPs that normally is occupied by D-alanyl-D-alanine, which are the terminal amino acid residues on the sugar-amino acid precursor, UDP-*N*-acetylmuramic acid (UDP-MurNAc)-peptide subunits of the nascent peptidoglycan layer (see Figure 1A).¹⁷ Thus, β -lactam antibiotics inhibit the synthesis of the peptidoglycan layer and, as a result, kill the bacteria via cell lysis.

An effective way for bacteria to counteract β -lactam antibiotics is by producing β -lactamases, which are enzymes that inactivate the drugs by hydrolyzing the β -lactam ring (see Figure 1B).¹⁶ This mode of action of bacterial resistance can be surpassed successfully by the administration of β -lactam antibiotics with β -lactamase inhibitors, but the effectiveness of current penicillin class antibiotics, cephalosporins, carbapenems, and mechanism-based β -lactamase inhibitors are suppressed by prevailing extended-spectrum β -lactamases (ESBLs),¹⁸ carbapenemases,¹⁹ and metallo- β -lactamases (MBLs).²⁰ Consequently, the synthesis of new antibiotics and broad-spectrum β -lactamase inhibitors is crucial.

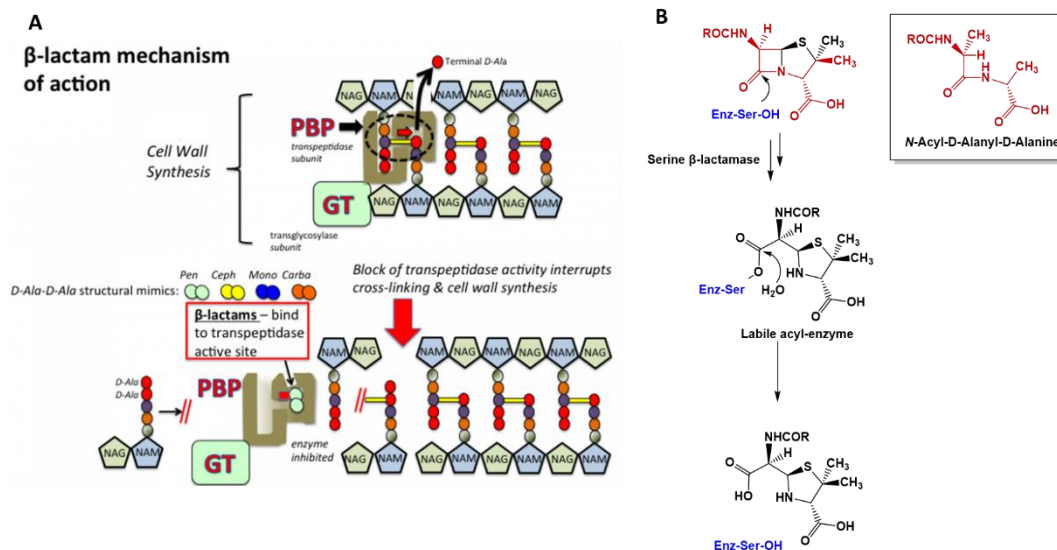


Figure 1. (A) Mechanism of action for the inhibition of bacterial peptidoglycan layer synthesis by β -lactam antibiotics. Fragments of glycan strands are represented by chains of pentagons representing *N*-acetyl glucosamine (NAG) and *N*-acetyl muramic acid (NAM). (B) Inactivation of β -lactam antibiotics (penicillin) by β -lactamase enzyme through hydrolysis of the β -lactam ring. The core structure of penicillin analogous to *N*-Acyl-*N*-Alanyl-D-Alanine is highlighted in red. Copyright: Tulane University, School of Medicine, TMedWeb, 2015.

Electrophilic Covalent Reactive Groups in Drug Discovery

Covalent inhibitors are typically small molecules that form a covalent bond with their biological targets such as enzymes and/or receptors and inactivate their biological activities. Irreversible covalent inhibitors typically consist of an electrophilic functional group that is expected to react with nucleophilic amino acid residues, including serine, cysteine, tyrosine, threonine, or lysine.²¹ These electrophilic covalent reactive groups (CRG) are known as warheads in the context of drug design and development. Depending on the type of selected warhead, the covalent bond formed with the biological target could be either reversible or irreversible. In drug design, the most frequently used CRGs are acrylamides and other substituted α,β -unsaturated groups, boronic acids, and α -halogen

ketones.²² Furthermore, some unique covalent reactive groups such as cyclobutanones captivated our interest, and we are investigating the inhibitory potencies of the cyclobutanone inhibitors against therapeutical target enzymes which will be discussed in Chapters Three and Four.

Historic Overview

The discovery of covalent-binding drugs has been more often serendipitous rather than following a rational drug design process, as in the discovery of penicillin as an antibiotic. Aspirin (acetylsalicylic acid) is one of the early examples and is a common covalently-modifying drug that has been used clinically from 1899 as a pain killer (see Figure 2). Aspirin irreversibly acetylates a nucleophilic serine residue of cyclooxygenase-1 (COX-1) that is responsible for the biosynthesis of prostaglandin.^{23, 24}

The development of reactive covalently-binding drugs is historically considered highly risky, and irreversible covalent inhibitors were underutilized in medicinal chemistry because of the presumed off-target reactivity leading to potential toxicity. The deleterious effect on human health elicited by some covalent drug metabolites was reported in 1973 regarding the hepatotoxicity caused by the cellular metabolites (reactive quinone intermediates and benzoquinone) of acetaminophen.²⁵ Haptenization of proteins that might stimulate an immune response, and idiosyncratic drug reactions, a rare adverse episode that is observed after administration of certain drugs and is frequently immunogenic in origin, are some of the concerns and off-target toxic effects that made medicinal chemists and drug discovery programs hesitant toward the development of

covalent modifier drugs. In this context, it is therefore critically important to tune the reactivity of the electrophilic warhead to the target enzyme of interest to avoid the off-target reactivity.²³ Additionally, to overcome the above-mentioned undesired potential toxic effects, reversible covalent inhibition (for example, inhibition of serine proteases by cyclobutanone inhibitors) of the target enzyme could be the solution.²⁶

In the last 50 years, research and development of covalent inhibitors has reemerged, and it has been established that the unique strengths of covalent and non-covalent modes of drug action could be combined by designing compounds that consist of meticulously tuned reactivity with specific selectivity to the target. Currently, about 50 drugs with a covalent mode of action are approved by the FDA (see Figure 2).²⁷

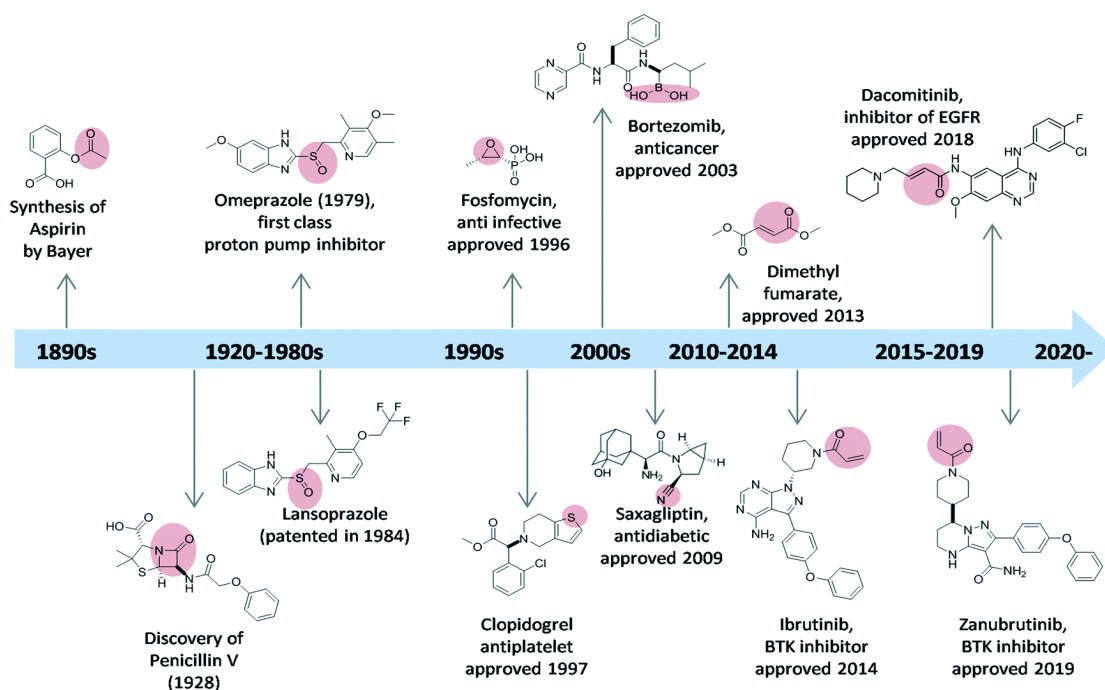


Figure 2. Historic advancement of approved covalent drugs. Covalent warheads are highlighted in pink. Thiophene is a pre-electrophile that undergoes oxidation to the CRG, the thiol/sulfenic acid.²⁷

Mechanistic Characteristics and Kinetics of Covalent Inhibitors

The general approach in drug design is to develop small-molecule drugs to interact with their biological target under equilibrium-binding conditions through the formation of swift and reversible desired drug-protein interactions. Covalent inhibitors are generally developed via structure-based design by incorporating an electrophilic covalent reactive group to the optimized reversible ligand. Binding of a covalent inhibitor with the target enzyme takes place in two steps. In the first step, the inhibitor binds to the enzyme via the reversible non-covalent interactions through which the reactive warhead of the inhibitor will be placed in close proximity to the targeted nucleophilic amino acid residue for a successive covalent bond formation in the second step. The formation of this covalently bonded inhibitor-protein complex can result in the irreversible inhibition of the targeted enzyme. Thus, the irreversible inhibitors follow non-conventional equilibrium kinetics and provide a prolonged therapeutic response (see Figure 3).²⁸

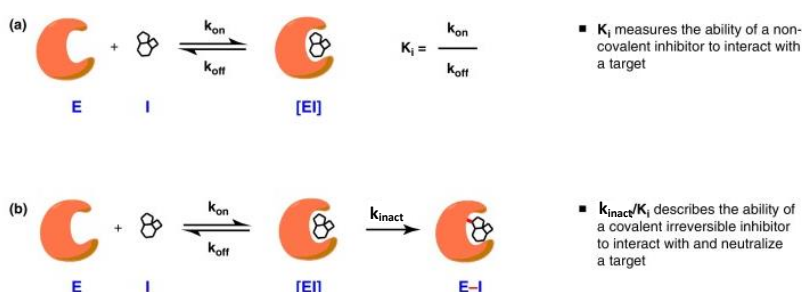


Figure 3. Binding modes and kinetic parameters of (a) conventional non-covalent inhibitors and (b) covalent inhibitors.²⁸ E represents the enzyme, and the inhibitor is denoted as I.

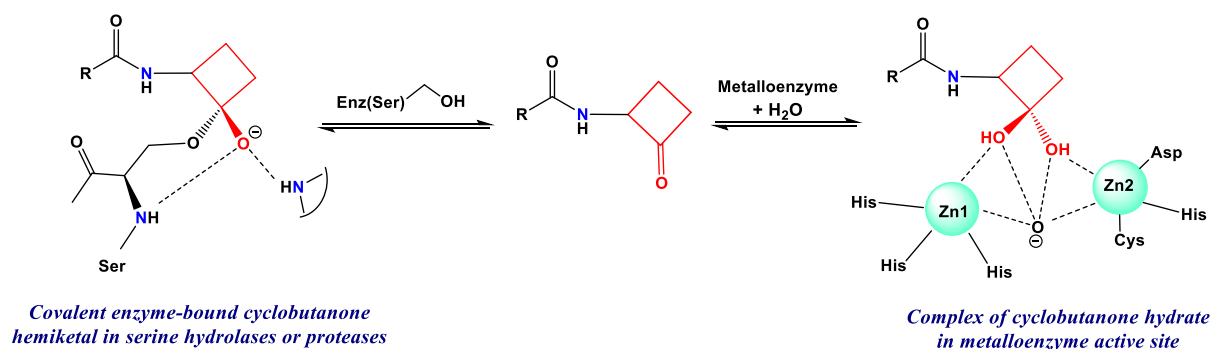
As explained above, the binding kinetics of the covalent inhibitors are substantially distinct from the equilibrium kinetics of the reversible inhibitors. For traditional reversible inhibitors, potency and selectivity are typically assessed by measuring the equilibrium binding affinity for the target (K_i) and/or by measuring the concentration of the inhibitor at which 50% inhibition (IC_{50}) of the enzymatic activity is achieved in a biochemical assay. If sufficient time is given to react, covalent inhibitors can completely inactivate the targeted protein as opposed to traditional reversible inhibitors. Therefore, considering the rate of inactivation of a target (k_{inact} , see Figure 3) will better represent the potencies of the covalent inhibitors rather than the time-dependent IC_{50} s. Hence, the k_{inact}/K_i ratio is generally preferred over IC_{50} in the assessment of potency, selectivity, and structure-activity relationship (SAR) for the covalent irreversible inhibitors.²⁹

Achieving desirable potency and selectivity in a drug is challenging. Numerous examples of clinically approved covalent drugs show that with optimized covalent inhibitors, high selectivity along with improved biochemical efficiency can be achieved.²¹ Moreover, covalent inhibitors provide a range of advantages, including a reduced chance of drug resistance where a noncatalytic amino acid is targeted, less frequent dosing related to the extent and duration of the resulting pharmacological effect, and the ability of the covalent inhibitors to access shallow binding sites. Once the target protein is inactivated by the covalent inhibitor and if the kinetic half-life of the covalent adduct is higher than the re-synthesis of the target protein, regaining the activity of the protein via a feedback

mechanism is hard to achieve. Thus, covalent inhibitors can provide excellent antibiotics and anticancer drugs.²³

Cyclobutanones as Covalent Inhibitors

Diseases that involve inappropriate proteolytic activity may be treated by selectively inhibiting the implicated protease enzyme,³⁰ for which cyclobutanones offer a compact scaffold with the opportunity to form a covalently bound but reversible hemiacetal enzyme-inhibitor adducts with active-site nucleophilic residues, such as the catalytic serine residue in a serine hydrolase, or the reversible formation of a hydrated inhibitor-enzyme adduct bound to the active site metal center of most metallohydrolases. In both mechanisms of inhibition, formation of a transition state mimetic enzyme-inhibitor complex is enabled by the strain inherent in the four-membered cyclobutanone ring as illustrated in Scheme 1.^{31, 32}



Scheme 1. *N*-Functionalized cyclobutanones as inhibitors of serine hydrolases and proteases and metalloenzymes.^{31, 32}

Cyclobutanones are a bioisostere of the β -lactam ring, and cyclobutanone analogs of β -lactams were explored as potential β -lactamase inhibitors and antibiotics in the early 1980s. In 1983, Gordon Lowe and coworkers proposed that cyclobutanone analogs of β -lactams generated by replacing the nitrogen atom that is pyramidal due to the ring fusion in penicillins and cephalosporins, with an sp^3 hybridized carbon and further hypothesized that cyclobutanone analogs of β -lactams should be stereochemically compatible with the active site of the transpeptidases and D,D-carboxypeptidases that are key enzymes in bacterial cell wall biosynthesis^{33,34} (see Figure 4).

β -Lactams are classified based on the ring system fused to the core four-membered cyclic amide. Most common clinically administered β -lactam antibiotics (cephalosporins, penicillins, and carbapenems) have an additional five- or six-membered ring with the β -lactam scaffold (see Figure 4). The monobactams, unlike the other bicyclic β -lactams, have a monocyclic moiety, and currently, the only commercially available monobactam antibiotic is aztreonam.³⁵

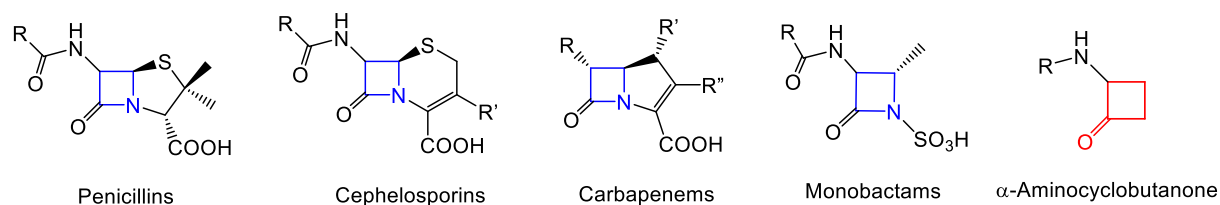


Figure 4. Core structures of clinically used antibiotics with β -lactam ring shown in blue and a general cyclobutanone analog of monobactam with cyclobutanone shown in red where the nitrogen atom of the β -lactam ring is replaced with a methylene (CH_2) group.

Cyclobutanone analogs of β -lactams were explored as β -lactamase inhibitors in the early 1980s, uncovering modest inhibition of R-TEM-2 β -lactamase, Bcl β -lactamase, and R61 transpeptidase (penicillin binding protein).^{34, 36-38} Oligopeptide cyclobutanones were shown to inhibit the serine protease elastase.³⁹ In 2007, Rutledge and coworkers reported cyclobutanone analogs as mechanistic probes targeting isopenicillin N synthase.⁴⁰ Strynadka and Dmitrienko reported cyclobutanone inhibitors of serine- and metallo- β -lactamases including an X-ray crystal structure of a cyclobutanone covalently bound to a class D β -lactamase OXA-10 as a serine hemiketal.³¹ More recently, Abboud and Dmitrienko published an X-ray crystal structure of a class B metallo- β -lactamase, SPM-1, with a hydrated cyclobutanone coordinated to the di-zinc metal center (see Figure 5A and 5B).³² We have reported the X-ray crystal structure of the 2-allyl benzenesulfonamide cyclobutanone covalently bound to an esterase from *Francisella tularensis* (Figure 5C).⁴¹ For serine and cysteine proteases, cyclobutanone derivatives can function as covalent yet reversible inhibitors through the formation of a hemiketal adduct with the active site serine or cysteine residue, respectively, analogous to the mode of action of medicinally useful trifluoromethyl ketone protease inhibitors⁴² and alpha-ketoamide protease inhibitors.⁴³

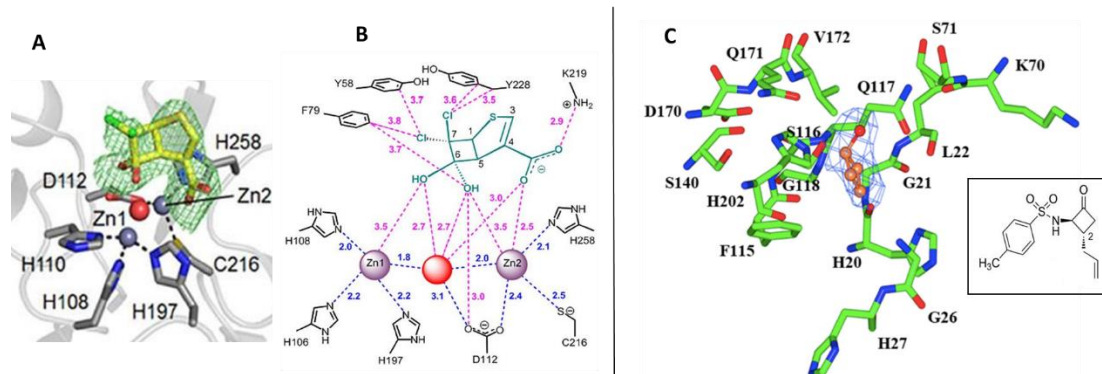


Figure 5. Binding mode of β -lactam analog of cyclobutanone to metallo- β -lactamase SPM-1 as observed in crystallography. (A) Cyclobutanone analog (yellow) bound to the SPM-1 active site. (B) Interactions of cyclobutanone analog with SPM-1. Distances between the cyclobutanone (cyan) and the SPM-1 active site are in magenta. Distances between active site atoms are in blue. The red sphere represents the bridging water molecule or hydroxide. Distances are given in Å.³² (C) Open cyclobutanone inhibitor-bound carboxylesterase (FTT258) binding pocket is shown. The inhibitor is shown (brown) as a ball and stick model. The chemical structure of the cyclobutanone analog is highlighted in the box.⁴¹

Synthetic Strategies in the Preparation of *N*-Functionalized 2-Aminocyclobutanones

Background and Previous Work

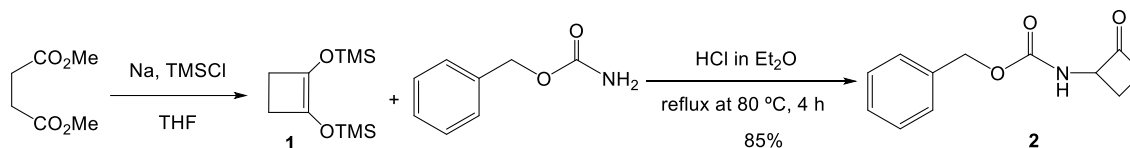
Cyclobutanones are crucial synthetic intermediates and target compounds with useful applications in medicinal chemistry, as discussed previously. Even though cyclobutanones are molecular scaffolds with high potential, comparatively few methods to prepare simple 2-aminocyclobutanones and multi-substituted complex cyclobutanone analogs are found in the literature.⁴⁴

Most of the methods published in the synthesis of cyclobutanone analogs of monobactams had included an aminoacyl functional group at the respective position on the monocyclic cyclobutanone⁴⁴ to mimic the functionalities of β -lactam antibiotics (see Figure

4). Ghosez and coworkers reported the synthesis of a set of substituted enantiopure 2-aminocyclobutanone analogs as well as a range of corresponding cyclobutanol precursors. In this work, the cyclobutanone ring was formed via [2+2] cycloaddition between a ketene and an oxazoline yielding a bicyclic cyclobutanone intermediate and the acid catalyzed ring opening reaction of oxazoline provided the 2-aminocyclobutanol precursor which then oxidized to give the final monocyclic cyclobutanone analog.⁴⁵ Utilizing trans-2-aminocyclobutanol as the cyclobutanone precursor, Reid and coworkers prepared 2-aminoacyl monocyclic cyclobutanones. Through a sequence of peptide coupling reactions, oligopeptide-functionalized cyclobutanols are generated, which are then oxidized to the corresponding cyclobutanones.³⁹ Both methods mentioned above, among several other reported synthetic routes, access the cyclobutanone ring via the oxidation of a cyclobutanol precursor.

A number of research groups including our lab have worked on developing novel synthetic routes to prepare the monocyclic *N*-functionalized 2-aminocyclobutanones where the alpha position can be readily functionalized to provide multi-substituted 2-aminocyclobutanone analogs. In addition, we envisioned protected 2-aminocyclobutanones as an intermediate to afford peptidomimetic cyclobutanones. Vederas and coworkers synthesized the racemic benzyl carbamate (Cbz) protected 2-aminocyclobutanone (**2**) by reacting 1,2-bis(trimethylsilyloxy)cyclobutene (**1**) with benzyl carbamate in the presence of HCl in ether.⁴⁶ The cyclobutene intermediate was prepared via acyloin condensation of dimethyl succinate with chlorotrimethylsilane in molten sodium (Scheme 2).⁴⁷

In order to synthesize *N*-alkylated 2-aminocyclobutanones and derivatives with various *N*-protecting groups, our lab extended Vederas's approach by using a diverse set of nitrogen nucleophiles including carbamates, amides, sulfonamides, and anilines instead of benzyl carbamate to make a series of racemic 2-aminocyclobutanone derivatives.¹³



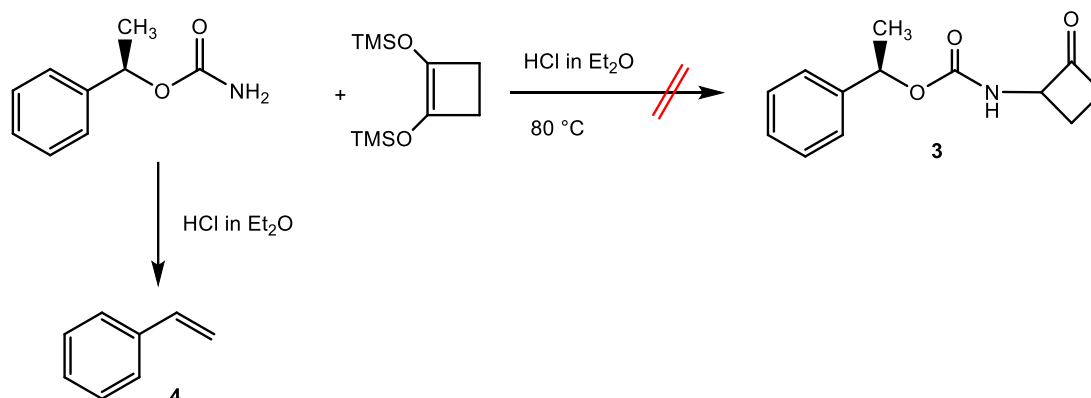
Scheme 2. Synthesis of benzyl (2-oxocyclobutyl) carbamate (**2**).^{13, 46}

Attempted Synthetic Methods to Make Enantiopure 2-Aminocyclobutanone

The synthesis of the enantiomerically pure 2-aminocyclobutanone synthon was a goal, specifically in preparing chiral peptidomimetic *N*-functionalized 2-aminocyclobutanones. Previously, in our lab, Dr. Cory Reidl attempted the synthesis of (*R*)-1-phenylethyl (2-oxocyclobutyl) carbamate (**3**) from (*R*)-1-phenylethyl carbamate and 1,2-bis(trimethylsilyloxy)cyclobutene (**1**) where a range of acid catalysts including hydrogen chloride and ferric-based Lewis acids were investigated. His effort to synthesize and separate the diastereomers of (*R*)-1-phenylethyl (2-oxocyclobutyl)carbamate (**3**) followed by deprotection of Cbz group in order to achieve enantiopure 2-aminocyclobutanone was not successful due to the acid catalyzed elimination reaction of carbamate **3** to vinylbenzene (**4**, see Scheme 3).

We sought to synthesize and isolate enantiopure Cbz-2-aminocyclobutanone, which could serve as a chiral intermediate in preparing the enantiomerically pure modular scaffold 2-aminocyclobutanone. We identified the racemic benzyl (2-oxocyclobutyl)

carbamate (**2**) as the desired protected 2-aminocyclobutanone from our library mentioned above, owing to the ease of removal of benzyl carbamate by hydrogenolysis. We investigated classical resolution techniques as well as more challenging enzymatic kinetic resolution methods in resolving the two enantiomers of 2-aminocyclobutanone synthon.



Scheme 3. Attempted synthesis (*R*)-1-phenylethyl (2-oxocyclobutyl)carbamate (**3**) and acid catalyzed elimination reaction producing ethenylbenzene (**4**).

Enzymatic Dynamic Kinetic Resolution

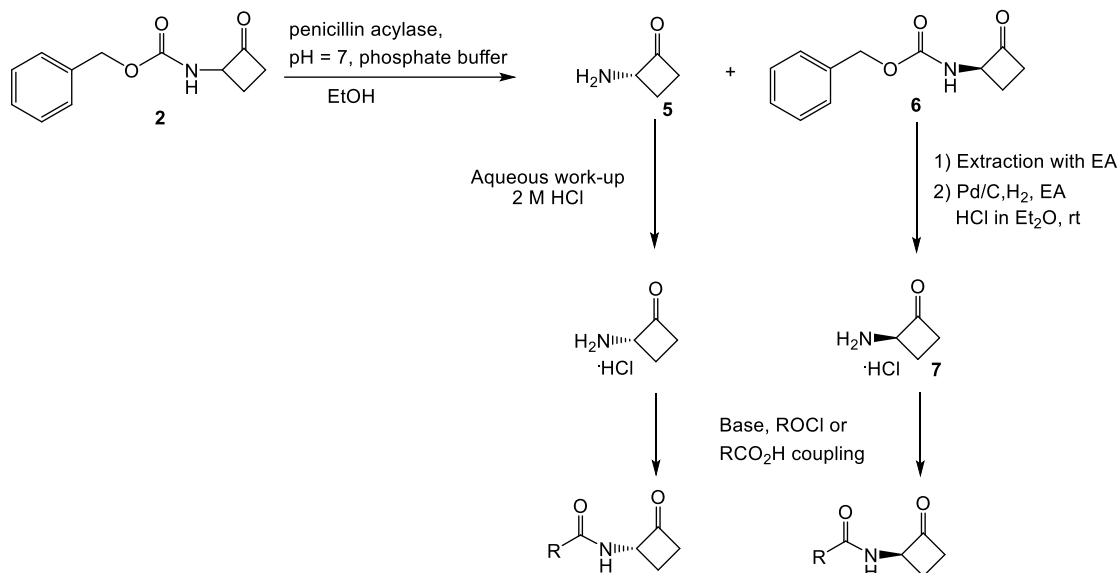
Enzymes as biocatalysts often possess high stereo-, substrate-, and regio-specificities under mild reaction conditions and are, therefore, considered to be attractive alternatives to conventional chemical methods in kinetic resolution and dynamic kinetic resolution. Furthermore, synthesis employing the enzymes are more environmentally friendly and cost effective compared to classical organic synthesis.⁴⁸

A kinetic resolution (KR) is defined as a process where the two enantiomers of a racemate are converted to products at different rates. If the kinetic resolution is efficient, one of the enantiomers of the racemic mixture reacts to form the desired product while the other enantiomer remains unreacted. One major disadvantage of KR is having a maximum

theoretical yield of 50%, and the remaining 50% will be discarded or recovered. Classical kinetic resolution has been advanced to include dynamic kinetic resolution (DKR) in order to obtain a quantitative yield of one of the enantiomers. Effectively, DKR combines the resolution step of the kinetic resolution with an *in-situ* equilibration or racemization of the chirally labile substrate. Racemization of the substrate can be performed chemically, biocatalytically, or even spontaneously.⁴⁹ The DKR transformations could be done either chemically (non-enzymatic) or bio-catalytically (enzymatic). The catalyst can selectively lower the transition state energy of a single enantiomer, leading to almost 100% yield of the kinetically favored reaction pathway over the other.

We attempted enzymatic hydrolysis of the Cbz group of the benzyl(2-oxocyclobutyl) carbamate (**2**) using commercially available penicillin amidase/penicillin acylase from *Escherichia coli*, which is a highly efficient enzyme employed in the industrial-scale hydrolysis of penicillin to 6-aminopenicillanic acid (6-APA).⁵⁰ Penicillin acylases selectively react with the S-isomer or L-amino acids and have been shown to efficiently resolve racemic mixtures of chiral compounds including amino acids and β -amino esters.⁵¹

Acylases, esterases, and proteases from various organisms including bacterial, bovine, and human erythrocytes, are shown to be utilized in carbamate hydrolysis.^{52, 53} Through the enzymatic resolution, we hoped to isolate the (*S*)-2-amiocyclobutanone (**5**) as well as the unreacted benzyl (*R*)-(2-oxocyclobutyl) carbamate (**6**), the Cbz group of which can be removed via hydrogenolysis to give the (*R*)-2-amiocyclobutanone (**7**, see Scheme 4).



Scheme 4. Attempted enzymatic resolution of racemic benzyl(2-oxocyclobutyl) carbamate (**2**).

Result and Discussion

The enzymatic reaction of benzyl(2-oxocyclobutyl) carbamate (**2**) was performed by dissolving compound **2** in a solution of ethanol buffered to pH 7 using phosphate buffer followed by the addition of penicillin acylase to the mixture. The hydrophobic compound **2** was only partially dissolved in ethanol, and it formed an unexpected and uncharacterized residue with 1M phosphate buffer. Ethanol or other water-soluble short chain alcohols have a lower inhibitory effect on the enzymatic activity and are used as a co-solvent for the reactions of penicillin acylase in aqueous medium.⁵¹

The enzymatic reaction was performed by stirring the reaction mixture at room temperature (RT) for 4 hours. The high-performance liquid chromatography (HPLC) data suggested the consumption of benzyl(2-oxocyclobutyl)carbamate (**2**) based on the ultra-

violet (UV) absorption at both 254 and 220 nm and toluene was identified and confirmed as the by-product of the enzymatic hydrolysis of benzyl carbamate protecting group. Since the desired product, 2-amincyclobutanone, lacks a chromophore we had to rely on thin-layer chromatography (TLC) to detect the formation of the primary amine product.

Once the reaction was complete, acetonitrile (ACN) was added to denature the enzyme and the inactivated enzyme was filtered off. After the removal of the solvent under reduced pressure, 2 M HCl was added to the aqueous solution until the pH reached to 3. In an acidic solution the newly formed amine of the desired product (**5**) is protonated and will be isolated as the hydrochloride salt of the amine (see Scheme 4). The enzymatic reaction was run with 12% and 9% ethanol to optimize the solubility of racemic compound **2** and the unhydrolyzed isomer of compound **2**, and during both trials, the cloudiness and a precipitate formed in the reaction made the purification very challenging. The solid adduct formed in the reaction could not be isolated and characterized.

We hypothesize that the formation of a salt-like precipitate is due to the high concentration of the phosphate buffer. Enzyme-catalyzed resolution of benzyl(2-oxocyclobutyl)carbamate (**2**) might be achieved by further optimization of the buffer identity and concentration as well as screening various organic co-solvents. Even though the starting material compound **2** was consumed in the enzyme catalyzed hydrolysis reaction, we faced several challenges in the purification of the water-soluble HCl salt of the amine product **5**. Enzymes as biocatalysts have many appealing features including stereospecificity, activity at moderate temperatures and atmospheric pressure, and

allowing the reaction to proceed in aqueous solution. However, there are shortcomings associated with biocatalysts due to the higher sensitivity to elevated temperatures and pressures and most enzymes are denatured by even relatively small amounts of organic solvents. Owing to the above-mentioned challenges and restrictions, we decided not to further pursue the enzymatic resolution route.

A New Synthetic Route to Make Protected 2-Aminocyclobutanone as a Modular Transition State Synthon

Furthering our interest in cyclobutanones as enzyme inhibitors^{13, 41} we envisioned a modular 2-aminocyclobutanone synthon that could be functionalized in a single step to provide a variety of derivatives including α -benzamide-, α -thiourea-, α -urea, and α -sulfonamide-cyclobutanones with potential activity against serine and metallo β -lactamases, di-zinc enzymes, and serine proteases.

Our efforts in synthesizing chiral 2-aminocyclobutanones utilizing a range of asymmetric synthesis methods including enzymatic resolution were not successful. As a result, we aimed to develop a new synthetic route to make racemic 2-aminocyclobutanone as a shelf-stable amine salt. This modular aminocyclobutanone is a useful intermediate in synthesizing peptidomimetic *N*-functionalized 2-aminocyclobutanones.

The hydrogenolysis and the acidolysis approaches were attempted in parallel to achieve the deprotection of the Cbz moiety. A neat acidolysis reaction of benzyl(2-oxocyclobutyl)carbamate was carried out using hydrobromic acid in acetic acid. The

acidolysis was unsuccessful, presumably due to the instability of the cyclobutanone ring under the strong acidic and reducing environment.

Optimization of the Hydrogenolysis Reaction Conditions

The traditional palladium (Pd/C) catalyzed hydrogenolysis was investigated to remove the benzyl carbamate group of the racemic benzyl(2-oxocyclobutyl)carbamate under acidic medium in the synthesis of the aminocyclobutanone hydrochloride salt. As the product of hydrogenolysis is an aminoketone, it is important to remove the benzyl carbamate group in the presence of an acid to form the salt of the amine directly to prevent the polymerization through imine formation and the subsequent reductive amination of the polymeric imine.

The most common solvents used in the Pd/C catalyzed hydrogenolysis, including ethyl acetate, ethanol, methanol, ethyl acetate/ethanol, and the less frequently utilized solvent dichloromethane, were screened at room temperature in the presence of HCl in diethyl ether. The acid lability of the ethyl acetate (EA) led us to choose methanol as our preferred solvent for the hydrogenolysis reaction. Thus, the acetalization of the aminocyclobutanone ketone was taken into account in designing the route. An acetal is formed through a condensation reaction of an aldehyde or a ketone with a large excess of an alcohol in the presence of a trace amount of strong acid. The equilibrium favoring the acetal is driven to the right either by the use of excess alcohol as the solvent or by removal of the water by-product, or both. Taking advantage of the reversibility of the reaction, we

decided to generate dimethyl acetal protected 2-aminocyclobutanone (**9**) as a precursor, which will be hydrolyzed in the subsequent synthetic steps revealing the cyclobutanone.

With the thermally and chemically labile cyclobutanone, and also under a hydrogen gas saturated closed vessel in which the hydrogenolysis reaction was performed, the removal of water as an azeotrope was not viable. Therefore, We investigated trimethyl orthoformate, 3Å molecular sieves,⁵⁴ and a solid-phase acid catalyst—mordenite molecular sieves as dehydrants suspended in the reaction mixture to selectively remove water at room temperature (see Table 1). We observed that trimethyl orthoformate reproducibly afforded complete conversion of the ketone to the acetal under reproducible and scalable conditions (Entry 5, see Table 1).

Table 1. Dehydrants Screening for the Hydrogenolysis and Acetalization of 2-aminocyclobutanone^(a)

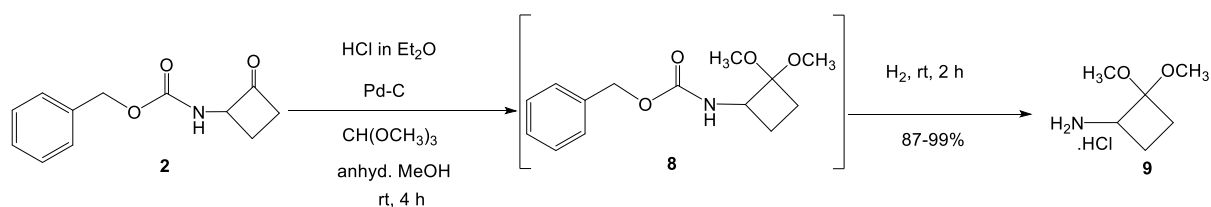
Exp	Dehydrant	Amount of dehydrant (mg)	2.0 M HCl	Time (min)	% Conversion ^(b)
1	3 Å Molecular sieves	250	1.1 eq	120	27
2	Mordenite molecular sieves	30	1.0 eq	120	84
3	Trimethyl orthoformate	19	1.1 eq	120	41
4	Trimethyl orthoformate	30	1.1 eq	120	69
5	Trimethyl orthoformate	119	1.1 eq	240	100

^(a)Reaction conditions: Cbz-cyclobutanone (30 mg, 1 eq, 0.14 mmol), 10% Pd-C (20mg/mmol) at 20-25 °C.

^(b)Determined by NMR.

With the optimized conditions, we designed this route to be a two-step one-pot reaction. First, the Cbz-cyclobutanone (**2**) was converted to the dimethyl acetal of Cbz-cyclobutanone (**8**), and the formation of the acetal intermediate was confirmed by HPLC

and TLC based on comparison with an authentic sample. The completion of the acetal formation was achieved by adding the trimethyl orthoformate in one-hour intervals to the reaction mixture. The use of hydrogen chloride in diethyl ether catalyzes the acetal formation and further enables the product 2,2-dimethylcyclobutanamine to be isolated in 87 to 96% yield as the hydrochloride salt (**9**) in a single-pot acetalization and deprotection of Cbz-2-aminocyclobutanone. HPLC and TLC indicated that the acetalization proceeds first to carbamate **2** based on comparison with an authentic sample, which then undergoes hydrogenolysis to yield the amine salt **9** (see Scheme 5).⁵⁵

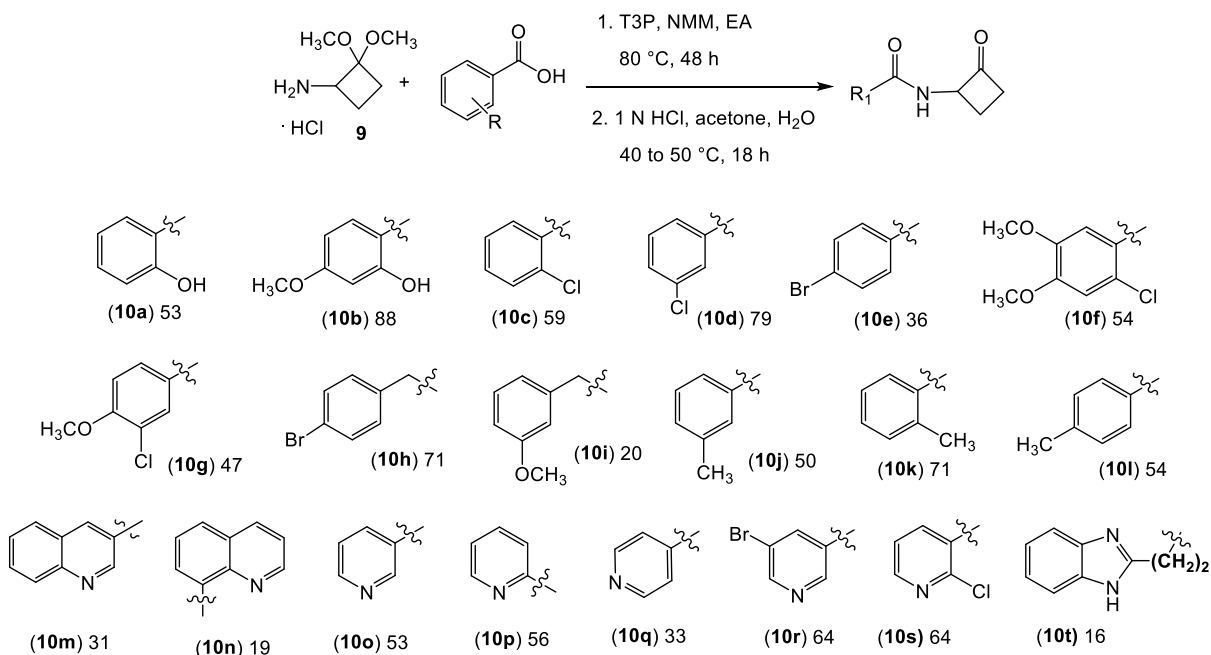


Scheme 5. Synthesis of 2,2-dimethoxycyclobutan-1-amine hydrochloride (**9**) via one-pot acetalization/debenzylation from carbamate **2**.

Preparation of *N*-Functionalized 2-Aminocyclobutanone Library

With the 2,2-dimethoxycyclobutan-1-amine salt (**9**) in hand, we proceeded to synthesize a library of *N*-functionalized 2-aminocyclobutanones which included α -benzamide (**10a-t**, see Scheme 6) and α -sulfonamide-functionalized cyclobutanones (see Scheme 7). In preparation of 2-aminocyclobutanones analogs, compound **9** was coupled with a series of substituted benzoic acids, pyridinecarboxylic acids, and quinoline carboxylic acids followed by the acid-catalyzed hydrolysis of the corresponding acetal, and the final products were isolated in moderate to good yields. In our published method⁵⁵ for

the synthesis of compound **9**, we utilized 1-ethyl-3-(3-dimethylaminopropyl)carbodiimide hydrochloride (EDCI), and hydroxybenzotriazole (HOBt), a set of reagents commonly used in peptide synthesis and the reaction was performed in anhydrous dimethylformamide (DMF).

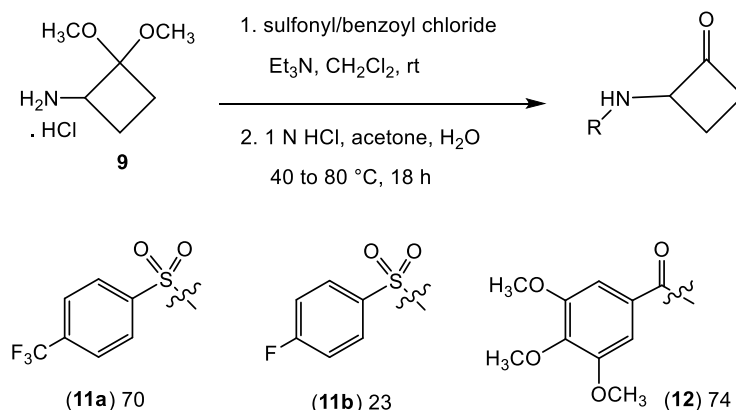


Scheme 6. Synthesis of cyclobutanone analogs from compound **9** and aromatic carboxylic acids via T3P coupling/hydrolysis reactions.

Coupling reactions performed in DMF were low yielding, and a significant effort was required (e.g., increased number of water washes during the workup) to remove the high boiling solvent from the acetal intermediate prior to the hydrolysis reaction. Moreover, we replaced EDCI/HOBt with propylphosphonic anhydride (T3P), which is a reactive cyclic anhydride of phosphoric acid and is a mild and low toxic coupling agent used in peptide synthesis. The formation of water-soluble by-products from the T3P coupling reaction makes the purification straightforward, and in most cases, column chromatography could

be avoided. Therefore, ethyl acetate was selected as the preferred solvent for the coupling reactions of compound **9** with aromatic carboxylic acids (see Scheme 6).

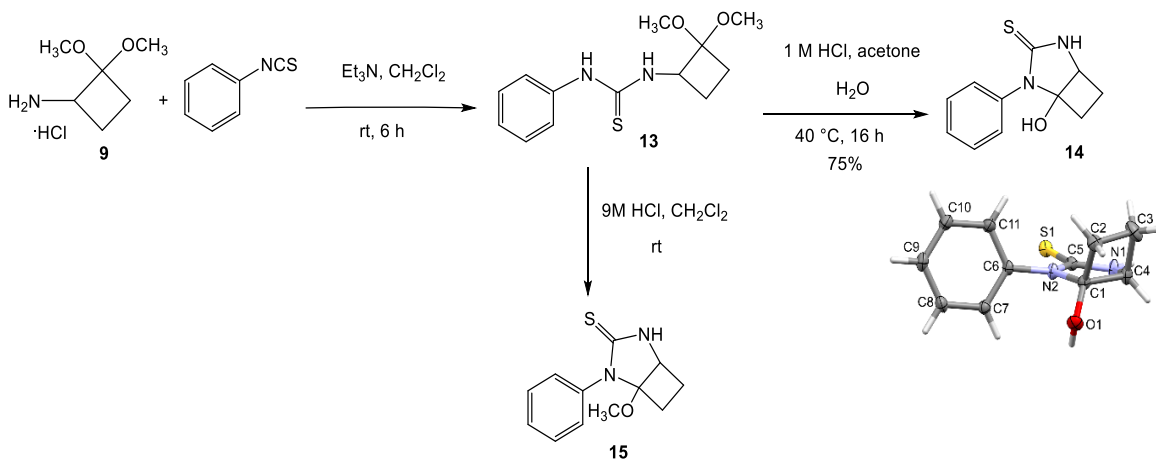
Extending the substrate scope, several sulfonyl chlorides and benzoyl chlorides were reacted with compound **9** in a base mediated coupling reaction in the presence of triethylamine (Et₃N), and the resulting acetal intermediates were subjected to acid-catalyzed hydrolysis to afford the α -sulfonamide (**11a-b**) and α -benzamide cyclobutanones (**12**) as shown in Scheme 7.



Scheme 7. Synthesis of α -sulfonamide (**11**) and α -benzamide cyclobutanones (**12**) from compound **9** via base catalyzed coupling/hydrolysis reactions.

The pivotal intermediate 2,2-dimethoxycyclobutan-1-amine hydrochloride (**9**) was also reacted with phenyl isothiocyanate with the expectation of obtaining the corresponding thiourea. Hydrolysis of the thiourea-acetal (**13**) under the general hydrolysis conditions (1 N HCl, acetone, H₂O, 40 °C), this reaction, provided the bicyclic thiourea **14** in 75% yield rather than the expected cyclobutanone-functionalized thiourea via an intramolecular nucleophilic attack by the thiourea nitrogen. The structure of **14** was confirmed by single crystal X-ray crystallography (Scheme 8). In order to screen solvents

and reaction temperatures for the acetal hydrolysis, thiourea-acetal (**13**) was stirred with 9 M HCl for 24 h at room temperature, and the methoxy-bicyclic thione **15** was formed where the thiourea nitrogen attacked the acetal carbon eliminating methanol and the hydroxy-bicyclic thione **14** was also observed along with other by-products (see Scheme 8). The structure of the methoxy-bicyclic thione **15** was confirmed by NMR and by high resolution mass spectrometry ((ESI): calculated for: (MH⁺) C₁₂H₁₅N₂O₃: 235.0900, Observed: 235.0899).



Scheme 8. Synthesis of bicyclic thiourea **14** from compound **9** via acetal **13** and the ORTEP structure of **14**.

Furthermore, a set of peptidomimetic cyclobutanones analogs was synthesized driven by computer-aided drug design to inhibit the SARS-CoV-2 target enzymes. Details of the *in silico* lead identification, syntheses, and biological testing data of peptidomimetic cyclobutanone analogs will be discussed in Chapter Three.

Solvent Dependency of Hydration Equilibria of

N-Functionalized 2-Aminocyclobutanones

Carbonyl groups establish an equilibrium with the corresponding hydrate formed via hydration reaction in water or in an organic solvent that contains residual water. Equilibrium kinetics and the stability of a hydrate in solution are determined by electronic and steric factors of the carbonyl group. In many cases, hydration of the carbonyl carbon results in an unstable hydrate that exists in a rapid equilibrium with the carbonyl group in solution. In an aqueous solution, aldehydes form about 60% of the hydrate at equilibrium, while ketones are less than 1% hydrated in solution because the electron donating alkyl groups stabilize the partial positive charge on the carbonyl carbon. In contrast, the addition of electron withdrawing groups destabilizes the carbonyl resulting in a comparatively stable hydrate.⁵⁶ Cyclobutanones are shown to form a moderately stable hydrate via a rapid equilibrium with the carbonyl enabled by the inherent strain of the ring that makes the ketone carbonyl more electrophilic than an unstrained ketone.⁵⁷

During the purity analysis of the several aminocyclobutanone analogs using reverse phase HPLC dissolved in ACN, an overlapping peak integrating to less than 5% was observed with the main compound peak. Initially, we surmised that this peak was due to an impurity present in the compound. However, using proton and carbon NMRs obtained in deuterated chloroform (CDCl₃) with less than 1% residual water, the purity of the above-mentioned cyclobutanones assessed to be higher than 95%. Based on the NMR purity, we hypothesize that the overlapping peak observed in the HPLC chromatogram is the hydrate

of cyclobutanone formed during the HPLC run since the mobile phase consists of water and ACN. HPLC chromatogram highlighting the overlapping peak and the proton NMR of compound **12** are shown in Figure 6.

Conclusion

We have developed a synthetic route to prepare the modular 2-aminocyclobutanone synthon **9** as a shelf-stable HCl salt. A library of *N*-functionalized 2-aminocyclobutanones of α -benzamide and α -sulfonamide-functionalized cyclobutanones have been prepared from aminocyclobutanone acetal **9** to demonstrate the synthetic compatibility of this synthon with a range of electrophiles including aryl carboxylic acids, pyridinecarboxylic acids, and sulfonyl chlorides under coupling conditions. We believe that the aminocyclobutanone building block **9** will find utility in lead development of inhibitors for serine and metallo proteases and for esterases. We have further shown that the unusual 1-hydroxy-2,4-diazabicyclo[3.2.0]heptane-3-thione bicyclic adduct was obtained *via* the reaction of **9** with phenyl isothiocyanate as confirmed by single crystal X-ray structure of bicyclic thiourea **14**.

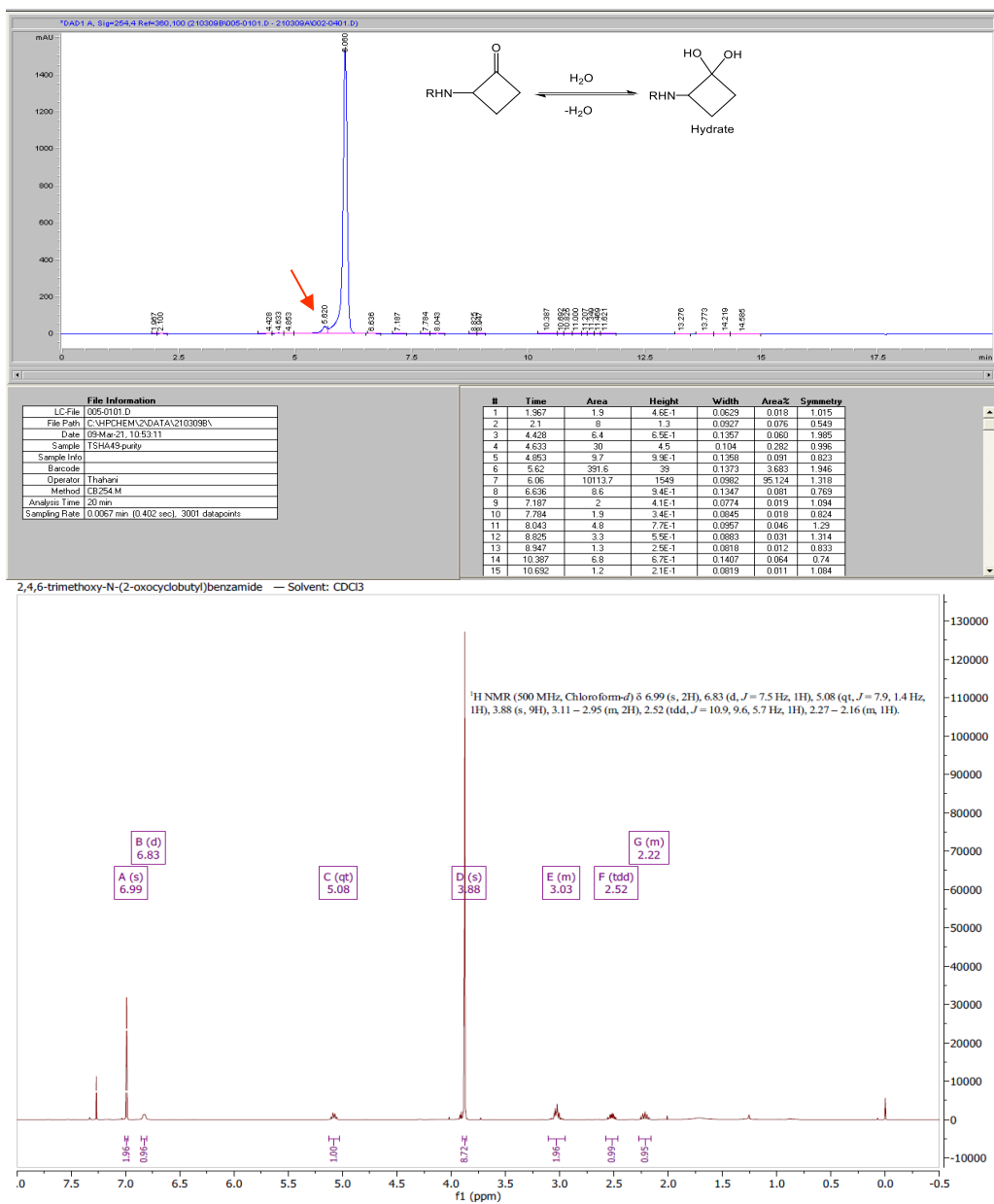


Figure 6. (A) HPLC and (B) proton NMR of compound **12** highlighting the shoulder peak of potential hydrate and absence of hydrate peaks in the NMR.

Experimental

Methods and Materials

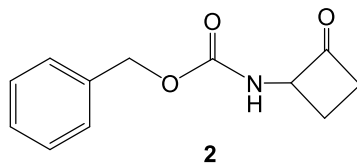
All solvents were distilled prior to use or purchased as anhydrous grade and all reagents were used without further purification unless otherwise noted. Molecular sieves were activated at 300-350 °C under vacuum unless stated otherwise. Penicillin acylase from *Escherichia coli* was purchased from Sigma-Aldrich. Propylphosphonic anhydride (T3P) was purchased from Sigma-Aldrich as ≥ 50 weight % concentrated solution in ethyl acetate. All synthetic reactions were conducted under an atmosphere of nitrogen. Silica gel 60 Å, 40–75 μm (200 \times 400 mesh) was used for column chromatography. Aluminum-backed silica gel 200 μm plates were used for TLC. ^1H NMR spectra were obtained using a 500 MHz spectrometer with tetramethylsilane (TMS) as the internal standard. ^{13}C NMR spectra were obtained using a 75 or 125 MHz spectrometer. The purity of all compounds was determined to be $\geq 95\%$ unless otherwise noted by high performance liquid chromatography (HPLC) employing a mobile phase A = 5% acetonitrile B in water and a mobile phase B = 0.1% TFA in acetonitrile with a gradient of 60% B increasing to 95% over 10 min, holding at 95% B for 5 min, then returning to 60% B and holding for 5 min. HRMS spectra were measured on a TOF instrument by electrospray ionization (ESI). HRMS spectra were collected using a Waters Acquity I class UPLC and Xevo G2-XS QToF mass spectrometer with Waters Acquity BEH C18 column (1.7 μm , 2.1 \times 50 mm). Single crystal XRD data for **14** were collected on a Bruker Quest X-ray diffractometer at 150 K. Complete crystallographic data, in CIF format, have been deposited with the Cambridge

Crystallographic Data Centre. CCDC Deposition Number 1966012 contains the supplementary crystallographic data. These data can be obtained free of charge from The Cambridge Crystallographic Data Centre via www.ccdc.cam.ac.uk/data_request/cif.

Attempted Enzymatic Hydrolysis of Benzyl(2-oxocyclobutyl)carbamate (2)

Penicillin acylase (76427 Sigma, 5-10 units/mg protein) from *Escherichia coli* (10.0 mg) was added to a pH 7 solution of the carbamate **2** (165 mg, 0.75 mmol) in 1 M phosphate buffer (5 mL) and ethanol (0.7 mL, 12 v/v %). The reaction mixture was allowed to stir at room temperature for 4 hours until the consumption of carbamate **2** as determined by HPLC. Then, acetonitrile was added to denature the enzyme, and the residue formed was removed by filtration. The cloudiness formed during the reaction persisted even after the addition of acetonitrile. The reaction mixture was concentrated by removing the solvent under reduced pressure, and 2 M HCl was added to the aqueous solution until the pH was reduced to 3. The cloudiness of the reaction mixture and the formation of an emulsion complicated the extraction of the products. Thus, the enzymatic reaction was not pursued further.

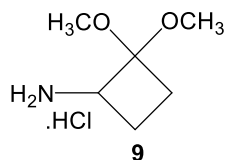
Benzyl(2-oxocyclobutyl)carbamate (2)



Following the method reported by Vederas,⁴⁶ under an atmosphere of argon, commercially available 1,2-bis(trimethylsilyloxy)cyclobutene (3.5 g, 15 mmol) was added dropwise to a stirring solution of *N*-benzyl carbamate (2.067 g, 13.68 mmol) in 1 M HCl

solution in diethyl ether (27 mL) at 0 °C for 5 min. The reaction was allowed to reflux for 4 hours at 80 °C. Upon completion, the reaction mixture was concentrated under reduced pressure providing the crude product as a yellow oil. Purification of the crude mixture was performed on a Teledyne Isco Rf Flash chromatography unit eluting with Et₂O/hexane (50/50) to afford Cbz-cyclobutanone **2** (2.83 g, 94.6%) as a clear crystalline product: mp 51-54 °C. R_f = 0.2 (Pet. ether/ethyl ether = 50/50). Both proton and carbon NMR of the product matched the published characterization data.⁴⁶

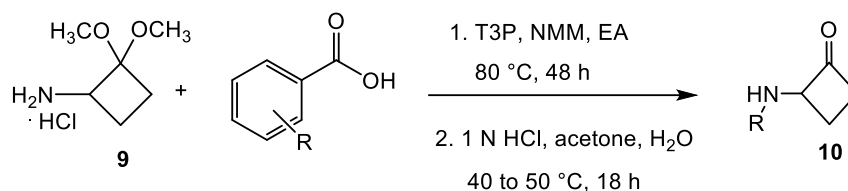
Synthesis of 2,2-dimethoxycyclobutan-1-aminium Chloride (9)



To a solution of benzyl(2-oxocyclobutyl)carbamate (448 mg, 2.04 mmol) in anhydrous MeOH (10.2 mL) was added 2.0 M HCl in diethyl ether (1.10 mL, 2.24 mmol) via syringe and vigorously stirred for 5 min under N₂. Trimethyl orthoformate (1.88 mL, 16.3 mmol) was added to the reaction mixture in four portions over 1 hour intervals as the reaction stirred at rt for 4 hours. The reaction progress was monitored by TLC (diethyl ether/hexane = 50/50) for consumption of the benzyl carbamate **2** whereupon Pd/C (10%, 20 mg/mmol) was added in a single portion to the reaction mixture. Alternatively, Pd/C may be added to the reaction mixture along with compound **2** in the beginning of the reaction, which affords comparable isolated yields of acetal hydrochloride **9**. Hydrogen was then introduced from a balloon, and the reaction was stirred at room temperature under an atmosphere of hydrogen until completion of the hydrogenolysis determined by TLC

(diethyl ether/hexane = 1/1) and HPLC. The catalyst was removed by filtration through a bed of Celite using MeOH as eluent. Concentration of the filtrate gave 2,2-dimethoxycyclobutan-1-aminium chloride (**9**) as a white crystalline solid (329 mg, 96.2%). ^1H NMR (500 MHz, D_2O) δ 3.77 (1H, t, $J=8.0$ Hz), 3.16 (3H, s), 3.11 (3H, s), 2.35 – 2.25 (1H, m), 2.15 – 2.04 (1H, m), 1.85 (1H, dt, $J= 3.1, 9.3$ Hz), 1.61 (1H, dddd, $J = 12.1, 10.5, 8.8, 7.2$ Hz). ^{13}C NMR 100.6, 50.6, 48.9, 48.5, 26.6, 17.6. MS (ESI) m/z (relative intensity): 167.21 (95.84), 168.18 (22.77). HRMS (ESI) calcd for $\text{MH}^+ \text{C}_6\text{H}_{13}\text{NO}_2$: 132.1025, found 132.1090, (M - OCH_3) 100.0756.

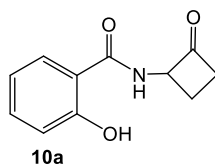
General Procedure for Alpha-Benzamide Cyclobutanones (**10a-10l**)



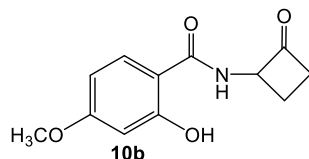
To a solution of substituted benzoic acid (1 eq, 0.249 mmol) and acetal **9** (1.2 eq, 0.298 mmol) in ethyl acetate (1.25 mL), *N*-methyl morpholine (5.0 eq, 1.24 mmol) was added. Then propylphosphonic anhydride (2.5 eq, 0.62 mmol) was added to the above mixture as a solution in ethyl acetate (purchased as ≥ 50 weight % in EA). The reaction mixture was stirred under N_2 at 80°C for 48 hours or until complete consumption of the benzoic acid determined by TLC (EA/hexane = 50/50 and ~ 3 to 4 drops of glacial acetic). The reaction was quenched by adding water (3 mL), then the organic product was extracted using ethyl acetate (3 x 3 mL). The combined organic layers were washed successively with water (3 x 3 mL) and 1N HCl (3 mL) and then dried over Na_2SO_4 . The solvent was removed by evaporation under reduced pressure providing the corresponding

acetal intermediate. Without further purification, crude acetal (1 eq) was subjected to hydrolysis conditions, wherein the crude mixture was dissolved in acetone (1.2 mL), water (0.17 mL, 10% v/v), and 1N HCl (0.34 mL, 30% v/v). Then the reaction mixture was stirred at 50°C for 18 hours with periodic TLC and HPLC monitoring. Upon completion, the organic product was extracted using ethyl acetate (3 x 3 mL) or methylene chloride for highly water-soluble analogs, and the combined organic layers were dried over Na₂SO₄. The solvent was evaporated under reduced pressure, and the crude mixture was purified by column chromatography to afford the corresponding alpha-benzamide cyclobutanone.

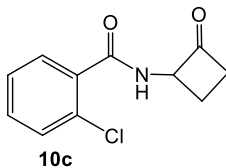
2-Hydroxy-N-(2-oxocyclobutyl)benzamide (10a)



The crude mixture of **10a** was purified by column chromatography using ethyl acetate/hexane (50/50) to afford cyclobutanone **10a** as a white crystalline solid (49.0 mg, 88%): mp 149-151°C. ¹H NMR (500 MHz, CDCl₃) δ 11.76 (OH, s, 1H), 7.40 – 7.28 (m, 1H), 7.28 (dd, *J* = 8.0, 1.6 Hz, 1H), 6.91 (dd, *J* = 8.4, 1.2 Hz, 1H), 6.88 – 6.73 (m, 2H), 5.10 – 5.01 (m, 1H), 3.05 – 2.92 (m, 2H), 2.55 – 2.43 (m, 1H), 2.12 (dtd, *J* = 11.1, 9.6, 8.2 Hz, 1H). ¹³C NMR (126 MHz, CDCl₃) δ 203.52, 168.59, 160.65, 133.78, 124.57, 117.82, 117.71, 112.32, 62.94, 41.37, 18.68.

2-Hydroxy-4-methoxy-N-(2-oxocyclobutyl)benzamide (10b)

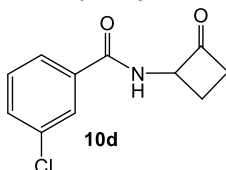
The crude product of **10b** was purified by column chromatography using ethyl acetate/hexane (50/50) to afford cyclobutanone **10b** as a white crystalline solid (38.4 mg, 88%): mp 131-133 °C. ¹H NMR (500 MHz, CDCl₃) δ 12.20 (s, 1H), 7.30 – 7.25 (m, 1H), 6.96 (NH, d, *J* = 7.7 Hz, 1H), 6.41 (d, *J* = 2.6 Hz, 1H), 6.37 (dd, *J* = 8.8, 2.6 Hz, 1H), 5.09 (dt, *J* = 9.9, 7.7 Hz, 1H), 3.79 (s, 3H), 3.01 (dd, *J* = 9.4, 7.8 Hz, 2H), 2.55 – 2.44 (m, 1H), 2.26 – 2.14 (m, 1H). ¹³C NMR (126 MHz, CDCl₃) δ 205.02, 169.47, 164.79, 164.02, 126.89, 107.27, 106.34, 101.58, 63.96, 55.47, 42.28, 19.79.

2-Chloro-N-(2-oxocyclobutyl)benzamide (10c)

The crude product of **10c** was purified by column chromatography on a Teledyne Isco Rf Flash chromatography unit eluting with ethyl acetate/hexane (40/60) to afford cyclobutanone **10c** as a white crystalline solid (32.5 mg, 59%): mp 102-103 °C. ¹H NMR (500 MHz, CDCl₃) δ 7.71 (dd, *J* = 7.6, 1.7 Hz, 1H), 7.45 – 7.35 (m, 2H), 7.33 (td, *J* = 7.3, 1.9 Hz, 1H), 6.81 (NH, d, *J* = 7.2 Hz, 1H), 5.16 (dt, *J* = 10.3, 7.9 Hz, 1H), 3.03 (dd, *J* = 9.6, 7.7 Hz, 2H), 2.57 (tt, *J* = 10.6, 7.2 Hz, 1H), 2.24 – 2.13 (m, 1H). ¹H NMR (500 MHz, CDCl₃) δ 7.76 – 7.70 (m, 1H), 7.46 – 7.35 (m, 2H), 7.35 (ddd, *J* = 7.5, 6.8, 1.8 Hz, 1H), 6.85 (d, *J* = 7.6 Hz, 1H), 5.23 – 5.14 (m, 1H), 3.10 – 3.01 (m, 2H), 2.64 – 2.53 (m, 1H), 2.20 (dtd, *J* = 11.0, 9.6, 8.2 Hz, 1H).

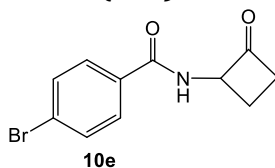
^{13}C NMR (126 MHz, CDCl_3) δ 204.41, 165.80, 133.50, 131.85, 130.80, 130.64, 130.37, 127.19, 64.53, 42.37, 19.69.

3-Chloro-N-(2-oxocyclobutyl)benzamide (10d)

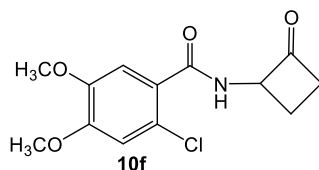


The crude product of **10d** was purified by column chromatography using ethyl acetate/hexane (50/50) to afford compound **10d** as a white solid (47.6 mg, 79%): mp 64-66 °C. ^1H NMR (500 MHz, CDCl_3) δ 7.77 (t, J = 1.9 Hz, 1H), 7.65 (dt, J = 7.7, 1.4 Hz, 1H), 7.50 (ddd, J = 8.0, 2.1, 1.0 Hz, 1H), 7.38 (t, J = 7.9 Hz, 1H), 6.82 (d, J = 7.1 Hz, 1H), 5.23 – 5.14 (m, 1H), 3.12 – 2.97 (m, 2H), 2.62 – 2.51 (m, 1H), 2.18 (dtd, J = 11.0, 9.6, 8.2 Hz, 1H). ^{13}C NMR (126 MHz, CDCl_3) δ 205.12, 165.61, 134.87, 132.04, 129.99, 127.52, 125.19, 64.51, 42.30, 19.74.

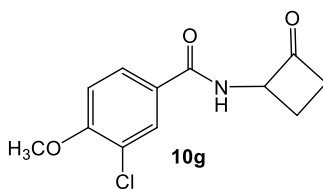
4-Bromo-N-(2-oxocyclobutyl)benzamide (10e)



The crude product of **10e** was purified by column chromatography on a Teledyne Isco Rf Flash chromatography unit eluting with ethyl acetate/hexane (30/70) to afford compound **10e** as a white crystalline solid (23.7 mg, 36%): mp 104-105 °C. ^1H NMR (500 MHz, CDCl_3) δ 7.69 – 7.61 (m, 2H), 7.58 (dd, J = 8.6, 2.0 Hz, 2H), 6.85 – 6.77 (NH, s, 1H), 5.15 (tdd, J = 9.6, 7.8, 1.4 Hz, 1H), 3.04 (ddd, J = 9.5, 7.8, 1.6 Hz, 2H), 2.55 (dtdd, J = 12.3, 9.7, 6.9, 2.1 Hz, 1H), 2.19 (dtd, J = 11.0, 9.6, 8.1 Hz, 1H). ^{13}C NMR (126 MHz, CDCl_3) δ 205.24, 165.94, 131.91, 128.71, 126.81, 64.53, 42.28, 19.72.

2-Chloro-4,5-dimethoxy-N-(2-oxocyclobutyl)benzamide (10f)

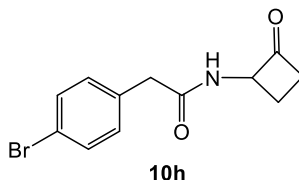
The crude product of **10f** was purified by column chromatography eluting with ethyl acetate/hexane (60/40) to afford **10f** as a white solid (38.2 mg, 54%): mp 123-125 °C. ^1H NMR (500 MHz, CDCl_3) δ 7.43 (s, 1H), 7.40 – 7.29 (m, 1H), 7.24 (NH, d, $J = 7.5$ Hz, 1H), 6.83 (s, 1H), 5.13 – 5.04 (m, 1H), 3.90 (d, $J = 4.6$ Hz, 6H), 3.14 – 2.85 (m, 2H), 2.59 – 2.42 (m, 1H), 2.24 (dddd, $J = 11.0, 10.1, 9.0, 8.0$ Hz, 1H). ^1H NMR (500 MHz, CDCl_3) δ 7.46 (s, 1H), 7.25 (d, $J = 7.6$ Hz, 1H), 6.85 (s, 1H), 5.10 (tdd, $J = 10.0, 7.1, 2.2$ Hz, 1H), 3.92 (d, $J = 4.4$ Hz, 6H), 3.15 – 3.05 (m, 1H), 3.08 – 2.98 (m, 1H), 2.55 (dtd, $J = 11.0, 10.1, 5.1$ Hz, 1H), 2.26 (dddd, $J = 11.1, 10.1, 9.1, 8.1$ Hz, 1H). ^{13}C NMR (126 MHz, CDCl_3) δ 204.75, 164.97, 151.52, 148.02, 124.15, 122.75, 113.63, 112.82, 64.78, 56.33, 56.23, 42.32, 19.59.

3-Chloro-4-methoxy-N-(2-oxocyclobutyl)benzamide (10g)

The crude product of **10g** was purified by column chromatography on a Teledyne Isco Rf Flash chromatography unit eluting with ethyl acetate/hexane (40/60) to afford compound **10g** as a white solid (29.5 mg, 47%): mp 134-136 °C. ^1H NMR (500 MHz, CDCl_3) δ 7.80 (d, $J = 2.2$ Hz, 1H), 7.70 – 7.65 (m, 1H), 6.94 (d, $J = 8.8$ Hz, 1H), 6.63 (d, $J = 7.4$ Hz, 1H), 5.18 – 5.09 (m, 1H), 3.95 (s, 3H), 3.06 – 2.99 (m, 2H), 2.54 (tt, $J = 10.5, 7.2$ Hz, 1H), 2.21 –

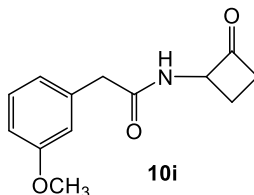
2.10 (m, 1H). ^1H NMR (500 MHz, CDCl_3) δ 7.80 (d, $J = 2.3$ Hz, 1H), 7.66 (dd, $J = 8.6, 2.3$ Hz, 1H), 6.97 (d, $J = 7.7$ Hz, 1H), 6.92 (d, $J = 8.6$ Hz, 1H), 5.12 (dt, $J = 9.8, 7.6$ Hz, 1H), 3.94 (s, 3H), 3.01 (dd, $J = 9.4, 7.8$ Hz, 2H), 2.57 – 2.46 (m, 1H), 2.20 (dtd, $J = 11.0, 9.5, 8.1$ Hz, 1H). ^{13}C NMR (126 MHz, CDCl_3) δ 206.00, 165.37, 157.83, 129.35, 127.29, 126.07, 122.65, 111.46, 64.53, 56.32, 42.17, 19.63.

2-(4-Bromophenyl)-N-(2-oxocyclobutyl)acetamide (10h)



The crude product of **10h** was purified by column chromatography using ethyl acetate/hexane (50/50) isocratic elution to afford compound **10h** as a white crystalline solid (49.7 mg, 71%): mp 124-127 °C. ^1H NMR (500 MHz, CDCl_3) δ 7.51 – 7.43 (m, 2H), 7.20 – 7.11 (m, 2H), 5.95 (d, 1H), 4.89 (dt, $J = 10.3, 8.0$ Hz, 1H), 3.53 (s, 2H), 3.02 – 2.86 (m, 2H), 2.40 (tt, $J = 10.5, 7.2$ Hz, 1H), 2.01 (dtd, $J = 11.1, 9.5, 8.0$ Hz, 1H). ^{13}C NMR (126 MHz, CDCl_3) δ 205.06, 169.96, 133.19, 132.15, 131.13, 121.58, 64.23, 42.36, 42.13, 19.54.

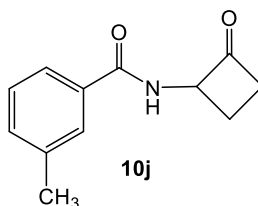
2-(3-Methoxyphenyl)-N-(2-oxocyclobutyl)acetamide (10i)



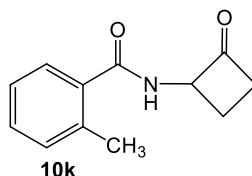
The crude product of **10i** was purified by column chromatography using ethyl acetate/hexane (40/60) where compound **10i** was isolated as an off-white crystalline solid (26 mg, 88% HPLC purity). Recrystallization of above-mentioned solid from hot ethyl

acetate afforded compound **10i** as white crystals (11.4 mg, 20%): mp 104-105 °C. ^1H NMR (500 MHz, CDCl_3) δ 7.27 (dd, $J = 8.3, 7.4$ Hz, 1H), 6.87 – 6.81 (m, 2H), 6.80 (t, $J = 2.1$ Hz, 1H), 5.94 (NH, d, $J = 7.4$ Hz, 1H), 4.86 (dtd, $J = 9.6, 7.4, 6.7, 1.2$ Hz, 1H), 3.81 (s, 3H), 3.56 (s, 2H), 2.99 – 2.84 (m, 2H), 2.44 – 2.33 (m, 1H), 2.02 (dtd, $J = 11.0, 9.6, 8.1$ Hz, 1H). ^{13}C NMR (126 MHz, CDCl_3) δ 205.15, 170.50, 160.09, 135.68, 130.18, 121.71, 115.04, 113.09, 64.23, 55.27, 43.22, 42.07, 19.51.

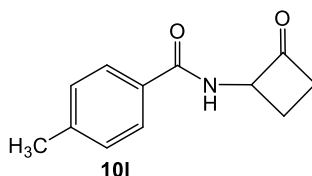
3-Methyl-N-(2-oxocyclobutyl)benzamide (10j)



The crude product of **10j** was purified by column chromatography on a Teledyne Isco Rf Flash chromatography unit eluting with ethyl acetate/hexane (20/80) to afford compound **10j** as a white crystalline solid (25.5 mg, 50%): mp 94-96 °C. ^1H NMR (500 MHz, CDCl_3) δ 7.52 (s, 1H), 7.51 – 7.43 (m, 1H), 7.32 – 7.21 (m, 2H), 6.56 (NH, d, $J = 7.4$ Hz, 1H), 5.14 – 5.05 (m, 1H), 2.95 (dd, $J = 9.5, 7.8$ Hz, 2H), 2.53 – 2.43 (m, 1H), 2.32 (d, $J = 0.8$ Hz, 3H), 2.07 (dtd, $J = 11.0, 9.6, 8.2$ Hz, 1H). ^{13}C NMR (126 MHz, CDCl_3) δ 204.12, 166.02, 137.54, 132.09, 131.72, 127.64, 127.52, 126.84, 123.04, 76.25, 76.00, 75.74, 63.58, 41.24, 20.30, 18.90.

2-Methyl-N-(2-oxocyclobutyl)benzamide (10k)

The crude product of **10k** was purified by column chromatography using ethyl acetate/hexane (40/60) to afford compound **10k** as a white solid (35.7 mg, 71%): mp 100-102 °C. ¹H NMR (500 MHz, CDCl₃) δ 7.40 (dd, *J* = 7.6, 1.5 Hz, 1H), 7.35 (td, *J* = 7.5, 1.5 Hz, 1H), 7.30 – 7.18 (m, 2H), 6.30 (NH, d, *J* = 7.8 Hz, 1H), 5.21 – 5.12 (m, 1H), 3.10 – 2.96 (m, 2H), 2.63 – 2.52 (m, 1H), 2.47 (s, 3H), 2.16 (dtd, *J* = 11.0, 9.6, 8.2 Hz, 1H). ¹³C NMR (126 MHz, CDCl₃) δ 204.95, 169.42, 136.60, 134.84, 131.21, 130.37, 126.80, 125.76, 64.45, 42.27, 19.88.

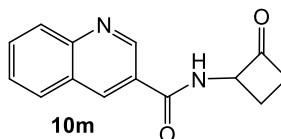
4-Methyl-N-(2-oxocyclobutyl)benzamide (10l)

The crude product of **10l** was purified by column chromatography using ethyl acetate/hexane (40/60) to afford compound **10l** as a white solid (27.4 mg, 50.6%): mp 149-150 °C. ¹H NMR (500 MHz, CDCl₃) δ 7.68 (d, 2H), 7.23 (d, *J* = 7.9 Hz, 2H), 6.80 (NH, d, *J* = 7.6 Hz, 1H), 5.19 – 5.10 (m, 1H), 3.05 – 2.96 (m, 2H), 2.59 – 2.48 (m, 1H), 2.40 (s, 3H), 2.18 (dtd, *J* = 11.0, 9.6, 8.1 Hz, 1H). ¹³C NMR (126 MHz, CDCl₃) δ 205.62, 166.84, 142.51, 130.27, 129.30, 127.14, 64.59, 42.19, 21.49, 19.82.

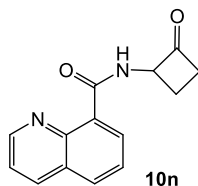
General Procedure for *N*-Heterocyclic Benzamide Cyclobutanones (**10m-10t**)

The general procedure for the synthesis of benzamide cyclobutanones (**10a-10l**) was followed. In order to neutralize and isolate the desired product as the free base, hydrolysis reaction was quenched by adding saturated Na₂CO₃ until effervescence ceased. The organic product was extracted using ethyl acetate (3 x 3 mL) or methylene chloride for highly water-soluble analogs and the combined organic layers were dried over Na₂SO₄. Then the solvent was evaporated under reduced pressure and the resultant crude product was purified by column chromatography to afford the heterocyclic benzamide cyclobutanones.

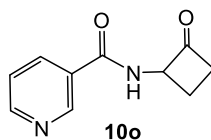
N-(2-Oxocyclobutyl)quinoline-3-carboxamide (**10m**)



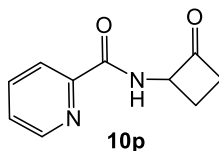
The crude product of **10m** was purified by column chromatography using ethyl acetate/hexane (80/20) to afford compound **10m** as a white solid (30.0 mg, 50%): mp 155-156 °C. ¹H NMR (500 MHz, CDCl₃) δ 9.18 (d, *J* = 2.3 Hz, 1H), 8.52 (dd, *J* = 2.3, 0.8 Hz, 1H), 8.04 (dd, *J* = 8.4, 1.1 Hz, 1H), 7.79 (dd, *J* = 8.2, 1.4 Hz, 1H), 7.73 (ddd, *J* = 8.4, 6.9, 1.4 Hz, 1H), 7.53 (ddd, *J* = 8.1, 6.9, 1.2 Hz, 1H), 7.21 (NH, s, 1H), 5.15 (dt, *J* = 9.9, 7.7 Hz, 1H), 2.99 (dd, *J* = 9.4, 7.8 Hz, 2H), 2.57 – 2.46 (m, 1H), 2.19 (dtd, *J* = 11.1, 9.6, 8.2 Hz, 1H). ¹³C NMR (126 MHz, CDCl₃) δ 205.26, 165.18, 149.28, 147.99, 136.17, 131.61, 129.28, 128.86, 127.68, 126.80, 125.76, 77.29, 77.04, 76.78, 64.57, 42.37, 19.71.

***N*-(2-Oxocyclobutyl)quinoline-8-carboxamide (10n)**

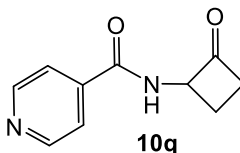
The crude product of **10n** was purified by column chromatography using ethyl acetate/hexane (70:30) to afford compound **10n** as a white soft solid (11.8 mg, 19%): mp 89-91 °C. ¹H NMR (500 MHz, CDCl₃) δ 11.83 (NH, d, *J* = 7.3 Hz, 1H), 8.93 (dd, *J* = 4.3, 1.8 Hz, 1H), 8.83 (dd, *J* = 7.4, 1.6 Hz, 1H), 8.29 (dd, *J* = 8.4, 1.8 Hz, 1H), 7.99 (dd, *J* = 8.1, 1.6 Hz, 1H), 7.68 (dd, *J* = 8.1, 7.3 Hz, 1H), 7.51 (dd, *J* = 8.3, 4.3 Hz, 1H), 5.25 – 5.15 (m, 1H), 3.16 (dddd, *J* = 17.5, 10.1, 4.6, 2.7 Hz, 1H), 3.04 (dddd, *J* = 17.6, 10.6, 8.8, 2.0 Hz, 1H), 2.56 (qd, *J* = 10.5, 4.7 Hz, 1H), 2.39 (dddd, *J* = 11.0, 10.1, 8.8, 8.0 Hz, 1H). ¹³C NMR (126 MHz, CDCl₃) δ 206.28, 165.71, 149.44, 145.52, 137.84, 134.18, 132.44, 128.51, 127.81, 126.57, 121.04, 64.95, 42.22, 19.66.

***N*-(2-Oxocyclobutyl)nicotinamide (10o)**

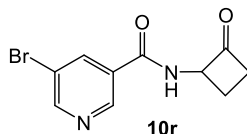
The crude product of **10o** was purified by column chromatography using methanol/ethyl acetate (1/99) to afford compound **10o** as a white solid (25.3 mg, 53%): ¹H NMR (500 MHz, CDCl₃) δ 8.98 (dd, *J* = 2.3, 0.8 Hz, 1H), 8.68 (dd, *J* = 4.9, 1.7 Hz, 1H), 8.12 (dt, *J* = 8.0, 2.0 Hz, 1H), 7.68 (d, *J* = 7.7 Hz, 1H), 7.37 (ddd, *J* = 8.0, 4.9, 0.9 Hz, 1H), 5.13 (dt, *J* = 10.3, 7.9 Hz, 1H), 3.01 (dd, *J* = 9.4, 7.7 Hz, 2H), 2.51 (tt, *J* = 10.7, 7.1 Hz, 1H), 2.24 (dtd, *J* = 11.0, 9.6, 8.1 Hz, 1H). ¹³C NMR (126 MHz, CDCl₃) δ 205.79, 165.15, 152.34, 148.02, 135.59, 129.11, 123.67, 64.41, 42.23, 19.39.

***N*-(2-Oxocyclobutyl)picolinamide (10p)**

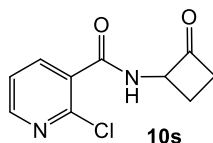
The crude product of **10p** was purified by column chromatography using ethyl acetate/hexane (40/60) to afford compound **10p** as a white solid (37.7 mg, 79.5%): mp 97-99 °C. ¹H NMR (500 MHz, CDCl₃) δ 8.56 (ddd, *J* = 4.8, 1.7, 0.9 Hz, 1H), 8.50 (NH, d, *J* = 8.1 Hz, 1H), 8.18 (dt, *J* = 7.8, 1.1 Hz, 1H), 7.87 (td, *J* = 7.7, 1.7 Hz, 1H), 7.46 (ddd, *J* = 7.6, 4.8, 1.3 Hz, 1H), 5.22 (dt, *J* = 9.9, 7.8 Hz, 1H), 3.05 (dd, *J* = 9.7, 7.9 Hz, 2H), 2.56 (tt, *J* = 10.6, 7.1 Hz, 1H), 2.24 (dtd, *J* = 11.0, 9.6, 8.3 Hz, 1H). ¹³C NMR (126 MHz, CDCl₃) δ 205.18, 164.06, 149.03, 148.20, 137.43, 126.56, 122.43, 64.05, 42.26, 19.61.

***N*-(2-Oxocyclobutyl)isonicotinamide (10q)**

The crude product of **10q** was purified by column chromatography using methanol/ethyl acetate (1/99) to afford compound **10q** as a white solid (15.4 mg, 33%): mp 119-121 °C. ¹H NMR (500 MHz, CDCl₃) δ 8.77 – 8.72 (m, 2H), 7.64 – 7.59 (m, 2H), 7.10 (NH, d, *J* = 7.4 Hz, 1H), 5.22 – 5.12 (m, 1H), 3.13 – 2.98 (m, 2H), 2.64 – 2.52 (m, 1H), 2.20 (dtd, *J* = 11.1, 9.6, 8.2 Hz, 1H). ¹³C NMR (126 MHz, CDCl₃) δ 204.73, 165.03, 150.64, 140.27, 120.94, 77.29, 77.04, 76.78, 64.40, 42.41, 19.59.

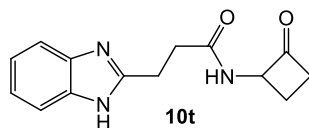
5-Bromo-N-(2-oxocyclobutyl)nicotinamide (10r)

The crude product of **10r** was purified by column chromatography using ethyl acetate/hexane (50/50) to afford compound **10r** as a white crystalline solid (25.3 mg, 64%). %): mp 114-115 °C. ¹H NMR (500 MHz, CDCl₃) δ 8.89 (d, *J* = 2.3 Hz, 1H), 8.80 (d, *J* = 2.2 Hz, 1H), 8.27 (t, *J* = 2.1 Hz, 1H), 7.06 (NH, d, *J* = 7.4 Hz, 1H), 5.18 (dddd, *J* = 11.0, 9.5, 8.0, 1.6 Hz, 1H), 3.14 – 2.99 (m, 2H), 2.58 (tdd, *J* = 10.8, 8.4, 5.8 Hz, 1H), 2.27 – 2.15 (m, 1H). ¹³C NMR (126 MHz, CDCl₃) δ 204.73, 163.71, 153.73, 145.94, 138.03, 130.31, 121.04, 77.29, 77.03, 76.78, 64.40, 42.40, 19.62. HRMS (ESI): Calcd for (MH⁺) C₁₀H₁₀BrN₂O₂: 268.9920, found 268.9916 (⁷⁹Br), 269.9948, 270.9896 (⁸¹Br).

2-Chloro-N-(2-oxocyclobutyl)nicotinamide (10s)

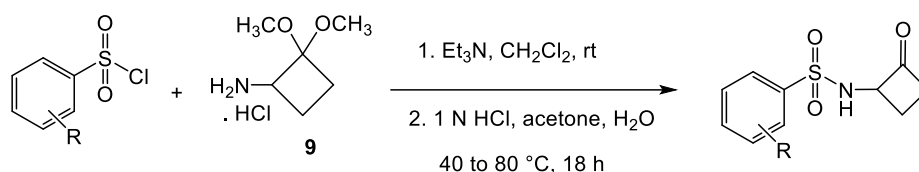
The crude product of **10s** was purified by column chromatography using ethyl acetate/hexane (70/30) to afford compound **10s** as a white crystalline solid (25.3 mg, 64%). %): mp 80-82 °C. ¹H NMR (500 MHz, CDCl₃) δ 8.48 (dd, *J* = 4.7, 2.0 Hz, 1H), 8.14 (dd, *J* = 7.7, 2.0 Hz, 1H), 7.37 (dd, *J* = 7.6, 4.7 Hz, 1H), 7.18 (NH, s, 1H), 5.20 – 5.11 (m, 1H), 3.11 – 3.03 (m, 2H), 2.64 – 2.53 (m, 1H), 2.23 (dtd, *J* = 11.1, 9.6, 8.2 Hz, 1H). ¹³C NMR (126 MHz, CDCl₃) δ 204.02, 164.08, 151.41, 147.20, 140.19, 129.88, 122.85, 77.30, 77.05, 76.79, 64.51, 42.46, 19.48.

3-(1H-Benzo[d]imidazol-2-yl)-N-(2-oxocyclobutyl)propenamide (10t)

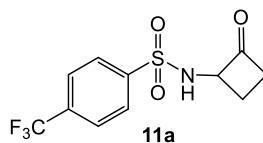


2-Benzimidazolepropionic acid was reacted with acetal **9** following the general T3P coupling reaction method. Upon the completion of the acetal hydrolysis, acetone was evaporated off under reduced pressure. Then the reaction was quenched by adding saturated Na₂CO₃ until effervescence ceased. The organic product was extracted using methylene chloride (5 x 2 mL) and the combined organic layers were dried over Na₂SO₄. Then the solvent was evaporated under reduced pressure, and the resultant crude product was purified by column chromatography using methanol/ethyl acetate (3/97) isocratic elution to afford an off-white solid with 93% HPLC purity. This solid was washed with ethyl acetate (3 x 0.5 mL) to yield cyclobutanone **10t** as a white crystalline solid (10.5 mg, 16%). %): mp 179-181 °C. ¹H NMR (500 MHz, CDCl₃) δ 7.54 (dt, *J* = 6.7, 3.3 Hz, 2H), 7.26 (NH, s, 1H), 7.21 (dt, *J* = 7.0, 3.5 Hz, 2H), 7.14 (NH, d, *J* = 7.6 Hz, 1H), 4.78 (tdd, *J* = 7.7, 5.9, 4.2 Hz, 1H), 3.27 – 3.13 (m, 2H), 3.03 – 2.87 (m, 2H), 2.82 – 2.62 (m, 2H), 2.44 – 2.31 (m, 1H), 2.12 (tt, *J* = 10.0, 9.0 Hz, 1H). ¹³C NMR (126 MHz, CDCl₃) δ 205.75, 172.60, 153.65, 122.39, 64.37, 42.11, 33.43, 24.61, 19.11.

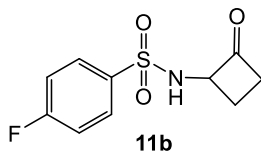
General Procedure for Sulfonamide Cyclobutanones (11a and 11b)



Acetal **9** (50.0 mg, 0.298 mmol) was suspended in methylene chloride (0.8 mL) and the reaction was cooled to 0°C. Triethylamine (82.6 μL , 0.596 mmol) was then added to the solution, followed by dropwise addition of 4-(trifluoromethyl)benzenesulfonyl chloride (87.6 mg, 0.358 mmol) in methylene chloride (0.7 mL). The reaction was stirred at 0°C for 5 minutes, then allowed to warm to room temperature and stirred overnight at room temperature. Once the reaction was deemed complete by TLC, the organic layer was washed successively with water (2 x 3 mL), 1N HCl (3 mL), and saturated Na_2CO_3 . Then, the organic layer was dried over sodium sulfate, and the solvent was removed under reduced pressure to afford the crude acetal intermediate. Without further purification, the crude material (97.9 mg) was subjected to hydrolysis by dissolving in a mixture of acetone (2.0 mL), water (0.30 mL), and 1N HCl (0.60 mL) and allowed to stir at 40°C overnight. The reaction was then partitioned between water and methylene chloride, and the organic product was extracted with methylene chloride (2 x 3 mL). The combined organic fractions were dried over Na_2SO_4 and concentrated under reduced pressure. The resultant crude product was purified by column chromatography to give the corresponding sulfonamides.

***N*-(2-Oxocyclobutyl)-4-(trifluoromethyl)benzenesulfonamide (11a)**

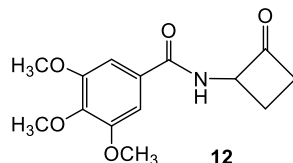
The crude product of **11a** was purified by column chromatography eluting with ethyl acetate/hexane (30/70) to afford benzenesulfonamide **11a** as a clear oil (60.8 mg, 70%), which formed needle like crystals in ethyl acetate/hexane (10/90). mp 74-76 °C. ¹H NMR (500 MHz, CDCl₃) δ 8.12 – 8.02 (m, 2H), 7.85 – 7.79 (m, 2H), 5.53 (NH, d, *J* = 8.0 Hz, 1H), 4.82 – 4.72 (m, 1H), 2.97 (dddd, *J* = 17.5, 11.3, 9.9, 1.7 Hz, 1H), 2.81 (dddd, *J* = 17.4, 9.9, 4.2, 2.5 Hz, 1H), 2.49 (tdd, *J* = 11.1, 10.1, 4.2 Hz, 1H), 1.88 (dtd, *J* = 11.2, 9.9, 8.5 Hz, 1H). ¹³C NMR (126 MHz, CDCl₃) δ 201.30, 142.80, 133.71 (q, *J*_{C-F} = 33.2 Hz), 126.50, 125.36 (q, *J*_{C-F} = 3.8 Hz), (ortho carbons of aryl-CF₃ long range F splitting: 123.22, 121.05, 118.87), 76.23, 75.98, 75.73, 64.81, 40.91, 19.92. HRMS (ESI): Calcd for (MH⁺) C₁₁H₁₁F₃NO₃S: 294.04, found 294.0405, Calcd for: (M+Na⁺) C₁₁H₁₁F₃NO₃SNa⁺: 316.0231, found 316.0222.

***N*-(2-Oxocyclobutyl)-4-(fluoro)benzenesulfonamide (11b)**

The crude product of **11b** was purified by column chromatography on a Teledyne Isco Rf Flash chromatography unit eluting with a gradient of 100% hexane, 5% EA in hexane, and 10% EA in hexane to afford compound **11b** as a clear oil (13.6 mg, 23%). ¹H NMR (500 MHz, CDCl₃) δ 8.00 – 7.90 (m, 1H), 7.93 – 7.85 (m, 1H), 7.27 – 7.15 (m, 2H), 5.52 (d, *J* = 8.2 Hz, 1H), 4.72 (dtt, *J* = 10.3, 8.3, 2.2 Hz, 1H), 2.93 (dddt, *J* = 17.4, 11.3, 9.8, 1.7 Hz,

1H), 2.77 (dddd, $J = 17.3, 9.9, 4.2, 2.5$ Hz, 1H), 2.47 – 2.36 (m, 1H), 1.83 (dtd, $J = 11.1, 9.9, 8.5$ Hz, 1H). ^{13}C NMR (126 MHz, CDCl_3) δ 202.96, 165.29 (d, $J_{\text{C-F}} = 255.3$ Hz), 136.31 (d, $J_{\text{C-F}} = 3.6$ Hz), 129.81 (d, $J_{\text{C-F}} = 9.4$ Hz), 116.47 (d, $J_{\text{C-F}} = 22.9$ Hz), 65.91, 41.91, 20.82.

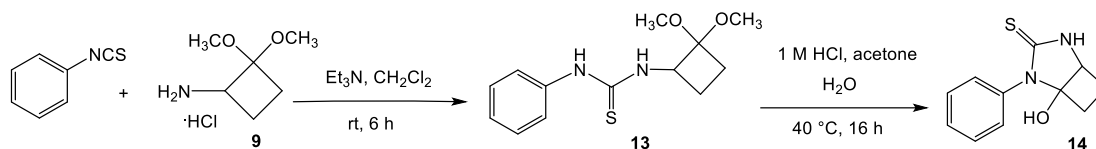
3,4,5-Trimethoxy-N-(2-oxocyclobutyl)benzamide (12)



Acetal **9** (30 mg, 0.18 mmol) was suspended in methylene chloride (0.9 mL) and cooled to 0°C. Triethylamine (49.9 μL , 0.36 mmol) was then added to the solution, followed by dropwise addition of 3,4,5-trimethoxybenzoyl chloride (41.5 mg, 0.18 mmol). The reaction was allowed to stir for 5 hours at room temperature with periodic TLC (hexane/diethyl ether = 50/50) and HPLC monitoring. Upon completion, the reaction mixture was successively washed with 1 M HCl (3 mL) and water (3 mL). Then this methylene chloride layer containing the acetal intermediate was subjected to hydrolysis by vigorously stirring with 1 M HCl (1 mL) overnight. After the hydrolysis was determined to be complete by TLC and HPLC, the organic layer was successively washed with water (3 mL), brine (3 mL), and dried over Na_2SO_4 . Then the solvent was removed under reduced pressure, and the resultant crude product was purified by column chromatography using ethyl acetate/hexane (50/50) to afford compound **12** as a white solid (25 mg, 21%): mp 144-146 °C. ^1H NMR (500 MHz, CDCl_3) δ 6.99 (s, 2H), 6.83 (NH, d, $J = 7.5$ Hz, 1H), 5.08 (qt, $J = 7.9, 1.4$ Hz, 1H), 3.88 (s, 9H), 3.11 – 2.95 (m, 2H), 2.52 (tdd, $J = 10.9, 9.6, 5.7$ Hz, 1H), 2.27

– 2.16 (m, 1H). ^{13}C NMR (126 MHz, CDCl_3) δ 205.90, 166.60, 153.17, 141.29, 128.30, 104.54, 77.29, 77.04, 76.79, 64.70, 60.93, 56.31, 42.25, 19.66.

1-Hydroxy-2-phenyl-2,4-diazabicyclo[3.2.0]heptane-3-thione (14)



Acetal **9** (100.0 mg, 0.597 mmol) was suspended in methylene chloride (2.98 mL) and cooled to 0°C. Triethylamine (124 μL , 0.895 mmol) was then added to the reaction, followed by the dropwise addition of phenyl isothiocyanate (85.6 μL , 0.716 mmol). The reaction was allowed to stir at room temperature and monitored by TLC (EA/DCM = 60/40 and 5% NH_3 in MeOH). After the consumption of acetal **9** (6 h), the methylene chloride layer was washed successively with water (2 x 3 mL) and 1N HCl (2 mL) and then dried over Na_2SO_4 . The solution was concentrated under reduced pressure to provide the crude acetal intermediate **13**, which was dissolved in a mixture of acetone (2.0 mL), water (0.20 mL), and 1 N HCl (0.56 mL) and stirred at 40°C for 16 h. Upon consumption of acetal **13**, the reaction was partitioned between ethyl acetate (3 mL) and water, and the aqueous layer was then extracted with two more portions (3 mL each) of ethyl acetate. The combined organic fractions were dried over Na_2SO_4 and concentrated under reduced pressure to afford a crude product mixture which was purified by column chromatography using ethyl acetate/hexane (50/50) to afford the bicyclic thione **14** (57.0 mg, 75%) as a white crystalline solid: mp 204–205°C. ^1H NMR (500 MHz, acetone- d_6) δ 7.96 (s, 1H), 7.48 (t, J = 1.8 Hz, 1H), 7.47 (dd, J = 2.0, 1.0 Hz, 1H), 7.42 – 7.37 (m, 2H), 7.34 – 7.30 (m, 1H), 6.18

(d, $J = 4.6$ Hz, 1H), 4.22 (ddd, $J = 7.3, 4.4, 2.0, 0.9$ Hz, 1H), 2.49 – 2.43 (m, 1H), 2.39 – 2.27 (m, 2H), 1.81 – 1.75 (m, 1H). ^{13}C NMR (126 MHz, MeOD) δ 183.17, 136.63, 129.47, 128.22, 127.42, 93.66, 59.64, 48.11, 47.94, 47.77, 47.60, 47.43, 47.26, 47.09, 31.67, 22.43. HRMS (ESI) calcd for (MH⁺) C₁₁H₁₄N₂O₂S: 221.0749, found 221.0743. The crystalline solid was recrystallized from methylene chloride to obtain crystals suitable for single crystal X-ray crystallography.

X-ray Crystallography Method

Single crystals of 1-hydroxy-2-phenyl-2,4-diazabicyclo[3.2.0]heptane-3-thione (**14**) were coated with a trace of Fomblin oil and were transferred to the goniometer head of a Bruker Quest diffractometer with a fixed chi angle, a Mo K α wavelength ($\lambda = 0.71073$ Å) sealed tube fine focus X-ray tube, single crystal curved graphite incident beam monochromator, and a Photon100 CMOS area detector. The instrument is equipped with an Oxford Cryosystems low temperature device, and examination and data collection were performed at 150 K. Data were collected, reflections were indexed and processed, and the files scaled and corrected for absorption using APEX3⁵⁸ and SADABS.⁵⁹ The space groups were assigned, and the structures were solved by direct methods using XPREP within the SHELXTL suite of programs^{60, 61} and refined by full matrix least squares against F^2 with all reflections using Shelxl2018⁶² using the graphical interface Shelxle.⁶³ Phenyl H atoms were placed in calculated positions with C-H = 0.95 Å. Positions of H atoms attached to N and O atoms and on the four membered ring were refined, and the X-H distances were restrained to target values (N-H = 0.88(2), CH₂ C-H = 0.99(2), CH C-H = 1.00(2)) Å. $U_{\text{iso}}(\text{H})$ values were

set to 1.5 (O-H) or 1.2 (C-H, N-H) times U_{eq} . Complete crystallographic data in CIF format have been deposited with the Cambridge Crystallographic Data Centre. CCDC Deposition Number 1966012 contains the supplementary crystallographic data for compound **14**. These data can be obtained free of charge from The Cambridge Crystallographic Data Centre via www.ccdc.cam.ac.uk/data_request/cif.

CHAPTER THREE

INHIBITION AND MOLECULAR DYNAMICS OF BACTERIAL ENZYME

N-SUCCINYL-L,L-2,6-DIAMINOPIMELIC ACID DESSUCINYLAZE

Antibiotic resistance in pathogenic bacteria is rising at an alarming rate and infections caused by multiple drug resistant (MDR) bacteria pose a pandemic level threat to human health.¹¹ MDR has emerged in methicillin/oxacillin-resistant *Staphylococcus aureus* (MRSA), vancomycin-resistant enterococci (VRE), extended-spectrum beta-lactamases (ESBLs), and penicillin-resistant *Streptococcus pneumoniae* (PRSP) due to the inheritance of drug resistant genes between strains and even between species.⁴ Growing MDR in common bacterial strains including *Escherichia coli*,⁵ and *Mycobacterium tuberculosis*⁶⁴ that cause life-threatening diseases is a global health concern.

Unfortunately, in the past five decades, only a few antibacterial agents were identified to replace the antibiotics that are no longer clinically effective against several bacterial infections. A common approach in developing new antibiotics to overcome bacterial resistance is chemically modifying the existing antibacterial drugs. However, only a limited number of classes of antibiotics including diarylquinolines, oxazolidinones, pleuromutilins, lipopeptides, and streptogramins have been marketed in the last four decades.⁶⁵ Furthermore, biological targets of clinically used antibiotics belong to a small set of bacterial cellular pathways and are not well diversified.⁶⁶ Therefore, the development of

small molecule inhibitors of novel bacterial target enzymes with a new mechanism of action is critically important.

We have identified a previously unexplored and a promising bacterial target enzyme known as *N*-succinyl-L,L-diaminopimelic acid desuccinylase (DapE) toward the discovery of novel antibiotics. We have structurally characterized this enzyme and made a significant contribution to elucidate the mechanism of action enabled by protein crystallography and computer simulations in collaboration with Dr. Richard Holz, Dr. Ken Olsen, and Dr. Boguslaw Nocek. This chapter focuses on the synthesis of DapE inhibitors belonging to various chemical classes, *in vitro* testing of those inhibitors, and molecular dynamics experiments performed to increase our understating of conformational changes of DapE enzyme during the catalytic cycle.

DapE as a Novel Antibiotic Target

The *dapE*-encoded *N*-succinyl-L,L-diaminopimelic acid desuccinylase (DapE, EC 3.5.1.18) is a key enzyme in the late stages of bacterial *meso*-diaminopimelate (*m*-DAP)/lysine biosynthetic pathway, and DapE is present in all Gram-negative bacteria and most Gram-positive bacteria. In plants and bacteria *m*-DAP, the precursor for lysine, is synthesized from L-aspartate via three parallel pathways, namely the succinylase, dehydrogenase, and acetylase pathways, wherein the succinylase pathway is the most common pathway in the lysine biosynthesis pathway (see Figure 7).⁶⁷

DapE catalyzes the hydrolysis of *N*-succinyl-L,L-diaminopimelic acid (L,L-SDAP) to succinic acid and L,L-diaminopimelate (DAP). Then, DAP is converted to *m*-DAP and

ultimately to lysine via decarboxylation (see Scheme 9). Products of the *m*-DAP/lysine biosynthetic pathway, *m*-DAP and lysine are precursors in peptide and bacterial peptidoglycan cell wall synthesis. The deletion of the *dapE* gene that encodes the DapE enzyme proved to be lethal to *Helicobacter pylori*⁶⁸ and *Mycobacterium smegmatis*.⁶⁹ Moreover, the *Helicobacter pylori* mutant with the deletion of the *dapE* gene was unable to grow even in the lysine supplemented media, but the bacteria in the *m*-DAP alone supplemented media showed growth. This confirms that the *m*-DAP/lysine biosynthetic pathway is indispensable in bacterial survival, and it is the only source of *m*-DAP and also shows that lysine is essential in bacterial cell wall synthesis. Alternatively, in humans, no lysine biosynthetic pathway is present. Therefore, the essential amino acid lysine must be obtained as part of our diet. Therefore, inhibitors of enzymes in the succinylase pathway, specifically DapE, are promising drug targets that should exert selective toxicity toward bacterial strains with no mechanism-based toxicity in humans.⁶⁷

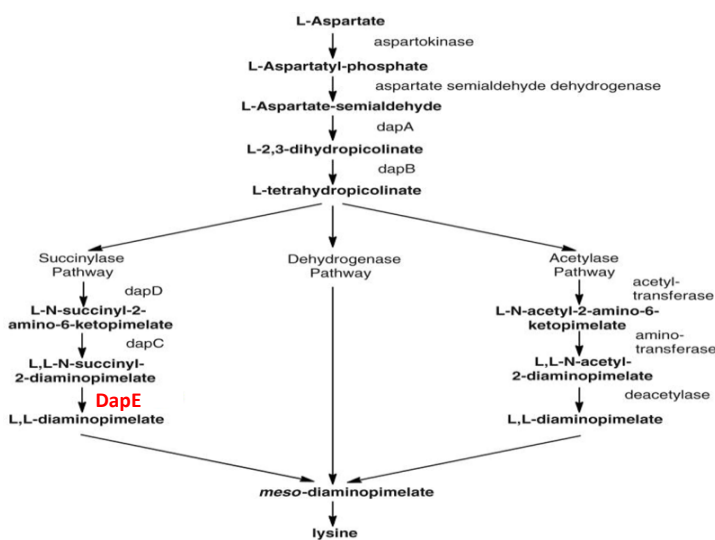
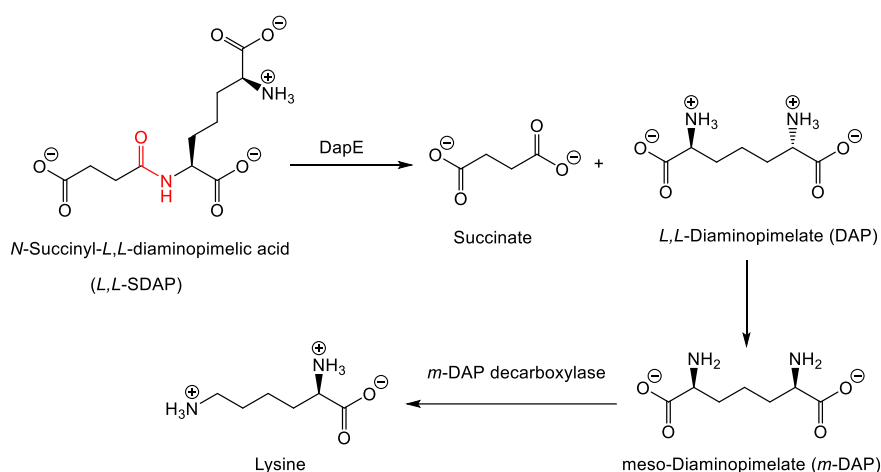


Figure 7. Lysine and *m*-DAP biosynthesis via bacterial succinylase pathway.

The presence of DapE in pathogenic bacteria including *Mycobacterium tuberculosis*,⁷⁰ *Escherichia coli* (O157:H7), *Vibrio cholerae*, *Pseudomonas aeruginosa*, and *Staphylococcus aureus* (strain MRSA252)⁶⁷ in particular, targeting ESKAPE pathogens⁷¹ confirms that inhibitors of DapE could serve as broad-spectrum antibiotics. These facts demonstrate that DapE is an attractive target to fight the rising bacterial resistance via a new mechanism of action without mechanism-based side effects in humans.



Scheme 9. Hydrolysis of L,L-SDAP to succinate and DAP by DapE.

In drug discovery, protein crystallography is exceptionally valuable providing structural insights into the binding site of the target enzyme. Key amino acid residues responsible for the catalysis, substrate identification, and inhibitor binding could be determined via ligand-bound enzyme crystal structures.

X-ray Crystal Structures and Conformational Changes of DapE during Catalysis

DapE enzyme is a di-metallo homodimer (subunit $M_r = 41.6$ kDa) with each subunit comprised of a catalytic domain and a dimerization domain which plays a critical role in catalysis (see Figure 8A). The first X-ray crystal structure of an apo DapE from *Neisseria*

meningitidis (*NmDapE*) was reported in 2005.⁷² 3D structure of the enzyme with no metal ion in the active site provide a limited structural knowledge of the enzyme, as metal ion-bound structures are critical in determining the spatial arrangements of key amino acid residues involved in the catalysis. In 2010, our collaborators reported the first metal ion-bound crystal structures of DapE. These crystal structures of mono- and di-zinc forms of *Haemophilus influenzae* (*HiDapE*) were determined at 2.0 Å (PDB ID: 3ISZ) and 2.3 Å (PDB ID: 3IC1) resolution, respectively.⁷³ Furthermore, we determined structures of mono- and di-zinc forms of *NmDapE*.⁷⁴ Significantly, the structure of the DapE inhibitor, captopril, bound to the active site of the di-zinc *NmDapE* at 1.8 Å resolution demonstrated interactions of the thiol moiety with the active site zinc atoms.

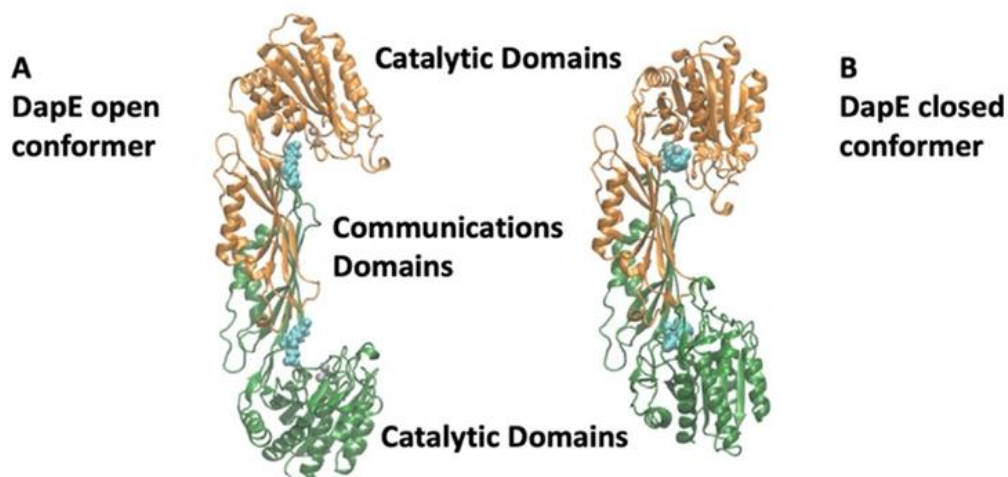


Figure 8. (A) Open conformation of *NmDapE* enzyme [PDB ID: 5UE], (B) Closed conformation of *HiDapE* products-bound structure [PDB ID: 5VO3].⁷⁵ Catalytic and dimerization domains of the homodimer are colored in orange and green. Zinc ions are highlighted in grey. Products bound to the active site are shown in cyan.

Active Site Architecture of DapE Enzymes

The active site of DapE is located in the catalytic domain comprised of a di-zinc metal center. Each Zn(II) ion adopts a distorted tetrahedral geometry and is coordinated by histidine and glutamate residues. In addition, both Zn(II) ions are bridged by an aspartate on one side and a water/hydroxide on the opposite side, while the Zn(II) ions are separated by approximately 3.3 Å (see Figure 9). The *HiDapE* crystal structure revealed that Glu134 acts as the general base during catalysis and that the Thr325 belonging to the loop positioned right above the active site is critical in substrate recognition and transition-state stabilization.⁷³

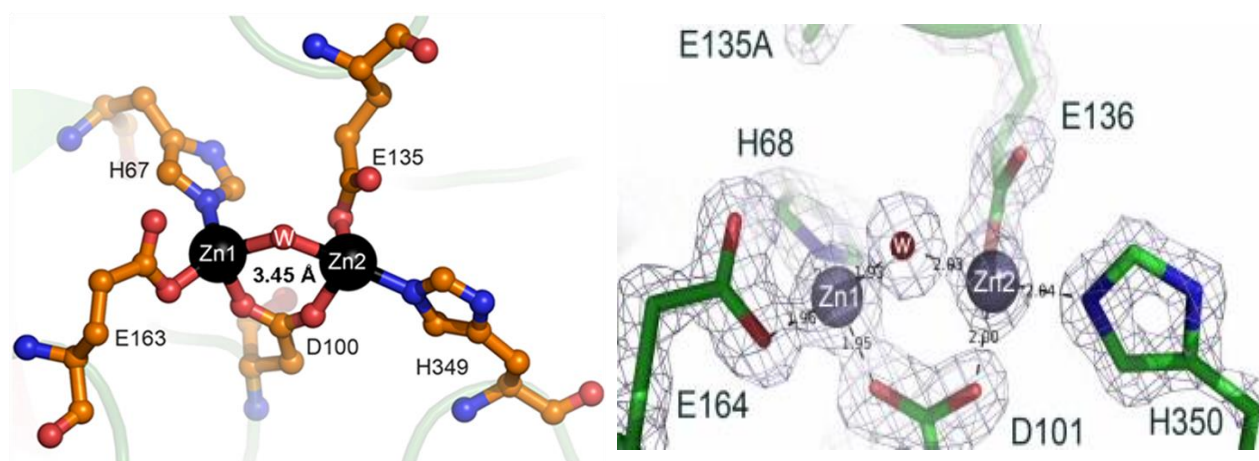


Figure 9. Architecture of di-zinc active sites of (A) *HiDapE* enzyme⁷³ and (B) *NmDapE* with 1.3 Å resolution (PDB ID: 5UEJ).⁷⁵

In 2018, our group reported a *HiDapE* crystal structure with the products of enzymatic cleavage, succinate and diaminopimelic acid bound in the active site revealing the previously unknown closed conformation and the flexibility of dimeric DapE (PDB ID: 5V03).⁷⁶ Overlaid structures of the open wild type (di-Zn *HiDapE*) with the closed (di-Zn

HiDapE) products-bound structure indicated that in the conformation bound to products, the catalytic domain rotates $\sim 50^\circ$ and shifts up to 29 Å at the exterior of the protein and 10 Å at the center of the catalytic domains (measured with respect to the position of Zn(II) atoms). The DapE substrate binding pocket consists of two distinct binding regions to accommodate succinic acid and L,L-DAP (see Figure 10A), and the succinic acid binding pocket resides next to the di-zinc active site (see Figure 10B).

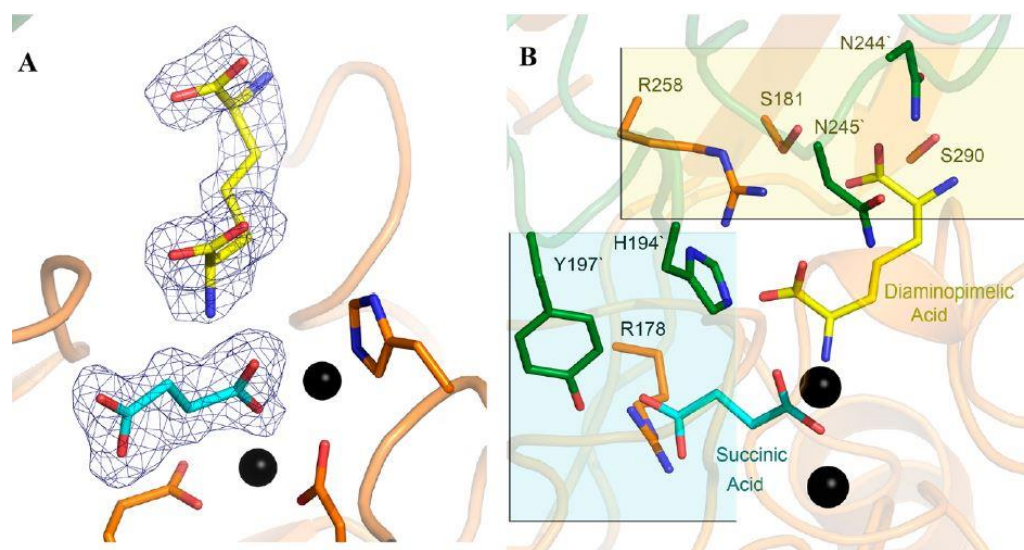


Figure 10. (A) Succinic acid (cyan) and L,L-diaminopimelic acid (yellow) binding regions are highlighted to show the individual binding pockets. (B) Amino acid side chains interacting with the products of hydrolysis. Zinc ions are shown as black spheres.⁷⁶

The products-bound structure also revealed the previously unknown role of His194.B, a residue on the dimerization domain of the opposite subunit that moves ~ 10 Å forming a key hydrogen bond with the substrate in the active site (see Figure 11A). This H-bond (2.9 Å) between the imidazole hydrogen of His194.B and the oxygen atom of succinic acid bound to Zn₂ in the active site facilitates the formation of an oxyanion hole consists of

Zn(II) and His194.B in the closed di-Zn *HiDapE* structure (see Figure 11B).⁷⁶ His194.B is a key residue involved in catalysis and aid in transition state stabilization. The movement of His194.B is crucial in activating the scissile carbonyl carbon of the SDAP substrate enabling the nucleophilic attack by a hydroxide nucleophile. Furthermore, it has been shown that the activity of di-zinc *NmDapE* enzyme drops to only ~3% of its wildtype (WT) activity when His195.B (that translates to H194.B in *HiDapE*) is mutated.⁷⁴

We utilized this products-bound structure in a product-bound transition state modeling (PBTSM) approach developed by Dr. Cory Reidl using the Chemical Computing Group's Molecular Operating Environment (MOE) modeling suite⁷⁷ to study and refine the proposed reaction mechanism of DapE. PBTSM is an integrated reverse approach of molecular mechanics and molecular dynamics. The modeling starts from the di-zinc *HiDapE* products-bound structure and generates ligand-enzyme complex models for the lowest-energy structures of each major catalytic step in reverse chronological order.⁷⁸

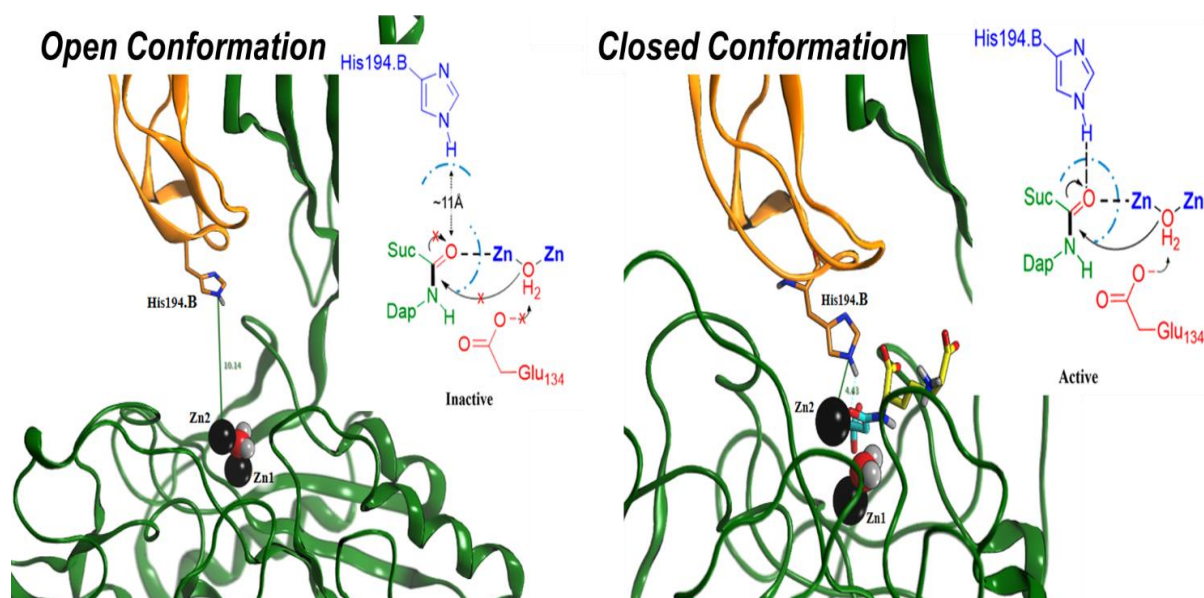


Figure 11. (A) The position of His194.B (orange) is shown in the open conformation of *HiDapE*. (B) Structure of proposed oxyanion hole constitute with His194.B and a Zn(II) ion in the *HiDapE* closed conformation.⁷⁶

A High-Resolution X-ray Crystal Structure of DapE

We recently reported a new atomic-resolution (1.3 Å) X-ray crystal structure of *NmDapE* (PDB ID: 5UEJ)⁷⁵ with sulfate ions bound in the substrate binding pocket. Our previous closed product-bound structure of *HiDapE* in combination with this new high-resolution open structure further defines the dramatic conformational range of motion that occurs for DapE during its catalytic cycle. The new high-resolution X-ray structure of *NmDapE* (PDB ID: 5UEJ) showed several structure similarities with previously reported *HiDapE* structures. *HiDapE* and *NmDapE* share a high degree of sequence identity of 55% with no sequence gaps and have the same active site architectures, including metal binding residues and essential substrate binding residues responsible for the hydrolytic activity.⁷⁵ Both *HiDapE* and *NmDapE* are dimers with two domains (a catalytic and communication/

dimerization domain) in each monomer (see Figure 8A). The catalytic domain in the new *NmDapE* open structure interacts with the communication domain of the other subunit as we previously observed with products-bound *HiDapE* structure, but most of the inter-subunit contacts were identified in the communication domains of the two monomers.⁷⁵

There is a significant conformational change observed between the open and closed forms of the enzyme presumably induced by substrate binding (see Figure 8A, B), and this dynamic conformational change is in agreement with a hinge domain mechanism that enables both domains to interact with the substrate. Based on the products-bound *DapE* structure and through PBTM simulations, we previously suggested that Arg residues of the *DapE* active site likely to involve in the substrate binding and may stabilize transition-state complex via hydrogen bonding interactions with the substrate.⁷⁶ The new 1.3 Å structure validates the importance of active site arginine residues (Arg179 and Arg259 in *NmDapE*) in substrate recognition and binding through sulfates observed in the substrate carboxylate binding regions.

Inhibition of *DapE* by Sulfate

We hypothesized that the two sulfate ions bound in the new open *NmDapE* structure (PDB ID: 5UEJ) are from the crystallization buffer (Li_2SO_4 , $(\text{NH}_4)_2\text{SO}_4$, and 5% DMSO), and occupy the same locations as two of the negatively charged carboxylates of the substrate. This was confirmed by direct comparison of the products-bound *HiDapE* closed structure (PDB ID: 5VO3) with the sulfate-bound *NmDapE* open structure (PDB ID: 5UEJ), where the carboxylates are observed to electrostatically bind to Arg178 and Arg258 of

HiDapE, analogous to the sulfates binding Arg179 and Arg259 of *NmDapE*, respectively (see Figure 12).

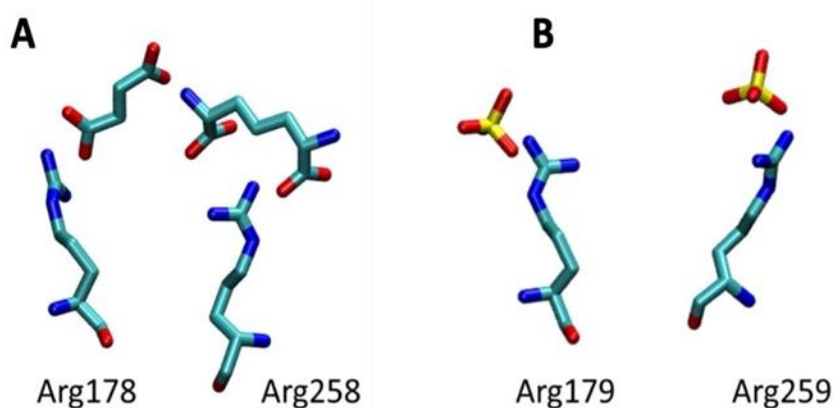


Figure 12. Key Coulombic interactions of (A) the terminal substrate derived carboxylates of the products in *HiDapE* (PDB ID: 5V03) with Arg178 and Arg258 and (B) the two bound sulfate ions in the open conformation of *NmDapE* (PDB ID: 5UEJ) with the corresponding arginine residues, Arg179 and Arg259, respectively.⁷⁵

Arginine residues were found in these positions in all 99 sequences similar to *NmDapE* found by a blastp search. Reviewing all eleven DapE structures deposited in the PDB, we found that six of the crystal structures had one or two sulfates bound in their active sites. DapE crystal structures with at least one bound sulfate in the active sites include PDB entries 3IC1 and 3ISZ,⁷³ as well as PDB entries 4O23, 4PPZ, and 4PQA.⁷⁴ The DapE structure that was first reported is an apo structure, PDB entry 1VGY,⁷² which lacks bound sulfates. For the apo structure, crystallization conditions were not reported making it impossible to know if sulfate ions were present in the crystallization solution. Several truncated DapE proteins have been expressed lacking the linker domains and were crystallized in the presence of acetate rather than sulfate (PDB entries 4ONW, 4OP4, and

4H2K)⁷⁹ and therefore do not have bound sulfate, but neither do they exhibit bound acetate in their active sites. These truncated DapE proteins are missing the Arg residues that bind the sulfates, or these Arg residues are near the new termini of the protein and thus are in very flexible regions of the structure. Therefore, sulfate binding to these residues would not be expected. Sulfates are well-known to bind at protein phosphate sites,^{80,81} and sulfate ions can also compete with carboxylate ions for binding sites.⁸²

Realizing that sulfate may compete with the substrate in the active site, we determined the inhibitory potency of sulfate to be 13.8 ± 2.8 mM (IC_{50}) using our ninhydrin-based assay.⁸³ The concentration of sulfate in the crystallization buffer of PDB 5UEJ was 1.46 M, which is 106 times higher than the IC_{50} of sulfate, consistent with its presence in the active site. The only reported products-bound structure (PDB ID: 5VO3) did not have sulfate in its crystallization buffer, which was likely more advantageous for substrate binding given the absence of competing sulfate. To investigate the nature of sulfate binding to the DapE active site, we performed a kinetic assay with various substrate and sulfate concentrations. Sulfate inhibition of *HiDapE* followed a competitive inhibition pattern as summarized in Table 2, and the saturation curves are shown in Figure 13. The saturation of activity with an increasing substrate concentration was not observed; rather, the enzymatic activity was inconsistent as the pH of the solution started to decline with an increase in *N*-methyl-L,L-SDAP substrate concentration above 5.5 mM. The decrease in the pH of the solution was attributed to the fact that *N*-methyl-L,L-SDAP was synthesized and is

used as the trifluoroacetate salt of the amine (see Scheme 10, compound **37**); hence, at higher concentrations, it ultimately affects the pH of the solution.

Table 2. Kinetic Parameters for *HiDapE* with *N*-Methyl-L,L-SDAP as the substrate⁷⁵

Assay	Sulfate (mM)	V_{\max} (AU/min)	$S_{0.5}$ (mM)
Control	0	0.068 ± 0.0055	1.21 ± 0.15
Inhibition	10	0.073 ± 0.0072	2.50 ± 0.29
	20	0.080 ± 0.0098	2.72 ± 0.066
	30	0.084 ± 0.0052	2.92 ± 0.098

These data combined with our previously published crystal structures of DapE from various organisms, including *NmDapE* and *HiDapE*, provides a fundamental understanding of the structural features, mechanistic insights, and crucial active site residues responsible for both catalysis and substrate identification.

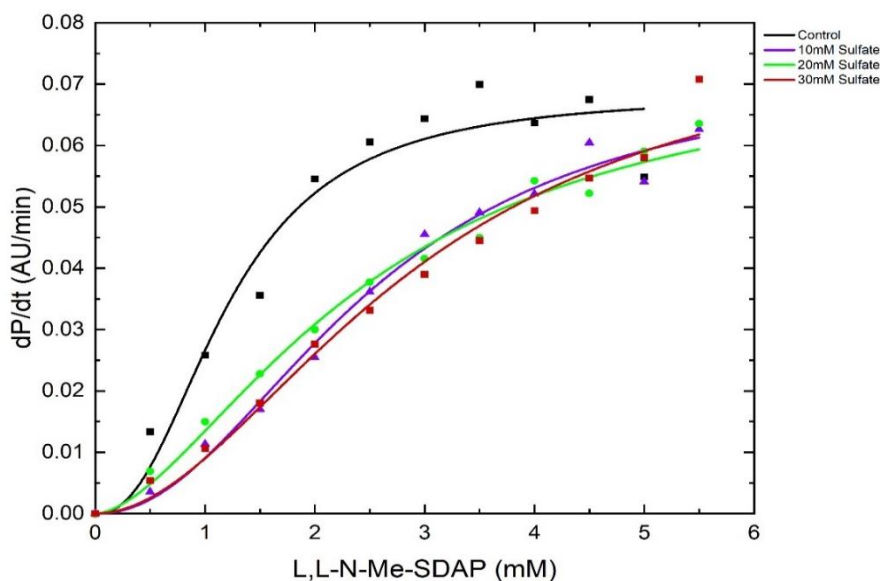


Figure 13. *HiDapE* saturation curves with varying substrate and sulfate concentrations.

Targeted Molecular Dynamics

Our products-bound closed *HiDapE*, and open structures of *NmDapE* (PDB ID: 5UEJ) and *HiDapE* (PDB ID: 3IC1) demonstrated the dynamic modulation between the open and closed conformation of the enzyme and the closed structure also provided many new ligand-protein interactions as discussed in the previous sections. These binding interactions and key residues were not predicted by our docking experiments or molecular dynamics simulations reported by Dutta and Mishra.⁸⁴ To better understand the catalytically important conformational change of DapE from the open to the closed conformer, a former master's student Matt Kochert, with the help of Dr. Ken Olsen, performed Targeted Molecular Dynamics (TMD) experiments using Visual Molecular Dynamics (VMD)⁸⁵ and a molecular dynamics program, Nanoscale Molecular Dynamics (NAMD).⁸⁶

TMD is a valuable computer simulation tool in studying the movements of atoms of a molecule at a finite temperature triggered by an applied force. As opposed to standard molecular dynamics (MD), a constraint is directed toward a target atom or a coordinate in the designated target structure in a time-dependent manner. TMD involves the application of an additional force on selected atoms in the direction of the positions of their counterparts in the target structure.^{87, 88} This force depends on the number of atoms selected, the selected force constant, and the root-mean-square deviation (RMSD) between the coordinates at any given time during the simulation and the final coordinates. Three TMD runs were performed from the open to the closed conformation using the new

NmDapE (PDB ID: 5UEJ) as the open starting conformation and the products-bound structure (PDB ID: 5VO3) as the closed target conformation.

Atoms identified to apply force were either all of the α -carbons in both subunits or all of the α -carbons in just one of the two subunits. Structure preparations of the protein models were performed prior to TMD simulations. The native substrate L,L-SDAP was built into the active sites of both the initial and target structures. In the open structure, the placement of the substrate was guided by the positions of the two sulfate ions found in the active site of the crystal structure to model the positions of the substrate terminal carboxylates. The substrate was placed in the active site of the closed structure in a manner consistent with the binding of the products in PDB entry 5VO3.

Simulation boxes generated with initial and target models were relaxed using NAMD. The relaxation process involved following subsequence steps. An energy minimization with and without restraints on the protein coordinates, slow heating from 10 to 310 K, and then the pressure and temperature equilibration using a Langevin piston followed by unrestrained dynamics for 2 ns. These equilibrated structures were subjected to 50 ns TMD simulations. During the TMD, when a force was applied to both subunits/monomers of DapE in the open conformation, both subunits approached the closed conformation as estimated by their degree of overlap and a comparison of RMSD values with the target structure. TMD experiments applying the additional force only to one subunit at a time were also performed to investigate if closing one subunit might induce the closure of the other subunit. These calculations indicated that the conformational change of

the subunits is independent since the force applied to one subunit did not induce the closure of the opposite subunit toward the target coordinates to any significant extent.

New Insights into DapE Catalytic Mechanism

TMD experiments were performed with no force on the SDAP substrate, and calculated interaction energies between the substrate and the enzyme demonstrate that the conformational change in the protein facilitates the movement and correct positioning of the substrate in the active site. As the protein closes, the binding affinity of substrate increases leading to a tighter binding of substrate to the enzyme (see Figure 14C, D). Additionally, a rotation of the catalytic domains around the dimerization domains was observed during the TMD simulations, as was observed in the product-bound *HiDapE*⁷⁶ structure and as previously suggested by Dutta and Mishra.⁸⁴ These results strengthen the proposed catalytic mechanism of DapE as they confirm the dynamic modulation of DapE between an open and a closed conformation induced by substrate binding. The importance of the Coulombic interactions between negatively charged carboxylates of L,L-SDAP substrate, and the binding pocket residues in substrate binding was highlighted by the sulfates bound in the active site in the new 1.3 Å DapE crystal structure. Our TMD simulations indicate that DapE inhibitors that result in a closed or partially closed structure upon binding the enzyme might be energetically favored over the inhibitors that solely bind the open conformer of DapE. Furthermore, TMD results and the new high-resolution DapE structure provided critical information in better understanding the structural

changes and key binding interactions in catalysis, which will guide us in the rational design of novel DapE inhibitors and in lead optimization to develop more potent inhibitors.

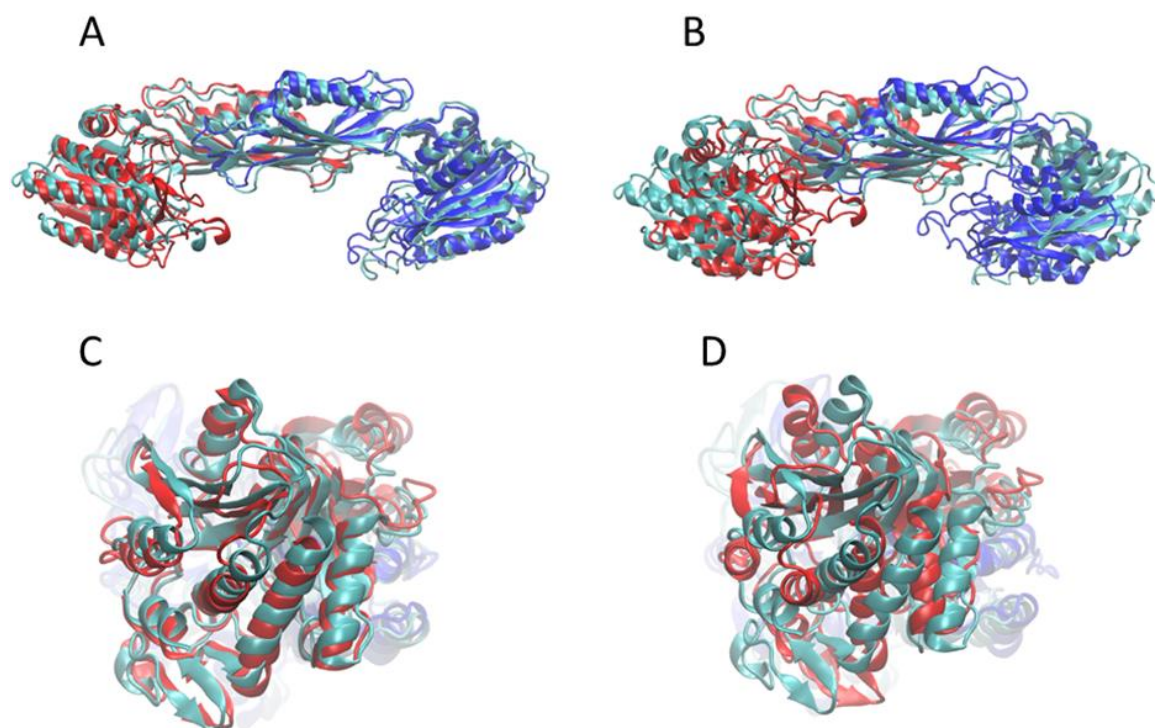


Figure 14. (A) DapE at 0 and 12.5 ns showing the conformational change in the catalytic domains moving toward the dimerization domains with force applied to both subunits. The dimer at time zero is colored cyan, and the dimer at 12.5 ns is colored red (chain A) and blue (chain B). (B) Same as panel A, but at 40 ns. (C) Same as panel A, but viewed so that the rotation of the catalytic domain relative to the dimerization domain can be seen easily. No rotation occurred during the first 12.5 ns of the TMD simulation. (D) Same as panel C but at 40 ns. The large rotation of the catalytic domain relative to the initial structure can be seen.⁷⁵

Synthesis of DapE Substrate Analogs as Potential Inhibitors and Biochemical Tools

Our work on substrate analogs of DapE started in collaboration with Dr. Rick Holz, a pioneer in studying DapE bacterial enzyme. Synthetic substrate analogs were utilized in kinetic experiments and crystallization of DapE.

Development of Ninhydrin Inhibition Assay for DapE

Our former research team member Dr. Tahirah Heath developed a convenient enzymatic assay to assess the inhibition of DapE employing the fundamental reaction between ninhydrin and the primary amine formed by hydrolysis of the SDAP substrate.

The need for a new DapE inhibition assay can be attributed to the lack of reproducibility and limitations of the existing assays. Further, we sought to expand the scope in order to develop an effective screening assay as an important tool in identifying drug-like lead molecules. Commonly, DapE inhibition has been measured using a spectrophotometric assay that utilizes L,L-SDAP as a substrate and monitors the amide bond cleavage of L,L-SDAP at 225 nm. This rapid assay is straightforward and can be performed in a 96-well plate. However, the 225 nm assay lack the ability to provide accurate and reliable inhibitory data for test compounds with a strong UV absorption, limiting the application of this assay in testing medicinal chemistry target compounds.⁸⁹

The original DapE assay was developed by Gelb *et al.* by taking advantage of the rapid reaction of L,L-DAP (product of the enzymatic reaction) with ninhydrin vs the reaction with the L,L-SDAP substrate,⁹⁰ but this assay was not reproducible. The same

group developed two different assays for DapE. The first assay utilized ^{14}C -labeled SDAP followed by scintillation counting of liberated radioactive ^{14}C -succinate. This substrate assay required working with radioactivity with extra safety protocols and waste disposal issues. The second is a complex, coupled assay employing several successive enzymatic reactions to capture and quantify the product succinate. This coupled assay is expensive, and the reproducibility is poor due to technical challenges. When developing an assay, it is wise to avoid secondary enzymes as they can result in possible false positives. Thus, we refrained from commercially available kits that monitor the formation of succinate through coupled enzyme assays. More importantly, these kits are not cost-effective for higher-throughput assays.⁸³ Our robust ninhydrin-based assay was developed to overcome the limitations of previous assays and to guide us in the ultimate discovery of novel antibiotics against DapE.

Previous Work on Substrate Analogs for Ninhydrin Assay

The reaction between the newly formed primary amine of L,L-DAP via amide hydrolysis of L,L-SDAP substrate and ninhydrin was the key detection method in the ninhydrin assay. It was shown that DapE is inactive toward the substrate analog lacking the free N^6 -amino group.⁹¹ Taking these requirements into consideration, we previously designed N^6 -methylated (**15b**), N^6,N^6 -dimethyl L,L-SDAP(**15c**), and N^6 -acetylated (**15d**) derivatives of L,L-SDAP with methyl or acetyl cap on the free amine of L,L-SDAP to prevent its interference by blocking the reactivity (see Figure 15). Synthesis of these analogs were

prioritized using molecular docking and modeling⁸³ performed by Dr. Cory Reidl using MOE, as summarized below.

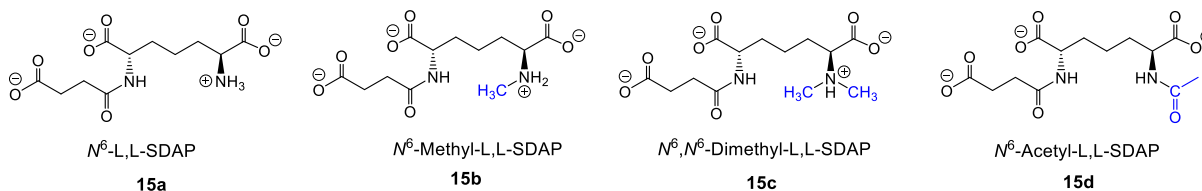


Figure 15. N⁶-Methyl (**15b**), N⁶,N⁶-dimethyl (**15c**), and N⁶-acetylated (**15d**) substrate analogs of L,L-SDAP (**15a**).

Molecular Modeling of Substrate Analogs

MD simulations were performed utilizing the products-bound *HiDapE* crystal structure (PDB ID:5V03) in its closed conformation. Structure models of L,L-SDAP (**15a**), N⁶-methyl-L,L-SDAP (**15b**), and N⁶,N⁶-dimethyl-L,L-SDAP (**15c**) were built using the Molecular Operating Environment (MOE) computational suite's Builder utility and a minimization in the gas phase using the force field MMFF94X was performed. Following the molecular docking, the docking poses for all three ligands were compared to the binding interactions found in the DapE crystal structure with products bound to the active site.⁸³ Molecular dynamics of selected docked models of all three ligands provided comprehensive binding interaction maps for L,L-SDAP, and substrate analogs **15b** and **15c** (see Figure 16).

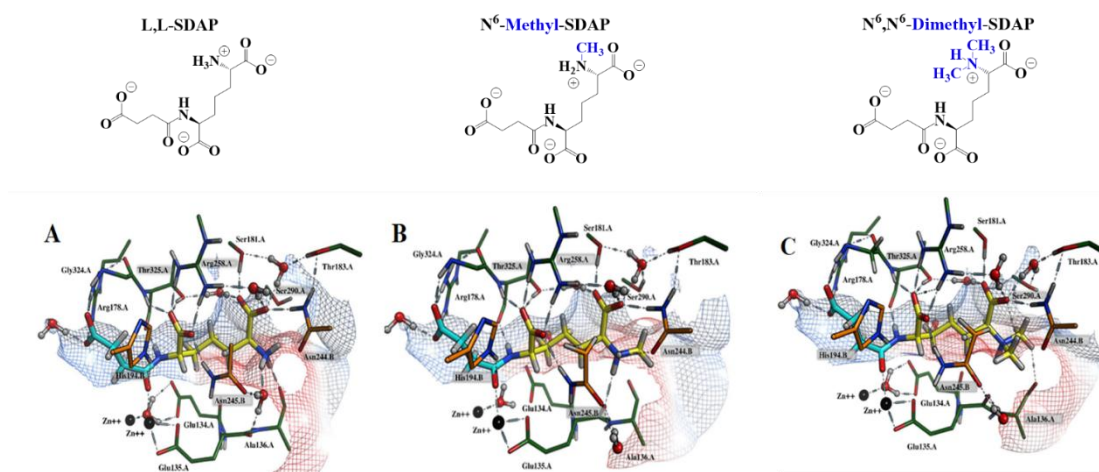


Figure 16. Docked and modeled (A) native substrate L,L-SDAP, (B) N^6 -methyl-L,L-SDAP, and (C) N^6,N^6 -dimethyl-L,L-SDAP in the DapE active site. The diaminopimelate moiety is shown in yellow, and the succinate in turquoise. The catalytic domain of Subunit A is colored in green, and the dimerization domain of Subunit B is colored orange.⁸³

Binding interactions predicted via molecular modeling are consistent with the interactions observed in both open and closed crystal structures of DapE and residues identified during TMD simulations, confirming the importance of key residues in substrate binding and catalysis. Specifically, the final models obtained from MD experiments highlighted the binding orientations of Arg258.A and Thr325.A, responsible for the substrate identification and binding, and His194.B critical in catalysis facilitating the formation of closed active DapE form (see Figure 16). The monomethyl-L,L-SDAP analog **15b** shared similar interactions with the native substrate, with an exception of a loss of the H-bond interaction between the methyl group on the primary amino group and the backbone carbonyl of Ala136.A (see Figure 16B). Alternatively, the dimethyl-L,L-SDAP analog **15c** binding was distinct from the binding interactions of the native substrate, notably, the elimination of interconnecting H-bond between the backbone carbonyl of

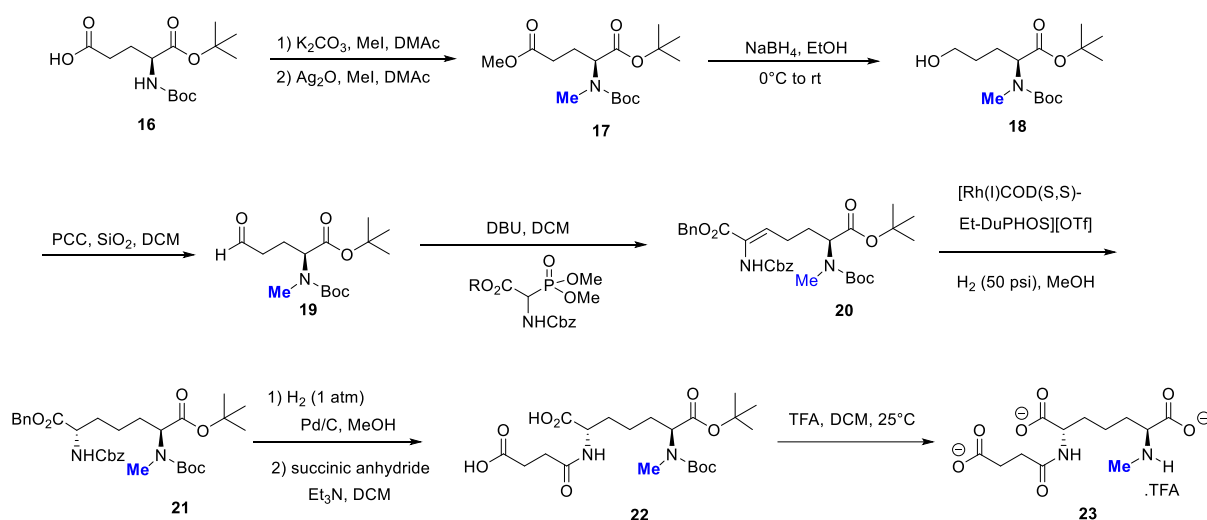
Glu135.A and the side chain carbonyl of Asn245.B through the secondary amine N-H. As demonstrated, the monomethyl-L,L-SDAP analog binds to the DapE active site in a similar manner as the native substrate whereas, the dimethyl-L,L-SDAP analog bearing an extra methyl group lacked some key binding interactions. This suggests that dimethyl-L,L-SDAP could serve as a competitive inhibitor of DapE leading to the partially closed enzyme.

During the MD simulation, the *N*⁶-acetyl-L,L-SDAP (**15d**) went under significant binding alterations due to loss of the positive charge and the presence of the acetyl group. Based on these results, the synthesis of *N*⁶-methyl-L,L-SDAP (**15b**) was prioritized over *N*⁶,*N*⁶-dimethyl-L,L-SDAP (**15c**) as the modified substrate for the ninhydrin assay. Both molecular modeling and TMD results integrated with structural insights from our new high-resolution *NmDapE* structure will enable us to design inhibitors that bind DapE in a similar fashion to the native substrate as well as inhibitors that inhibit DapE by disrupting the closing of the open enzyme conformer.

Synthesis of *N*⁶-methyl-L,L-SDAP (**15b**)

The asymmetric synthesis of *N*²-succinyl-*N*⁶-methyl-L,L-diaminopimelic acid substrate **15b** was developed by Dr. Marlon Lutz, as shown in Scheme 10.⁸³ Two key steps of this scalable synthetic route are olefination and asymmetric hydrogenation. The first step of this route is the one-pot methylation of Boc-L-glutamic acid *t*-butyl ester **16** using potassium carbonate and methyl iodide, followed by silver oxide catalyzed methylation providing the α -*N*-methylated ester **17**. The methyl ester was reduced using sodium borohydride, and the resultant primary alcohol **18** was oxidized to give aldehyde **19** with

pyridinium chlorochromate (PCC). Then compound **19** was subjected to Horner-Wadsworth-Emmons olefination with benzyl 2-[[[(benzyloxy)carbonyl]amino]-2-(dimethoxyphosphoryl)acetate providing olefin **20**, followed by an enantioselective hydrogenation using catalytic amounts of 1,2-bis[(2*S*,5*S*)-2,5-diethylphospholano]benzene(1,5-cyclooctadiene)rhodium(I) trifluoromethanesulfonate to give the L,L-Cbz-protected amino acid **21**. Hydrogenolysis debenzoylation of both benzyl and Cbz groups afforded the zwitterionic compound which, then reacted with succinic anhydride providing the succinamide **22**. The Boc group and *tert*-butyl ester group were removed in the presence of trifluoroacetic acid (TFA) in methylene chloride to afford the *N*-methyl L,L-SDAP as a trifluoroacetate salt (**23**).



Scheme 10. Asymmetric synthesis of *N*⁶-methyl-L,L-SDAP substrate analog **23**.

The *N*⁶-methyl-L,L-SDAP substrate analog enabled us to develop an effective DapE inhibition assay that detects the newly formed primary amine from succinate amide hydrolysis. This assay takes advantage of the selective formation of a Schiff base known as

Ruhemann's purple ($\lambda_{\max} = 570 \text{ nm}$) when ninhydrin selectively reacts with primary amines versus secondary amines.

Thioamide Analogs of DapE Substrates

Lead molecules designed as L,L-SDAP and *N*⁶-methyl-L,L-SDAP (**15b**) derivatives with key carboxylates and amide isosteres to retain the key binding interactions with the DapE active site could provide competitive inhibitors of DapE. Our Molecular Modeling⁸³ and Targeted Molecular Dynamics experiments⁷⁵ suggested that substrate-derived inhibitors may be energetically favored via the formation of a stable inhibitor-enzyme complex.

We investigate *NmDapE* and *HiDapE* to obtain 3D crystal structures in collaboration with Dr. Boguslaw Nocek and Dr. Jerzy Osipiuk at Argonne National Laboratories. Up until now, our group has deposited several crystal structures of DapE in the Protein Data Bank, including open form (PDB ID: 3IC1), and closed form with products bound (PDB ID: 5V03) DapE enzyme from *Haemophilus influenzae*, and open form DapE (PDB entry 5UEJ) from *Neisseria meningitidis* (*NmDapE*). Recently, we reported a crystal structure of DapE, solved by Dr. Osipiuk from pathogenic Gram-negative bacteria, *Shigella flexneri*. This structure is released in the Worldwide Protein Data Bank⁹² as PDB ID: 7LGP.

We are currently working on experiments to co-crystallize DapE in the presence of both L,L-SDAP and *N*⁶-methyl-L,L-SDAP (**15b**) in collaboration with Dr. Nicole Inniss at Northwestern University, Center for Structural Genomics of Infectious Diseases (CSGID).

DapE structures with native substrate or substrate analogs bound to the active site will aid in identifying key residues enabling a more potent and efficient inhibitor design.

Alternatively, we are preparing novel thioamide derivatives of L,L-SDAP and *N*⁶-methyl-L,L-SDAP (**15b**) substrates and beta-lactams as co-crystallization tools of dimetalloenzymes with extended applications. Beta-lactam thioamide analogs are being synthesized in an effort to co-crystallize with New Delhi Metallo- β -lactamase-1 (NDM-1), which catalyzes the hydrolysis of β -lactam drugs such as penicillins, cephalosporins, and carbapenems.⁹³ NDM-1 is a key enzyme responsible for multi-drug resistance found in pathogenic bacteria, including *Klebsiella pneumoniae* and *Pseudomonas aeruginosa*.⁹⁴

Chemistry and Significance of Thioamides

A thioamide group is isosteric to the amide bond, where the carbonyl oxygen atom is replaced with a sulfur atom. Thioamides are scaffolds with unique properties and are found in natural products.⁹⁵ The C-S bond of the thioamide, unlike the C-O bond of the corresponding amide, is less polarized because of the similarity of the electronegativity of carbon and sulfur atoms making the thioamide less polar than the amide. Yet, the thioamide moiety has a greater dipole moment and a higher rotational barrier endowing the C-N bond with more double bond character than the corresponding amides (see Figure 17).

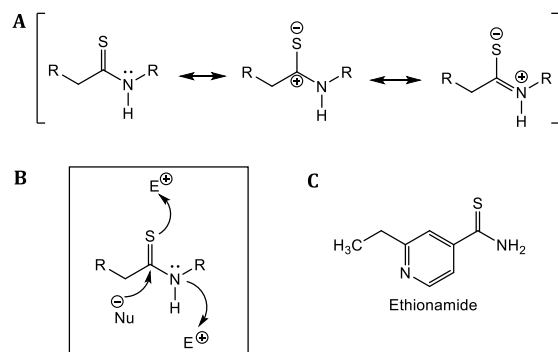


Figure 17. (A) The resonance structures of thioamide. (B) Thioamide reactive centers and (C) the structure of ethionamide.

The H-bonding pattern of thioamide has been extensively studied and applied in thiopeptide chemistry.⁹⁶ Typically, thioamides are weaker hydrogen bond acceptors, and the N-H proton is a stronger hydrogen bond donor and more acidic ($\sim pK_a=12$) than of an oxoamide ($\sim pK_a=17$).⁹⁵ Thioamides are less electrophilic than their amide isologues, but more reactive than amides with electrophiles through either sulfur or nitrogen nucleophilic centers. Thus, thioamides are useful precursors in the synthesis of a wide range of heterocyclic compounds.⁹⁷ Stronger S-metal coordination leads to the enhanced affinity of thioamides towards metals, which is advantageous in selective metal catalyzed reactions and in designing inhibitors targeting metalloenzymes.⁷⁴

Applications of thioamides are not limited to synthetic intermediates but extend to enzyme inactivators, co-crystallization tools, and even clinically approved drugs, for example, ethionamide, a second line antitubercular agent for the treatment of tuberculosis.⁹⁸ Several mechanism-based inhibitors of sirtuins (regulatory deacylases responsible for healthspan of cells) containing a thioamide moiety were previously studied

and resulted in some of the most potent sirtuin inhibitors to date. Thioamide analogs of sirtuins' native substrate were shown to provide potent inhibitors of the enzyme, and some thioamide analogs were reported as co-crystallization tools⁹⁹ providing useful structural information in inhibitor design.

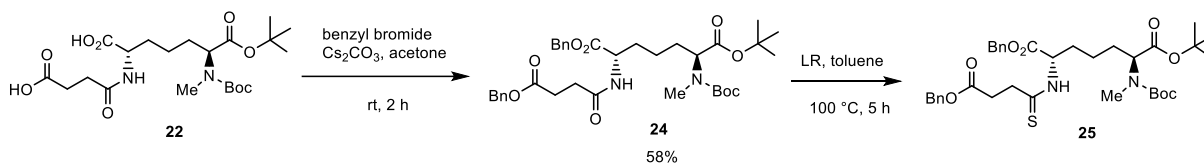
In this project, targeting DapE, substrate thioamide analogs were rationally designed by replacing the succinamide of the SDAP with a thioamide. Thioamide analogs of SDAP are expected to bind the DapE native substrate binding pocket through a strong sulfur-zinc interaction and should be hydrolyzed at a slower rate due to the lower electrophilicity of thioamides than the amide of the SDAP substrate. As a result, thioamide SDAP analogs, as well as thiono- β -lactams against NDM-1, could serve as competitive inhibitors of the target enzymes or as slowly hydrolyzed substrates.

Synthesis of the *N*⁶-Methyl-L,L-SDAP Thioamide Analog

Initially, we attempted to synthesize thioamide analogs of DapE substrates by reacting L,L-SDAP and *N*⁶-methyl-L,L-SDAP (**23**) with Lawesson's reagent (LR). Lawesson's reagent is the most common thionating agent in organic synthesis in addition to phosphorus pentasulfide (P₂S₅). Lawesson's reagent is a convenient and mild thionating reagent and is sometimes preferred over P₂S₅ that needs higher temperatures, longer reaction times, and a larger excess of reagent.¹⁰⁰ The order of reactivity of functional groups toward Lawesson's reagent is as follows: alcohols > amides > ketone > esters. It has been suggested that the reactivity and the mechanism of carboxylic reaction with Lawesson's reagent are similar to the reaction with alcohols.¹⁰¹ Reactions of both

substrates with Lawesson's reagent were not successful, presumably due to the reactivity of free carboxylic acid and the amine toward Lawesson's reagent forming the corresponding thioacid¹⁰¹ and an ammonium complex through a ring opening reaction of Lawesson's reagent with the amine.¹⁰² Thus, we required to protect labile carboxylic acids and the amine moieties of both L,L-SDAP and *N*⁶-methyl-L,L-SDAP (**23**) to prevent these side reactions.

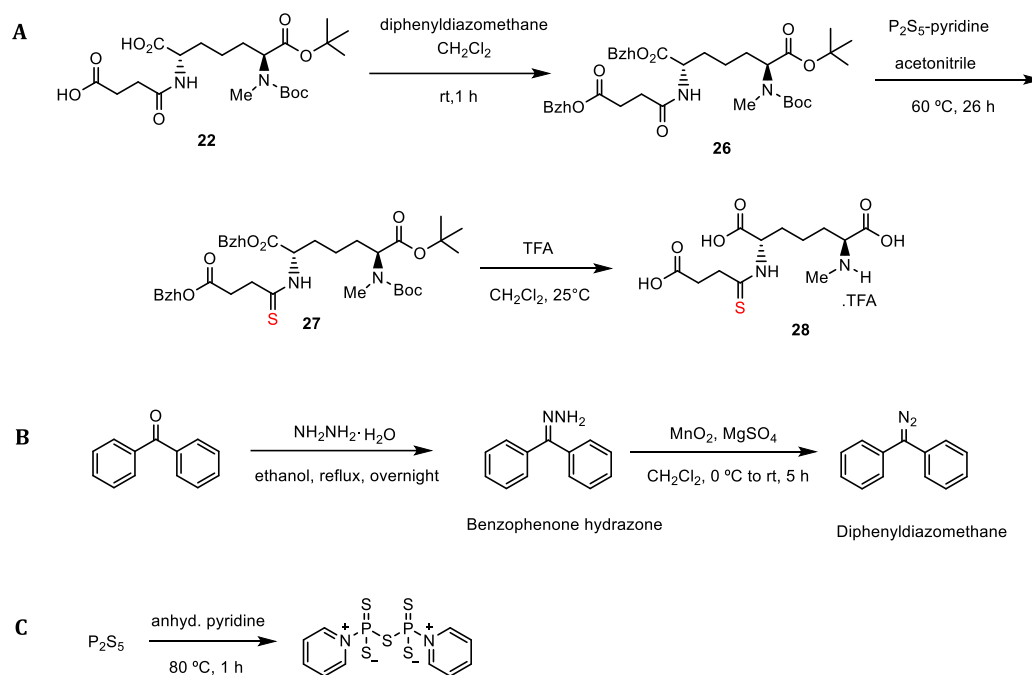
A modified *N*⁶-methyl-L,L-SDAP synthetic route was employed in the preparation of thiono *N*⁶-methyl L,L-SDAP (**28**). For the efficient synthesis of the thioamide analog, a benzyl and a benzhydryl ester protection step of the carboxylic acid and a thionation step were incorporated into our reported route. Succinamide **22** was reacted with benzyl bromide in the presence of Cs₂CO₃ in acetone to give benzyl ester protected succinate amide **24** in 58% yield. The thionation was then attempted by refluxing the protected *N*-methyl SDAP with Lawesson's reagent in toluene at 100 °C (see Scheme 11). In this reaction, compound **24** was completely consumed providing several less polar by-products than compound **24** that eluted close to one another with similar retention times in HPLC analysis (the method reported in the experimental section). The crude product was purified using column chromatography, and characterization of isolated products through NMR and mass spectrometry indicated that the desired thioamide **25** was not formed in the reaction of benzyl ester analog **24** with Lawesson's reagent.



Scheme 11. Attempted thionation of benzyl ester protected succinate amide **24** using LR.

Alternatively, we explored other thionating agents, including a combination of P_2S_5 with hexamethyldisiloxane (HMDO). By-products from a thionation reaction with HMDO can be removed in an aqueous workup followed by a mild base hydrolysis or via a silica plug filtration, whereas by-products from Lawesson's reagent can only be removed through column chromatography.¹⁰³ The reaction of benzyl ester derivative **24** with P_2S_5 /HMDO in DCM at room temperature was not successful.

Benzyl ester derivative (**24**) was unstable during the reaction with both Lawesson's reagent and P_2S_5 leading to several decomposed products. A similar trend was observed when benzyl *N*-Boc-7 α -amino-3-deacetoxycephalosporinate (7-ADCA) was reacted with Lawesson's reagent and P_2S_5 /HMDO to prepare thioamide analog of 7-ADCA as a co-crystallization tool for NDM-1. We then employed the benzhydryl ester protection group that is more hydrolytically stable than benzyl ester even at elevated temperatures. Diphenyldiazomethane was prepared freshly from benzophenone hydrazone in the presence of activated MnO_2 and MgSO_4 in DCM. The resultant partially solidified crude product of diphenyldiazomethane was immediately reacted with compound **22** in DCM at room temperature to afford the globally protected *N*-methyl-L,L-SDAP (**26**, see Scheme 12).



Scheme 12. Synthesis of *N*⁶-methyl-L,L-SDAP thioamide analog (**28**).

We then sought to react compound **26** under mild thionation conditions in terms of temperature and functional group compatibility. The P_2S_5 -pyridine complex is a convenient thionating agent that can be synthesized by heating P_2S_5 and pyridine to 80 °C (reaction b, see Scheme 12). The zwitterionic P_2S_5 -pyridine complex has many preferred advantages, including increased solubility that enables thionation of polar compounds at a comparatively lower temperature, selectivity, and less reagent-derived by-products than Lawesson's reagent.¹⁰⁴ Globally protected thiono succinamide **27** was synthesized by reacting the succinamide **26** with P_2S_5 -pyridine complex in ACN at 60 °C. This reaction produced only a few by-products (add up to less than 20% of the crude mass), including excess pyridine from the reagent that were separated from the desired product by column chromatography. Then the Boc, benzhydryl, and *tert*-butyl ester groups will be removed in

a one-pot reaction using trifluoroacetic acid in methylene chloride to afford the thioamide analog of *N*-methyl-L,L-SDAP as its TFA salt (**28**).

The thioamide substrate analog **28** will be tested against DapE in our ninhydrin assay to study the affinity of this substrate analog toward DapE. We expect that *N*-methyl-L,L-SDAP thioamide analog may inhibit DapE through stronger coordination with the active site zinc ions, and the rate of catalytic hydrolysis of the thioamide should be lower due to the low electrophilicity of the thiocarbonyl center. Further, co-crystallization of DapE with the *N*-methyl-L,L-SDAP thioamide analog should provide us a substrate-bound crystal structure of DapE that will enable us to map the key active site residues in substrate binding and identification. These structural insights will guide us in designing novel substrate mimetic inhibitors of DapE as well as in optimizing identified lead compounds.

Synthetic Strategies and Inhibitory Potencies of DapE Inhibitors

Previously, the original DapE assay that monitors the cleavage of the SDAP substrate amide bond at 225 nm,⁹¹ was utilized to screen a selected library of potential DapE inhibitors containing zinc-binding groups, including thiols, boronic acids, hydroxamates, and phosphates. We identified captopril as a fairly potent lead that showed competitive inhibition with an IC₅₀ of 3.3 μM, and a K_i of 1.8 μM.⁸⁹ Captopril is an angiotensin converting enzyme (ACE) inhibitor used to treat hypertension, thus, it can be considered a lead molecule for medicinal chemistry. However, concerns were raised regarding the selectivity of the thiol moiety of captopril leading to side effects observed in patients.¹⁰⁵ Furthermore, synthesis, purification, and characterization of thiol containing compounds

can lead to challenges due to increased reactivity and sensitivity of thiols to oxidation. Even though captopril showed inhibition of DapE and exhibited dose-responsive antibiotic activity, Creus and Uda reported that the antibiotic activity of captopril is independent of DapE inhibition.¹⁰⁶ They suggested that the antibacterial efficacy of captopril could be due to inhibition of multiple target enzymes consistent with the selectivity of promiscuous thiol moiety. In order to validate DapE as an antibiotic target, we employed a lead search via high-throughput screening (HiTS) of existing target compound libraries.

We have identified five inhibitor molecules from our high-throughput screen (HiTS) screen from ChemBridge Corporation using an automated enzyme-coupled assay with >20% inhibition of DapE at 12 μ M inhibitor concentration. These lead molecules belong to four distinct chemical classes as follow, two *N*-acyl-sulfonamide indolines (**29**, **30**), a simple sulfone amide (**31**), a difluoromethyl sulfonamide (**32**), and a phenyltetrazole thioether (**33**, see Figure 18).

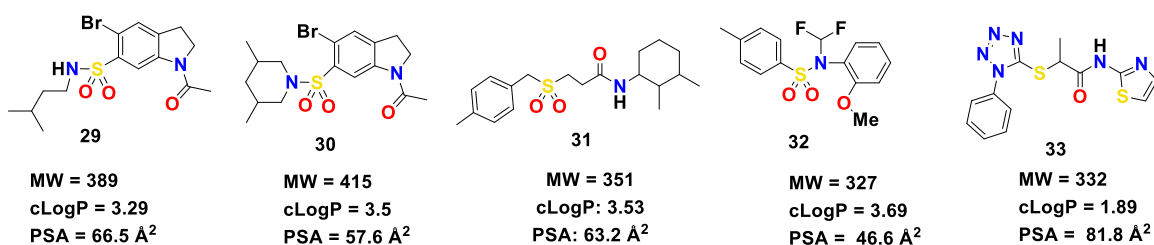


Figure 18. DapE hit compounds with calculated physicochemical properties.

For our advantage, all five lead compounds satisfy Lipinski's rule of five¹⁰⁷ and possess ≤ 10 rotatable bonds and a polar surface area ≤ 140 Å² consistent with Veber's rules for drug likeness of inhibitors.¹⁰⁸ All five hits are free of PAINS (pan assay interference

compounds) structural motifs. PAINS are compounds that are not selective toward a particular target and, as a result, give rise to false positive results in a high-throughput screen.¹⁰⁹⁻¹¹¹ SwissADME¹¹² predicted that our five hits should be orally bioavailable and all are predicted to exhibit blood-brain barrier (BBB) penetration except tetrazole hit **33**. The docking studies using SwissDock¹¹³ and MOE⁷⁷ suggest that all four classes of lead molecules consist of atoms that could coordinate with both zinc ions of the DapE active site. Furthermore, inhibitors of dimetalloenzymes with functional groups that could bridge the two active site zinc ions, including *N*-acyl-sulfonamide indolines, are less common. The presence of these structural features in our hits could be beneficial in designing potent inhibitors of DapE.

Synthesis of indoline sulfonamide series and tetrazole series were prioritized since indoline moieties are found in drugs and bioactive natural products.¹¹⁴ Previously, Dr. Tahirah Heath and Dr. Cory Reidl prepared a set of hit-derived *N*-acetyl 6- and 7-indoline sulfonamide analogs and demonstrated the inhibitory potencies against DapE using the ninhydrin assay. Our group's recent publication reports the synthesis and *in vitro* testing of *N*-acetyl-5-halo-6-indoline sulfonamide analogs against DapE,¹¹⁵ and is the first reported inhibitor series with SAR analysis and enzyme inhibition data validating DapE as a novel antibiotic target in the discovery of antibiotics with a new mechanism of action.

Synthesis and Docking of Difluoromethyl Sulfonamides Inhibitors of DapE

The *N*-(difluoromethyl)-*N*-(2-methoxyphenyl)-4-methylbenzenesulfonamide (**32**) was identified as a lead molecule that includes a difluoromethyl group. Difluoromethyl

moieties are relevant in drug discovery as a metabolically stable lipophilic hydrogen bond donors.^{116,117} The CF₂H group is known to aid in the efficient binding of biologically active compounds through favorable hydrogen-bonding interactions.¹¹⁷ A difluoromethyl group is considered as a potential lipophilic isostere of the hydroxyl, thiol, hydroxamic acid, and amine moieties¹¹⁷ in SAR analysis and lead optimization and found in clinically approved drugs. For example, Roflumilast used for the treatment of obstructive pulmonary disease contains a difluoromethoxy group.¹¹⁸

Difluoromethyl sulfonamide-based inhibitors can bind to the DapE active site through the coordination of sulfone oxygens as well as the methoxy oxygen atom to the zinc ions in the active site. To explore the SAR of the difluoromethyl sulfonamide series, we proposed several derivatives of the original hit compound (**32**), as shown in Figure 19.

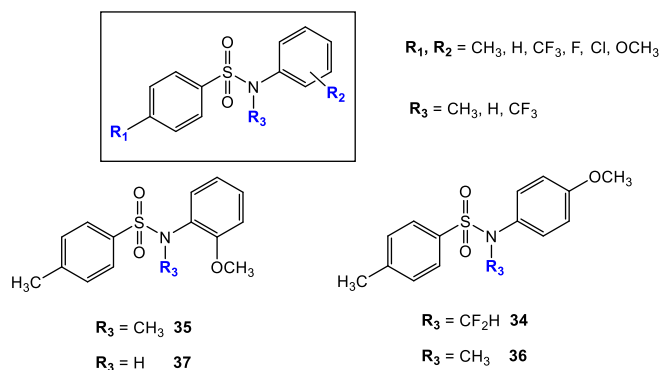


Figure 19. SAR functional group derivatizations of difluoromethyl sulfonamide series.

First, we identified the *p*-methoxy analog (**34**) to study the importance of the position of the aryl methoxy group. Additionally, the *N*-difluoromethyl group was replaced by an isosteric methyl group (compounds **35**, **36**) in investigating the role of *N*-difluoromethyl moiety in the binding of the inhibitor. *N*-Methyl analogs **35**, **36** were

previously synthesized, and **35** showed 60 % inhibition at 100 μM , where compound **36** showed an IC_{50} of 151 μM against DapE. The *N*-unsubstituted sulfonamide analog **37** reported no detectable inhibition at 100 μM . We designed synthetically accessible analogs where R1 and R2 can be varied by incorporating a range of functional groups, including CH_3 , CF_3 , F, Cl, OCH_3 , and H, and these analogs (Figure 19) can be readily synthesized from substituted aryl sulfonamides and substituted anilines.

Molecular Docking

Previously, we performed docking studies of the hit compound **32**, *p*-methoxy analog **34**, and the corresponding methyl analogs **35** and **36** in SwissDock using DapE open crystal structure (PDB ID: 3IC1). Calculated binding energies of the *N*-methyl sulfonamide analogs indicated a tighter binding than the corresponding *N*-difluoromethyl analogs. Present docking experiments were performed using MOE utilizing our new *NmDapE* open crystal structure (PDB ID: 5UEJ) with an atomic-level resolution and a high-quality refinement at the dimerization loops for a better understanding of ligand binding modes.

Molecular docking results showed that both *o*- OCH_3 and *p*- OCH_3 analogs of difluoromethyl sulfonamide (**32**, **34**) bind to the di-zinc active site suggesting a competitive inhibition of DapE. The original hit, *o*- OCH_3 difluoromethyl sulfonamide **32**, is predicted to bind to one of the zinc ions through coordination of sulfonamide oxygen atom, whereas the sulfonamide oxygen of the *p*- OCH_3 analog **34** is predicted to bridge the zinc ions (see Figure 20A, B). In addition, a cation- π interaction between the guanidine moiety of Arg179 and the tosyl aromatic ring was observed enabling a tighter binding of the inhibitor.

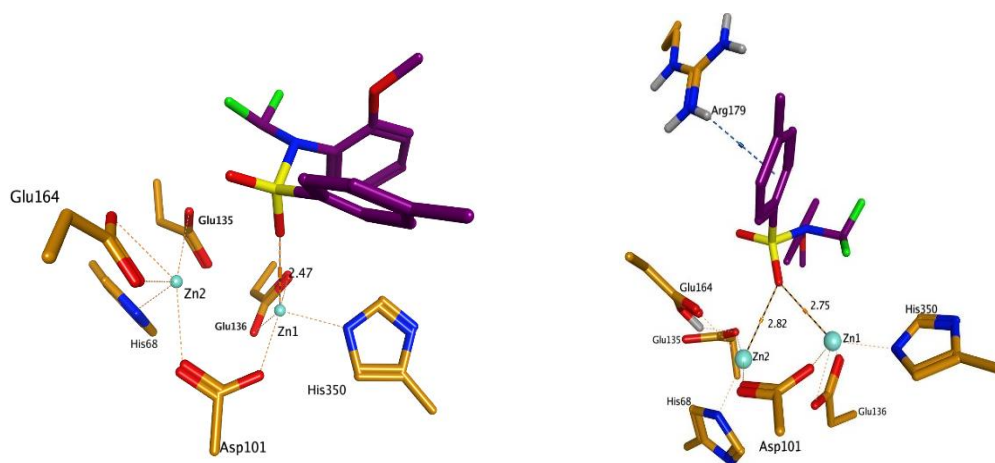
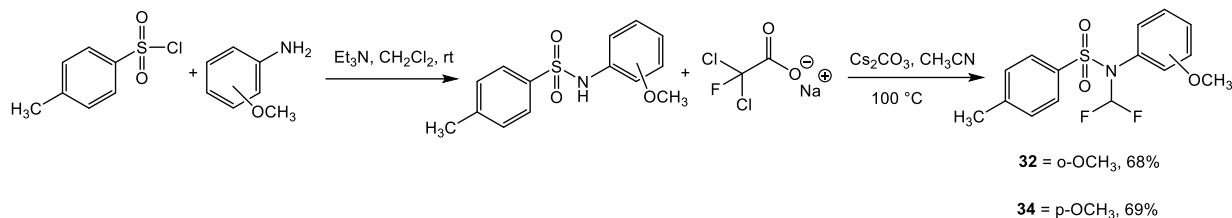


Figure 20. Docked (A) *o*-OCH₃ difluoromethyl sulfonamide (**46**) and (B) *p*-OCH₃ analog (**48**) into DapE di-zinc active site.

Synthesis and Inhibitory Potencies

N-difluoromethyl-(*o*-methoxy)-sulfonamide (**32**) was synthesized in a base-mediated coupling reaction of *p*-toluenesulfonyl chloride and *o*-anisidine yielding the sulfonamide intermediate, which then reacted with the fluorinating agent, sodium chlorodifluoroacetate in the presence of cesium carbonate and the final product **32** was isolated in 68% yield. The *p*-methoxy analog **34** was synthesized in parallel with compound **32** following the same route using *p*-anisidine (see Scheme 13). Compounds **32** and **34** were tested using the ninhydrin assay to assess the inhibitory potencies against *Hi*DapE. The original hit, *o*-methoxy analog **32** gave a calculated IC₅₀ of 72.9 μM, and *p*-methoxy analog (**34**) was more potent than the original hit with an IC₅₀ of 52.6 μM.



Scheme 13. Synthesis of *N*-difluoromethyl sulfonamides **32** and **34**.

Inhibitory data of the difluoromethyl sulfonamide series is promising and prompted us to explore the SAR via rational design of inhibitors guided by molecular docking. We collaborate with Dr. Innocent Demshemino at Georgetown College Kentucky to synthesize a focused *N*-difluoromethyl sulfonamide library in developing more potent DapE inhibitors.

Design, Synthesis, and Docking of Tetrazole- and Pyrazole-based DapE Inhibitors

Our five hits against DapE include a tetrazole compound (**33**) that consists of two heteroatom aromatic ring systems linked via a thioether moiety, as shown in Figure 21. Tetrazoles are planer aromatic heterocycles that contain an electron-rich ring system with four nitrogens and a carbon atom. The *1H*- or *2H*, 5-substituted tetrazole motif is a non-classical carboxylate bioisostere,^{119, 120} and 1,5-substituted tetrazoles serve as a bioisostere of *cis*-amide bonds of peptides.^{119, 121} Tetrazoles are found in 23 FDA approved drugs, including a cephalosporin antibiotic, Cefoperazone.¹²² The utility of tetrazole moiety as a synthetic scaffold in medicinal chemistry and pharmacology has drastically increased in recent years due to enhanced metabolic stability that they provide, favorable physicochemical properties, and tighter binding as a result of an increased number of ligand-receptor interactions.^{123, 124}

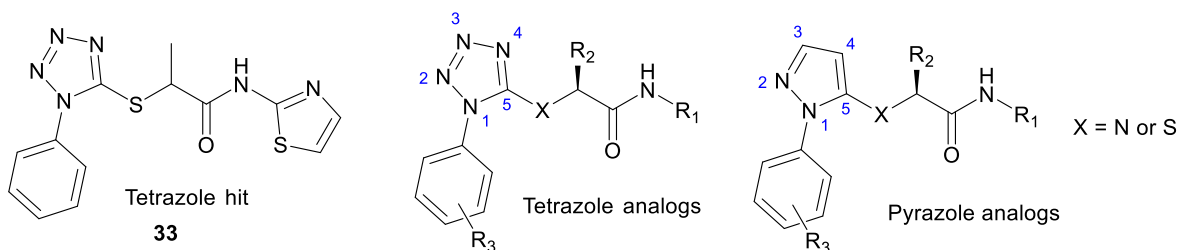


Figure 21. Plausible point derivatization of tetrazole and pyrazole derived DapE inhibitors.

An analogous series of tetrazole hit **33** where the sulfur atom of the thioether is replaced with a nitrogen was proposed as readily available natural and unnatural amino acids could be utilized in the synthesis. Moreover, a tetrazole isostere, pyrazole analogs were designed to enhance the drug-likeness of the inhibitor molecules with increased solubility, oral bioavailability and are also expected to provide tighter binding in the DapE active site. Both tetrazole and pyrazole scaffolds enable three-point functional group derivatization, as shown in Figure 21, to drive the SAR in expanding our substrate scope in synthesizing more potent and efficacious drug candidates. Selected heterocyclic moieties can replace the thiazole ring at R₁ providing H-bond acceptors, whereas R₃ can be modified with substituted phenyl groups. Furthermore, for the *N*-linked series, we are incorporating a range of amino acids with hydrophobic side chains at R₂, including Val, Ile, and Phe.

Docking

The molecular docking of the tetrazole hit with the DapE open crystal structure (PDB ID: 3IC1) using SwissDock performed by Dr. Tahirah Heath showed a significant difference in the binding affinity of DapE toward tetrazole hit **33** where (R)-enantiomer ($\Delta G = -8.59$ kcal/mol) enantioselectively binds to the active site with a preference for the (R)-enantiomer over the (S)-enantiomer ($\Delta G = -7.74$ kcal/mol). During docking, the (S)

isomer of tetrazole **33** interacted with one of the zinc atoms in the di-zinc active site, whereas the (R) isomer was bound to a distal binding pocket rather than the di-zinc active site indicating the possibility of allosteric inhibition of DapE by non-competitive or uncompetitive inhibitors (see Figure 22).

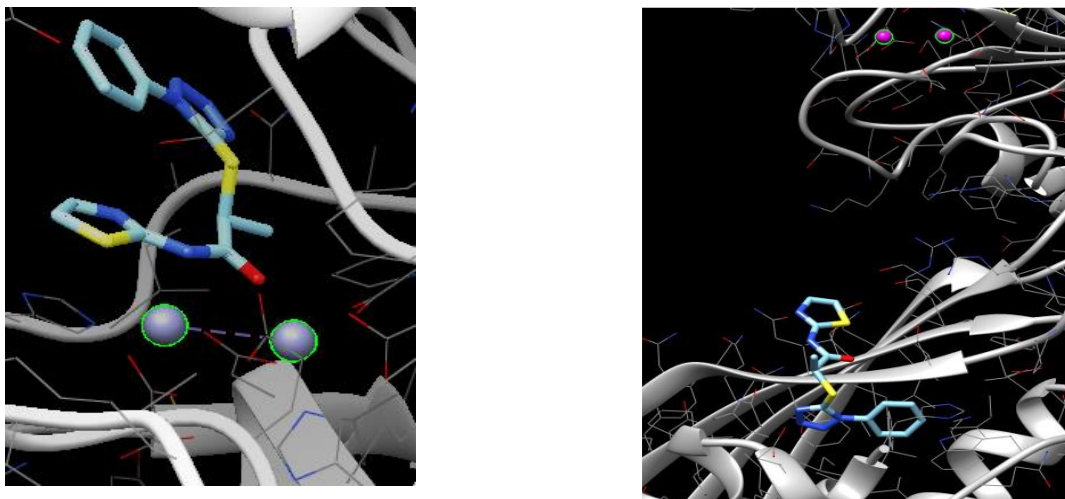


Figure 22. Docked (A) (S)-enantiomer is interacting with the zinc atoms (grey spheres) in the active site. (B) The (R)-enantiomer is bound to an allosteric site. The zinc atoms of DapE active site are highlighted as purple spheres.

During the docking experiments performed using MOE, the tetrazole original hit-derived *N*-linked pyrazole analog was bound to the DapE active site. These results indicated the importance of the pyrazole ring that forms a π -hydrogen interaction with the imidazole NH of H195 (see Figure 23). The H-bond between the pyrazole nitrogen and asparagine 246 suggests that an H-bond acceptor at this position is critical in binding. The amide moiety of the inhibitor could play a key role in binding as it provides two favorable H-bonds through an H-bond with the NH and His350, and an H-bond between the amide oxygen and a water molecule. The thiazole ring is bound to a hydrophobic pocket, and the

nitrogen atom could form H-bond interactions with the active site residues. We believe that the protonation state of the thiazole nitrogen should be neutral in the solution (see Figure 23).

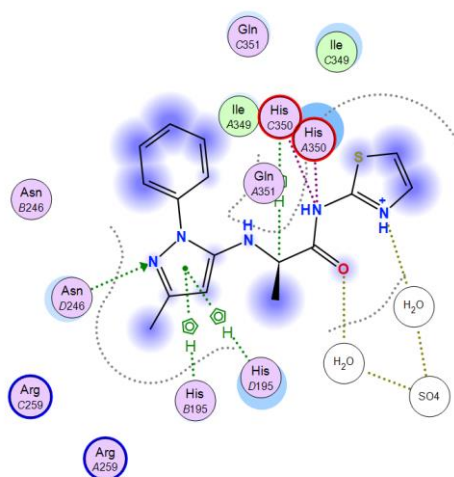
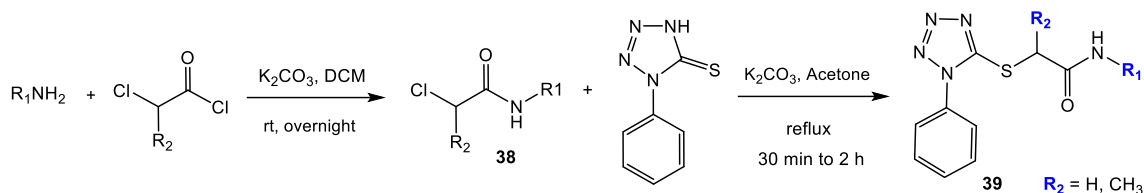


Figure 23. Hit-derived pyrazole bound to DapE active site through favorable interactions with active site residues.

Synthesis and Inhibitory Potencies

We developed a synthetic route to prepare thio-linked tetrazole and pyrazole inhibitors utilizing the nucleophilic substitution of alpha-halo amide intermediates with respective tetrazole and pyrazole thiones. The synthesis of the tetrazole analogs is achieved by two successive base-mediated coupling reactions following the route illustrated in Scheme 14. First, the heterocyclic amine is reacted with chloroacetyl chloride in DCM at room temperature with K_2CO_3 present where R_2 is a proton, and with alpha-chloropropionyl chloride where R_2 is a methyl group providing the corresponding alpha-halo amides (**38**). The tetrazole ring was introduced by refluxing each alpha-halo amide intermediate with commercially available 1,2-dihydro-1-phenyl-5H-tetrazole-5-thione in

acetone in the presence of K_2CO_3 , affording the corresponding phenyl tetrazole thio-linked analogs (**39**) (see Scheme 14).

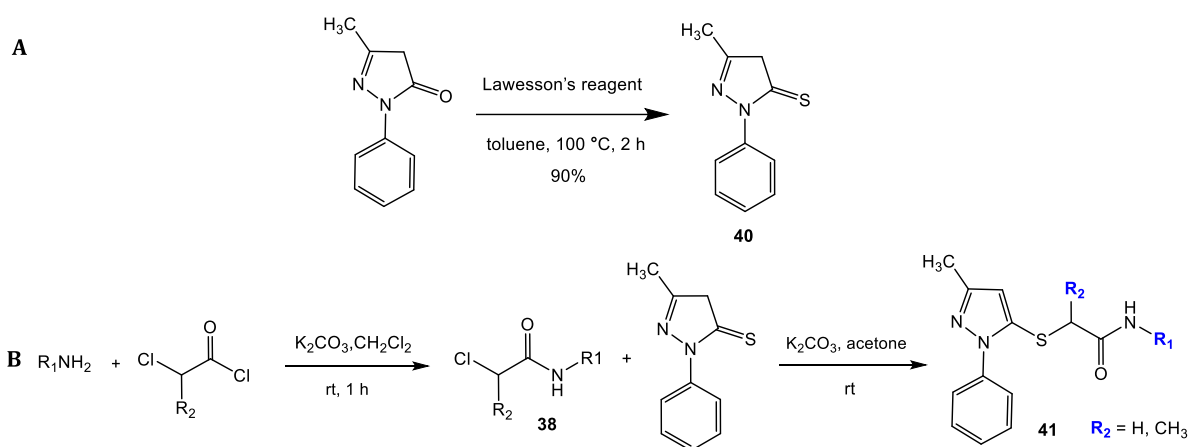


Scheme 14. Synthesis of phenyl tetrazole thio-linked DapE inhibitors.

Synthesis of pyrazoles followed the synthetic route shown in Scheme 15. Edaravone was utilized as a precursor, and the thionation using Lawesson's reagent afforded 5-methyl-2-phenyl-2,4-dihydro-3H-pyrazole-3-thione (**40**). Similar to the tetrazole synthesis, each isolated alpha-halo amide intermediate was reacted with thione **40** in the presence of K_2CO_3 , providing the corresponding phenyl pyrazole thio-linked analogs (**41**) as shown in Scheme 15. A master's student in our laboratory, Thomas DiPuma, and an undergraduate researcher, Katie Jane Torma, are currently preparing tetrazole and pyrazole inhibitors. The *in vitro* testing of the series is in progress.

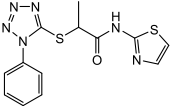
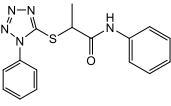
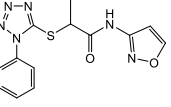
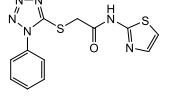
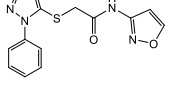
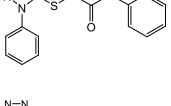
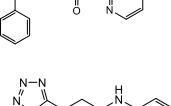
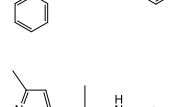
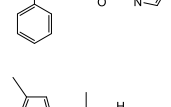
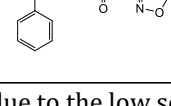
Inhibitory potencies of tetrazole analogs tested against DapE at 200 μM are listed in Table 3. Interestingly, tetrazole analogs with an alpha-proton in place of the alpha-methyl group are more potent with a significant increase in the percent inhibition. Compound **39d** shows 95.1% inhibition at 200 μM , where the corresponding racemic alpha-methyl tetrazole analog **39a** inhibits DapE only by 60.3% at the same concentration. A similar trend is observed between compound **39f** (92.4%) and **39b** (75.6%), indicating a possible steric clash of the alpha-methyl group with the amino acid residues in the DapE active site. This suggests that an alkyl group at the alpha position of tetrazole analogs might not be

critical in inhibitor binding leading to a stable inhibitor-enzyme complex. When comparing the inhibitory potencies of pyrazole analogs with the corresponding tetrazole parent compounds, an increased percent inhibition of DapE was seen with pyrazole analogs as in pyrazole **41a** (79.4%) vs tetrazole **39a** (60.3%). A moderate preference observed for the pyrazole moiety over tetrazole validates the importance of the nitrogen atom at position 2 of the pyrazole ring in inhibitor binding. In contrast, tetrazole nitrogen atoms in 3rd and 4th positions might not participate in ligand binding since the activity was not lost when the tetrazole was replaced with pyrazole, rather, pyrazoles are somewhat more potent than the respective tetrazoles as discussed above. IC₅₀s of inhibitors showed greater than 90% inhibition at 200 μM will be determined using the ninhydrin assay.



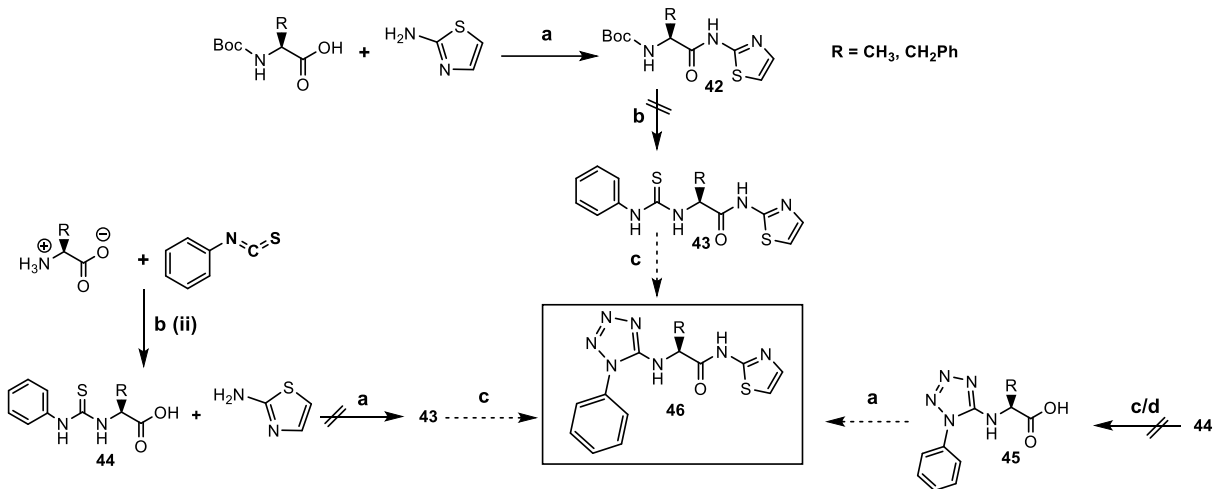
Scheme 15. Synthesis of (A) phenyl pyrazole thione **40** and (B) phenyl pyrazole thio-linked DapE inhibitors.

Table 3. Preliminary inhibition data and percent yields for selected tetrazole and pyrazole analogs.

Compound	Structure	% Yield	% Inhibition at 200 μ M
39a		34	60.3
39b		65	75.6
39c		45	0
39d		56	95.1
39e		68	67.4
39f		78	92.4
39g		38	100
39h		78	^[a] 39.5
41a		60	79.4
41b		50	61.4

^[a]Inhibition measured at 75 μ M due to the low solubility of the inhibitor at 200 μ M.

Encouraged by the docking results of the *N*-linked series, two synthetic routes were designed to prepare tetrazole inhibitors following the reported methods using Mukaiyama's reagent (2-chloro-1-methylpyridinium iodide)¹²⁵ and copper catalysts¹²⁶ via one-pot desulphurization/substitution/electro cyclization of the corresponding thiourea intermediate as illustrated in Scheme 16. The reaction proceeds through a nucleophilic substitution of the sulfur from thioureas by N_3^- forming an alkyl azide intermediate which then cyclizes to form the tetrazole ring. In the attempted synthetic routes, to synthesize tetrazoles analogs **46**, alanine/phenylalanine (route A) and thiourea **44** (route B) were coupled with 2-aminothiazole in two different routes anticipating making the thiourea-amide analog **43**, which should react with Mukaiyama's reagent forming a carbodiimide. Then the carbodiimide will react with sodium azide in a subsequent electrocyclization forming the 5-aminotetrazole (see Scheme 16).



Reagents and conditions: (a) EDCl.HCl, HOBT, NMM, anhyd. DMF, 50 °C, overnight; (b) (2 steps) (i) CF₃COOH, CH₂Cl₂, rt, 2h; (ii) 1M KOH, acetone, rt, 7h; (c) Mukaiyama's reagent, Et₃N, NaN₃, anhyd. DMF; (d) (2 steps) (i) Cu(OAc)₂·2H₂O, Et₃N, DMSO, rt, 1h; (ii) NaN₃, rt, 1h.

Scheme 16. Attempted synthetic routes in preparation of hit-derived tetrazole analogs **46**.

In either route, the synthesis of thiourea-amide analog **43** was not successful, presumably due to the intramolecular hydrolysis of the thiazole-amide bond where the nitrogen atom of the thiourea acted as a nucleophile in the presence of a Brønsted base. In both attempted routes, HPLC and NMR confirmed the formation of carboxylic acid analog **44** through hydrolysis. In addition, we approached the tetrazole analog synthesis by interchanging the order of the reactions specifically, the direct formation of 5-aminotetrazole intermediate **45** from alanine/phenylalanine was explored (route C, Scheme 16). Unfortunately, the tetrazole ring formation was not observed with either copper or with Mukaiyama's reagent. We hypothesize that the failure to form the tetrazole ring is due to the coordination of the carboxylic acid with the copper catalyst. When the carboxylic acid intermediate **45** is treated with Mukaiyama's reagent, a nucleophilic substitution of the chlorine on electrophilic carbon of Mukaiyama's reagent by the carboxylate under basic conditions is possible. Even the protected carboxylic acid, including the methyl and *tert*-butyl ester analogs of **44**, underwent hydrolysis to give the free carboxylic acid rather than the desired reaction.

We are investigating alternative reaction conditions to prepare the *N*-linked tetrazole and pyrazole analogs incorporating amino acids. One practical method reported by Batey and co-workers is to approach the formation of the tetrazole ring using C-terminus solid-supported precursors to avoid the above-mentioned side reactions of carboxylate.¹²⁵ With the protected carboxylic acid, the free amine of the amino acid can be reacted with phenyl isothiocyanate to form the thiourea intermediate **46** (see Scheme 16)

followed by electrocyclization with azide in the presence of Mukaiyama's reagent generating the *N*-substituted tetrazole compounds. The generic reactions are shown in Scheme 16. We believe that the development of efficient synthetic routes along with our in-house DapE inhibition assay will enable us to further explore the SAR of tetrazole and pyrazole series leading to the discovery of more potent inhibitors of DapE.

Inhibitory Potencies of Cyclobutanone Inhibitors of DapE

An *N*-functionalized 2-aminocyclobutanone library consisting α -benzamide-, α -nicotinamide- and α -sulfonamide-cyclobutanones was designed to act as covalent but reversible inhibitors of serine and metallo β -lactamases, di-zinc enzymes, and serine proteases. Cyclobutanones can inhibit most metallohydrolases through the reversible formation of a hydrated inhibitor-enzyme adduct bound to the active site metal center due to the inherent ring strain of the cyclobutanone scaffold. Thiabicyclo-cyclobutanone analogs of β -lactam antibiotics were reported to inhibit a class of di-zinc metallo β -lactamases,³² confirming that cyclobutanone-based compounds can provide inhibitors of metalloenzymes. Even though cyclobutanones are expected to bind to the di-zinc active site through hydrate oxygen coordination to the Zn(II) ions, a comprehensive map of the pharmacophore is unknown. Currently, co-crystallization experiments utilizing two potent inhibitors representing α -benzamide- and α -Ts-amino acid cyclobutanones (**12** and **48h**) are being performed by Dr. Nicole Inniss at CSGID. We believe that an inhibitor-bound DapE crystal structure will reveal the key binding interactions in ligand binding leading to inactivation of the enzyme as well as previously unknown possible allosteric binding sites

of DapE. Synthetic method development of our cyclobutanone library is extensively discussed in Chapter Two.

The cyclobutanone library was tested against the bacterial di-zinc enzyme, *HiDapE* using ninhydrin assay to study the inhibitory potencies and SAR of diversely substituted 2-aminocyclobutanone analogs as metalloenzyme inhibitors. Preliminary screening of the cyclobutanone was performed at 100 μM inhibitor concentration. We then analyzed the concentration-dependent inhibition (dose-response) of the inhibitors with above 70% inhibition at 100 μM through IC_{50} analysis. Interestingly, cyclobutanones showed promising inhibitory potencies against DapE where several analogs had measured IC_{50} s below 60 μM . Inhibitory data of cyclobutanones and two cyclobutanone isosteres **51** and **52** are listed in Tables 4 and 5.

DapE inhibition by cyclobutanones demonstrate an array of SAR with a preference for α -benzamide- and α -sulfonamide-cyclobutanones over α -nicotinamide- and quinoline-cyclobutanone analogs (**10m-10s**) where the highest inhibiting heterocyclic cyclobutanone, *N*-(2-oxocyclobutyl)quinoline-3-carboxamide (**10m**, Table 4) showed only 48% inhibition of DapE at 100 μM . α -Benzamide cyclobutanones with less polar *meta*- and *para*-aryl substituents showed higher percent inhibition than the corresponding halo substituted benzamides. Notably, *m*-chloro-benzamide cyclobutanone (**10c**) and *p*-bromo-benzamide cyclobutanone (**10e**) showed 34% and 25% inhibition, whereas *m*- CH_3 - (**10j**) and *p*- CH_3 -benzamide cyclobutanone (**10l**) showed 85% and 58% inhibition, respectively (see Table 4).

Table 4. Inhibition of DapE by α -benzamide- and α -sulfonamide-cyclobutanones.

Compound	Structure	IC ₅₀ (μ M) or % inhibition at 100 μ M	Compound	Structure	IC ₅₀ (μ M) or % inhibition at 100 μ M
10a		29%	10m		48%
10b		66.4 \pm 2.9	10n		0%
10c		34%	10o		25%
10d		46%	10p		26%
10e		25%	10q		0%
10f		24%	10r		35%
10g		29%	10s		0%
10h		59%	10t		52.4 \pm 7.4
10i		27%	11a		23%
10j		85%	11b		53.3 \pm 5.4
10k		17%	12		39.6 \pm 1.1
10l		58%	14		50%

Out of two sulfonamide cyclobutanones (**11a**, **11b**) tested, 4-fluoro sulfonamide cyclobutanone (**11b**) exhibited moderate inhibition of DapE with an IC_{50} of $53.3 \pm 5.4 \mu\text{M}$. In contrast, 4- CF_3 sulfonamide cyclobutanone (**11a**) showed only 23% inhibition at $100 \mu\text{M}$, about four times less potent than **11b** with a *p*-F group, indicating the selectivity toward polar aryl substituents at the *para* position. Moreover, a higher binding affinity of DapE was demonstrated toward both *p*- OCH_3 substituted benzamides, **10b** and **12** compared *p*- CH_3 - and *p*-Br benzamide cyclobutanone. Measured IC_{50} s for compound **10b** and **12** are $66.4 \pm 2.9 \mu\text{M}$ and $39.6 \pm 1.1 \mu\text{M}$, respectively suggesting that H-bond acceptors at 3,4,5 aryl positions might be crucial in inhibitor binding.

Benzimidazoles are heterocyclic aromatic systems containing a fused scaffold of an imidazole and a benzene ring. These structures are unique and typically found in bioactive compounds and pharmacophores of inhibitor molecules. Thus, benzimidazoles are privileged scaffolds in medicinal chemistry.¹²⁷ Benzimidazoles provide both an H-bond acceptor and a favorable H-bond donor via NH, potentially leading to stronger binding of an inhibitor. Further, the ability of benzimidazole to form salts makes this scaffold more appealing in designing water soluble and orally bioavailable drug candidates. It is rewarding that the benzimidazole cyclobutanone exhibited potency against DapE with an IC_{50} of $52.4 \pm 7.4 \mu\text{M}$. Exploring the SAR of benzimidazole cyclobutanone analogs is worthwhile in identifying more potent DapE inhibitors.

To our pleasant surprise, *N*-protected amino acid cyclobutanone analogs showed promising results during the preliminary assays with $100 \mu\text{M}$ inhibitor, as shown in Table

5. Briefly, it is clear that DapE selectively binds to amino acid-derived cyclobutanones consisting of hydrophobic side chains, including Phe and Val, regardless of the tosyl or Cbz group on the alpha-amino moiety. In comparison, Ts-L-Trp analog **48c** (20%) and Cbz-L-Tyr analog **54b** (16%) were significantly less potent than the corresponding Ts-L-Phe analog **48a** (93%) and Cbz-L-Phe analog **54c** (96%) indicating the presence of a hydrophobic binding region in the DapE active site that forms favorable hydrophobic binding interactions with the inhibitors enabling a stable inhibitor-enzyme complex. The L isomer of Ts-Phe cyclobutanone (**48a**) showed 93% inhibition, and the D-isomer **48b** showed an essentially identical inhibitory potency against DapE with 88% inhibition at 100 μM . This lack of preference was also observed between potent L- and D-isomers of Cbz-Phe cyclobutanone with 96% and 98% inhibition, respectively (**54c**, **54d**, see Table 5).

Table 5. Inhibition of DapE by peptidomimetic cyclobutanones.

Compound	Structure	% inhibition at 100 μM	Compound	Structure	% inhibition at 100 μM
48a		93%	52		36%
48b		88%	54a		54%
48c		20%	54b		16%
48h		100%	54c		96%
51		19%	54d		98%

Compound **48h** exhibited 100% inhibition, the highest inhibition of DapE at 100 μ M in the focused subset of peptidomimetic cyclobutanones (see Table 5). As of today, **48h** is the only D-valine analog that consists of an *N*-terminus 4-OCH₃-benzene sulfonamide we have successfully synthesized and tested against DapE. Therefore, to draw conclusions based on the inhibitory potency of **48h**, we require to synthesize and test at least a few more analogs incorporating D-Val, L- and D-Phe and also replace the 4-OCH₃ group with CH₃, CF₃, and H to investigate the role of the 4-OCH₃ group in inhibitor binding.

Two cyclobutanone isosteres containing hydroxyl groups, namely, Ts-L-Phe isopropanol (**51**) and Ts-L-Phe cyclopropanol (**52**) derivatives were tested to validate the importance of cyclobutanone moiety in the binding and inhibition of DapE. As expected, the loss of cyclobutanone ring resulted in less potent inhibitors where compound **51** only showed 19% inhibition and compound **52** exhibited only 36% inhibition compared to the corresponding Ts-L-Phe cyclobutanone (**48a**) with 93% inhibition at 100 μ M (see Table 5). IC₅₀ determination of amino acid derivatives of cyclobutanone inhibitors with >70% inhibition at 100 μ M is in progress.

Through the DapE inhibition assay, we demonstrated that cyclobutanones could provide potent inhibitors of di-zinc metalloenzymes. We hypothesize that cyclobutanone inhibitors may find applications beyond just DapE as metalloenzyme inhibitors containing a general class of reactive group. Our rational design approaches in the synthesis of peptidomimetic cyclobutanones will be discussed in Chapter Four.

Dose-Response Curves of Cyclobutanone Inhibitors and Observed Hill Coefficients

Hill Equation

DapE inhibitory data from the ninhydrin assay was processed where IC_{50} s and kinetic constants were obtained by fitting the data following the modified Hill equation. The Hill equation was originally introduced by A.V. Hill in 1910 to describe the sigmoidal binding curve of the equilibrium relationship between oxygen tension and the percent saturation of haemoglobin with oxygen. The original Hill equation is utilized in studying non-linear biochemical and physicochemical reactions, including enzymatic reactions through the determination of three kinetics parameters: V_{max} , $X_{0.5}$, and n .¹²⁸ The general Hill equation can be expressed as, $V = V_{max} X^{nH} / (X^{nH_{0.5}} + X^{nH})$. The maximum velocity can be achieved at saturating concentrations of the substrate is V_{max} , X is the concentration of the substrate, $X_{0.5}$ is the substrate ($S_{0.5}$) concentration at 50% maximum velocity, and Hill coefficient is denoted as n_H .

In pharmacology, to study the biological effect of drug vs the drug/inhibitor concentration, it is required to incorporate a baseline response V_0 in the mathematical expression. V_0 is the velocity/effect in the absence of a drug or an inhibitor in inhibition assays. Thus, the fundamental Hill equation is modified to generate the four-parameter fit (4PL). Dose-response curves for inhibitors and drugs are typically plotted and analyzed using 4PL fits enabling the estimation of IC_{50} , background (V_0), V_{max} , and Hill coefficient (n_H).^{125, 128} The modified Hill equation utilized in our experiments is as follow, $V = V_0 + (V_{max}-V_0) X^{nH} / (X^{nH_{0.5}} + X^{nH})$. The velocity in the absence of the substrate is V_0 , the velocity

at saturating concentrations of the substrate or with no inhibitor for the inhibition assay is V_{\max} , X is the concentration of the substrate or inhibitor, $X_{0.5}$ is the substrate ($S_{0.5}$), and inhibitor ($I_{0.5}$) concentration at 50% maximum velocity and 50% inhibition, respectively.

Experimental IC₅₀ Curves and Hill Coefficients

Experimental IC₅₀ curves for cyclobutanone inhibitors against DapE were identified as sigmoidal shaped response curves as opposed to simple hyperbolic plots. Further, the calculated Hill coefficients were greater than one, with an average value of 2.8 for all four cyclobutanone inhibitors analyzed for IC₅₀ determinations. IC₅₀ curves with the corresponding Hill coefficients are reported in Appendix B. Experimental Hill coefficients may provide information on the number of binding sites of a biological target (receptors and enzymes) interacting with ligands.¹²⁹ Although $n_H > 1$ could demonstrate the cooperative binding mechanism of ligands with the target enzyme, a Hill coefficient alone does not represent the type of inhibition and is not adequate to distinguish between competitive, non-competitive, or allosteric binding mechanisms. It is suggested that elucidating mathematical expressions and data fitting for enzyme dose-response curves in the presence of an inhibitor could be challenging compared to the dose-response curves for receptors because of the inclusion of the substrate concentration as an additional unknown parameter.¹²⁹

It is important to note that DapE is a dimer with two explicit di-zinc binding sites located in the catalytic domain. Furthermore, DapE exists in a dynamic conformational change between open and closed conformers likely triggered by native substrate binding

leading to an active closed form of the enzyme. Therefore, competitive, non-competitive, or allosteric DapE inhibitors are expected to provide Hill coefficients greater than one indicating the number of inhibitor-bound binding sites. For example, if two inhibitor molecules bind to both di-zinc active sites of each subunit, the calculated Hill coefficient for this particular inhibitor could be at least two or greater than two in the case of allosteric inhibition at higher inhibitor concentrations that involves an allosteric binding site. Experimental Hill coefficients for DapE cyclobutanone inhibitors were 2-3 within the error range consistent with the statement supported by statistics that the maximum experimentally calculated Hill coefficient should be equal to or smaller than the number of binding sites interacting with the ligands in facilitating the biological response. Based on the mounting high-throughput screening experimental evidence, it is concluded that the shape of the dose-response curve and the corresponding Hill coefficient are determined based on the type of ligand under study.¹²⁹ Presently, binding modes of cyclobutanone inhibitors and the mechanism leading to the inactivation of DapE are unknown. We believe that crystal structures of DapE bound to cyclobutanone inhibitors will validate the mechanism of inhibition and provide structural insight into ligand binding modes.

Conclusion

Among our previously reported crystal structure of DapE, we recently reported a new atomic-resolution (1.3 Å) X-ray crystal structure of *NmDapE* (PDB ID: 5UEJ) with sulfate ions bound in the substrate binding pocket. Our TMD simulations performed utilizing the new 1.3 Å DapE crystal structure indicated that DapE inhibitors that result in a

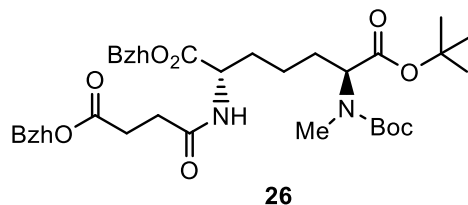
closed or partially closed structure upon binding the enzyme might be energetically favored over the inhibitors that solely bind the open conformer of DapE. Furthermore, TMD results and the new high-resolution DapE structure provided critical information in better understanding the structural changes and key binding interactions in catalysis. Specifically, the importance of the Coulombic interactions between negatively charged carboxylates of L,L-SDAP substrate, and active site Arg residues in ligand binding was highlighted by the sulfates bound in the active site in the new 1.3 Å DapE crystal structure. These data combined with our previously published crystal structures of DapE from various organisms, including *NmDapE* and *HiDapE* provided a fundamental understanding of the structural features, mechanistic insights of DapE. Furthermore, these results enabled us to identify crucial active site residues responsible for both catalysis and substrate identification, which will guide us in the rational design of novel DapE inhibitors and in lead optimization to develop more potent inhibitors.

The thioamide analog of *N*-methyl-L,L-SDAP will be synthesized as a TFA salt and will be tested against DapE in our ninhydrin assay to study the affinity of this substrate analog toward DapE. We expect that *N*-methyl-L,L-SDAP thioamide analog **28** may inhibit DapE through stronger coordination with the active site zinc ions and the rate of catalytic hydrolysis of the thioamide should be lower due to the low electrophilicity of the thiocarbonyl center. Further, co-crystallization of DapE with *N*-methyl-L,L-SDAP thioamide analog should provide us a substrate-bound crystal structure of DapE that will allow us to map the key active site residues in substrate binding and identification. Inhibition of DapE

by the *N*-difluoromethyl-sulfonamide series was established by synthesizing and determining the inhibitory potencies of the original hit, *N*-difluoromethyl-(*o*-methoxy)-sulfonamide (**32**), that gave a calculated IC₅₀ of 72.9 μM, and *p*-methoxy analog **34** was more potent than the original hit with an IC₅₀ of 52.6 μM. In addition, we pursue tetrazole and tetrazole isosteres, namely, pyrazole-based inhibitors, where we have successfully synthesized a set of thio-linked tetrazoles and pyrazole inhibitors. This series shows promising inhibition of DapE in a single concentration screening with a few analogs inhibit up to 100% at 200 μM. IC₅₀ determinations of the highest inhibiting analogs are in progress. Cyclobutanone-based compounds were identified as a new class of DapE inhibitors, and so far, inhibitory potencies of four cyclobutanones were demonstrated where more potent cyclobutanone inhibiting DapE showed an IC₅₀ of 39.6 μM. We are currently working on co-crystallization experiments of DapE using two cyclobutanone inhibitors as well as both *N*-difluoromethyl-sulfonamide inhibitors. Crystal structures of inhibitor-bound DapE will shed light on structural insights and guide us in designing more potent inhibitors of DapE as well as aid in optimizing identified lead compounds.

Experimental

Synthesis of *N*⁶-methyl-*L,L*-SDAP thioamide analog: 1-benzhydryl 7-(*tert*-butyl) (2*S*,6*S*)-2-(4-(benzhydryloxy)-4-oxobutanamido)-6-((*tert*butoxycarbonyl)(methyl)amino) heptanedioate (26)

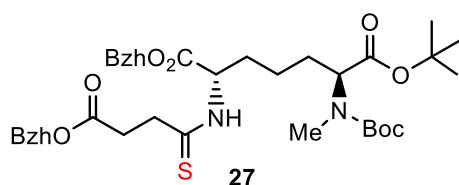


(2*S*,6*S*)-7-(*tert*-Butoxy)-6-((*tert*-butoxycarbonyl)(methyl)amino)-2-(3-carboxypropanamido)-7-oxoheptanoic acid (**22**) was synthesized by following our published *N*-Me-SDAP synthetic method (PLoS ONE, 2018).⁸³ Diphenyldiazomethane was prepared from benzophenone via benzophenone hydrazone following the general literature procedures published by Yang,¹³⁰ Tian,¹³¹ and Schmitt.¹³²

A vial was charged with a magnetic stirrer and (2*S*,6*S*)-7-(*tert*-butoxy)-6-((*tert*-butoxycarbonyl)(methyl)amino)-2-(3-carboxypropanamido)-7-oxoheptanoic acid (**22**) and the vial was sparged with argon for one minute. Then, dry methylene chloride was injected to the vial and the mixture was stirred at room temperature until the solid dissolved. The reaction mixture was then cooled to 0 °C in an ice bath. To the stirring reaction mixture at 0 °C, freshly prepared diphenyldiazomethane was added in excess until the solution retained the purple color. The reaction was then allowed to warm up to room temperature and stirred at room temperature for one hour. Completion of the reaction was monitored by TLC (diethyl ether/hexane = 10:90). Upon completion, solvent was evaporated off and

the crude was purified through a flash column in a gradient elution starting with neat hexane to diethyl ether/hexane (90/10). Combined fractions gave compound **26** (41.5 mg, 47%) as a white solid. ^1H NMR (500 MHz, CDCl_3) δ 7.36 – 7.28 (m, 20H), 6.87 (s, 2H), 6.12 (NH, dd, $J = 8.0, 2.9$ Hz, 1H), 4.73 (q, $J = 6.8$ Hz, 0.5H, amide rotamers of α -protons), 4.67 (td, $J = 7.8, 4.9$ Hz, 0.5H, amide rotamers of α -protons), 4.45 (dd, $J = 10.7, 4.8$ Hz, 1H), 2.83 – 2.75 (m, 2H), 2.68 (d, $J = 12.9$ Hz, 3H), 2.53 (t, $J = 7.1$ Hz, 2H), 1.89 – 1.81 (m, 2H), 1.46 – 1.39 (m, 20H), 1.25 (t, $J = 7.5, 6.6$ Hz, 2H). ^{13}C NMR (126 MHz, CDCl_3) δ 171.69, 171.33, 171.01, 170.92, 170.75, 156.45, 140.05, 139.98, 139.58, 139.39, 139.29, 128.62, 128.56, 128.49, 128.21, 128.11, 128.05, 127.91, 127.89, 127.22, 127.09, 127.03, 126.98, 126.95, 81.27, 80.06, 79.84, 78.13, 60.39, 59.64, 58.38, 52.17, 52.03, 31.96, 31.79, 30.84, 30.74, 29.72, 28.60, 28.39, 28.37, 28.03, 21.93, 21.84.

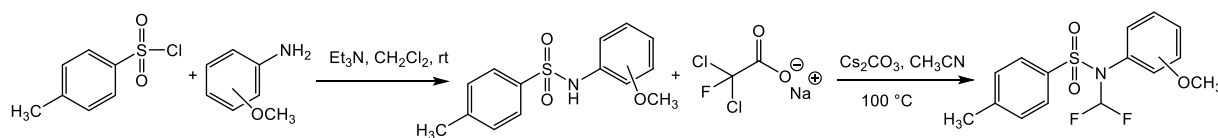
Synthesis of 1-benzhydryl 7-(tert-butyl) (2S,6S)-2-(4-(benzhydryloxy)-4-oxobutanethioamido)-6-((tert-butoxycarbonyl)(methyl)amino)heptanedioate (27)



Protected succinamide **26** (19.7 mg, 0.027 mmol) and P_2S_5 -pyridine complex (10.3 mg, 0.027 mmol) were heated in dry acetonitrile (270 μL , 0.1 M) at 60 $^\circ\text{C}$ for 26 hours under nitrogen. Once the reaction was deemed complete by HPLC analysis at both 254 nm and 220 nm and the solvent was evaporated off under reduced pressure. Then, the crude was partitioned between water (1 mL) and ethyl acetate (1 mL) and the organic product

was extracted using ethyl acetate (1 mL x 5). The combined organic layers were washed with brine (2 mL), dried over Na₂SO₄, and concentrated under reduced pressure to give the crude product as a yellow foam-like solid (17.5 mg). The crude was purified by column chromatography using diethyl ether/hexane (40/60) to provide compound **27** a colorless solid (10 mg, 46%). ¹H NMR (500 MHz, CDCl₃) δ 7.40 – 7.28 (m, 20H), 6.94 – 6.86 (m, 1H), 6.17 (NH, d, 1H), 5.21 (dq, *J* = 32.7, 6.5 Hz, 1H), 4.46 (ddd, *J* = 15.6, 10.7, 4.7 Hz, 1H), 3.06 – 2.91 (m, 4H), 2.70 (dd, *J* = 11.2, 5.9 Hz, 3H), 1.99 (dt, *J* = 16.2, 6.0 Hz, 2H), 1.86 (d, *J* = 11.8 Hz, 2H), 1.48 – 1.42 (m, 18H), 1.34 (t, 3H). ¹³C NMR (126 MHz, CDCl₃) δ 203.86, 203.65, 172.02, 171.72, 171.15, 170.78, 170.41, 156.45, 155.79, 140.04, 139.94, 128.63, 128.56, 128.49, 127.95, 127.93, 127.89, 127.34, 127.12, 127.09, 127.03, 126.98, 81.33, 80.09, 79.91, 78.39, 78.13, 60.40, 59.66, 40.52, 40.41, 33.30, 33.20, 30.91, 30.58, 28.38, 28.18, 28.03, 21.94, 21.86.

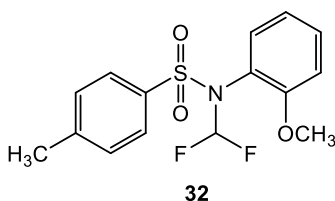
General Procedure for Synthesis of *N*-(Difluoromethyl)-sulfonamide DapE Inhibitors (**32** and **34**)



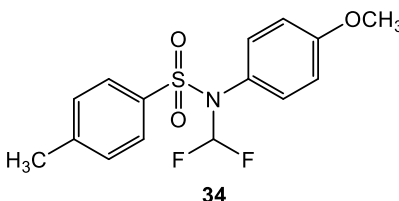
In a pressure flask, *N*-(2-methoxyphenyl)-4-methylbenzenesulfonamide/*N*-(4-methoxyphenyl)-4-methylbenzenesulfonamide (100 mg, 0.36 mmol), sodium chlorodifluoroacetate (164.9 mg, 1.08 mmol) and cesium carbonate (381 mg, 1.08 mmol) were suspended in anhydrous acetonitrile (3.6 mL, 0.1 M) and the reaction was refluxed at

100 °C under nitrogen with periodic TLC (ethyl acetate/hexane = 40/60) and HPLC monitoring. Upon completion, acetonitrile was evaporated off, and the resultant crude was suspended in water (4 mL). The organic product was extracted using ethyl acetate (4 x 3 mL), and the combined organic layers were dried over Na₂SO₄. Then the solvent was removed by evaporation under reduced pressure providing a crude product mixture as a yellow oil which was purified by column chromatography on a Teledyne Isco Rf 200 flash chromatography unit to afford the corresponding *N*-(difluoromethyl)-sulfonamide.

***N*-(Difluoromethyl)-*N*-(2-methoxyphenyl)-4-methylbenzenesulfonamide (32)**



The reaction was refluxed at 100 °C for 7 days. The crude (107.6 mg) was eluted through a flash column using ethyl acetate/hexane (10/90) and *N*-difluoromethyl *o*-CH₃-sulfonamide **32** was isolated as a clear crystalline solid (79.9 mg, 68%): mp = 84-86 °C. ¹H NMR (500 MHz, CDCl₃) δ 7.62 (t, *J* = 61.4 Hz, 2H), 7.38 (ddd, *J* = 8.3, 7.4, 1.8 Hz, 1H), 7.30 – 7.27 (m, 2H), 7.18 (t, *J*_{H-F} = 60.9 Hz, 1H), 6.94 (dd, *J* = 7.8, 1.8 Hz, 1H), 6.91 (dd, *J* = 8.4, 1.3 Hz, 1H), 6.87 (td, *J* = 7.6, 1.3 Hz, 1H), 3.60 (s, 3H), 2.44 (s, 3H). ¹³C NMR (126 MHz, CDCl₃) δ 158.37, 144.37, 136.29, 133.41, 131.70, 129.45, 128.01, 120.36, 119.62, 111.49 [(113.20, 111.22, 109.24) t, *J*_{C-F} = 249.4, 248.0 Hz), 112.30, 77.28, 77.03, 76.78, 55.61, 21.62.

***N*-(Difluoromethyl)-*N*-(4-methoxyphenyl)-4-methylbenzenesulfonamide (**34**)**

The reaction was refluxed at 100 °C for 36 hours. The crude product of **34** was eluted in step-gradient of 100% hexane (50 mL), 5% ethyl acetate in hexane (50 mL), and 10% ethyl acetate in hexane (60 mL) providing *N*-difluoromethyl *p*-OCH₃-sulfonamide **34** as a clear colorless oil (81.3 mg, 69%). ¹H NMR (500 MHz, CDCl₃) δ 7.60 – 7.51 (m, 2H), 7.29 (dd, *J*_{H-F} = 64.0, 58.7 Hz, 1H), 7.31 – 7.25 (m, 2H), 6.99 – 6.92 (m, 2H), 6.85 – 6.78 (m, 2H), 3.79 (s, 3H), 2.44 (s, 3H). ¹³C NMR (126 MHz, CDCl₃) δ 160.63, 144.74, 135.18, 132.80, 129.71, 127.96, 123.25, 114.31, 112.99, 111.02 (t, *J*_{C-F} = 248.0 Hz), 109.04, 55.43, 21.66.

DapE Enzyme Inhibition by Sulfate: IC₅₀ Determination

The inhibition of *HiDapE* by sulfate was assessed using lithium sulfate following the protocol detailed by us previously.⁸³ Sulfate inhibition assays were conducted with a reaction volume of 200 μL, 2 mM *N*⁶-methyl-L,L-SDAP,⁸³ and 8 nM *HiDapE*. To a 50 mM HEPES, pH 7.5 buffered solution at 0 °C was added lithium sulfate followed by *HiDapE* and incubated for 10 min. *N*⁶-Methyl-L,L-SDAP was added and allowed to react for 10 min followed by heating to 100 °C for 1 min and cooled on ice to 0 °C. A 2% ninhydrin solution (100 μL) was added, and the mixture was vortexed. The reaction was heated to 80 °C for 15 min followed by cooling on ice. The absorbance of an 80 μL aliquot was recorded at 570 nm on a BioTek Synergy 2 microplate reader. The inhibition assay of *HiDapE* by lithium sulfate

was performed in triplicate, and the IC_{50} was determined to be 13.8 ± 2.81 mM. The IC_{50} and kinetics constants were obtained by fitting the data following modified Hill equation: $V = V_0 + (V_{max} - V_0) X^{n_H} / (X^{n_H_{0.5}} + X^{n_H})$ using the graphing suite Origin 9.1 with the Levenberg-Marquardt non-linear least-squares algorithm. The velocity in the absence of the substrate is V_0 , the velocity at saturating concentrations of the substrate or with no inhibitor for the inhibition assay is V_{max} , X is the concentration of the substrate or inhibitor, $X_{0.5}$ is the substrate ($S_{0.5}$), and inhibitor ($I_{0.5}$) concentration at 50% maximum velocity and at 50% inhibition, respectively. Hill coefficient is represented as n_H .

Kinetic Studies

A discontinuous kinetic assay was performed on a Techne PCR Thermal Cycler System utilizing a modified ninhydrin assay protocol⁸³. The volume of each component was adjusted to fit the total reaction volume of 50 μ L, and the enzyme concentration was 0.12 μ M. Inhibition of *HiDapE* with 10 mM, 20 mM, and 30 mM lithium sulfate was studied in triplicate while changing the substrate concentration from 0.5 mM to 5.5 mM. The amount of *N*-methyl-L,L-DAP formed over 10 minutes was monitored by measuring the absorbance of the complex formed by reacting *N*-methyl-L,L-DAP with 2% ninhydrin. The enzymatic activity was reported as the rate of formation of the product, *N*-methyl-L,L-DAP in absorbance unit per minute (AU/min). The kinetic constants were reproducible within \pm 10% using the modified Hill equation utilizing the Levenberg-Marquardt non-linear least-squares algorithm.

DapE Enzyme Inhibition: IC₅₀ Determinations

The inhibition of *HiDapE* by synthesized inhibitors was assessed using a modified ninhydrin assay protocol of our original published protocol.⁸³ All the inhibition assays were performed on a Thermo Fisher MiniAmp PCR Thermal Cycler. Assays were conducted with a reaction volume of 100 μ L, 2 mM *N*⁶-methyl-L,L-SDAP, 8 nM *HiDapE*. Inhibitors that are insoluble in HEPES buffer were dissolved in neat DMSO (stock stored at -10 °C), and the pre-assay concentrations were adjusted to give a final concentration of 5% DMSO in the assay. To a 50 mM HEPES pH 7.5 buffered solution at 30 °C was added the selected inhibitor followed by *HiDapE* and incubated for 10 min. *N*⁶-Methyl-L,L-SDAP was added and allowed to react for 10 min followed by heating at 100 °C for 1 min and cooled to 0 °C. A 2% ninhydrin solution (100 μ L) was added, and the mixture was vortexed/mixed well by pipetting while cooled at 0 °C. The reaction was then heated at 80 °C for 15 min. The absorbance of an 80 μ L aliquot was recorded at 570 nm on a BioTek Synergy 2 microplate reader. All the inhibition assays of *HiDapE* were performed in triplicate, and the IC₅₀s were determined by fitting the data following the modified Hill equation as explained above. Inhibition plots (IC₅₀) are included in Appendix B.

Molecular Docking Protocol

Recent docking experiments utilized the new 1.30 Å resolution DapE structure from *Neisseria meningitidis* (PDB ID: 5UEJ) as the docking receptor due to the high quality of refinement at the dimerization loops that is critical in substrate binding. Ligand molecular models were generated using Molecular Operating Environment (MOE) computational

suite's Builder utility. Protonation states of ligands were optimized at pH 7.4 and relaxed through energy minimization in the gas phase using the MMFF94X1 force field. Ligand models were then sampled via a conformational search that generates energetically reasonable 3D atomic configurations of ligands with or without geometric constraints and analyzed for potential energy local minima. Depending on the ligand, a set of stable conformers or the most stable conformer was identified as the preferred docking ligand model. Then the X-ray crystal structure of *NmDapE* (PDB ID: 5UEJ) was loaded into MOE and prepared for docking using MOE's Structure Preparation utility. The hydrogen-bonding network of the docking receptor was further optimized at physiological conditions (pH 7.4, T = 310 K) by automatically sampling different tautomer/protomer states using Protonate3D, which calculates optimal protonation states, including titration, rotamer, and "flips" using a large-scale combinatorial search. The substrate-binding pocket of chain A/B where the di-zinc metal center is located was analyzed using MOE's Site Finder utility and populated with inactivated dummy atoms that define the docking location. Following preparation of the *NmDapE* docking receptor model, an induced-fit molecular docking using the previously identified ligand conformers (a database or a single conformer) was carried out with solvent atoms inactivated at the docking site. The docking site was specified by the dummy atoms populating the substrate-binding site of the docking receptor. The Alpha triangle placement with Affinity dG scoring generated 1000 data points, which were further refined using the induced fit method with GBVI/WSA dG scoring to obtain the top 300 docking results. These calculations were performed using

Amber12:EHT3 force field. Then the ligand poses were analyzed and selected based on the docking score and the observed desired interactions. For DapE inhibitors, the top ligand docking poses that coordinate to the active site zinc ions along with other favorable interactions (Coulombic and hydrophobic) were selected.

CHAPTER FOUR
DESIGN AND SYNTHESIS OF INHIBITORS TARGETING DRUGGABLE ENZYMES OF
SARS-COV-2 THROUGH COMPUTER-AIDED DRUG DESIGN

Introduction

In December 2019, a new species of coronavirus was identified. This novel coronavirus was reported as the cause of the epidemic of severe respiratory infections in Wuhan, the capital of the Hubei province of China.¹³³ The disease caused by the novel severe acute respiratory syndrome coronavirus 2 (SARS-CoV-2) is designated as coronavirus disease 2019 (COVID-19).¹³⁴ As of today (April 2021), this fatal and highly contagious coronavirus has caused 143 million COVID-19 cases globally, resulting in 3 million deaths. In the United States alone, up to 31.9 million COVID-19 cases were reported.¹³⁵ In the scientific community, there is a consensus that SARS-CoV-2 originated from bat coronaviruses,¹³⁶ yet the origin of the coronavirus outbreak is unknown and is still under investigation.¹³⁷

Coronaviruses

Viruses are parasitic microorganisms that lack the ability to replicate in the absence of a host. A virus is made up of a core of genetic material, either DNA or RNA, encapsulated in a protective layer called a capsid comprised of protein, lipid, or glycoprotein. The nucleic acid genome and the capsid, collectively known as a virion, is the infectious particle.

Viruses replicate and reproduce by manipulating the host cell machinery to transcribe the viral genetic material to synthesize the critical proteins and the viral genome.¹³⁸ SARS-CoV-2 is an airborne virus that transmits from person-to-person contact.¹³⁹ The typical symptoms of the SARS-CoV-2 infection are cough, fever, shortness of breath, fatigue, loss of taste and smell, and as an additional adverse effect, the virus can cause atypical pneumonia.¹³³ Coronaviruses (CoVs) belong to the *Coronaviridae* family, a large family of single-stranded, positive-sense RNA viruses that can infect animals and humans.

Coronaviruses can cause respiratory, hepatic, gastrointestinal, and neurologic diseases.¹⁴⁰

The RNA genomes of this family of viruses are the largest genomes of all RNA viruses and vary in size from 25 to 32 kilobases.¹⁴¹ CoVs are classified into four genera: α -coronavirus, β -coronavirus, γ -coronavirus, and δ -coronavirus.¹⁴² SARS-CoV-2, severe acute respiratory syndrome-CoV (SARS-CoV), and Middle East respiratory syndrome-CoV (MERS-CoV) are categorized as β -coronaviruses. The SARS-CoV epidemic was first reported in China in November 2002, and within a year, the virus was transmitted to other parts of the world.¹⁴³ Globally, SARS cases were reported in 29 countries, with 8,096 patients leading to 774 deaths. A decade later, in 2012, the MERS epidemic originated in Saudi Arabia¹⁴⁴ and continues to cause endemics in Middle Eastern countries and occasionally cases reported in other regions of the world.¹⁴⁵

Genetically, SARS-CoV-2 is closely related to SARS-CoV as it shares about 79.5% genomic identity with SARS-CoV,¹⁴⁶ but only about 50% similarity with MERS-CoV.¹⁴⁷ The 5' end of the coronavirus genome encodes the viral replicase-transcriptase (a functional

protein), while the 3' end encodes the viral structural proteins.¹⁴⁷ There are four conserved structural proteins that make virions of coronaviruses: the spike (S) protein, which is responsible for binding to host cell receptors and virus entry into cells; the membrane (M) protein; the envelope (E) protein, which facilitates virion assembly, budding, envelope formation; and the nucleocapsid (N) protein. N protein and genomic RNA make up the nucleocapsid.¹⁴¹

Development of Therapeutic Agents against SARS-CoV-2

Academic researchers and pharmaceutical companies are working toward the development of therapeutic agents that can treat COVID-19, including inhibitors of SARS-CoV-2 target enzymes. In this global effort, some researchers were focused on repurposing clinically approved drugs at the early stages of the SARS-CoV-2 outbreak to accelerate COVID-19 therapeutics following the WHO's guidance. This approach was effective in identifying remdesivir, and possibly lopinavir as potential anti-SARS-COV-2 agents. In October 2020, the FDA issued an emergency use authorization (EUA) of remdesivir for the treatment of COVID-19 in hospitalized adult and pediatric patients.¹⁴⁸

Among other reports of repurposed drugs targeting SARS-COV-2, our collaborator, Dr. Prakasha Kempaiah from the Mayo Clinic, Florida, published a detailed computer-aided drug design (CADD) method that is enabled through a high-throughput virtual screening (HTVS) in identifying potential anti-SARS-CoV-2 agents.¹⁴⁹ The virtual screen revealed Bisindolylmaleimide IX (BIM IX), a known inhibitor of protein kinase C isoforms, as an inhibitor of SARS-CoV-2 main protease (also known as 3CLpro).¹⁵⁰

The role of repurposed drugs in treating COVID-19 and mitigating the symptoms in some patients has been verified.¹⁴⁸ A vaccine is a sustainable answer to a highly infectious disease. However, while vaccination of the general population is proceeding, many countries are experiencing a second wave of the SARS-CoV-2 pandemic. SARS-CoV-2 continues to mutate, and as of today, six different variants have been identified in the USA alone. These genetic variations of the virus can affect transmission, virulence and might compromise the effectiveness of existing vaccines.¹⁵¹ A global effort to develop an antiviral drug to treat COVID-19 is an ongoing process along with other potential therapies, including monoclonal antibodies. However, currently, there are no clinically approved anti-SARS-CoV-2 drugs.¹⁵² Thus, the development of small-molecule drugs to selectively target SARS-CoV-2 is a crucial clinical need, especially as the virus continues to mutate.

Computer-aided Drug Design and Target Identification

Computer-aided drug design (CADD) is an attractive tool of the modern drug discovery process that enables the search and optimization of potential lead compounds with a considerable saving of time and cost.¹⁴⁹ CADD is advantageous over high-throughput screening (HiTS) assays to identify drug targets and hits of highly contagious pathogens with little or no prior knowledge, as in the case of SARS-CoV-2. In this project, we virtually screened 80 cyclobutanone compounds using Schrödinger docking suite (LLC 2020-1) against potential targets of SARS-CoV-2. The list of the target enzymes and the descriptions are reported in the section below. The computer simulations were performed by Dr. Yash Gupta at Stritch Medical School.¹⁵⁰

Method Outline

The 3D structures were obtained from Protein Data Bank (PDB) X-ray crystal structures, and the predicted structures (homology modeled) were obtained from the I-Tasser server.¹⁵³ The energy minimizations and accompanying relaxations of 3D structure models (crystal structures and modeled proteins) were performed using the Protein Preparation Wizard, followed by a short 20 ns MD simulation.¹⁵⁴ Active site identification was performed utilizing data mining and COACH predictions, followed by a high-throughput virtual screening (HTVS) of *N*-functionalized 2-aminocyclobutanones and their corresponding hydrates. The screening was performed in three consecutive docking processes (HTVS, SP, and XP) using the Virtual Screening Wizard.¹⁵⁴ Preliminary *in silico* virtual screening provided potential inhibitors depending on the criteria, including energy, docking parameters, ligand and binding site strain energies, and fit scores. Compounds were classified based on their selective binding to each target protein and were further analyzed for binding free energy perturbation by the molecular mechanics' method using Prime MM-GBSA.¹⁵⁴ Lead compounds were prioritized based on the binding free energies of the hits. Molecular dynamic simulations (MDS) using the Desmond module were performed on the highest scoring lead compounds from each target group to validate our *in-silico* screening method (see Figure 24).

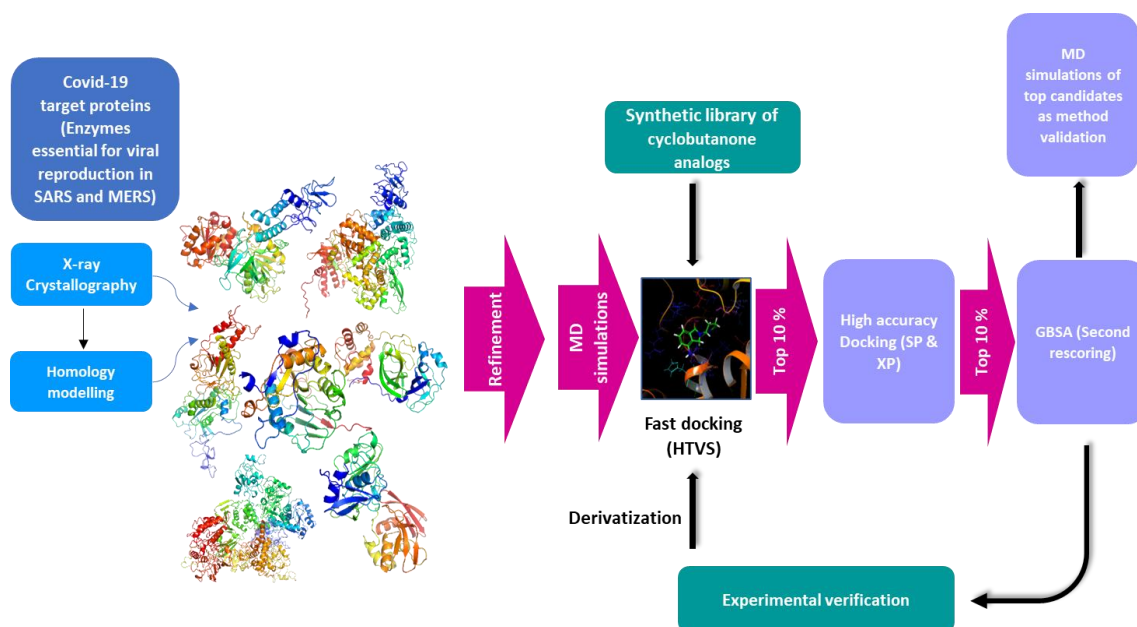


Figure 24. Schematic roadmap of the *N*-functionalized 2-aminocyclobutanone library screening against the seven SARS-CoV-2 target proteins. 3D protein models from the Protein Data Banks and other sources were optimized and relaxed by MD simulations. Active sites of the minimized structures were then mapped, and a GLIDE Grid was generated for a high-throughput virtual screening. The top 10% of the candidates were then subjected to high accuracy SP and XP dockings. The resultant top 10% were further refined in subsequent secondary rescoring (GBSA). Our method was validated via MD simulations of the highest scoring lead molecules specific to each target pool.¹⁵⁰

Target Identification

Functional proteins including enzymes, are common drug targets since the inactivation of a critical enzyme is detrimental to the microorganism. Thus, enzymes are preferred antiviral drug targets over structural proteins of a virus. SARS-CoV-2 produces about 29 known proteins that are classified into structural and nonstructural (functional) proteins. Seven key nonstructural proteins in the viral lifecycle, namely 3CLpro, PLpro, RdRP, Helicase, NendoU, ExoN, and 2OMT (see Figure 25), were virtually screened following the method outlined in Figure 24.

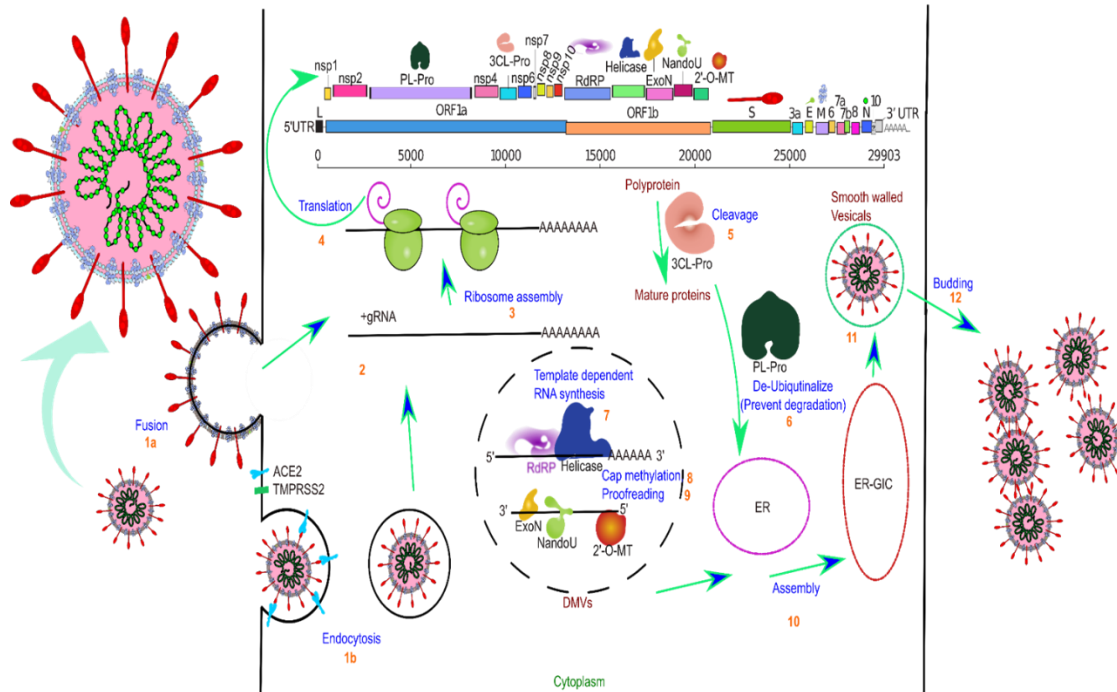


Figure 25. The SARS-CoV-2 life cycle highlighting HTVS target proteins. Replicase translates the viral genomic RNA to synthesize pp1a and pp1ab, two replicase polyproteins (4). These polyproteins are proteolytically cleaved by two proteases, PLpro and 3CLpro, producing 16 nonstructural proteins (5). Viral Helicase is responsible for accelerating the required folding in viral replication (7). RdRp catalyzes the template synthesis of RNA genome that is critical in viral-host cell replication. ExoN is a viral exoribonuclease. Both 2'-O-MT (8) and ExoN are critical for coronaviruses to escape the recognition of viral RNA by the host immune system (9). NandoU is suggested to suppress the host cell immune response.¹⁵⁰

Coronavirus replicase is part of the transcription machinery that mediates the translation of most of the viral genomic RNA to synthesize two replicase polyproteins, pp1a and pp1ab (see Figure 25). These two polyproteins are proteolytically cleaved by two proteases, the coronavirus main protease or 3-Chymotrypsin-Like Protease (3CLpro) and Papain-Like Protease (PLpro), producing 16 nonstructural proteins (Nsp1 to Nsp16). These nonstructural proteins are enzymes responsible for core enzymatic functions involved in RNA synthesis and host immune evasion.¹⁵⁵ Viral proteases are proven to be effective drug

targets that resulted in several approved drugs. For example, the human immunodeficiency virus (HIV) drug ritonavir targets an aspartyl protease, and telaprevir, a hepatitis C virus (HCV) drug inhibits a serine protease.

Main Protease (M^{pro})

The main protease of SARS-CoV-2 is one of the target enzymes extensively investigated for designing inhibitors due to its unique characteristics, including the recognition of a specific amino acid sequence during catalysis. The first drug candidate against SARS-CoV-2 to reach Phase 1 clinical trials (as of April 2021) is an inhibitor of the main protease developed by Pfizer. A combination of lopinavir-ritonavir (HIV-protease inhibitors) was shown effective against SARS-CoV-2 by inhibiting the main protease.¹⁵⁶ The SARS-CoV-2 main protease sequence is 96% identical to the SARS-CoV main protease amino acid sequence.¹⁵⁷ The main protease is a cysteine protease involved in the processing of replicase polyproteins pp1a and pp1ab.

The SARS-CoV-2 main protease is a homodimeric enzyme. Dimerization is essential for the catalytic activity of the enzyme, and the monomer has been shown to be inactive.¹⁵⁷ The active site of the main protease consists of a catalytic dyad with a nucleophilic cysteine and a basic histidine residue. The main protease cleaves the peptide bond that connects glutamine and serine in an amino acid sequence of Leu-Gln-Ser-Ala-Gly, which is unique for the main protease, as there are no human proteases known to have a comparable sequence recognition. Thus, inhibitors of SARS-CoV-2 main protease could prevent the viral replication with minimal off-target toxic effects.^{157, 158}

Papain-Like Protease (PLpro)

As discussed in the previous section, similar to the main protease, PLpro is responsible for cleaving the *N*-terminus of the replicase polyproteins and produces three nonstructural proteins that are part of the functional replication machinery. The active site of PLpro also consists of a cysteine-histidine catalytic dyad. In contrast to the main protease, PLpro has de-ubiquitinating activity because of structural similarities with cellular de-ubiquitinating enzymes. The de-ubiquitination interferes with human innate immune sensing.¹⁵⁹

Exoribonuclease (ExoN)

Viral nonstructural protein 14 (Nsp14) of SARS-CoV-2 is responsible for an exoribonuclease (ExoN) activity degrading RNA of terminal nucleotides in a 3' to 5' direction and an *N7*-guanine methyltransferase activity (*N7*-MTase). The latter mediates 2'-*O*-ribose methylation of the viral mRNA cap. Mutations in the ExoN active site were shown to disrupt the RNA synthesis and lower the replication fidelity.¹⁴⁹

2'-*O*-Methyltransferase (2'-*O*-MT)

After the addition of the *N7*-methyl guanosine cap as mentioned above, Nsp10 (a co-factor) activates 2'-*O*-MT (Nsp16), which then facilitates the mRNA cap 2'-*O*-ribose methylation to the 5'-cap structure of viral mRNAs. This methylation reaction is universal to coronaviruses, including SARS-CoV and MERS-CoV. Studies performed on SARS-CoV mutants that lack 2'-*O*-MT reported a significant attenuation of SARS-CoV replication both

in vitro and *in vivo*. This conclusion was drawn from reduced viral titers and viral replication observed in cell assays.¹⁶⁰

Both 2'-O-MT and ExoN are vital for coronaviruses to escape the recognition of viral RNA by the host immune system. Therefore, 2'-O-MT and ExoN have been selected as potential targets even though, as of today, there are no clinically approved SARS and MERS drugs that inhibit these enzymes.¹⁴⁹

Nonstructural Uridylate-Specific Endoribonuclease (NendoU) Nsp-15

This endoribonuclease is a highly conserved protein in coronaviruses. NendoU can cleave single and double-stranded RNA at a uridine residue and may play a key role in viral RNA replication. NendoU is a type I interferon (IFN) antagonist that down-regulates the immune response, leading to increased immunopathogenesis. Inhibitors that target NendoU could provide effective antivirals against SARS-CoV-2.¹⁶¹

RNA-directed RNA Polymerase (RdRp)

RdRp is part of the replication-transcription complex of coronaviruses, which catalyzes template synthesis of polynucleotides in the 5'-3' direction in making copies of the RNA genome during replication. RdRp is also responsible for generating structural and other proteins encoded by the viral genome and is essential for the viral infectious cycle as it initiates RNA replication in the host cell. RdRp of SARS-CoV-2 is 93% homologous to the polymerase of SARS-CoV.

In 2020, James Russo and co-workers demonstrated that a SARS-CoV mutant with no RdRp activity was unable to replicate and proliferate.¹⁶² Several groups have studied

inhibitors of RdRp and shown that nucleoside analogs of adenine or guanine derivatives can block viral RNA synthesis of human coronaviruses. Influenza drugs favipiravir and remdesivir, are nucleoside-based drugs, and favipiravir is being studied in clinical settings to mitigate the symptoms in COVID-19 patients.¹⁶³ Moreover, there is no human counterpart to RdRp. Thus, RdRp is a promising druggable protein in designing inhibitors that target SARS-CoV-2 with little or no off-target inhibition of human polymerase.

Helicase

Similar to RdRp, helicase is an enzyme found in the viral replication transcription complex. The nonstructural protein 13 (Nsp13) of SARS-CoV-2 was shown to have nucleoside triphosphate hydrolase, NTPase activity, and RNA helicase activity.¹⁶⁴ Helicases are motor proteins that utilize the free energy from NTP hydrolysis in unwinding helical duplex DNA and RNA. This helicase activity is vital in viral genome replication, recombination, transcription, and repair. Coronavirus Nsp13 is the most conserved protein across CoV genera, and the SARS-CoV-2 helicase has a 99.8% sequence identity to SARS-CoV helicase. This high level of conservation shows the importance of the helicase for the survival of coronaviruses.¹⁶⁵

X-ray crystal structures of MERS-CoV and SARS-CoV Nsp13s revealed that coronavirus helicases are highly similar in structure. Helicases consist of multiple domains including an *N*-terminal Zn(II) binding domain (ZBD), a hinge domain (stalk), and a 1B domain; those together connect the helicase core (SF1).¹⁶⁵ Xi Zhuo and co-workers (2020) demonstrated the magnesium dependency of SARS-CoV-2 helicase, and they reported the

bismuth inhibition of both NTPase and RNA helicase activities of SARS-CoV-2 Nsp13.¹⁶⁴

However, a drug candidate targeting helicase is yet to be developed.

Rational Design of Cyclobutanone Analogs Driven by Computer-Aided Drug Design and Structure-Activity Relationship

Our CADD high-throughput screening of cyclobutanone analogs provided insights into hit-target binding interactions and will allow us to identify key amino acid residues in the catalysis of SARS-CoV-2 druggable proteins. A better understanding of active site structures and binding modes of the inhibitors can be achieved by computer simulations. This approach integrated with *in vitro* testing will enable us to design potent small molecule inhibitors of SARS-CoV-2.

Peptidomimetic *N*-functionalized 2-aminocyclobutanone analogs could provide inhibitors of serine and cysteine proteases, among other therapeutically targeted serine hydrolases as discussed previously in Chapter two. Expanding our scope, we sought to synthesize peptidomimetic cyclobutanone derivatives utilizing 2-aminocyclobutanone synthon **9**. The hemiacetal enzyme-inhibitor complex of these cyclobutanone derivatives will resemble the oligopeptide substrates of the proteases, and as a result, peptidomimetic cyclobutanones could covalently yet reversibly inhibit the proteases.

We identified *N*-tosyl-L-phenylalanine chloromethyl ketone (TPCK), a known covalent inhibitor of chymotrypsin (a serine protease), as our lead compound.¹⁶⁶ The α -chloro ketone covalent warhead of the TPCK was replaced with the cyclobutanone ring in designing the *N*-tosyl-L-phenylalanine cyclobutanone (see Figure 26), and a series of

natural and unnatural amino acid-based cyclobutanone derivatives was designed based on the results obtained from the preliminary virtual screening which will be discussed in the sections below.

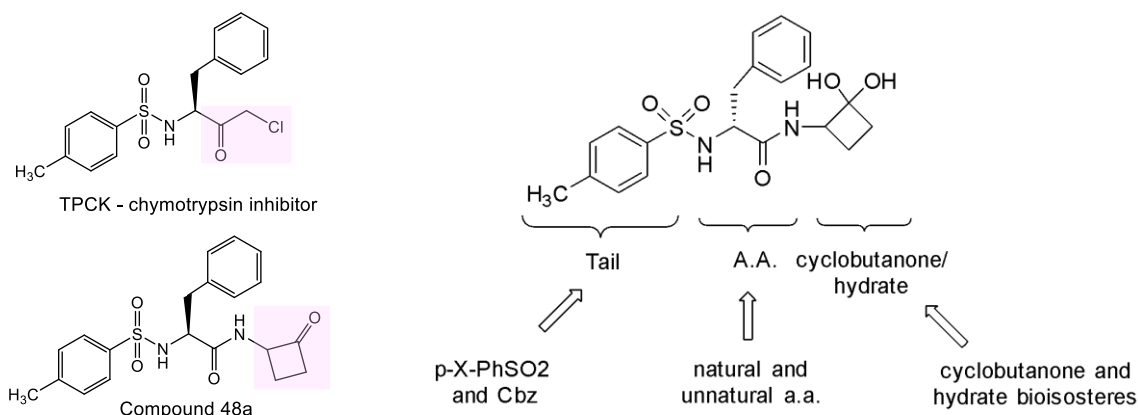


Figure 26. Rational design of (A) cyclobutanone analog of TPCK by replacing the α -chloro ketone covalent warhead with a cyclobutanone ring and (B) cyclobutanone analogs via functional group derivatization including Cbz, natural and unnatural amino acids, and cyclobutanone isosteres from Ts-D-Phe cyclobutanone hydrate (HT-virtual screening original hit).

Preliminary Virtual Screening of the Cyclobutanone Library

A preliminary screening of 62 compounds, 31 *N*-functionalized 2-aminocyclobutanone analogs (see Schemes 6 and 7), and the corresponding hydrates was performed utilizing the virtual screening method discussed in the previous section (see Figure 25). During the *in silico* screenings, hydrates of 2-aminocyclobutanone analogs were expected to bind to the SARS-CoV-2 proteases (M^{pro} and PL^{pro}) as transition state mimetic inhibitors through favorable interactions with the active site amino acid residues.

3D structures of ligands were preprocessed using LigPrep (Schrödinger) prior to loading into the screening pipeline. Preprocessing of the ligand includes energy

minimization and structure preparation (confirming correct Lewis structures and ionization states). All the possible stereoisomers of ligands were generated in LigPrep for an accurate screening. The crystal structures (PDB files) and the I-TASSER models (homology models) of selected seven SARS-CoV-2 target enzymes (referred to as receptors in this context) were energy minimized using the Protein Preparation Wizard of the Schrödinger suite, followed by a short 20 ns MD simulation.

The virtual screening was performed by employing three consecutive docking runs (HTVS, SP, and XP) using the Virtual Screening Wizard. First, a high-throughput virtual screening (HTVS) ligand docking was performed, followed by an SP docking of the top 10 % compounds from the HTVS run that are refined in the torsional space of the receptors.¹⁵⁴ Then, the top 10% of scoring hits from SP docking were subjected to an XP docking. The XP docking removes false positives, as the scoring function is highly selective for ligand-receptor shape complementarity than the HTVS. Potential inhibitors were identified through the initial dockings based on docking parameters, ligand and binding site strain energies, and fit scores. A higher XP Glide score means the better the calculated affinity of the hit in binding to the protein target.

Rational Design

Following criteria for drug-likeness of molecules were taken into account when designing all our synthetic target compounds. Molecular weight was confirmed to be less than 500 Dalton, no more than five hydrogen bond donors, no more than ten hydrogen bond acceptors, and an octanol-water partition coefficient (log P) value less than 5.¹⁶⁷ Hit

compounds were categorized based on the selective binding to each target protein and were further refined by calculating binding free energies for the top hit-receptor complexes utilizing the molecular mechanics' method using Prime MM-GBSA. During this final MM-GBSA refinement, the torsional strain on both ligand and receptor within the complex was estimated using interaction energies including Coulomb, Van der Waals, covalent-covalent binding, lipophilic, and generalized Born electrostatic solvation. Corrections including hydrogen-bonding, pi-pi stacking, and self-contact in the hit-receptor complex were also taken into consideration for the final binding energy calculation. Our lead compounds were prioritized based on the binding free energies of the hits.

Hits identified through our CADD screenings provided us comprehensive ligand binding interaction profiles. We developed structure-based pharmacophore models for each target hit pool using PharmaGist¹⁶⁸ and the Molecular Operating Environment (MOE).⁷⁷ Pharmacophore models combined with the ligand binding profiles enabled us to generate series of hit-derived compounds through functional group modifications. Improved cyclobutanone analogs were virtually screened against corresponding target enzymes. Top scoring cyclobutanone derivatives were then synthesized, and *in vitro* activities of these hits were validated through biochemical assays. Syntheses of hit compounds and the biological testing data will be discussed in the following section.

Results and Discussion

Preliminary screening of the 2-aminocyclobutanones provided *N*-tosyl-D-Phe cyclobutanone (**48b**) as a hit against SARS-CoV-2 helicase. The cyclobutanone hit is

predicted to bind as the hydrate of the cyclobutanone carbonyl to the adenosine triphosphate (ATP) binding site of the helicase, revealing the pharmacophore as shown in Figure 27.

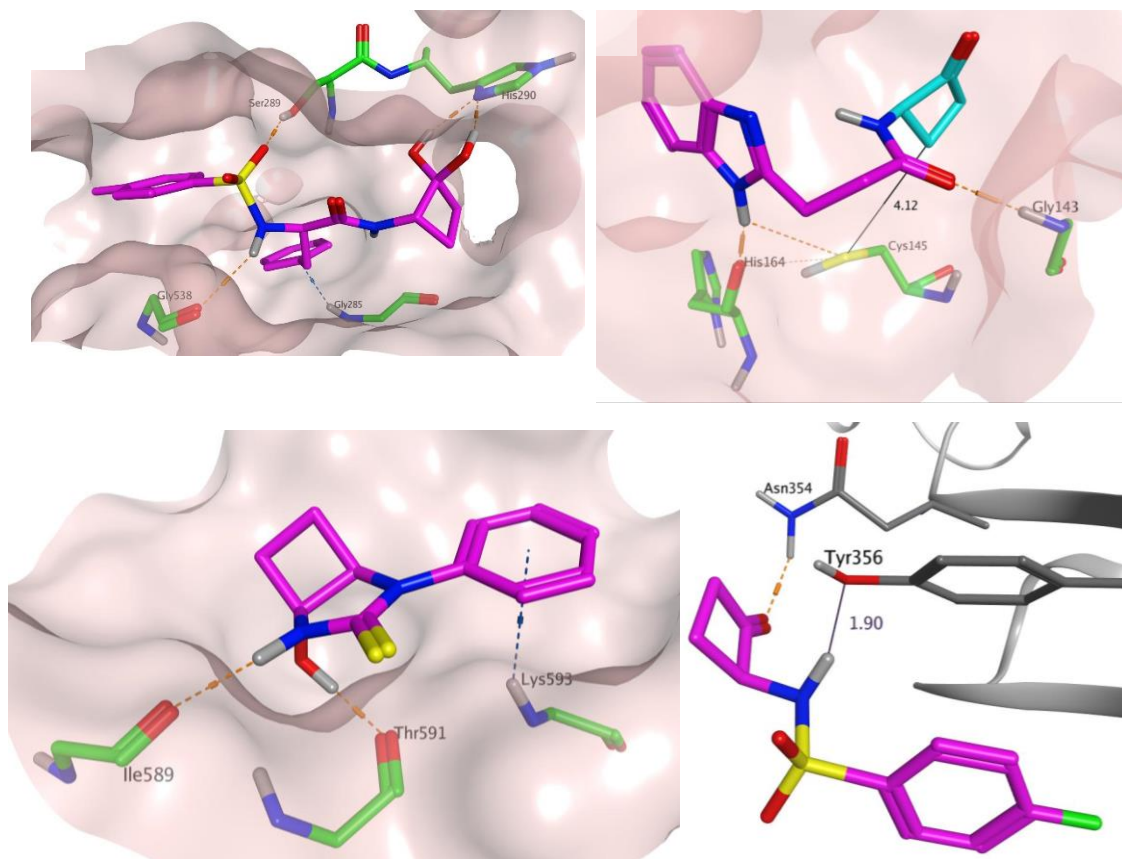


Figure 27. Docking images showing binding interactions of (A) Ts-D-Phe cyclobutanone (**48b**) in the ATP binding site where cyclobutanone hydrate is hydrogen bonded to His290, (B) benzimidazole cyclobutanone **10t** in the M^{pro} active site with residues highlighting the proximal positioning of cyclobutanone ring to the catalytic Cysteine 145, (C) bicyclic thiourea **14** in the RdRp active site, and (D) 4-fluoro benzene sulfonamide cyclobutanone **11b** bound to the PLPro active site and the residues interacting are highlighted.

This suggests that a stable cyclobutanone hydrate scaffold formed in solution could inhibit the target enzyme via a stable inhibitor-enzyme complex. Calculated energy and other docking parameters of the helicase hit are listed in Table 6 (entry 6).

In addition to the helicase original hit, we selected three top-scoring 2-aminocyclobutanone analogs from the virtual docking screens that showed *in silico* affinity toward SARS-CoV-2 M^{Pro}, PL^{pro}, and RdRp, enzymes that are promising drug targets (Figure 27). These selected compounds were not refined through molecular mechanics (MM-GBSA) binding energy calculations. We refer to these molecules as “seed” compounds because of their moderate binding affinity toward the target enzymes. Further optimization and functional group modification of these seed compounds could provide potent SARS-CoV-2 inhibitors. Benzimidazole cyclobutanone (**10t**) was predicted to bind the main protease, while 4-fluoro benzene sulfonamide **11b** was bound to the PL^{Pro} during the virtual screen. Bicyclic thiourea **14** was identified as a seed compound against the RdRp. Sulfonamide and bicyclic thiourea are reserved as our backup molecular scaffolds and will be subjected to functional group modification and optimization as needed. We pursued benzimidazole seed hit to design potential main protease inhibitors driven by SAR and *in silico* screening. Our approach in the development of main protease inhibitors is discussed in the sections below.

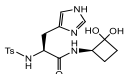
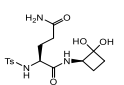
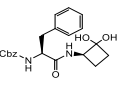
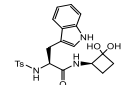
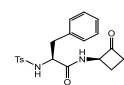
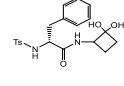
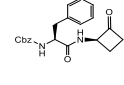
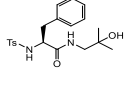
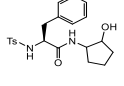
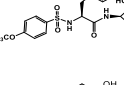
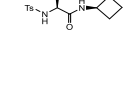
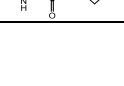
Rational Design of Peptidomimetic 2-Aminocyclobutanone Helicase Inhibitors

We pursued tosyl-D-phenylalanine-cyclobutanone (**48b**) as the lead molecule to design potential SARS-CoV-2 helicase inhibitors. Functional group permutations were made, as shown in Figure 26. Both (S) and (R) enantiomers of aryl, hydrophobic, and polar amino acids (Phe, Trp, Tyr, His, Val, Ile, Ala, Gly, Ser, Gln), as well as unnatural amino acid derivatives of helicase hit, were proposed. In addition, various *para*-substituted

arylsulfonamide (4-CH₃, 4-CF₃, 4-F, 4-Cl, 4-MeO, and 4-H), *N*-Cbz-amino acid cyclobutanone analogs, and cyclobutanone/hydrate isosteres including cyclopentanone, isopropanol, cyclopropanol analogs were designed (see Figure 26). The alpha carbon of the helicase original hit (**48b**) is racemic by synthesis. Our virtual high-throughput screening generated all the possible stereoisomers of each inhibitor. As such, all four diastereomers (S and R isomers of cyclobutanone α -carbon and L and D isomers of phenylalanine) of compound **48b** were generated and screened to investigate the stereospecific binding of each SARS-CoV-2 inhibitors.

Forty nine helicase hit-derived molecules, including Ts- and Cbz-amino acid-cyclobutanone analogs, their corresponding hydrates, and cyclobutanone isosteres, were virtually screened using our high-throughput *in silico* screening method. The lead optimization screening provided eleven helicase hits with significantly improved MM-GBSA estimated binding energies and Glide scores (see Table 6). The glide energy of the helicase original hit-enzyme complex was estimated to be -45.5 with a Glide score (GScore) of -6.96. Glide score is a scoring function used to calculate the ligand binding free energy using OPLS3e force field (electrostatic and van der Waals interactions were considered in the calculation). As shown in Table 6, four cyclobutanone analogs have higher (better) Glide scores suggesting that these analogs could provide potent helicase inhibitors due to their increased affinity toward helicase enzyme.

Table 6. Docking parameters and calculated energies of amino acid-derived cyclobutanone hits against SARS-CoV-2 helicase

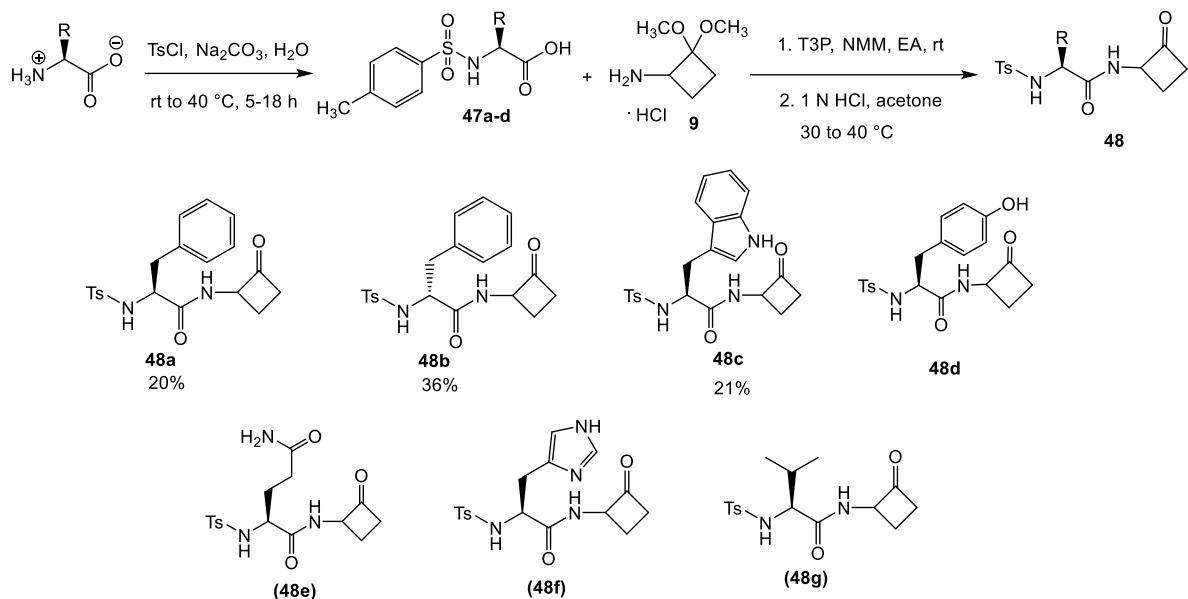
Entry	Structure	GScore	Glide Energy	DockScore	LipophilicEvdW	HBond	Electro	RotPenal
1		-8.34	-51.87	-7.87	-3.66	-2.58	-1.15	0.38
2		-7.48	-56.85	-7.48	-3.7	-2.9	-1.34	0.45
3		-7.38	-54.13	-7.38	-4.51	-2.36	-1	0.45
4		-7.08	-56.92	-7.08	-4.18	-1.98	-1.2	0.3
5		-6.96	-45.5	-6.96	-3.97	-2.38	-1.37	0.25
6		-6.86	-49.17	-6.86	-4.78	-1.63	-0.66	0.36
7		-6.62	-51.33	-6.62	-4.4	-1.24	-0.76	0.43
8		-6.48	-51.26	-6.48	-4.87	-1	-0.85	0.44
9		-6.46	-48.86	-6.46	-5.36	-0.64	-0.66	0.36
10		-6.45	-49.72	-6.45	-4.06	-1.83	-0.97	0.34
11		-6.15	-45.23	-6.15	-4.04	-1.97	-0.7	0.36
12		-6.04	-44.78	-6.04	-3.18	-1.94	-0.99	0.39

Interestingly, *N*-Cbz-L-Phe cyclobutanone (entry 7, see Table 6), the only Cbz cyclobutanone analog screened against helicase, was identified as a hit. The predicted affinity of compound **54c** toward helicase suggested that incorporating a Cbz group into our structure design might improve the potency of the inhibitor through efficient ligand binding.

All eleven hit compounds bind to the ATP binding site of helicase through hydrogen bonding, pi-cation, and pi-pi stacking interactions with Gly287, Ser289, His290, Lys320, and Arg442. Inhibitors and repurposed drugs were shown to bind the SARS-CoV-2 helicase ATP binding site in recent studies.^{149, 169} We believe that helicase cyclobutanone hits could serve as potent competitive SARS-CoV-2 helicase inhibitors and provide effective antivirals.

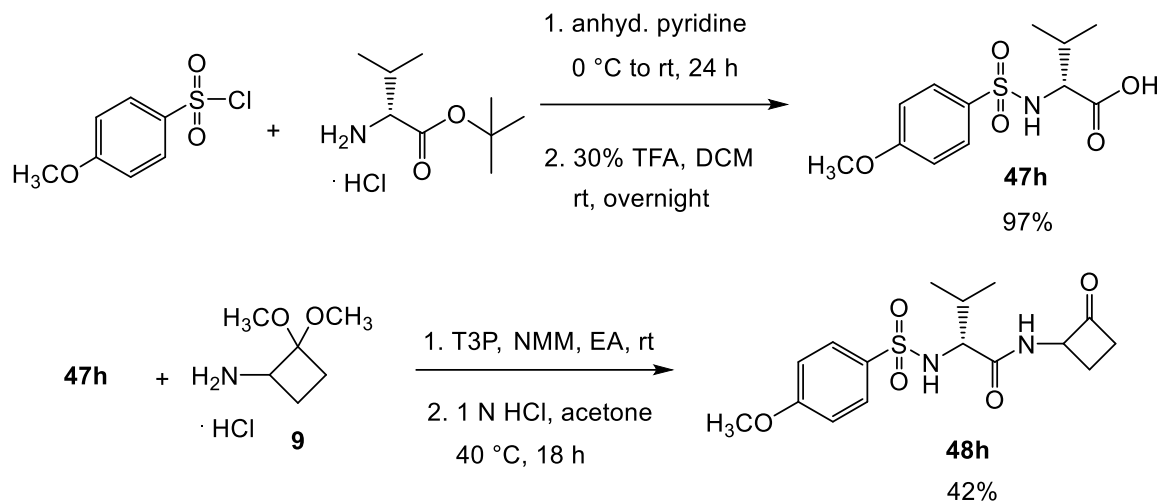
Synthesis of Helicase Inhibitors

Hit compounds were prioritized based on the binding energies, docking scores, and predicted synthetic challenges. In a parallel synthesis setting, aryl sulfonyl chlorides were reacted with amino acids in a base-mediated coupling reaction using Na₂CO₃ following a published general procedure.¹⁷⁰ Sulfonamide intermediates of free carboxylic acids (**47a-c**) were then reacted in a T3P coupling reaction with the 2-aminocyclobutanone synthon **9** to give acetal intermediates. Acetal hydrolysis under general reaction conditions (1 M HCl, acetone, H₂O, rt to 40 °C) yielded the final benzenesulfonamide-amino acid-cyclobutanone analogs (**48a-c**, see Scheme 17).



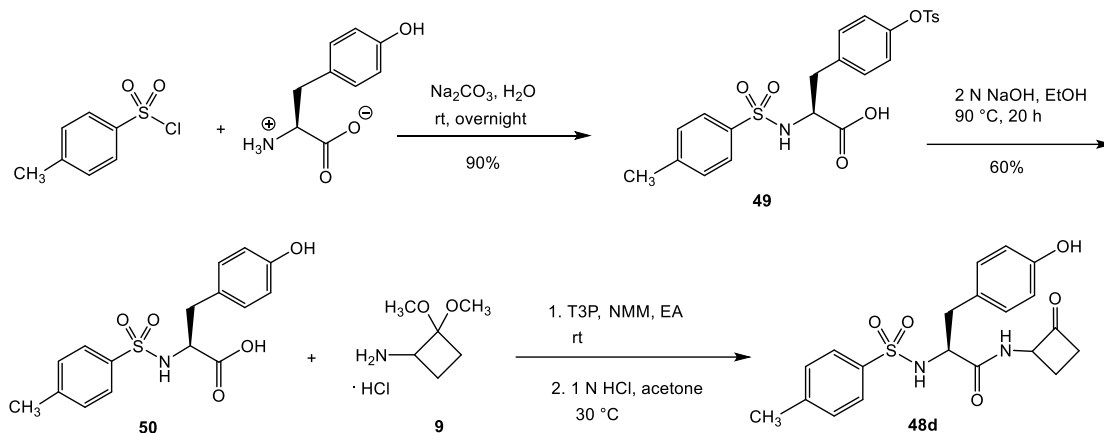
Scheme 17. Synthesis of tosyl-amino acid cyclobutanone analogs **48** using 2-aminocyclobutanone synthon **9**. Prospective cyclobutanone analogs are also shown (**48d-g**).

4-Methoxybenzene sulfonamide cyclobutanone analog consist of D-valine amino acid (**48h**) was synthesized in a sequence of *N*-sulfonylation, ester hydrolysis, and amine-carboxylic acid coupling reactions utilizing D-valine *tert*-butyl ester. A base-mediated coupling reaction of D-valine *tert*-butyl ester HCl salt with 4-methoxybenzenesulfonyl chloride using pyridine as solvent yielded the corresponding sulfonamide intermediate. Deprotection of the *tert*-butyl ester was achieved by stirring the ester protected sulfonamide intermediate with trifluoroacetic acid (TFA). The cyclobutanone analog **48h** was synthesized by reacting 2-aminocyclobutanone synthon **9** with ((4-methoxyphenyl)sulfonyl)-D-valine under T3P coupling conditions as shown in Scheme 18.



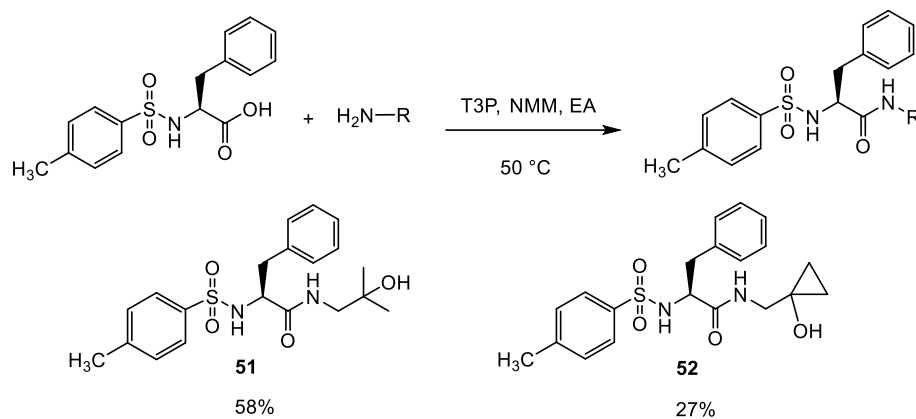
Scheme 18. Synthesis of 4-(OCH₃)-benzenesulfonamide-D-valine cyclobutanone (**48h**).

Synthesis of Ts-L-Tyr-, Ts-L-His-, Ts-L-Gln-cyclobutanones was attempted without much success following the general synthetic route shown in Scheme 17. Challenges in these syntheses arise from the reactivities of the side chain phenol of tyrosine, the basic imidazole nitrogen atom of the histidine, and the reactive primary amide in glutamine. During the reaction with tosyl chloride, the *p*-hydroxyl group of the tyrosine side chain was also reacted to form the *N*-Ts tyrosine sulfonate ester (**49**). In a subsequent reaction, the sulfonate ester **49** was hydrolyzed by refluxing in ethanol using 2 N NaOH. A T3P coupling reaction of Ts-L-Tyr-OH (**50**) with 2-aminocyclobutanone acetal **9** was attempted by heating the reaction to 60 °C for 10 days (see Scheme 19). HPLC analysis indicated the formation of a new peak (presumably the desired product). However, the reaction was not moving forward even after seven days, and compound **50** degraded with time. We believe that with optimized reaction conditions, Ts-Tyr cyclobutanone can be accessed as we continue to work on the synthesis of these hits to overcome synthetic limitations.



Scheme 19. Synthesis of Ts-L-tyrosine cyclobutanone analog **48d** in progress.

Synthesis of cyclobutanone hydrate isostere analogs **51** and **52** was achieved by reacting Tosyl-L-phenylalanine under T3P coupling conditions with dimethylethanolamine and 1-(aminomethyl)cyclopropanol in the presence of *N*-methylmorpholine (NMM) to give compounds **51** and **52**, respectively (see Scheme 20).

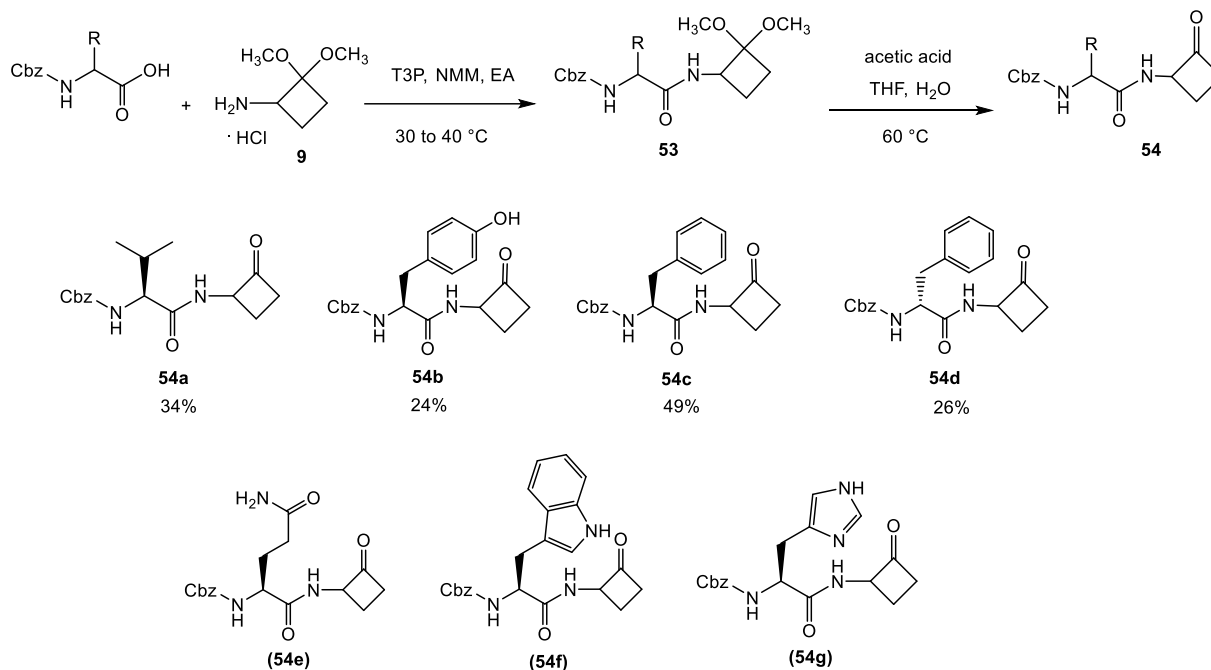


Scheme 20. Synthesis of cyclobutanone isostere compounds **51** and **52**.

We then sought to synthesize four Cbz-amino acids (L- and D-Phe, L-Val, L-Tyr) cyclobutanone derivatives. First, Cbz-amino acids were coupled with acetal **9** using T3P as the coupling agent. When the acetal intermediates **53a-d** were subjected to hydrolysis in 1 M HCl and acetone, the Cbz group was hydrolyzed to the respective amines under aqueous

acidic conditions. To find a mild reaction condition for the hydrolysis of Cbz-acetal intermediates, we screened 1 M H₂SO₄, *p*-toluene sulfonic acid (TsOH), and acetic acid as alternative acid catalysts. It was found that a 40% v/v acetic acid solution in THF (40% v/v) and water selectively hydrolyzed the acetal moiety of the Cbz acetal intermediates even at elevated temperatures as high as 60 °C. Cbz cyclobutanone analogs **54 a-d** were synthesized following the route shown in Scheme 21.

Both *N*-Ts- and *N*-Cbz-amino acid cyclobutanone analogs were purified through manual silica gel columns with silica gel packed in glass Pasteur pipettes. This is because of the low crude mass obtained from small-scale reactions (50 mg), and the resolution between the desired product and by-products was poor on TLC. The crude products of *N*-Ts- and *N*-Cbz-amino acid cyclobutanone analogs were chromatographed by carefully controlling the flow rate (~5 mL/min) using the identified solvent systems (eluent) to afford the desired products in >95 % HPLC purity.



Scheme 21. Synthesis of Cbz-amino acid cyclobutanone analogs **54a-d**. Prospective analogs are listed as **54e-g**.

Lead Optimization and Rational Design of Main Protease Inhibitors

Seed compound benzimidazole cyclobutanone (**10t**) is predicted to bind to the coronavirus main protease (M^{Pro}) through favorable interactions with amino acid residues. Intriguingly, the *in silico* ligand-bound enzyme structure shows that the carbonyl carbon of the cyclobutanone ring is in a proper alignment for a nucleophilic attack by the catalytic cysteine (Cys145) of the main protease (see Figure 27B). A reversible inhibitor, the seed compound in this context, with moderate (*in silico*) activity, can be chemically modified to design a potent covalent inhibitor of the cysteine protease (M^{Pro}). Thus, we designed benzimidazole-based covalent inhibitors by replacing the cyclobutanone ring with known protease specific covalent warheads (discussed in Chapter Two), including acrylamide, α -

chloroamide, and α -cyanoacetamides. These alkylating groups are common Michael acceptors that are frequently utilized in rationally designed covalent inhibitors of cysteine proteases.²² A nucleophilic cysteine in the active site of the target enzyme forms a covalent bond with the vinyl carbon of the acrylamide facilitated by the conjugation with the carbonyl, as a result, the enzyme will be irreversibly inactivated. In inhibiting the enzyme, α -chloroamides form a covalent bond with cysteine through the loss of a chloride ion.

Halopyridine moieties, specifically 4-bromopyridine and 2-chloropyridine, were also incorporated in our design as 4-bromopyridine scaffolds shown to irreversibly inhibit a hydrolase involved in nitric oxide production.¹⁷¹ Inhibitory potency of a halopyridine ligand is enabled by covalent bond formation with the active site cysteine via displacement of the 4- or 2-Cl/Br atom. The covalent modifiers were designed as reverse amide analogs of the benzimidazole seed compound **10t**. Furthermore, we included two cyclobutanone isosteres containing hydroxyl groups to mimic the cyclobutanone hemiacetal-protease enzyme complex that can form a stable inhibitor-enzyme adduct via strong binding interactions with the active site amino acid residues. Our rational design of benzimidazole-based inhibitors is shown in Figure 28.

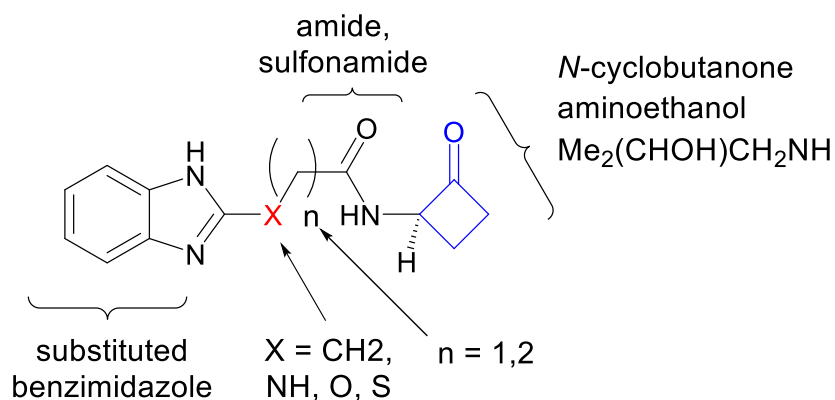
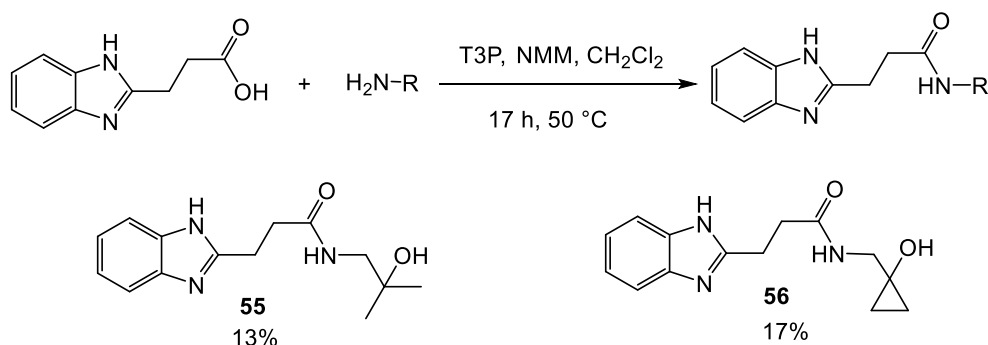


Figure 28. Rational design of benzimidazole-based main protease inhibitors.

Synthesis of Benzimidazole-Based Main Protease Inhibitors

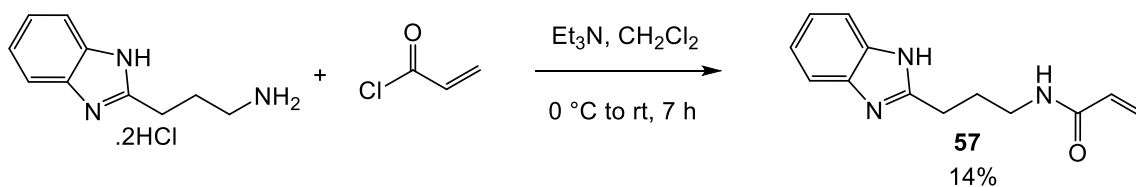
Synthesis of seed compound **10t** is reported in chapter two as part of the 2-aminocyclobutanone library preparation. To explore SAR, we designed and synthesized two cyclobutanone isostere analogs of compound **10t**. Benzimidazole propanoic acid was subjected to T3P coupling reactions with dimethylethanolamine and 1-(aminomethyl)cyclopropanol in the presence of *N*-methylmorpholine (NMM) to give benzimidazole analogs **55** and **56**, respectively (see Scheme 22).



Scheme 22. Synthesis of benzimidazole analogs **55** and **56**.

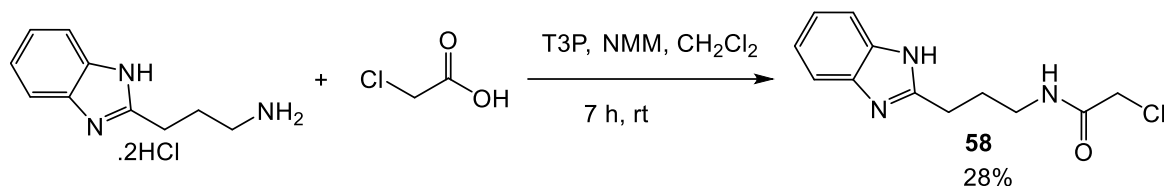
Reverse amide analogs were synthesized by coupling benzimidazole 2-propanamine with various electrophiles. Benzimidazole acrylamide analog (**57**) was prepared by

reacting benzimidazole 2-propanamine with acryloyl chloride in the presence of triethylamine in methylene chloride at room temperature (see Scheme 23). Reaction progress was monitored by HPLC analysis. Under these conditions, complete consumption of benzimidazole 2-propanamine was not achieved even after 20 hours of stirring at room temperature, and prolonged reaction time tends to form several by-products. HPLC analysis indicated the depletion of the desired product with time, presumably due to a reaction between the imidazole nitrogen and acryloyl chloride. As a result, the reaction was quenched prematurely, and the final product **57** was isolated in a low yield (14%) yet in a sufficient amount for the *in vitro* testing.

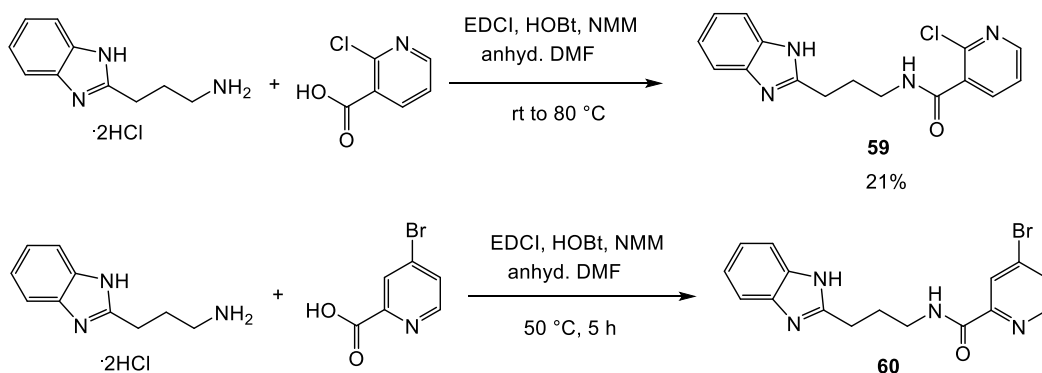


Scheme 23. Synthesis of benzimidazole acrylamide analog **57** from acryloyl chloride.

Alpha-chloro benzimidazole analog **58** was synthesized in a T3P coupling reaction of benzimidazole 2-propanamine with 2-chloroacetic acid, and the final product was isolated in 28 % yield (see Scheme 24). In the synthesis of halopyridine benzimidazole analogs, benzimidazole 2-propanamine was reacted with 2-Cl pyridinecarboxylic acids using EDCI, HOBT, and NMM affording compound **59**, and the 4-bromo pyridine benzimidazole analog **60** is currently being synthesized as shown in Scheme 25.



Scheme 24. Synthesis of α -chloro benzimidazole analog **58**.



Scheme 25. Synthesis of benzimidazole 2-chloronicotinamide **59** and 4-bromo pyridine benzimidazole analog **60**.

Antiviral Assay

The preliminary *in vitro* testing of fourteen selected helicase and main protease inhibitors (see Table 7) was performed at the United States Army Medical Research Institute of Infectious Diseases (USAMRIID) BSL-3 lab (Drs. S. Bradfute and J. M. Dye). Vero E6 cells (ATCC Cell Lines) were seeded into 96-well culture plates 24 h before infection with SARS-CoV-2 (Coronavirus 2 Isolate USA-WA1/2020, BEI Resources). After 24 hours, in a fresh medium, cells were treated with test compounds at 5 μ M and 50 μ M concentrations followed by 48 hours of incubation period. Mammalian cell viability and cytotoxicity in the presence of the test compounds were measured via a cell rescue assay. We calculated the percentage of viable cells remaining after an incubation period with SARS-CoV-2 that

promoted the viral lysis of living cells. Additionally, nuclei from living cells were also counted to assess test compounds' cytotoxic effects.

Results and Discussion

Several helicase and main protease hits showed promising *in vitro* antiviral activity with little to no cytotoxicity at 5 μM and 50 μM (see Table 7). The cell survival assay measured the ability of the tested inhibitors to prevent cell death caused by SARS-CoV-2 by calculating the number of living cells that escaped viral cell lysis. Assay data is listed in Table 7 indicating the dose-response of each inhibitor in cell viability and relative cytotoxicity. Higher cell survival means the better anti-SARS-CoV-2 activity of the inhibitors.

Out of the fourteen hits tested, Ts-L-tryptophan cyclobutanone analog **48c** targeting helicase showed the highest cell survival percentage indicating antiviral activity as well as the potent anti-SARS-CoV-2 efficacy. Negative values in the chart represent cell death due to the toxic effects posed by the inhibitors. Only α -chloro benzimidazole cyclobutanone analog **58** showed cell toxicity at 50 μM yet, the antiviral activity at 5 μM is significant as 47 % cell survival was recorded. The cytotoxicity of compound **58** is presumably caused by off-target reactions and high reactivity, and the resultant off-target modification is one of the main concerns raised in designing covalent modifier inhibitors.

Table 7. Percent cell survival of SARS-CoV-2 inhibitors obtained via a cell survival assay.

Compound ID	Structure	50 μ M	5 μ M	Compound ID	Structure	50 μ M	5 μ M
48a		49.8	39.3	54b		28.1	- 3.0
48b		35.9	26.6	54c		57.5	41.7
48c		70.9	54.3	54d		34.7	24.2
48h		49.1	32.0	55		60.4	31.9
51		59.2	36.7	56		34.9	34.4
52		30.7	29.9	57		42.9	37.3
54a		54.9	37.9	58		-10.0	47.4

When comparing the activities of Ts-phenylalanine cyclobutanone **48a** (L isomer) and **48b** (D isomer) at both 5 μ M and 50 μ M, there is a significant increase in the activity of the L isomer over D isomer (see Table 7). A similar trend is observed between Cbz-phenylalanine cyclobutanone, where at 5 μ M L isomer **54c** showed 41.5 % cell survival with only 24.2 % activity in the presence of D isomer **54d**. Benzimidazole acrylamide analog **57** designed to covalently inhibit the main protease did not show any toxicity even at 50 μ M. When treated with benzimidazole acrylamide analog **57** at 50 μ M and 5 μ M

concentrations, 43 % and 32 % cells were viable, respectively, indicating the potential efficacy of inhibitors bearing an acrylamide moiety.

Anti-SARS-CoV-2 data obtained by measuring the cell survival percentage is very promising. The observed activities validate our multi-targeted CADD approach and provided insights into SAR exploration. The most potent nine compounds are currently being tested using enzymatic assays to determine dose-response activities by measuring IC_{50} s. Based on the biological data, we continue to develop more potent inhibitors of SARS-CoV-2 target enzymes. We believe that cyclobutanone analogs and benzimidazole-based compounds provide attractive lead molecules with numerous opportunities for ligand-based inhibitor design.

Conclusion

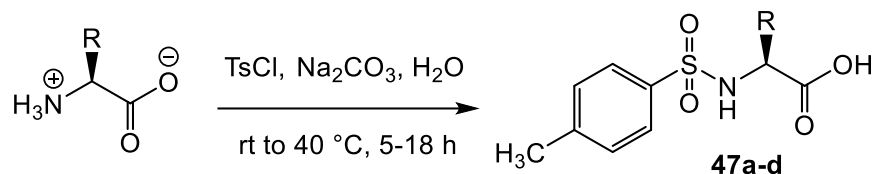
The COVID-19 pandemic continues to cause catastrophic effects on public health and the economy globally, and the loss of human lives in unprecedented numbers is devastating. Even as vaccines are rolled out, most countries are still struggling to cope with this fatal virus, and highly contagious and potent SARS-CoV-2 variants have worsened the adversity. Therefore, developing effective therapeutic agents is a timely and critical need in treating COVID-19. Our efforts in developing potential drug candidates against SARS-CoV-2 focuses on multi-targeted computer-aided drug design (CADD). Drugs targeting essential viral proteins are preferred over antivirals targeting the host cell to avoid or minimize adverse effects on human health, as they are designed to show higher specificity toward the virus. We identified a set of hit compounds against SARS-CoV-2 helicase and against the

main protease enabled by virtual high-throughput screening of a synthesized cyclobutanone library against seven identified druggable SARS-CoV-2 target enzymes utilizing the Schrödinger suite and Molecular Operating Environment (MOE). Antiviral activity of *N*-functionalized 2-aminocyclobutanone hits, as well as the hit-derived compounds, were tested *in vitro* using a cell survival assay to measure the inherent toxicity and the efficacy of these effective antiviral agents. Six rationally designed peptidomimetic cyclobutanone hits against helicase and three benzimidazole-based covalent inhibitors of the main protease showed promising antiviral activities with no toxic effects on mammalian host cells in the cell survival assay, validating out multi-target CADD approach in developing small-molecule antivirals against SARS-CoV-2. Currently, inhibitory potencies of these inhibitors are being tested using *in vitro* enzymatic assays to establish the dose-response profile against both SARS-CoV-2 helicase and main protease. Designing potent and selective inhibitors with improved efficacy against SARS-CoV-2 enabled by CADD driven by SAR is in progress. The emergence of drug resistance in rapidly mutating RNA viruses is inevitable. Therefore, the discovery of new anti-SARS-CoV-2 therapeutic agents is critical in alleviating the adverse impacts of the COVID-19 pandemic.

Experimental

General Procedure for the Synthesis of *N*-Aryl Sulfonamide-Amino Acid Analogs

47a-d

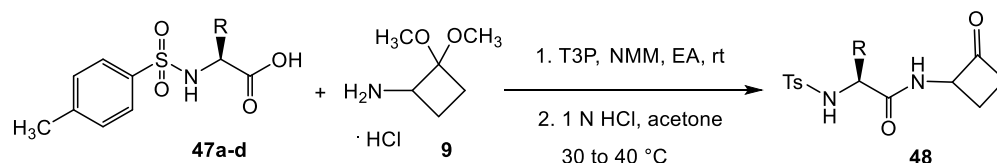


Following the general method reported by Misra and co-workers,¹⁷⁰ to a vigorously stirring solution of the amino acid (1.21 mmol) in water (1.5 mL), sodium carbonate (179.8 mg, 1.45 mmol) was added. Once all of the solutes were dissolved, the solution was cooled to 0°C and the respective aryl sulfonyl chloride (1.45 mmol) was added to the stirring reaction mixture in four portions over 1 h. Then the reaction was allowed to warm up to rt and the slurry was stirred at rt for 4 h or until completion. The reaction progress was monitored by TLC (methanol/methylene chloride = 10/90). Once completed, the mixture was acidified using 2 N HCl until the pH of the solution was reduced to 2. Crystals formed during the acidification were filtered and washed with pH 2.2 buffer. Final pure products (**47a-d**) were dried under high vacuum. Both proton and carbon NMR spectra of pure products **47a-c** matched the reported characterization data as indicated.

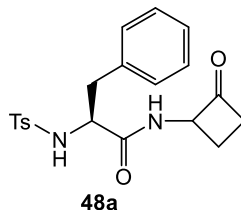
Tosyl-L-tryptophan

Upon acidifying the reaction mixture, a green solid formed. This solid was filtered, washed with water, and pH 2.2 buffer, respectively. The resultant paste-like solid was recrystallized from hot methylene chloride. While cooling to rt, needle-like crystals formed, which then dried under high vacuum.

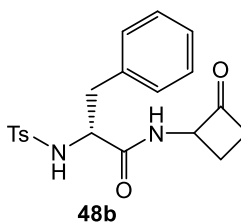
General Procedure for the Synthesis of Amino Acid Cyclobutanone Analogs **48a-c**



To a solution of substituted *N*-benzene sulfonamide amino acids **47a-c** (1 eq) and acetal **9** (1.2 eq) in ethyl acetate (0.2 M), *N*-methyl morpholine (4.0 eq) was added. Then propylphosphonic anhydride (T3P, 2.5 eq) was added to the above mixture as a solution in ethyl acetate (purchased as ≥ 50 weight % in EA). The reaction mixture was stirred under N_2 at rt to 40°C for 18 hours or until complete consumption of protected carboxylic acid intermediates determined by HPLC analysis. The reaction was quenched by adding water (3 mL) and then the organic product was extracted using ethyl acetate (3 x 3 mL). The combined organic layers were washed successively with water (3 x 3 mL) and 1N HCl (3 mL) and then dried over Na_2SO_4 . The solvent was removed by evaporation under reduced pressure providing the corresponding acetal intermediate. Without further purification, crude acetal (1 eq, final concentration was 0.1 M) was subjected to hydrolysis conditions, wherein the crude mixture was dissolved in acetone, water (10% v/v) and 1N HCl (30% v/v). Then the reaction mixture was stirred at 40°C for overnight with periodic HPLC monitoring. Upon completion, the organic product was extracted using ethyl acetate (3 x 3 mL) or methylene chloride for highly water-soluble analogs, and the combined organic layers were dried over Na_2SO_4 . The solvent was evaporated under reduced pressure, and the crude mixture was purified by column chromatography to afford the corresponding amino acid-derived cyclobutanone (**48a-c**).

(2S)-2-((4-Methylphenyl)sulfonamido)-N-(2-oxocyclobutyl)-3-phenylpropanamide**(48a)**

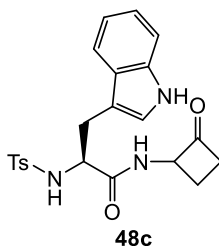
The *N*-Ts-carboxylic intermediate **47a** (50.0 mg, 0.129 mmol) was used in the reaction. The crude mixture of **48a** was purified by column chromatography eluting with a gradient of ethyl acetate/hexane (20/80) and ethyl acetate/hexane (40/60) followed by recrystallization from hot EA to afford compound **48a** (9.8 mg, 20%) as white crystalline solid. ¹H NMR (500 MHz, CDCl₃) δ 7.57 – 7.44 (m, 2H), 7.25 – 7.15 (m, 5H), 6.96 – 6.87 (m, 2H), 6.72 (d, *J* = 8.3 Hz, 1H), 4.97 (dtt, *J* = 10.1, 8.2, 2.1 Hz, 1H), 4.85 (d, *J* = 6.6 Hz, 1H), 3.85 (dt, *J* = 7.3, 6.4 Hz, 1H), 3.01 – 2.89 (m, 3H), 2.88 (dddd, *J* = 17.4, 9.9, 4.7, 2.3 Hz, 1H), 2.43 (s, 3H), 2.46 – 2.35 (m, 1H), 1.86 (dtd, *J* = 11.1, 9.7, 8.3 Hz, 1H). HRMS (ESI): Calcd for (MH⁺) C₂₀H₂₃N₂O₄S: 387.1373, found 387.1366.

(2R)-2-((4-Methylphenyl)sulfonamido)-N-(2-oxocyclobutyl)-3-phenylpropanamide**(48b)**

The *N*-Ts-carboxylic intermediate **47b** (50.0 mg, 0.129 mmol) was used in the reaction. The crude mixture of **48b** was purified by column chromatography eluting with a gradient of ethyl acetate/hexane (20/80) and ethyl acetate/hexane (30/70) to afford

compound **48b** (18.1 mg, 36.2%) as white solid: mp 190-192 °C. ¹H NMR (500 MHz, CDCl₃) δ 7.57 – 7.48 (m, 2H), 7.24 – 7.14 (m, 5H), 6.95 – 6.86 (m, 2H), 6.75 (NH, d, *J* = 8.3 Hz, 1H), 4.98 (dtt, *J* = 10.2, 8.3, 1.9 Hz, 0.5H), 4.87 (NH, d, *J* = 6.6 Hz, 0.5H), 4.82 (NH, d, *J* = 6.8 Hz, 0.5H), 4.78 – 4.68 (m, 0.5H), 3.87 (dtd, *J* = 16.8, 7.0, 6.1 Hz, 1H), 3.07 – 2.93 (m, 1.5H), 2.96 – 2.91 (m, 1H), 2.93 – 2.85 (m, 1H), 2.83 (dd, *J* = 14.1, 5.8 Hz, 0.5H), 2.44 (s, 1.5H), 2.43 (s, 1.5H), 2.43 – 2.36 (m, 0.5H), 2.39 – 2.31 (m, 0.5H), 2.16 (dddd, *J* = 11.2, 10.3, 8.9, 8.0 Hz, 0.5H), 1.86 (dtd, *J* = 11.2, 9.7, 8.4 Hz, 0.5H). ¹³C NMR (126 MHz, CDCl₃) δ 204.49, 204.40, 170.23, 169.93, 144.15, 144.09, 135.42, 135.30, 134.92, 134.71, 129.95, 129.90, 129.26, 129.14, 129.04, 127.42, 127.39, 127.21, 127.19, 77.27, 77.02, 76.77, 64.30, 63.68, 57.62, 57.29, 42.33, 42.13, 38.19, 37.74, 21.61, 21.59, 19.43, 18.90.

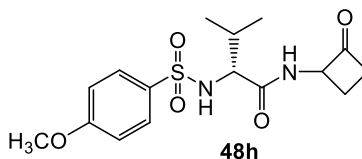
(2S)-3-(1H-Indol-3-yl)-2-((4-methylphenyl)sulfonamido)-N-(2-oxocyclobutyl)propanamide (48c)



The *N*-Ts-carboxylic intermediate **47c** (50.0 mg, 0.139 mmol) was used in the reaction. The crude mixture of **48c** was purified by column chromatography on a Teledyne Isco Rf Flash chromatography unit eluting with a gradient of ethyl acetate/hexane (20/80), ethyl acetate/hexane (30/70), and ethyl acetate/hexane (40/60) to afford compound **48c** (12.4 mg, 21%) as an off-white solid: mp 200-201 °C. ¹H NMR (500 MHz, CD₃CN) δ 9.07 (NH, s, 1H), 7.48 – 7.41 (m, 2H), 7.41 – 7.32 (m, 2H), 7.16 – 7.09 (m, 3H), 7.10 (NH, d, *J* = 7.5 Hz,

1H), 7.07 – 6.96 (m, 2H), 5.82 (NH, s, 1H), 4.68 (dtt, $J = 10.2, 8.0, 2.2$ Hz, 1H), 3.90 (dd, $J = 8.1, 5.7$ Hz, 1H), 3.14 – 3.06 (m, 1H), 2.95 – 2.73 (m, 3H), 2.35 (s, 3H), 2.21 – 2.10 (m, 1H), 1.82 (tt, $J = 10.5, 8.6$ Hz, 1H). ^{13}C NMR (126 MHz, CD_3CN) δ 205.61, 170.72, 143.47, 136.61, 136.41, 129.35, 127.10, 126.57, 126.51, 124.06, 121.41, 118.88, 111.33, 108.97, 63.62, 63.60, 57.04, 41.40, 41.34, 28.72, 28.58, 20.60, 20.58, 18.18, 18.11. HRMS (ESI): Calcd for (MH^+) $\text{C}_{22}\text{H}_{24}\text{N}_3\text{O}_4\text{S}$: 426.1482, found 426.1472.

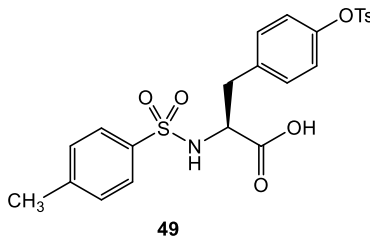
(2R)-2-((4-Methoxyphenyl)sulfonamido)-3-methyl-N-(2-oxocyclobutyl)butanamide (48h)



D-Valine *tert*-butyl ester HCl salt (100 mg, 0.477 mmol) was dissolved in anhydrous pyridine (1.0 mL) and stirred until all of the solutes were dissolved. The reaction mixture was cooled to 0 °C with an ice bath, and 4-methoxybenzenesulfonyl chloride (98.5 mg, 0.477 mmol) was added to the stirring reaction mixture. Then the reaction was allowed to warm up to rt and stirred at rt for 24 h with periodic monitoring using HPLC. Upon completion, the reaction mixture was diluted with methylene chloride (3 mL) and the organic layer was washed successively with water (3 mL), 1N HCl (10 x 3 mL), and brine (3 mL) and then dried over Na_2SO_4 . The solvent was removed by evaporation under reduced pressure providing a pale-yellow solid. Without further purification Ts-D-valine *tert* butyl ester was subjected to hydrolysis conditions. To a solution of crude Ts-D-valine *tert* butyl ester (64.7 mg, 0.188 mmol) in methylene chloride (0.94 mL), TFA (282 μL , 30% v/v) was

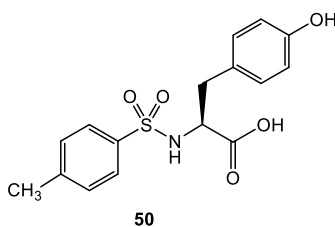
added under nitrogen. The mixture was stirred at room temperature overnight and monitored by TLC (EA/hexane = 50/50). The solvent was evaporated under reduced pressure. To the resultant residue, toluene (2 mL) was added to enable the formation of an azeotrope. The excess TFA was removed by evaporation on a rotary evaporator at 50°C providing a yellow crystalline solid (52.6 mg, 97%). HPLC purity of the product **47h** was 97%. Proton and carbon NMR spectra of the ((4-methoxyphenyl)sulfonyl)-D-valine (**47h**) matched the published data.¹⁷² Compound **48h** was synthesized from intermediate **47h** (30 mg, 0.104 mmol) following the general procedure of the T3P coupling reactions of *N*-Ts amino acids with 2-aminocyclobutanone synthon **9** and the acetal intermediate was subjected to hydrolysis using general reaction conditions (1 M HCl, acetone, H₂O) and stirred at 40 °C for 18 hours. The crude mixture of **48h** was purified by column chromatography using ethyl acetate/hexane (60/40) to afford Ts-D-valine cyclobutanone analog **48h** (15.5 mg, 42%) as a white solid: mp 179-181. ¹H NMR (500 MHz, CDCl₃) δ 7.84 – 7.77 (m, 2H), 7.04 – 6.96 (m, 2H), 6.51 (dd, *J* = 16.8, 7.7 Hz, 1H), 5.08 (dd, *J* = 13.7, 7.8 Hz, 1H), 4.89 – 4.76 (m, 1H), 3.90 (s, 1.5H), 3.89 (s, 1.5H), 3.48 (ddd, *J* = 16.5, 7.8, 5.1 Hz, 1H), 2.99 – 2.87 (m, 2H), 2.43 – 2.30 (m, 1H), 2.17 – 2.06 (m, 1H), 2.01 – 1.94 (m, 0.5H), 1.87 (dtd, *J* = 11.0, 9.6, 8.1 Hz, 0.5H), 0.87 (dd, *J* = 6.9, 3.2 Hz, 3H), 0.81 (t, *J* = 6.7 Hz, 3H). ¹³C NMR (126 MHz, CDCl₃) δ 204.22, 170.37, 170.30, 163.28, 130.53, 129.59, 114.37, 64.08, 63.90, 61.82, 61.80, 55.68, 42.29, 42.21, 31.11, 31.05, 19.19, 19.04, 17.15, 17.12. HRMS (ESI): Calcd for (MH⁺) C₁₆H₂₃N₂O₅S: 355.1322, found 355.1309.

Synthesis of (S)-(S)-3-(4-hydroxyphenyl)-2-((4-methylphenyl) sulfonamido)propanoic 4-methylbenzenesulfonic anhydride (49)



L-Tyrosine (200 mg, 1.10 mmol) was reacted with tosyl chloride (524.3 mg, 2.75 mmol) in the presence of Na₂CO₃ following the general procedure to afford sulfonate ester **18** (510.2 mg, 94.7%) as a white solid. ¹H NMR (500 MHz, CDCl₃) δ 7.74 – 7.65 (m, 2H), 7.59 – 7.52 (m, 2H), 7.31 (d, *J* = 8.1 Hz, 2H), 7.27 – 7.15 (m, 2H), 7.06 – 6.97 (m, 2H), 6.88 – 6.78 (m, 2H), 5.32 (d, *J* = 8.6 Hz, 1H), 4.12 (ddd, *J* = 8.7, 7.1, 5.2 Hz, 1H), 3.07 (dd, *J* = 14.0, 5.1 Hz, 1H), 2.91 (dd, *J* = 14.0, 7.2 Hz, 1H), 2.44 (s, 3H), 2.40 (s, 3H). ¹³C NMR (126 MHz, CDCl₃) δ 174.14, 148.79, 145.55, 144.06, 136.24, 134.16, 132.23, 130.72, 129.85, 129.77, 128.48, 127.03, 122.46, 56.30, 38.11, 21.74, 21.54.

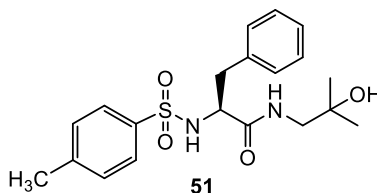
Synthesis of tosyl-L-tyrosine (50)



To a solution of sulfonate ester **49** (100 mg, 0.204 mmol) in absolute ethanol was added 2 N NaOH and the reaction mixture was allowed to stir at 90 °C for 20 hours. Upon completion, pH of the solution brought down to 2 by adding 2 N HCl. While acidifying, a white crystalline solid formed. Precipitation of the product was completed over the period

of 18 hours. Crystals were filtered and rinsed with water to afford compound **50** (40.8 mg, 60%) as a pale-brown needle-like crystals. ^1H NMR (500 MHz, MeOD) δ 7.56 – 7.50 (m, 2H), 7.24 (d, J = 8.0 Hz, 2H), 6.96 – 6.89 (m, 2H), 6.64 – 6.58 (m, 2H), 3.94 (dd, J = 8.4, 5.5 Hz, 1H), 2.95 (dd, J = 13.9, 5.5 Hz, 1H), 2.74 (dd, J = 13.9, 8.5 Hz, 1H), 2.41 (s, 3H). ^{13}C NMR (126 MHz, MeOD) δ 173.28, 155.97, 143.01, 138.22, 129.99, 129.06, 129.04, 127.07, 126.59, 114.72, 57.72, 37.67, 20.04.

Synthesis of (S)-N-(2-hydroxy-2-methylpropyl)-2-((4-methylphenyl)sulfonamido)-3-phenylpropanamide (51)

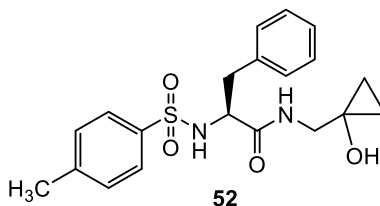


Ts-L-phenylalanine (50 mg, 0.129 mmol) was reacted with dimethylethanolamine (14.4 μL , 0.155 mmol) following the general T3P coupling procedure and stirred at 50 to 60 $^{\circ}\text{C}$ for 6 days until completion. The crude product (oil) of **51** was crystallized from hot EA/hexane = 20/80. When the EA/hexane solution was cooled to rt the product became an oil. Therefore, it is important to maintain the temperature of the solution to stay between 50 to 60 $^{\circ}\text{C}$ to allow a slow crystallization of the final product. Recrystallization provided compound **51** (29 mg, 58%) as clear needle-like crystals: mp 131-133 $^{\circ}\text{C}$. ^1H NMR (500 MHz, CDCl_3) δ 7.53 – 7.47 (m, 2H), 7.23 – 7.14 (m, 5H), 6.96 – 6.90 (m, 2H), 6.74 (s, 1H), 4.93 (d, J = 6.2 Hz, 1H), 3.84 (dt, J = 7.8, 6.1 Hz, 1H), 3.29 (dd, J = 13.7, 6.9 Hz, 1H), 3.12 (dd, J = 13.7, 5.5 Hz, 1H), 2.97 (dd, J = 14.0, 5.9 Hz, 1H), 2.91 (dd, J = 14.0, 7.7 Hz, 1H), 2.43 (s, 3H), 1.16 (d, J = 2.2 Hz, 6H). ^{13}C NMR (126 MHz, CDCl_3) δ 170.92, 144.05, 135.19, 135.16, 129.87,

129.09, 129.04, 127.37, 127.23, 70.85, 58.06, 50.30, 38.29, 27.17, 27.10, 21.58. HRMS (ESI):

Calcd for (MH⁺) C₂₀H₂₇N₂O₄S: 391.1686, found 391.1680.

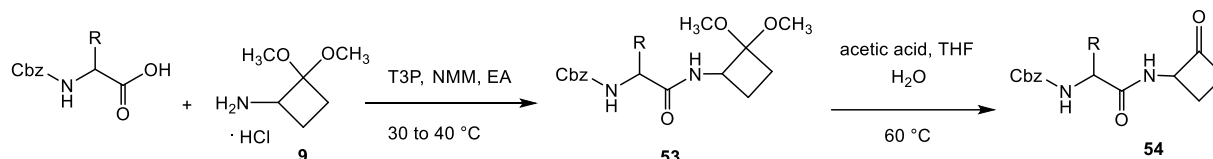
Synthesis of (S)-N-((1-hydroxycyclopropyl)methyl)-2-((4-methylphenyl) sulfonamido)-3-phenylpropanamide (52)



Ts-L-phenylalanine (50 mg, 0.129 mmol) was reacted with 1-(aminomethyl)cyclopropanol (14.4 μ L, 0.155 mmol) following the general T3P coupling procedure and stirred at 50 $^{\circ}$ C for 4 days. The crude mixture of **52** was purified by column chromatography on a Teledyne Isco Rf Flash chromatography unit eluting with a gradient of ethyl acetate/hexane (20/80) and ethyl acetate/hexane (30/70). Appropriate fractions were combined and concentrated to give white solid which then subjected to recrystallization. The product was dissolved in minimum amount of hot methylene chloride and hexane was added dropwise until cloudiness was observed. While cooling needle-like crystals formed providing compound **52** (13.6 mg, 27%): mp 131-133 $^{\circ}$ C. ¹H NMR (500 MHz, CDCl₃) δ 7.51 (dd, J = 8.1, 2.4 Hz, 2H), 7.25 (d, J = 13.9 Hz, 1H), 7.21 (dd, J = 12.2, 7.2 Hz, 5H), 6.94 (d, J = 7.1 Hz, 2H), 6.75 (NH, d, J = 6.3 Hz, 1H), 4.96 (NH, d, J = 5.7 Hz, 1H), 3.86 – 3.80 (m, 1H), 3.39 (ddd, J = 14.3, 6.8, 2.4 Hz, 1H), 3.30 – 3.22 (m, 1H), 3.20 (OH, s, 1H), 2.95 (tt, J = 14.1, 10.3, 8.5, 4.4 Hz, 2H), 2.43 (d, J = 2.4 Hz, 3H), 0.79 (s, 2H), 0.64 – 0.56 (m,

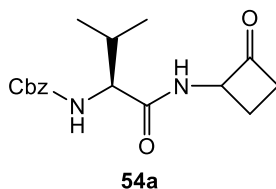
1H), 0.56 – 0.50 (m, 1H). ¹³C NMR (126 MHz, CDCl₃) δ 171.13, 144.15, 135.17, 135.03, 129.88, 129.09, 129.06, 127.41, 127.26, 58.15, 55.43, 47.73, 38.32, 21.60, 12.84, 12.48.

Synthesis of Cbz-Amino Acid Cyclobutanone Analogs 54a-d



Cbz protected amino acids (Phe, Try, Val, 50 mg) were coupled with 2-aminocyclobutanone synthon **9** following the general T3P coupling reaction procedure. The resulting acetal intermediates **53a-d** were subjected to hydrolysis without further purification. To a solution of crude acetal product (1 eq, concentration = 0.1 M) in THF (40% v/v), water (20% v/v) and acetic acid were added, and the reaction mixture was stirred at 60 °C overnight or until deemed complete by HPLC. Upon completion, excess acetic acid was neutralized by adding a solution of saturated Na₂CO₃ until pH of 8 was achieved and the organic product was extracted with methylene chloride (3 x 3 mL). The combined organic layers were dried over Na₂SO₄, and the solvent was evaporated under reduced pressure. The crude mixture was purified by column chromatography to afford the corresponding Cbz protected amino acid-derived cyclobutanone (**54a-d**).

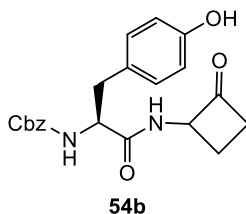
Benzyl ((2S)-3-methyl-1-oxo-1-((2-oxocyclobutyl)amino)butan-2-yl)carbamate (54a)



The crude mixture of **54a** was purified by column chromatography eluting with a gradient of ethyl acetate/hexane (20/80) to (30/70). Appropriate fractions were combined

and concentrated to give a white solid which then subjected to recrystallization. The product was dissolved in a minimum amount of methylene chloride and hexane was added dropwise until cloudiness was observed. Over 24 hours, needle-like crystals formed providing compound **54a** (21.3 mg, 34%): mp 140-144. ^1H NMR (500 MHz, CDCl_3) δ 7.38 (s, 3H), 7.43 – 7.32 (m, 2H), 6.44 – 6.39 (d, 1H), 5.26 (d, $J = 8.9$ Hz, 1H), 5.14 (s, 2H), 4.91 (dt, $J = 10.1, 7.9$ Hz, 1H), 4.01 (dd, $J = 8.8, 6.0$ Hz, 1H), 2.98 (t, $J = 8.8$ Hz, 2H), 2.46 (dd, $J = 13.3, 5.3$ Hz, 1H), 2.18 (h, $J = 6.8$ Hz, 1H), 2.13 – 2.06 (m, 1H), 1.00 (d, $J = 6.8$ Hz, 3H), 0.95 (d, $J = 6.8$ Hz, 3H). ^{13}C NMR (126 MHz, CDCl_3) δ 204.44, 170.99, 152.17, 136.09, 128.61, 128.31, 128.13, 67.27, 64.17, 60.03, 42.28, 30.79, 29.71, 19.48, 19.18. HRMS (ESI): Calcd for (MH^+) $\text{C}_{17}\text{H}_{23}\text{N}_2\text{O}_4$: 319.1652, found 319.1641.

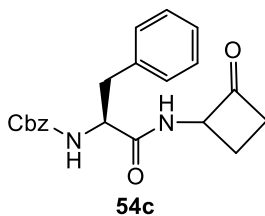
Benzyl ((2S)-3-(4-hydroxyphenyl)-1-oxo-1-((2-oxocyclobutyl)amino)propan-2-yl)carbamate (54b)



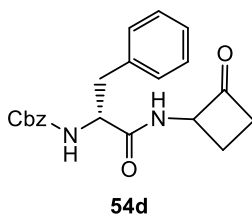
The crude mixture of **54b** was purified by column chromatography eluting with a gradient of ethyl acetate/hexane (20/80) to (30/70). Combined fractions were recrystallized from hot methylene chloride to afford compound **54b** (14.6 mg, 24%) as small needle-like crystals: mp 154-155 °C. ^1H NMR (500 MHz, CD_3CN) δ 7.42 – 7.26 (m, 4H), 7.23 – 7.13 (m, 1H), 7.11 – 7.04 (m, 2H), 6.77 – 6.71 (m, 2H), 5.88 (dd, $J = 12.9, 8.5$ Hz, 1H), 5.08 (d, $J = 12.8$ Hz, 1H), 4.99 (d, $J = 12.7$ Hz, 1H), 4.80 (dddd, $J = 20.0, 10.0, 5.9, 2.1$ Hz, 1H), 4.25 (dtd, $J = 17.5, 8.7, 5.3$ Hz, 1H), 3.04 (ddd, $J = 13.6, 7.8, 5.4$ Hz, 1H), 2.96 – 2.81 (m, 1H),

2.79 (dddd, $J = 14.1, 12.0, 8.3, 2.7$ Hz, 1H), 2.15 – 1.91 (m, 1H). ^{13}C NMR (126 MHz, CD_3CN) δ 206.08, 171.17, 171.10, 155.73, 137.13, 130.43, 128.45, 128.27, 128.22, 127.86, 127.51, 115.09, 66.07, 63.71, 63.63, 56.31, 56.14, 41.39, 41.37, 18.33, 18.14.

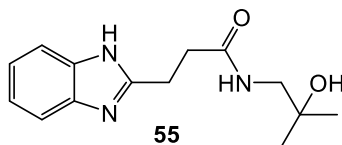
Benzyl ((2S)-1-oxo-1-((2-oxocyclobutyl)amino)-3-phenylpropan-2-yl)carbamate (54c)



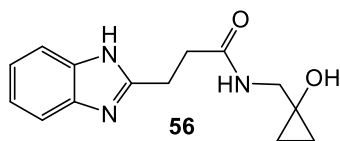
The crude mixture of **54c** was purified by column chromatography eluting with a gradient of ethyl acetate/hexane (20/80) to (30/70). Appropriate fractions were combined and concentrated to give white solid (94% HPLC purity) which was then recrystallized from hot methylene chloride to give a white needle-like crystals of compound **54c** with 97% HPLC purity (30.2 mg, 49%): mp 100-101 °C. ^1H NMR (500 MHz, CDCl_3) δ 7.40 – 7.23 (m, 8H), 7.23 – 7.17 (m, 2H), 6.63 (NH, d, $J = 7.6$ Hz, 0.5H), 6.48 (NH, d, $J = 7.9$ Hz, 0.5H), 5.46 (t, $J = 10.6$ Hz, 1H), 5.07 (t, $J = 3.3$ Hz, 2H), 4.96 – 4.87 (m, 0.5H), 4.78 (qt, $J = 7.9, 1.4$ Hz, 0.5H), 4.45 (d, $J = 7.0$ Hz, 1H), 3.09 (d, $J = 6.7$ Hz, 2H), 2.98 – 2.83 (m, 2H), 2.38 (dd, $J = 10.9, 5.2$ Hz, 0.5H), 2.33 (dd, $J = 10.3, 4.7$ Hz, 0.5H), 2.03 (q, $J = 9.6$ Hz, 0.5H), 1.90 – 1.73 (m, 0.5H). ^{13}C NMR (126 MHz, CDCl_3) δ 204.79, 204.76, 170.84, 170.69, 156.03, 136.23, 136.23, 136.08, 129.40, 129.38, 128.76, 128.58, 128.26, 128.01, 127.14, 67.16, 64.03, 63.72, 55.97, 55.75, 42.16, 42.06, 38.63, 38.43, 19.35, 19.13. HRMS (ESI): Calcd for (MH⁺) $\text{C}_{21}\text{H}_{23}\text{N}_2\text{O}_4$: 367.1652, found 367.1646.

Benzyl ((2R)-1-oxo-1-((2-oxocyclobutyl)amino)-3-phenylpropan-2-yl)carbamate (54d)

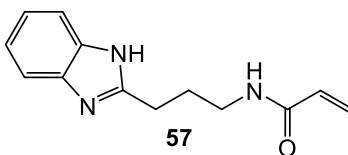
The crude mixture of **54d** was purified by column chromatography eluting with a gradient of ethyl acetate/hexane (20/80) and ethyl acetate/hexane (30/70). Appropriate fractions were combined and concentrated to give white solid (93% HPLC purity) which then subjected to recrystallization. The product was dissolved in minimum amount of methylene chloride and hexane was added dropwise until cloudiness was observed. Colorless crystals were formed providing compound **54d** (16.1 mg, 26%): mp 98-100 °C. ¹H NMR (500 MHz, CDCl₃) δ 7.41 – 7.24 (m, 8H), 7.21 (t, *J* = 6.0 Hz, 2H), 6.35 (d, *J* = 7.6 Hz, 0.5H), 6.20 (d, *J* = 8.0 Hz, 0.5H), 5.32 (s, 0.5H), 5.27 (s, 0.5H), 5.10 (s, 2H), 4.92 (q, *J* = 9.0 Hz, 0.5H), 4.81 (q, *J* = 8.7 Hz, 0.5H), 4.42 (q, *J* = 7.3 Hz, 1H), 3.17 – 3.11 (m, 1H), 3.06 (td, *J* = 13.5, 12.9, 7.6 Hz, 1H), 2.99 – 2.85 (m, 2H), 2.39 (dq, *J* = 15.8, 9.7 Hz, 1H), 2.06 - 2.03 (m, 0.5H), 1.88 – 1.81 (m, 0.5H). ¹³C NMR (126 MHz, CDCl₃) δ 204.33, 170.65, 170.49, 155.97, 136.02, 136.02, 129.39, 129.37, 128.84, 128.59, 128.30, 128.29, 128.09, 127.22, 67.23, 64.05, 63.76, 56.03, 42.21, 42.12, 38.56, 38.19, 19.42, 19.22.

3-(1H-Benzo[d]imidazol-2-yl)-N-(2-hydroxy-2-methylpropyl)propanamide (55)

To a solution of 2-benzimidazolepropionic acid (30 mg, 0.158 mmol) and dimethylethanolamine (17.6 μ L, 0.189 mmol) in dry methylene chloride (790 μ L, 0.2 M), *N*-methyl morpholine (34.8 μ L, 0.316 mmol) was added. Then propylphosphonic anhydride (T3P, 158 μ L, 0.395 mmol) was added to the above mixture as a solution in ethyl acetate (purchased as ≥ 50 weight % in EA). The reaction mixture was stirred under N_2 at 50°C for 17 hours while monitoring the reaction progress by HPLC analysis. The reaction was quenched by adding water (1 mL), and then the organic product was extracted using methylene chloride (5 x 2 mL). The combined organic layers were dried over Na_2SO_4 . The solvent was removed under reduced pressure, and the resultant crude product was purified by recrystallization. The crude product was dissolved in a minimum amount of methylene chloride, and petroleum ether was added dropwise until cloudiness was observed. Compound **55** (5.2 mg, 13%) was isolated as white crystals: mp 139-141 °C. 1H NMR (500 MHz, MeOD) δ 7.93 (NH, dd, $J = 7.8, 1.4$ Hz, 1H), 7.73 – 7.63 (m, 2H), 7.46 – 7.36 (m, 2H), 3.34 – 3.24 (m, 4H), 3.00 (t, $J = 6.9$ Hz, 2H), 1.73 – 1.62 (m, 6H). ^{13}C NMR (126 MHz, MeOD) δ 170.96, 148.36, 128.38, 125.08, 124.05, 118.86, 112.54, 63.85, 54.97, 34.06, 20.59. HRMS (ESI): Calcd for (MH^+) $C_{14}H_{20}N_3O_2$: 262.1550, found 262.1542.

3-(1H-Benzo[d]imidazol-2-yl)-N-((1-hydroxycyclopropyl)methyl) propanamide (56)

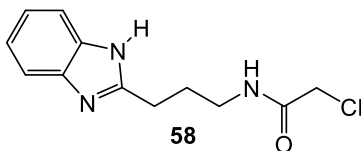
Compound **56** was synthesized by reacting 2-benzimidazolepropionic acid (30 mg, 0.158 mmol) and 1-(aminomethyl)cyclopropanol (16.5 mg, 0.189 mmol) using the T3P coupling reaction conditions utilized in the synthesis of compound **55**. The crude mixture of **56** was purified by column chromatography using 2% methanol in ethyl acetate to afford compound **56** (6.9 mg, 17%) as a white solid. ^1H NMR (500 MHz, MeOD) δ 7.98 – 7.90 (m, 1H), 7.71 (dt, J = 6.8, 3.4 Hz, 2H), 7.50 (dt, J = 6.1, 3.3 Hz, 2H), 3.34 – 3.24 (m, 4H, mixture of amide rotamers), 3.03 (t, J = 7.1 Hz, 2H), 1.10 – 0.97 (m, 6H). ^{13}C NMR (126 MHz, MeOD) δ 170.97, 148.36, 125.07, 124.95, 124.03, 118.84, 113.44, 112.53, 53.15, 50.95, 34.05, 20.58.

N-(3-(1H-Benzo[d]imidazol-2-yl)propyl)acrylamide (57)

1H-Benzimidazole-2-propanamine dihydrochloride (40 mg, 0.16 mmol) was suspended in methylene chloride (0.8 mL) and triethylamine (78.2 μL , 0.56 mmol) was added to the solution. The reaction mixture was cooled to 0°C, and acryloyl chloride (19.6 μL , 0.24 mmol) was added dropwise to the stirring solution under N_2 . The reaction was allowed to warm to room temperature and stirred at rt for 7 hours while monitoring the reaction progress using HPLC. Upon completion, the reaction was quenched by adding water (2 mL), and the organic product was extracted using ethyl acetate (5 x 2 mL). The combined organic layers were dried over Na_2SO_4 . The solvent was removed under reduced

pressure, and the resultant crude product was purified by recrystallization. The crude product was dissolved in a minimum amount of methanol, and diethyl ether was added dropwise until a cloudy solution is formed. Needle-like crystals of compound **57** (5.3 mg, 14%) formed over a period of 18 hours: mp 106-108 °C. ^1H NMR (500 MHz, CDCl_3) δ 7.65 – 7.58 (m, 2H), 7.25 (dd, $J = 6.0, 3.2$ Hz, 2H), 6.50 (s, 1H), 6.38 (dd, $J = 16.9, 1.3$ Hz, 1H), 6.16 (dd, $J = 16.9, 10.3$ Hz, 1H), 5.74 (dd, $J = 10.3, 1.3$ Hz, 1H), 3.49 (q, $J = 6.2$ Hz, 2H), 3.03 – 2.96 (m, 2H), 2.07 – 1.98 (m, 2H). ^{13}C NMR (126 MHz, CDCl_3) δ 167.11, 154.28, 130.41, 127.43, 122.23, 38.27, 28.72, 25.53. HRMS (ESI): Calcd for (MH^+) $\text{C}_{13}\text{H}_{16}\text{N}_3\text{O}$: 230.1288, found 230.1282.

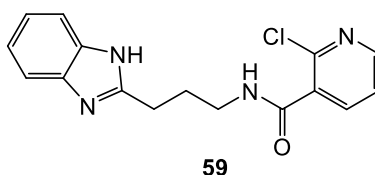
***N*-(3-(1*H*-Benzo[d]imidazol-2-yl)propyl)-2-chloroacetamide (58)**



To a solution of 1*H*-benzimidazole-2-propanamine dihydrochloride (50 mg, 0.201 mmol) and 2-chloroacetic acid (20.9 mg, 0.221 mmol) in dry methylene chloride (1.0 mL, 0.2 M), *N*-methyl morpholine (110.7 μL , 1.01 mmol) was added. Then propylphosphonic anhydride (T3P, 300.5 μL , 0.502 mmol) was added to the above mixture as a solution in ethyl acetate (purchased as ≥ 50 weight % in EA). The reaction mixture was stirred under N_2 at rt for 7 hours while monitoring the reaction progress using HPLC. The reaction was quenched by adding water (3 mL), and a solution of saturated NaHCO_3 was added until the pH of the reaction mixture reached 8-9. A crystalline solid formed in solution. The solid was filtered and washed with water. The resultant crude product was recrystallized from hot

methylene chloride providing compound **58** (13.2 mg, 28%) as pink crystals: mp 171-173 °C. ¹H NMR (500 MHz, MeOD) δ 7.54 – 7.48 (m, 2H), 7.24 – 7.17 (m, 2H), 4.90 (s, 1H), 4.04 (s, 2H), 3.36 (t, *J* = 8.5, 6.9 Hz, 2H), 2.95 (t, *J* = 7.6 Hz, 2H), 2.07 (q, *J* = 7.1 Hz, 2H). ¹³C NMR (126 MHz, CDCl₃) δ 167.62, 153.83, 138.33, 122.34, 114.84, 42.61, 38.84, 28.21, 25.82. HRMS (ESI): Calcd for (MH⁺) C₁₂H₁₅ClN₃O: 252.0898, found 252.0886.

***N*-(3-(1*H*-Benzo[d]imidazol-2-yl)propyl)-2-chloronicotinamide (59)**



To a solution of 1*H*-benzimidazole-2-propanamine dihydrochloride (50 mg, 0.201 mmol), 1-ethyl-3-(3-dimethylaminopropyl)carbodiimide hydrochloride (191.7 mg, 0.242 mmol), hydroxybenzotriazole (135.12 mg, 0.242 mmol), and 2-chloronicotinic acid (50.0 mg, 0.201 mmol) in anhydrous dimethylformamide (670 μL, 0.3 M), *N*-methyl morpholine (93.2 μL, 0.846 mmol) was added via syringe before the vial was degassed with N₂ and stirred at 80 °C for 36 hours until deemed complete by HPLC. The reaction was quenched by adding water (1 mL), and a solution of saturated NaHCO₃ was added until the pH of the reaction mixture reached 8. The organic product was extracted using methylene chloride (6 x 2 mL). The combined organic layers were dried over Na₂SO₄, and the solvent was removed by evaporation under reduced pressure. The crude product was purified by column chromatography on a Teledyne Isco Rf Flash chromatography unit eluting with 1% methanol in ethyl acetate. Then the compound was further purified by recrystallization. The solid obtained from the column was dissolved in a minimum amount of methanol, and

diethyl ether was added dropwise until a cloudy solution is formed. Crystals were allowed to form at rt, and the crystals were washed with methylene chloride to afford compound **59** (18.3 mg, 29%) as clear needle-like crystals: mp 164-166 °C. ¹H NMR (500 MHz, MeOD) δ 8.21 (dd, *J* = 7.5, 1.8 Hz, 1H), 8.06 (dt, *J* = 3.5, 1.9 Hz, 1H), 7.62 (ddd, *J* = 8.2, 6.8, 0.9 Hz, 1H), 7.57 – 7.48 (m, 2H), 7.24 – 7.16 (m, 2H), 3.62 (t, *J* = 6.9 Hz, 2H), 3.07 (t, *J* = 7.6 Hz, 2H), 2.25 (q, *J* = 7.2 Hz, 2H). ¹³C NMR (126 MHz, MeOD) δ 164.74, 158.74, 154.66, 148.75, 143.13, 140.50, 128.67, 125.02, 121.87, 121.76, 119.23, 118.14, 48.11, 47.94, 47.77, 47.60, 47.43, 47.26, 47.09, 39.27, 27.43, 25.85.

In silico Methods

Protein/Receptor Structure Models

The crystal structures of Nsp3 (PDB ID: 6W02), Nsp9 (PDB ID: 6W4B), and Nsp15 (PDB ID: 6VWW) of SARS CoV-2 were obtained from Protein Data Bank. The crystal structures of SARS-CoV-2 main protease (Nsp5) in complex with Z44592329 (ID: 5r83) were obtained from the Protein Structure Database of Europe. The I-TASSER models for Nsp3 (QHD43415_3), Nsp5 (QHD43415_5), Nsp11 (QHD43415_11), Nsp12 (QHD43415_12), Nsp13(QHD43415_13), and Nsp14 (QHD43415_14) were used.¹⁵³

Protein (Receptor) Preparation

Protein preparation was performed using the Protein Preparation Wizard in Maestro.¹⁵⁴ Crystallization ions present in the crystal structure, including calcium and chloride, were deleted. Crystallization ligands present in the active site were not deleted as they were utilized for grid generation. All water molecules with less than three hydrogen

bonds (Sample water orientation) with the receptor or the ligand were deleted. Structure preparation of all seven receptor models developed was performed in the Wizard in Maestro. Each of the corrected receptor complexes was optimized with minimized hydrogens and then minimized using the OPLS3e force field.¹⁵⁴ Then, MD simulations (MDS) of the receptor models were performed under physiological conditions (0.15 M NaCl) by solvating the models in water. A simulation (water) box covering the entire receptor model was created with a 10 Å buffer space. The MD simulation was run for 20 ns at 300 K and standard pressure (1.01325 bar). Interacting residues were studied via a target complex trajectory analysis performed using the Desmond software.¹⁵⁴

Ligand Library Preparation

Ligand preparation was performed on LigPrep, where potential structural variations of ligands were generated, reactive species were eliminated, and ligands were optimized. Optimization was performed utilizing the OPLS3e force field. Protonation states of ligands at pH 7.0 ± 2.0 were taken into consideration and an EPIK minimization was performed on all possible protonated species. Tautomers of each ligand were created while retaining the chirality combinations with a maximum of 32 structures for each ligand.

Receptor Grid Preparation

Active sites of the receptors were located, and the size was estimated using COACH analysis. A grid with appropriate shapes and properties of each receptor was created for more accurate and refined screening and to avoid the exclusion of possible active compounds. Binding pocket residues predicted using the centroid of the COACH, through

which grids were generated using default values of protein atom scaling (1.0 Å) within a cubic box and ligand docking set to a length of 20 Å. OPLS3e force field was employed in grid generation. During the grid generation, the Receptor Grid Generation wizard of the Glide module intrinsically determined rotatable groups. COACH predicted binding site residues of each target were represented as; **Main protease (M^{pro})**; in accordance with PDB ID: 2q6gB amino acids constitute the substrate-binding site were 25, 26, 27, 41, 49, 140, 141, 142, 143, 144, 145, 163, 164, 165, 166, 168, 172, 187, 189, 190, and 192. **PLpro (Papain-like protease)**; Based on sequence similarity with SARS-CoV PLpro model (PDB ID: 3mj5B) and catalytic triad of Cys–His–Asp, the binding site consist of amino acids 209, 223, 230, 233, 234, 235, 236, 237, 238, 239, 293, 318, 321, 324, 325, 327, 349, 350, 352, 353, 354, 356, and 763. **RNA directed RNA polymerase (RdRP)**; based on a model (PDB ID: 3ol9I) with a comparable active site, the nucleic acid binding site consist of amino acid residues 500, 501, 507, 512, 543, 545, 557, 559, 560, 569, 580, 589, 590, 591, 592, 682, 683, 684, 685, 686, 758, 857, 860, 864 and 914. **Helicase**; deduced from a homolog model (PDB ID: 4N00), nucleic acid binding site comprise of amino acid residues 177, 178, 179, 180, 181, 197, 214, 309, 310, 311, 334, 335, 336, 337, 338, 339, 408, 409, 410, 411, 412, 413, 414, 485, 486, 516, 534, 554 and 560. **Exoribonuclease (ExoN)**; Based on the active site similarity with PDB ID: 5C8T, S-Adenosyl-L-Methionine (SAM) binding site residues were identified as 292, 333, 335, 352, 353, 366, 367, 368, 385, 386, 387, and 426. **2'-O-methyltransferase (2'-O-MT)**; Based on sequence similarity with a homolog protein (PDB ID: 4N48), the SAM binding site was 46, 74, 133, 134, 170, and 203. **Nonstructural**

Uridylate-specific endoribonuclease (NendoU); The COACH hit was PDB ID: 2C1W and the active site residues identified were, 234, 249, 289, 291, 292, 293, 332, 334, 339, 340, 341 and 342.

High-Throughput Virtual Screening (HTVS)

The HTV screening was performed in Glide (a Grid-based ligand docking that utilizes energy calculations) module of the Schrödinger suite.¹⁵⁰ Default parameters, including ionization states at defined pH, and Epik state penalties (for ionization and/or tautomeric states at physiological pH) were taken into consideration. The scaling factor was fixed at a default of 0.8 and a 0.15 partial charge cut-off was selected. The force field used docking was OPLS3e. An HTVS ligand docking was performed first, followed by SP and XP docking on the top 10% scoring hits from the appropriate previous step. The XP docking is an accurate analysis that eliminates false positives through a rigorous scoring function than the HTVS. The binding affinity of the ligand is determined by the Glide score. The greater the XP GScore, the better the estimated affinity of the hit towards the protein target. Binding free energies of the best docked ligand-receptor complexes were calculated using MM force fields and implicit solvation was performed using the in-built molecular mechanics/generalized Born surface area (MM-GBSA) method of the Schrödinger virtual screening platform.¹⁵⁴ The binding energy calculation used the following equation.

$$\Delta G = E_{\text{complex}}(\text{minimized}) - (E_{\text{ligand}}(\text{minimized}) + E_{\text{receptor}}(\text{minimized}))$$

The test ligands were ranked based on the estimated binding free energy for the corresponding ligand-receptor complexes.

Molecular Dynamics Simulation (MDS)

The stability of the ligand-receptor complex and the energetic strain on the docked ligand during the induced fit (flexible binding site) docking screening were measured. An increased strain energy of the ligand could result in immediate fly-off (<10 ns). Our integrated HTVS and MM-GBSA screening pipeline was validated via a 20 ns MD simulation of top hits from each target pool following the method stated in the protein/receptor preparation section. When the ligand/hit experienced a major conformation change, it flew off immediately from the receptor binding site. In that case, a 20 ns simulation of the free receptor was performed until it reached a stable state, and the ligand screening was repeated with the resulting minimized receptor.

CHAPTER FIVE
CHARACTERIZATION OF PA3944 GCN5-RELATED *N*-ACETYLTRANSFERASE
BACTERIAL ENZYME

Introduction

The Gcn5-related *N*-acetyltransferase (GNAT) superfamily is found in all kingdoms of life with diverse functionality and plays key roles in cellular and metabolic processes, including histone modification, xenobiotic metabolism, and aminoglycoside antibiotics resistance.^{173,174} GNATs are one of the bacterial acetyltransferases studied extensively among other acetyltransferases, including arylamine *N*-acetyltransferase (NAT).¹⁷⁵ Typically, acetyltransferases are classified into different families based on their structural folds and the types of substrates they acetylate. The GNATs transfer an acyl group from an active donor, typically acetyl-coenzyme A (AcCoA), to an acceptor substrate. Polyamine antibiotics, such as polymyxin B and other biomolecules, including peptides and proteins, can act as acceptor substrates.¹⁷⁴ The catalysis of the acetyl transfer reaction is facilitated by various structural scaffolds, active site residues, and specific kinetic mechanisms adopted by acetyltransferases. Only a small number of GNAT enzymes have been structurally and functionally characterized, while the vast majority of enzymes within this superfamily remain uncharacterized.

The three-dimensional structure of the ligand-bound protein is a powerful tool in identifying the active site and the ligand-binding site residues through which modern computer simulations can predict protein functions or modes of ligand binding.¹⁷⁶ The X-ray crystal structures of hundreds of AcCoA/CoA bound GNATs can be found in the Protein Data Bank (PDB) to date, but relatively few have a functionally relevant ligand bound in the acceptor substrate binding site. In collaboration with Dr. Misty Kuhn from San Francisco State University (SFSU), we are investigating bacterial GNATs with unknown biological functions from *Pseudomonas aeruginosa* to advance our understanding of the functionalities, structural features, and variations within the diverse family of GNATs.

X-ray Crystal Structures of GNATs

The two distinct substrate-binding sites of the GNATs are the donor (AcCoA) binding site and the acceptor substrate binding site. The conservation of the AcCoA/CoA binding site enables facile prediction of the AcCoA binding mode interactions in newly discovered GNATs. On the other hand, often highly selective acceptor substrate binding site is diverse among GNATs making it very difficult to predict the binding modes of ligands.

The predominant challenges in obtaining structures of acceptor substrate-bound GNATs are a lack of knowledge of GNAT functions and difficulties in co-crystallizing the enzyme with previously identified potential acceptor substrates. The following two strategies are used in obtaining ligand-bound structure of proteins, (1) chemically synthesize modified substrates that can be used for the synthesis of bisubstrates in the crystal or during co-crystallization, and (2) co-crystallize or soak crystals with covalent

alkylating agents with a high affinity toward the protein and that will label active site residues through the formation of a covalent complex.^{177,178} It is reasonable to assume that an enzyme will bind more tightly to a bisubstrate via a significantly higher number of interactions than the substrate alone in the crystal. Several other groups were able to crystallize and obtain functionally relevant ligand-bound structures GNATs in the presence of bisubstrates synthesized either by the enzyme or via chemical synthesis prior to crystallization.¹⁷⁸ As part of this collaborative effort, Dr. Mateusz Czub conducted protein crystallization experiments at the University of Virginia. The mutagenesis studies were performed under the direction of Professor Misty Kuhn of SFSU.

Design and Syntheses of Biochemical Tools Useful in Crystallization and Kinetic Studies of GNAT Enzymes

The identity of a functionally relevant substrate plays a key role in understanding the structural features of an enzyme. Acceptor substrate-binding domains of particular GNATs are highly specific, making it challenging to predict the acceptor substrates solely through X-ray crystal structures of the enzyme.¹⁷⁹ Previously, our collaborator, Dr. Misty Kuhn at SFSU, performed a broad-substrate screening assay against 10 kinetically uncharacterized GNATs using 95 compounds belong to a wide range of biochemical classes that included amino acids, commercially available peptides, and different classes of antibiotics. This screening provided acceptor substrates for PA4794, PA3944, and PA2271 GNATs, and their substrate specificities for the acetylation are as follow, PA4794 acetylates the dipeptide *N*-phenylacetyl glycine lysine (NPAcGK), PA3944 acetylates the dipeptide

aspartame as well as two peptide antibiotics (polymyxin B and colistin), and PA2271 acetylates spermine and spermidine (see Figure 29).¹⁷⁹

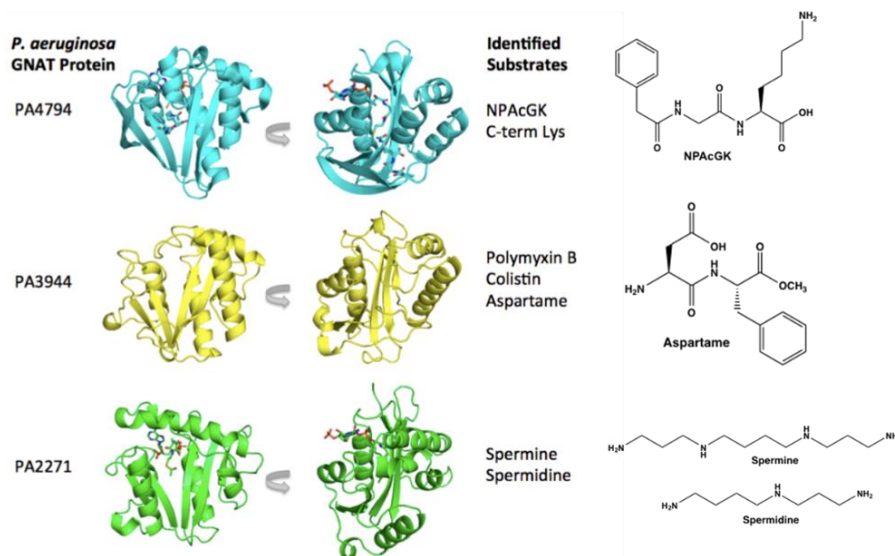


Figure 29. Acceptor substrates for PA4794, PA3944, and PA2271 GNATs, identified via a broad-substrate screening assay.¹⁷⁹

Our past research group member Dr. Cory Reidl in collaboration with Dr. Kuhn, reported two different three-dimensional structures of PA4794 with NPAcGK analog-derived bisubstrates formed in the active site with CoA (PDB ID: 5VDB) and (PDB ID 5VD6).¹⁷⁸ Dr. Reidl synthesized derivatives of NPAcGK substrates targeting PA4794, including analogs with a α -haloacetyl group on the ϵ -nitrogen of the lysine and an alkene lysine analog. The electrophilic α -haloacetyl group was installed on the ϵ -amino group of the acceptor substrate to alkylate the thiol of free CoA and produce a bisubstrate in the active site of the protein. Interestingly, two different three-dimensional structures of PA4794 were obtained with NPAcGK substrate-derived bisubstrates bound to the active site. These bisubstrates comprised of the acceptor substrate and coenzyme A (CoA) were

generated through two different mechanisms. The first bisubstrate was formed through the enzyme-catalyzed direct alkylation of CoA (PDB ID: 5VDB, see Figure 30A), and the second bisubstrate was showed to form through an X-ray induced radical-mediated addition to the alkene moiety of the substrate analog (PDB ID: 5VD6, see Figure 30B).¹⁷⁸ The feasibility of our approach in obtaining the bisubstrates in the active site during the crystal soak or co-crystallization led us to focus on synthesizing modified substrates of aspartame, a simple dipeptide, over highly complex structures of polymyxin B and colistin, and analyze GNAT PA3944 in a comparable manner to PA4794.

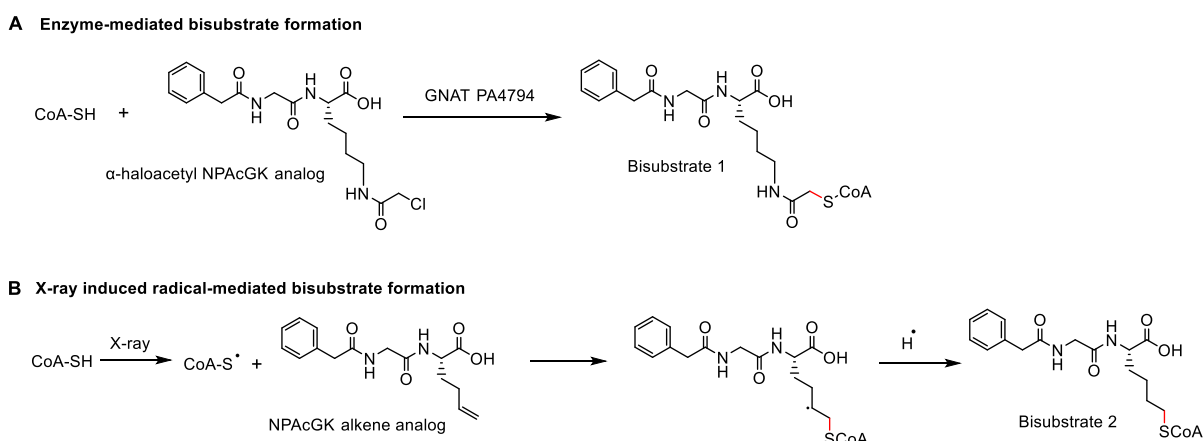


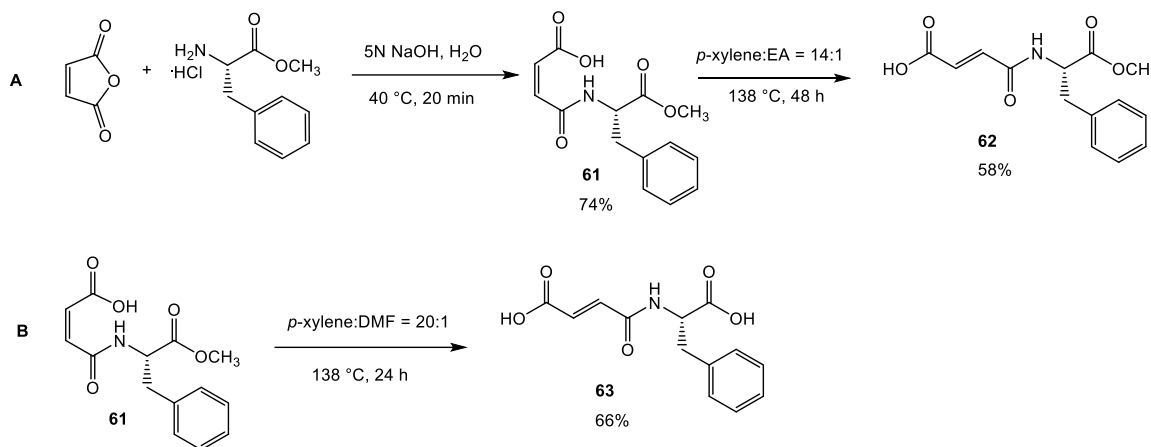
Figure 30. (A) Formation of bisubstrate 1 between CoA and α -haloacetyl NPACGK analog via enzyme-mediated alkylation of CoA. (B) X-ray induced radical-mediated addition of CoA to the alkene analog of NPACGK forming bisubstrate 2.

Design and Synthesis of Small Molecule Biochemical Tools Targeting PA3944

Rational Design and Synthesis of Aspartame Substrate Analogs

In the broad substrate screening assay, PA3944 GNAT was demonstrated to acetylate aspartame, the methyl ester of aspartic acid-phenylalanine dipeptide (see Figure 29). We successfully synthesized internal alkene analogs of aspartame, including *N*-maleyl-

L-phenylalanine methyl ester (**61**), *N*-fumaryl-L-phenylalanine methyl ester (**62**), and *N*-fumaryl-L-phenylalanine (**63**) targeting PA3944 (Scheme 26). The internal alkene analogs can act as radical or Michael acceptors and are expected to react with the thiol moiety of CoA in the ternary complex of enzyme-CoA-modified substrate during X-ray data collection and form respective bisubstrates as we observed previously.¹⁷⁸



Scheme 26. Synthesis of internal alkene analogs of aspartame (A) *N*-maleyl-L-phenylalanine methyl ester (**61**), *N*-fumaryl-L-phenylalanine methyl ester (**62**), and (B) *N*-fumaryl-L-phenylalanine (**63**) targeting PA3944.

The *N*-maleyl-L-phenylalanine methyl ester (**61**, cis isomer) was synthesized following the literature procedure¹⁸⁰ from maleic anhydride and L-phenylalanine methyl ester (see Scheme 8). We then pursued literature precedent for the cis-trans isomerization of *N*-maleyl-L-phenylalanine methyl ester to prepare the *N*-fumaryl-L-phenylalanine methyl ester (**62**, trans isomer) using 20:1 ratio of *p*-xylene to DMF. After 24 hours of reflux, the methyl ester of compound **61** was hydrolyzed to give *N*-fumaryl-L-phenylalanine (**63**). Optimized reaction conditions with *p*-xylene and dry ethyl acetate (14:1) were utilized in driving the cis-trans isomerism to completion and yielded *N*-

fumaryl-L-phenylalanine methyl ester (**62**) as shown in Scheme 26. Up until now, our efforts in obtaining a crystal structure with aspartame substrate analogs have not been successful. Thus, no acceptor substrate-bound PA3944 crystals were obtained to advance the investigation to date.

Rational Design of Small-Molecule Substrate Analogs of Polymyxin B

Colistin (polymyxin E) and polymyxin B are macrocyclic polyamines and were identified as acceptor substrates of PA3944 in Kuhn's broad-substrate screening assay.¹⁷⁹ Polymyxins are an older class of cationic, macrocyclic cyclic polypeptide antibiotics that have received a renewed interest due to rising antibiotic resistance toward other clinically relevant antibiotics.¹⁸¹ Polymyxin B is one member of this family of highly complex macrocyclic structures that contain five diaminobutyric acid (Dab) residues. We previously showed the PA3944 bacterial GNAT enzyme specifically acetylates the 3-Dab residue of polymyxin antibiotics.¹⁸² This residue is situated in the acyclic portion of the polypeptide between the fatty acid and cyclic peptide of polymyxin antibiotics (see Figure 31). Unfortunately, Dr. Karolina Majorek and Dr. Mateusz Czubs' attempts in protein crystallization and interpretation of kinetic data of polymyxin B faced challenges due to the complex structure of polymyxin B. As a result, they were unable to obtain crystals of GNAT PA3944 with the polymyxin bound to the acceptor site. Therefore, we have designed and synthesized small molecule analogs of polymyxin B as biochemical tools that are expected to bind the acceptor binding pocket and allow us to identify the active site residues and design substrates with an increased affinity toward PA3944. These insights into enzyme

structure will aid in further studies to identify homologs of GNAT with a similar catalytic mechanism.

The two small-molecule analogs *N*-(2-aminoethyl)-*N*-methyloctanamide (NANMO) and benzyl (*S*)-(4-amino-1-(methylamino)-1-oxobutan-2-yl)carbamate (BAMOC) were designed to mimic the indicated diaminobutyrate (Dab) moiety of polymyxin B (see Figure 31). Further, we proposed and synthesized an α -haloacetyl analog of NANMO (**65**) by installing an electrophilic α -chloroacetyl moiety to the nucleophilic terminal amine of NANMO, the amine that receives the acetyl group from AcCoA. The reactive electrophilic α -chloroacetyl moiety of NANMO should alkylate the thiol of free CoA to form a bisubstrate in the active site of GNAT PA3944 as we previously observed for PA4794.¹⁷⁸

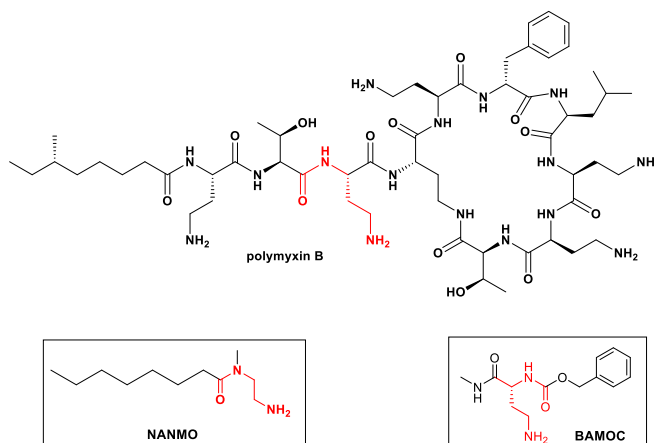


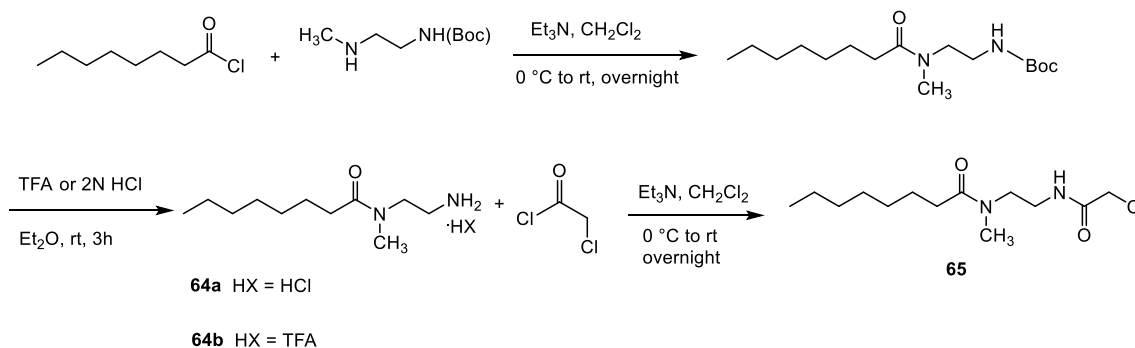
Figure 31. Structures of NANMO and BAMOC designed as small-molecule analogs of polymyxin B. The Dab moiety is highlighted in red.

Synthesis of Polymyxin B Substrate Analogs

The synthesis of NANMO was accomplished by reacting octanoyl chloride with *N*-Boc-protected-*N*-methyl ethylenediamine in the presence of triethylamine in methylene chloride. Then the Boc group was removed by reacting Boc protected NANMO with 2N HCl

in diethyl ether, providing NANMO (**64a**) as its HCl salt (see Scheme 27). NANMO was also synthesized as its TFA salt through the same route where TFA was used in the Boc deprotection reaction providing **64b** as shown in Scheme 27. We preferred the less hygroscopic TFA salt of NANMO over the HCl salt of NANMO, which turned into a sticky solid with time, making the transfer and storage of NANMO challenging.

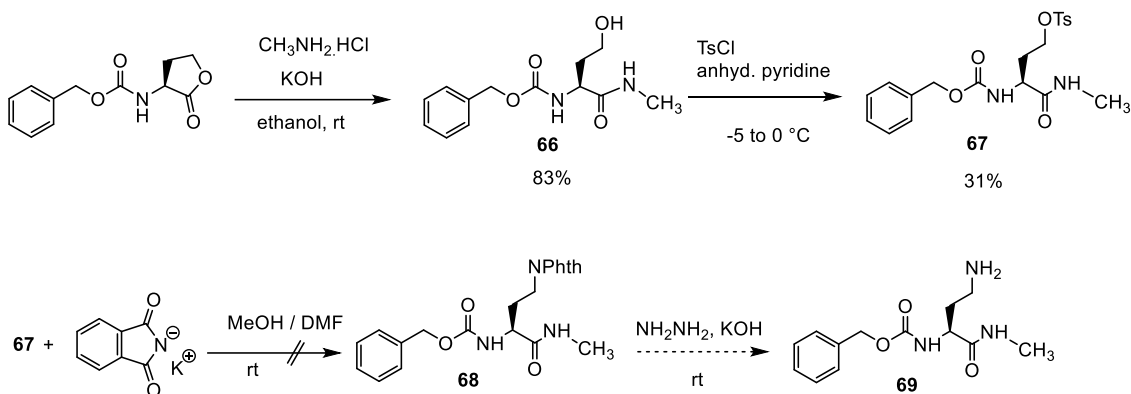
With NANMO in hand, we synthesized the alpha-chloro acetyl analog of NANMO, which could covalently alkylate nucleophilic active site residues through the formation of a covalent complex. *N*-(2-(2-Chloroacetamido)ethyl)-*N*-methyloctanamide (**65**) was synthesized via a base-mediated coupling of NANMO (**64a**) with 2-chloroacetyl chloride (see Scheme 27). Alpha-chloro NANMO will be tested against GNAT PA3944, and co-crystallization conditions will be explored.



Scheme 27. Synthesis of *N*-(2-aminoethyl)-*N*-methyloctanamide (NANMO, **64**) and α -chloro analog of NANMO (**65**).

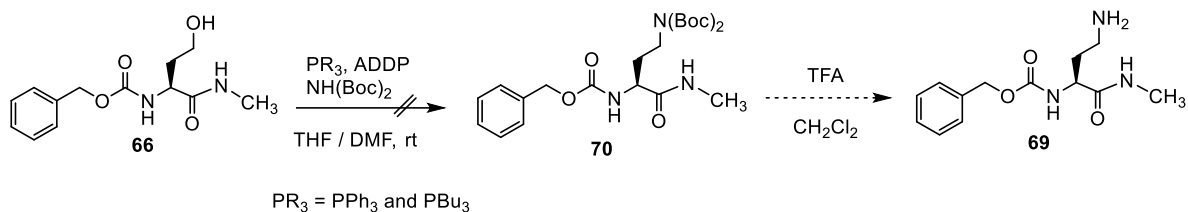
In addition to NANMO, we investigated another small-molecule analog of polymyxin B, benzyl (*S*)-(4-amino-1-(methylamino)-1-oxobutan-2-yl)carbamate (BAMOC, **69**) as an acceptor substrate against GNAT PA3944 (Figure 31). Our synthetic routes are designed to proceed at room temperature or lower to prevent the racemization of the chiral center of

BAMOC and the hydrolysis of the Cbz group (Scheme 28). The first step of the synthesis is the ring opening reaction of Cbz protected L-homoserine lactone with methylamine HCl salt in the presence of potassium hydroxide affording benzyl (S)-(4-hydroxy-1-(methylamino)-1-oxobutan-2-yl)carbamate (**66**) in 83% yield. In the next step, the alcohol analog **66** was converted to tosylate **67**. Tosylate is an excellent leaving group that can undergo nucleophilic displacements with ammonia, phthalimide, and azide. Then the *N*-alkyl phthalimide and alkyl azide derivatives should provide the final primary amine product under reducing conditions. In this route, although the tosylation of alcohol was successful, the yields were very low, and the purification of tosylate **67** was challenging due to the reactivity and instability of the tosyl group in the solvent. Therefore, tosylate **67** was reacted in the subsequent synthetic steps without further purification. The attempted reactions of tosylate **67** with potassium phthalimide in two different solvents, including methanol and DMF, to synthesize the phthalimide analog of BAMOC (**68**) were unsuccessful (see Scheme 28). We then focused on accessing BAMOC via an alkyl bromide intermediate, where the alcohol analog **66** was reacted with elemental bromine and triphenylphosphine in anhydrous pyridine. After 36 hours of stirring at room temperature, the reaction did not proceed as determined by HPLC and TLC analysis.



Scheme 28. Attempted synthesis of benzyl (*S*)-(4-amino-1-(methylamino)-1-oxobutan-2-yl) carbamate (BAMOC, **69**) via a tosylate intermediate (**67**).

The Mitsunobu reaction is an attractive alternative to synthesize primary amines in a single or two synthetic steps from an alcohol. Following a reported synthetic method,¹⁸³ we reacted the alcohol precursor of BAMOC (**66**) with $(\text{Boc})_2\text{NH}$, triphenylphosphine (PPh_3), and 1,1'-(azodicarbonyl)dipiperidine (ADDP) in anhydrous THF where the di-(Boc) amine should act as the nucleophile and displace the activated hydroxyl group, and the BAMOC could be isolated as the TFA salt via the deprotection of di-(Boc) protected BAMOC (**70**) as illustrated in Scheme 29. Even though the Mitsunobu condition gave a mixture of multiple products/by-products, the desired product was not observed among them. Then the triphenylphosphine was replaced with more reactive tributylphosphine, and the reaction was run at both room temperature and at elevated temperatures in THF as well as DMF to increase the solubility of the alcohol (see Scheme 29). Alcohol **66** was consumed in the reactions mentioned above, but it was not converted to the desired primary amine, instead, we identified several side products on TLC and HPLC. The by-products could not be isolated by column chromatography or characterized due to the low resolution of the components in the crude mixture.

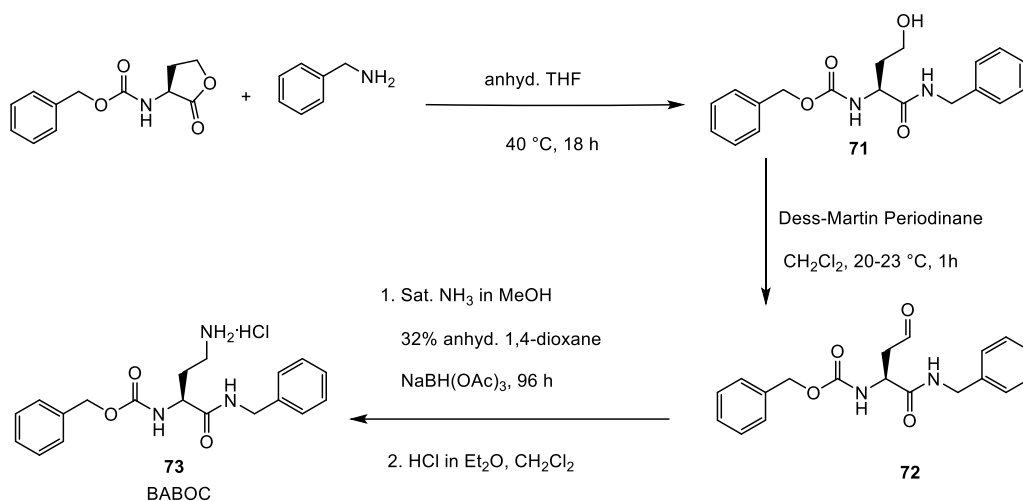


Scheme 29. Attempted synthesis of BAMOC (**69**). Mitsunobu conditions explored and the possible acid-catalyzed hydrolysis of di-(Boc) protection group of compound **70**.

The instability of the primary alcohol **66**, even in mild basic conditions, is presumably due to an intramolecular cyclization where the hydroxyl group can act as the nucleophile and attack the electrophilic carbonyl carbon of the amide/carbamate forming a five and/or a six-membered ring, respectively. In order to prevent the putative intramolecular cyclization and stabilize the substrate, we proposed benzyl (*S*)-(4-amino-1-(benzylamino)-1-oxobutan-2-yl)carbamate, abbreviated as BABOC (**73**), anticipating a moderate binding affinity toward GNAT PA3944.

A new synthetic route was developed to prepare BABOC that involves Dess-Martin oxidation and a reductive amination step. In the first step of this route, methylamine used in BAMOC synthesis (see Scheme 28) was replaced with benzyl amine in the ring-opening reaction of Cbz-homoserine lactone (Scheme 30). Benzyl (*S*)-(1-(benzylamino)-4-hydroxy-1-oxobutan-2-yl)carbamate (**71**) was synthesized from Cbz-homoserine lactone and benzylamine in anhydrous THF. Then, the alcohol analog **71** went under Dess-Martin oxidation, providing the aldehyde **72**. Without further purification, the reactive aldehyde intermediate **71** was reacted with ammonia in MeOH, forming an imine in situ, which then reduced using sodium triacetoxyborohydride to afford BABOC, and the final product was isolated as the HCl salt of BABOC (**73**) as shown in Scheme 30. The high-resolution mass

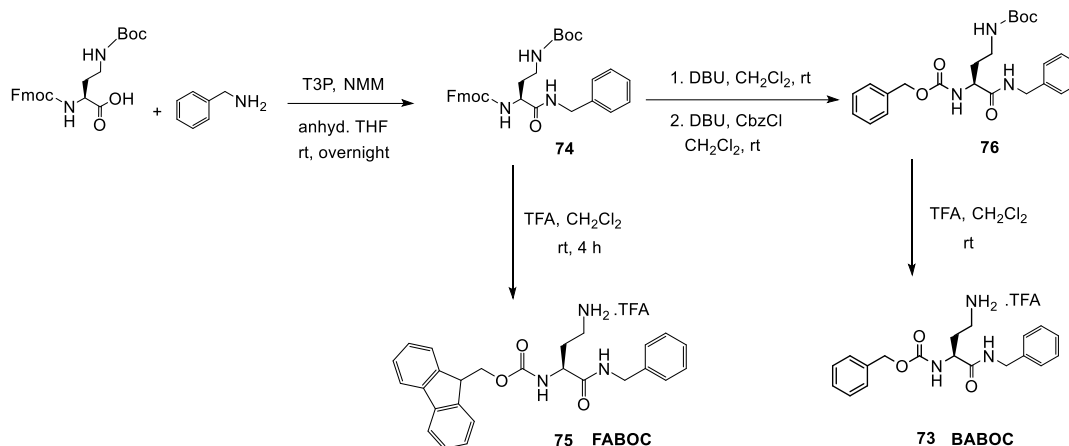
spectrometric analysis of BABOC using the electrospray ionization method was inconsistent with the calculated molecular ion ($M+H^+$). The NMR spectra of BABOC showed the expected chemical shifts (see experimental section and Appendix D). Consequently, we required to validate the structure of BABOC through a new synthetic route that could also provide high-yielding reactions.



Scheme 30. BABOC (**73**) synthesis via Dess-Martin oxidation/reductive amination route.

Our new route utilizes commercially available N_{α} -Fmoc- N_{γ} -Boc-L-2,4-diaminobutyric acid as a precursor that provides the core 2,4-Dab structure. Fmoc and Boc protected diaminobutyric acid was coupled with benzylamine using propylphosphonic anhydride (T3P), and globally protected benzylamide **74** was isolated in 96 % yield. Even though the (9H-fluoren-9-yl)methyl (*S*)-(4-amino-1-(benzylamino)-1-oxobutan-2-yl)carbamate (**75**, FABOC) is not a GNAT PA3944 small-molecule substrate analog by design, intermediate **74** was reacted with TFA in methylene chloride and the final amine product **75** was isolated as the TFA salt with 95 % yield (see Scheme 31). Currently, the

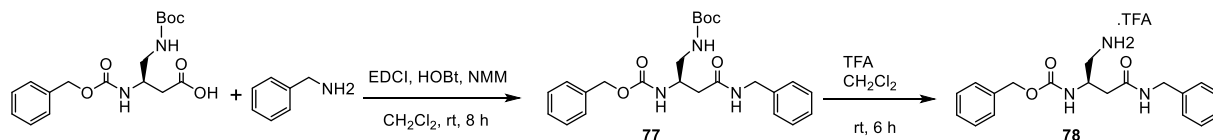
synthesis of BABOC from protected L-2,4-Dab intermediate **74** is in progress, as illustrated in Scheme 31.



Scheme 31. Synthesis of BABOC (**73**) and FABOC (**75**) from globally protected L-2,4-Dab.

We have also designed a homolog of 2,4-BABOC with the terminal β -amine in exploring the SAR of the polymyxin B substrate analogs. A master's student in our laboratory, Xhulio Arolli prepared the 3,4-BABOC analog (**78**) following the synthetic route shown in Scheme 32. In the first synthetic step, N_{β} -Cbz- N_{γ} -Boc-L-3,4-Dab was coupled with benzylamine under EDCI amide coupling conditions to afford the protected benzylamide **77**. Then the Boc group was removed by stirring benzylamide intermediate **77** in methylene chloride in the presence of TFA, and the final amine product 3,4-BABOC was isolated as its TFA salt (**78**) (Scheme 32). The docking of 3,4-BABOC performed using MOE, and the observed binding modes were consistent with other small molecule substrate analogs of GNAT PA3944, where 3,4-BABOC binds to the acceptor substrate-binding pocket of the enzyme. The docking results of polymyxin B substrate analogs will be discussed in the sections below. Our small-molecule acceptor substrate analogs are utilized in kinetics

studies in elucidating the chemical mechanism of the enzyme and in obtaining crystal structures of little-explored GNAT PA3944.



Scheme 32. Synthesis of 3,4-BABOC (**78**) from *N*_β-Cbz-*N*_γ-Boc-L-3,4-Dab.

PA3944 Acetylates NANMO and Polymyxin B with Similar Catalytic Efficiencies

Biochemical assays and kinetic experiments of our substrate analog were performed by Jackson Baumgartner, a member of Dr. Kuhn's research team at San Francisco State University. The GNAT PA3944 enzyme was screened to investigate the activity toward NANMO, where the assays were performed by varying the acceptor substrate concentration while maintaining a constant AcCoA concentration. It was demonstrated that NANMO can act as an acceptor substrate in a similar capacity to polymyxin B as shown in the substrate saturation curves of NANMO and polymyxin B (see Figure 32A).¹⁷⁵ Next, Dr. Kuhn further characterized the WT enzyme toward both NANMO and polymyxin B to compare kinetic parameters. While we characterized this enzyme toward polymyxin B previously,¹⁸² we chose to recharacterize it alongside the NANMO substrate and PA3944 mutant proteins (E102 and S148A) because polymyxin B is commercially available as a variable mixture. This approach was taken to ensure that potential differences or similarities in activity we observed between the two substrates were consistent and not due to different preparations or batches of polymyxin B. When we compared the kinetic parameters of the WT enzyme toward polymyxin B from our previous results and this new

preparation, we found the catalytic efficiencies were similar. The k_{cat}/K_m observed in our previous characterization was $2.54 \times 10^2 \text{ M}^{-1}\text{s}^{-1}$ compared to $3.0 \times 10^2 \text{ M}^{-1}\text{s}^{-1}$ for this preparation of WT PA3944 enzyme and polymyxin B (see Table 8). It was found that the WT enzyme used both polymyxin B and NANMO with similar catalytic efficiencies with $k_{\text{cat}}/K_m = 3.0 \times 10^2$ and 3.8×10^2 , respectively (see Table 8 and Figure 32A), which indicated NANMO could be used as an alternative substrate for further characterization of the PA3944 enzyme.¹⁷⁵

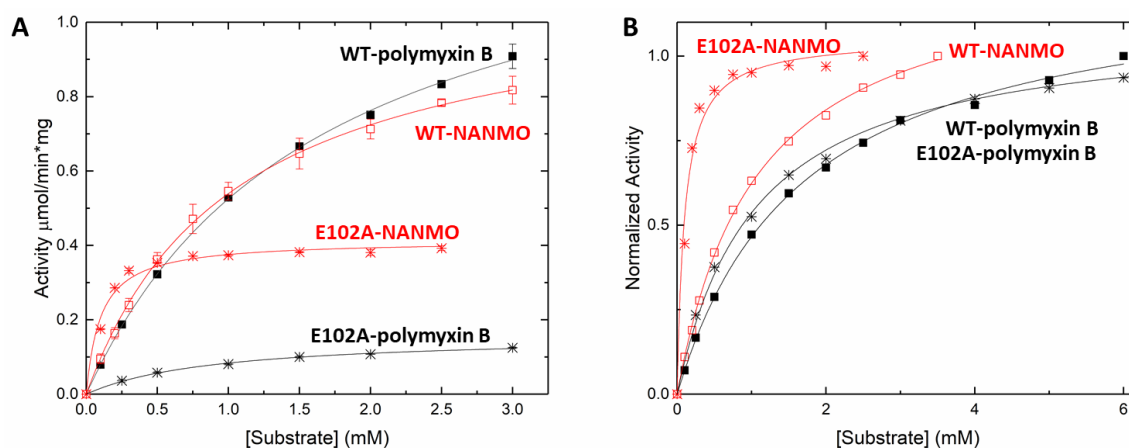


Figure 32. Substrate saturation curves of PA3944 WT and E102A mutant toward polymyxin B and NANMO. The concentration of acceptor substrate was varied while AcCoA was held constant at 0.5 mM. Curves in black correspond to polymyxin B as the substrate and curves in red correspond to NANMO as substrate. WT is shown as solid squares for polymyxin B and open squares for NANMO, E102A is shown as black stars for polymyxin B and red stars for NANMO. (A) Substrate saturation curves. (B) Normalized data from substrate saturation curves.¹⁷⁵

Table 8. PA3944 wild-type and mutant kinetic parameters toward NANMO and Polymyxin B¹⁷⁴

Substrate	Enzyme	K_m (mM)	k_{cat} (s ⁻¹)	k_{cat}/K_m (M ⁻¹ s ⁻¹)
NANMO	WT	1.07 ± 0.03	0.41	3.8x10 ²
	E102A	0.101 ± 0.013	0.15	1.5x10 ³
	S148A	N.D.		
Polymyxin B	WT	1.68 ± 0.07	0.51	3.0x10 ²
	E102A	1.05 ± 0.05	0.06	5.7x10 ¹
	S148A	N.D.		

Kinetics, Mutagenesis, and Molecular Docking Experiments in

Elucidating the Chemical Mechanism of GNAT PA3944

General Chemical Mechanism of GNATs

The primary chemical mechanism described for GNATs is a general acid/base mechanism that proceeds through the use of a tyrosine residue as a general acid and a glutamate residue as a general base. The base abstracts a proton from the conjugate acid of the acceptor amine, which enables the acceptor substrate to perform a nucleophilic attack on the acetyl donor; the general acid then protonates the thiolate anion of CoA. While this is the generally accepted mechanism, there have been examples of GNATs where a catalytic base could not be identified. In those cases, a water molecule or proton wire was proposed to deprotonate the acceptor substrate.¹⁸⁴ It has even been suggested that the approach of the acceptor substrate into the active site lowers the pKa of the acceptor amine or enables it to become deprotonated without the use of a general base.^{185, 186} Typical residues that can act as general acids are tyrosine and cysteine, while residues that can act as general bases include histidine, glutamate, and aspartate. Some reports have suggested that serine can act as a general acid, however, the pKa (~16) of serine side chain hydroxyl is too high

to serve as the general acid. Instead, it would more likely act as a nucleophile if it participates in the chemical mechanism. Therefore, the presence of a serine at the typical location of the general acid in a GNAT active site suggests the utilization of an alternative chemical mechanism. Furthermore, even when a tyrosine residue is placed appropriately to act as a general acid in a GNAT active site, it is not a definitive indication that it acts as an acid or that the enzyme utilizes a general acid/base mechanism.¹⁸⁷

Two main types of kinetic mechanisms for GNATs have been proposed: a direct transfer or sequential mechanism and a ping-pong mechanism. In a direct transfer mechanism, the acetyl group is transferred directly from AcCoA to the acceptor substrate. In contrast, in a ping-pong mechanism, the acetyl group is transferred first to the enzyme to form an acyl-enzyme intermediate and then from the enzyme to the acceptor substrate. For a ping-pong mechanism to occur, a nucleophilic residue such as cysteine or serine must be present at an appropriate position in the active site. Several GNATs have been described that have cysteine residues in their active sites.^{188, 189} However, all studies that have examined the criticality of these cysteines have shown they are not likely to be directly involved in catalysis. A few studies have reported a serine residue in GNAT active sites, but the role of this residue and potential involvement in the kinetic mechanism of the enzyme has only been suggested.¹⁸⁹ While a ping-pong mechanism has been widely proposed as a probable kinetic mechanism for GNATs in the literature, to our knowledge, only one example of a GNAT with evidence to support this mechanism has been described.¹⁹⁰

Significance of Serine148 for GNAT PA3944 Catalytic Activity

A general acid/general base mechanism of GNATs utilizing the relevant active site residues is well accepted. However, the PA3944 protein does not contain an obvious general acid, such as a tyrosine residue, in the active site (see Figure 33A). Instead, PA3944 has a serine (S148) in a comparable location where the critical tyrosine residue is usually found in GNATs. When the active sites of the PA3944 enzyme were compared with the GNAT PA4794 that was shown to have a functionally important tyrosine (Y128),¹⁸⁸ we observed there were no other residues in the PA3944 active site that could act as a general acid (see Figures 33A vs. C). While serine cannot act as a general acid due to its very high pKa (~16), we considered that it might play a role as a nucleophile in the enzymatic reaction. Therefore, we tested whether S148 was important for kinetic activity by mutating it to alanine and screened the S148A mutant protein toward both polymyxin B and NANMO. Dr. Kuhn found the S148A mutant was almost completely inactive with activity levels very near the baseline for both polymyxin B and NANMO. Further, it was showed that S148 is 100% conserved in 10 of the 11 closest homologs of WT PA3944 (PDB ID: 6EDV) identified through a homology search.¹⁷⁵ These results indicate that S148 is critical for PA3944 enzyme activity.

Substrate-Specific Catalytic Efficiency of PA3944 E102A Mutant

Our team searched the active site of the PA3944 protein to locate a viable candidate residue that could deprotonate the acceptor substrate during catalysis. The only residue that could potentially act as the general base was a glutamate residue (E102), so Dr.

Karolina Majorek mutated E102 to alanine and screened the enzyme for activity toward both polymyxin B and NANMO. The enzymatic activity of E102A mutant toward both substrates decreased compared to WT, with a more significant decrease in activity for polymyxin B compared to NANMO (see Figure 32). However, the catalytic efficiency of the E102A enzyme varied significantly depending upon the substrate. Specifically, the catalytic efficiency decreased by one order of magnitude compared to WT when polymyxin B was the substrate but increased by one order of magnitude compared to WT when NANMO was the substrate (see Table 8). Thus, when the catalytic efficiencies of the E102A protein toward NANMO and polymyxin B were compared, a substantial difference of two orders of magnitude was observed. This increased catalytic efficiency for the E102A mutant toward NANMO was primarily due to an improved apparent affinity of one order of magnitude compared to WT. On the other hand, the decreased catalytic efficiency for the E102A enzyme for polymyxin B was primarily due to one order of magnitude decrease in turnover (see Table 8 and Figure 32). Furthermore, our homology search showed that E102 is less conserved among homologs of PA3944, with only 6 of the 11 closest homologs having the corresponding E102 residue.¹⁷⁵ Based on these results, we suggest that E102 is more likely involved in substrate specificity rather than in the catalytic mechanism.

The significant improvement in catalytic efficiency of the PA3944 E102A mutant toward NANMO led our team to crystallize the protein in determining the structural changes that might help explain the kinetic observations. The E102A crystal structure (PDB ID: 7KPP) showed that the removal of the negative charge from the E102 side chain

provided space for the orientation of the phenyl ring of F89 to flip inward compared to the PDB ID: 6EDV WT structure (see Figures 33A,B,D).¹⁷⁵ Additionally, the removal of the negative charge of E102 increased the overall hydrophobicity of the acceptor substrate binding site. The change in hydrophobicity combined with the conformational change of the F89 residue validates the improvement in apparent affinity of the E102A protein for NANMO compared to polymyxin B.

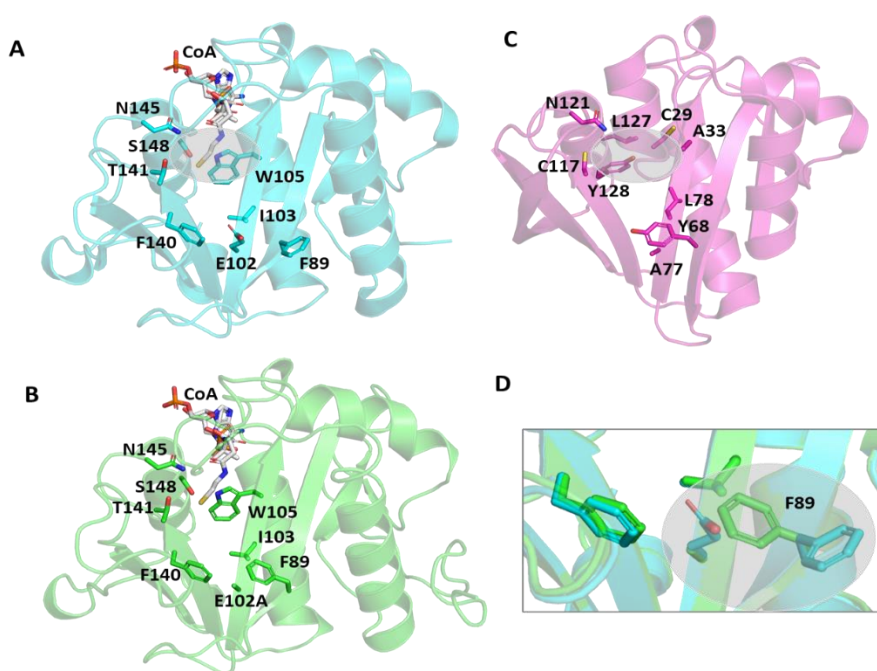


Figure 33. Comparison of PA3944 WT, PA3944 E102A, and PA4794 crystal structures and active sites. (A) WT PA3944 structure (cyan; PDB ID 6EDV). CoA is shown with white sticks and key active site residues are shown with cyan sticks. The gray bubble highlights the region of the active site where a general acid residue would typically be located. (B) WT PA3944 E102A crystal structure (green; PDB ID 7KPP). CoA is shown with white sticks and key active site residues are shown with green sticks. (C) PA4794 crystal structure (pink; PDB ID 5VDB). The ligand was removed for clarity and key active site residues are shown with pink sticks. The gray bubble highlights the region of the active site where a general acid residue would typically be located. (D) Overlay of PA3944 WT and E102A structures. The box highlights the F89 residue, which changes conformation when E102 is mutated to alanine. Figures were made using Pymol.¹⁷⁵

Substrate-Dependent Kinetic Mechanism of GNAT PA3944

Since we found that S148 is critical for enzyme activity, and there is no viable residue that could potentially act as a general acid, we suspected S148 may act as a nucleophile in the chemical reaction. Therefore, we sought to determine the PA3944 enzyme kinetic mechanism. Kinetics assays of GNAT PA3944 were performed by Jackson Baumgartner at San Francisco State University. Steady-state enzymatic assays were performed to generate a series of substrate saturation curves toward both NANMO and polymyxin B (acceptors) against four different concentrations of AcCoA (donor), and the data were fitted to a previously reported series of kinetic models.¹⁹¹ Since NANMO was the simpler substrate, the kinetic data was fitted to the classical ordered, random, and ping-pong kinetic models. The model with the best fit to the NANMO data was a ping-pong kinetic mechanism.¹⁷⁵ In this model, a covalent enzyme intermediate is implicated. AcCoA first binds to the enzyme, and an acyl-enzyme intermediate must be formed using a nucleophilic amino acid in the active site. Then, the acyl group is transferred from the acylated enzyme residue to the second substrate. A model of kinetic mechanisms is illustrated in Figure 34.

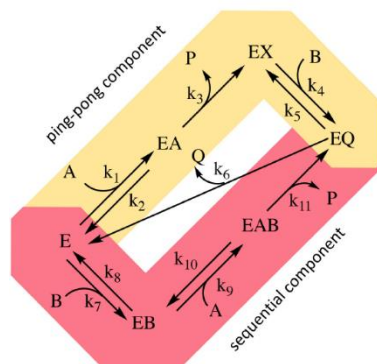


Figure 34. Hybrid ping-pong model with two components: a ping-pong path and a sequential path. E is enzyme, EX is acetylated enzyme, A is AcCoA, B is acceptor substrate (polymyxin B or NANMO), P is CoA, and Q is acetylated acceptor product. The hybrid model allows the free enzyme to bind AcCoA or acceptor substrate at the same time. If it binds AcCoA first, the enzyme becomes acetylated and the ping-pong path is used, whereas if acceptor substrate binds first the acetyl group of AcCoA can be transferred directly to acceptor substrate using the sequential path.¹⁷⁵

Next, the kinetic data obtained toward polymyxin B was fitted to the same set of traditional kinetic models as for NANMO. However, none of these models were sufficient to explain the enzyme behavior. Therefore, alternative models were explored which demonstrated a relatively simple hybrid ping-pong model for polymyxin B based on the kinetic data fitting.¹⁷⁵ A hybrid ping-pong mechanism implies that the enzyme is able to bind both donor and acceptor substrates at the same time. Our hybrid model contained two major paths: one is the classical ping-pong reaction and the second is the classical sequential scheme where AcCoA binds first to the enzyme and acylate the second substrate through direct transfer of the acyl group (see Figure 6B).

Based on these results, the data obtained when NANMO was the substrate was fitted to the hybrid model. These data fitting indicated that both ping-pong and hybrid models

were nearly similar for NANMO, indicating the ping-pong model is sufficient to explain the kinetics of NANMO.¹⁷⁵ It is possible that a fraction of the reaction can proceed through the sequential path of the hybrid model when NANMO is the substrate, but the rate constant for this path must be significantly lower than for the ping-pong path. On the other hand, when polymyxin B is the substrate, the rate constants for the two paths may not deviate as drastically, and therefore a larger fraction of the reaction compared to NANMO may proceed through the sequential path. The enzyme may exhibit this variability when polymyxin B is the substrate because it is a larger molecule than NANMO and is likely to remain in the active site longer. Thus, the acceptor substrate dictates the preferred path for acetylation, but in all cases, there is an underlying ping-pong component present. This indicates the role of serine as a nucleophile is plausible and must become acylated during the reaction. Even if a fraction of the reaction occurs via the sequential path, we cannot discount the possibility that S148 receives the acyl group from AcCoA and immediately transfers it to the acceptor substrate.

Since kinetic studies showed the enzyme utilized a ping-pong or hybrid ping-pong mechanism, our team attempted to obtain a crystal structure of GNAT PA3944 with S148 acetylated. All of our previous crystal structures of the enzyme were determined in the presence of CoA. Therefore, the protein was co-crystallized in the presence of AcCoA looking for density around S148 for an acetyl group. A crystal structure of GNAT PA3944 with AcCoA in one chain was obtained (PDB ID: 7KPS), but no additional density around S148 that would indicate its acetylation in the crystal was observed. However, a very small

amount of AcCoA cleavage in the presence of the enzyme was observed and the absence of acceptor substrates in our kinetic assays,¹⁷⁵ possibly indicating the enzyme could form an acyl-enzyme intermediate required for a kinetic mechanism with a ping-pong component.

Molecular Docking of NANMO with PA3944 WT and E102A Structures

Since we did not have a structure of the PA3944 WT or E102A proteins in complex with NANMO and we did not observe density for an acetylated S148 residue, we used molecular docking as a tool for addressing questions about how NANMO might bind and how the enzyme catalyzes its reaction. We chose to focus on NANMO due to its chemical homogeneity and simpler structure than polymyxin B. Docking experiments of NANMO were performed using MOE utilizing PA3944 WT (PDB ID: 6EDV or 7KPS) and E102A mutant (PDB ID: 7KPP) structure models. 6EDV structure is a complex with CoA present in the active site where we required AcCoA as the donor substrate for these simulations. Therefore, prior to the docking, CoA was acetylated using MOE's Builder utility and 6EDV protein was relaxed through energy minimization. NANMO was docked into both WT and E102A structures using MOE. We compared the results of CoA manually acetylated 6EDV structure with the 7KPS structure in complex with AcCoA but found no significant differences, so we used the higher resolution 6EDV structure for further analyses.¹⁷⁵

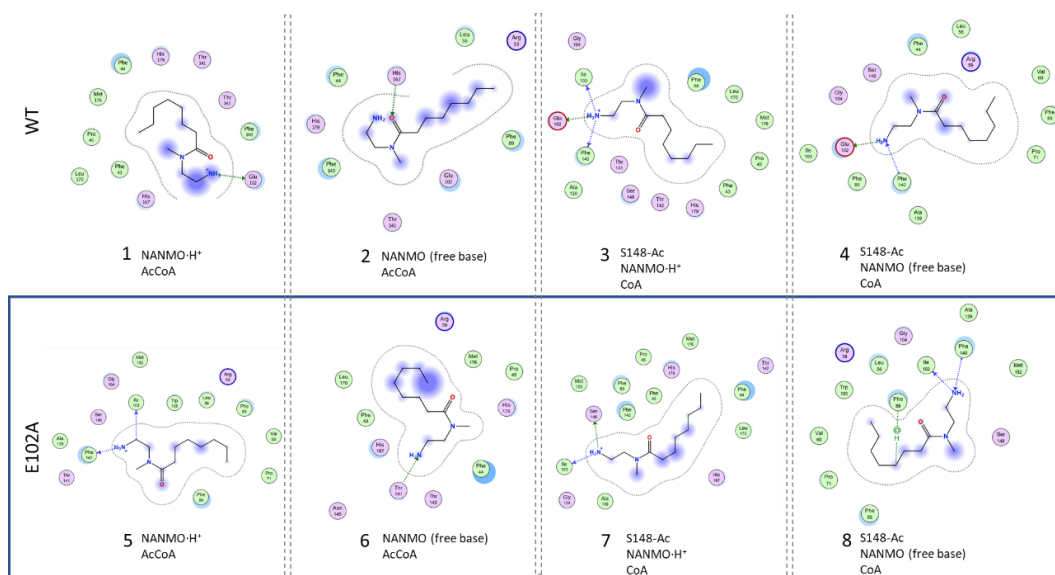


Figure 35. Ligand interaction maps for eight different conditions of NANMO docked into the PA3944 WT and E102A crystal structures. A single pose with the lowest binding energy for each of the eight experiments was selected. WT poses are numbered 1-4 and E102A are numbered 5-8. Ligands used for docking and modified residues (acetylated S148) are noted in each diagram. Purple circles are polar residues, green circles are hydrophobic residues, purple circles with a red border are acidic polar residues, purple circles with a blue border are basic polar residues. Ligand atoms highlighted in blue are exposed to solvent. Interaction diagrams were prepared in MOE.¹⁷⁵

We compared NANMO docking results of the protonated form and deprotonated form (NANMO free base) in structures with S148 either non-acetylated or acetylated (Ac-S148) and in the presence of AcCoA or CoA, respectively. Results of the selected eight docking experiments are shown in Figures 35 and 36.¹⁷⁵ Our docking experiments showed NANMO bound to the acceptor site of both the WT and E102A structures when either AcCoA or CoA was present and when S148 was acetylated or not acetylated. When we docked NANMO into the structure without AcCoA/CoA, the ligand binds to the AcCoA/CoA donor site of the protein. Therefore, the remainder of our experiments contained either AcCoA or CoA in the donor site, which is compatible with the hybrid kinetic model in which

both the acceptor and the donor can bind to the enzyme simultaneously. Moreover, the docking studies indicate S148 can be acetylated, and NANMO can still bind in the acceptor site in a suitable location for acetyl transfer to occur.

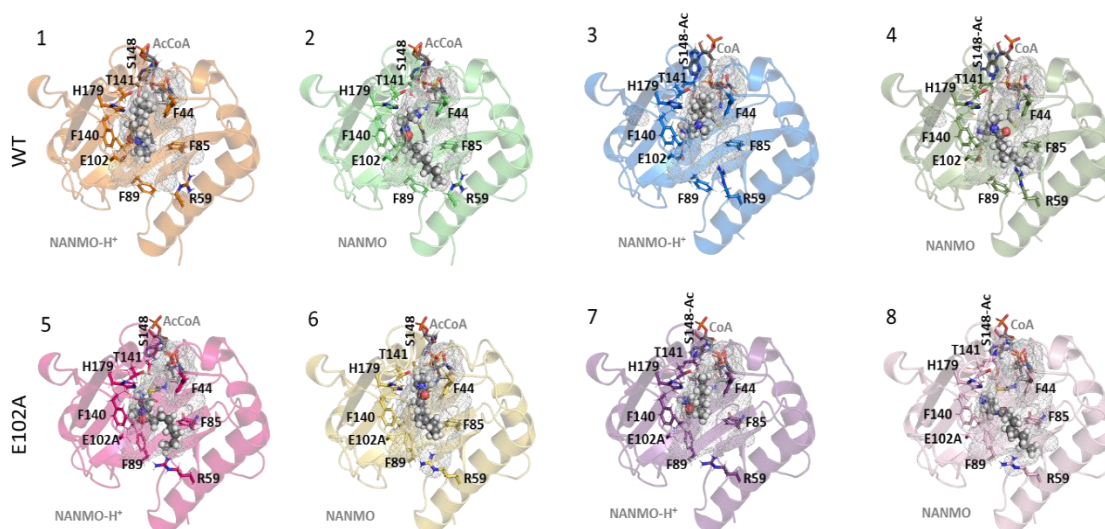


Figure 36. Eight poses of NANMO docked with WT and E102A PA3944. Key residues are shown with sticks and the PA3944 protein is shown as ribbons. The acceptor site of the enzyme is shown with gray mesh and NANMO is in spheres with red as oxygen, blue as nitrogen, white as hydrogen and gray as carbon atoms. CoA is shown as gray sticks. NANMO does not occupy the entire acceptor site and adopts a variety of conformations.¹⁷⁵

In order for the conjugate acid of the primary amine of an acceptor substrate to become acetylated, it must first be deprotonated. Therefore, we first docked NANMO into the WT structure with AcCoA to determine which residues might interact with the protonated and free base forms of the molecule. We selected representative docking poses with the lowest (best) docking scores and analyzed the binding orientations and interactions of NANMO (see Figures 35, 36).¹⁷⁵ When NANMO was protonated, its terminal amine formed an H-bond with E102 and with the carbonyl oxygen of AcCoA. NANMO also exhibited stabilizing interactions with F44, F140, H167, and H179. In contrast, when the

free base was docked, the carbonyl oxygen of NANMO formed an H-bond with H167, and the terminal amine formed an H-bond with the carbonyl oxygen of AcCoA. Ligand stabilizing interactions also occurred with F44, F89, F140, and E102. When we compared these results with the docking of protonated and free base forms of NANMO into the WT structure with S148 acetylated (S148-Ac) and CoA, we found the terminal amine of protonated NANMO formed H-bonds with the side chain of E102 and the backbone oxygens of I103 and F140. Significant stabilization of the amino-methyl group of NANMO occurred with F44. In the free base form, NANMO maintained H-bonding interactions with E102 and the backbone oxygen of I103. When we examined the same docking studies but in the PA3944 E102A structure, we found the protonated NANMO in the presence of AcCoA formed an H-bond with the backbone oxygen of F140, but the free base NANMO formed an H-bond with the backbone oxygen of F43. When S148 was acetylated, the terminal amine of protonated NANMO formed H-bonds with the backbone oxygens of I103 and F140 and the carbonyl oxygen of Ac-Ser148. The NANMO free base in the E102A structure formed H-bonds with the backbone oxygen of I103 and the carbonyl oxygen of Ac-Ser148. Therefore, it appears that backbone oxygens of I103 and/or F140 are critical for H-bonding to the NANMO substrate when S148 is acetylated regardless of NANMO protonation state in either WT or E102A enzymes. No clear pattern emerged when S148 was not acetylated and the protonation state of NANMO did not appear to drastically alter its interactions in either WT or E102A structures.

Size and Key Amino Acid Residues of the Acceptor Binding Pocket

The WT PA3944 acceptor site of the PA3944 enzyme contains predominantly non-polar residues and only a few polar residues, and its acceptor binding pocket is large enough to accommodate multiple conformations of the NANMO ligand. Therefore, we sought to determine which residues of the acceptor site more frequently interacted with the NANMO ligand across 100 of the lowest energy poses by analyzing the interaction maps generated for each of these poses. We selected poses for further analysis using the following criteria: NANMO needed to interact with acceptor site residues and have the terminal amine pointed toward the donor site. We found the residues that were in close proximity to NANMO across WT docking studies included: F43, F44, P45, L56, R59, P71, F85, F89, M93, E102, I103, G104, R106, F140, T141, T142, N145, S148, H167, L169, L170, M176, and H179. When we docked NANMO into the E102A structure, we found two additional residues located in close proximity to the molecule that were not observed in the WT docking: W105 and M152 (see Figure 37).¹⁷⁵ The residues with the highest frequency of interaction (>50% average across all perturbations) with NANMO included F43, F44, P45, F89, E102, F140, T141, T142, H167, and H179 and were primarily localized on one side of the acceptor pocket, with the exception of F44 and F45, which reside at the top of the pocket near the active center (see Figure 37).¹⁷⁵

Serine as a Nucleophile in GNAT Enzymatic Reactions: A New Paradigm for GNAT

Chemical Mechanisms

Kinetics data for the PA3944 enzyme demonstrates that of the models tested, the hybrid ping-pong kinetic mechanism, which contains both ping-pong and sequential components, explains data collected for both polymyxin B and NANMO acceptor substrates. Hybrid ping-pong mechanisms arise when there is a covalently modified enzyme intermediate in an enzyme with separate substrate binding sites.¹⁹² Since this mechanism requires formation of an acyl-enzyme intermediate, it must utilize a nucleophilic amino acid during the reaction. We have provided evidence that S148 plays the role of an active site nucleophile that enables the ping-pong component of the hybrid mechanism to proceed.¹⁷⁵

A proton wire has been proposed for several GNATs in the absence of a nearby viable acid or base.^{186, 193} This wire can allow the general base (or acid) residue to be located more distally from the active center and abstracts or donates a proton through a network of residues and/or ordered water molecules.¹⁹⁴ In addition, the CoA has been proposed to be reprotonated by the acceptor amine upon the collapse of the tetrahedral intermediate in the absence of a general acid.¹⁹⁵

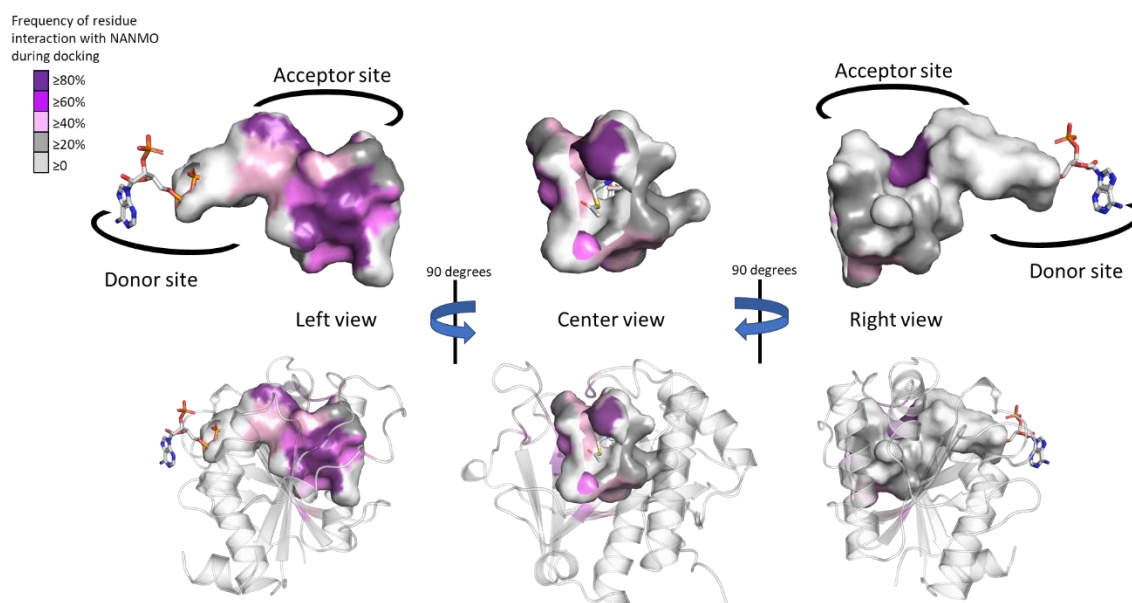


Figure 37. Frequency of WT PA3944 acceptor site interactions with NANMO during docking studies. All ligand interaction maps across all docking experiments with NANMO pointed toward the donor site were compiled and were analyzed to determine residues that most frequently interacted with NANMO. Residues were colored based on frequency (gradient from purple for high frequency to gray for low frequency) on the surface of the acceptor site. AcCoA is shown as sticks.¹⁷⁵

Our *in vitro* and *in silico* experiments provided evidence that PA3944 and its homologs represent an additional deviation from the canonical chemical mechanism for GNATs. Based on the results, we proposed the following chemical mechanism for the PA3944 ping-pong component (see Figure 38A and B).¹⁷⁵ We used NANMO as a representative substrate, but the mechanism applies to polymyxin B as well. First, AcCoA binds to the donor site of PA3944 and S148 is likely deprotonated by a water molecule concomitant with a nucleophilic attack on the carbonyl carbon of AcCoA. The tetrahedral intermediate is stabilized by an oxyanion hole formed by the side chain amide of N145 and the side chain hydroxyl of T141. A water molecule likely facilitates the collapse of this

complex and releases CoA to form the acetylated S148-enzyme intermediate. Next, NANMO is either deprotonated upon approach of the substrate into the active site through an unidentified base or is already deprotonated due to its relatively low pKa. NANMO then attacks the carbonyl carbon on the acetylated S148 residue and forms a second tetrahedral complex, again stabilized by a potential oxyanion hole with the side chain amide of N145 and the hydroxyl of T141. The protonation of the oxygen atom on S148 and delocalization of the electrons from the oxyanion releases the acetylated NANMO product and enables S148 to be restored for another round of catalysis when a new molecule of AcCoA binds. As there is no residue suitably placed for deprotonation of S148 we believe that a network of water molecules likely facilitates this process.

For the sequential component of the hybrid mechanism (see Figure 38C) to proceed, the free base of NANMO directly attacks AcCoA, providing the tetrahedral intermediate wherein the alkoxide moiety is stabilized by the oxyanion hole formed by Asn145 and Thr141, and possibly an additional water molecule. Collapse of the tetrahedral intermediate with the expulsion of CoA and proton transfers via a network of water molecules in the aqueous environment then provides the acetylated NANMO product.

Further studies of GNAT PA3944 are necessary to prove the formation of the acyl-enzyme complex, including acceptor substrate bound crystal structures of WT PA3944 protein. As discussed in the synthesis section, we have prepared a set of small-molecule analogs of polymyxin B to be utilized in enzyme activity and kinetics assays and co-crystallization experiments as acceptor substrates of GNAT PA3944.¹⁷⁵

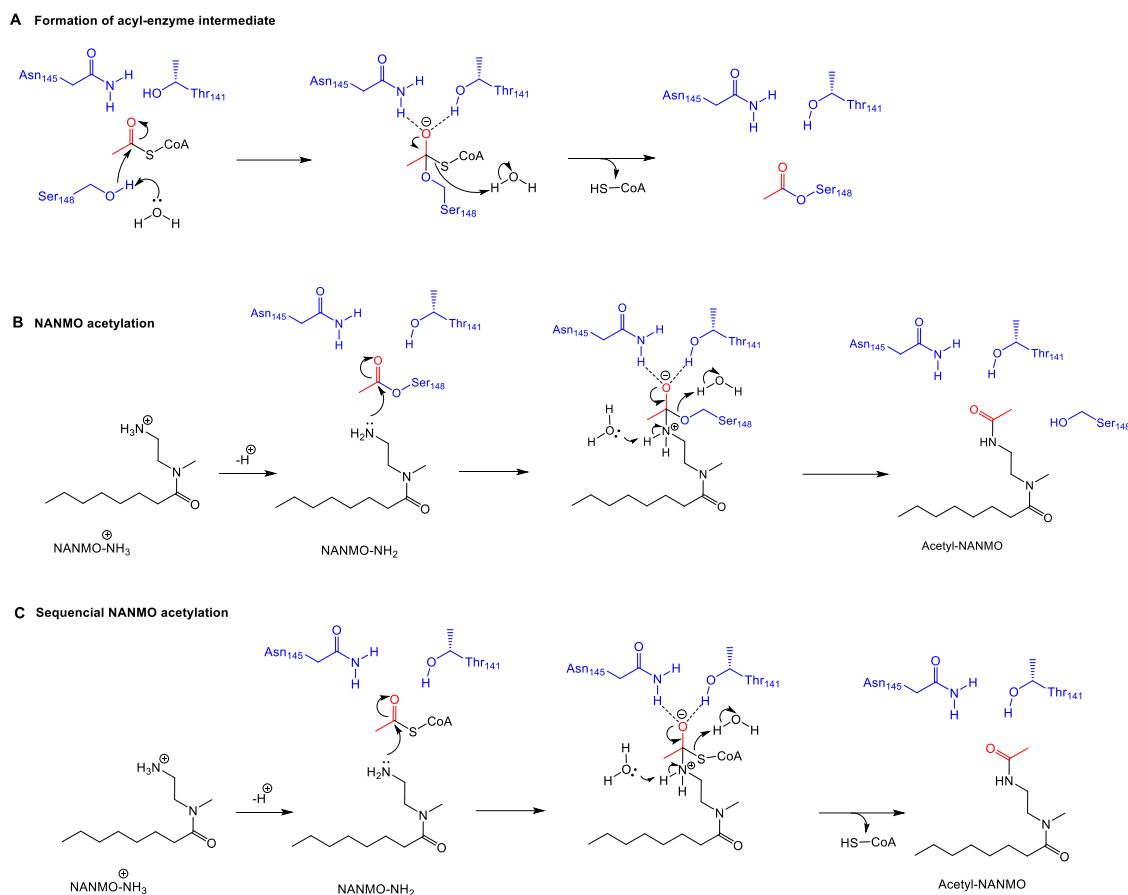


Figure 38. The proposed chemical mechanism for PA3944 using both ping-pong and sequential components of the hybrid mechanism. In the ping-pong component, (A) S148 acts as a nucleophile and is acetylated during the enzymatic reaction and then (B) deprotonated NANMO is acetylated by the acyl enzyme. In the sequential component, (C) direct enzyme-mediated acetylation of NANMO by AcCoA occurs.¹⁷⁵

Molecular Docking of Polymyxin B Substrate Analogs

Molecular docking experiments of the substrate analogs were performed using MOE utilizing PA3944 WT (PDB ID: 6EDV or 7KPS) and E102A mutant (PDB ID: 7KPP) structures. Docking experiments of BAMOC (**69**), BABOC (**73**), FABOC (**75**), and 3,4-BABOC

(78) with PA3944 WT (PDB ID: 6EDV) were performed using MOE following the docking protocol as for NANMO.

The predicted binding modes and interactions of NANMO using docking validate the affinity of PA3944 toward NANMO that was demonstrated using enzymatic assays. In addition, our *in silico* simulations allow us to identify the key residues and binding modes of NANMO and guided us in elucidating the proposed chemical mechanism of GNAT PA3944 (discussed in the previous section). Therefore, we chose NANMO as a reference in guiding the docking experiments of other small-molecule substrate analogs.

Preliminary docking studies suggested that protonated (NH_3^+) BAMOC, BABOC, 3,4-BABOC, and FABOC bind to the acceptor binding pocket of PA3944 in a similar fashion to NANMO in the presence of AcCoA where all four substrate analogs interact with common residues, including Phe140 and Glu102 (see Figure 39). The terminal amine of the protonated BAMOC formed bifurcated H-bonds with backbone oxygen of F140 and the imidazole nitrogen of H179 (see Figure 39B) where the terminal amine of BABOC formed two similar H-bonds with backbone oxygen of I103 and the side chain of E102 (see Figure 39C). When comparing the results, no significant change was observed in the binding orientations between BAMOC and BABOC caused by the introduction of a hydrophobic benzyl group in the place of the simple methyl moiety of the BAMOC. The protonated 3,4-BABOC analog showed an increased number of binding interactions compared to 2,4-BABOC (Figure 39C vs 39E). The terminal amine of 3,4-BABOC was H-bonded to the backbone oxygen of F140, and the polarized γ -methylene hydrogen formed an H-bond with

the side chain oxygen of E102. In addition, the carbamate oxygen atom was H-bonded to the imidazole hydrogen of H167 (see Figure 39E).

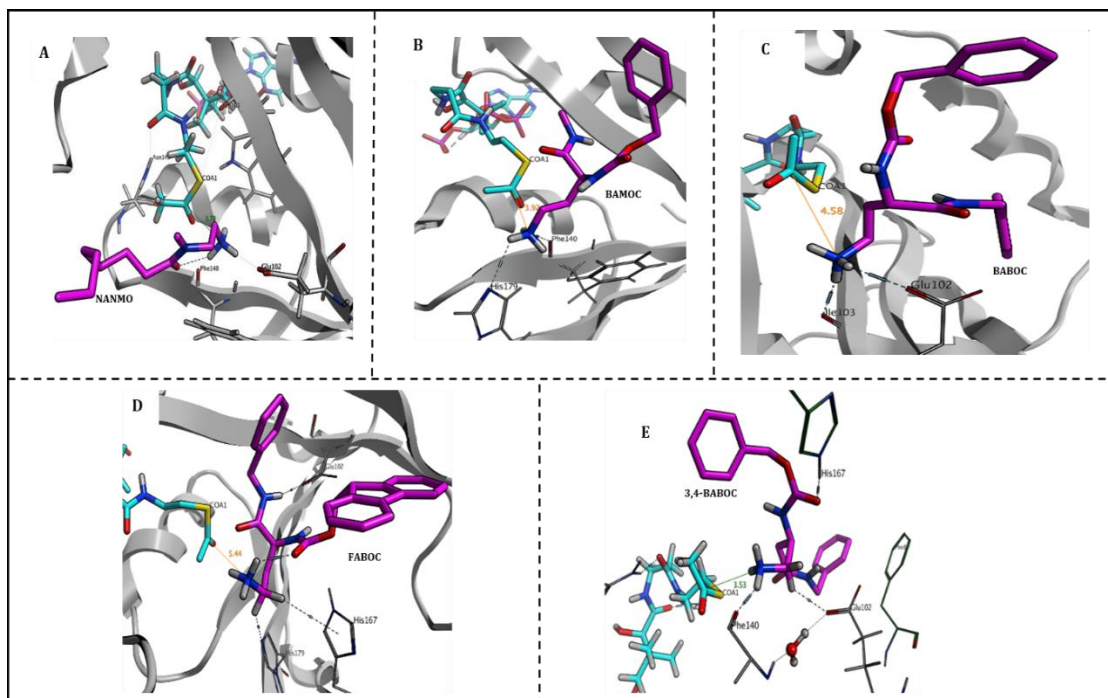


Figure 39. Substrates docked with PA3944 (PDB ID: 6EDV) in complex with AcCoA. All substrates are bound to the acceptor binding pocket where the terminal Dab amine moieties of (A) NANMO, (B) BAMOC, (C) BABOC, (D) 3,4-BABOC, and (E) FABOC placed in close proximity to the acetyl group of the AcCoA shown in cyan. Key interactions with residues and the distance between the terminal amine and the carbonyl carbon of AcCoA are visualized. Protein is shown as a gray ribbon and the ligands colored in magenta.

During docking, FABOC was also bound to the acceptor substrate site even though it is not a polymyxin B substrate analog by design, yet no interactions were observed between the amine and the active site residues. One of γ -methylene ($\text{CH}_2\text{-NH}_2$) hydrogens formed an H-bond with the imidazole nitrogen atom of H179, and a CH- π interaction was also observed between the γ -methylene hydrogen and H167 (see Figure 39D). The docking experiments indicate that these substrate analogs could provide GNAT PA3944 acceptor

substrates with comparable or better affinity than NANMO. Synthesized polymyxin B analogs will be screened as substrates with GNAT PA3944 and will be utilized in crystallization experiments to obtain acceptor substrate-bound crystal structures of PA3944. These results will provide further insights into amino acid residues involved in substrate identification and catalysis of GNAT PA3944 and provide us an increased understanding of the structural features and functions of the enzyme.

Conclusion

The Gcn5-related *N*-acetyltransferase (GNAT) superfamily is found in all kingdoms of life with diverse functionality and plays key roles in cellular and metabolic processes, including histone modification. Our efforts in this project focus on improving the structural and functional annotations of uncharacterized bacterial GNATs and contribute to the determination of diverse structures and functions of these enzymes. Previously, members of our team determined the structure of the PA3944 GNAT enzyme from *Pseudomonas aeruginosa* and found that it could acetylate polymyxin antibiotics, specifically the 3-Dab residue on polymyxin B and on colistin.¹⁸² We extensively studied GNAT PA3944 to determine the key residues that are critical in enzymatic activity and identifying functionally relevant acceptor substrates of PA3944. However, the complexities of the polymyxin B substrate complicated the interpretation of kinetic data as well as the ability to obtain a liganded crystal structure. Therefore, we designed and synthesized small-molecule substrate analogs of polymyxins, namely NANMO, BAMOC, BABOC, and 3,4-BABOC. Our *in vitro* and docking studies demonstrated that NANMO can act as an acceptor

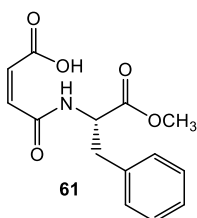
substrate in a similar capacity to polymyxin B, where GNAT PA3944 used both polymyxin B and NANMO with similar catalytic efficiencies as evidenced via the kinetic experiments. Thus, NANMO was utilized as an alternative substrate for further characterization of the PA3944 enzyme. Based on the crystal structures, kinetic data, and *in silico* simulations of PA3944 we have presented, it is clear that PA3944 does not proceed through a general acid/base mechanism as most other characterized GNATs; instead, the enzyme adopts a hybrid ping-pong kinetic mechanism, which contains both ping-pong and sequential components and demonstrates that the kinetic mechanism of the enzyme is substrate-dependent. It was further demonstrated that the S148 residue is critical for catalysis when either NANMO or polymyxin B are substrates and that S148 plays the role of an active site nucleophile in enabling the ping-pong component of the hybrid mechanism to proceed. Kinetic experiments and point mutations indicated that E102 more likely plays a role in substrate specificity rather than serve as a general base residue for the catalysis. Based on our *in vitro* and *in silico* studies, we proposed a chemical mechanism for the ping-pong component of GNAT PA3944. The synthesized substrate analogs will be utilized in further characterization and protein crystallization experiments of PA3944. We believe our results can be applied beyond just a single class of GNATs, and these results increase general understanding of the structural, functional, and mechanistic knowledge of GNATs.

Experimental

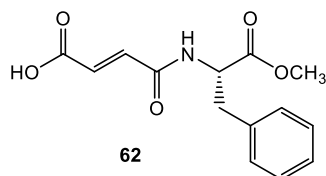
Synthesis of Aspartame Substrate Analogs (61-63)

Internal alkene substrate analogs of aspartame were synthesized following the general method reported by Keller¹⁸⁰ using alternative solvents for more effective transformations as stated below. Proton and carbon NMR spectra of final products were consistent with the reported characterization data.

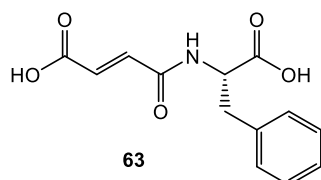
N-Maleyl-L-phenylalanine methyl ester (61)



L-Phenylalanine methyl ester hydrochloride (2.15 g, 10 mmol) was dissolved in water (10 mL), and the solution was brought to pH 6.0 using 5 N NaOH. Powdered maleic anhydride (0.9 mg, 10 mmol) was added in small portions to the stirring reaction mixture at 40 °C while maintaining the pH at 6.0 by adding 5 N NaOH. Once the addition was complete, the reaction was stirred for 10 minutes. When the reaction was deemed complete by HPLC, the pH of the reaction was brought down to 3.0 using 12.1 N HCl. Then the product was extracted with ethyl acetate (3 x 10 mL) and dried with MgSO₄. The solvent was evaporated under reduced pressure providing *N*-Maleyl-L-phenylalanine methyl ester (2.03 g, 74%) as a colorless crystalline solid.

N-Fumaryl-L-phenylalanine methyl ester (62)

p-Xylene (7 mL) was added to a solution of *N*-maleyl-L-phenylalanine methyl ester (100 mg, 0.35 mmol) in dry ethyl acetate (0.5 mL) in a pressure flask. The reaction mixture was heated to 138-142 °C for 48 h under nitrogen. A white solid formed as the solution was cooling to room temperature. The solid was filtered off and washed with *p*-xylene. The resultant crude product was dissolved in MeOH and filtered through a Celite/charcoal (1:1) plug to provide *N*-fumaryl-L-phenylalanine methyl ester as an off-white solid (58 mg, 58%).

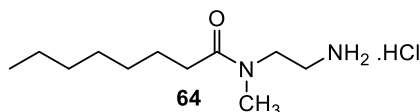
N-Fumaryl-L-phenylalanine (63)

p-Xylene (23 mL) was added to a solution of *N*-maleyl-L-phenylalanine methyl ester (1.54 g, 7 mmol) in DMF (1.2 mL). The reaction was refluxed for 24 h and deemed complete by HPLC. The product was then extracted into aq. NaOH solution (5 x 25 mL) of pH 10-12, and then the pH of the aqueous solution was brought down to 3.0 using 12.1N HCl in order to protonate the phenylalanine carboxylate. The carboxylic acid product extracted using ethyl acetate (5 x 25 mL) and dried over MgSO₄. The solvent was evaporated under

reduced pressure to afford *N*-fumaryl-L-phenylalanine (1.02 g, 66%) as an orange crystalline solid.

Synthesis of Polymyxin B Substrate Analogs

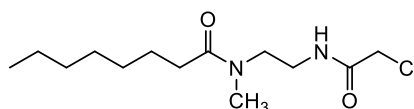
N-(2-Aminoethyl)-*N*-methyloctanamide hydrochloride (NANMO, 64)



Triethylamine (0.4 mL, 2.86 mmol) was added to a stirred solution of *N*-(*tert*-butoxycarbonyl)-*N*-methylethylenediamine (250 mg, 1.43 mmol) in methylene chloride (7.5 mL) at 0 °C in an ice bath followed by the dropwise addition of octanoyl chloride (0.3 mL, 1.72 mmol). The reaction was stirred at room temperature for 24 h. The resultant solution was washed successively with water (3 mL), 1 M aqueous HCl (3 mL) and 1 M aqueous NaOH (3 mL). The methylene chloride layer was dried over sodium sulfate and the solvent was evaporated under reduced pressure to give *tert*-butyl (2-(*N*-methyloctanamido)ethyl)carbamate (338 mg, 79% yield) as a colorless oil. Without further purification, *tert*-butyl (2-(*N*-methyloctanamido)ethyl)carbamate (338 mg, 1.13 mmol) was dissolved in diethyl ether (0.6 mL). Then, 2.0 M HCl in diethyl ether (0.2 mL, 4.11 mmol) was added to the reaction mixture and stirred 2 hours at room temperature. The resulting white precipitate was filtered off, washed with diethyl ether and dried under dry nitrogen to give *N*-(2-aminoethyl)-*N*-methyloctanamide (NANMO) as the hydrochloride salt (102 mg, 45 % yield). ¹H NMR (500 MHz, D₂O, doubling of some peaks due to amide rotamers) δ 3.67 (t, *J* = 6.9 Hz, 0.2H), 3.59 (t, *J* = 6.1 Hz, 1.8H), 3.18 (t, *J* = 6.8 Hz, 0.3H), 3.12 (t, *J* = 6.1 Hz, 1.7H), 3.03 (s, 2.5H), 2.86 (s, 0.5H), 2.39 – 2.33 (m, 2H), 1.50 (h, *J* = 7.3, 6.9 Hz, 2H), 1.29 –

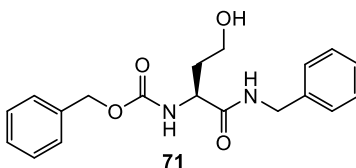
1.15 (m, 8H), 0.79 (t, 3H). ^{13}C NMR (126 MHz, MeOD, doubling of some peaks due to amide rotamers) δ 176.28, 176.02, 49.15, 48.13, 47.96, 47.79, 47.62, 47.45, 47.28, 47.11, 45.46, 37.77, 35.57, 35.55, 35.15, 32.97, 32.41, 31.53, 31.47, 29.02, 28.94, 28.88, 28.74, 27.38, 25.25, 24.56, 22.29, 22.28, 13.03, 13.01. HRMS (ESI) calcd (MH^+) $\text{C}_{11}\text{H}_{24}\text{N}_2\text{O}$: 201.1967, Obs: 201.1960 (100.00).

***N*-(2-(2-Chloroacetamido)ethyl)-*N*-methyloctanamide (65)**

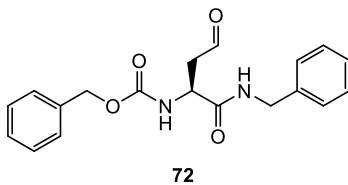


65

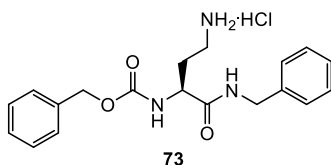
Triethylamine (134.4 μL , 0.964 mmol) was added to a stirring solution of *N*-(2-aminoethyl)-*N*-methyloctanamide hydrochloride (76.1 mg, 0.321 mmol) in methylene chloride (1.6 mL) at 0 $^\circ\text{C}$ in an ice bath followed by the drop wise addition of chloroacetyl chloride under an atmosphere of N_2 . The reaction was stirred at room temperature overnight and the reaction progress was monitored by HPLC. Upon completion, the methylene chloride layer was washed with water (3 X 3 mL) and 1 M HCl (2 X 3 mL) and dried over Na_2SO_4 . Then the solvent was evaporated under reduced pressure to give a yellow oil. This crude product was chromatographed using ethyl acetate/diethyl ether (50/50) as eluent and compound **65** was isolated as a clear oil (30.8 mg, 34.2%). ^1H NMR (500 MHz, CDCl_3) δ 7.39 (NH, s, 1H), 3.99 (s, 2H), 3.59 (dd, $J = 6.9, 4.7$ Hz, 2H), 3.47 (dt, $J = 10.2, 4.3$ Hz, 2H), 3.04 (s, 3H), 2.97 (s, 1H), 2.34 – 2.30 (m, 2H), 1.68 – 1.59 (m, 2H), 1.37 – 1.15 (m, 8H), 0.89 (td, $J = 7.1, 6.4, 4.0$ Hz, 3H). ^{13}C NMR (126 MHz, CDCl_3) δ 174.97, 166.81, 46.55, 42.48, 42.41, 39.14, 36.02, 33.60, 33.56, 31.73, 29.49, 29.41, 29.15, 29.10, 25.10, 22.63, 14.08. HRMS (ESI) Calcd for (MH^+): 201.19, Obs: 201.1960 (100.00), 202.14.

Benzyl (S)-(1-(benzylamino)-4-hydroxy-1-oxobutan-2-yl)carbamate (71)

To a solution of *N*-Cbz-L-homoserine lactone (500 mg, 2.13 mmol) in anhydrous THF (7.1 mL) benzylamine (695.8 μ L, 6.38 mmol) was added, and the reaction was stirred for 26 h at 40 °C while monitoring by TLC (ethyl acetate/petroleum ether = 80/20). During the reaction, the product precipitated as a white solid (the product was sparingly soluble in THF). Upon completion, the white solid was filtered off and washed with a minimum amount of THF and then with methylene chloride. In order to increase the percent isolation of the desired product, the filtrate was diluted with methylene chloride (20 mL), and the organic layer was washed with water (20 mL), 1 M HCl (20 mL), brine (20 mL) and dried over Na₂SO₄. Then the solution was concentrated under reduced pressure to afford alcohol analog **71** (601 mg, 87%) as a white solid. ¹H NMR (500 MHz, DMSO-*d*₆) δ 8.41 (t, *J* = 6.1 Hz, 1H), 7.43 (d, *J* = 7.9 Hz, 1H), 7.40 – 7.28 (m, 6H), 7.27 – 7.19 (m, 3H), 5.04 (d, *J* = 1.5 Hz, 2H), 4.55 (t, *J* = 5.0 Hz, 1H), 4.35 – 4.22 (m, 2H), 4.13 (tq, *J* = 7.9, 5.0 Hz, 1H), 3.50 – 3.39 (m, 2H), 1.89 – 1.78 (m, 1H), 1.71 (ddt, *J* = 14.2, 9.3, 5.7 Hz, 1H). ¹³C NMR (500 MHz, MeOD) δ 173.67, 157.32, 138.67, 136.98, 128.34, 128.30, 127.86, 127.73, 127.26, 126.99, 66.52, 48.09, 47.93, 47.76, 47.59.

Benzyl (S)-(1-(benzylamino)-1,4-dioxobutan-2-yl)carbamate (72)

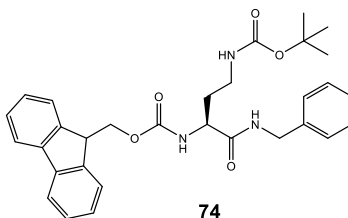
To a vial containing (*S*)-(1-(benzylamino)-4-hydroxy-1-oxobutan-2-yl)carbamate (100 mg, 0.29 mmol) and Dess-Martin periodinane (185.8 mg, 0.438 mmol), dry methylene chloride (2.9 mL) was added under N₂. The reaction was allowed to stir at room temperature for 40 min with periodic TLC monitoring using ethyl acetate/petroleum ether (80/20). Once completed, the organic layer was washed with water (3 X 4 mL), saturated NaHCO₃ (2 X 4 mL), and saturated Na₂S₂O₃ (2 X 4 mL). Then the solvent was evaporated under reduced pressure give the aldehyde analog **72** (83.1 mg, 83.6%) as a white solid. The aldehyde was utilized in the subsequent step as a crude product, and the product was not characterized due to the reactivity of the aldehyde intermediate.

Benzyl (S)-(4-amino-1-(benzylamino)-1-oxobutan-2-yl)carbamate hydrochloride (73)

Without further purification, the aldehyde **72** (100 mg, 0.294 mmol) was dissolved in 1,4-dioxane (1.4 mL), and a saturated solution of ammonia in methanol (3 mL) was added to the reaction and stirred at room temperature for 10 minutes. Then sodium triacetoxyborohydride (68.5 mg, 0.323 mmol) was added in a single portion, and the reaction mixture was continued to stir at room temperature. Ammonia gas was bubbled into the reaction in 6-hour intervals for 96 hours while monitoring the reaction by HPLC.

Then the reaction was quenched with water (3 mL), and the organic product was extracted with ethyl acetate (3 X 3mL). The combined organic layers were washed with water (5 X 3mL) and dried over Na₂SO₄. The crude amine product was isolated as a yellow oil (60.3 mg). To a solution of the crude product in methylene chloride (0.9 mL), 2.0 M HCl in diethyl ether (97.1 μL, 0.19 mmol) was added via syringe and stirred at room temperature for 15 minutes. A white solid was formed as the reaction mixture diluted with ethyl acetate (6 mL). The white solid was filtered off and washed with ethyl acetate (10 mL) to afford BABOC as its HCl salt (18 mg, 27%). ¹H NMR (500 MHz, MeOD) δ 7.43 – 7.30 (m, 10H), 5.22 – 5.09 (m, 2H), 5.02 – 4.94 (m, 2H), 4.36 (d, *J* = 15.6 Hz, 1H), 4.13 (dd, *J* = 11.0, 5.0 Hz, 1H), 3.01 (ddd, *J* = 14.8, 10.9, 7.9 Hz, 1H), 2.08 (ddd, *J* = 14.9, 5.0, 2.8 Hz, 1H). ¹³C NMR (500 MHz, MeOD) δ 173.27, 157.60, 136.61, 135.27, 128.87, 128.39, 128.04, 128.01, 127.99, 127.71, 127.69, 67.06, 63.93, 50.13, 44.59, 30.36. HRMS (ESI): calculated for (MH⁺) C₁₉H₂₄N₃O₃: 341.174, found 323.1388 (100.00), 340.1655. Even though NMR data confirmed the structure, the molecular ions observed during HRMS were inconsistent with the calculated values.

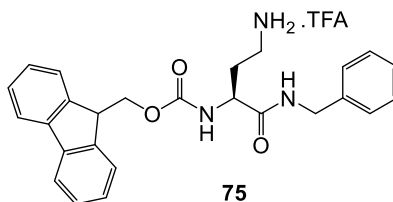
(9H-Fluoren-9-yl)methyl tert-butyl (4-(benzylamino)-4-oxobutane-1,3-diyl)-(S)-dicarbamate (74)



To a stirring solution of *N*_α-Fmoc-*N*_γ-Boc-L-2,4-diaminobutyric acid and *N*-methylmorpholine (99.2 μL, 0.908 mmol) in anhydrous tetrahydrofuran, propylphosphonic

anhydride (T3P, 377.2 μ L, 0.636 mmol) was added as a solution in EA (purchased as \geq 50 wt. % in EA) followed by the addition of benzyl amine (59.5 μ L, 0.545 mmol). The reaction was stirred overnight at room temperature and the consumption of protected 2,4-diaminobutyric acid was monitored by HPLC. Upon completion, the reaction was quenched by adding water (3 mL) and diluted with ethyl acetate (3 mL), and the organic product was extracted with ethyl acetate (3 X 3mL). The combined organic layers were washed with water (3 X 3 mL) and 1 M HCl (3 mL), dried over Na₂SO₄ and the solvent was removed under reduced pressure to give compound **74** (227.6 mg, 95.5%) as a white solid. ¹H NMR (500 MHz, MeOD) δ 7.84 – 7.78 (m, 2H), 7.69 (d, J = 7.5 Hz, 2H), 7.40 (tt, J = 7.5, 0.9 Hz, 2H), 7.35 – 7.27 (m, 6H), 7.23 (td, J = 5.9, 2.6 Hz, 1H), 4.40 (d, J = 5.7 Hz, 4H), 4.24 (t, J = 6.8 Hz, 1H), 4.19 – 4.09 (m, 1H), 3.11 (dt, J = 21.2, 7.1 Hz, 2H), 2.00 – 1.92 (m, 1H), 1.82 – 1.75 (m, 1H), 1.45 (s, 9H). ¹³C NMR (126 MHz, MeOD) δ 171.67, 161.13, 157.09, 143.87, 143.71, 141.28, 141.25, 138.26, 128.17, 127.44, 127.10, 126.91, 126.77, 124.70, 124.67, 119.58, 66.58, 65.51, 52.57, 48.11, 42.76, 36.44, 29.72, 14.04.

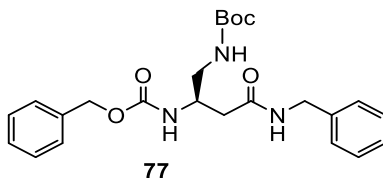
(9H-Fluoren-9-yl)methyl (S)-(4-amino-1-(benzylamino)-1-oxobutan-2-yl)carbamate 2,2,2-trifluoroacetic acid (75)



To a solution of globally protected benzylamide **74** (100 mg, 0.188 mmol) in methylene chloride (1.0 mL), trifluoroacetic acid (290.9 μ L, 30% v/v) was added and the reaction mixture was stirred at room temperature for 4 hours while monitoring the

reaction progress by HPLC. Upon completion, the reaction mixture was concentrated under reduced pressure and the resultant solution (~0.3 mL) was added dropwise to a stirring of solution of diethyl ether (50 mL) at room temperature. The precipitated solid was filtered off and washed with diethyl ether to afford TFA salt of FABOC (94.0 mg, 94.6%) as a white solid. $^1\text{H NMR}$ (500 MHz, MeOD) δ 8.48 (s, 1H), 7.82 (dq, $J = 7.8, 1.2$ Hz, 2H), 7.67 (t, $J = 6.4$ Hz, 2H), 7.45 – 7.38 (m, 2H), 7.33 (dt, $J = 7.5, 1.2$ Hz, 2H), 7.33 – 7.24 (m, 4H), 7.28 – 7.21 (m, 1H), 4.47 (d, $J = 6.5$ Hz, 2H), 4.41 (s, 2H), 4.29 – 4.21 (m, 2H), 3.02 – 2.93 (m, 2H), 2.21 – 2.10 (m, 1H), 1.97 (dtd, $J = 14.4, 8.6, 6.2$ Hz, 1H).

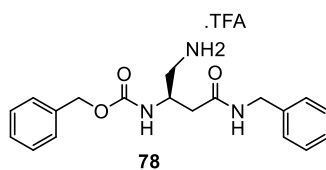
Benzyl tert-butyl (4-(benzylamino)-4-oxobutane-1,2-diyl)-(R)-dicarbamate (77)



To a solution of N_β -Cbz- N_γ -Boc-L-3,4-Dab (200 mg, 0.568 mmol) in anhydrous DMF (2.84 mL) were added 1-ethyl-3-(3-dimethylaminopropyl)carbodiimide hydrochloride (152.44 mg, 0.795 mmol), hydroxybenzotriazole (92.1 mg, 0.682 mmol), and benzylamine (74.45 μL , 0.682 mmol). N -Methyl morpholine (109.5 μL , 0.996 mmol) was added via syringe to the reaction mixture, and the reaction was stirred under N_2 at room temperature for 6 hours. Once completed, the reaction was quenched by adding water (3 mL), then the organic product was extracted using ethyl acetate (3x3 mL). The organic layer was washed with water (3 x 3 mL) and 1N HCl (3 mL) and dried over Na_2SO_4 . The solvent was removed by evaporation under reduced pressure, and the crude mixture was purified by column chromatography using ethyl acetate/hexane (60/40) to give the dicarbamate **77** (108.0 mg,

43.1%) as a white solid. ^1H NMR (500 MHz, CDCl_3) δ 7.37 – 7.31 (m, 2H), 7.33 (s, 3H), 7.34 – 7.22 (m, 5H), 6.85 (s, 1H), 6.11 (d, $J = 6.9$ Hz, 1H), 5.06 (s, 3H), 4.41 (qd, $J = 14.7, 5.6$ Hz, 2H), 3.90 (d, $J = 8.1$ Hz, 1H), 3.35 (dt, $J = 13.3, 6.3$ Hz, 1H), 3.26 (dt, $J = 13.7, 6.0$ Hz, 1H), 2.48 (qd, $J = 13.9, 5.5$ Hz, 2H), 1.42 (s, 9H).

Benzyl (R)-(1-amino-4-(benzylamino)-4-oxobutan-2-yl)carbamate 2,2,2-trifluoroacetic acid (78)



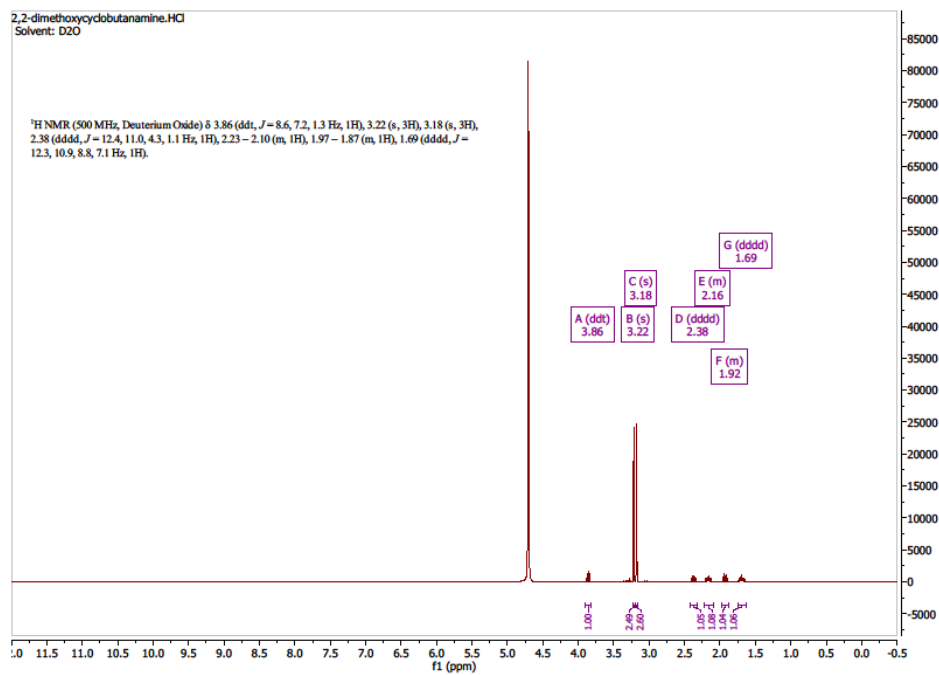
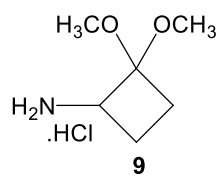
To a solution of dicarbamate **77** (75 mg, 0.170 mmol) in methylene chloride (1.7 mL) trifluoroacetic acid (509.6 μL , 30% v/v) was added and the reaction mixture was stirred at room temperature for 8 hours. Upon completion, the reaction mixture was concentrated under reduced pressure and the resultant solution (~ 0.3 mL) was added dropwise to a stirring of solution of diethyl ether (30 mL) at room temperature. The precipitated solid was filtered off and washed with diethyl ether to provide TFA salt of 3,4-BABOC (**78**, 57.0 mg, 73.7%) as a white solid. ^1H NMR (500 MHz, MeOD) δ 7.41 – 7.25 (m, 8H), 7.24 (td, $J = 6.0, 2.4$ Hz, 2H), 5.14 (d, $J = 12.2$ Hz, 1H), 5.08 (d, $J = 12.4$ Hz, 1H), 4.40 (d, $J = 14.9$ Hz, 1H), 4.34 (d, $J = 14.9$ Hz, 1H), 4.23 (dtd, $J = 10.7, 6.7, 4.1$ Hz, 1H), 3.19 (dd, $J = 13.0, 4.0$ Hz, 1H), 3.07 (dd, $J = 13.0, 9.8$ Hz, 1H), 2.58 (d, $J = 6.7$ Hz, 2H). ^{13}C NMR (126 MHz, MeOD) δ 170.29, 157.07, 138.31, 136.54, 128.19, 128.12, 127.75, 127.64, 127.19, 126.89, 66.53, 42.86, 42.82, 38.17.

Molecular Docking Protocol for GNAT Substrates

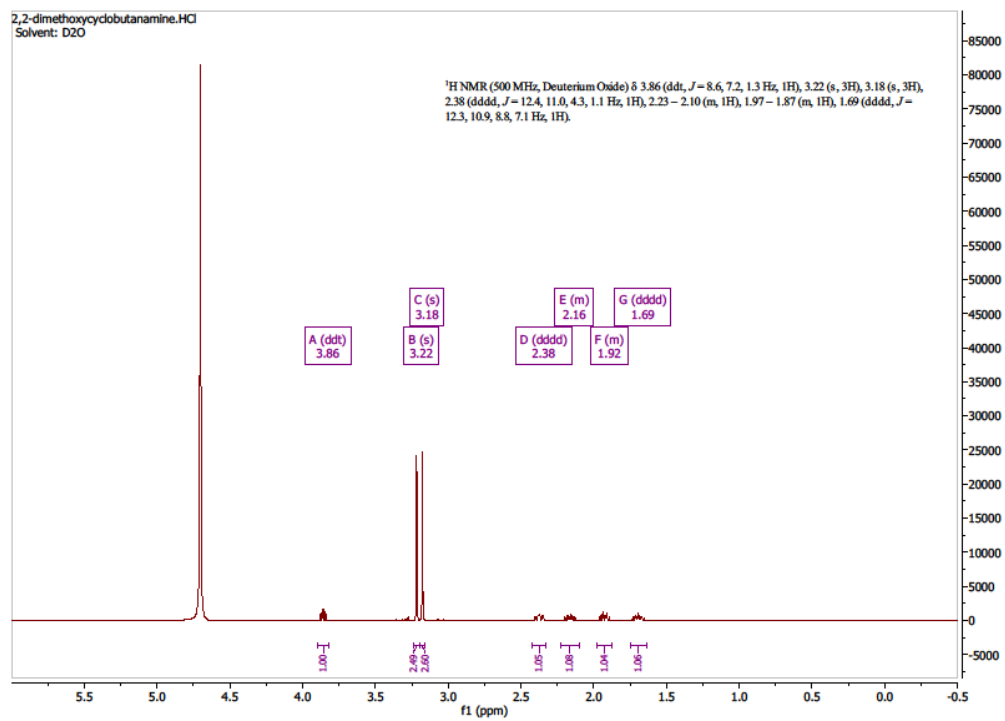
Molecular models of ligands were developed using the Molecular Operating Environment (MOE)⁷⁷ computational suite's Builder utility, followed by minimization in the gas phase using the MMFF94X force field. Structural models of PA3944 WT (PDB ID: 6EDV or 7KPS) and E102A mutant (PDB ID: 7KPP) were prepared in MOE with the Builder utility, then minimized before docking with NANMO. The hydrogen-bonding network of the docking model was further optimized at pH of 7.4 by automatically sampling different tautomer/protomer states using Protonate3D, which calculates optimal protonation states, including titration, rotamer, and "flips" using a large-scale combinatorial search. The active site was specified by the dummy atoms populating the binding pocket. Ligand placement employed the Alpha Triangle method with Affinity dG scoring to generate 1,000 data points per unique ligand that were further refined using the Induced Fit method with GBVI/WSA dG scoring to obtain the top 300 docking poses per ligand. The Amber12:EHT force field was used to perform these calculations. The docking poses were analyzed using the following criteria: (1) Substrate analogs needed to interact with acceptor site residues and have the terminal amine pointed toward the donor site. (2) Docking poses with the lowest docking score and energy were prioritized.

APPENDIX A
SUPPLEMENTAL DATA FOR CHAPTER TWO

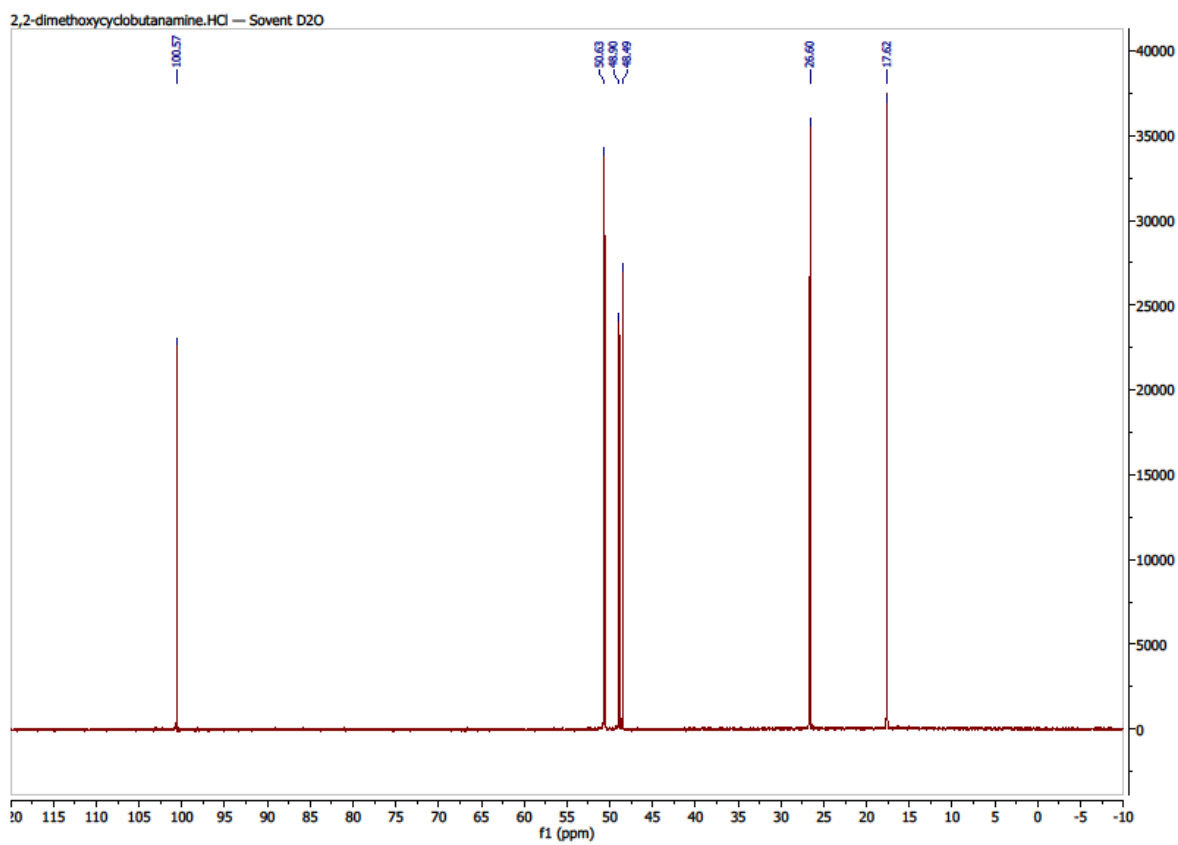
NMR spectra of the compounds reported in chapter two.



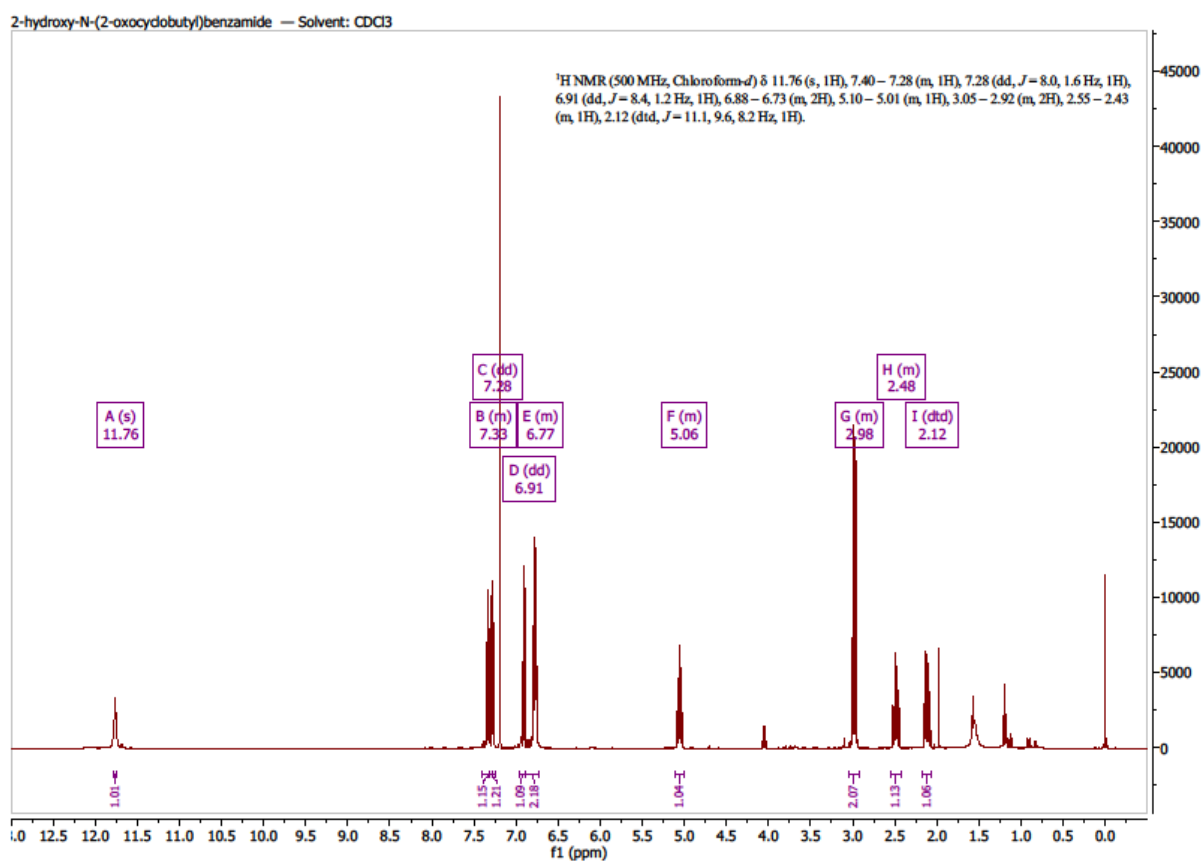
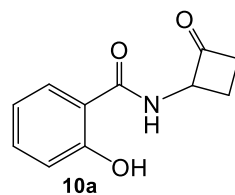
¹H spectrum of 2,2-dimethoxycyclobutan-1-aminium chloride (9).



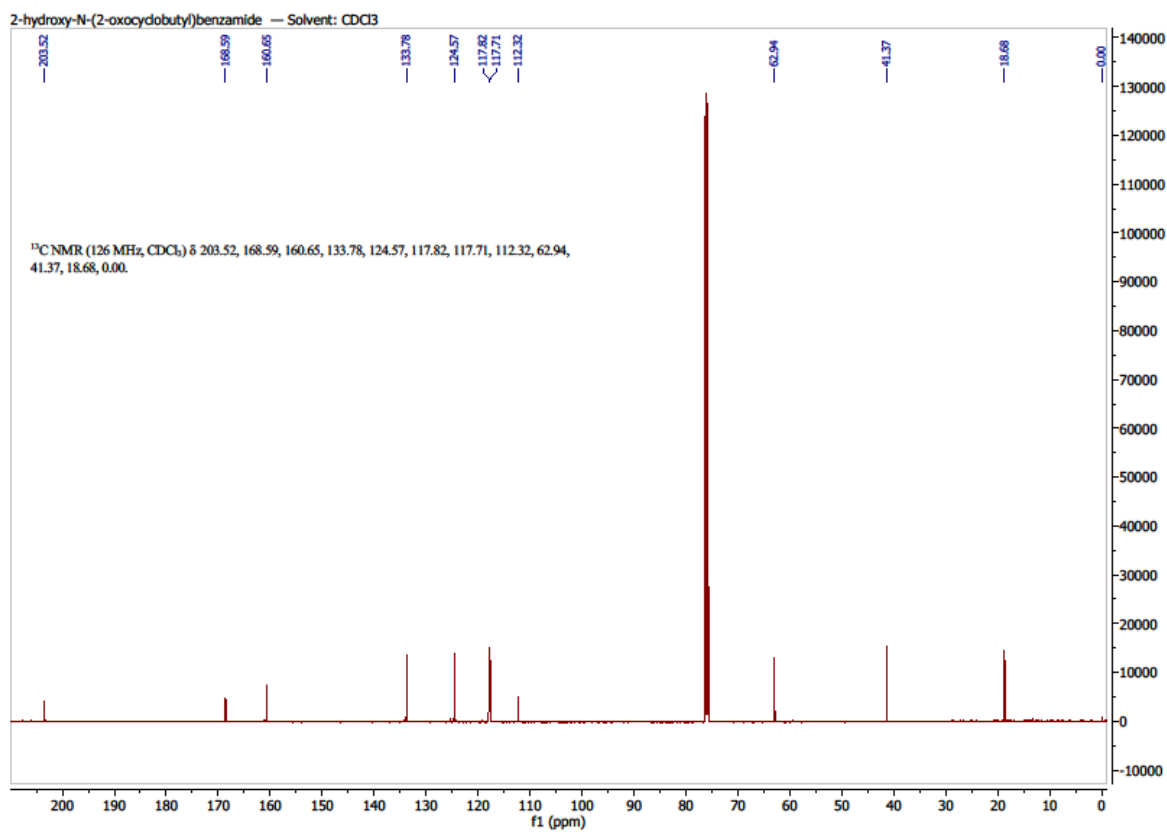
Expanded ¹H spectrum of 2,2-dimethoxycyclobutan-1-aminium chloride (**9**).



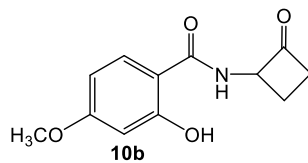
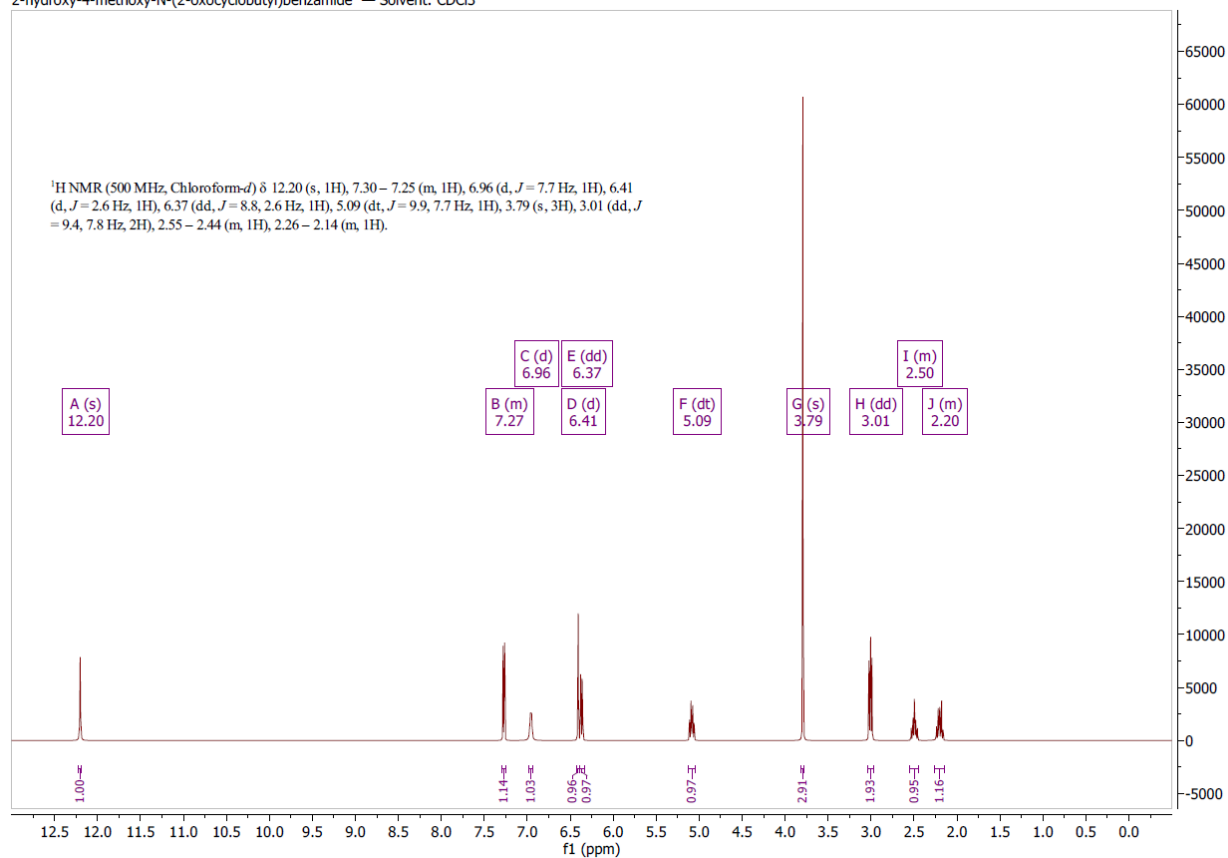
^{13}C spectrum of 2,2-dimethoxycyclobutan-1-aminium chloride (**9**).

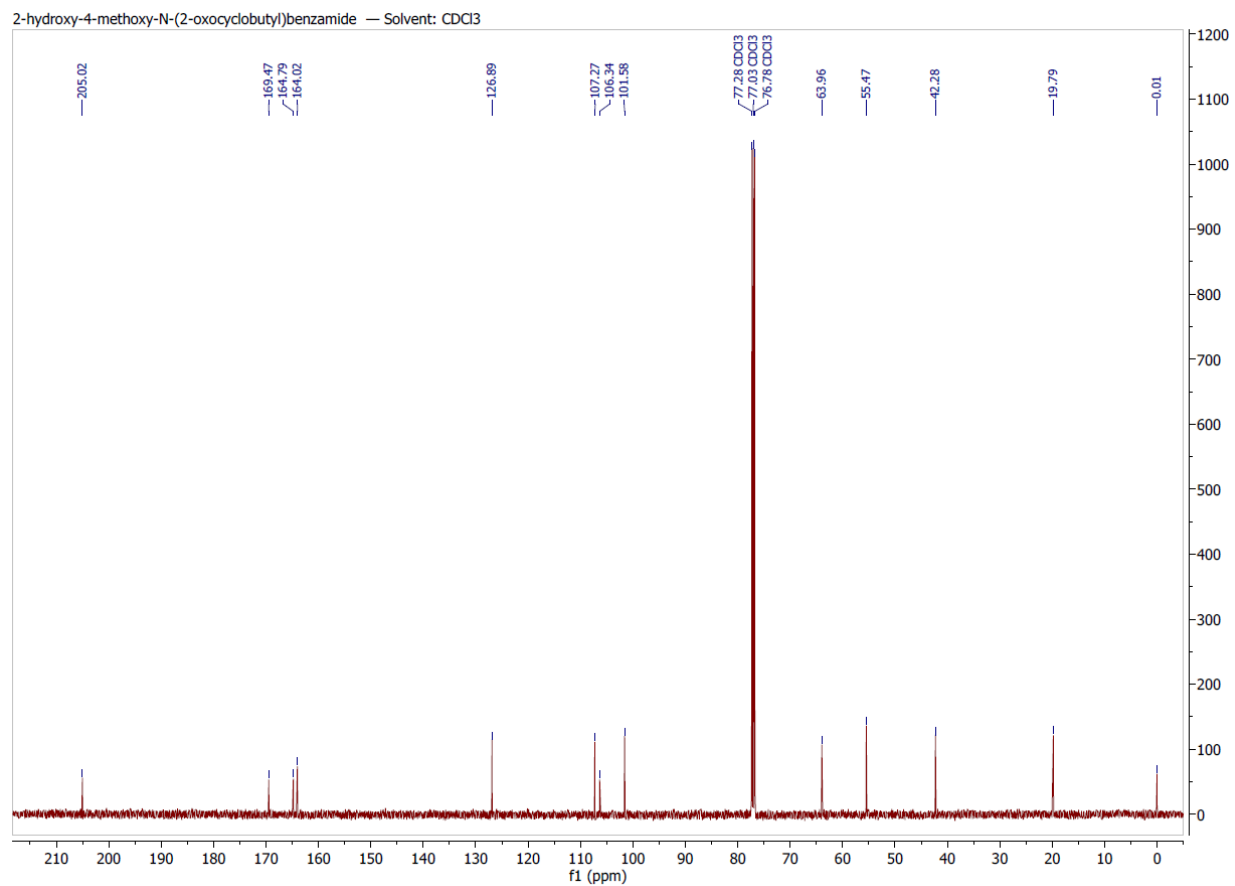


¹H spectrum of 2-hydroxy-N-(2-oxocyclobutyl)benzamide (**10a**)

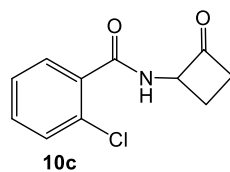


¹³C spectrum of 2-hydroxy-N-(2-oxocyclobutyl)benzamide (**10a**)

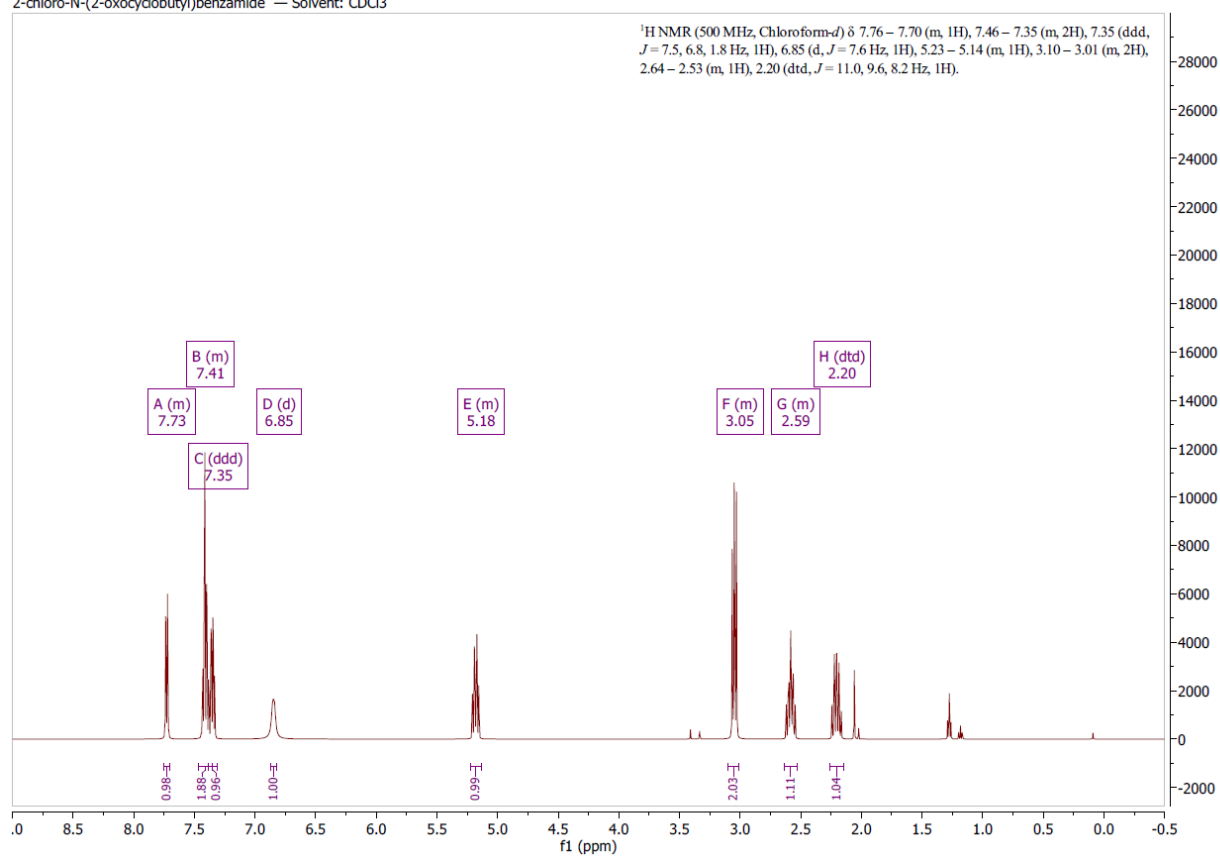
2-hydroxy-4-methoxy-N-(2-oxocyclobutyl)benzamide — Solvent: CDCl₃¹H spectrum of ¹H spectrum of 2-hydroxy-4-methoxy-N-(2-oxocyclobutyl)benzamide (**10b**).



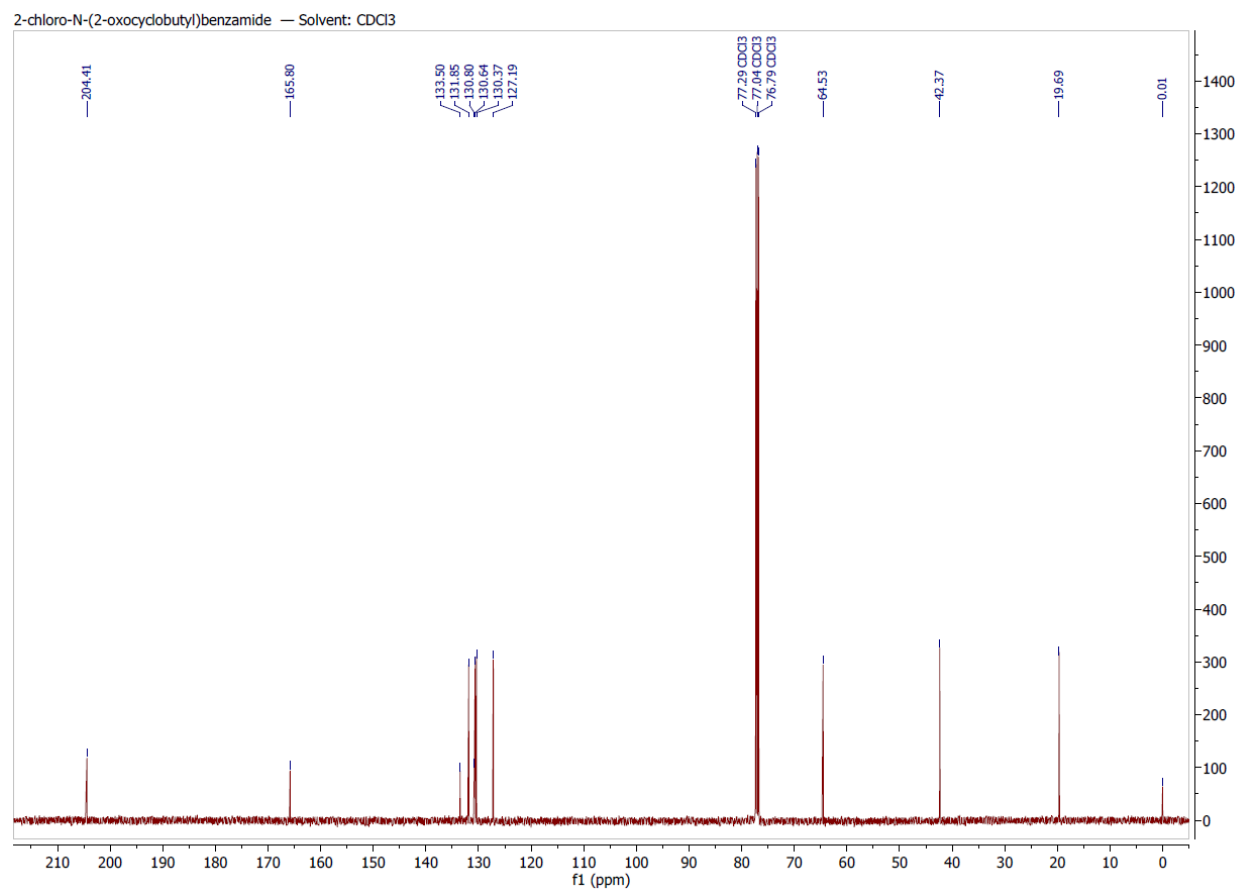
¹³C spectrum of 2-hydroxy-4-methoxy-*N*-(2-oxocyclobutyl)benzamide (**10b**).



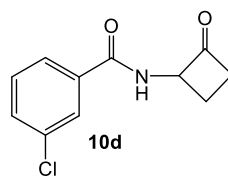
2-chloro-N-(2-oxocyclobutyl)benzamide — Solvent: CDCl₃



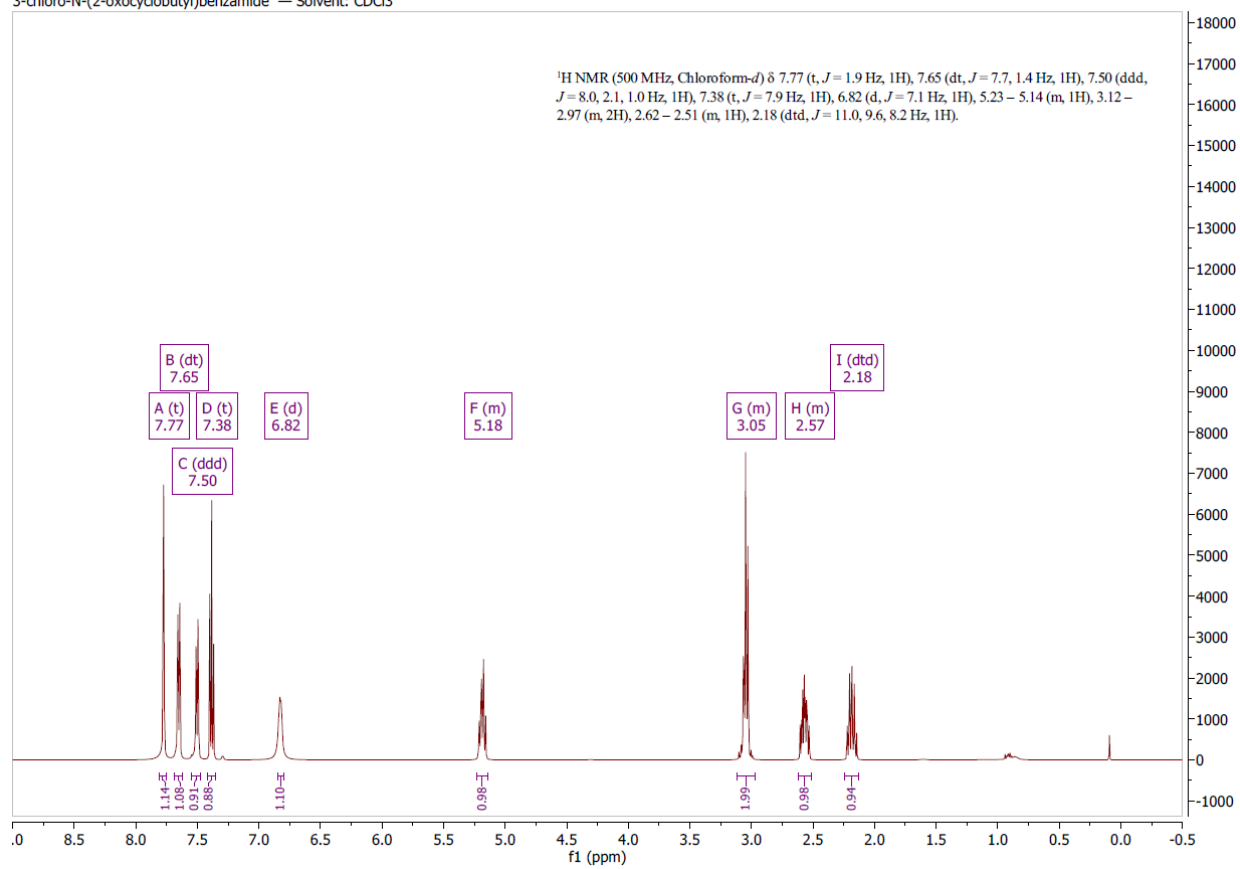
¹H spectrum of 2-chloro-N-(2-oxocyclobutyl)benzamide (**10c**).



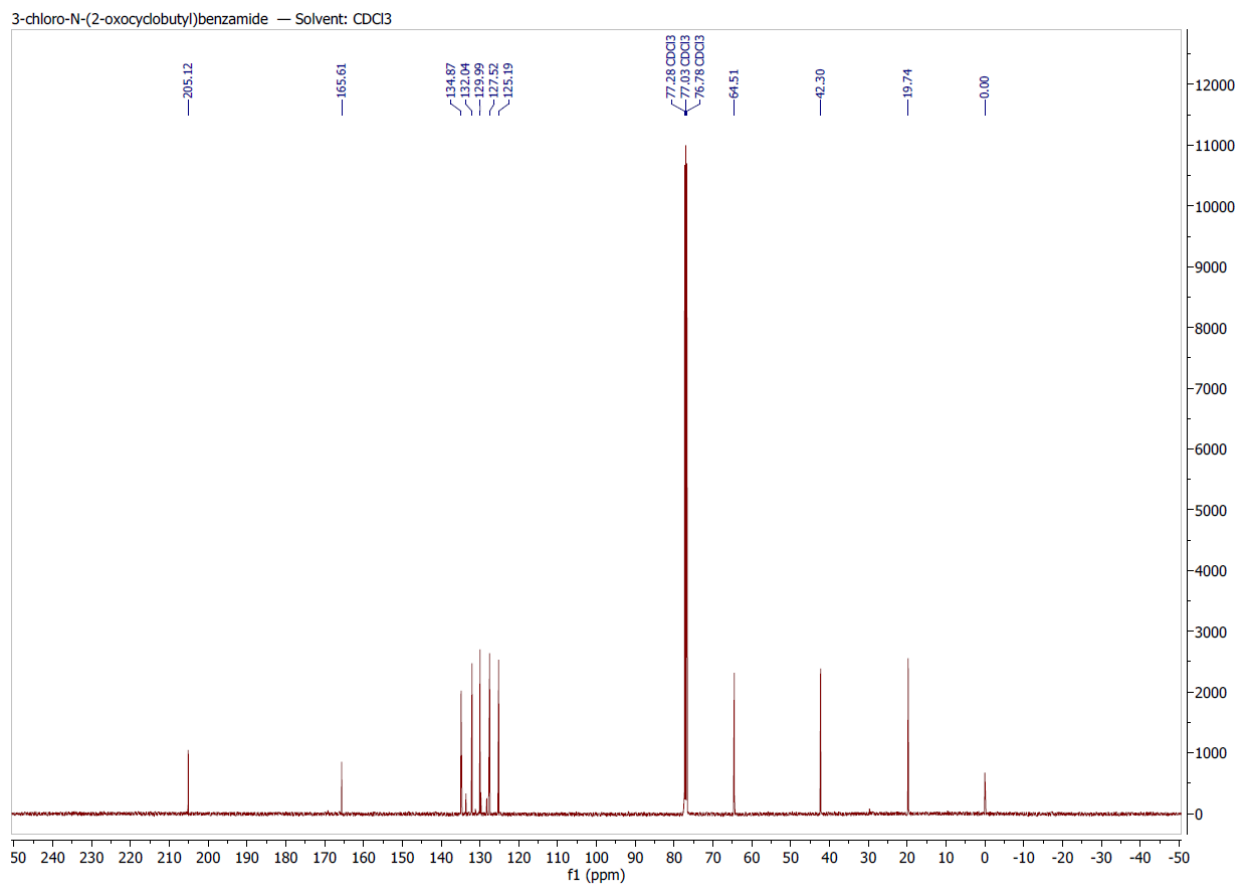
¹³C spectrum of 2-chloro-N-(2-oxocyclobutyl)benzamide (**10c**).



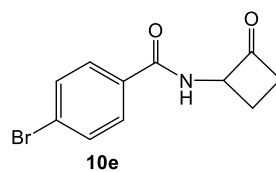
3-chloro-N-(2-oxocyclobutyl)benzamide — Solvent: CDCl₃



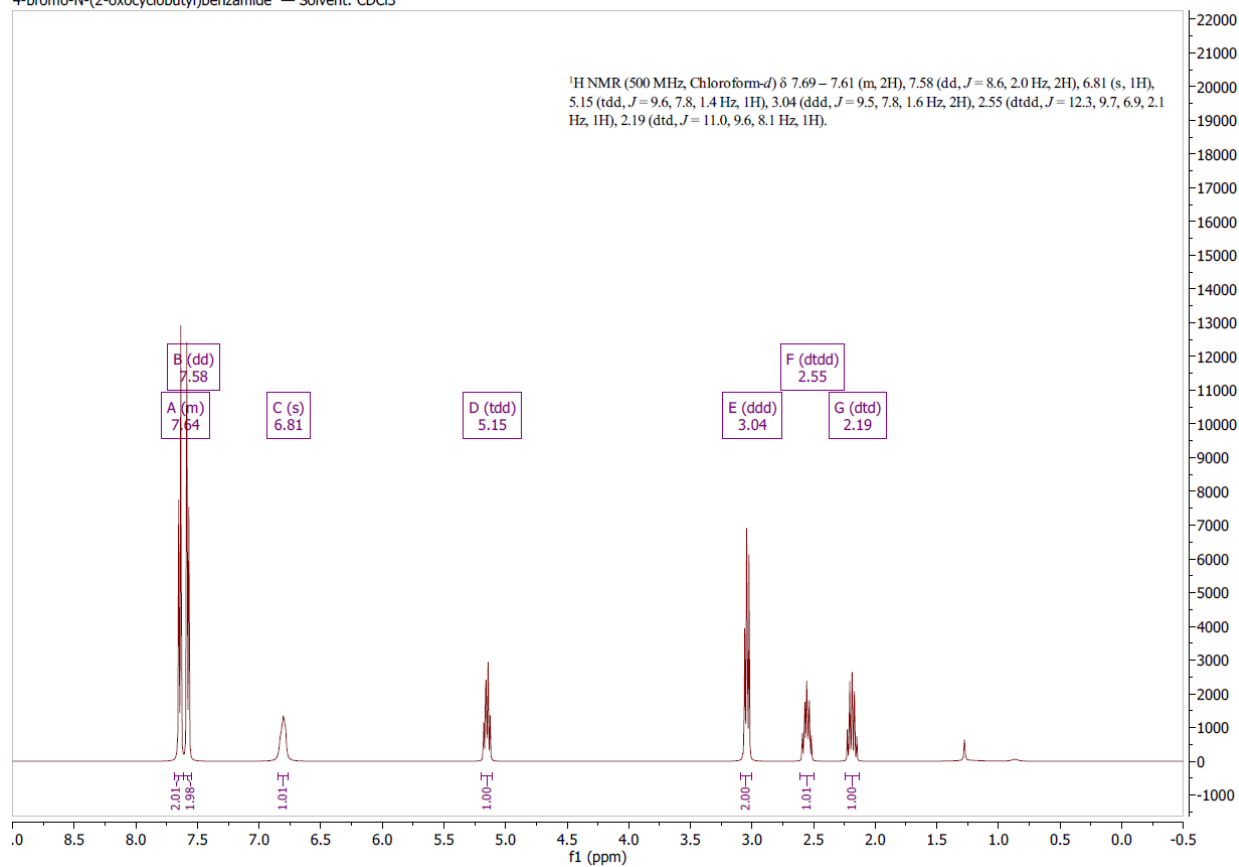
¹H spectrum of 3-chloro-N-(2-oxocyclobutyl)benzamide (**10d**).



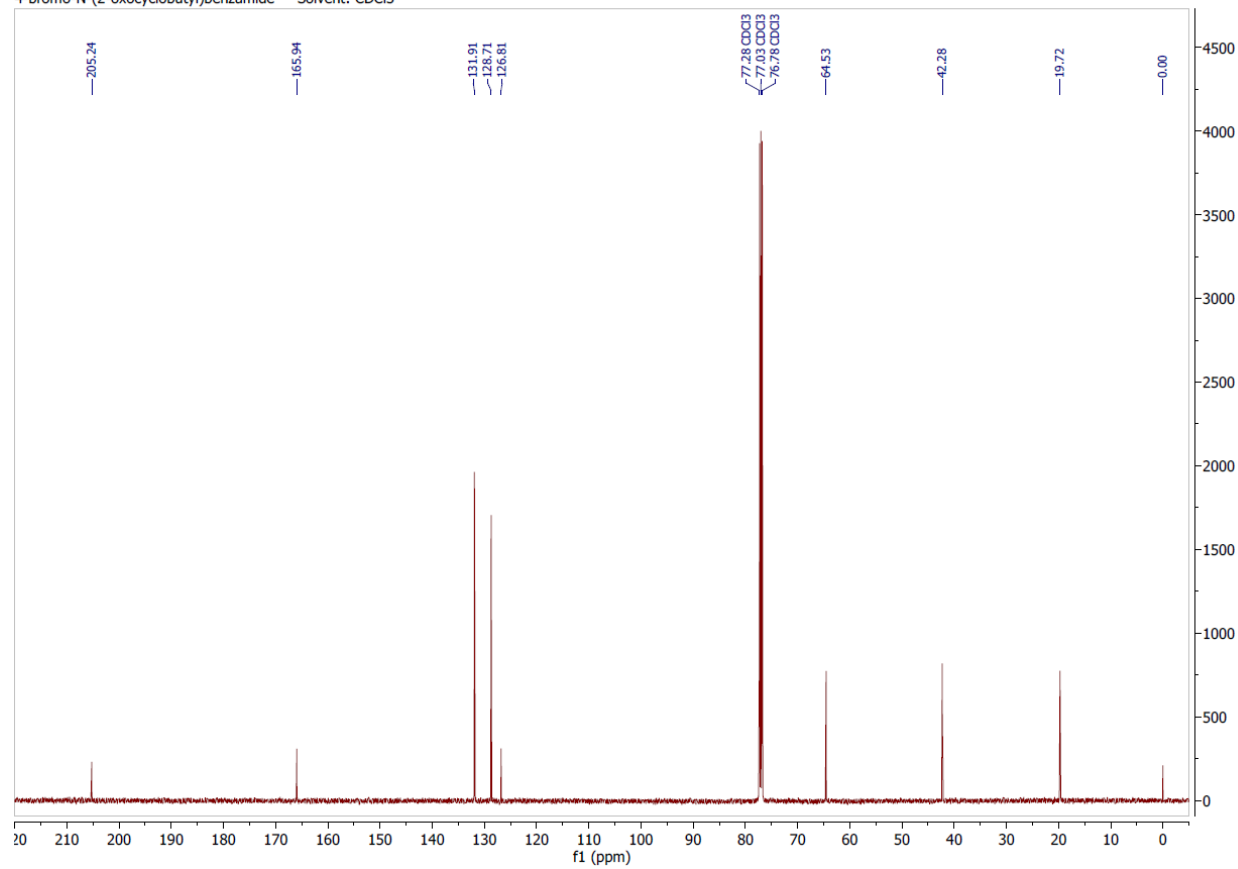
¹³C spectrum of 3-chloro-N-(2-oxocyclobutyl)benzamide (**10d**).



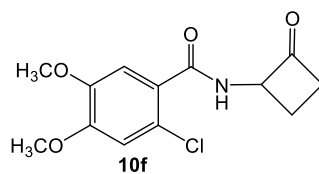
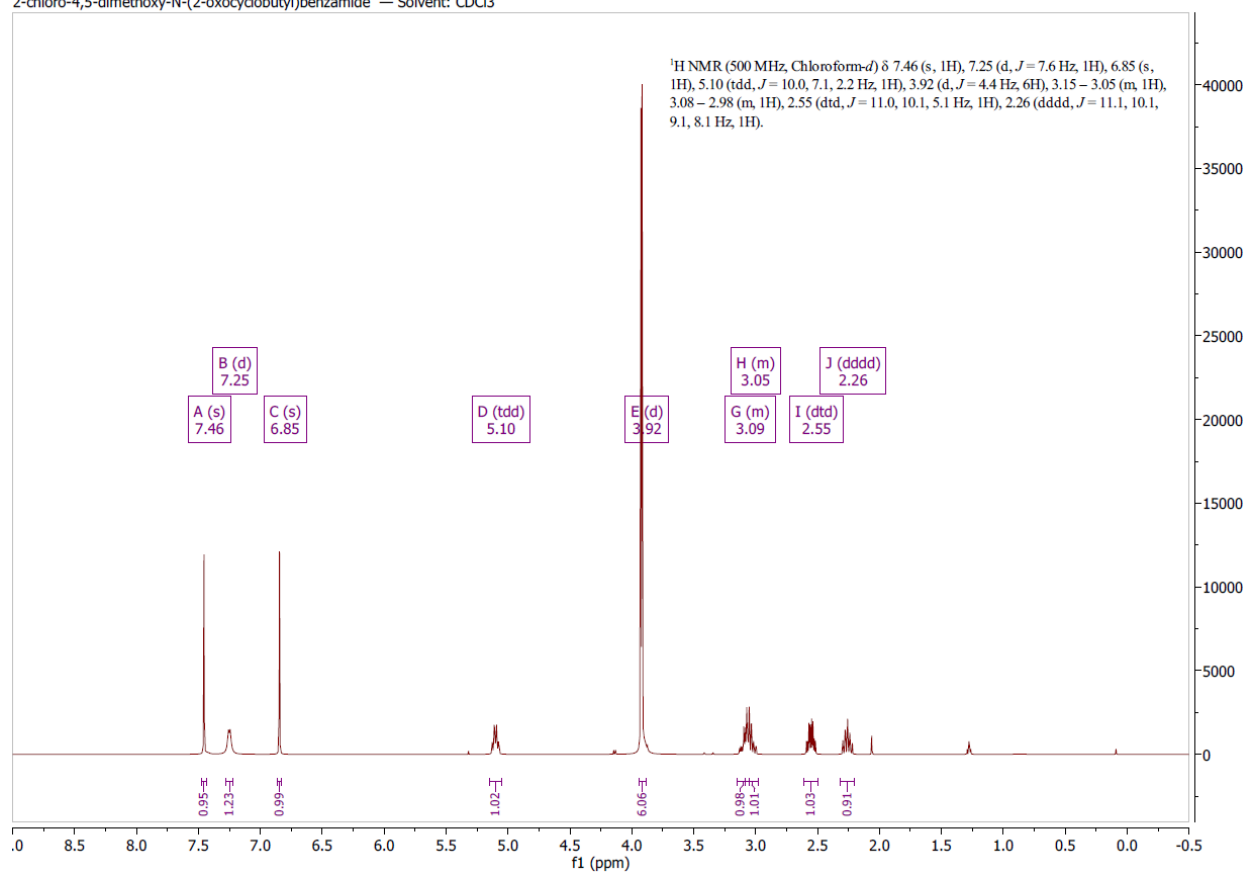
4-bromo-N-(2-oxocyclobutyl)benzamide — Solvent: CDCl₃

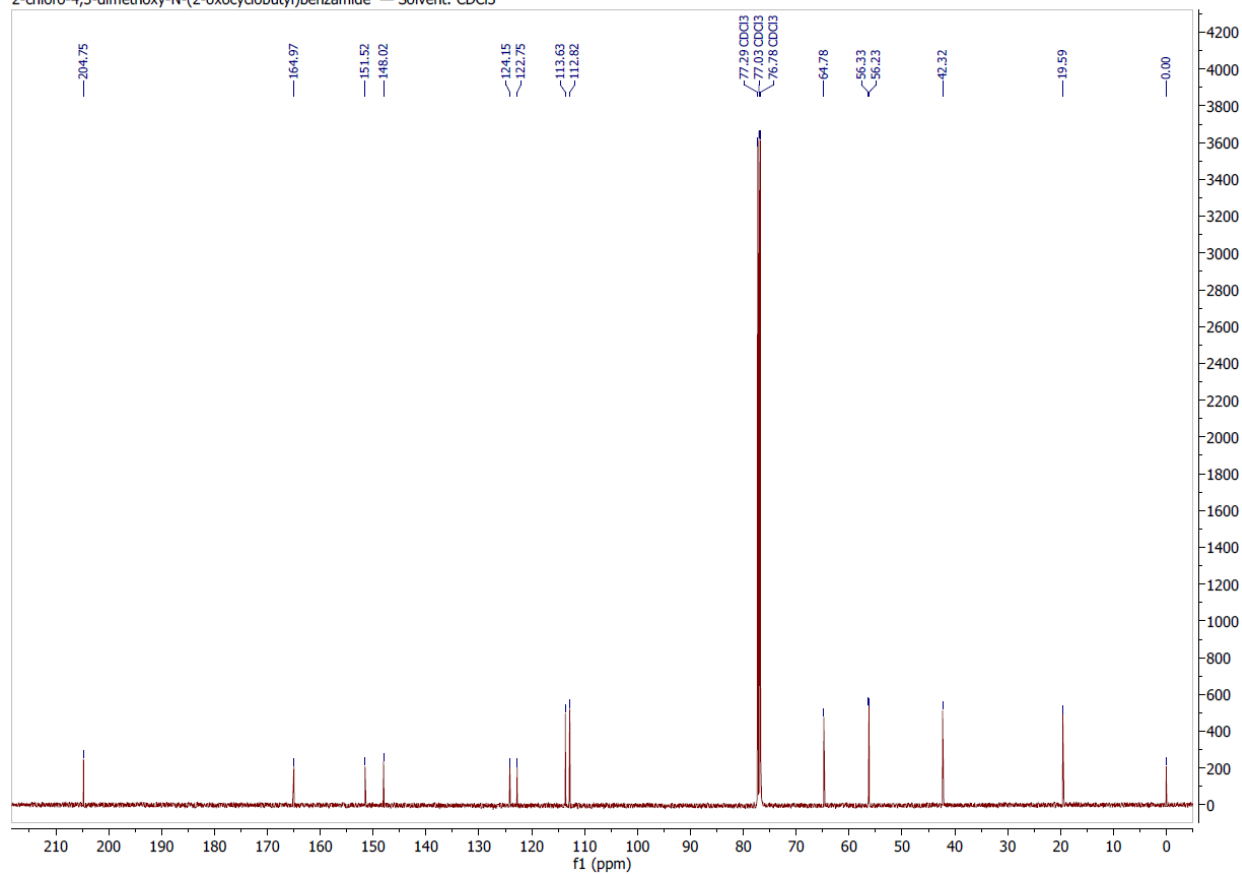


¹H spectrum of 4-bromo-N-(2-oxocyclobutyl)benzamide (**10e**).

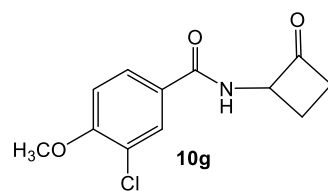
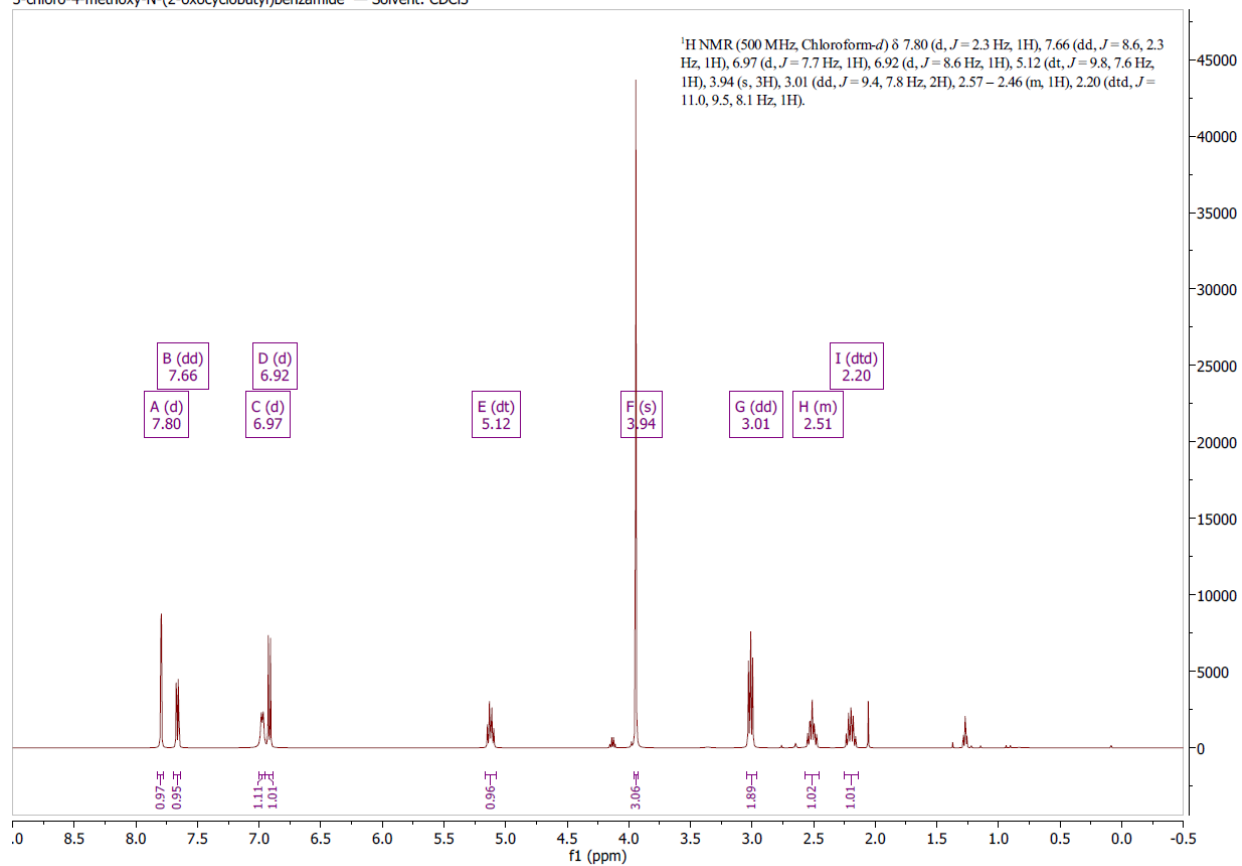
4-bromo-N-(2-oxocyclobutyl)benzamide — Solvent: CDCl₃

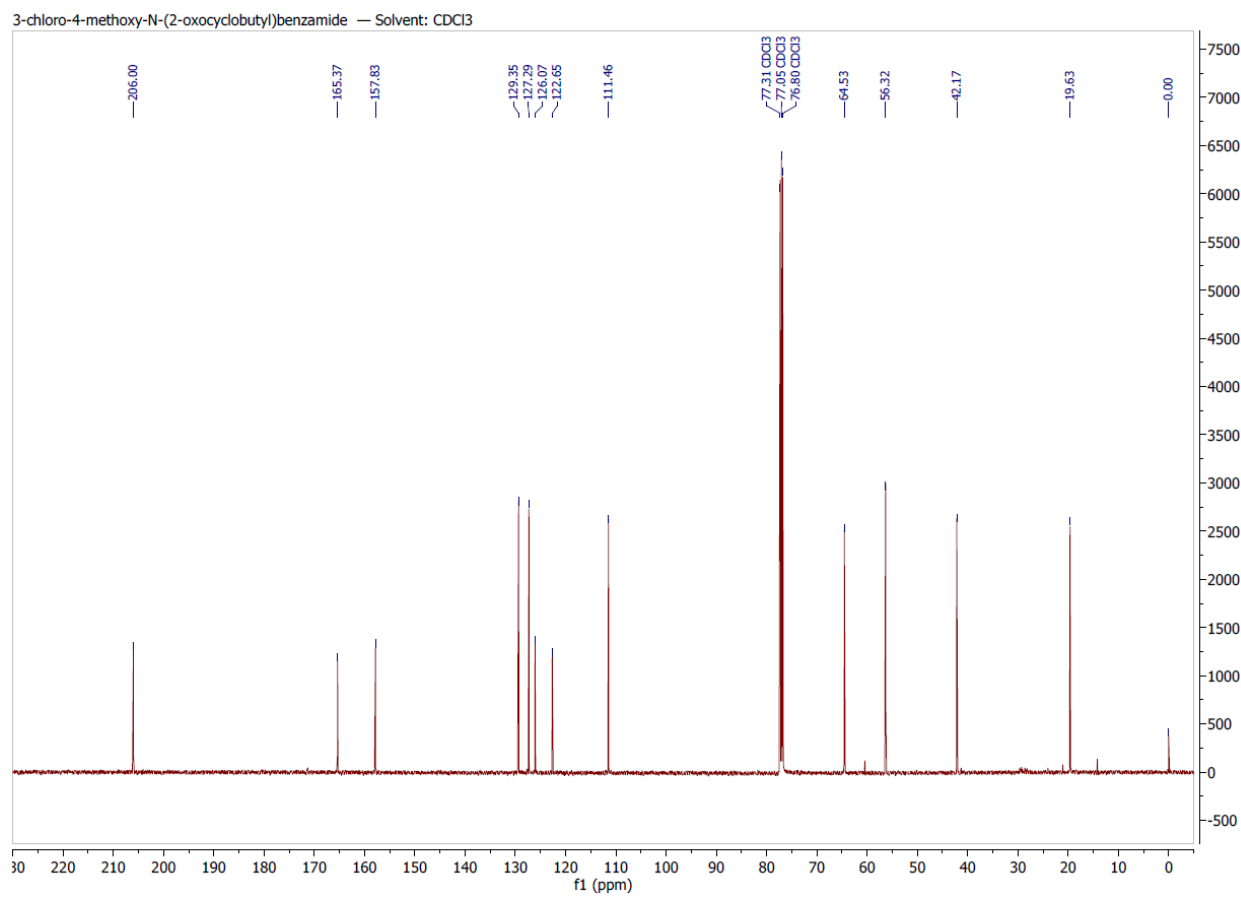
¹³C spectrum of 4-bromo-N-(2-oxocyclobutyl)benzamide (**10e**).

2-chloro-4,5-dimethoxy-N-(2-oxocyclobutyl)benzamide — Solvent: CDCl₃¹H spectrum of 2-chloro-4,5-dimethoxy-N-(2-oxocyclobutyl)benzamide (**10f**).

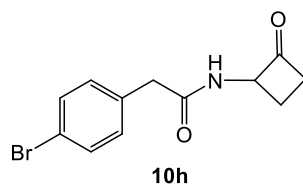
2-chloro-4,5-dimethoxy-N-(2-oxocyclobutyl)benzamide — Solvent: CDCl₃

¹³C spectrum of 2-chloro-4,5-dimethoxy-N-(2-oxocyclobutyl)benzamide (**10f**).

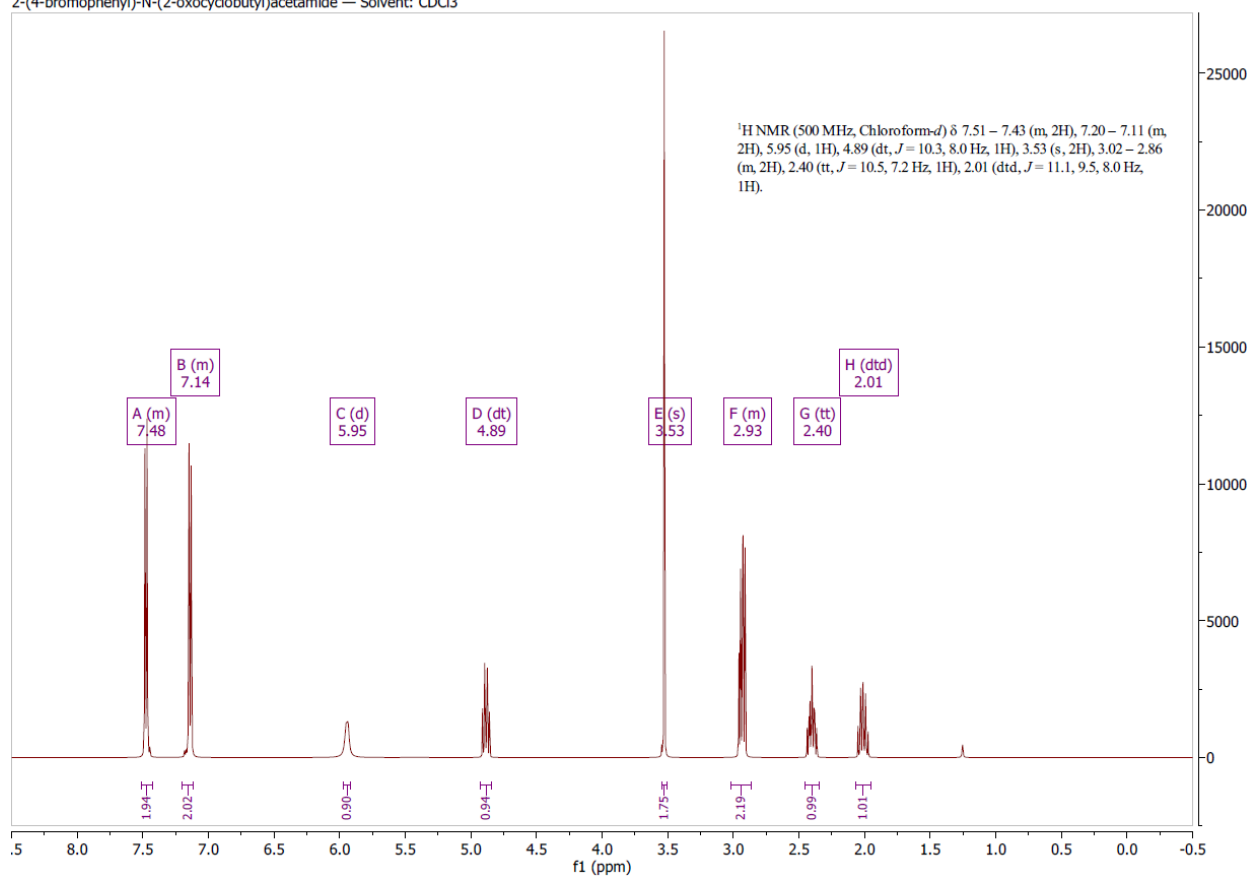
3-chloro-4-methoxy-N-(2-oxocyclobutyl)benzamide — Solvent: CDCl₃¹H spectrum of 3-chloro-4-methoxy-N-(2-oxocyclobutyl)benzamide (**10g**).



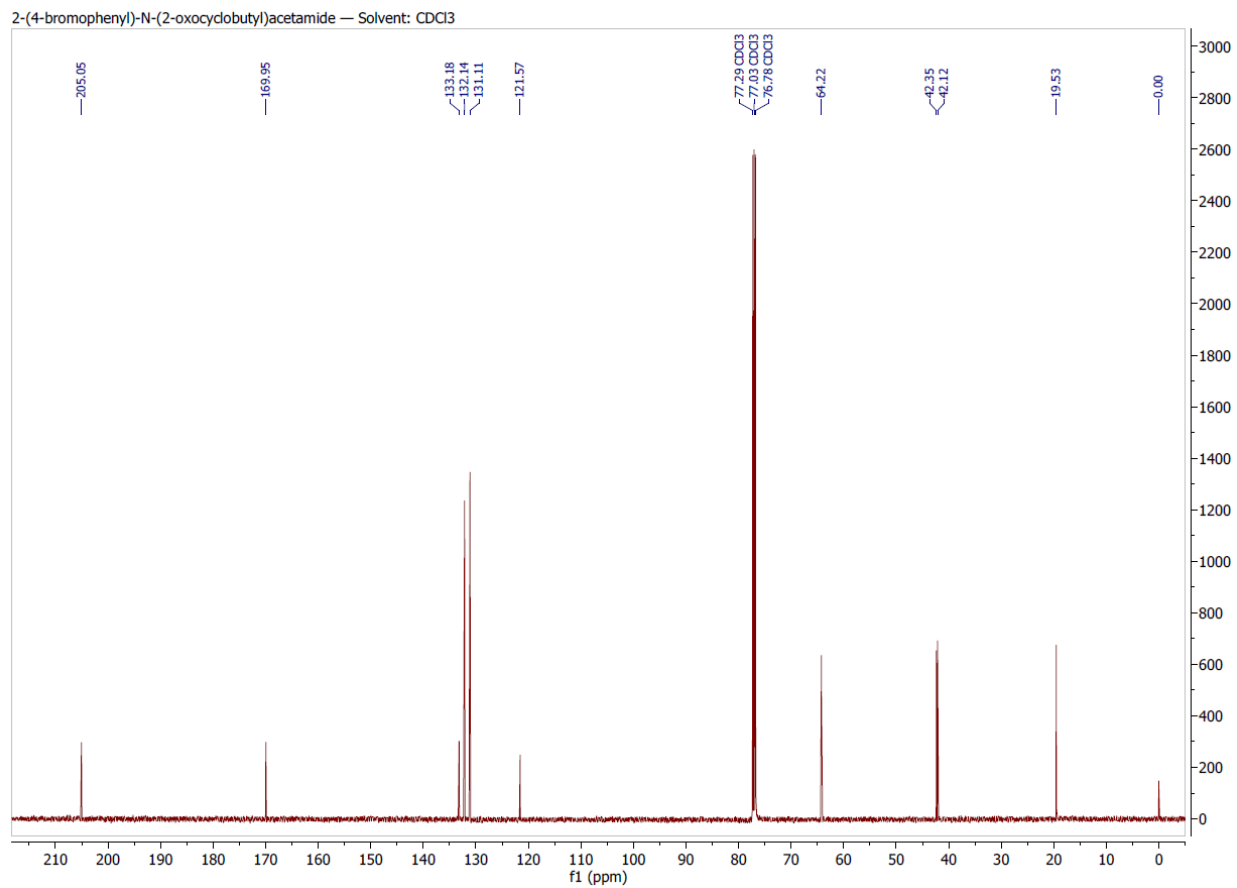
¹³C spectrum of 3-chloro-4-methoxy-*N*-(2-oxocyclobutyl)benzamide (**10g**).



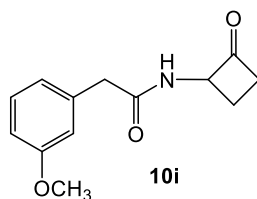
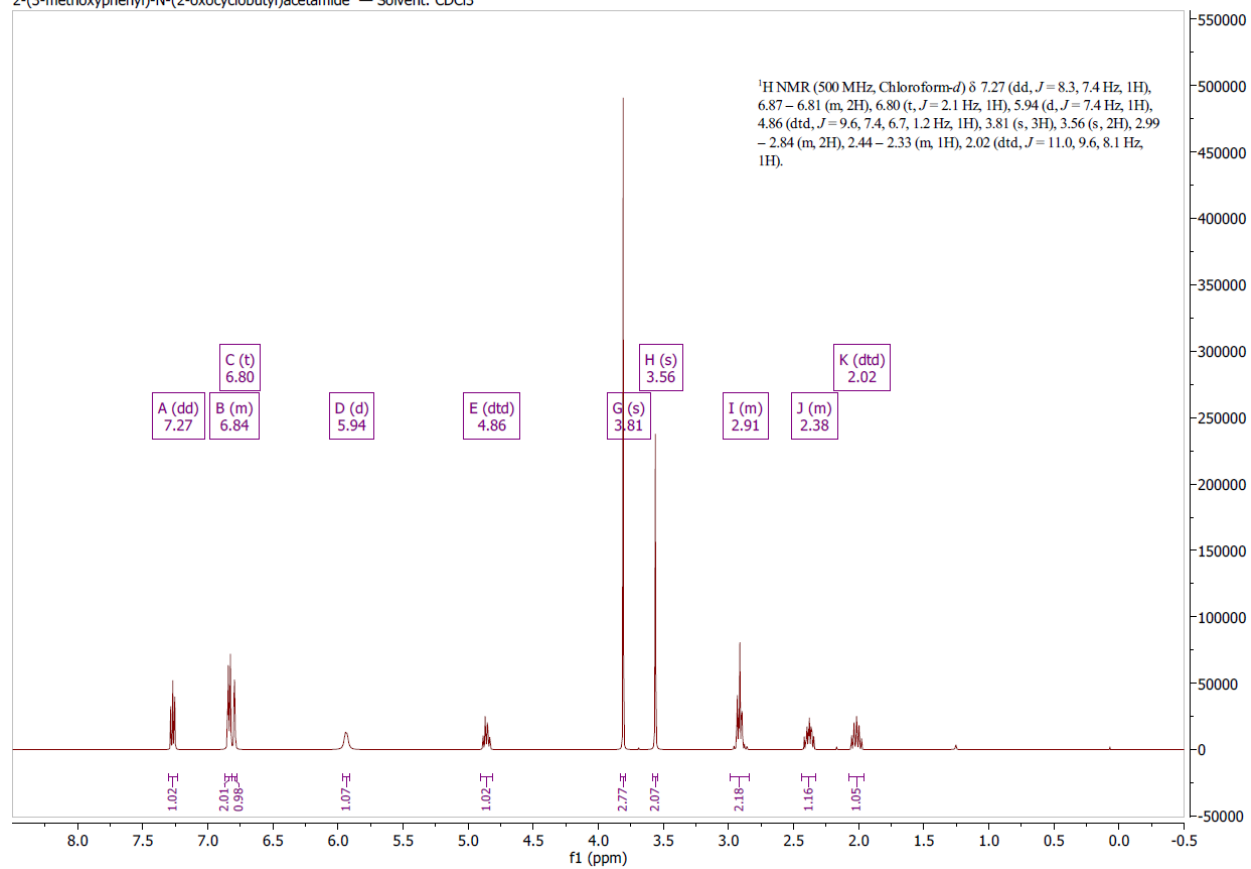
2-(4-bromophenyl)-N-(2-oxocyclobutyl)acetamide — Solvent: CDCl₃

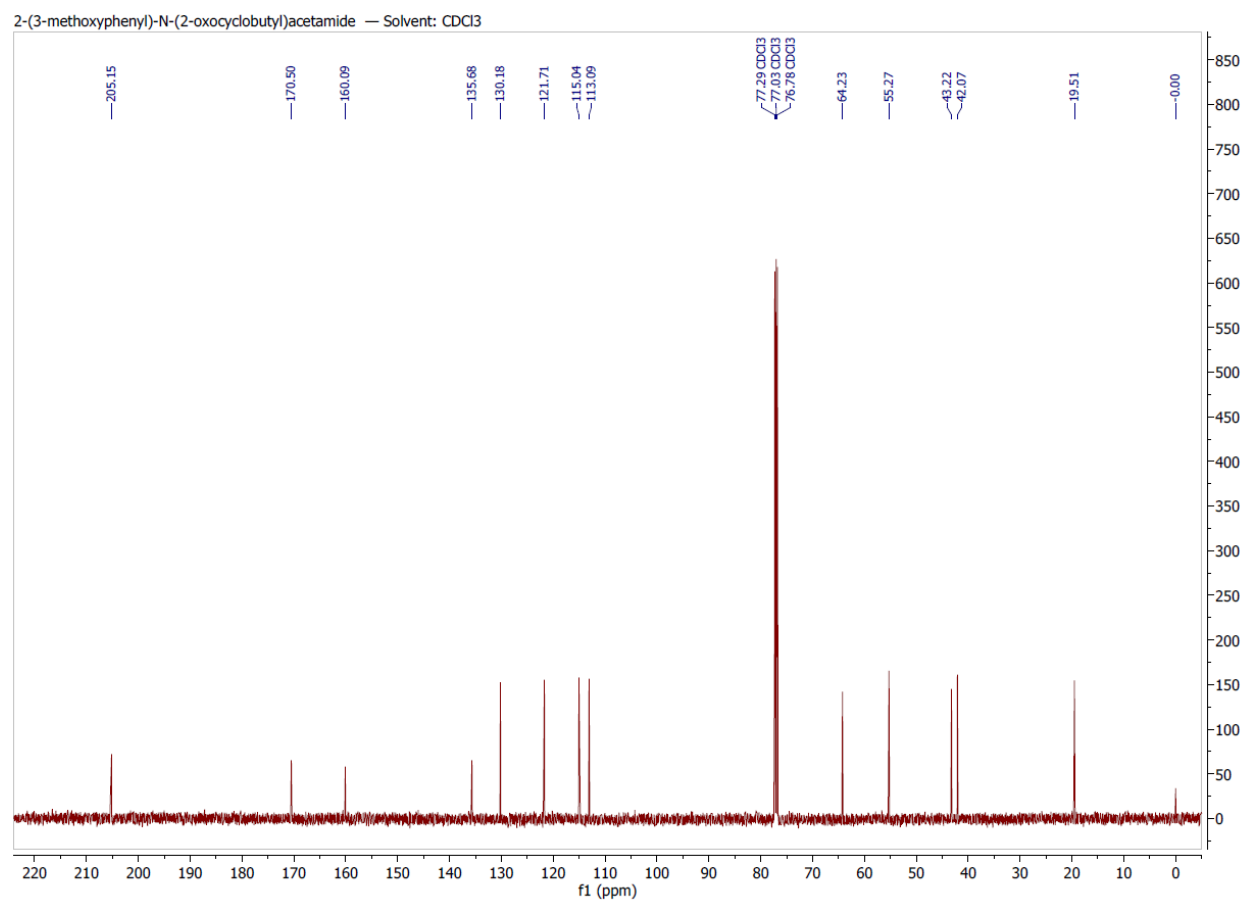


¹H spectrum of 2-(4-bromophenyl)-N-(2-oxocyclobutyl)acetamide (**10h**).

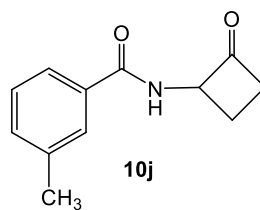
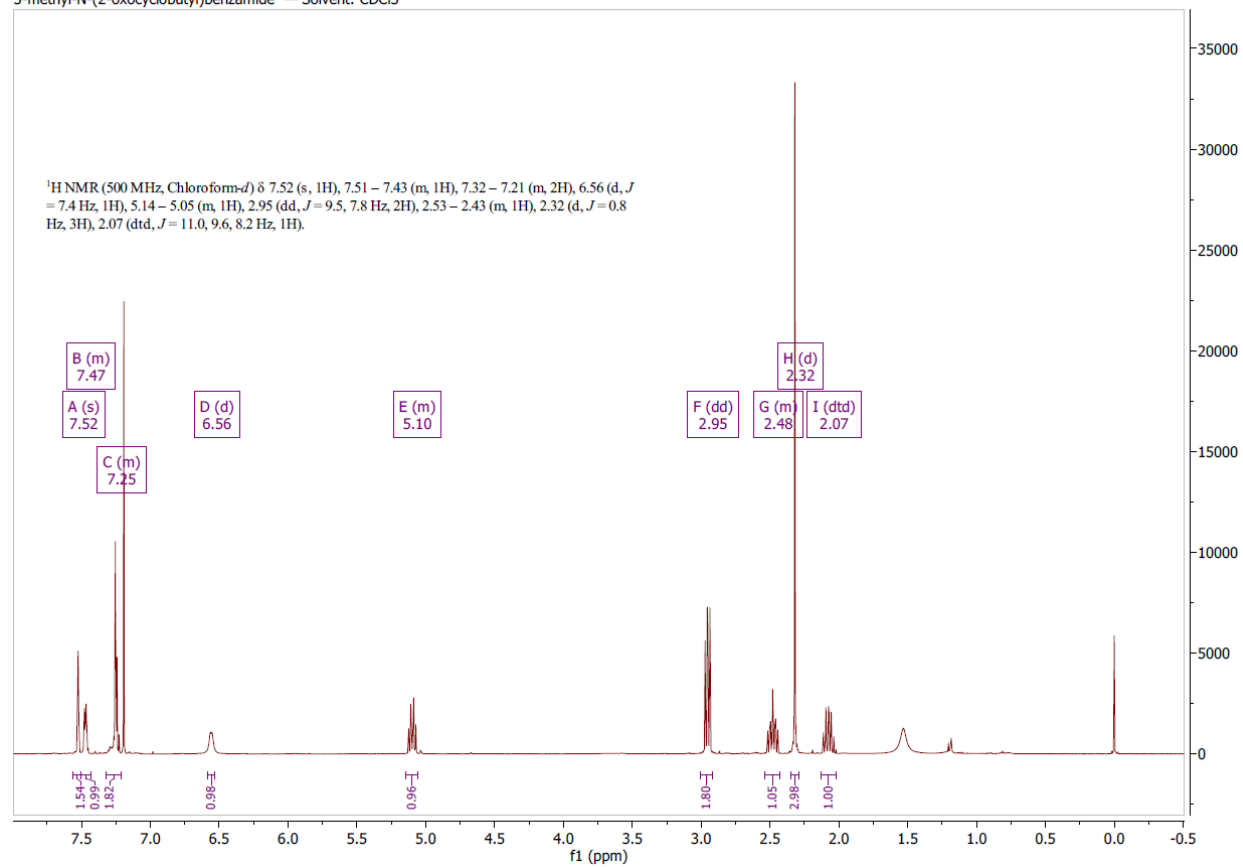


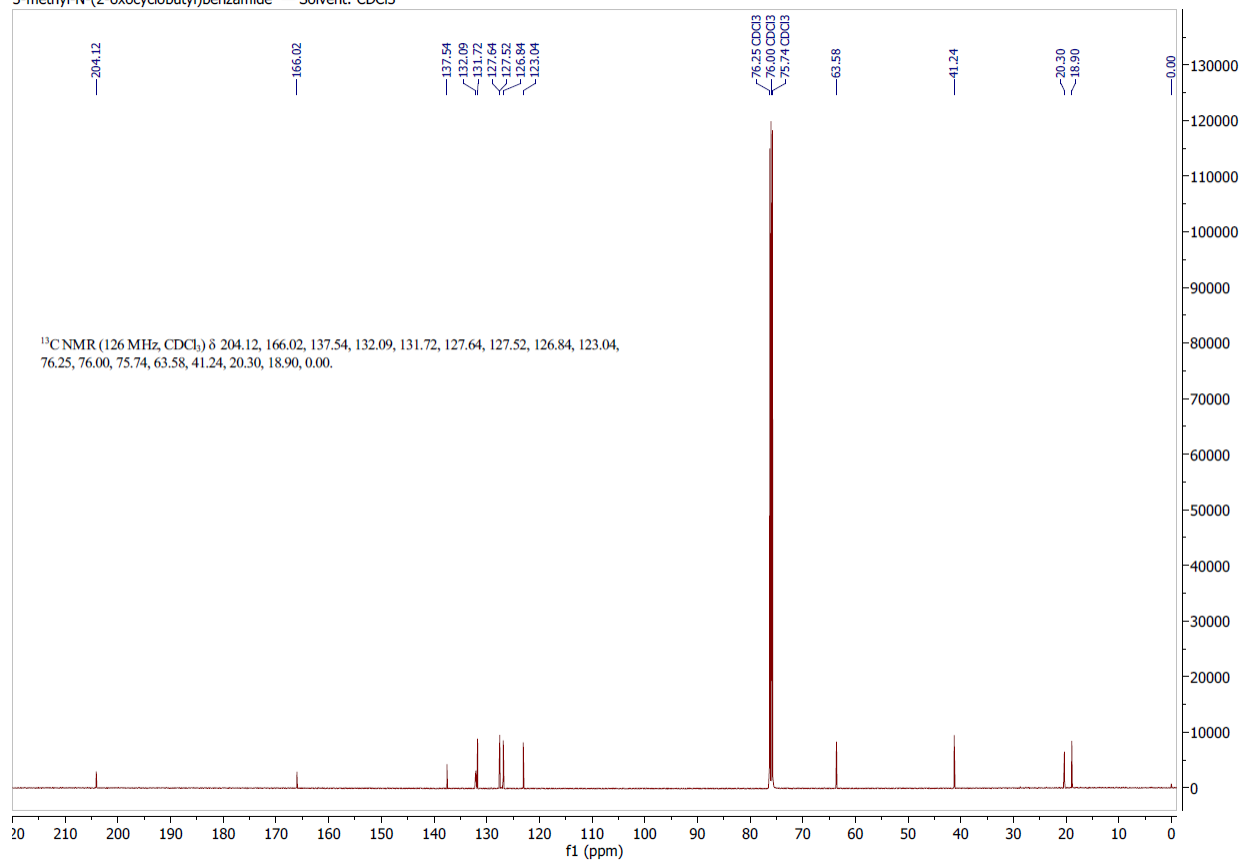
¹³C spectrum of 2-(4-bromophenyl)-N-(2-oxocyclobutyl)acetamide (**10h**).

2-(3-methoxyphenyl)-N-(2-oxocyclobutyl)acetamide — Solvent: CDCl₃¹H spectrum of 2-(3-methoxyphenyl)-N-(2-oxocyclobutyl)acetamide (**10i**).

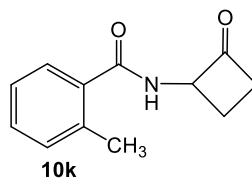


¹³C spectrum of 2-(3-methoxyphenyl)-N-(2-oxocyclobutyl)acetamide (**10i**).

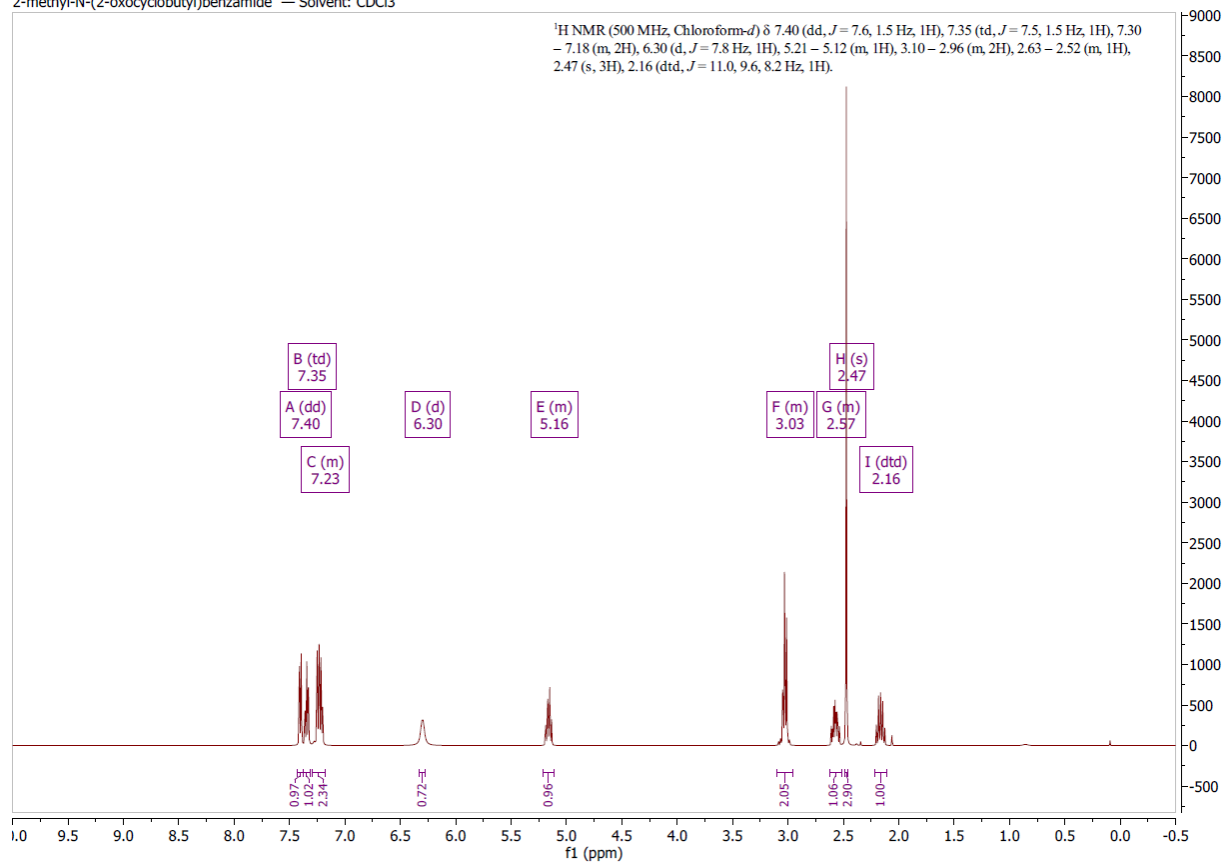
3-methyl-N-(2-oxocyclobutyl)benzamide — Solvent: CDCl₃¹H spectrum of 3-methyl-N-(2-oxocyclobutyl)benzamide (**10j**).

3-methyl-N-(2-oxocyclobutyl)benzamide — Solvent: CDCl₃

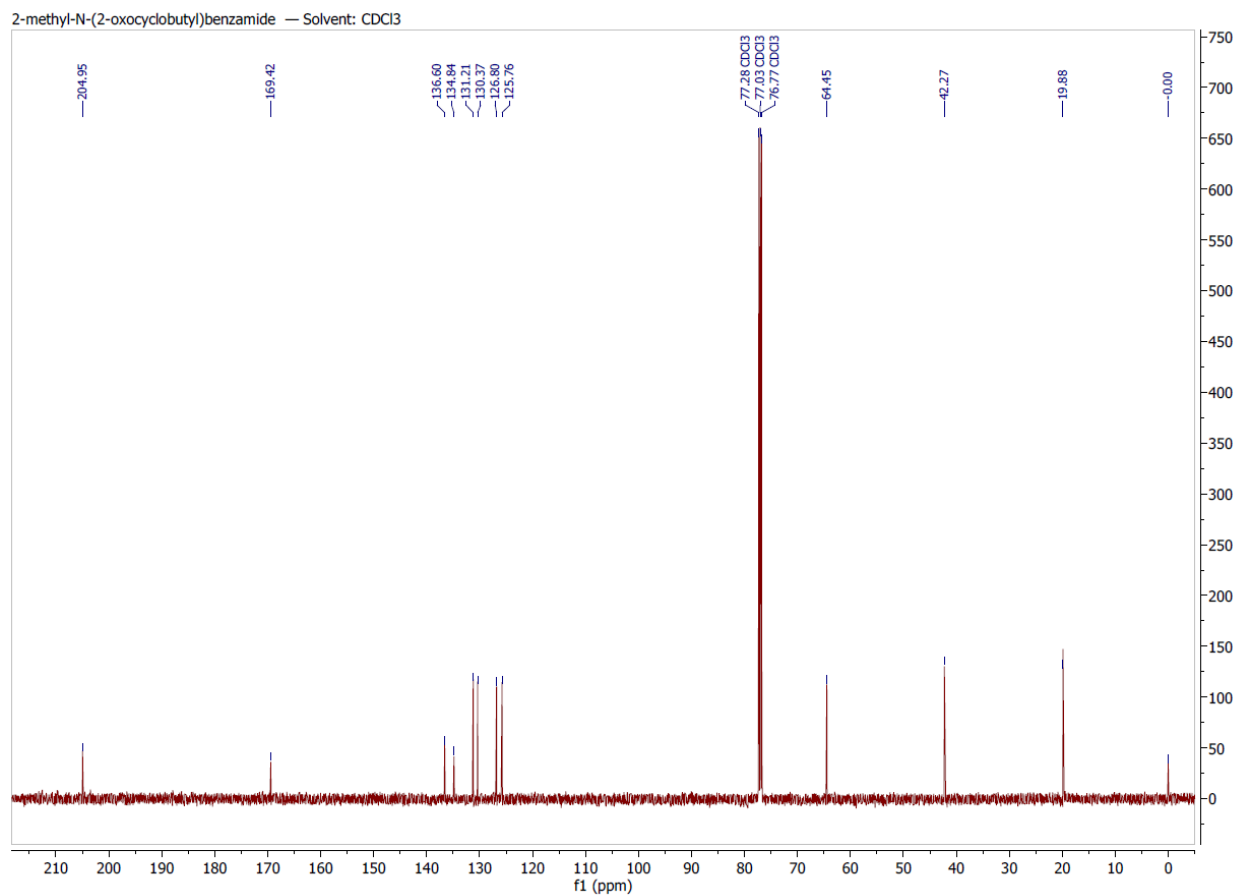
¹³C spectrum of 3-methyl-N-(2-oxocyclobutyl)benzamide (**10j**).



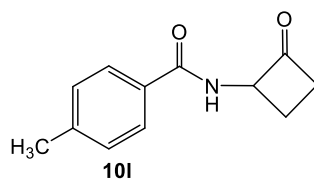
2-methyl-N-(2-oxocyclobutyl)benzamide — Solvent: CDCl₃



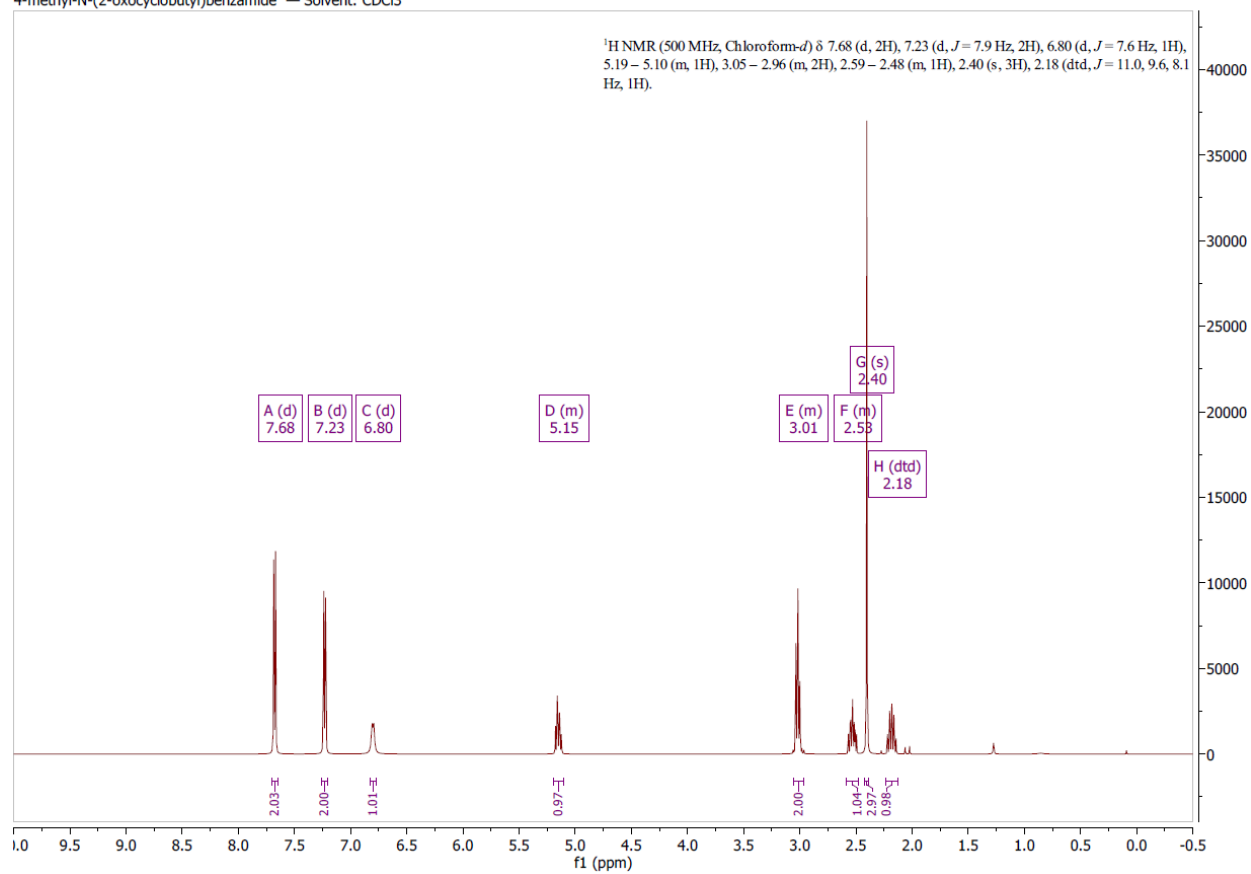
¹H spectrum of 2-methyl-N-(2-oxocyclobutyl)benzamide (**10k**).



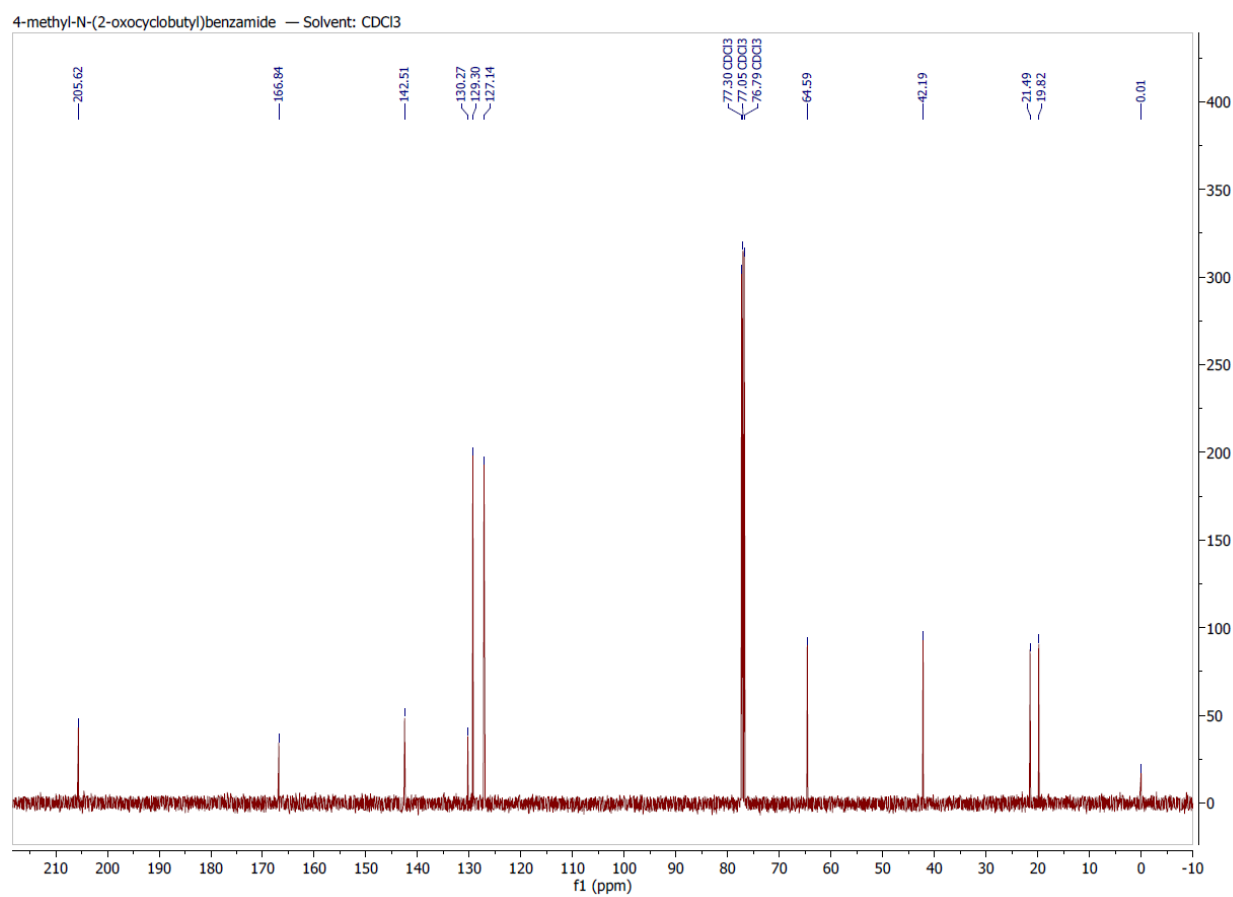
¹³C spectrum of 2-methyl-N-(2-oxocyclobutyl)benzamide (**10k**).



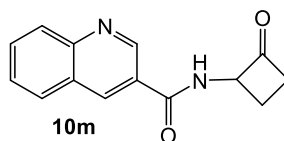
4-methyl-N-(2-oxocyclobutyl)benzamide — Solvent: CDCl₃



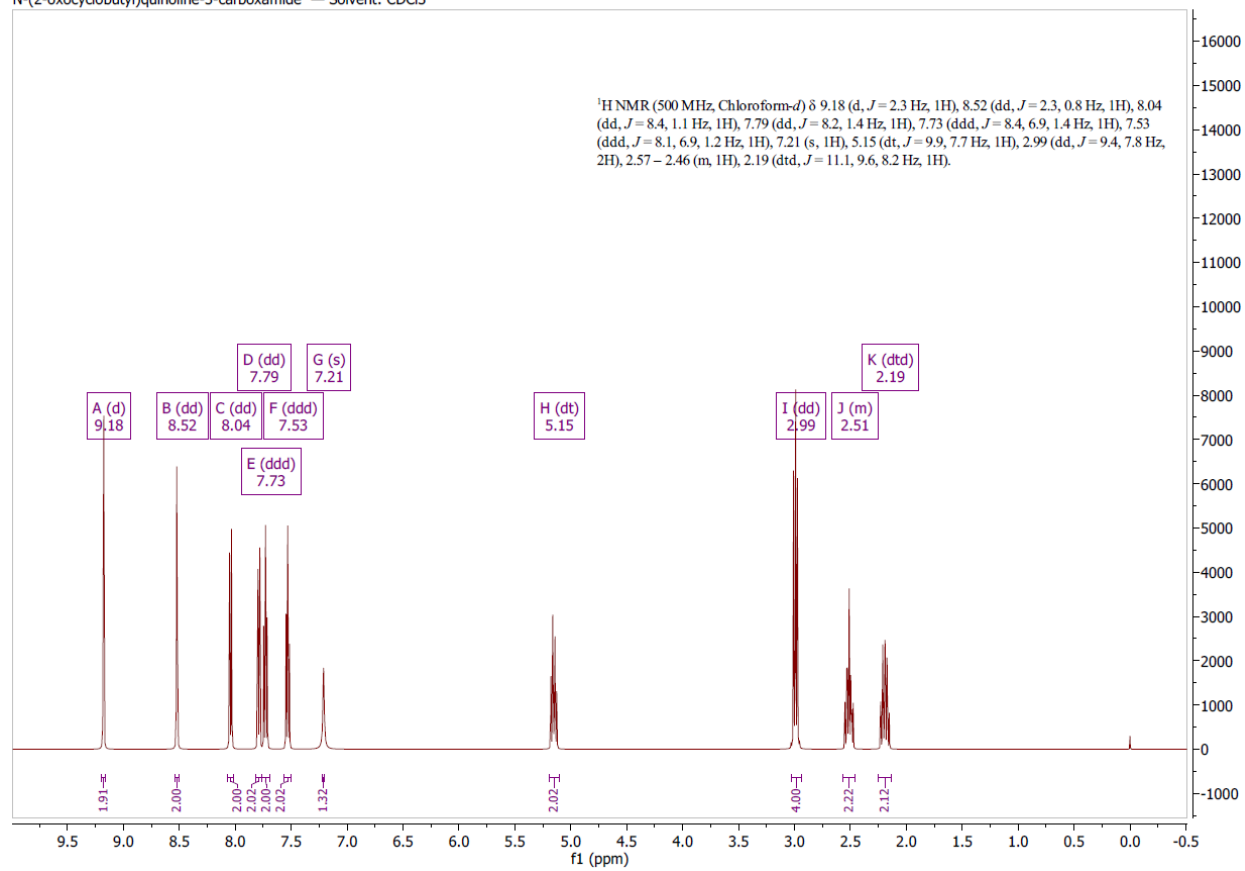
¹H spectrum of 4-methyl-N-(2-oxocyclobutyl)benzamide (**10I**).



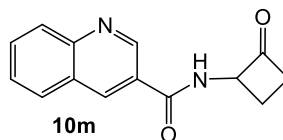
¹³C spectrum of 4-methyl-*N*-(2-oxocyclobutyl)benzamide (**101**).



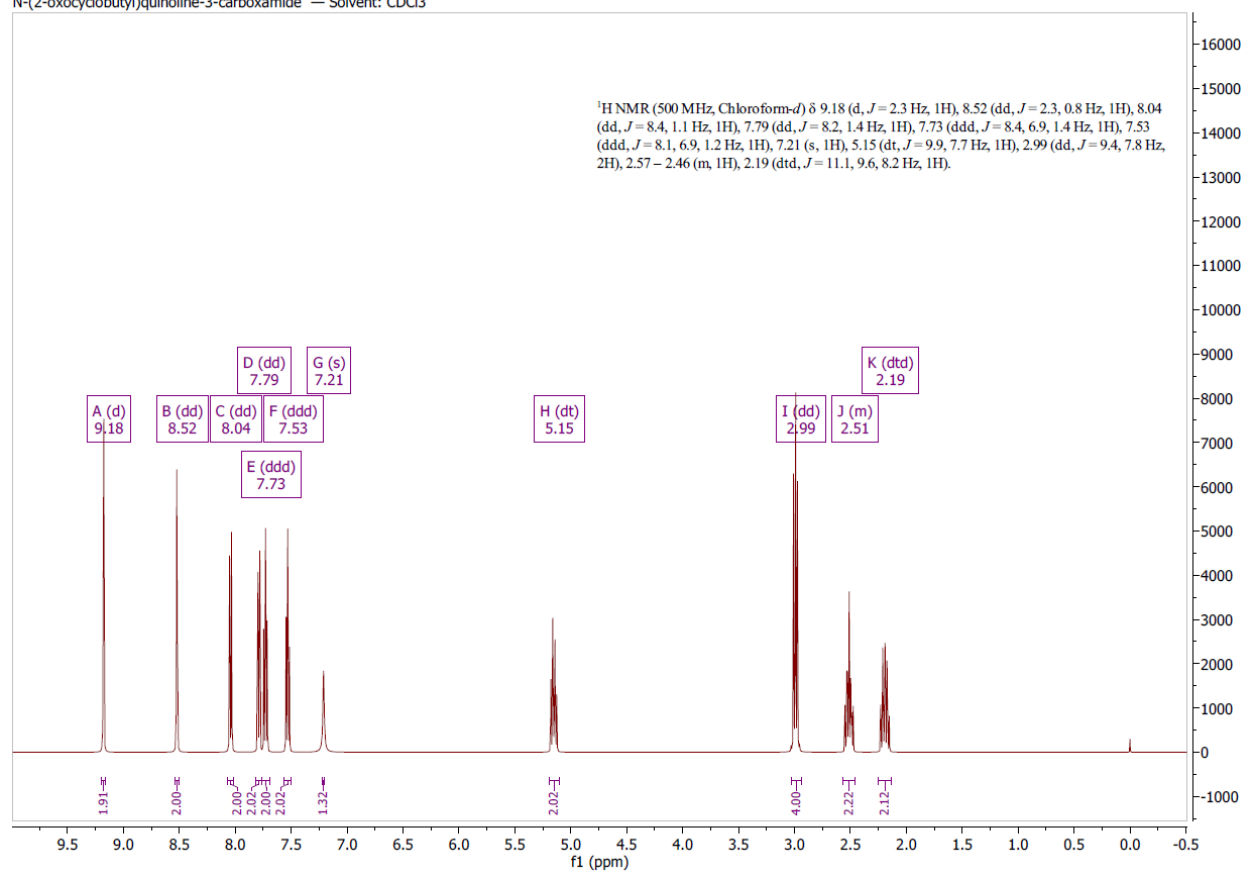
N-(2-oxocyclobutyl)quinoline-3-carboxamide — Solvent: CDCl₃



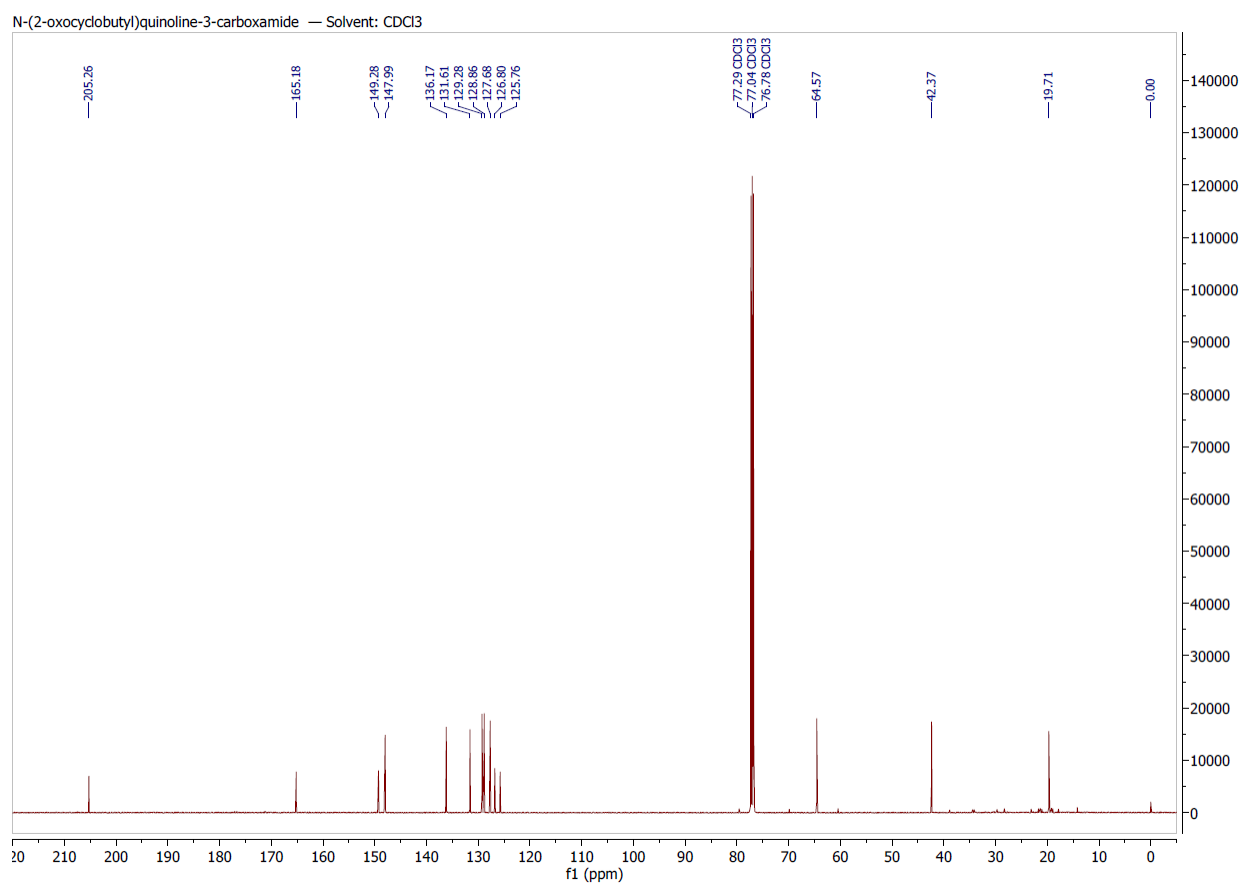
¹H spectrum of *N*-(2-oxocyclobutyl)quinoline-3-carboxamide (**10m**).



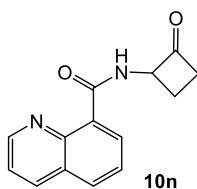
N-(2-oxocyclobutyl)quinoline-3-carboxamide — Solvent: CDCl₃



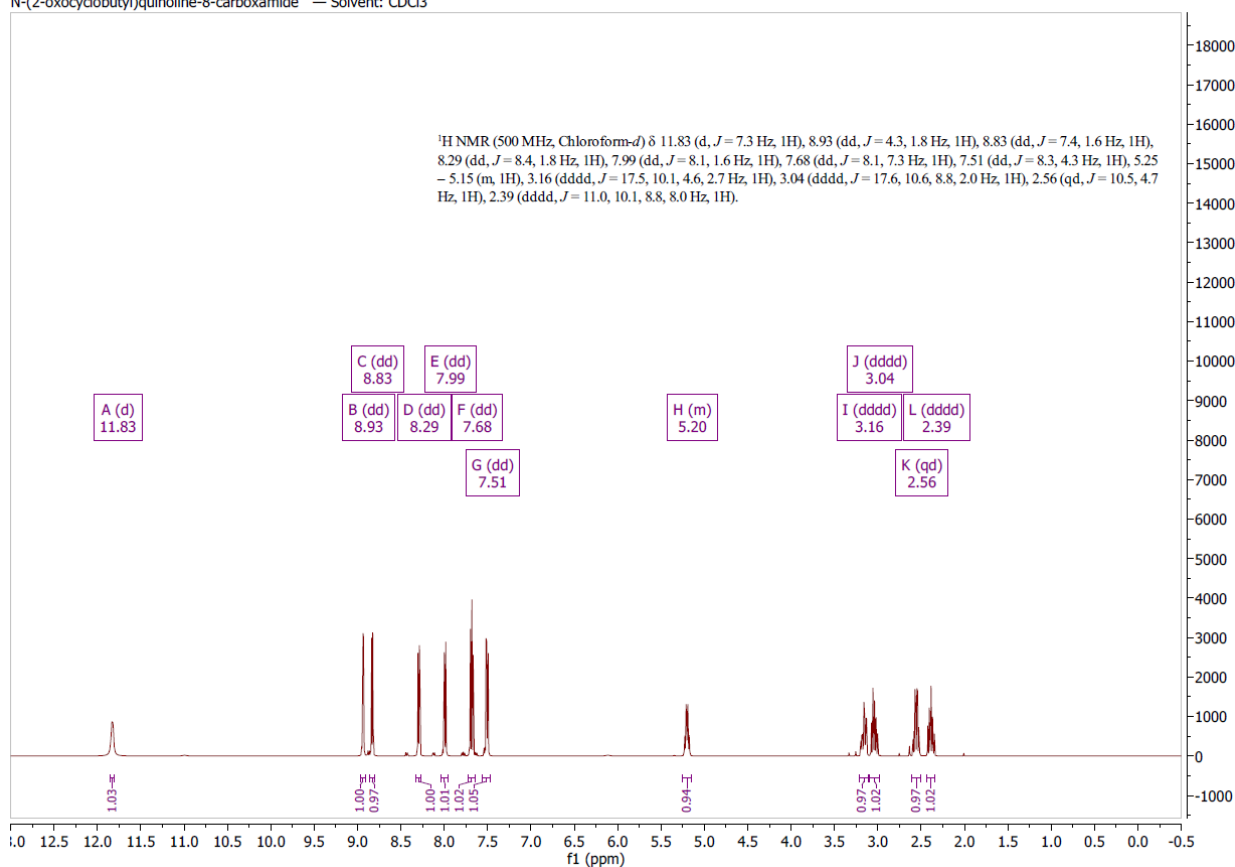
¹H spectrum of *N*-(2-oxocyclobutyl)quinoline-3-carboxamide (**10m**).



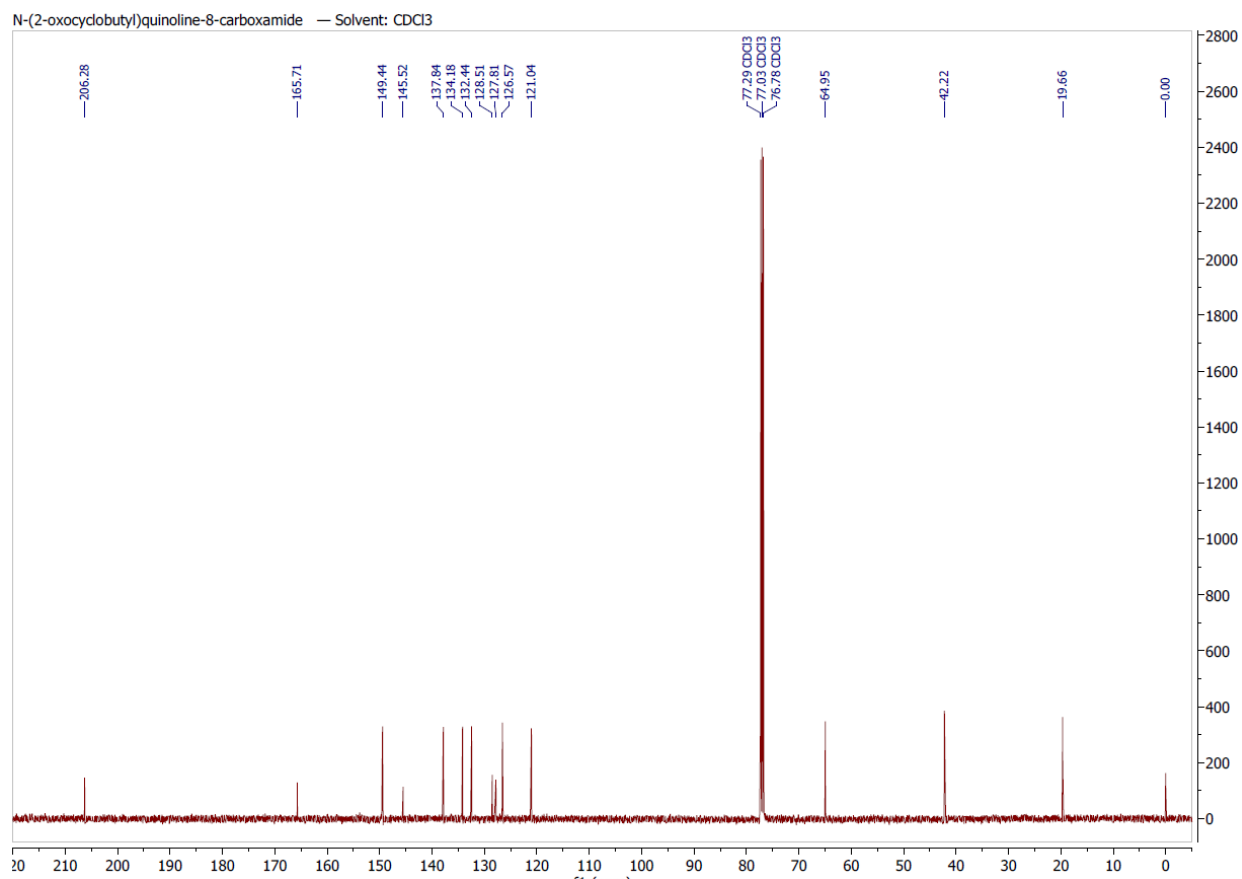
¹³C spectrum of *N*-(2-oxocyclobutyl)quinoline-3-carboxamide (**10m**).



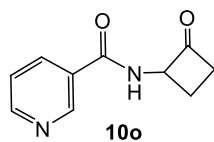
N-(2-oxocyclobutyl)quinoline-8-carboxamide — Solvent: CDCl₃



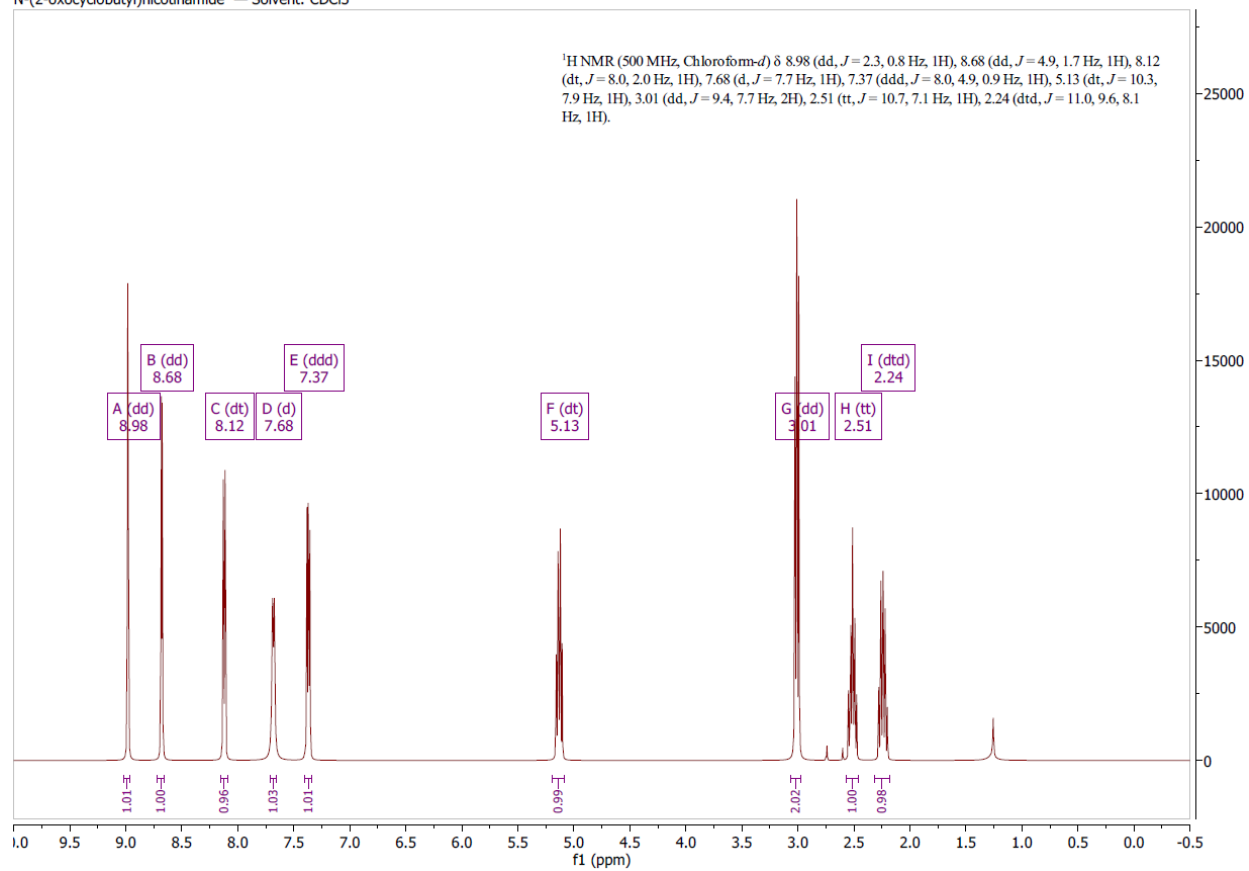
¹H spectrum of *N*-(2-oxocyclobutyl)quinoline-8-carboxamide (**10n**).



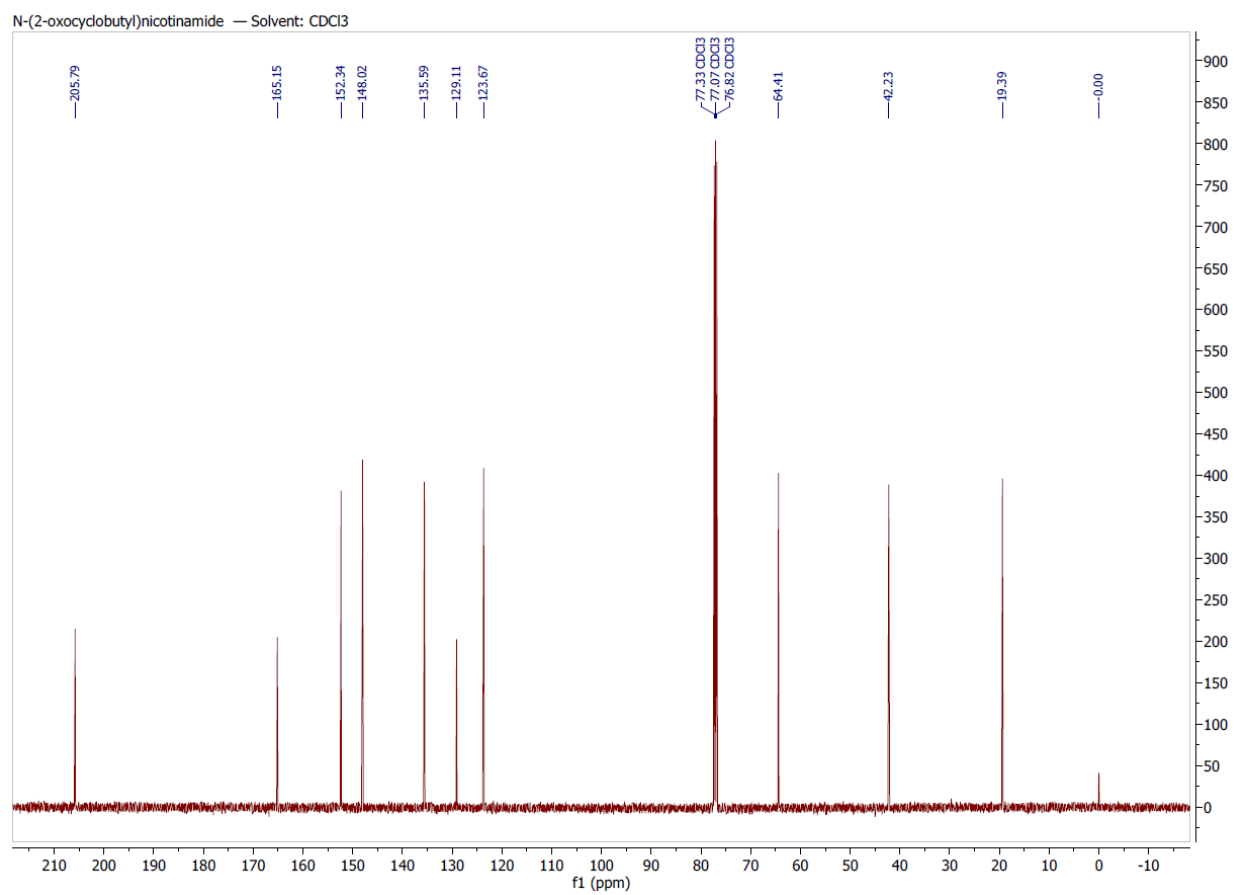
¹³C spectrum of *N*-(2-oxocyclobutyl)quinoline-8-carboxamide (**10n**).



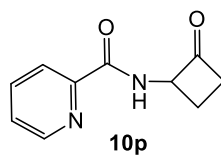
N-(2-oxocyclobutyl)nicotinamide — Solvent: CDCl₃



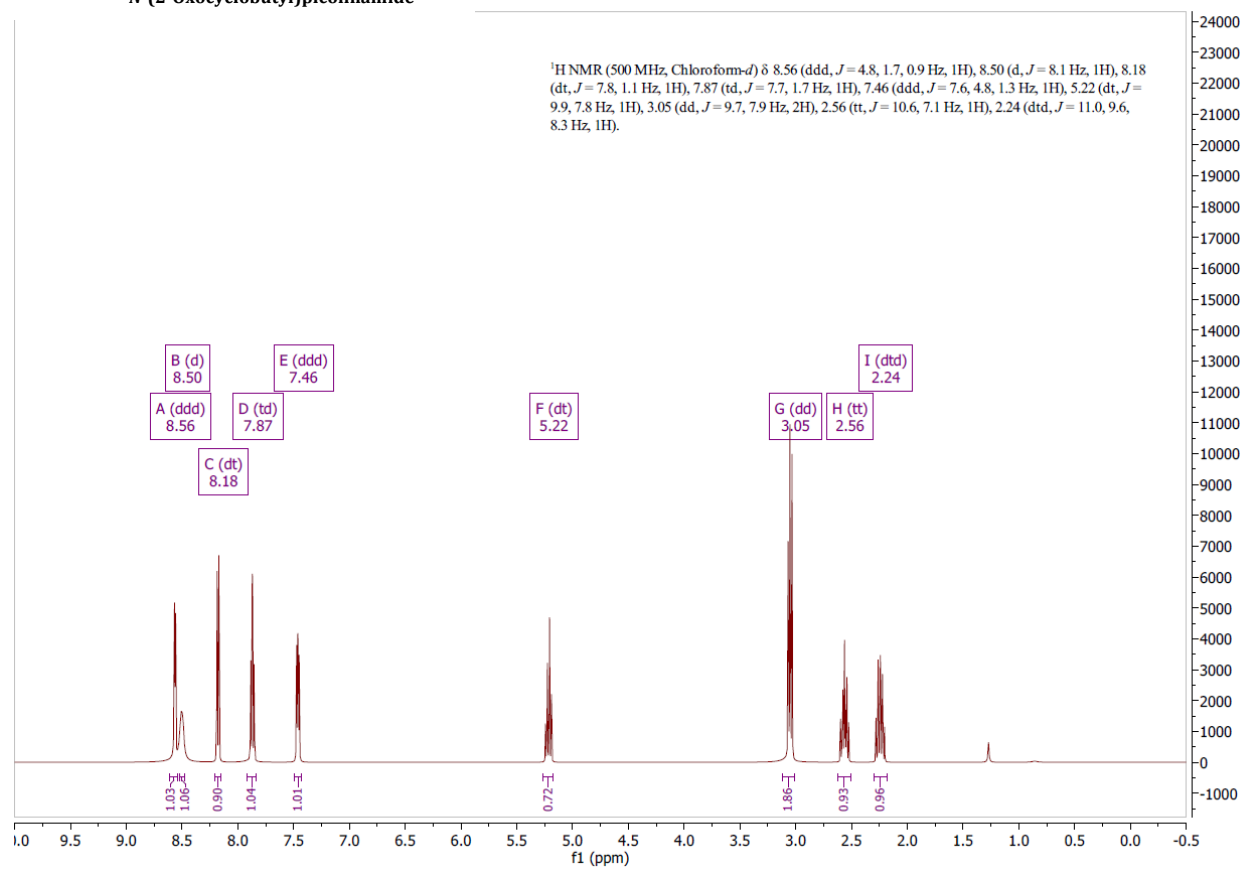
¹H spectrum of *N*-(2-oxocyclobutyl)nicotinamide (**10o**).



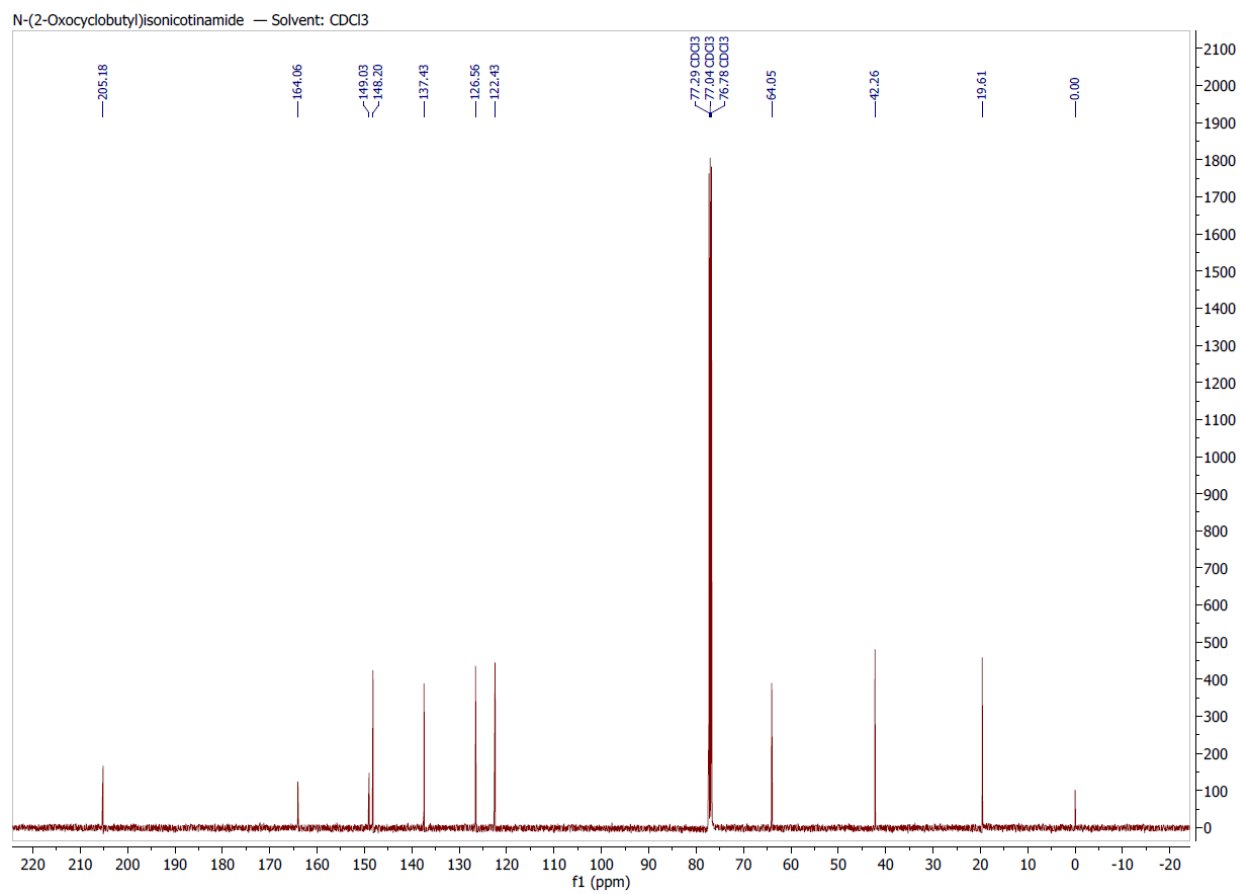
¹³C spectrum of *N*-(2-oxocyclobutyl)nicotinamide (**10o**).



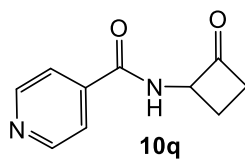
N-(2-Oxocyclobutyl)picolinamide -



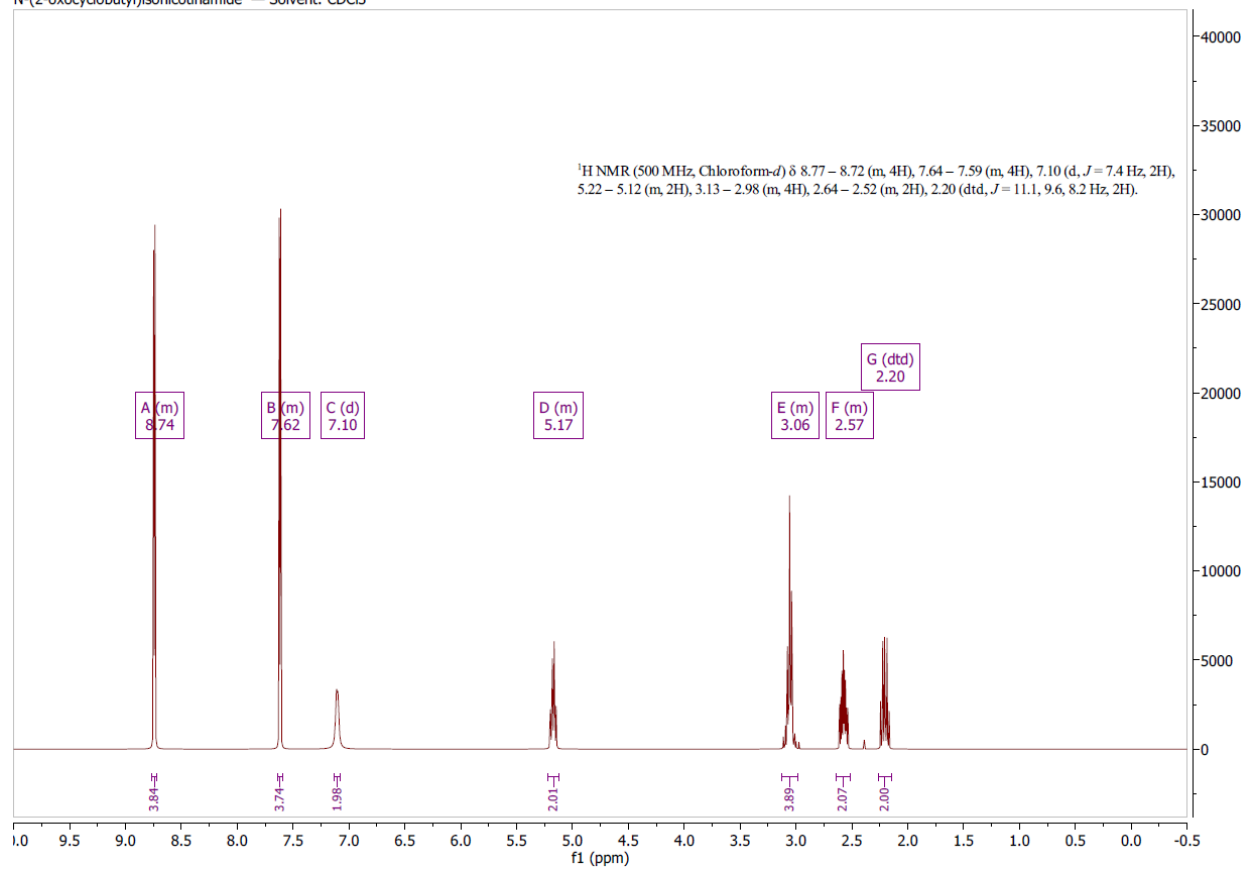
¹H spectrum of *N*-(2-oxocyclobutyl)picolinamide (**10p**).



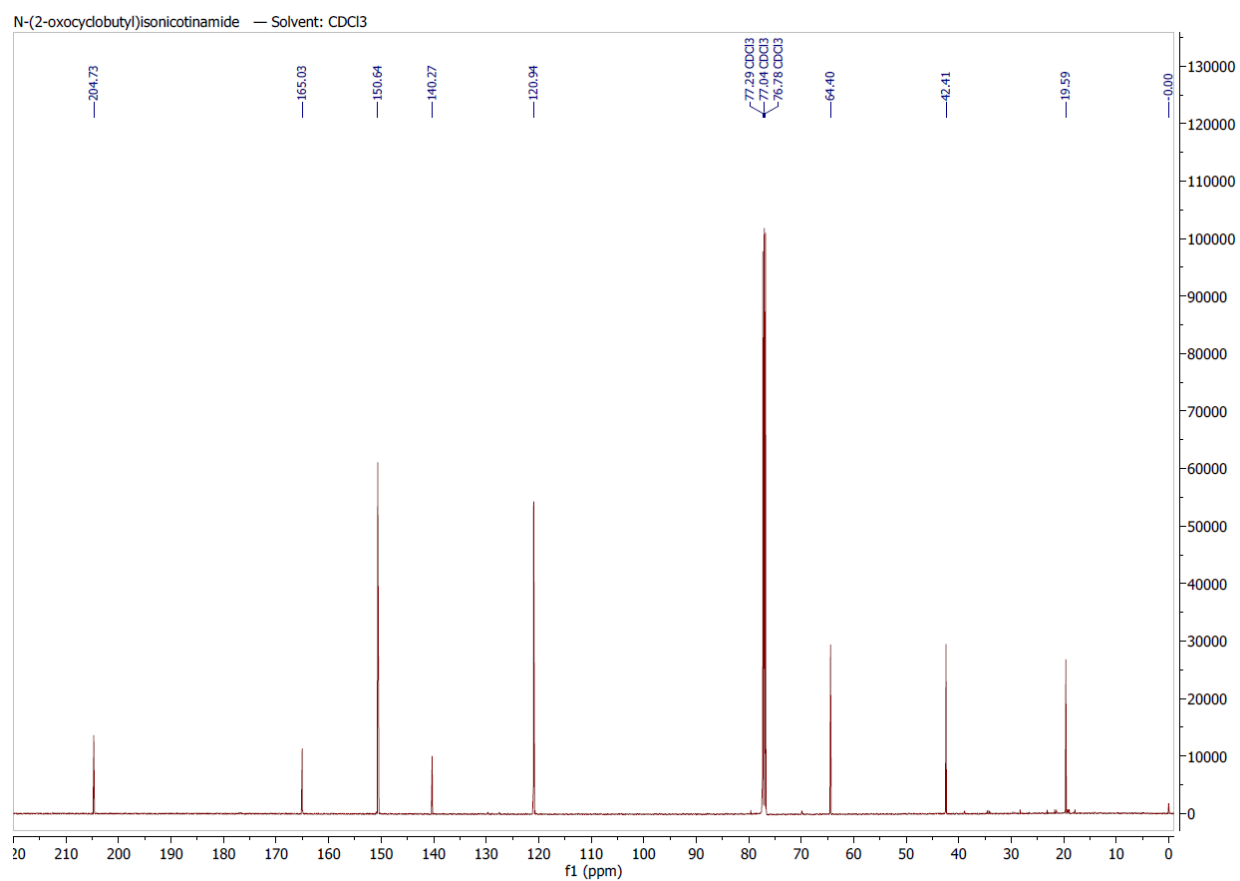
¹³C spectrum of *N*-(2-oxocyclobutyl)picolinamide (**10p**).



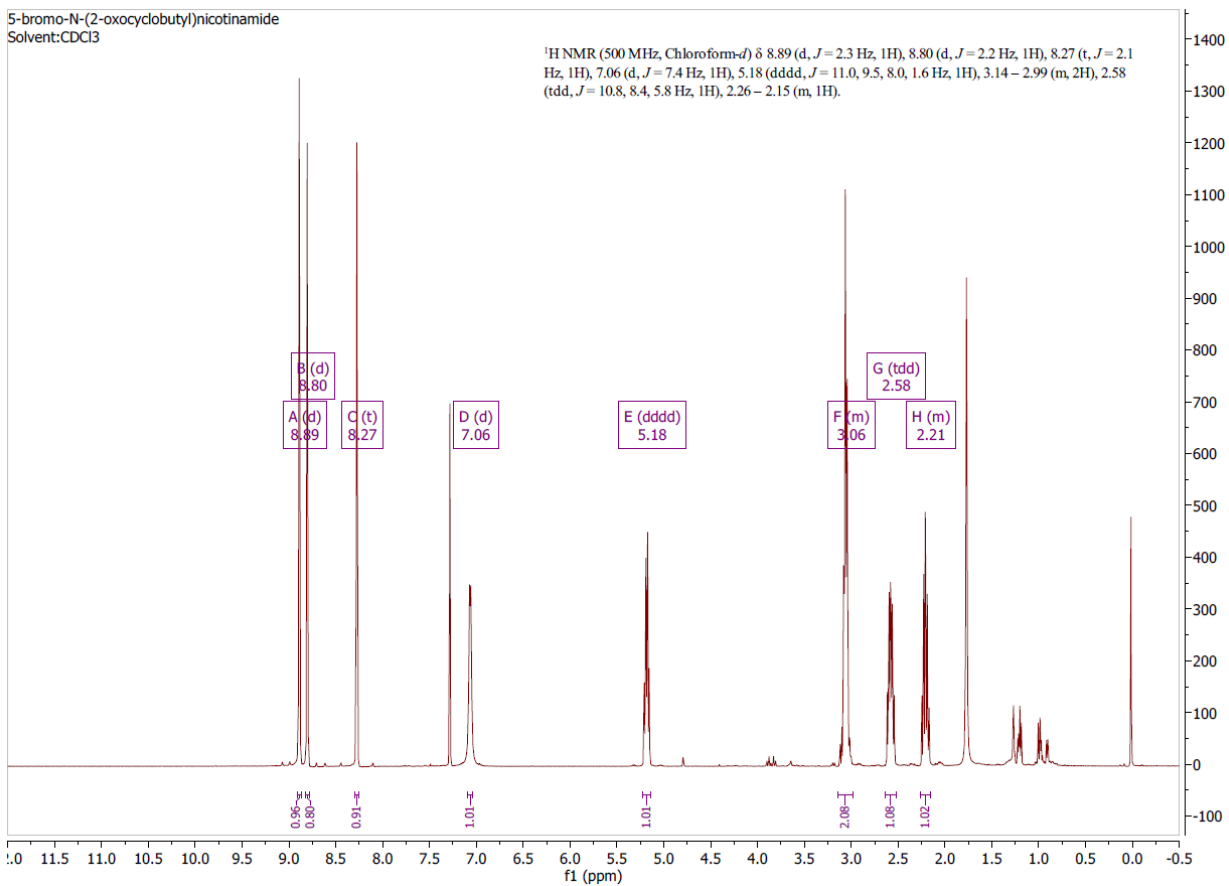
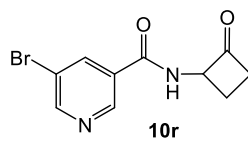
N-(2-oxocyclobutyl)isonicotinamide — Solvent: CDCl₃



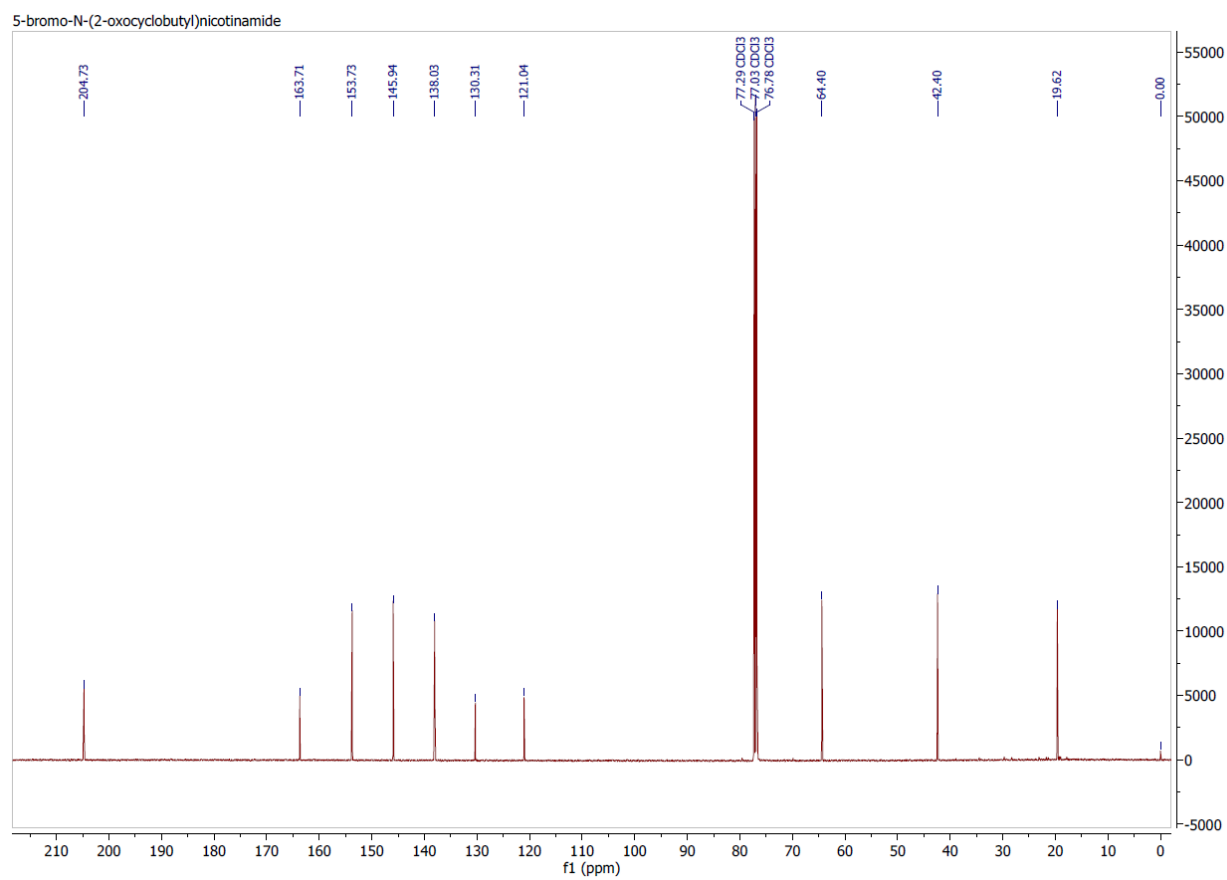
¹H spectrum of *N*-(2-oxocyclobutyl)isonicotinamide (**10q**).



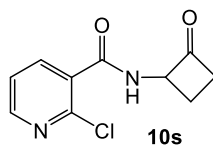
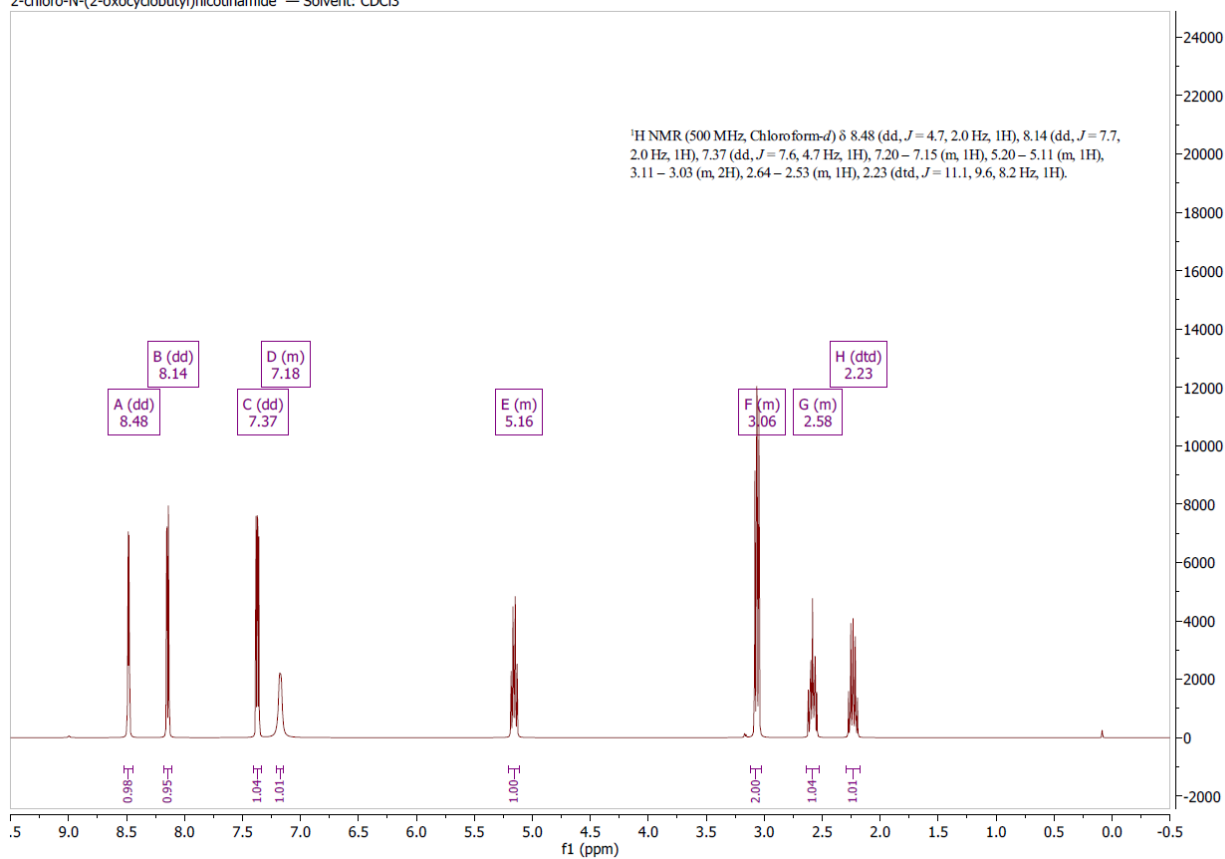
¹³C spectrum of *N*-(2-oxocyclobutyl)isonicotinamide (**10q**).

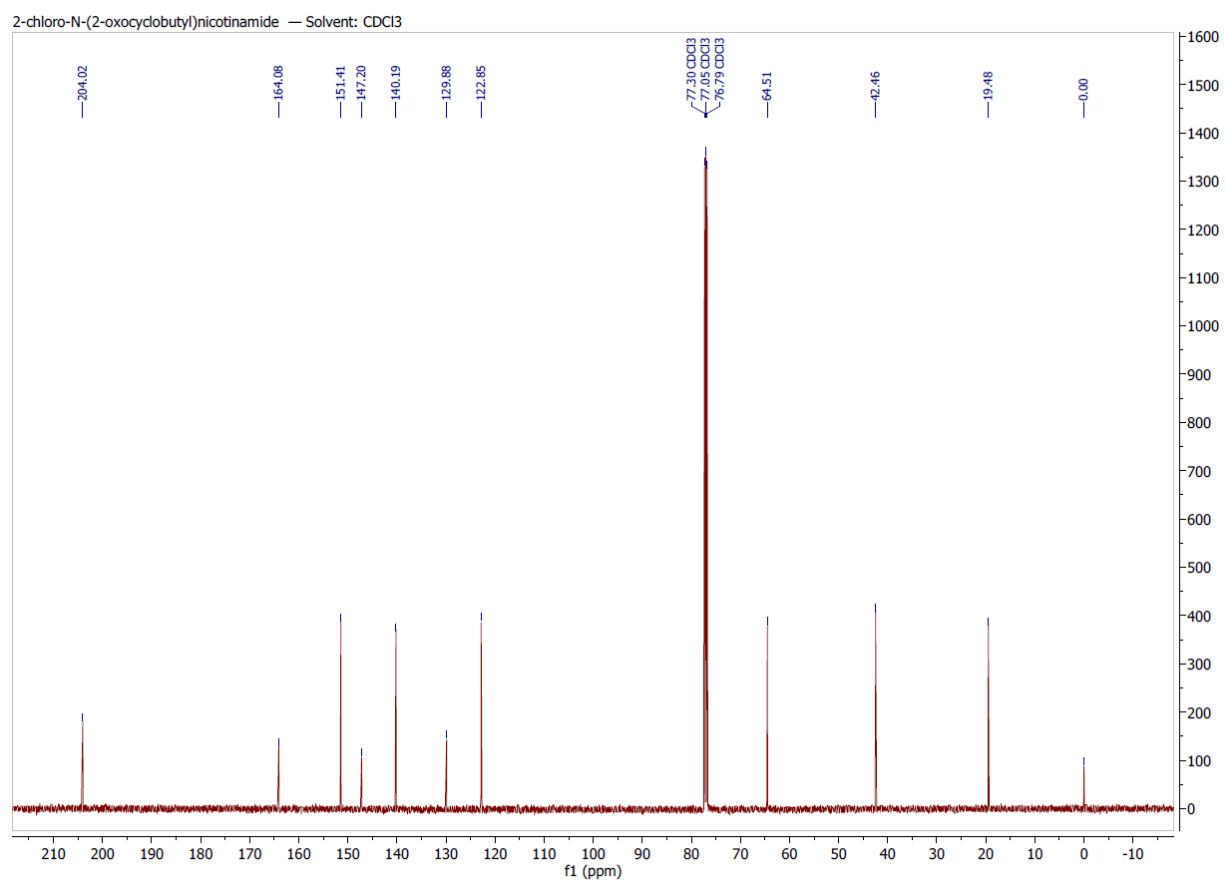


¹H spectrum of 5-bromo-N-(2-oxocyclobutyl)nicotinamide (**10r**).

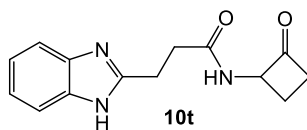


^{13}C spectrum of 5-bromo-N-(2-oxocyclobutyl)nicotinamide (**10r**).

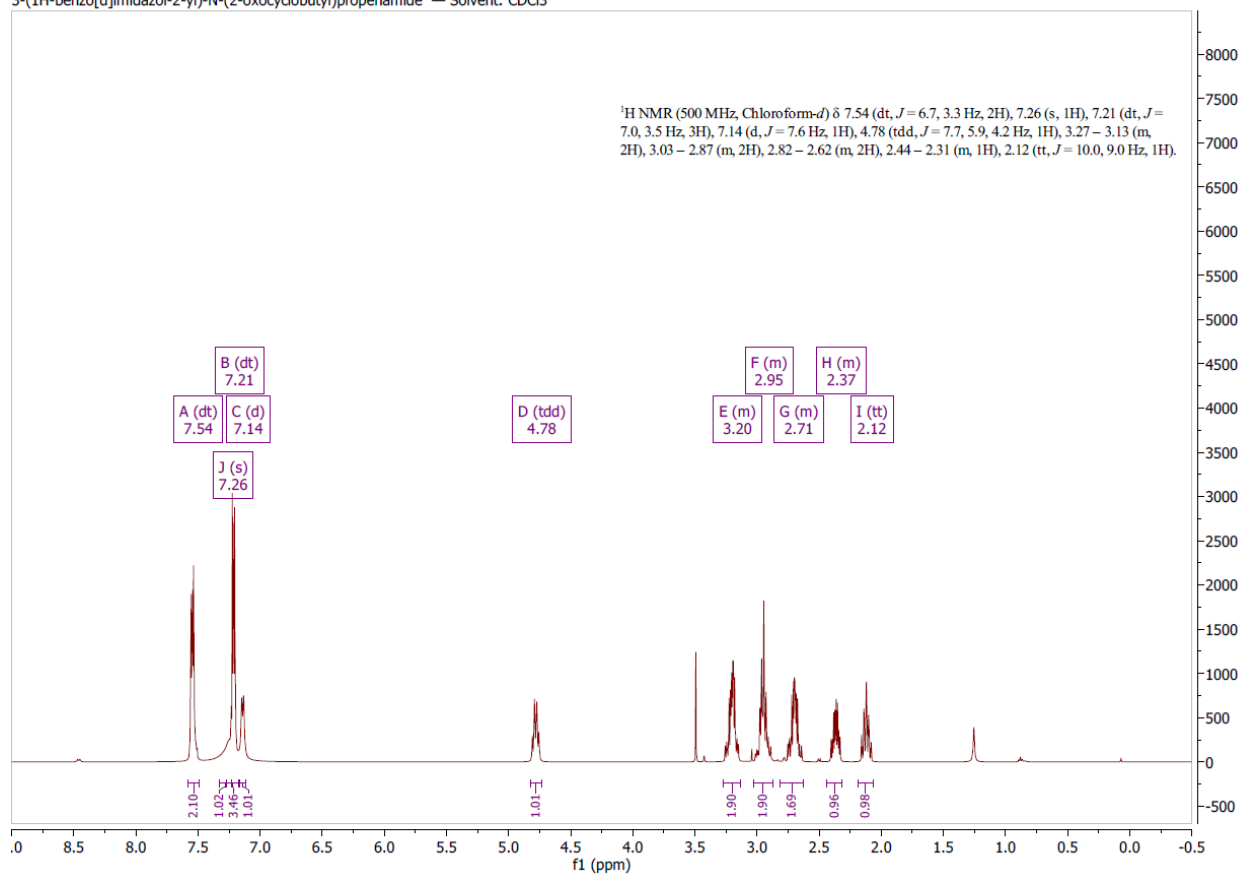
2-chloro-N-(2-oxocyclobutyl)nicotinamide — Solvent: CDCl₃¹H spectrum of 2-chloro-*N*-(2-oxocyclobutyl)nicotinamide (**10s**).



¹³C spectrum of 2-chloro-N-(2-oxocyclobutyl)nicotinamide (**10s**).

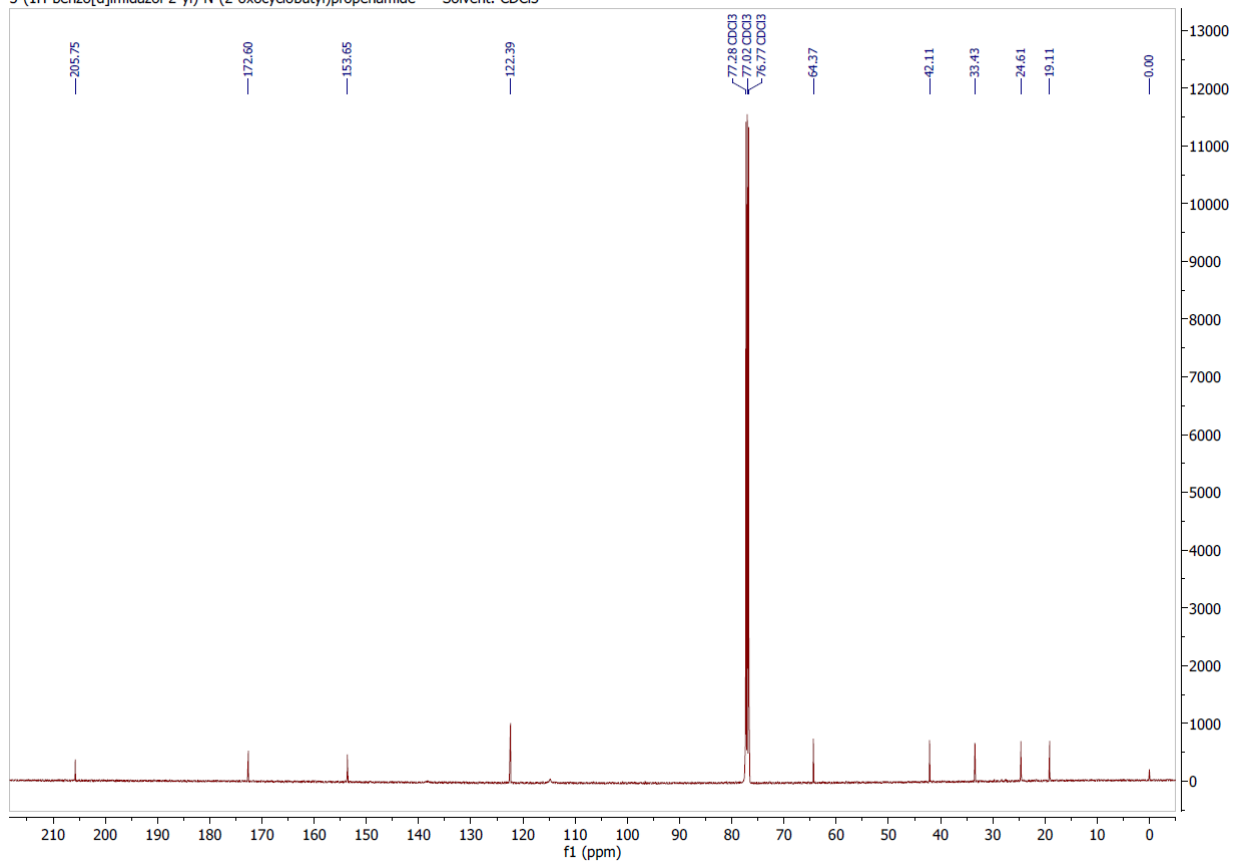


3-(1H-benzo[d]imidazol-2-yl)-N-(2-oxocyclobutyl)propanamide — Solvent: CDCl₃

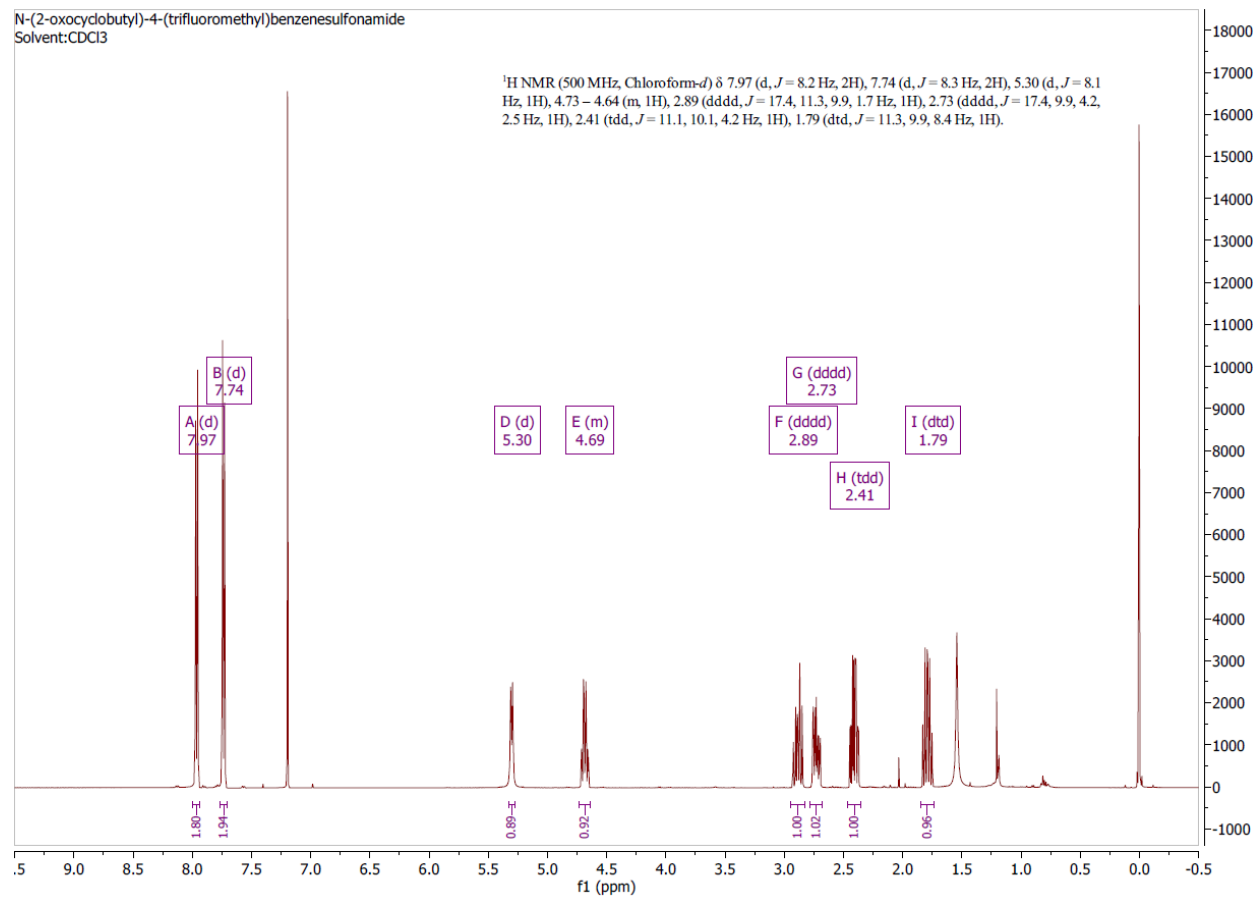
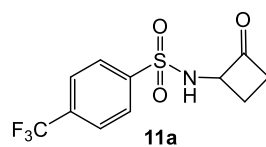


¹H spectrum of 3-(1H-benzo[d]imidazol-2-yl)-N-(2-oxocyclobutyl)propanamide (**10t**).

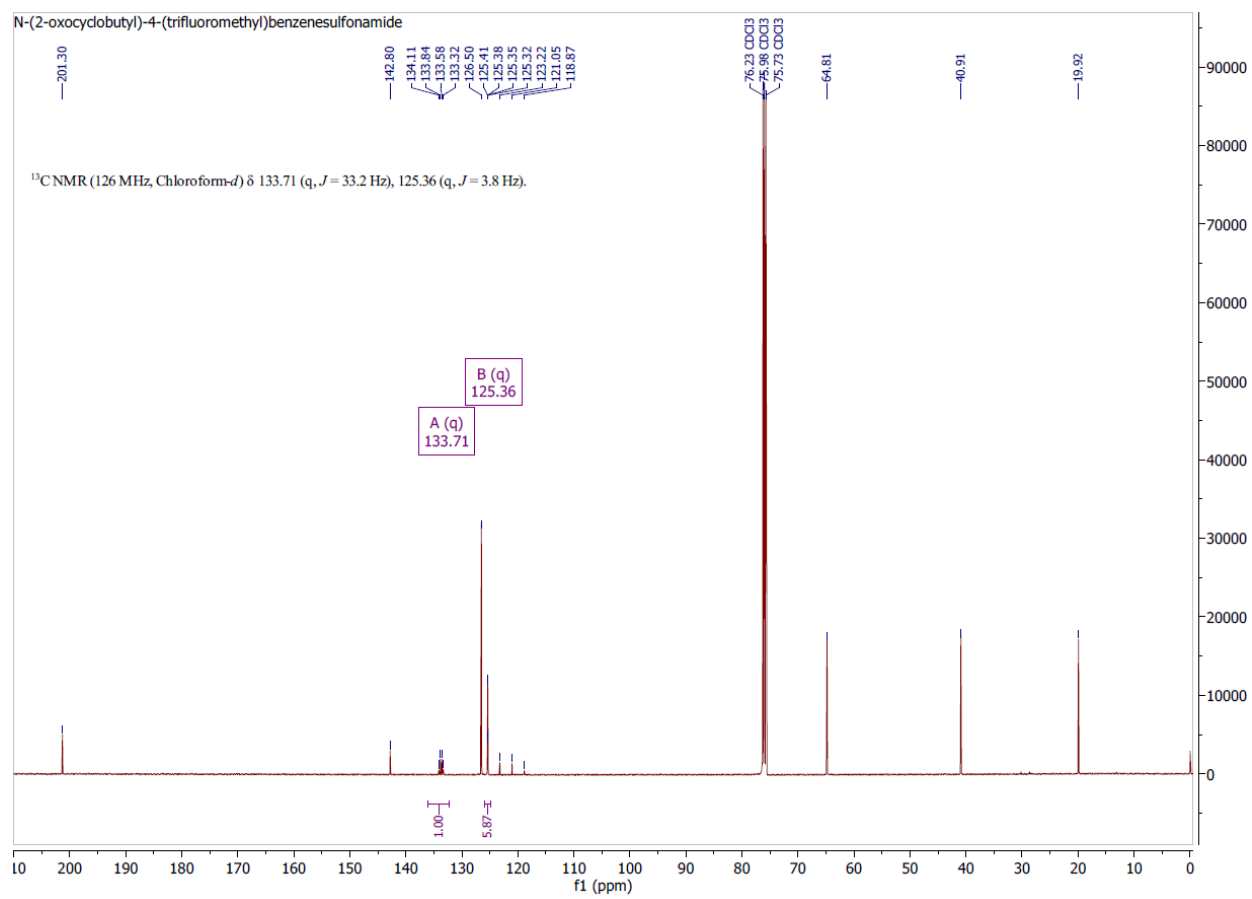
3-(1H-benzo[d]imidazol-2-yl)-N-(2-oxocyclobutyl)propanamide — Solvent: CDCl₃



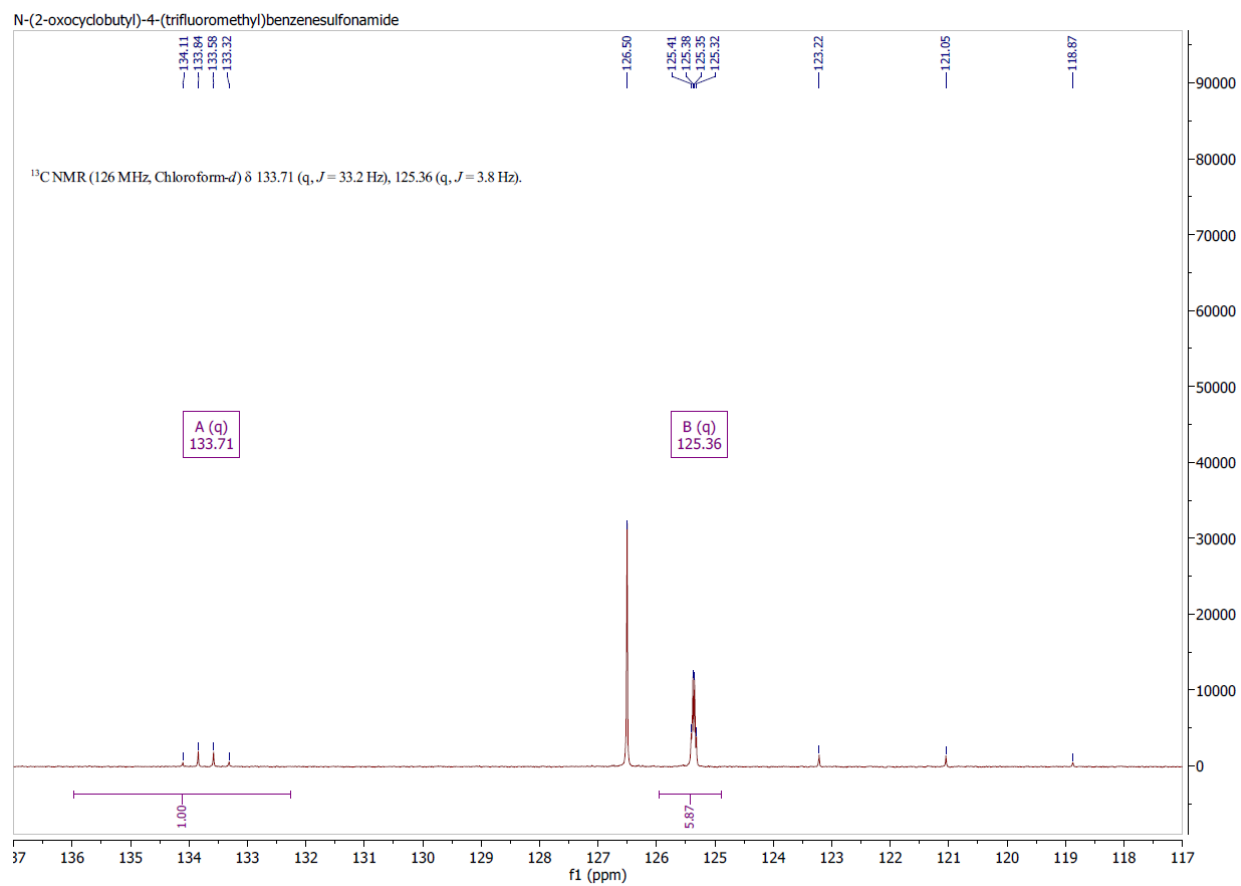
¹³C spectrum of 3-(1H-benzo[d]imidazol-2-yl)-N-(2-oxocyclobutyl)propanamide (**10t**).



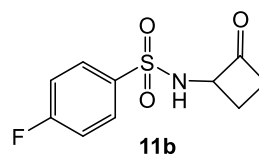
¹H spectrum of *N*-(2-oxocyclobutyl)-4-(trifluoromethyl)benzenesulfonamide (**11a**).



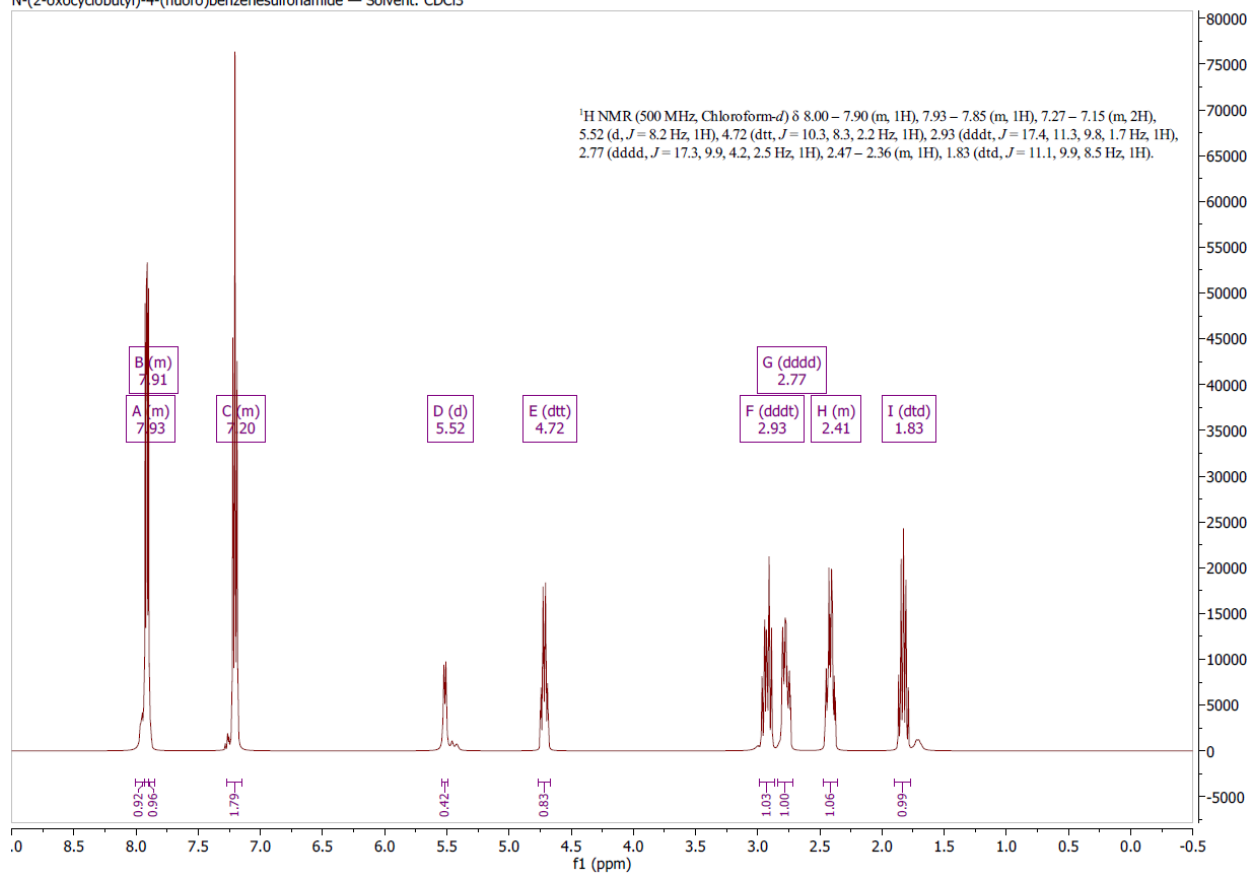
^{13}C spectrum of *N*-(2-oxocyclobutyl)-4-(trifluoromethyl)benzenesulfonamide (**11a**).



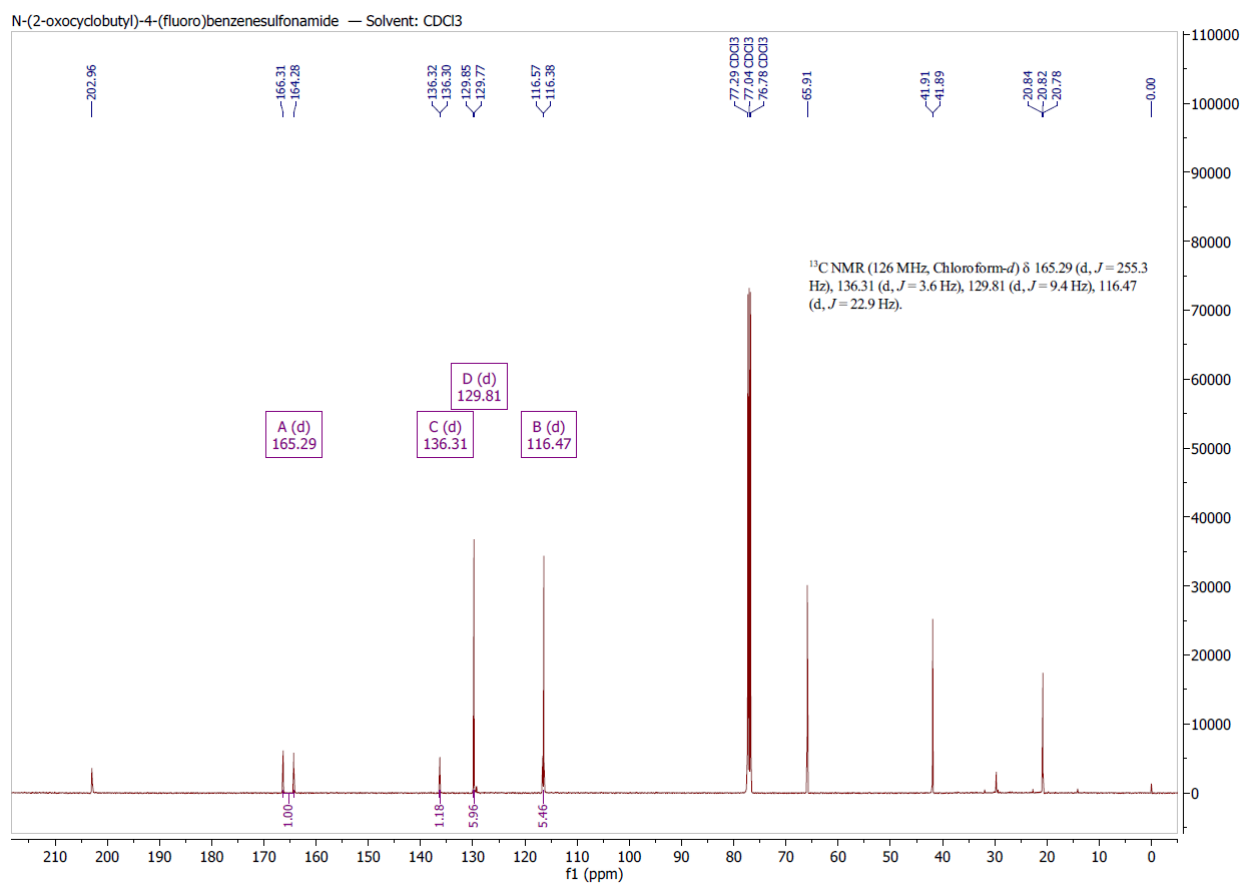
^{13}C spectrum of *N*-(2-oxocyclobutyl)-4-(trifluoromethyl)benzenesulfonamide (**11a**) indicating the ^{13}C 1, 2 and 3 bond splitting by ^{19}F .



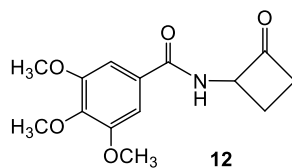
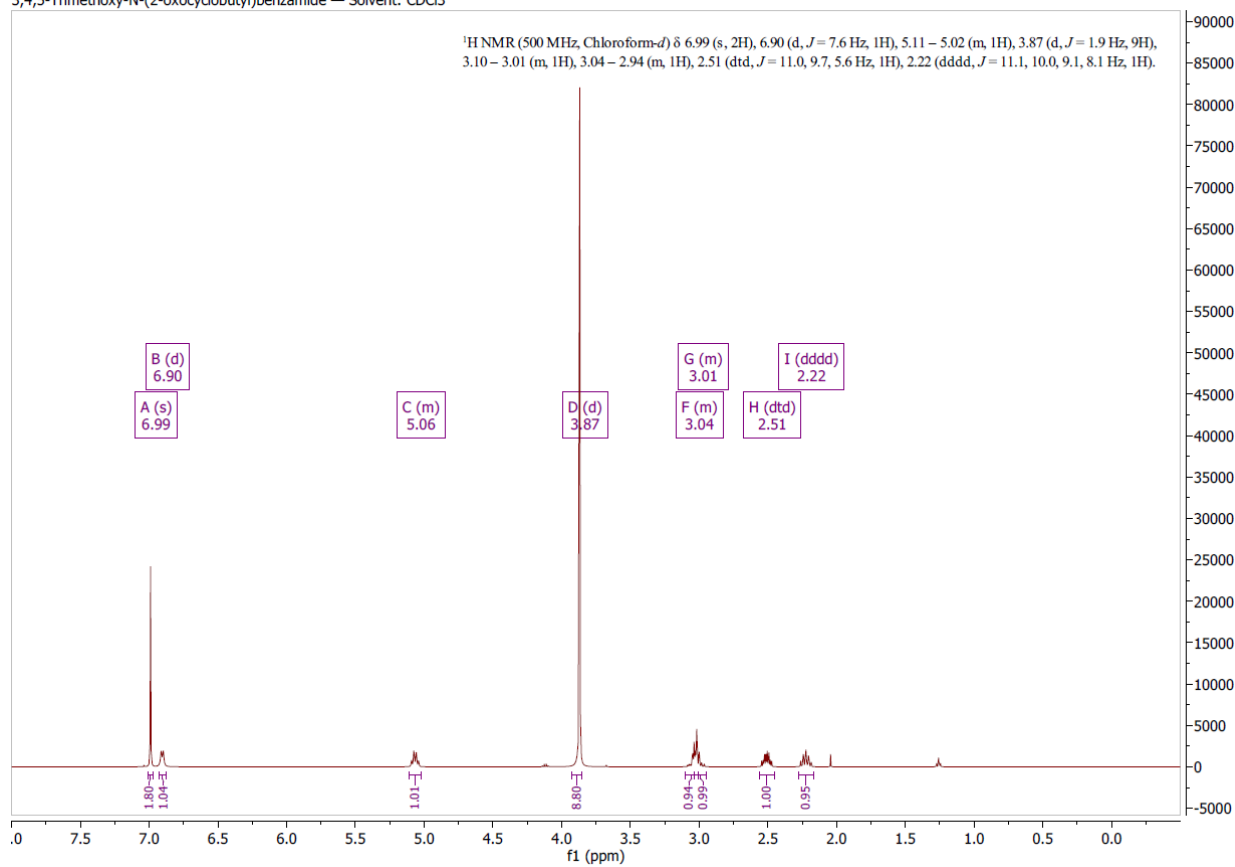
N-(2-oxocyclobutyl)-4-(fluoro)benzenesulfonamide — Solvent: CDCl₃

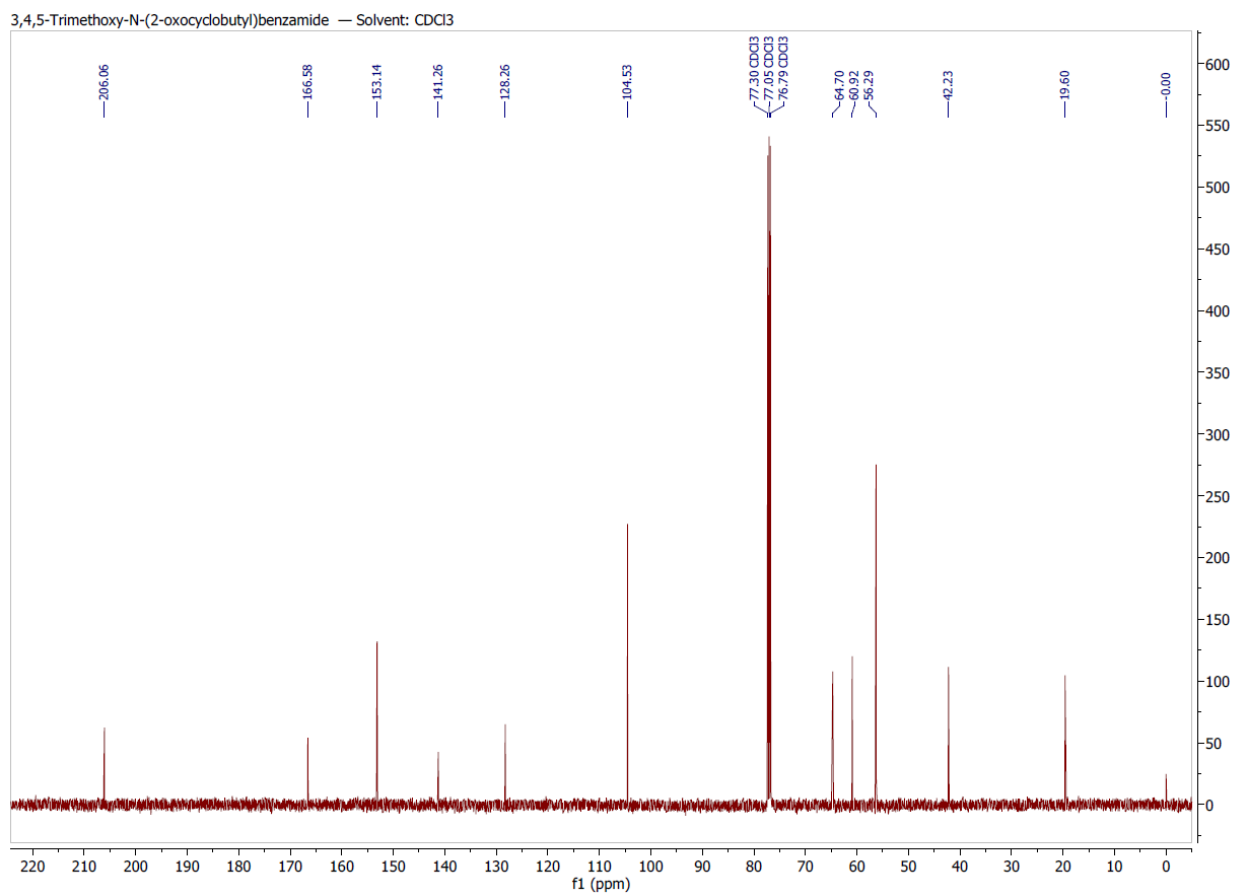


¹H spectrum of *N*-(2-oxocyclobutyl)-4-(fluoro)benzenesulfonamide (**11b**).

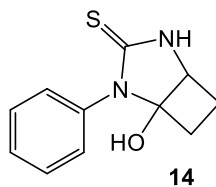
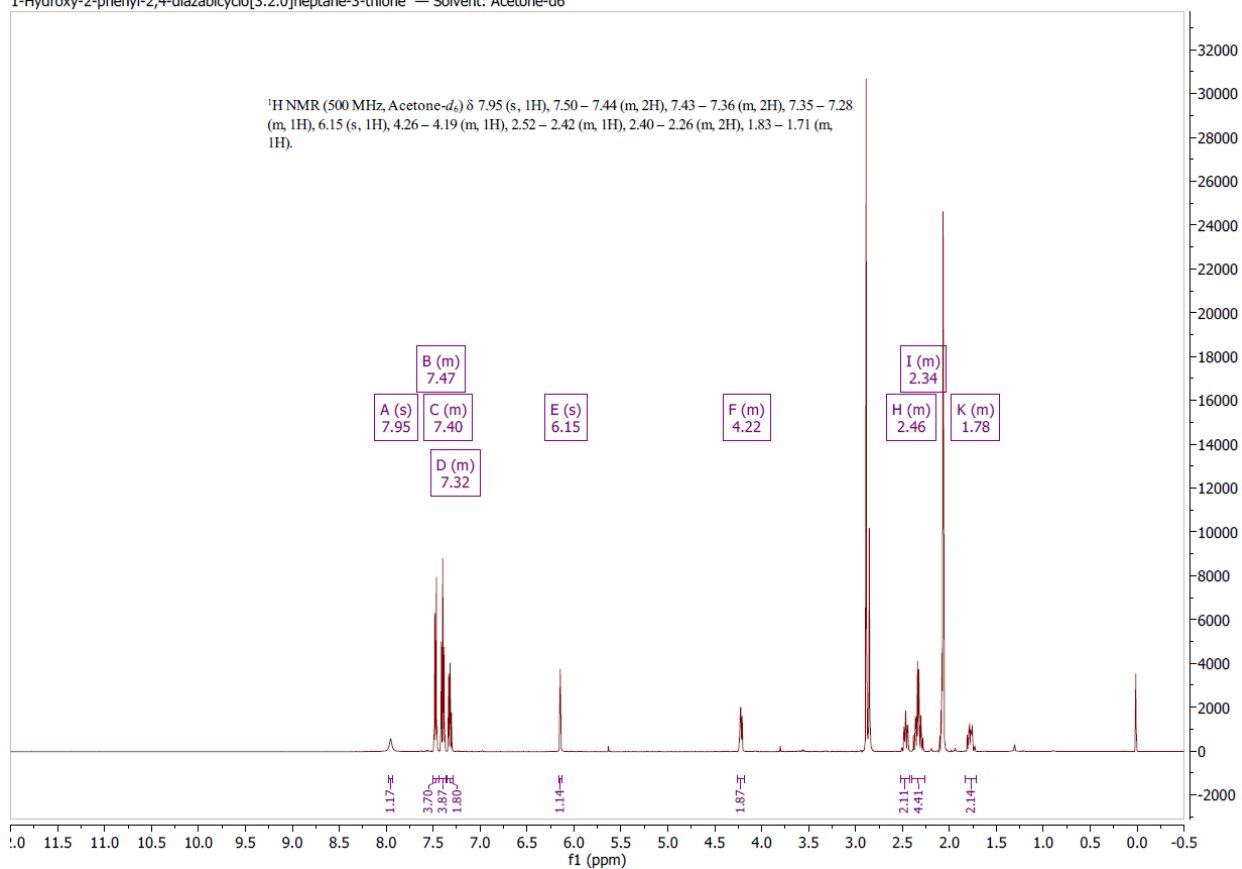


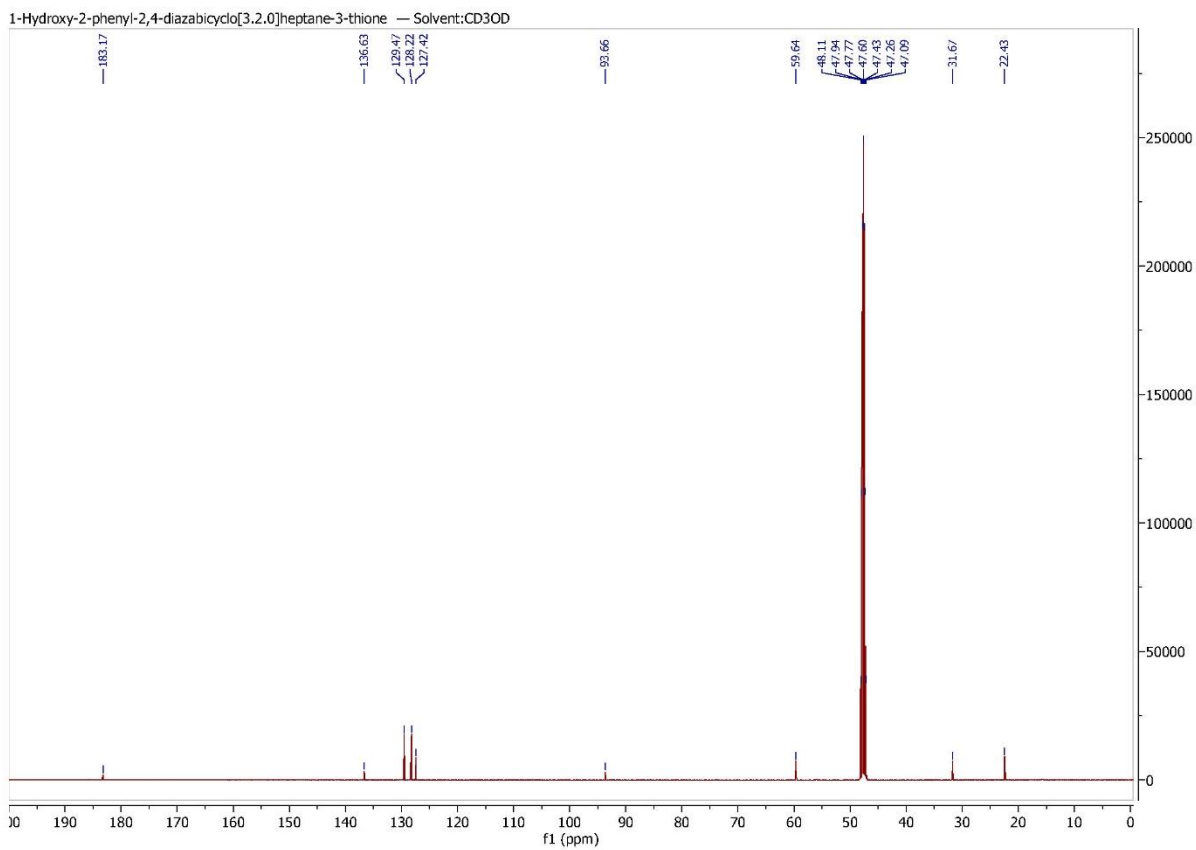
¹³C spectrum of *N*-(2-oxocyclobutyl)-4-(fluoro)benzenesulfonamide (**11b**).

3,4,5-Trimethoxy-N-(2-oxocyclobutyl)benzamide — Solvent: CDCl₃¹H spectrum of 3,4,5-trimethoxy-N-(2-oxocyclobutyl)benzamide (**12**).



¹³C spectrum of 3,4,5-trimethoxy-N-(2-oxocyclobutyl)benzamide (**12**).

1-Hydroxy-2-phenyl-2,4-diazabicyclo[3.2.0]heptane-3-thione — Solvent: Acetone- d_6  ^1H spectrum of 1-hydroxy-2-phenyl-2,4-diazabicyclo[3.2.0]heptane-3-thione (**14**).

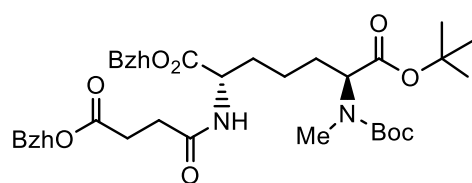


^{13}C spectrum of 1-hydroxy-2-phenyl-2,4-diazabicyclo[3.2.0]heptane-3-thione (**14**).

APPENDIX B

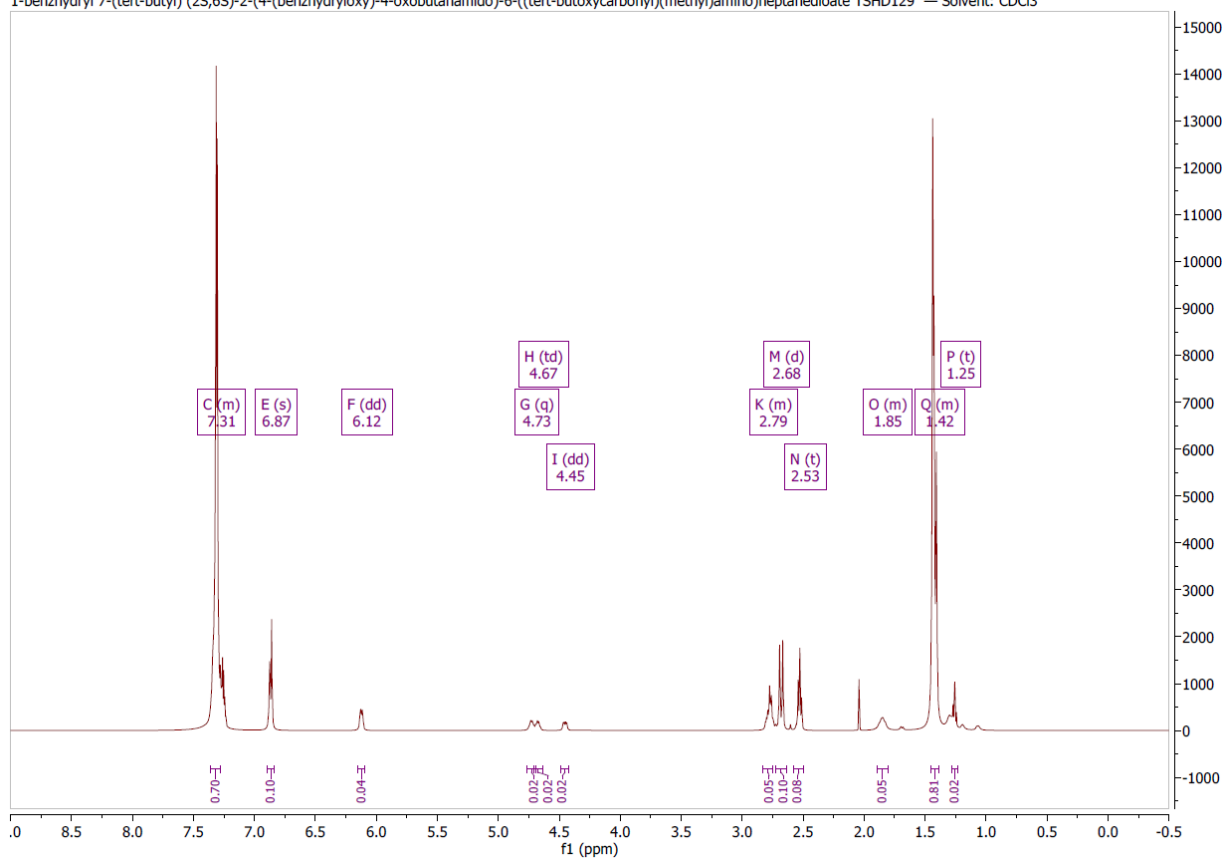
SUPPLEMENTAL DATA FOR CHAPTER THREE

NMR spectra of the compounds reported in chapter three.

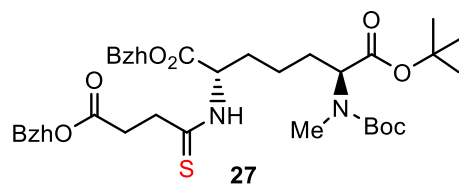


26

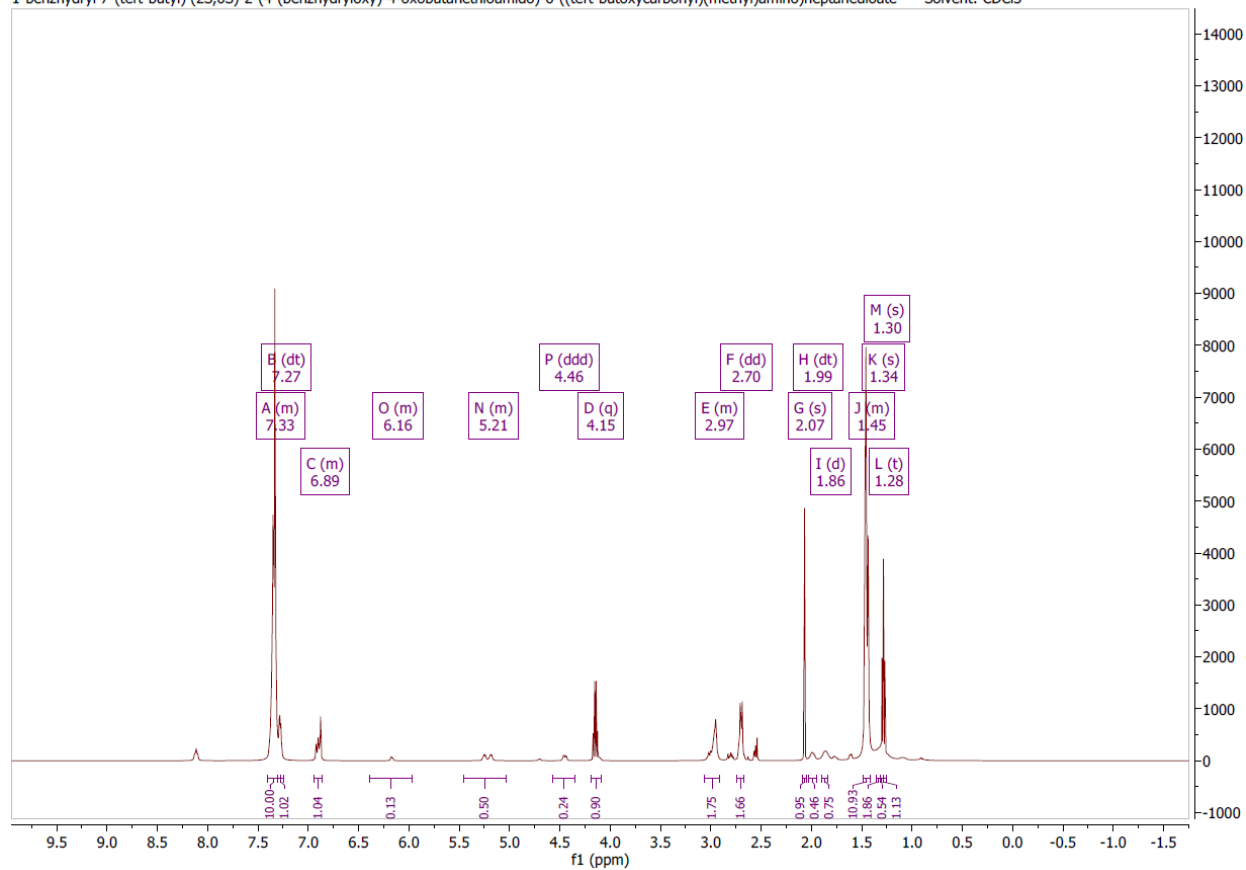
1-benzhydryl 7-(tert-butyl) (2S,6S)-2-(4-(benzhydryloxy)-4-oxobutanamido)-6-((tert-butoxycarbonyl)(methyl)amino)heptanedioate TSHD129 — Solvent: CDCl₃



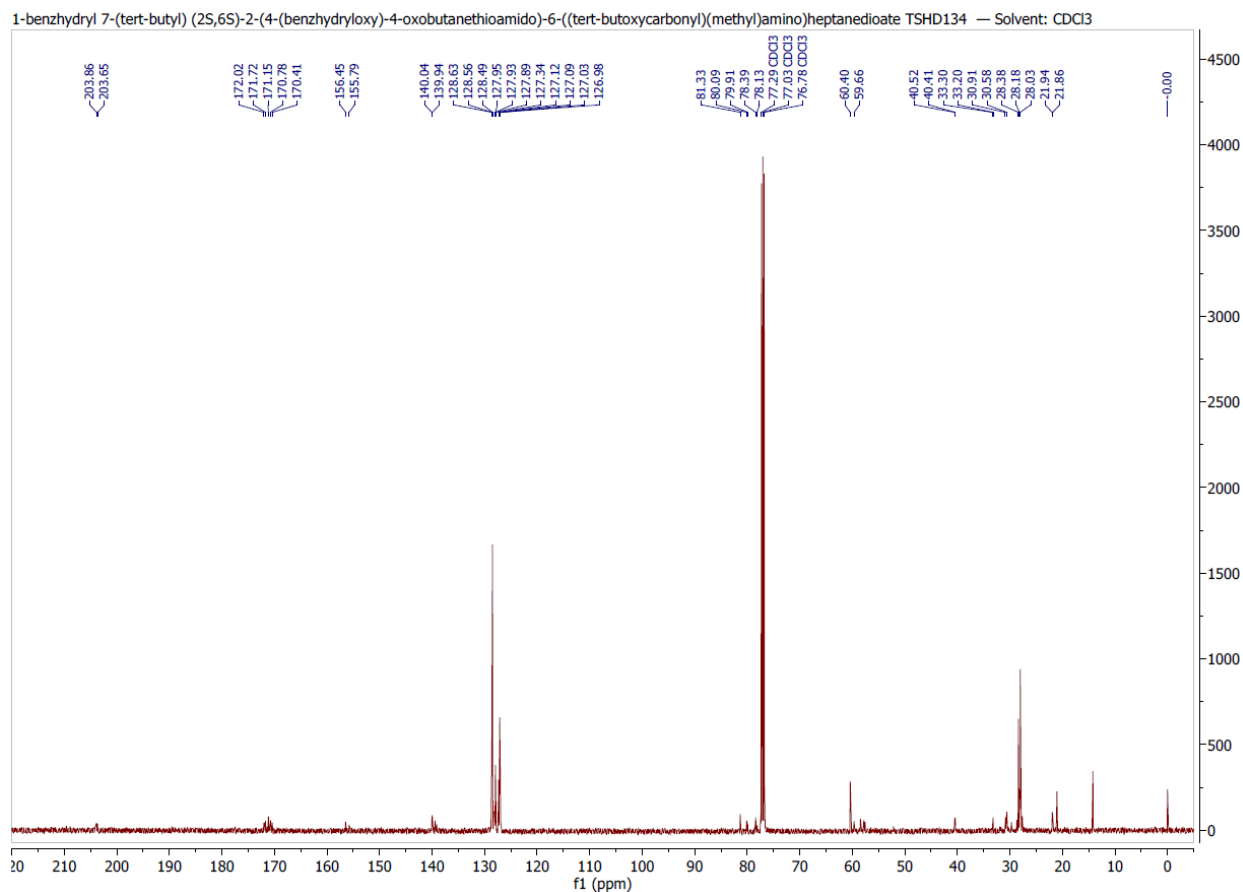
¹H NMR of *N*⁶-methyl-*L,L*-SDAP thioamide analog: 1-benzhydryl 7-(*tert*-butyl) (2*S*,6*S*)-2-(4-(benzhydryloxy)-4-oxobutanamido)-6-((*tert*butoxycarbonyl)(methyl)amino)heptanedioate (**26**).



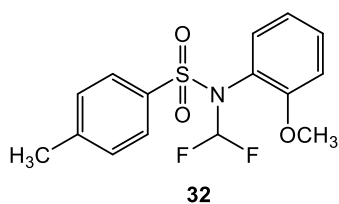
1-benzhydryl 7-(tert-butyl) (2S,6S)-2-(4-(benzhydryloxy)-4-oxobutanethioamido)-6-((tert-butoxycarbonyl)(methyl)amino)heptanedioate — Solvent: CDCl₃



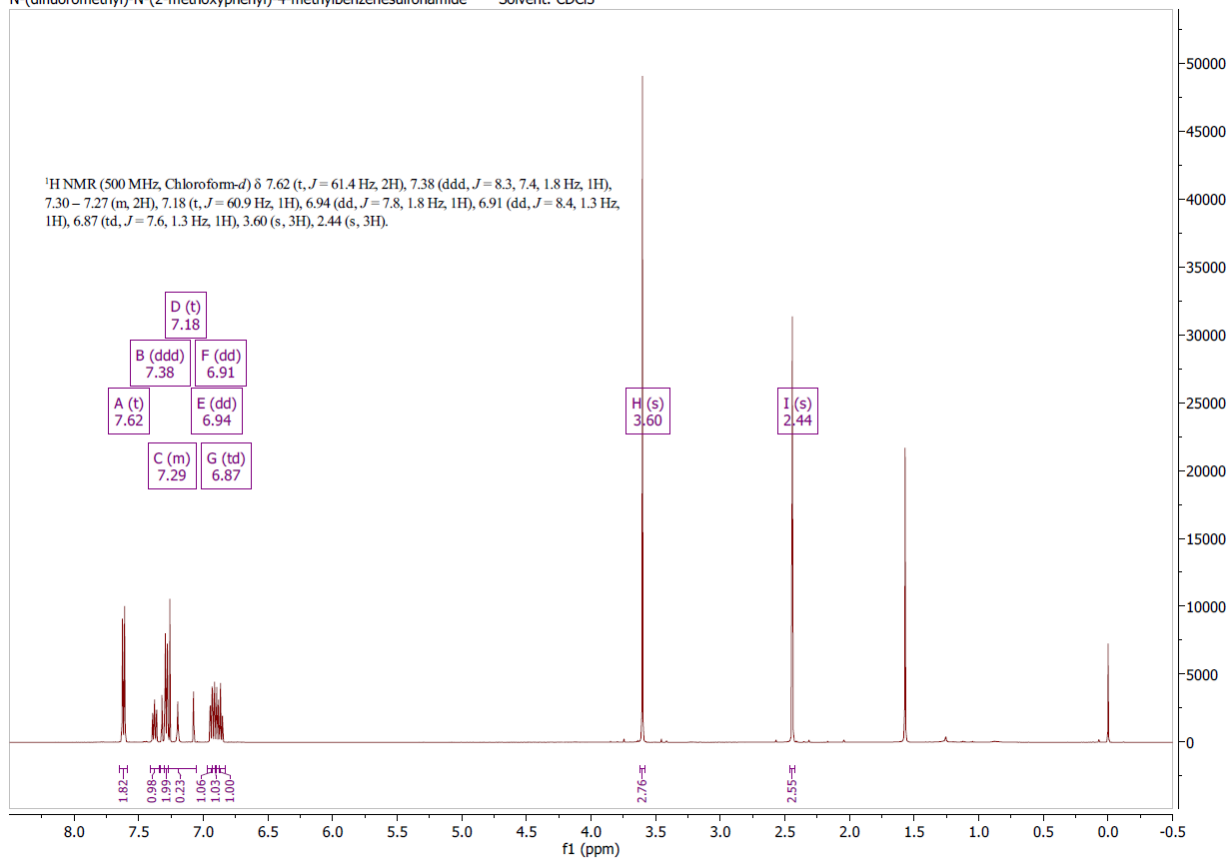
¹H NMR of 1-benzhydryl 7-(*tert*-butyl) (2S,6S)-2-(4-(benzhydryloxy)-4-oxobutanethioamido)-6-((*tert*-butoxycarbonyl)(methyl)amino)heptanedioate (**27**).



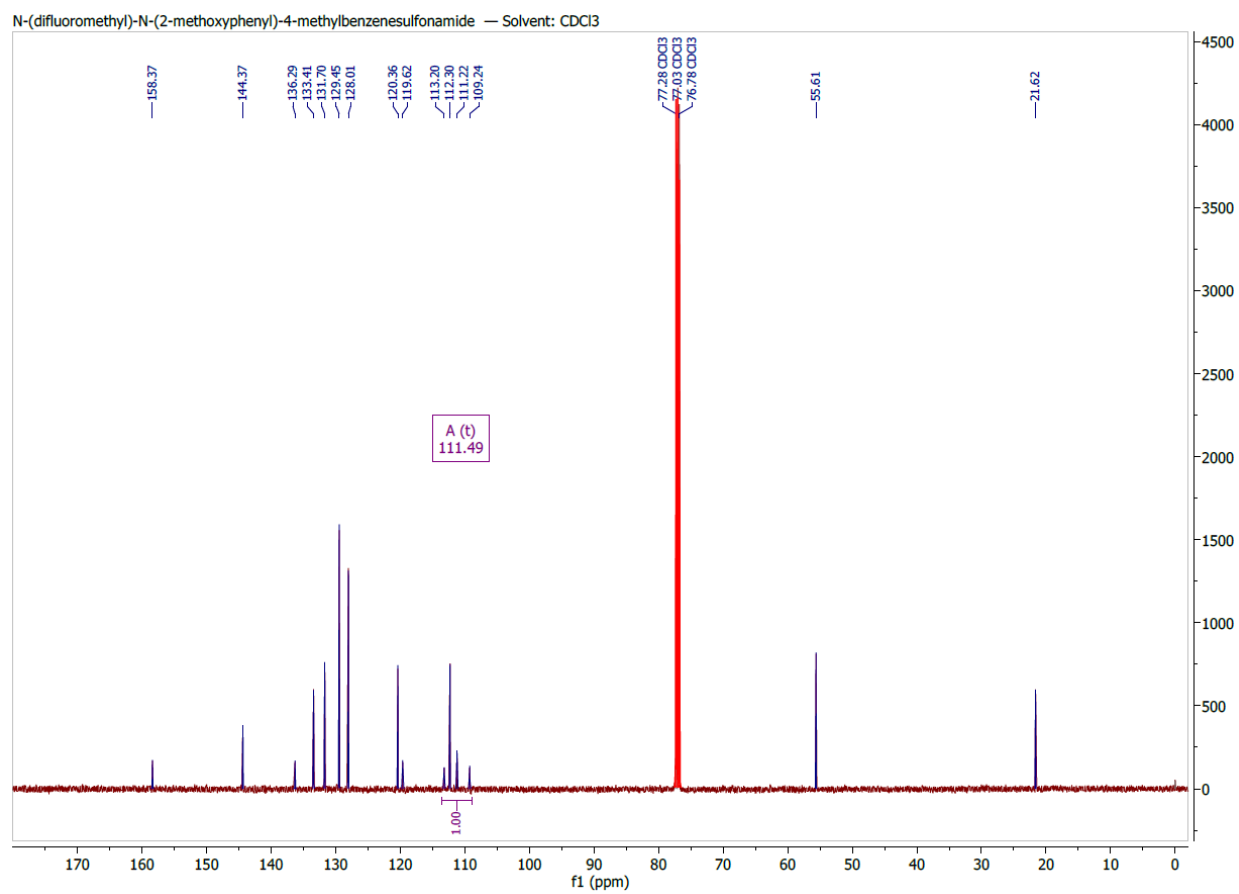
¹³C NMR of 1-benzhydryl 7-(*tert*-butyl) (2*S*,6*S*)-2-(4-(benzhydryloxy)-4-oxobutanethioamido)-6-((*tert*-butoxycarbonyl)(methyl)amino)heptanedioate (**27**).



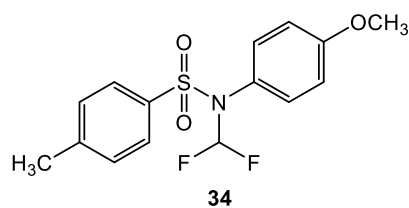
N-(difluoromethyl)-*N*-(2-methoxyphenyl)-4-methylbenzenesulfonamide — Solvent: CDCl₃



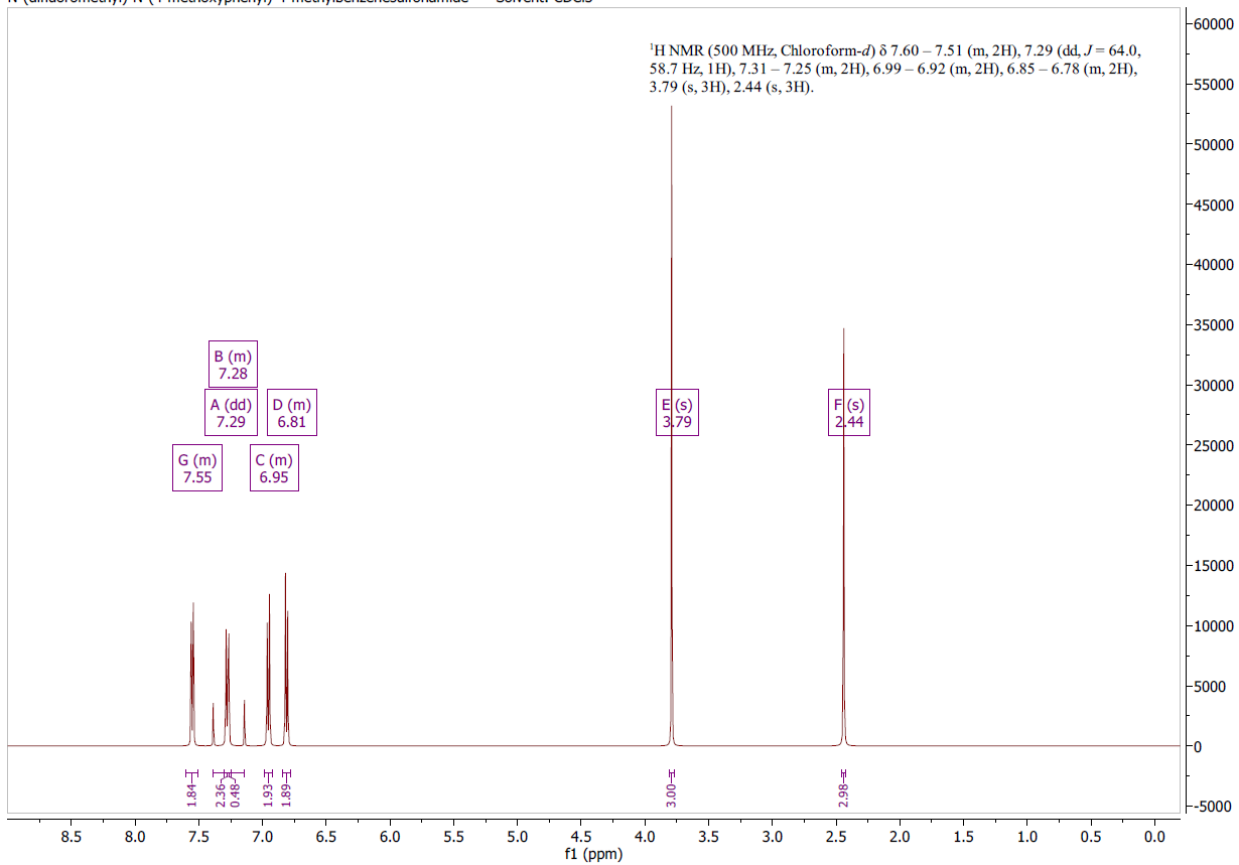
¹H NMR of *N*-(difluoromethyl)-*N*-(2-methoxyphenyl)-4-methylbenzenesulfonamide (**32**).



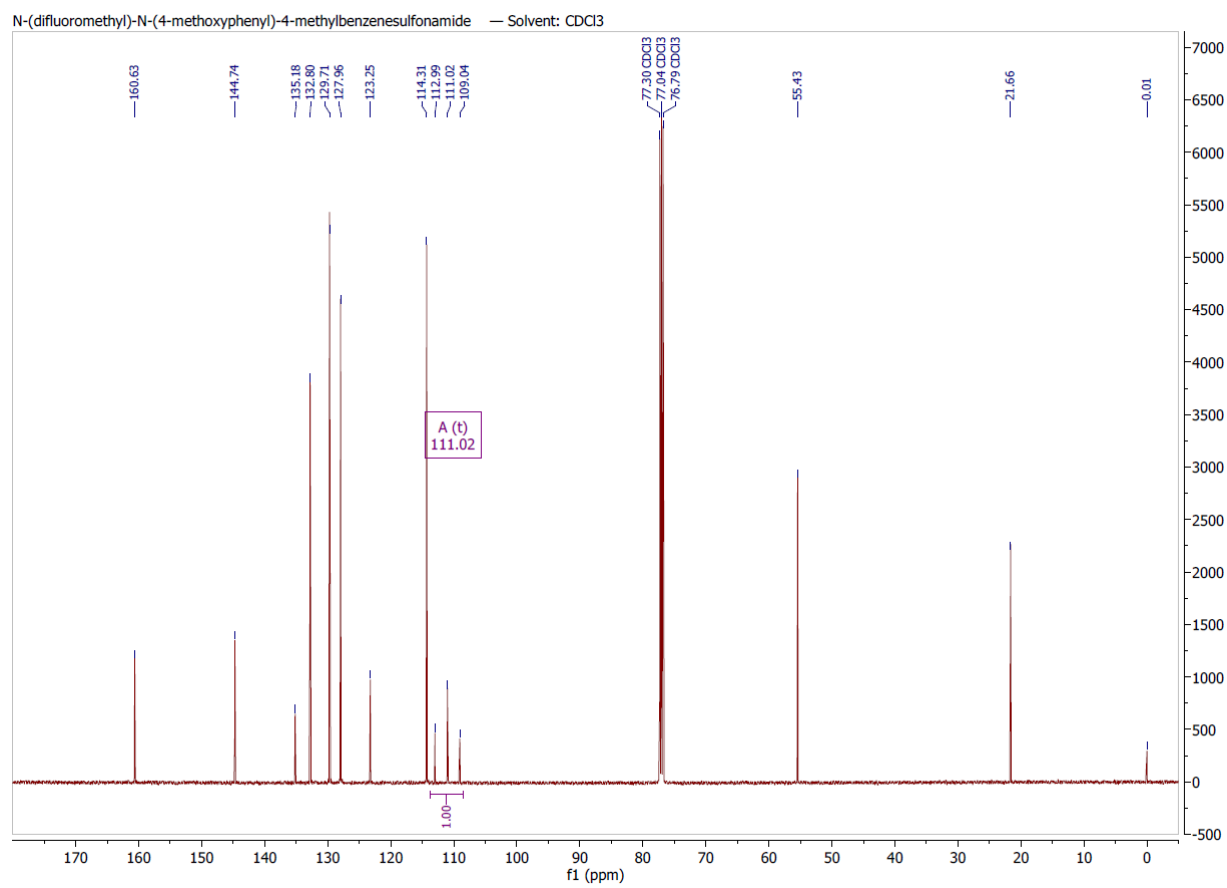
¹³C NMR of *N*-(difluoromethyl)-*N*-(2-methoxyphenyl)-4-methylbenzenesulfonamide (**32**).



N-(difluoromethyl)-*N*-(4-methoxyphenyl)-4-methylbenzenesulfonamide — Solvent: CDCl₃

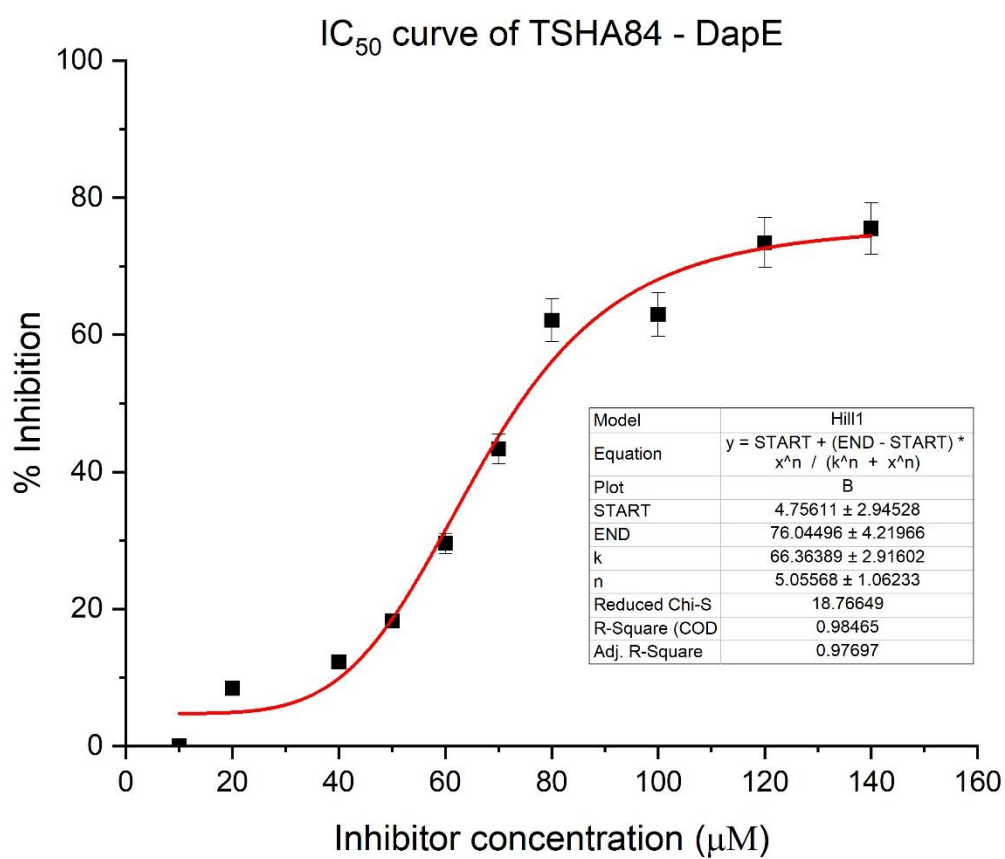
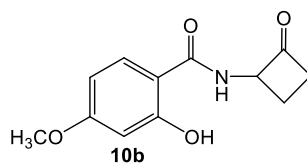


¹H NMR of *N*-(difluoromethyl)-*N*-(4-methoxyphenyl)-4-methylbenzenesulfonamide (**34**).

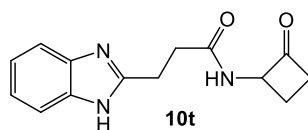


¹³C NMR of *N*-(difluoromethyl)-*N*-(4-methoxyphenyl)-4-methylbenzenesulfonamide (**34**).

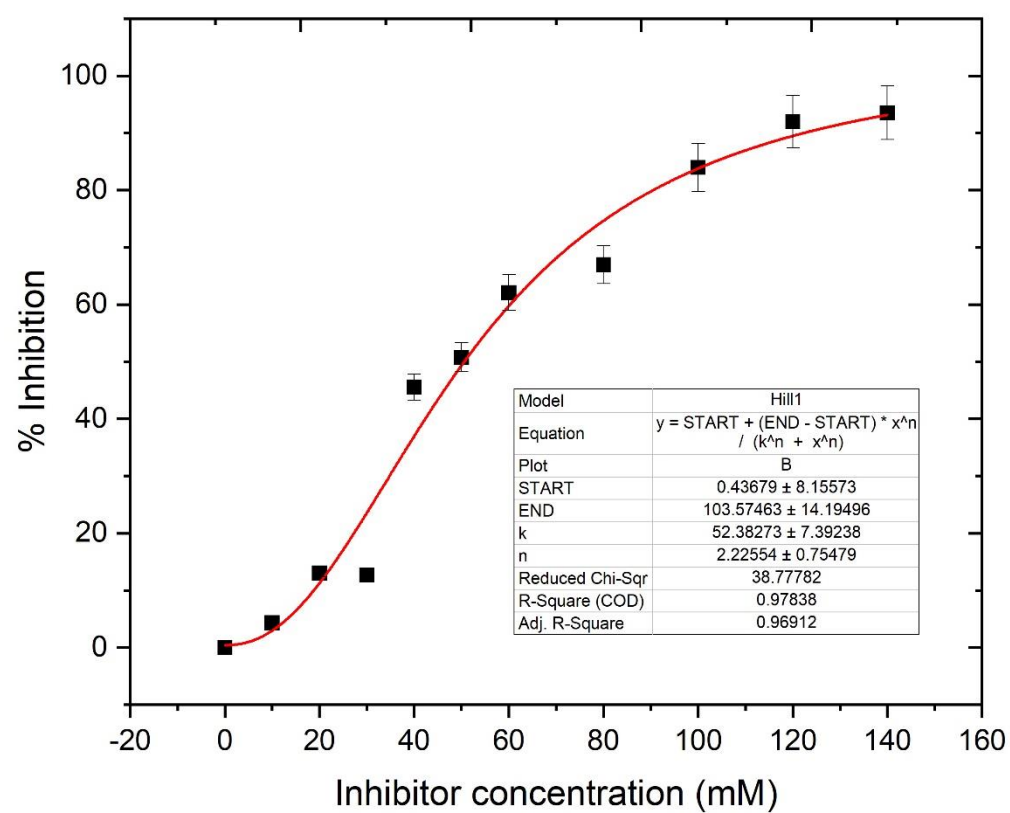
Inhibition curves for cyclobutanone inhibitors of DapE.



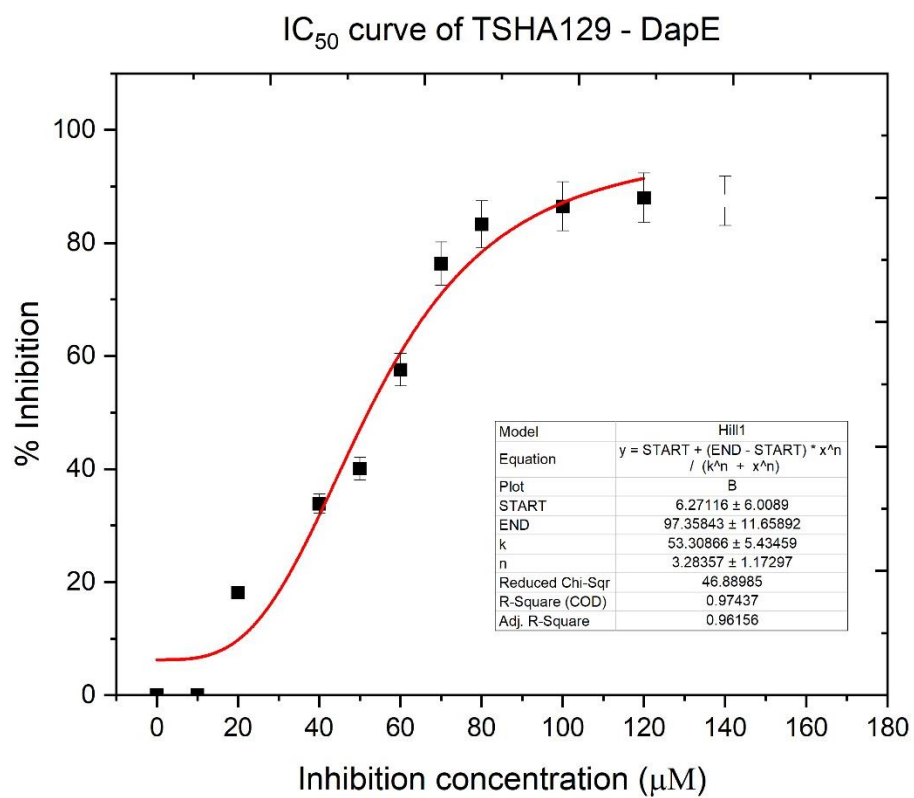
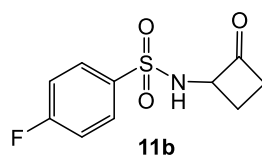
IC₅₀ plot for 2-hydroxy-4-methoxy-*N*-(2-oxocyclobutyl)benzamide (**10b**).



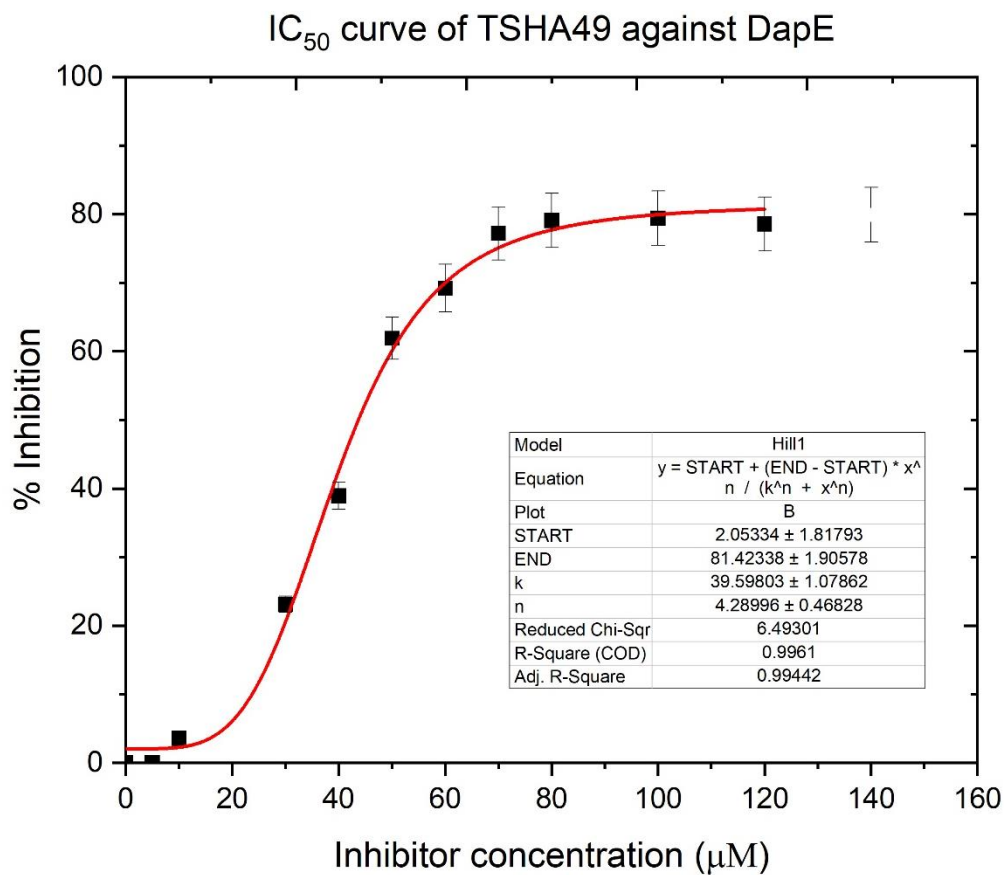
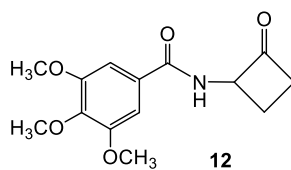
IC₅₀ curve of Benzimidazole cyclobutanone - DapE



IC₅₀ plot for 3-(1H-benzo[d]imidazol-2-yl)-N-(2-oxocyclobutyl)propenamide (**10t**).



IC₅₀ plot for *N*-(2-oxocyclobutyl)-4-(fluoro)benzenesulfonamide (**11b**).



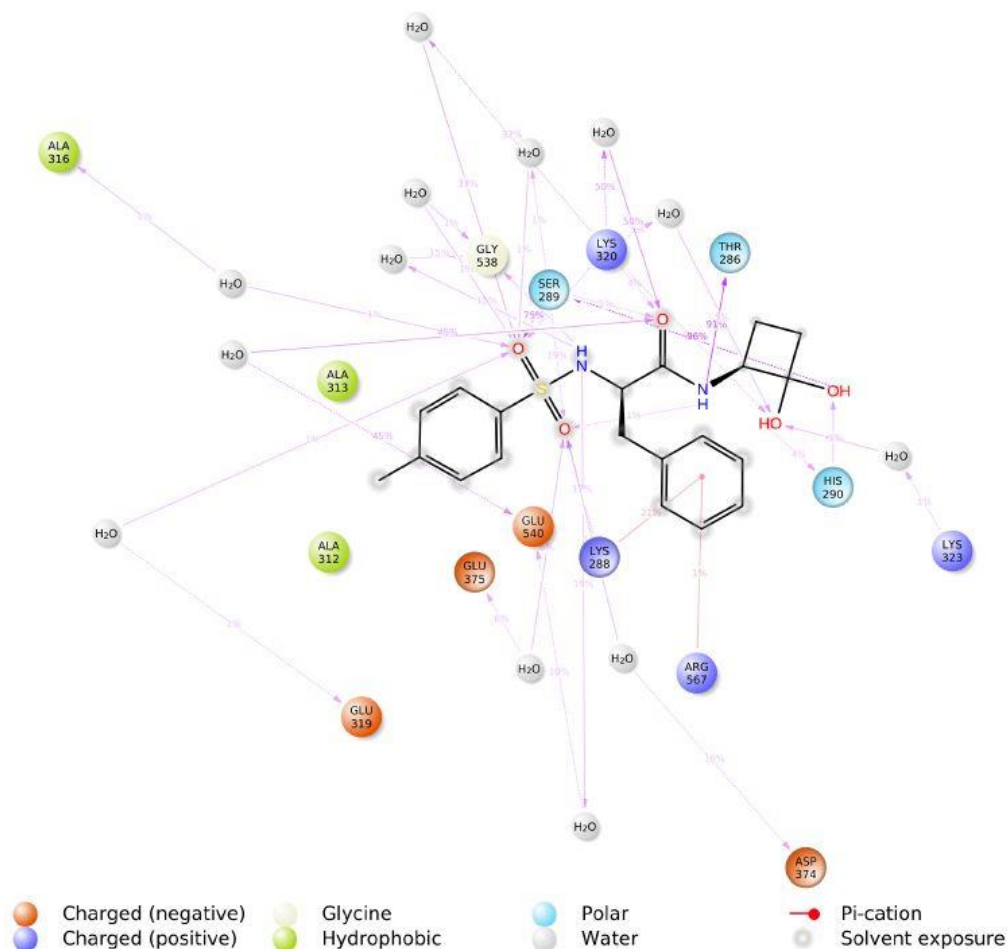
IC₅₀ plot for 3,4,5-trimethoxy-*N*-(2-oxocyclobutyl)benzamide (**12**).

APPENDIX C
SUPPLEMENTAL DATA FOR CHAPTER FOUR

Results of 20 nanoseconds MD simulation report for helicase original hit (48b)

generated in Schrödinger suite.

Ligand-Protein Contacts

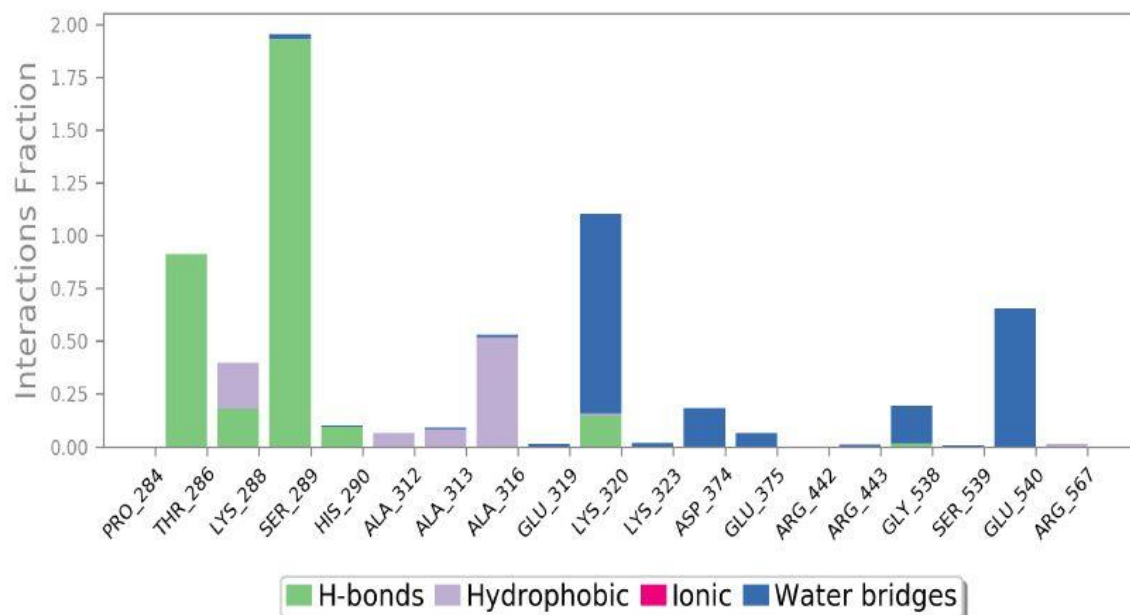


A schematic of detailed ligand atom interactions with the protein residues. Interactions that occur more than **1.0%** of the simulation time in the selected trajectory (0.00 through 20.00 nsec), are shown.

Note: it is possible to have interactions with >100% as some residues may have multiple interactions of a single type with the same ligand atom. For example, the ARG side chain has four H-bond donors that can all hydrogen-bond to a single H-bond acceptor.

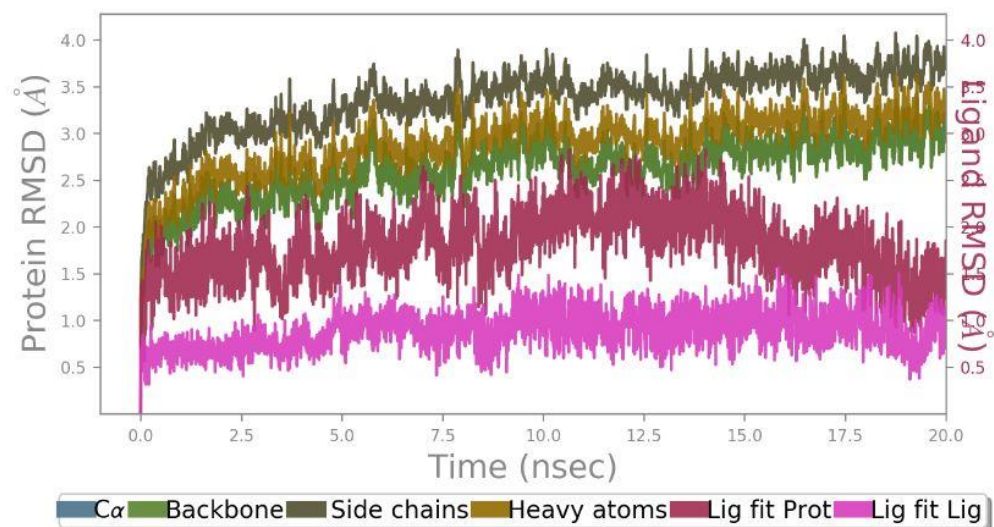
2D Representation of ligand interactions of compound **48b** with the active site residues throughout the simulation. Interactions that occur more than 1.0% of the simulation time in the selected trajectory (0.00 through 20.00 ns) are shown.

Protein-Ligand Contacts



Key protein ligand contacts of amino acid side chain residues with the interaction type.

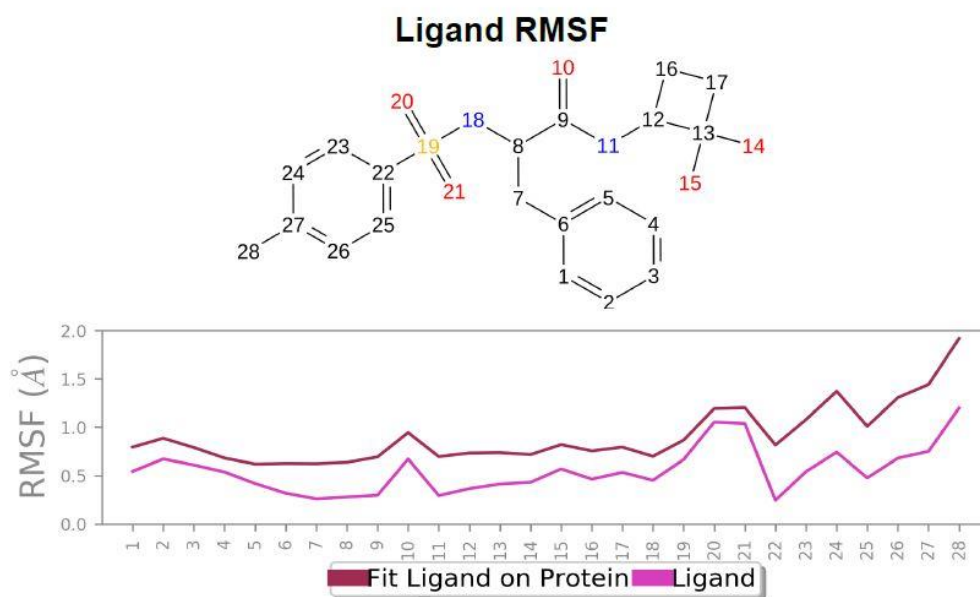
Protein-Ligand RMSD



The Root Mean Square Deviation (RMSD) is used to measure the average change in displacement of a selection of atoms for a particular frame with respect to a reference frame. It is calculated for all frames in the trajectory. The RMSD for frame x is:

$$RMSD_x = \sqrt{\frac{1}{N} \sum_{i=1}^N (r_i'(t_x) - r_i(t_{ref}))^2}$$

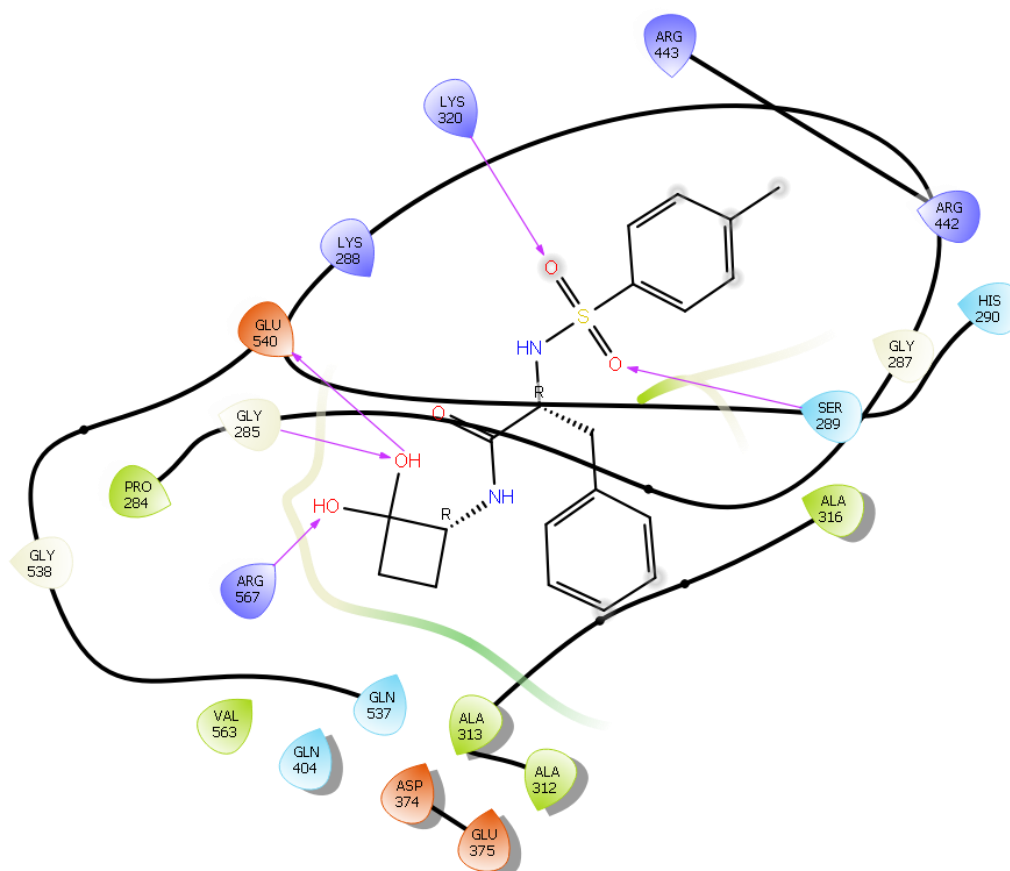
Root mean square deviations difference between helicase and bound ligand Ts-D-phenylalanine cyclobutanone (<4 Å).



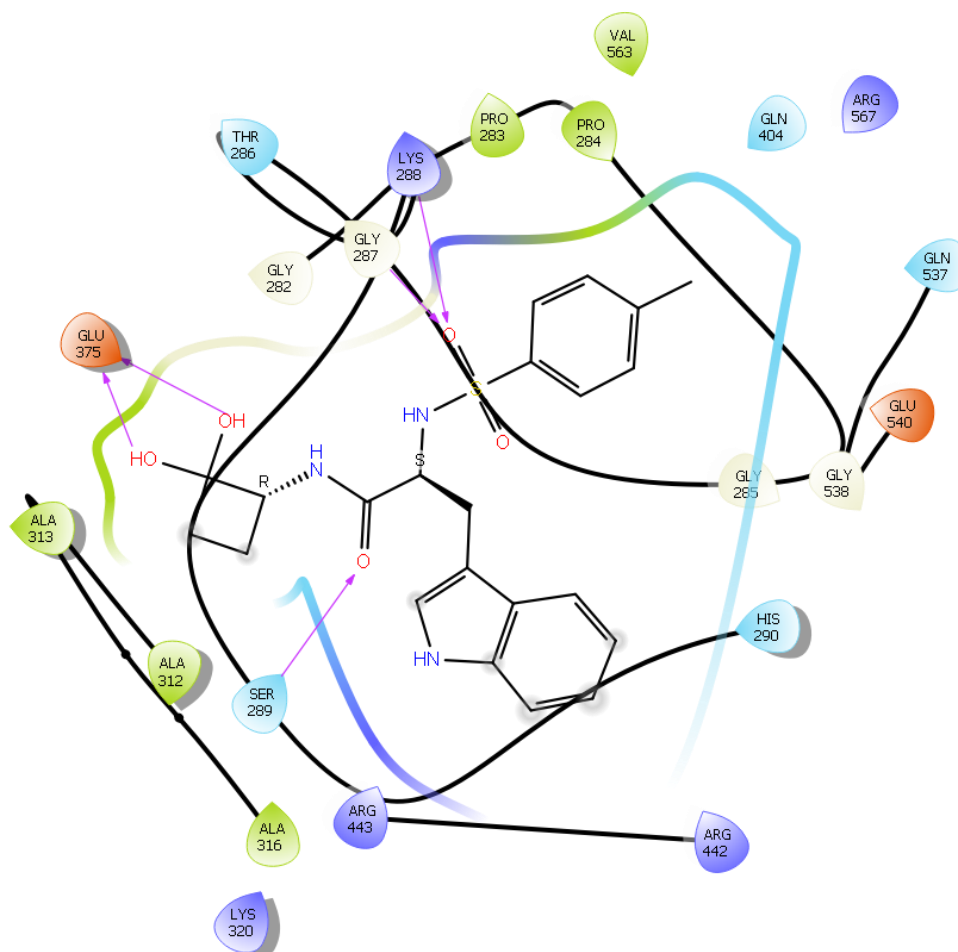
The Ligand Root Mean Square Fluctuation (L-RMSF) is useful for characterizing changes in the ligand atom positions. The RMSF for atom i is:

$$RMSF_i = \sqrt{\frac{1}{T} \sum_{t=1}^T (r_i(t) - r_i(t_{ref}))^2}$$

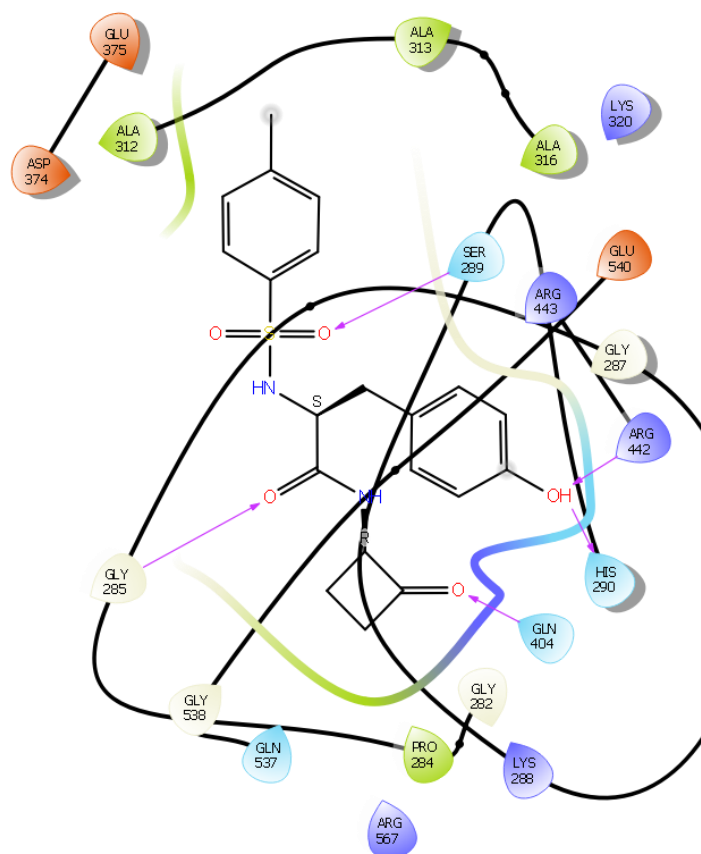
Root mean square fluctuation between the binding site of helicase and interacting ligand (48b).

Ligand interaction diagrams (2D) of 11 helicase amino acid-cyclobutanone hits.

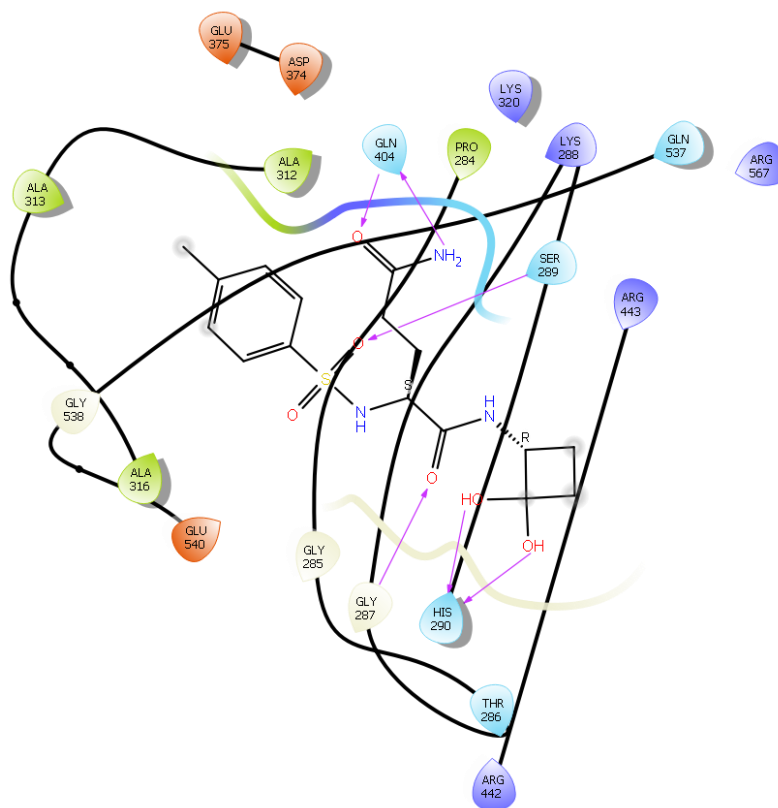
Ligand interaction diagram of (2R)-2-((4-methylphenyl)sulfonamido)-N-(2-oxocyclobutyl)-3-phenylpropanamide (**48b**) bound to the helicase active site as a hydrate.



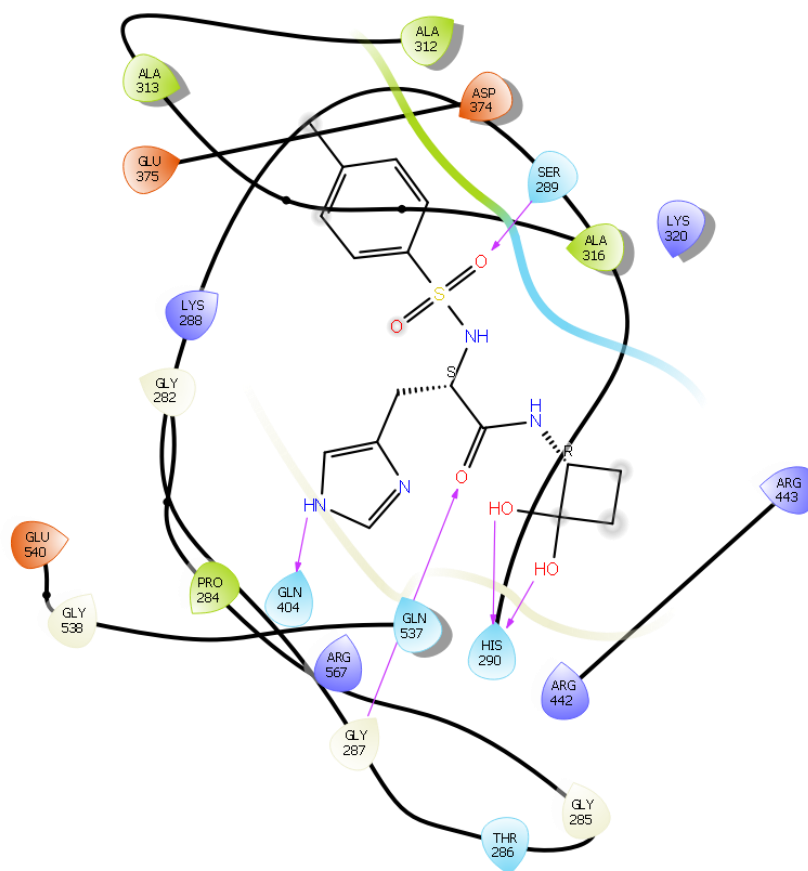
Ligand interaction diagram of (2S)-3-(1H-indol-3-yl)-2-((4-methylphenyl)sulfonamido)-N-(2-oxocyclobutyl)propanamide (**48c**) bound to the helicase active site as a hydrate.



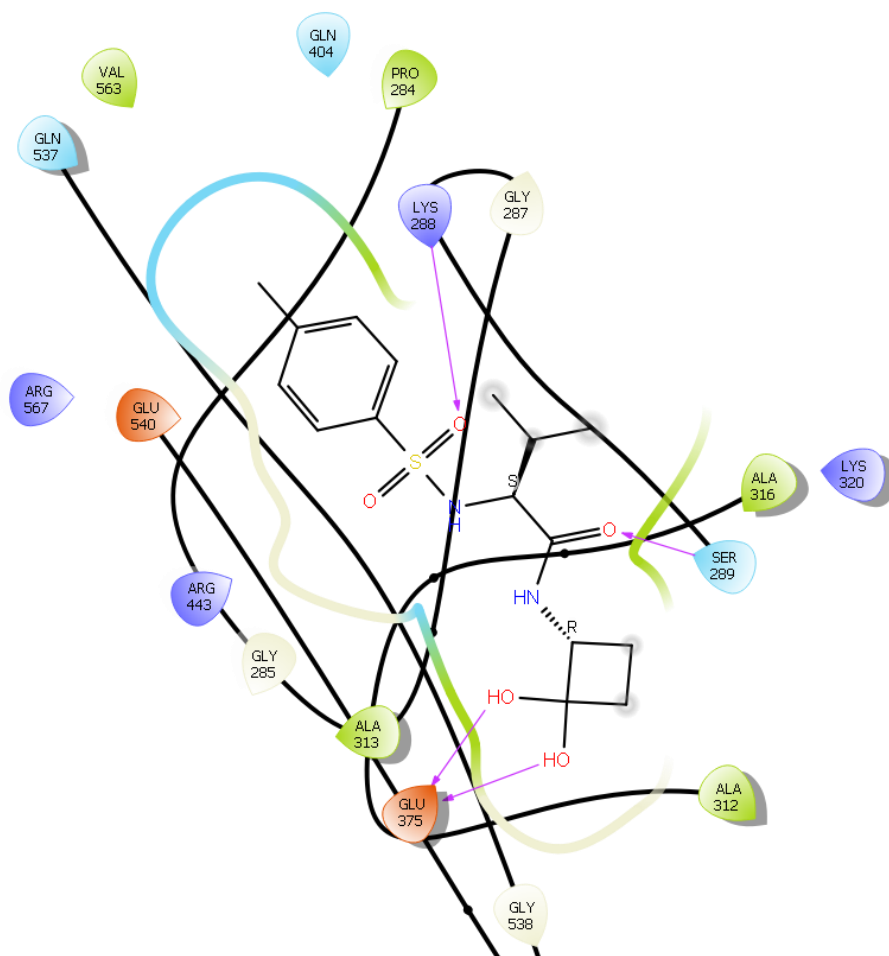
Ligand interaction diagram (2S)-3-(4-hydroxyphenyl)-2-((4-methylphenyl)sulfonamido)-N-(2-oxocyclobutyl)propanamide (**48d**).



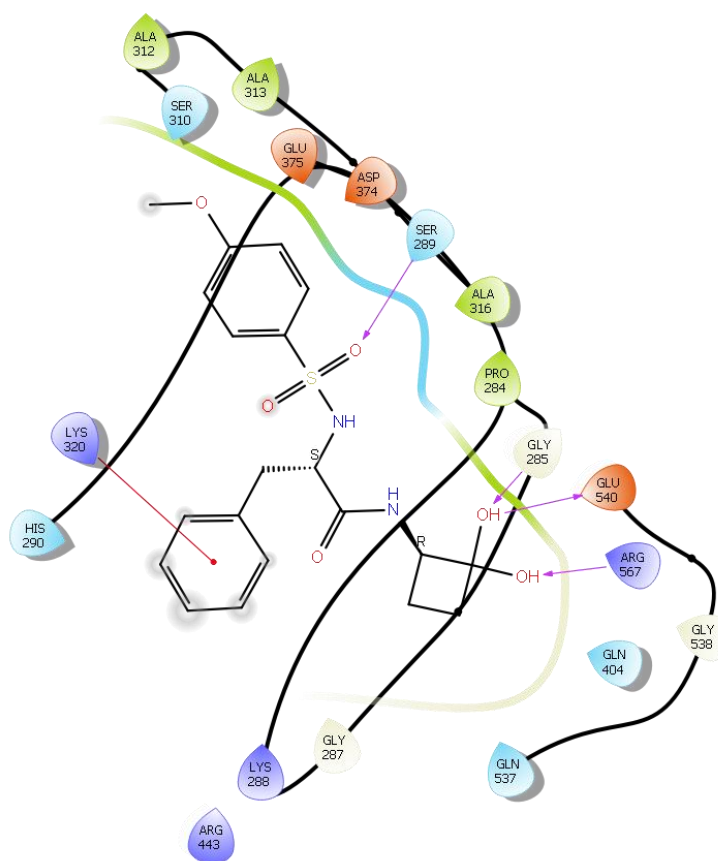
Ligand interaction diagram of (2S)-2-((4-methylphenyl)sulfonamido)-N¹-(2-oxocyclobutyl)pentanediamide (**48e**) bound to the helicase active site as a hydrate.



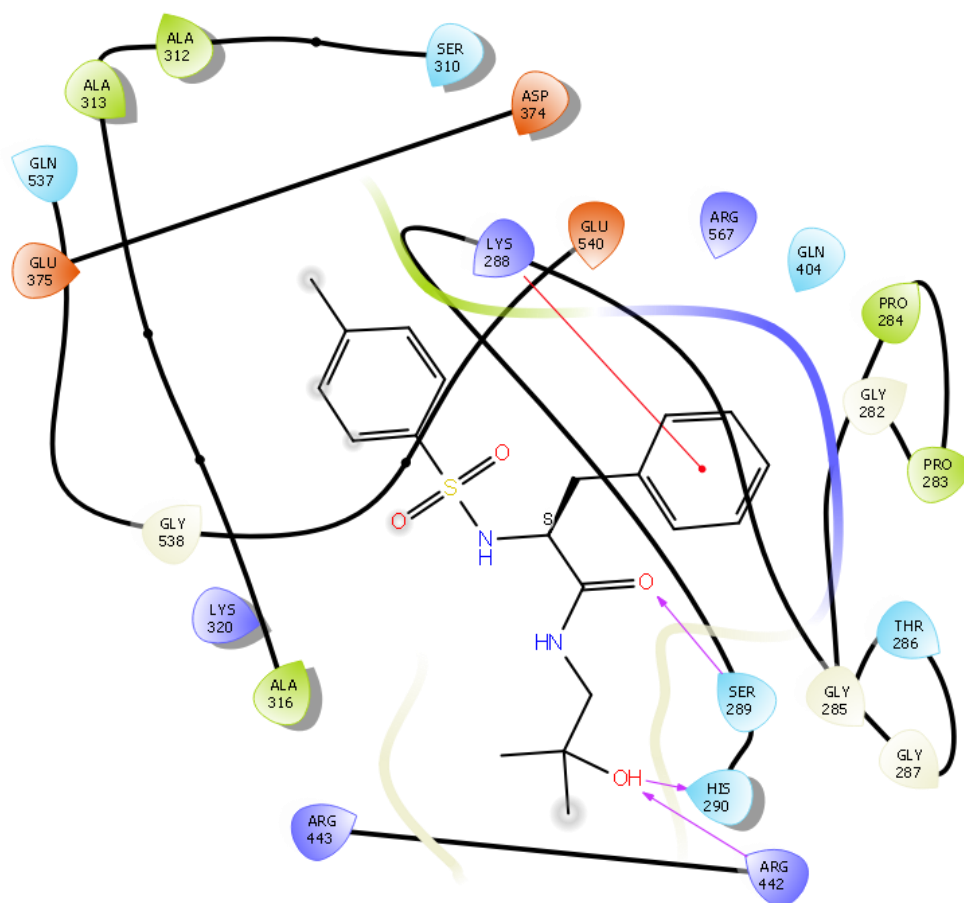
Ligand interaction diagram of (2S)-3-(1H-imidazol-4-yl)-2-((4-methylphenyl)sulfonamido)-N-(2-oxocyclobutyl)propanamide (**48f**) bound to the helicase active site as a hydrate.



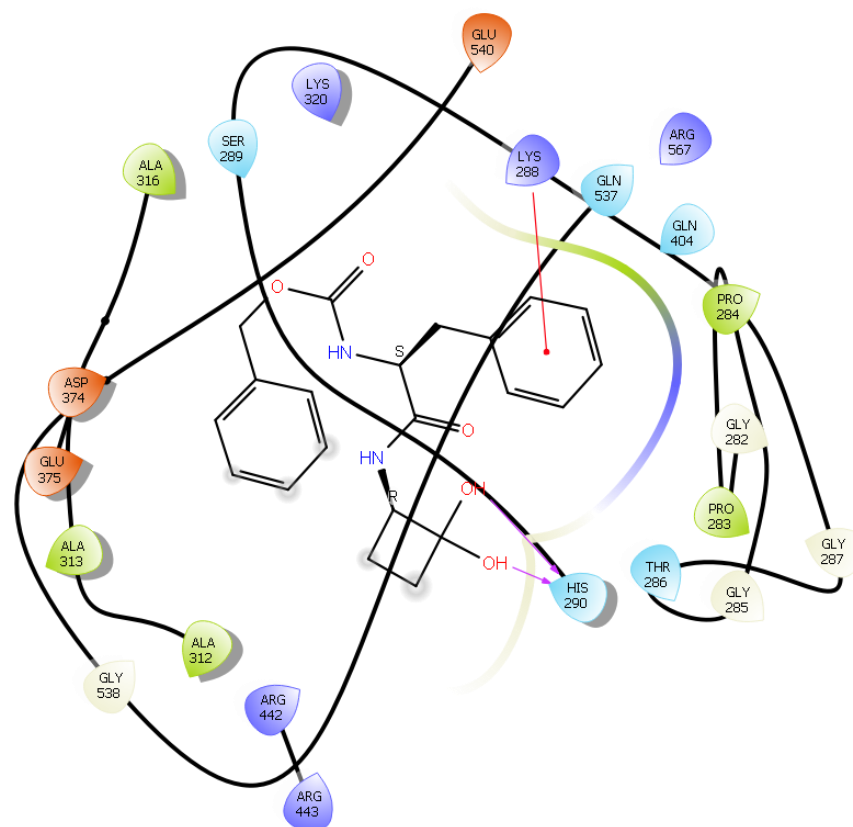
Ligand interaction diagram of (2S)-3-methyl-2-((4-methylphenyl)sulfonamido)-N-(2-oxocyclobutyl)butanamide (**48g**) bound to the helicase active site as a hydrate.



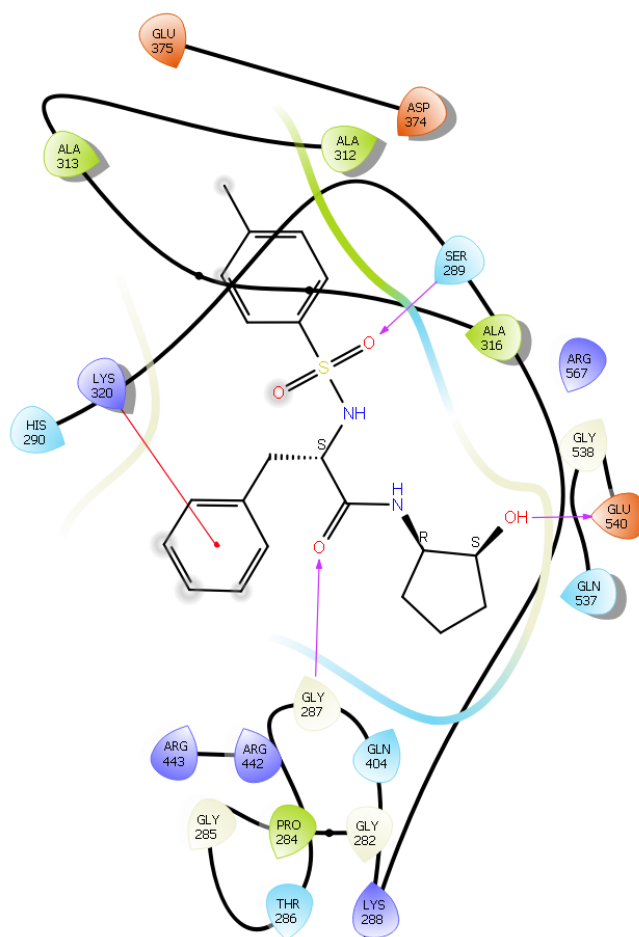
Ligand interaction diagram of (2R)-2-((4-methoxyphenyl)sulfonamido)-3-methyl-*N*-(2-oxocyclobutyl)butanamide (**48h**) bound to the helicase active site as a hydrate.



Ligand interaction diagram of (S)-N-(2-hydroxy-2-methylpropyl)-2-((4-methylphenyl)sulfonamido)-3-phenylpropanamide bound to helicase active site(51).

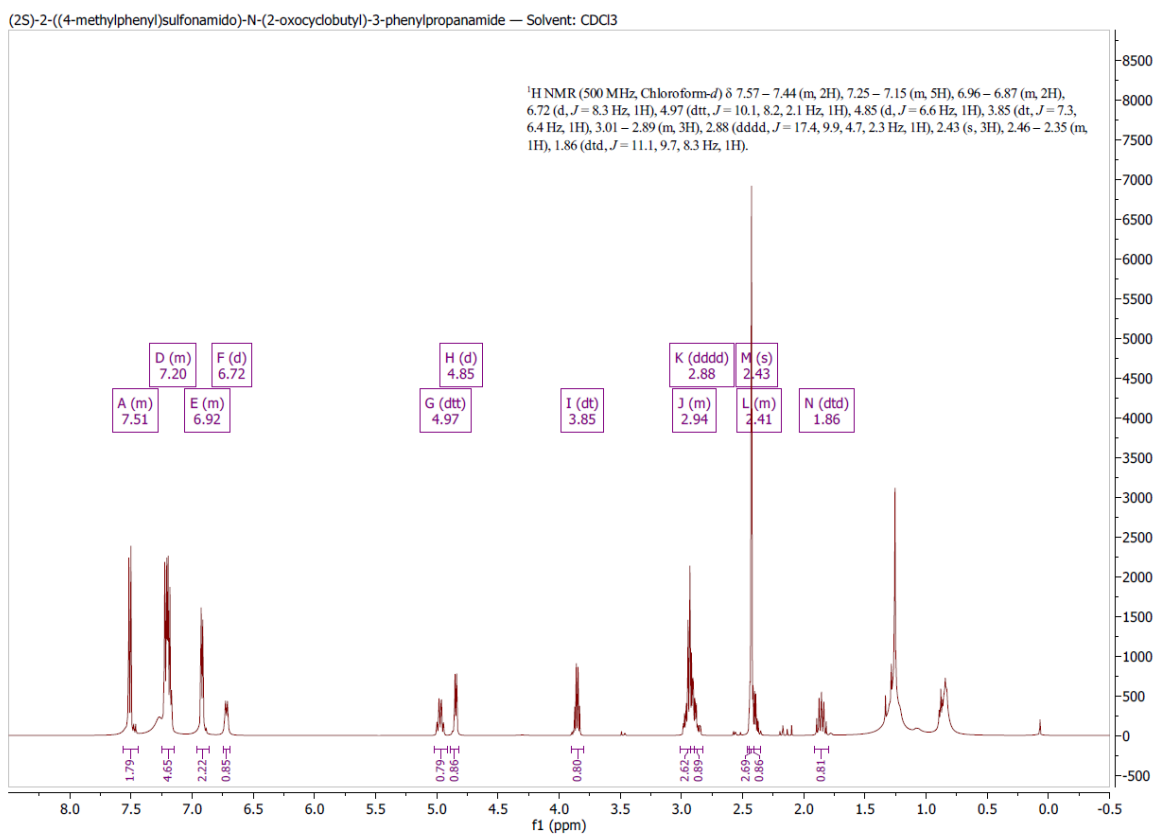
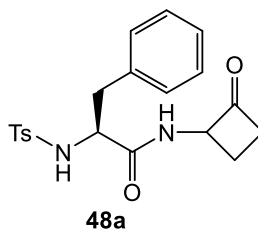


Ligand interaction diagram of benzyl ((2S)-1-oxo-1-((2-oxocyclobutyl)amino)-3-phenylpropan-2-yl)carbamate bound to the helicase active site as a hydrate (**54c**).

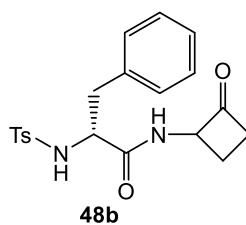


Ligand interaction diagram of (2S)-N-(2-hydroxycyclopentyl)-2-((4-methylphenyl)sulfonamido)-3-phenylpropanamide bound to the helicase active site.

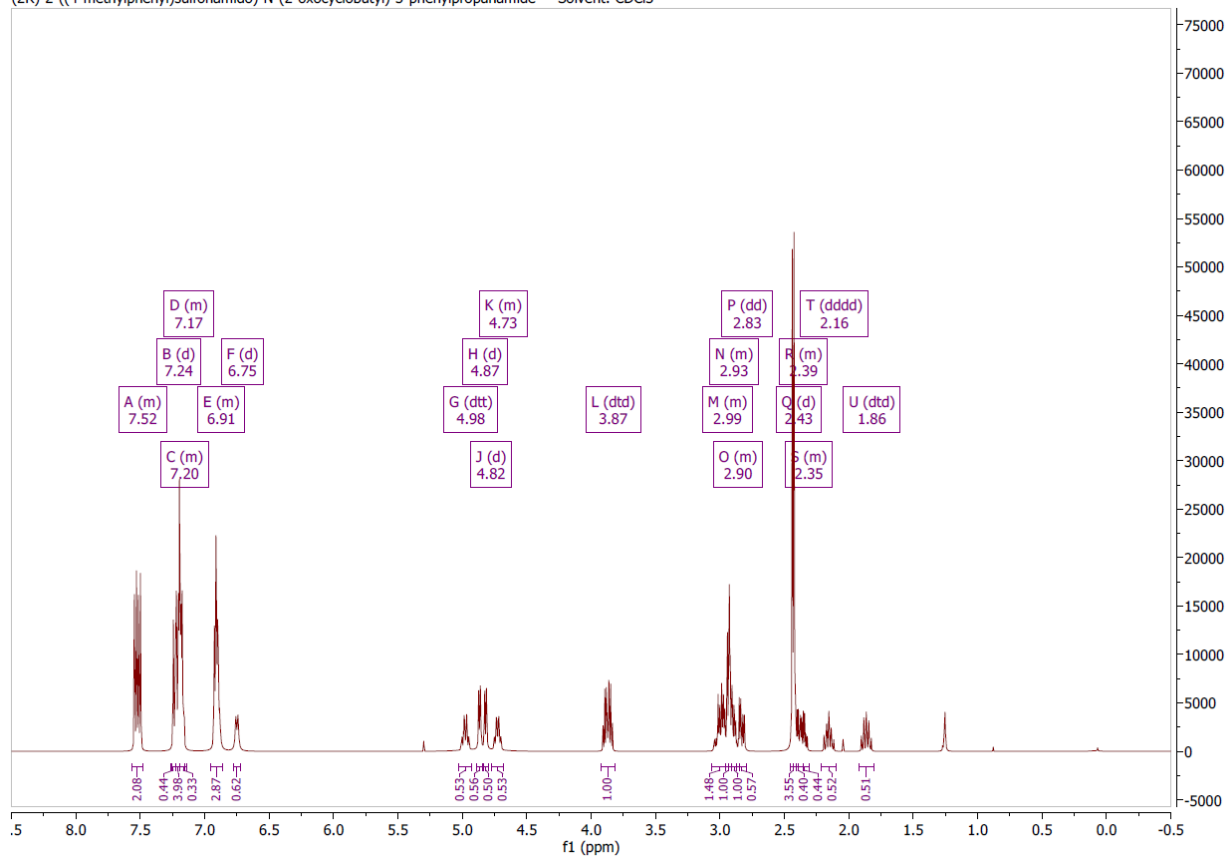
NMR spectra of the compounds reported in chapter four.



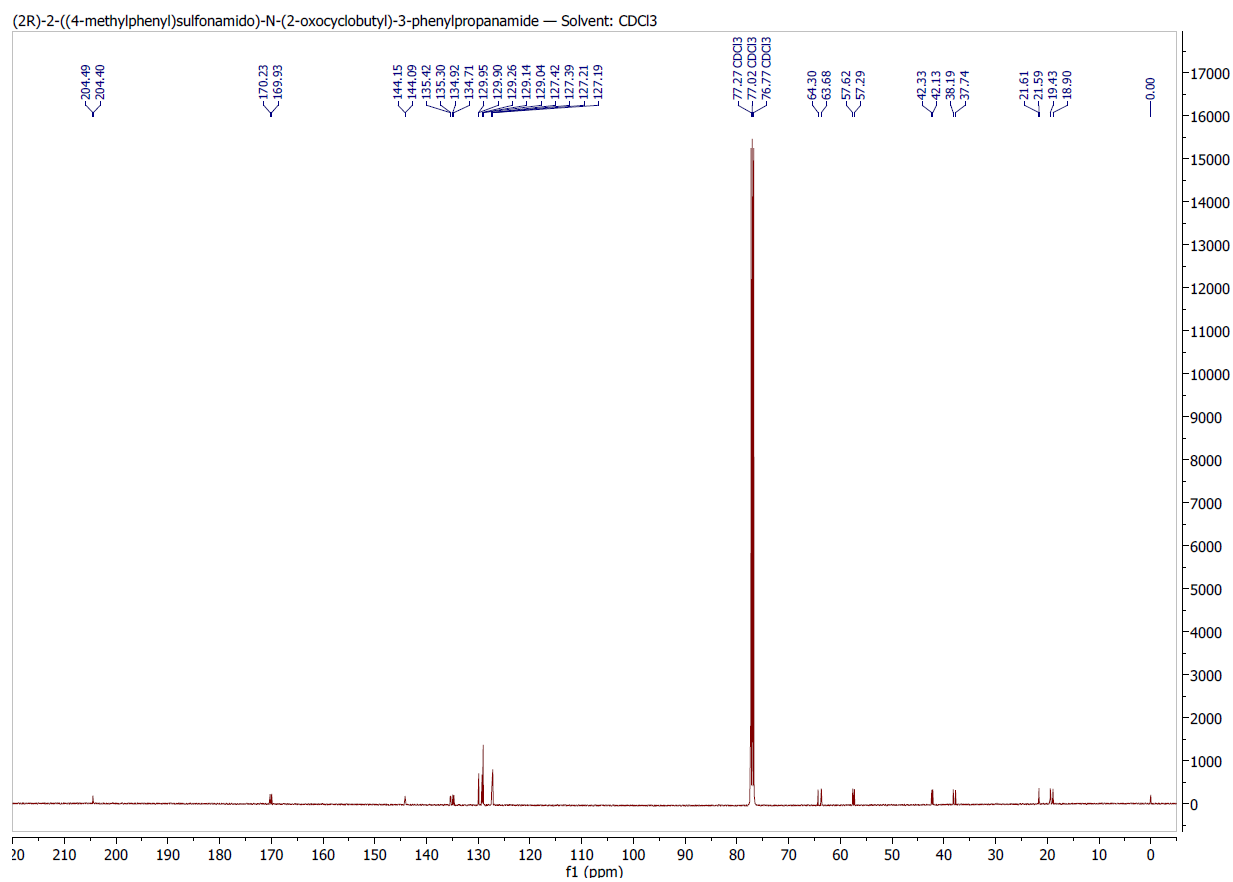
¹H NMR of (2S)-2-((4-methylphenyl)sulfonamido)-N-(2-oxocyclobutyl)-3-phenylpropanamide (**48a**).



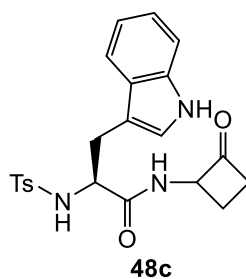
(2R)-2-((4-methylphenyl)sulfonamido)-N-(2-oxocyclobutyl)-3-phenylpropanamide — Solvent: CDCl₃



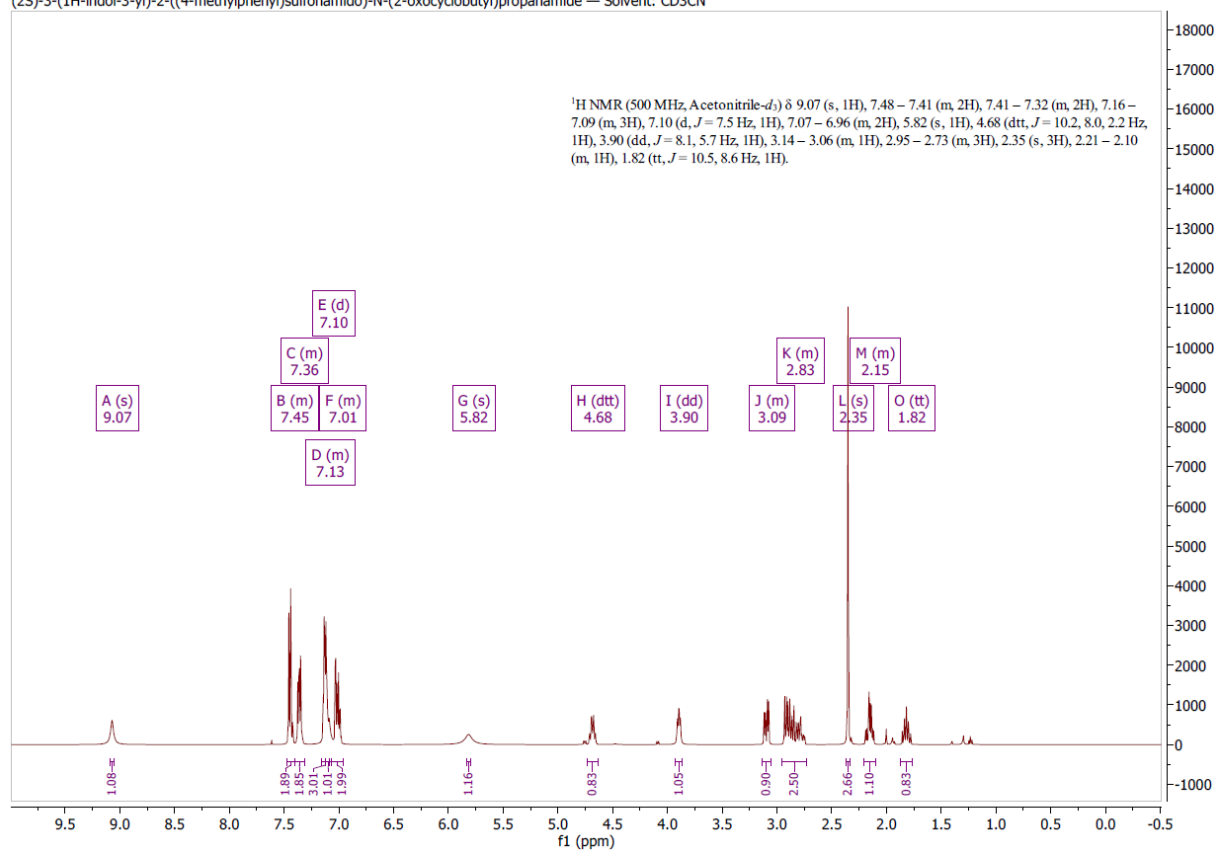
¹H NMR of (2R)-2-((4-methylphenyl)sulfonamido)-N-(2-oxocyclobutyl)-3-phenylpropanamide (**48b**).



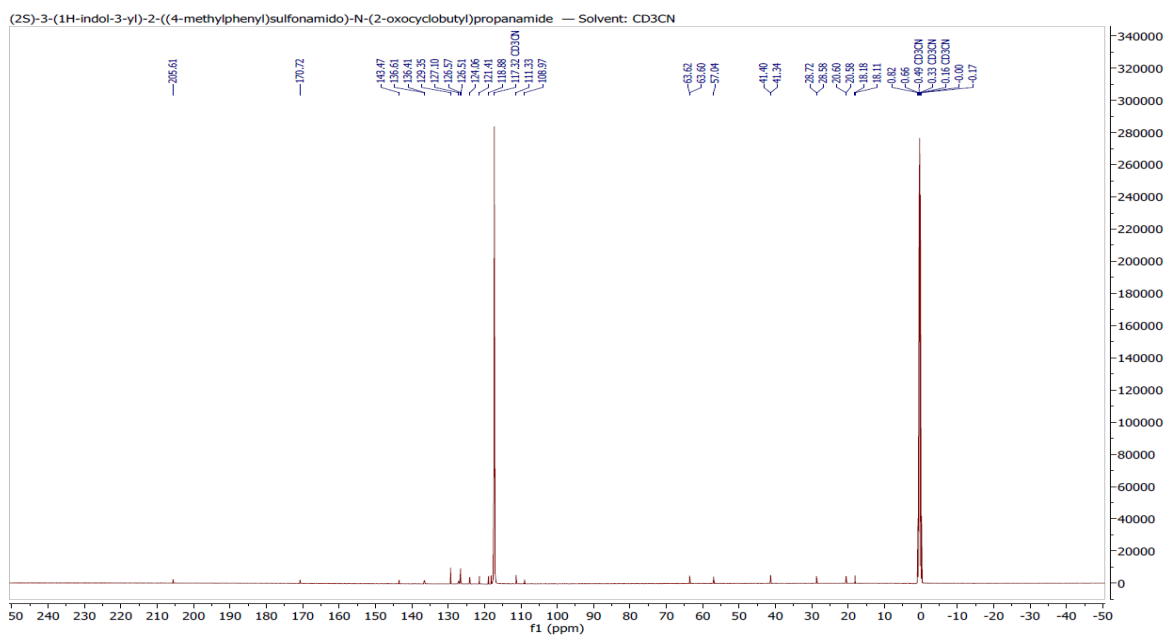
¹³C NMR of (2R)-2-((4-methylphenyl)sulfonamido)-N-(2-oxocyclobutyl)-3-phenylpropanamide (**48b**).



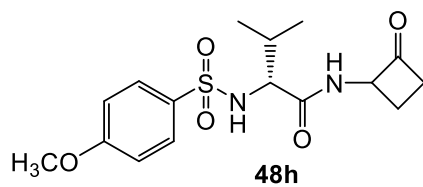
(2S)-3-(1H-indol-3-yl)-2-((4-methylphenyl)sulfonamido)-N-(2-oxocyclobutyl)propanamide — Solvent: CD₃CN



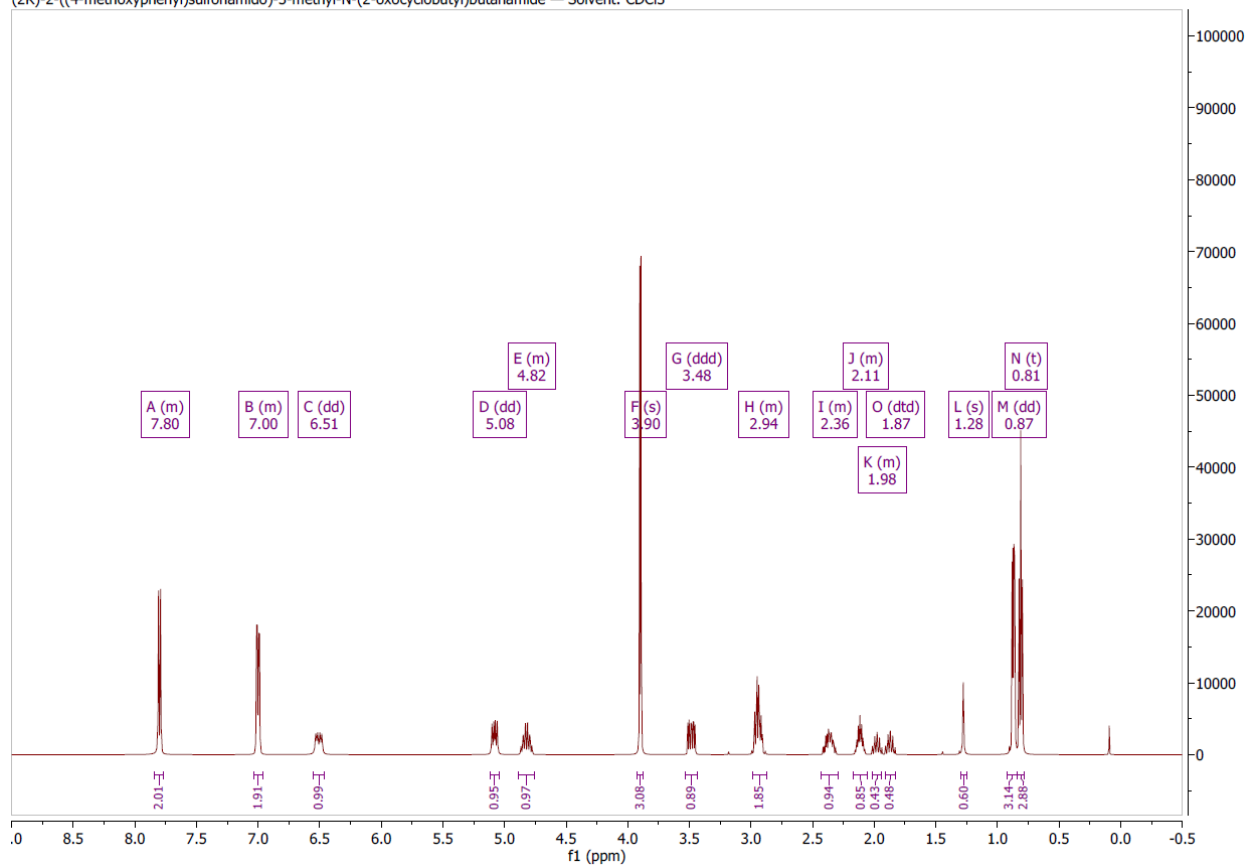
¹H NMR of (2S)-3-(1H-indol-3-yl)-2-((4-methylphenyl)sulfonamido)-N-(2-oxocyclobutyl)propanamide (**48c**).



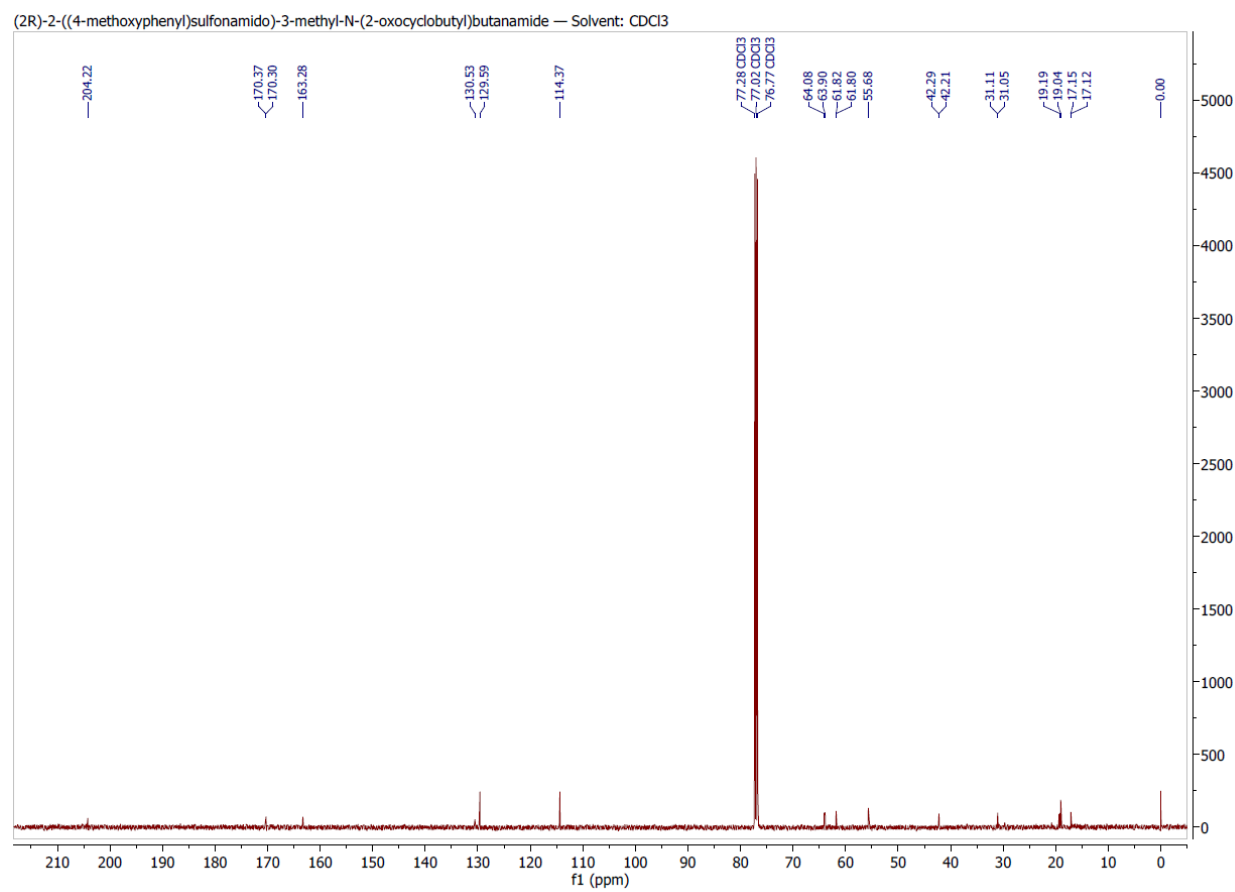
^{13}C NMR of (2S)-3-(1H-indol-3-yl)-2-((4-methylphenyl)sulfonamido)-N-(2-oxocyclobutyl)propanamide (**48c**).



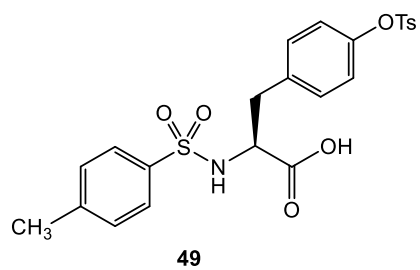
(2R)-2-((4-methoxyphenyl)sulfonamido)-3-methyl-N-(2-oxocyclobutyl)butanamide — Solvent: CDCl₃



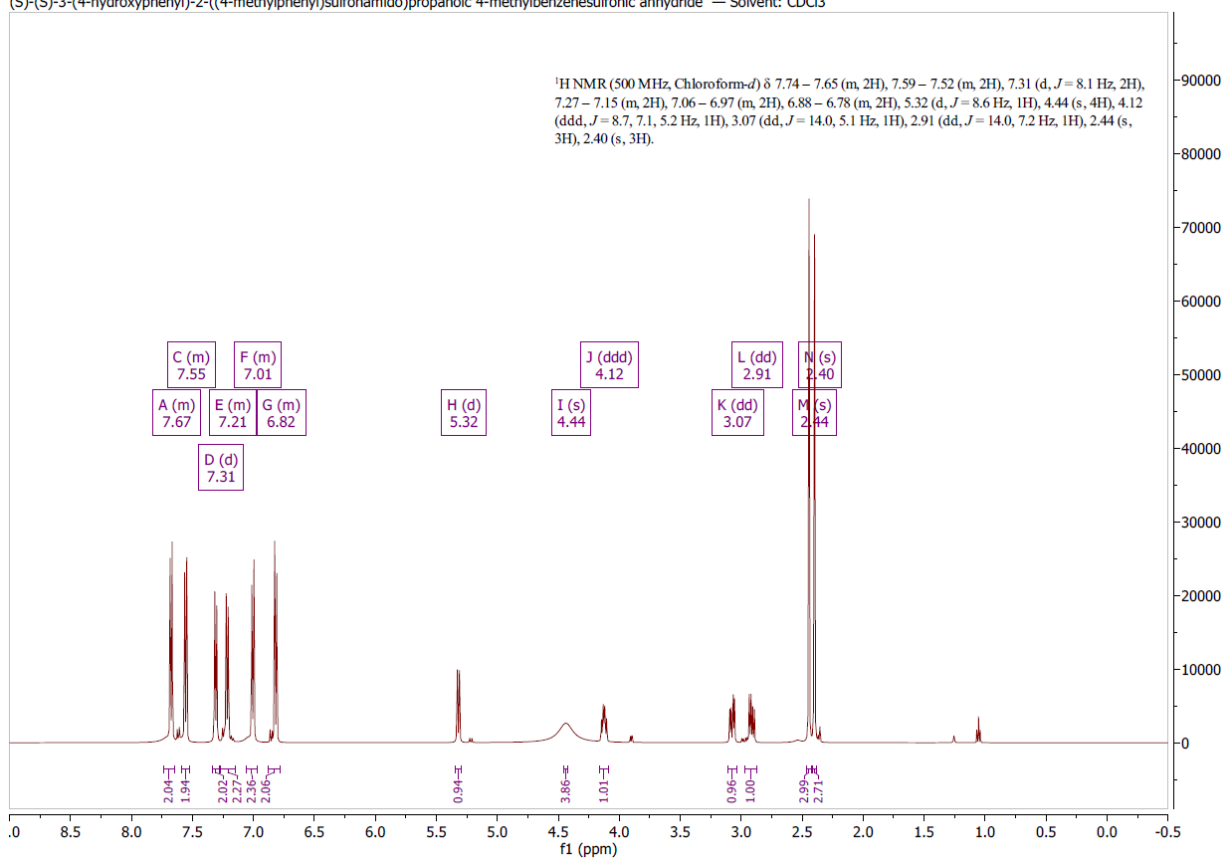
¹H NMR of (2R)-2-((4-methoxyphenyl)sulfonamido)-3-methyl-N-(2-oxocyclobutyl)butanamide (**48d**).



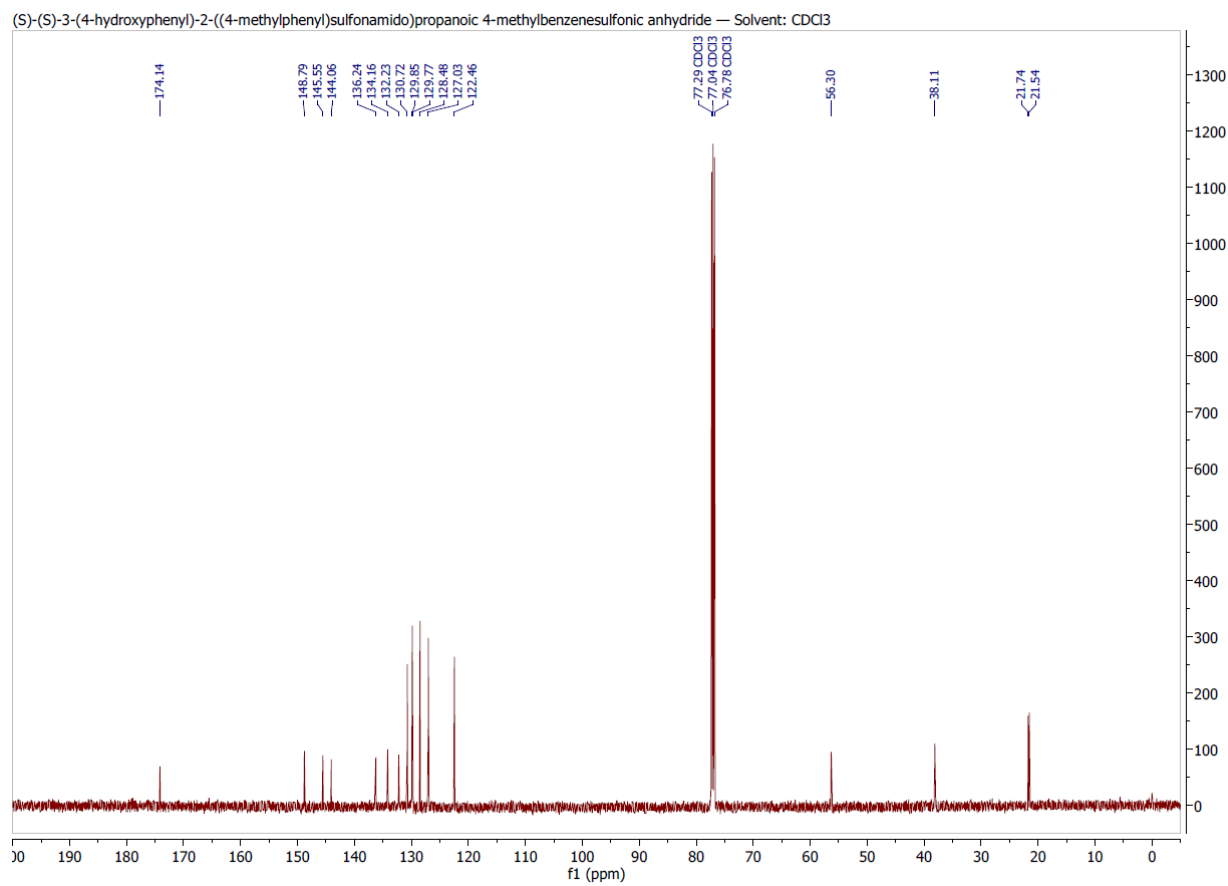
¹³C NMR of (2R)-2-((4-methoxyphenyl)sulfonamido)-3-methyl-N-(2-oxocyclobutyl)butanamide (**48d**).



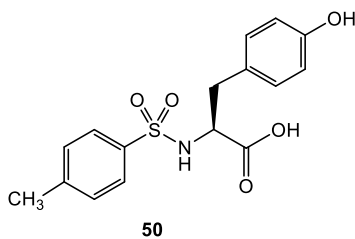
(S)-3-(4-hydroxyphenyl)-2-((4-methylphenyl)sulfonamido)propanoic 4-methylbenzenesulfonic anhydride — Solvent: CDCl₃



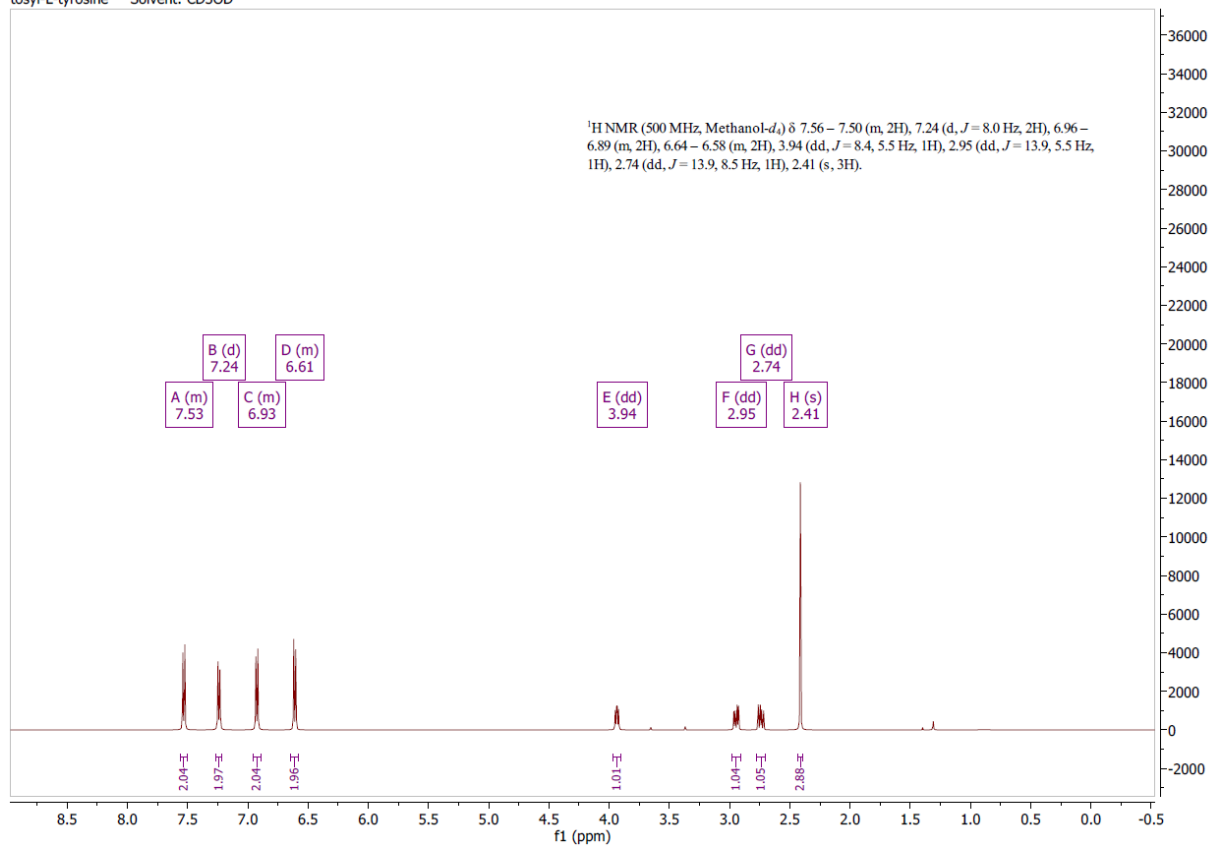
¹H NMR of (*S*)-3-(4-hydroxyphenyl)-2-((4-methylphenyl)sulfonamido)propanoic 4-methylbenzenesulfonic anhydride (**49**).

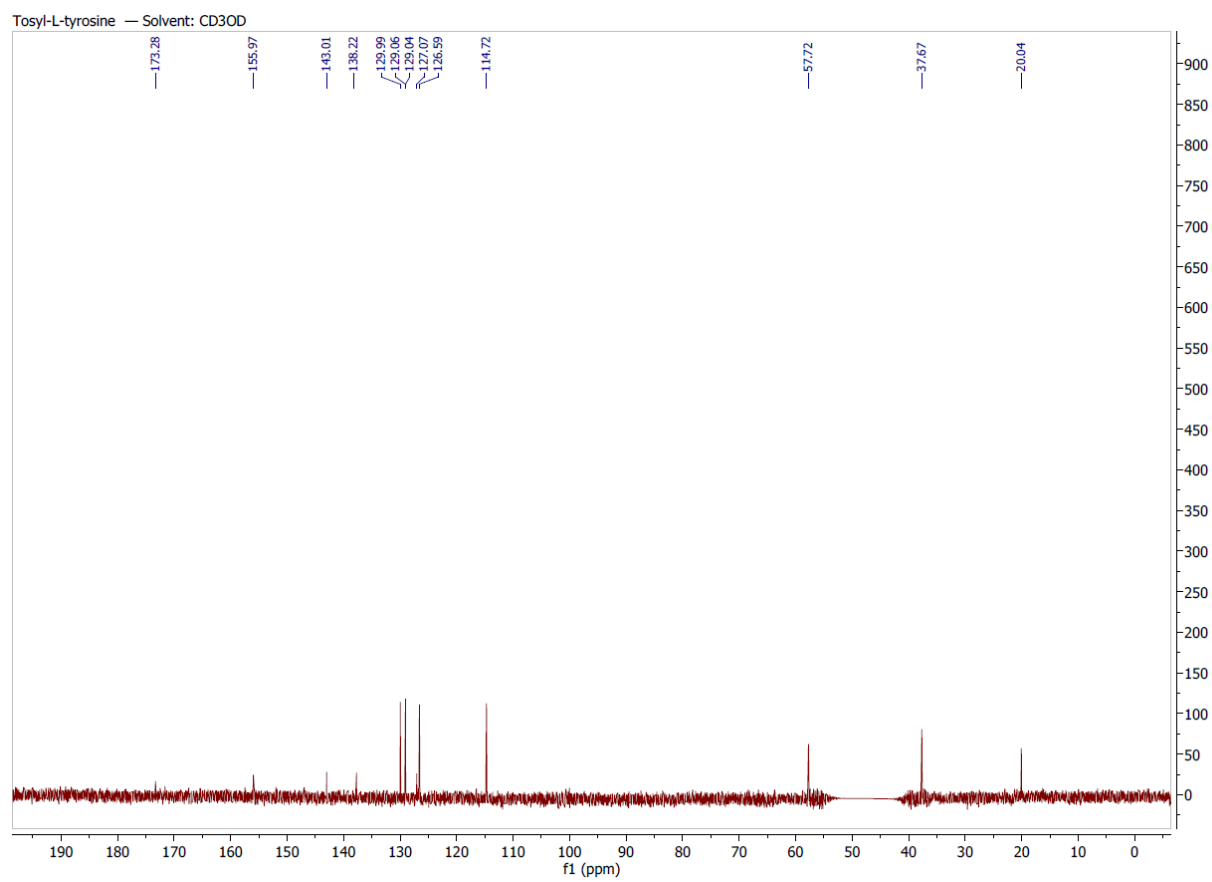


¹³C NMR of (S)-3-(4-hydroxyphenyl)-2-((4-methylphenyl)sulfonamido)propanoic 4-methylbenzenesulfonic anhydride (**49**).

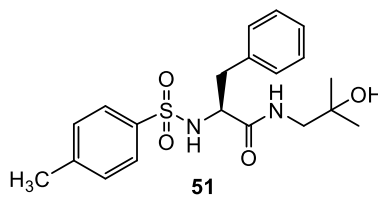


tosyl-L-tyrosine — Solvent: CD3OD

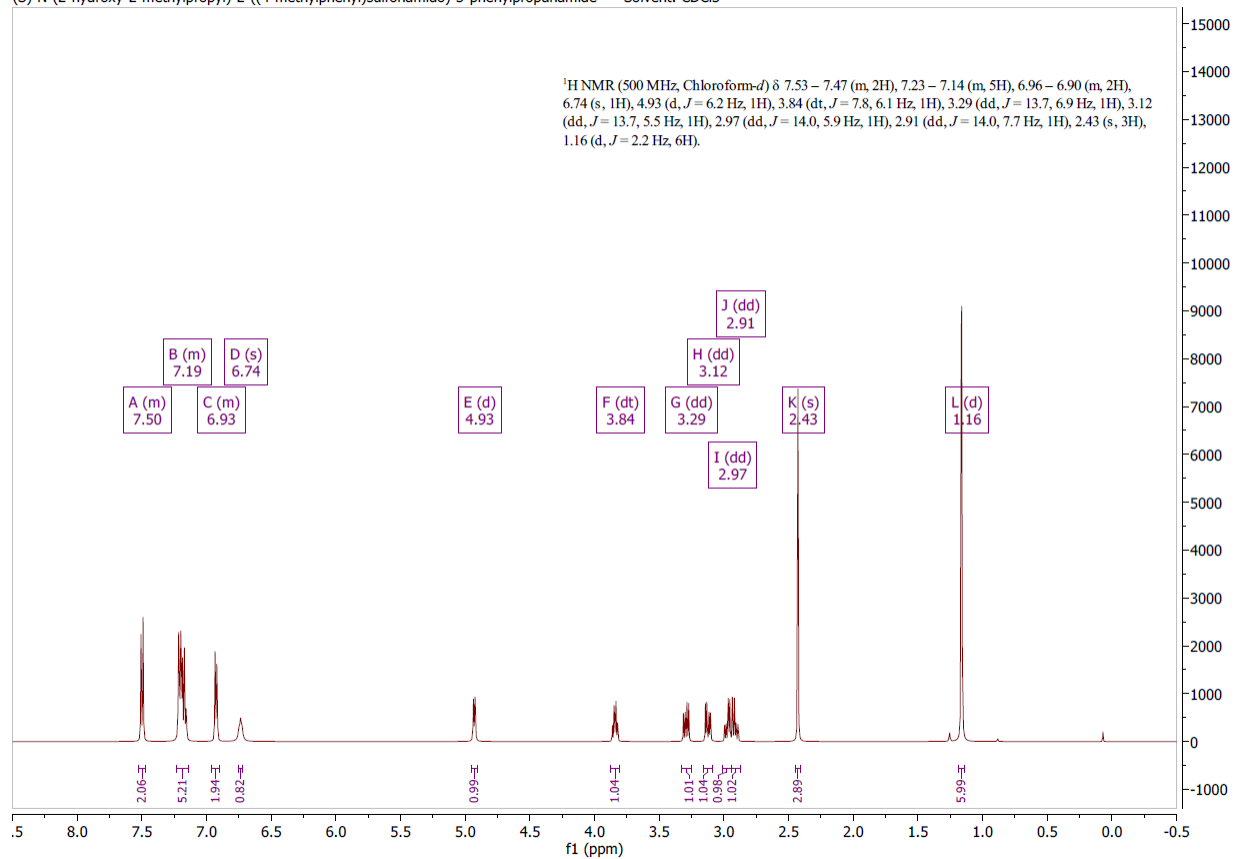
¹H NMR of tosyl-L-tyrosine (**50**).



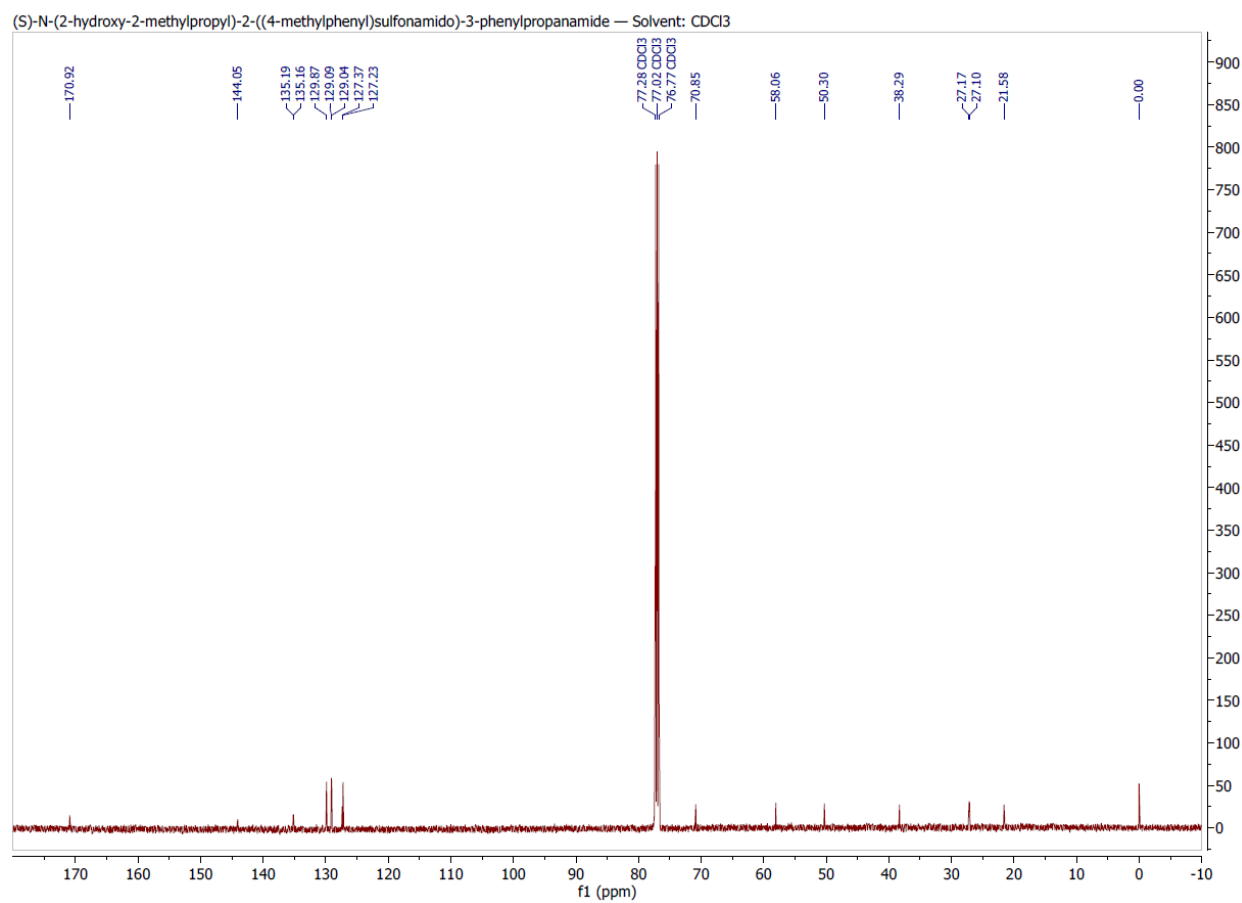
^{13}C NMR of tosyl-L-tyrosine (**50**).



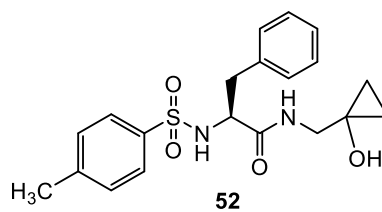
(S)-N-(2-hydroxy-2-methylpropyl)-2-((4-methylphenyl)sulfonamido)-3-phenylpropanamide — Solvent: CDCl₃



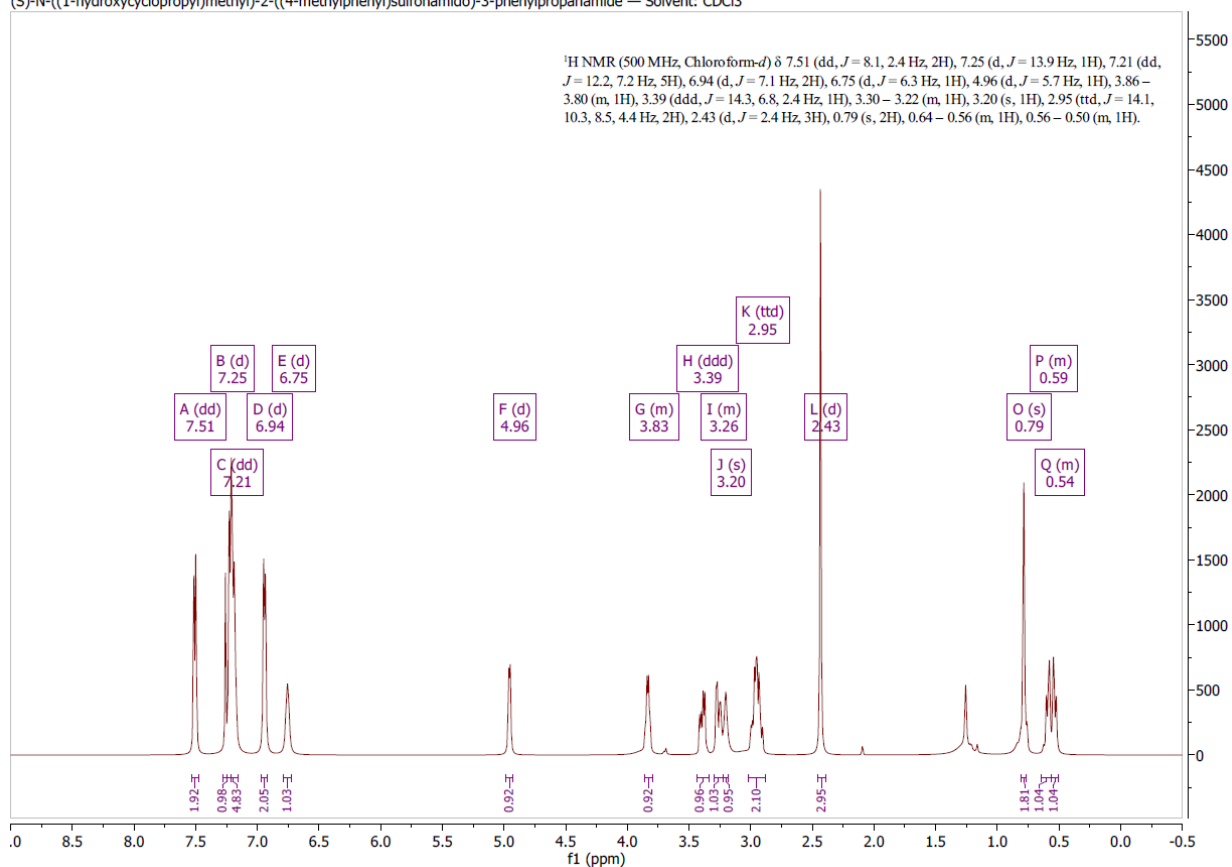
¹H NMR of (S)-N-(2-hydroxy-2-methylpropyl)-2-((4-methylphenyl)sulfonamido)-3-phenylpropanamide (**51**).



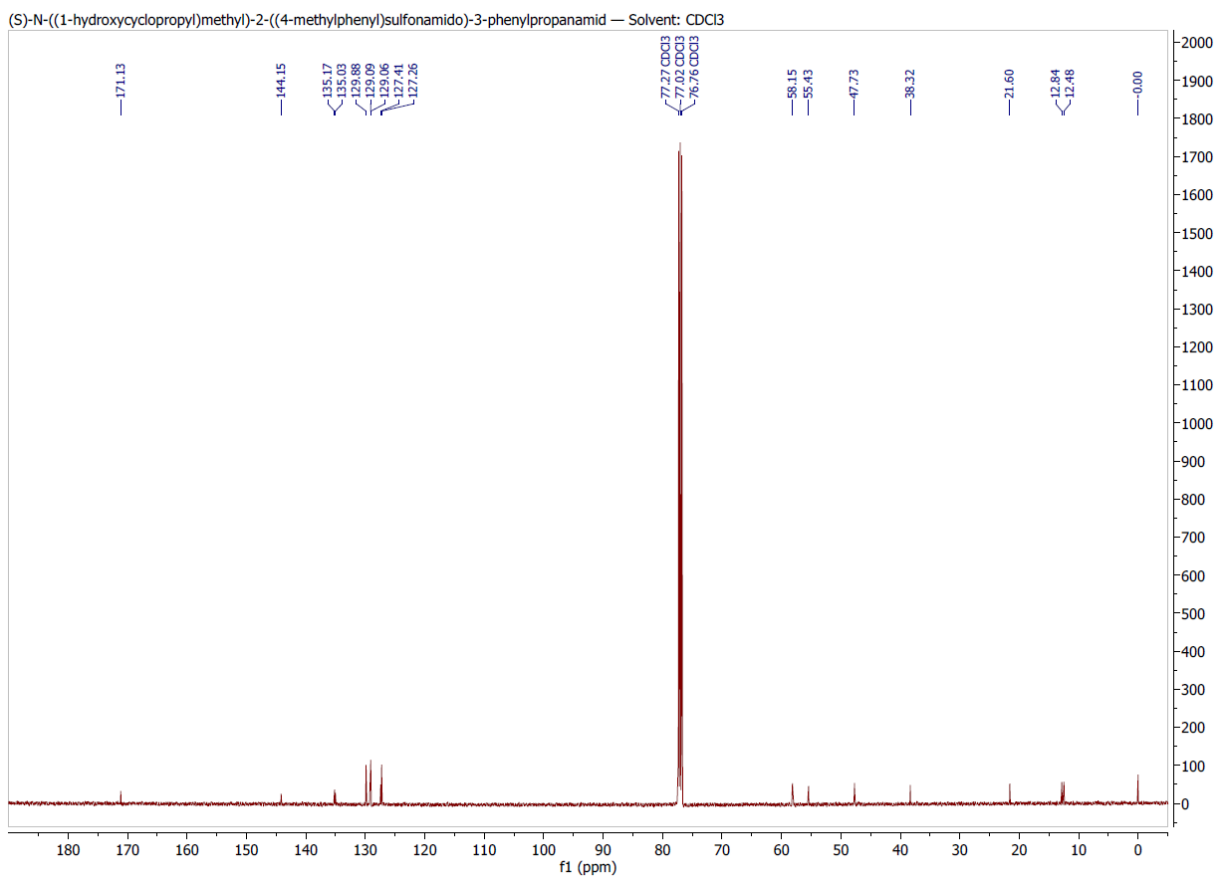
¹³C NMR of (S)-N-(2-hydroxy-2-methylpropyl)-2-((4-methylphenyl)sulfonamido)-3-phenylpropanamide (**51**).



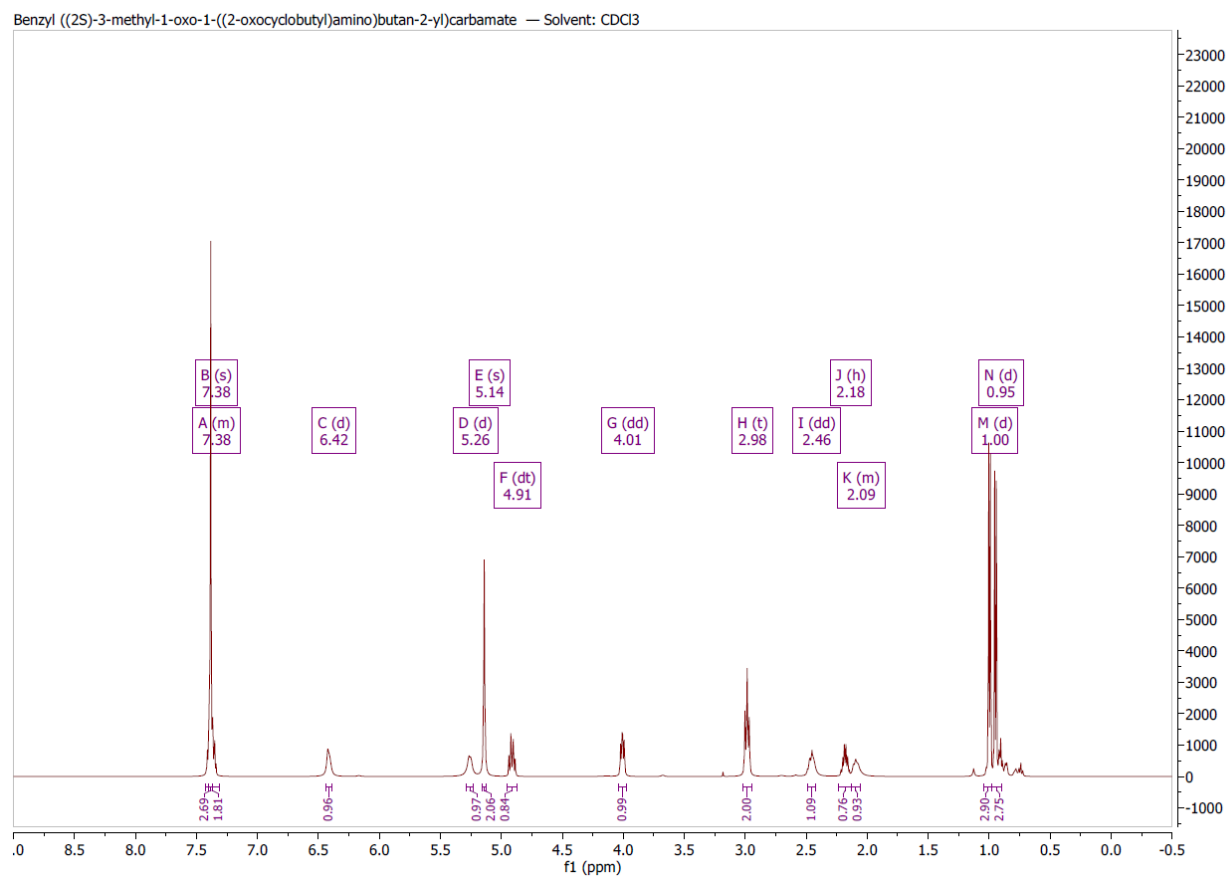
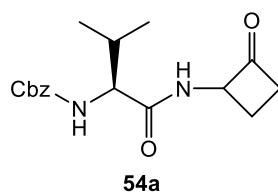
(S)-N-((1-hydroxycyclopropyl)methyl)-2-((4-methylphenyl)sulfonamido)-3-phenylpropanamide — Solvent: CDCl₃



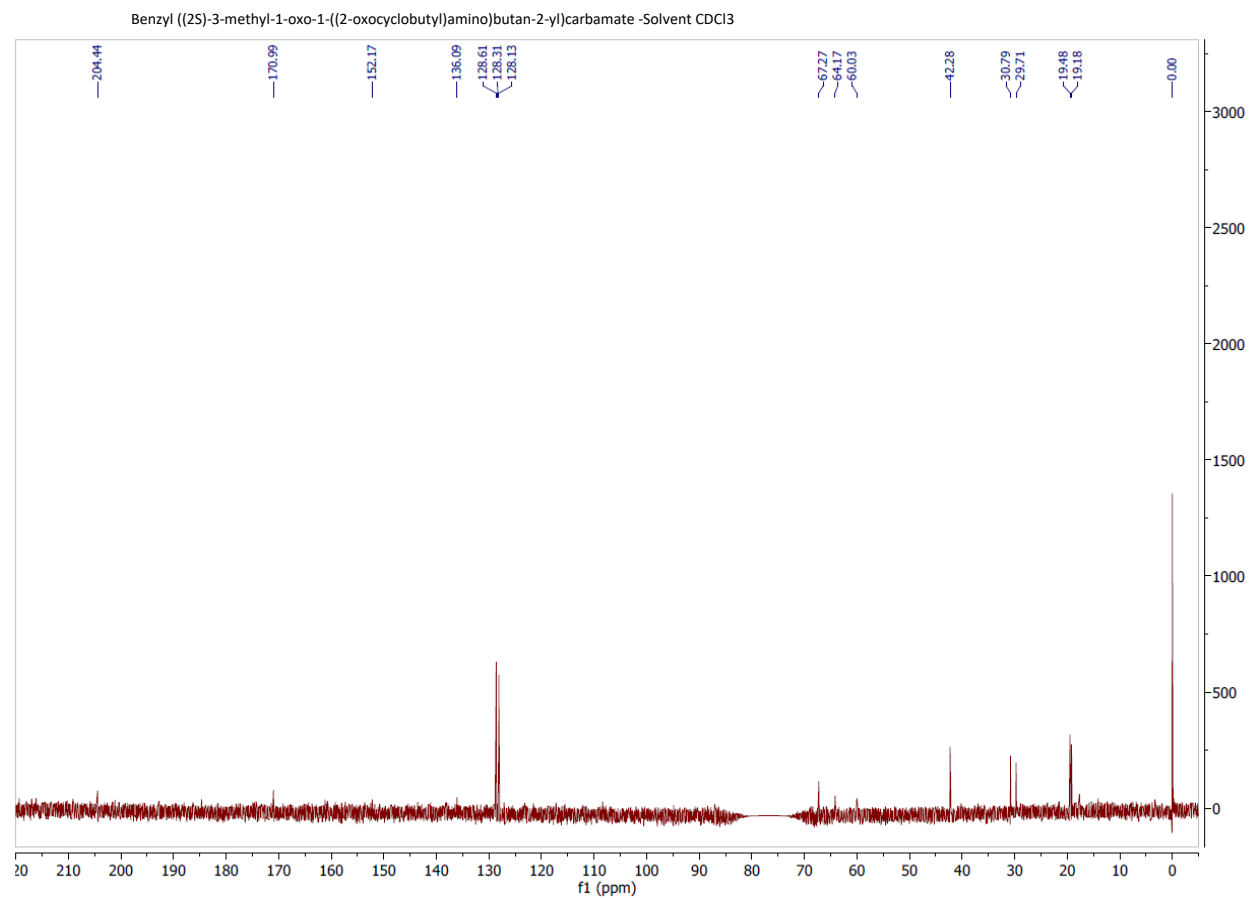
¹H spectrum of (S)-N-((1-hydroxycyclopropyl)methyl)-2-((4-methylphenyl)sulfonamido)-3-phenylpropanamide (**52**).



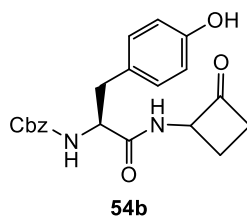
¹³C spectrum of (S)-N-((1-hydroxycyclopropyl)methyl)-2-((4-methylphenyl)sulfonamido)-3-phenylpropanamide (**52**).



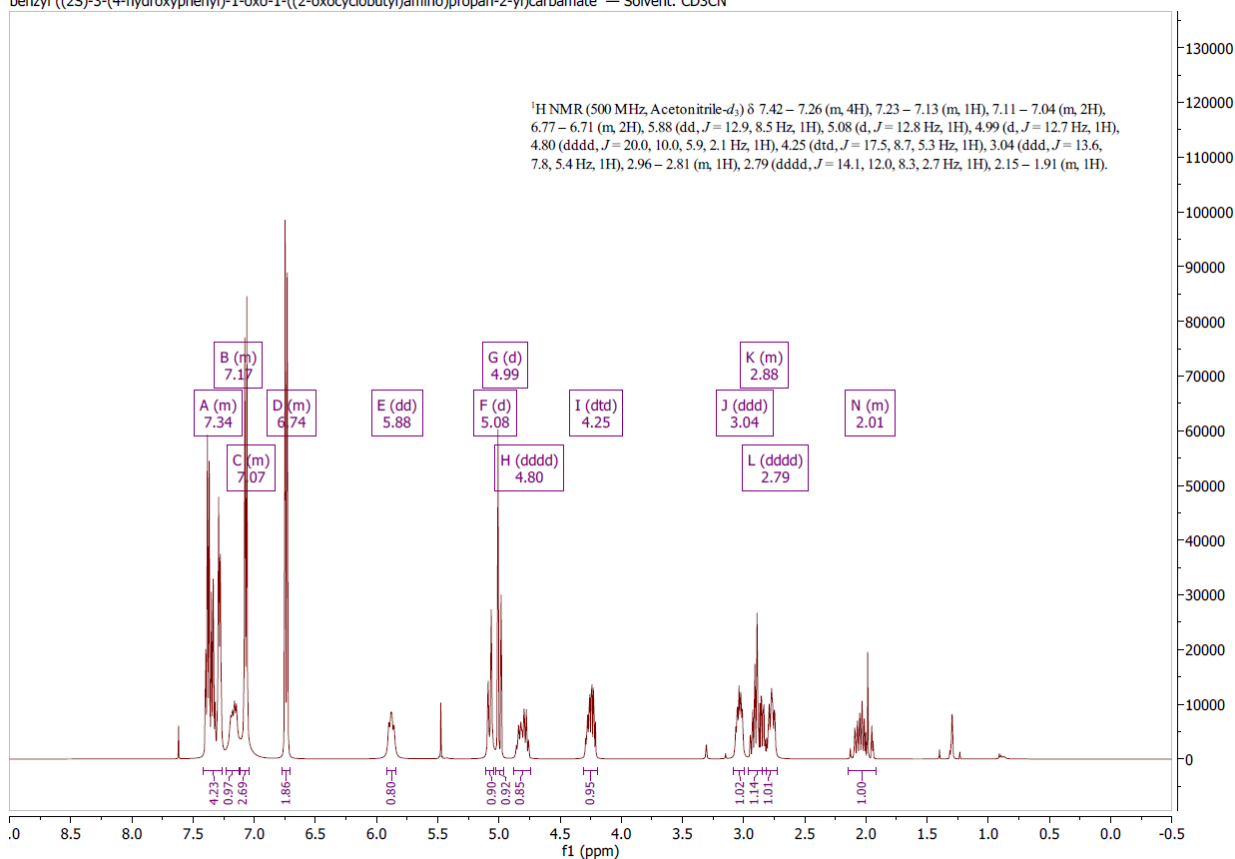
¹H spectrum of benzyl ((2S)-3-methyl-1-oxo-1-((2-oxocyclobutyl)amino)butan-2-yl)carbamate (**54a**).



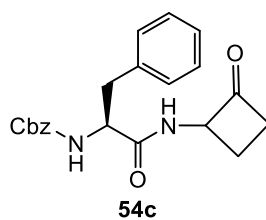
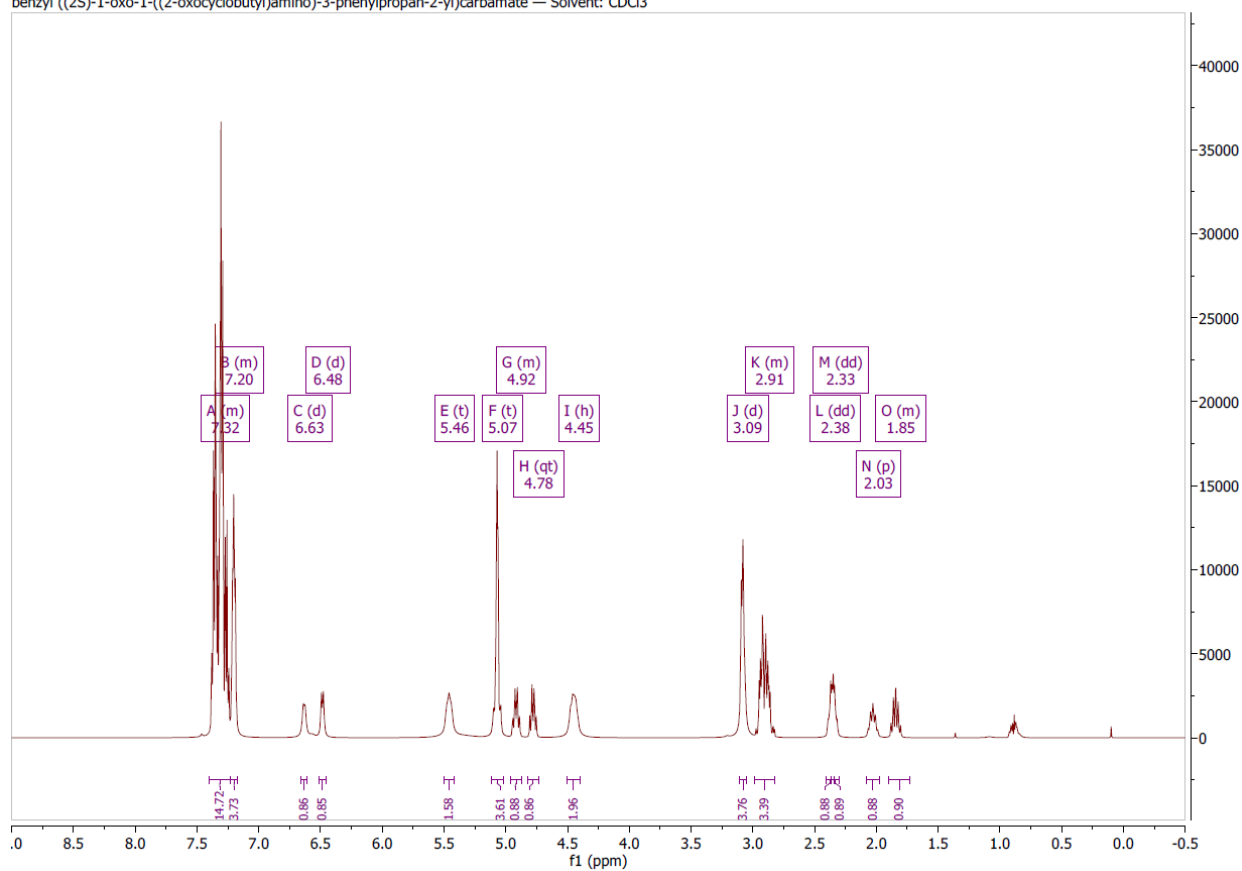
¹³C spectrum of benzyl ((2S)-3-methyl-1-oxo-1-((2-oxocyclobutyl)amino)butan-2-yl)carbamate (**54a**).



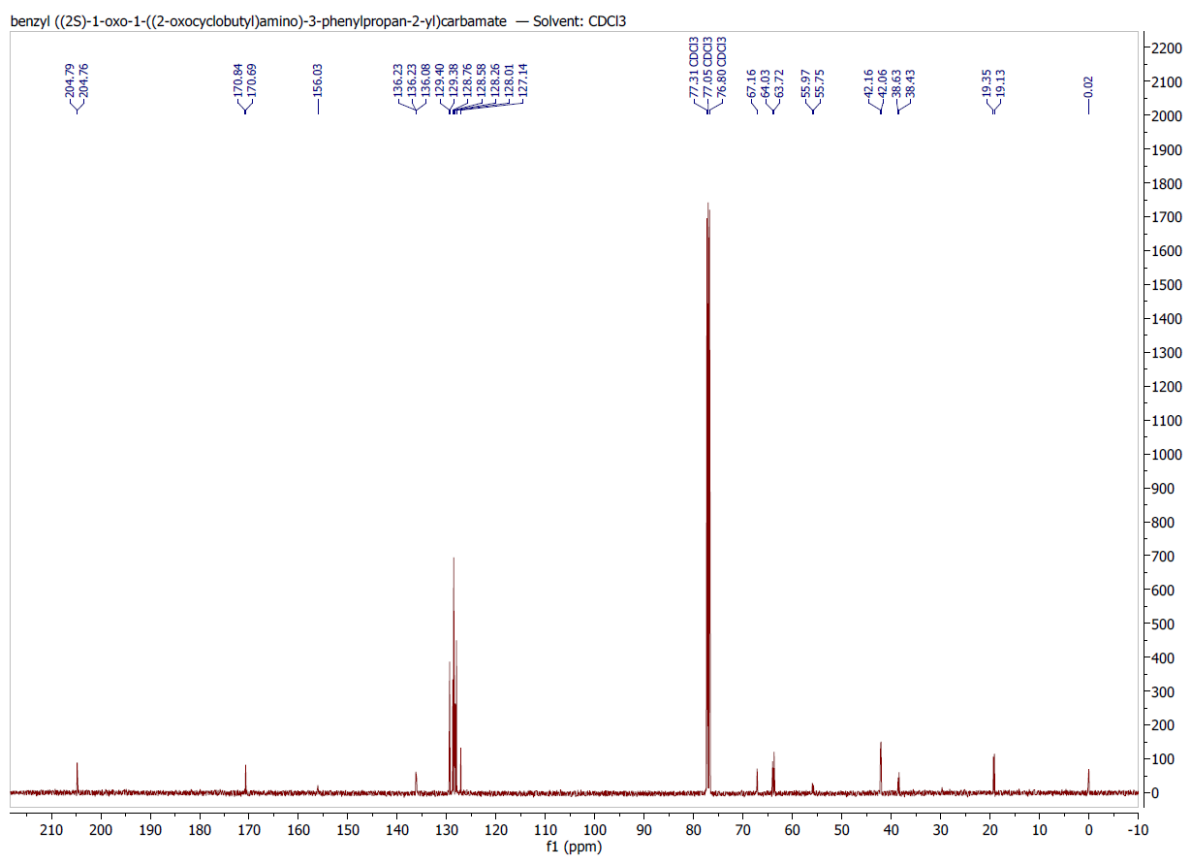
benzyl ((2S)-3-(4-hydroxyphenyl)-1-oxo-1-((2-oxocyclobutyl)amino)propan-2-yl)carbamate — Solvent: CD₃CN



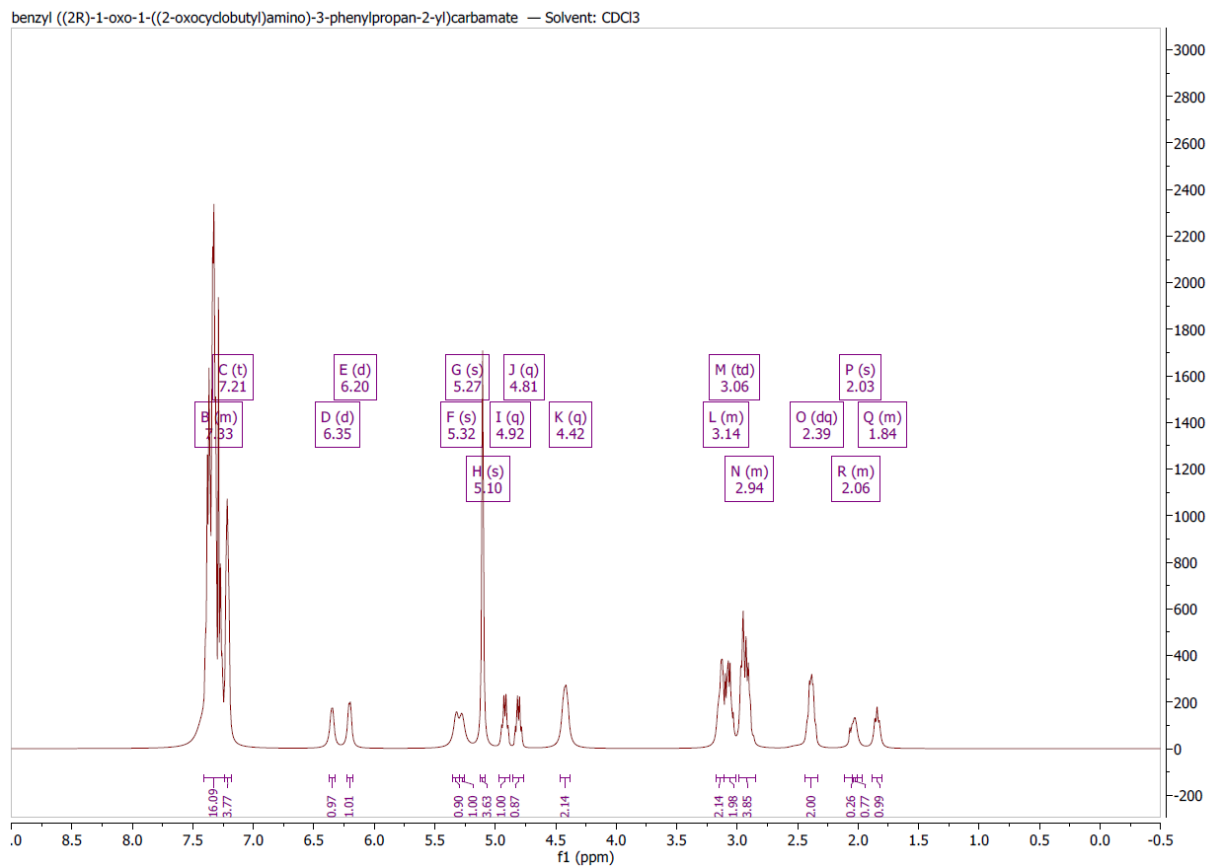
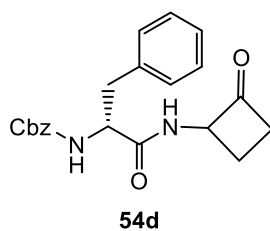
¹H spectrum of benzyl ((2S)-3-(4-hydroxyphenyl)-1-oxo-1-((2-oxocyclobutyl)amino)propan-2-yl)carbamate (**54b**).

benzyl ((2S)-1-oxo-1-((2-oxocyclobutyl)amino)-3-phenylpropan-2-yl)carbamate — Solvent: CDCl₃

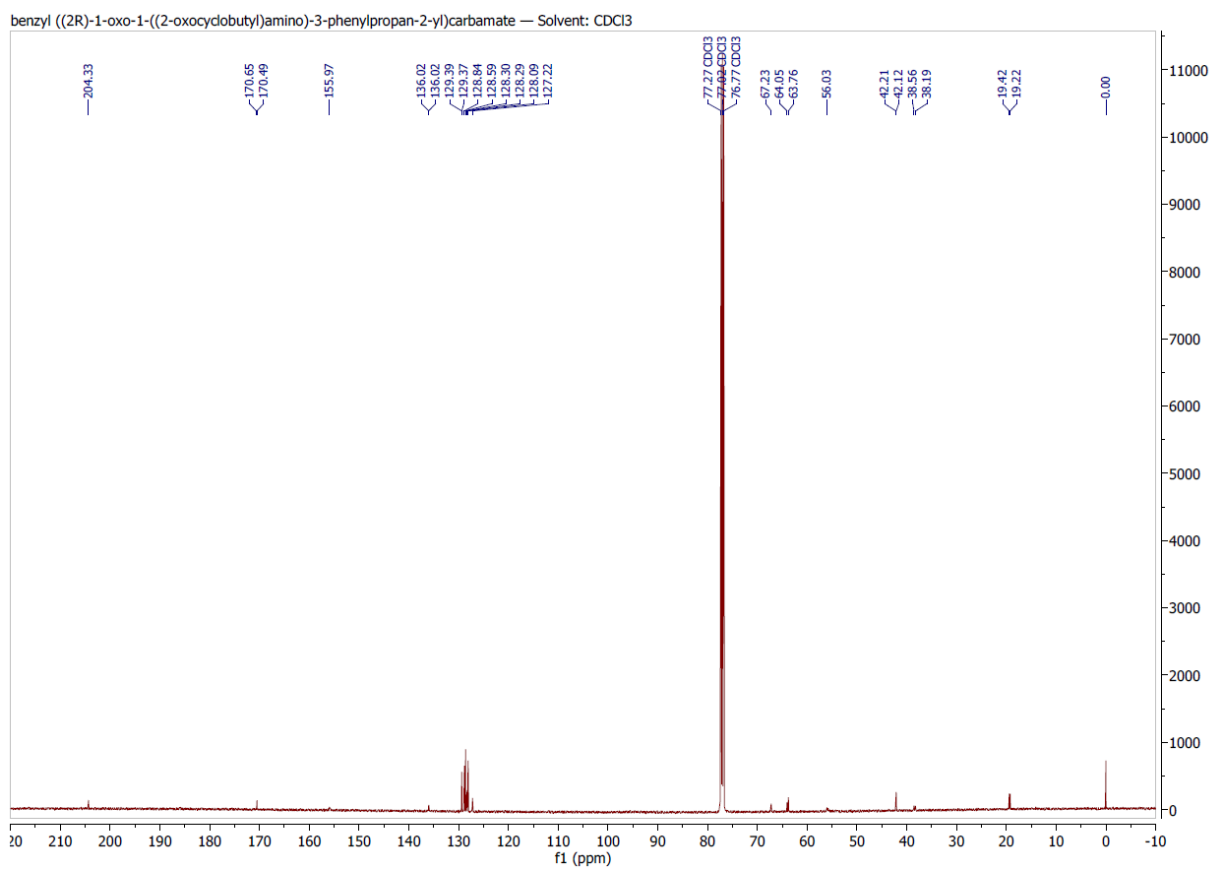
¹H spectrum of benzyl ((2S)-1-oxo-1-((2-oxocyclobutyl)amino)-3-phenylpropan-2-yl)carbamate (**54c**).



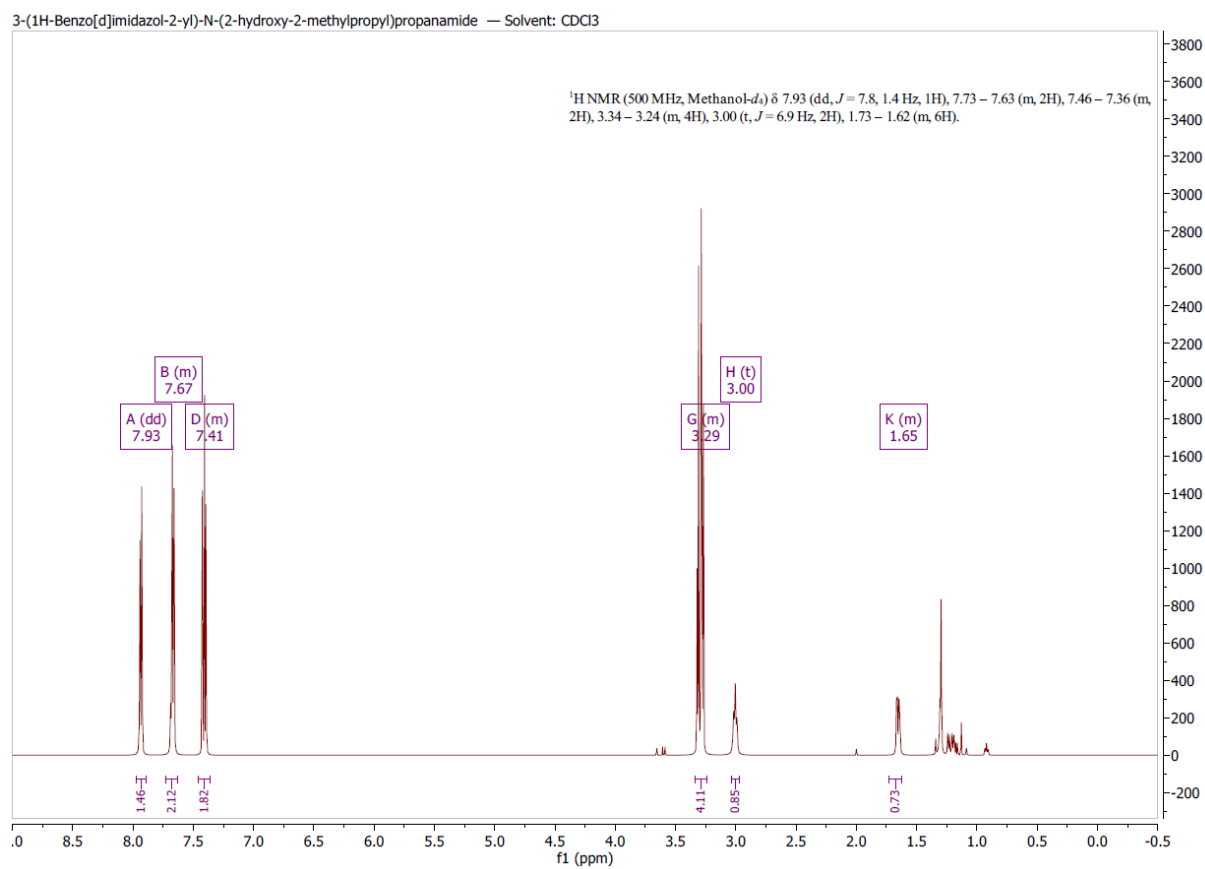
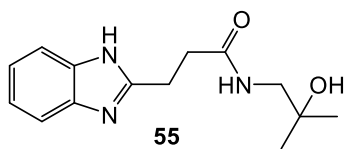
¹³C spectrum of benzyl ((2S)-1-oxo-1-((2-oxocyclobutyl)amino)-3-phenylpropan-2-yl)carbamate (**54c**).



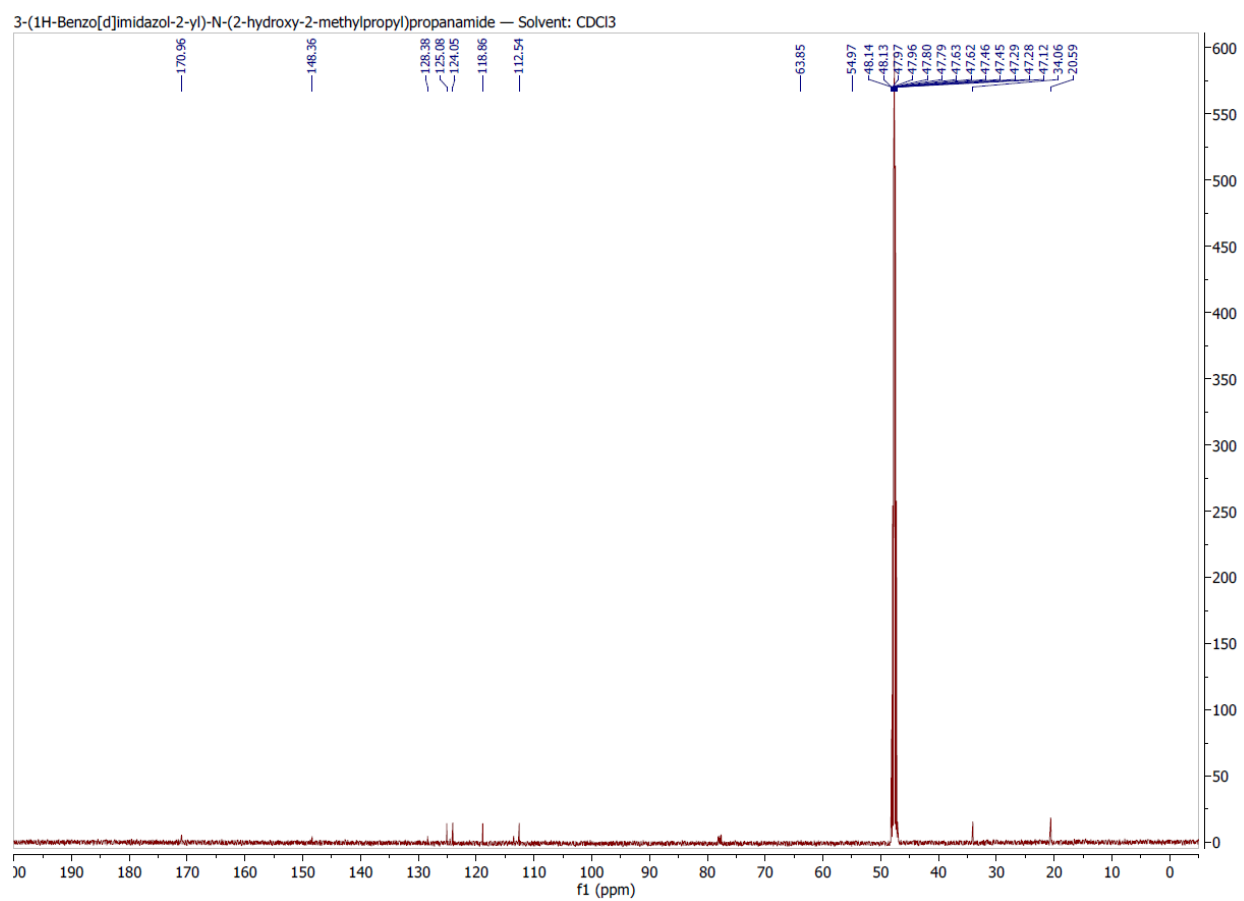
¹H spectrum of benzyl ((2R)-1-oxo-1-((2-oxocyclobutyl)amino)-3-phenylpropan-2-yl)carbamate (**54d**).



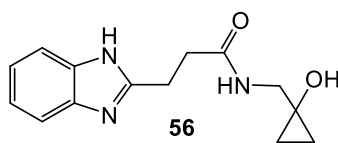
¹³C spectrum of benzyl ((2R)-1-oxo-1-((2-oxocyclobutyl)amino)-3-phenylpropan-2-yl)carbamate (**54d**).



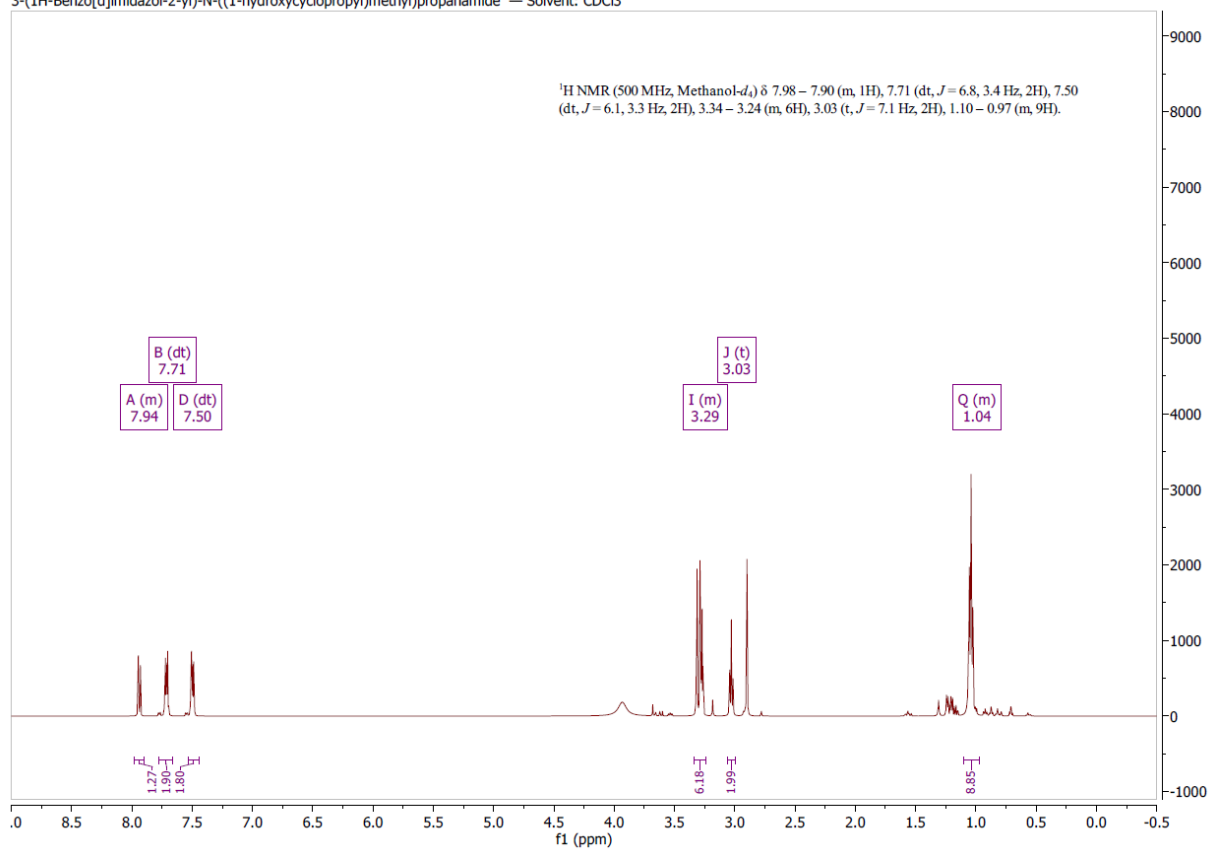
¹H spectrum of (3-(1*H*-benzo[*d*]imidazol-2-yl)-*N*-(2-oxocyclobutyl)propanamide (**55**).



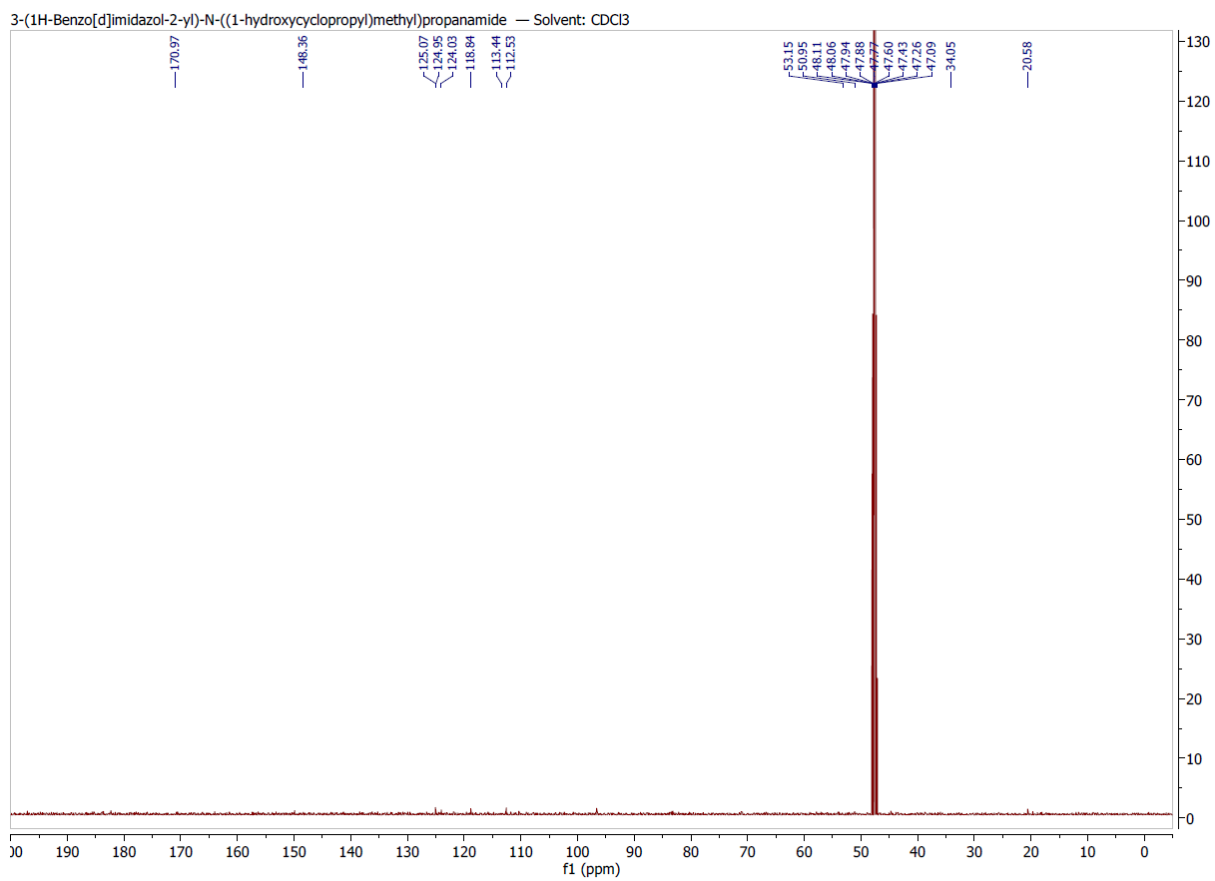
¹³C spectrum of (3-(1*H*-benzo[*d*]imidazol-2-yl)-*N*-(2-oxocyclobutyl)propanamide (**55**).



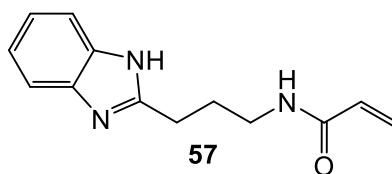
3-(1H-Benzo[d]imidazol-2-yl)-N-((1-hydroxycyclopropyl)methyl)propanamide — Solvent: CDCl₃



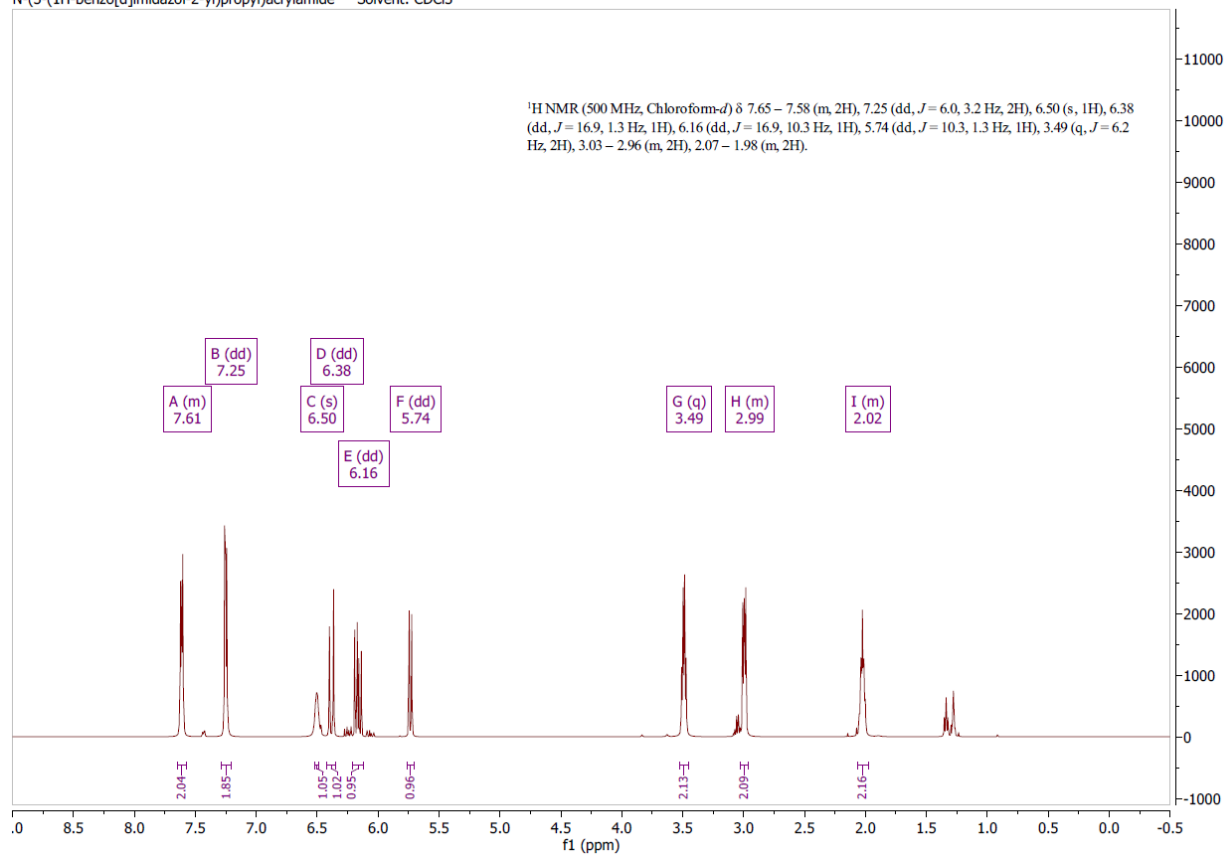
¹H spectrum of 3-(1H-benzo[d]imidazol-2-yl)-N-((1 hydroxycyclopropyl)methyl)propanamide (**56**).



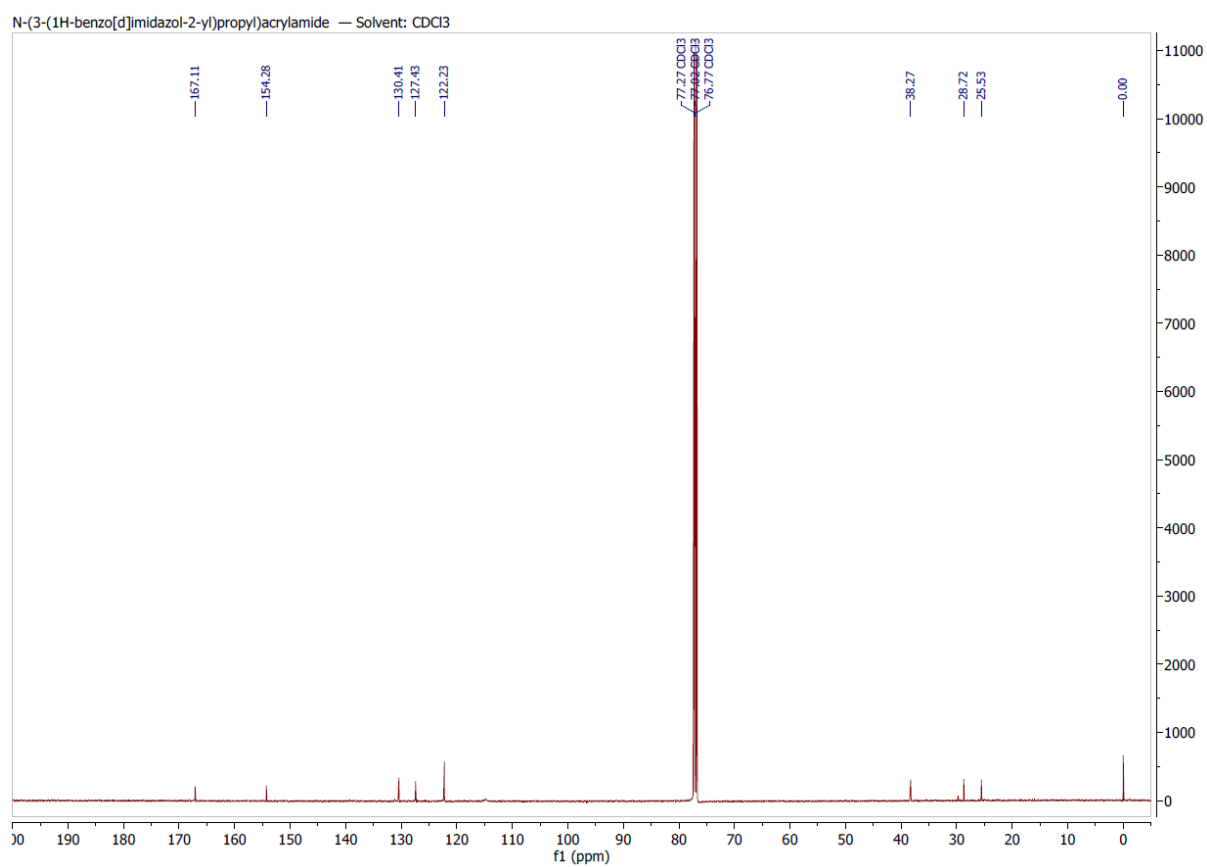
¹³C spectrum of 3-(1H-benzo[d]imidazol-2-yl)-N-((1-hydroxycyclopropyl)methyl)propanamide (56).



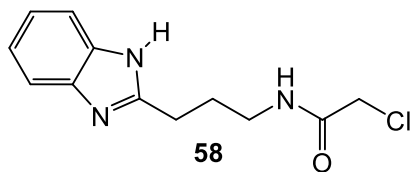
N-(3-(1H-benzo[d]imidazol-2-yl)propyl)acrylamide — Solvent: CDCl₃



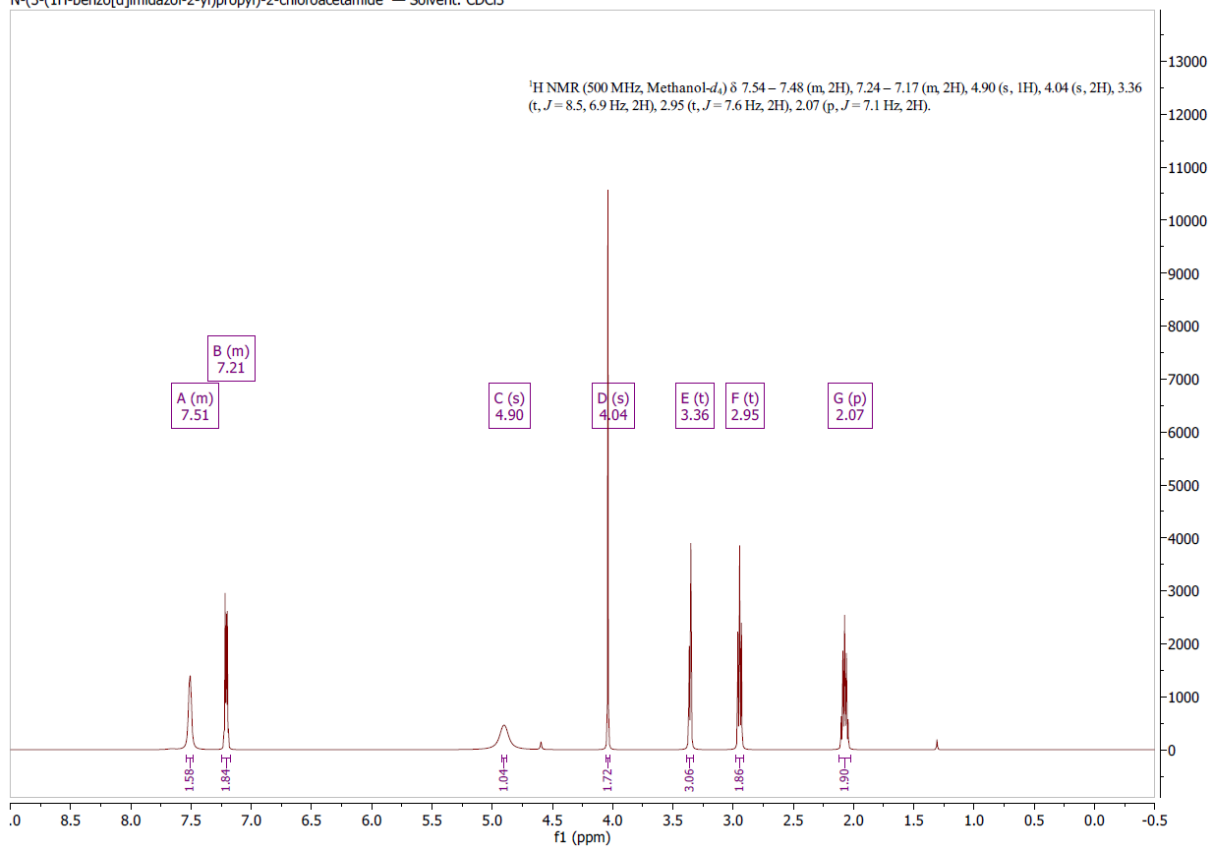
¹H spectrum of *N*-(3-(1H-benzo[d]imidazol-2-yl)propyl)acrylamide (**57**).



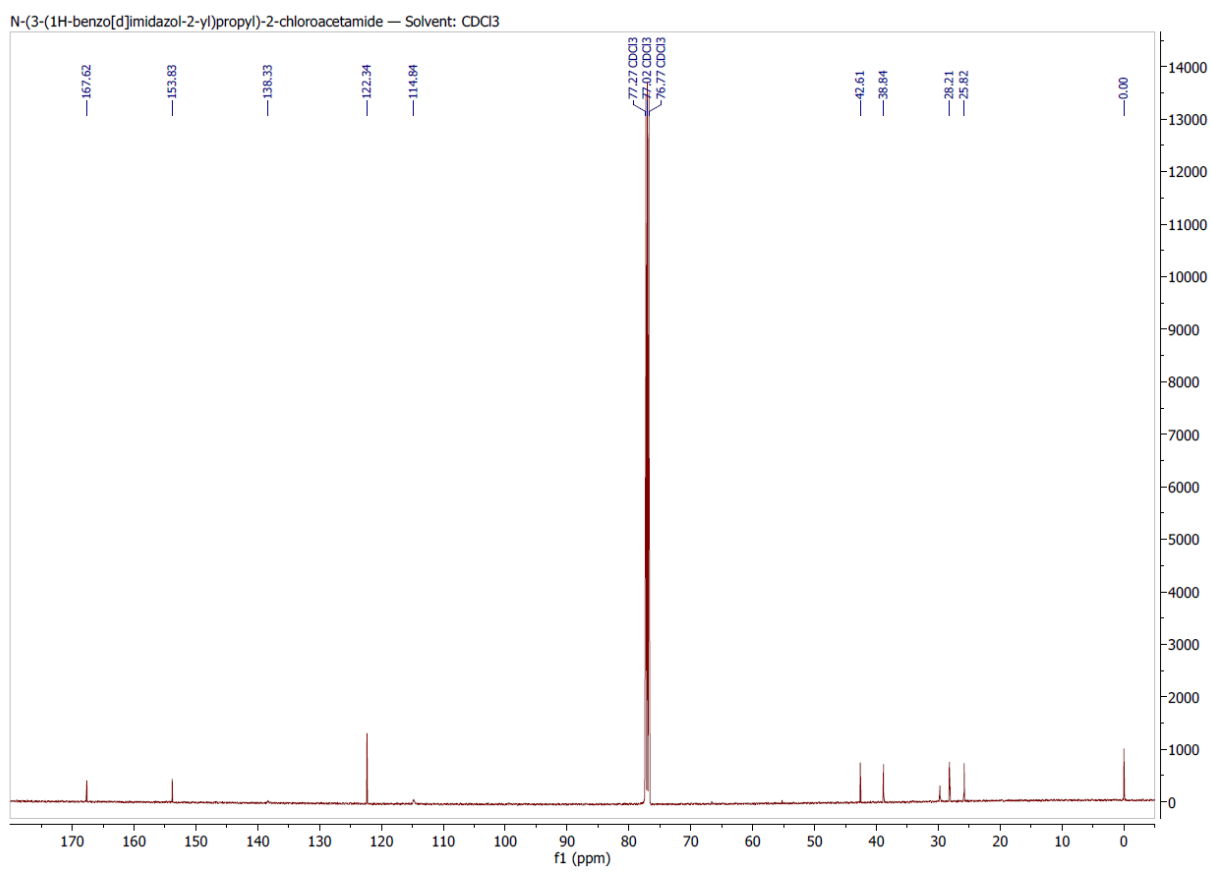
¹³C spectrum of *N*-(3-(1H-benzo[d]imidazol-2-yl)propyl)acrylamide (**57**).



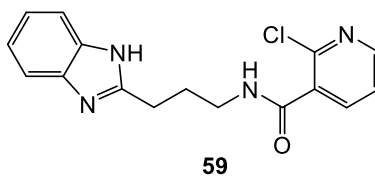
N-(3-(1H-benzo[d]imidazol-2-yl)propyl)-2-chloroacetamide — Solvent: CDCl₃



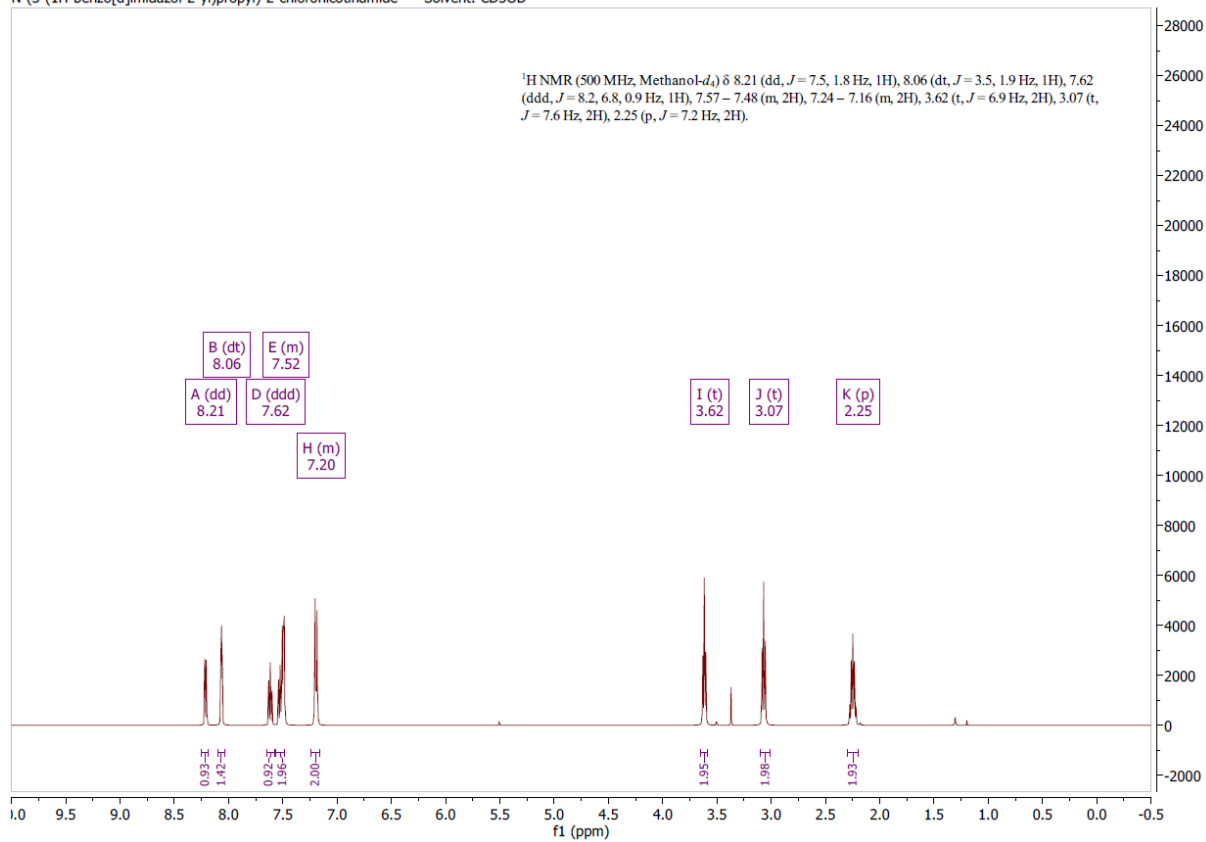
¹H spectrum of *N*-(3-(1H-benzo[d]imidazol-2-yl)propyl)-2-chloroacetamide (**58**).



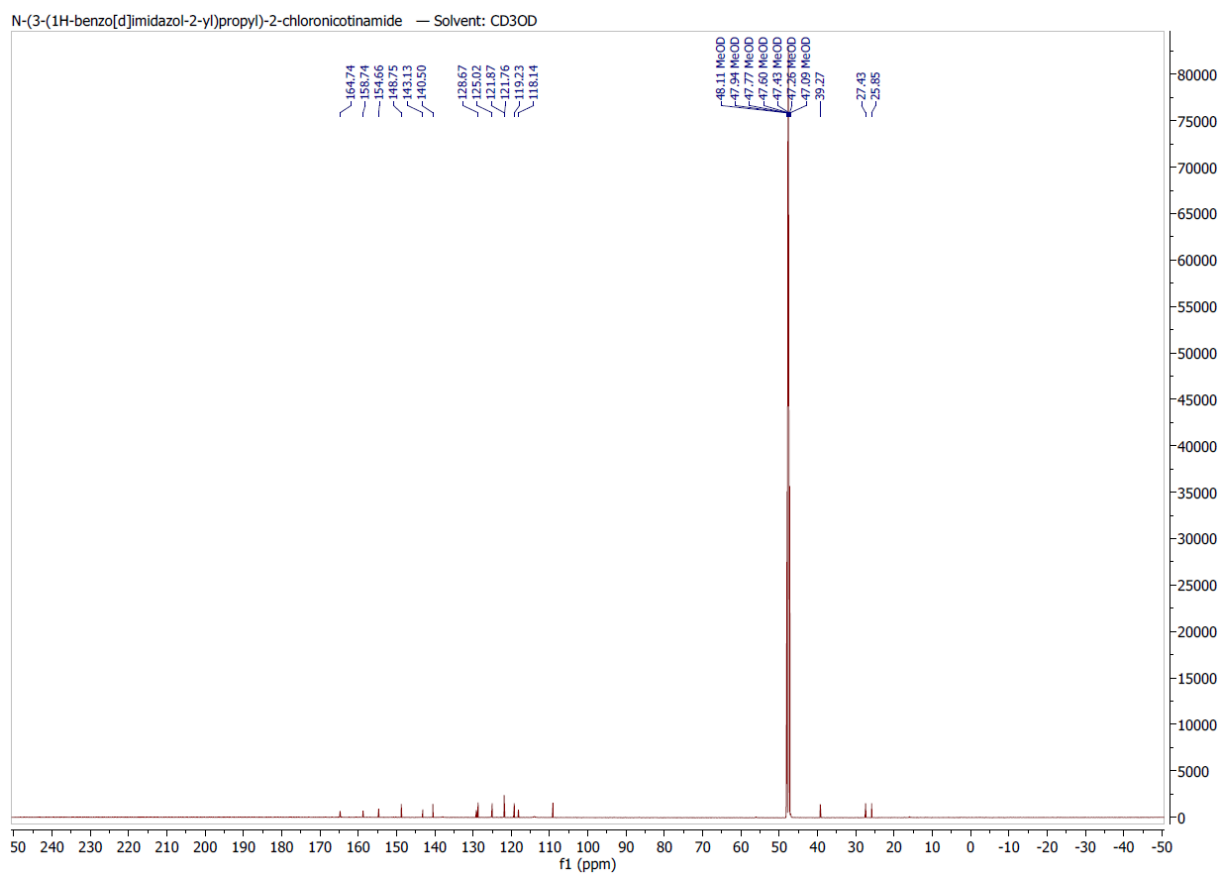
¹³C spectrum of *N*-(3-(1H-benzo[d]imidazol-2-yl)propyl)-2-chloroacetamide (**58**).



N-(3-(1H-benzo[d]imidazol-2-yl)propyl)-2-chloronicotinamide — Solvent: CD3OD



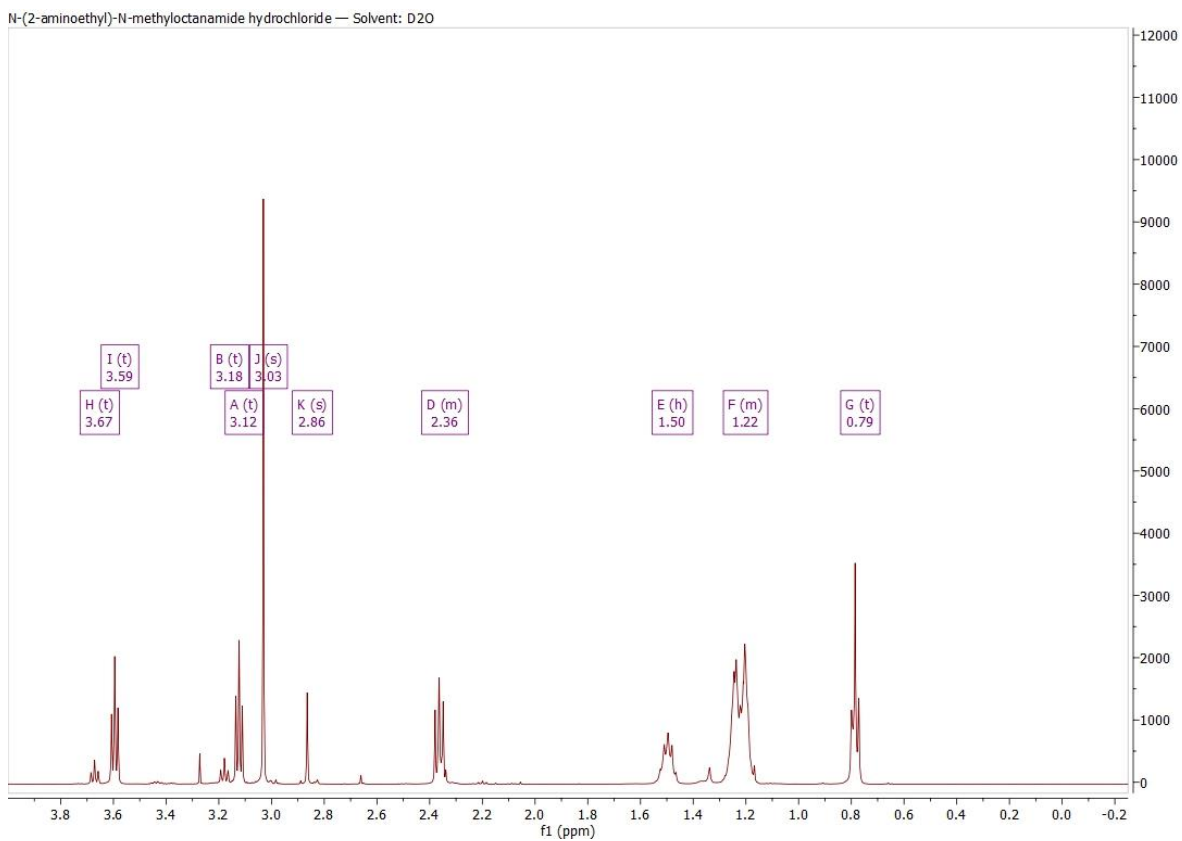
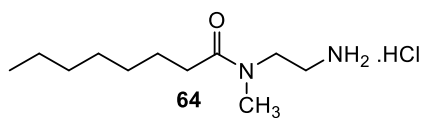
¹H spectrum of *N*-(3-(1H-benzo[d]imidazol-2-yl)propyl)-2-chloronicotinamide (**59**).



^{13}C spectrum of *N*-(3-(1H-benzo[d]imidazol-2-yl)propyl)-2-chloronicotinamide (**59**).

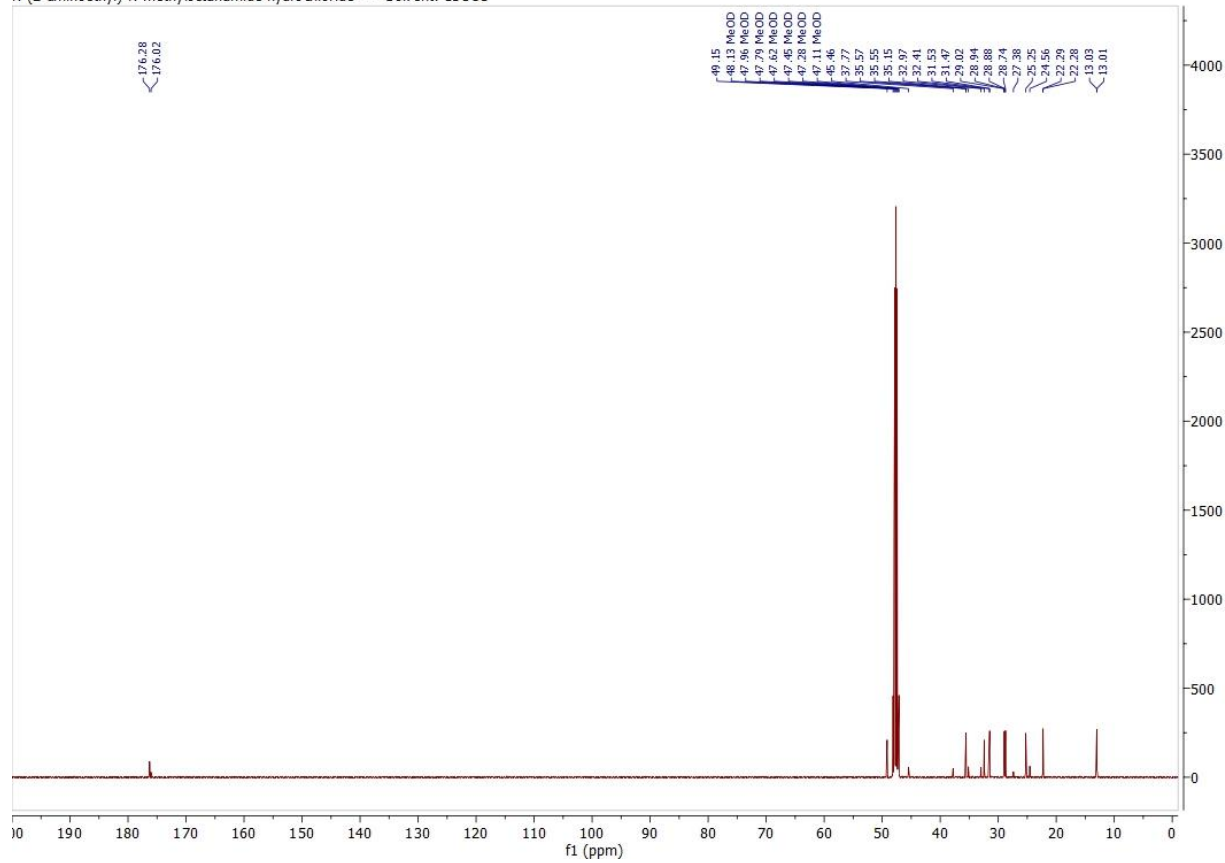
APPENDIX D
SUPPLEMENTAL DATA FOR CHAPTER FIVE

NMR spectra of the compounds reported in chapter five.

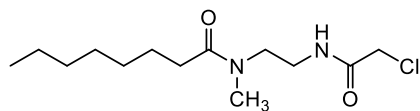


^1H NMR of *N*-(2-aminoethyl)-*N*-methyloctanamide hydrochloride (**64**, NANMO).

N-(2-aminoethyl)-N-methyloctanamide hydrochloride — Solvent: CD3OD



¹³C NMR of N-(2-aminoethyl)-N-methyloctanamide hydrochloride (**64**, NANMO).

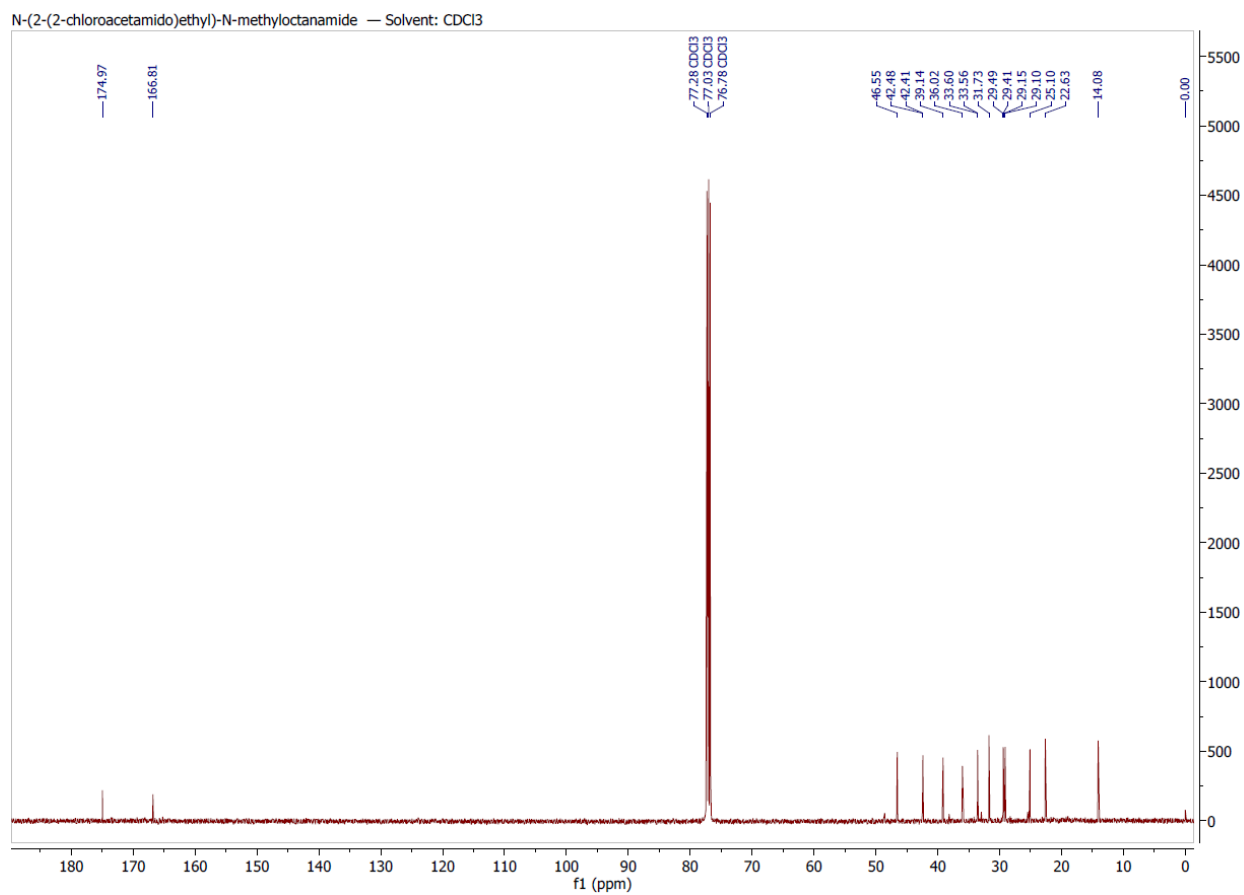


65

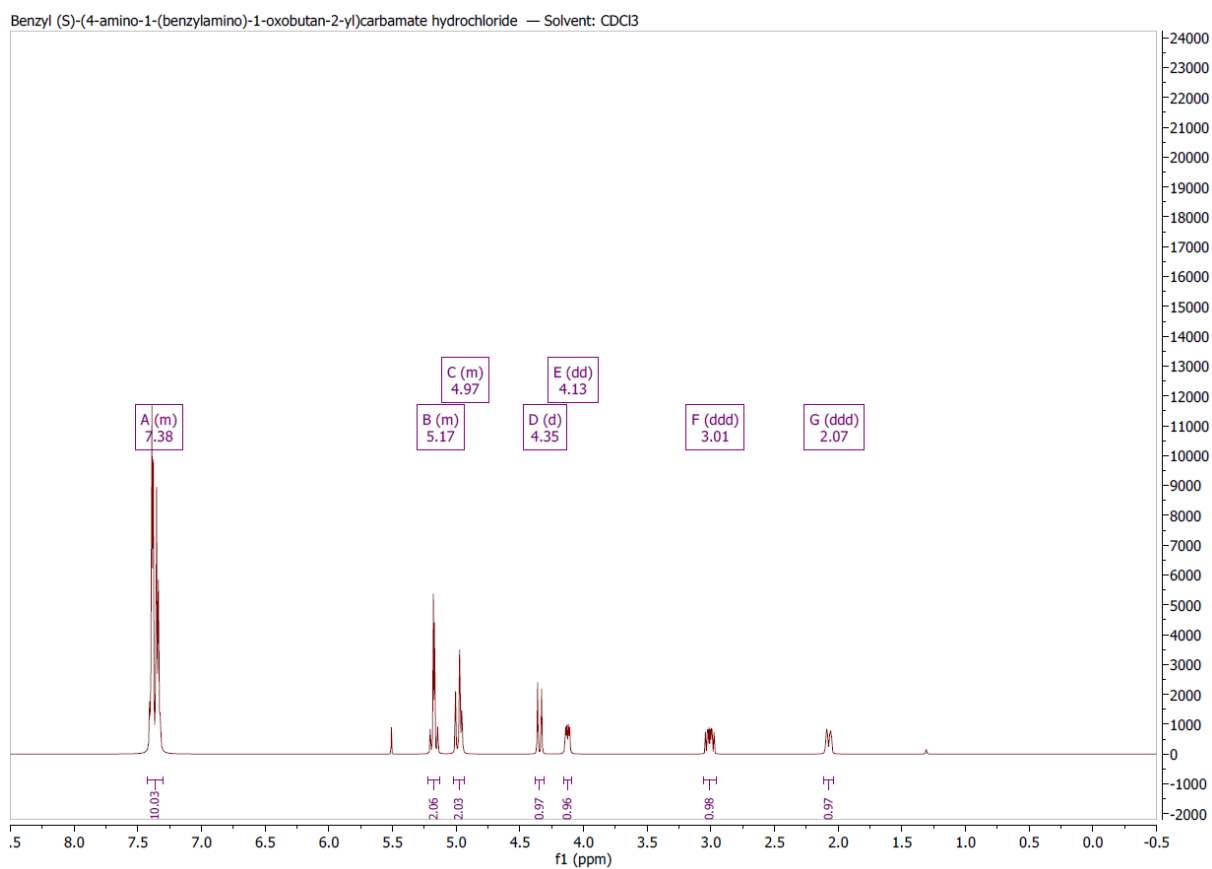
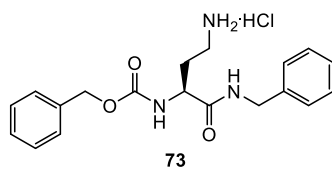
N-(2-(2-chloroacetamido)ethyl)-N-methyloctanamide — Solvent: CDCl₃



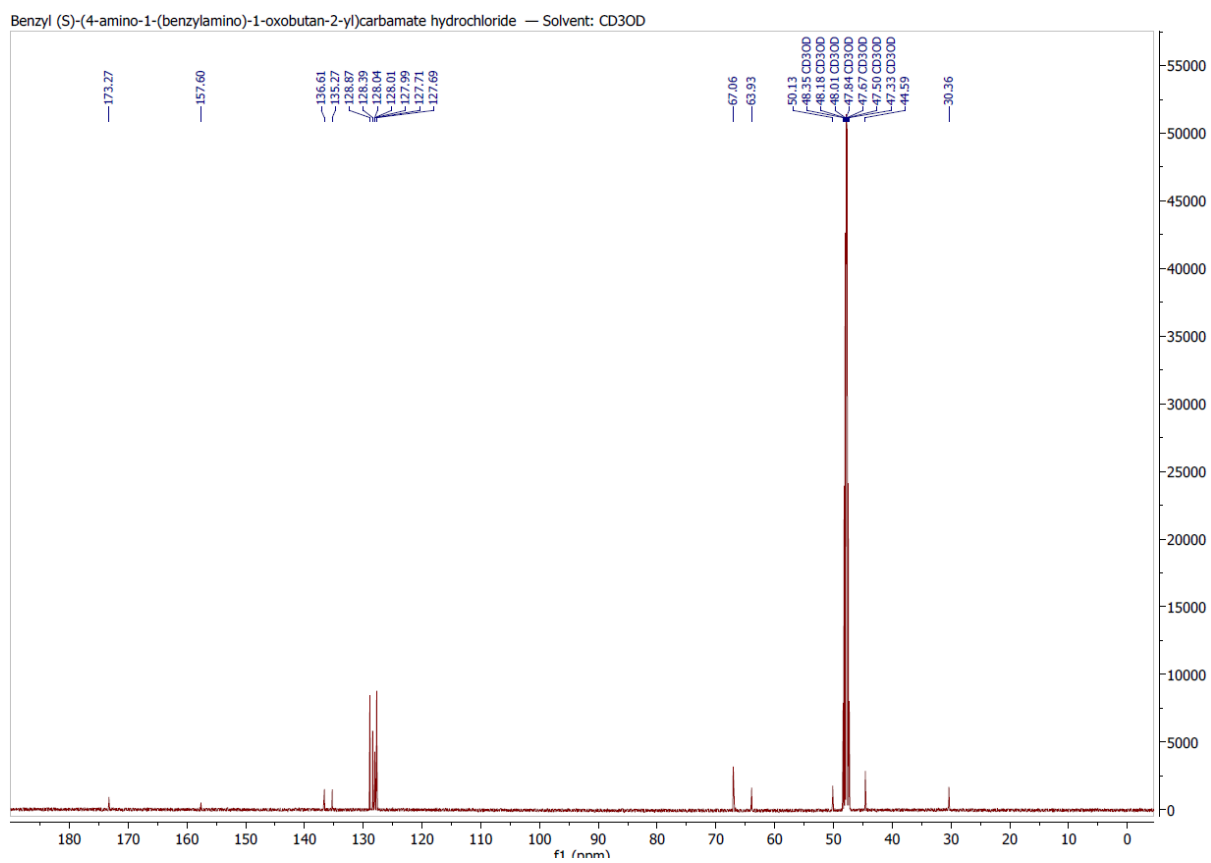
¹H NMR of *N*-(2-(2-chloroacetamido)ethyl)-*N*-methyloctanamide (**65**).



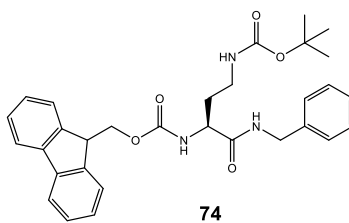
¹³C NMR of *N*-(2-(2-chloroacetamido)ethyl)-*N*-methyloctanamide (**65**).



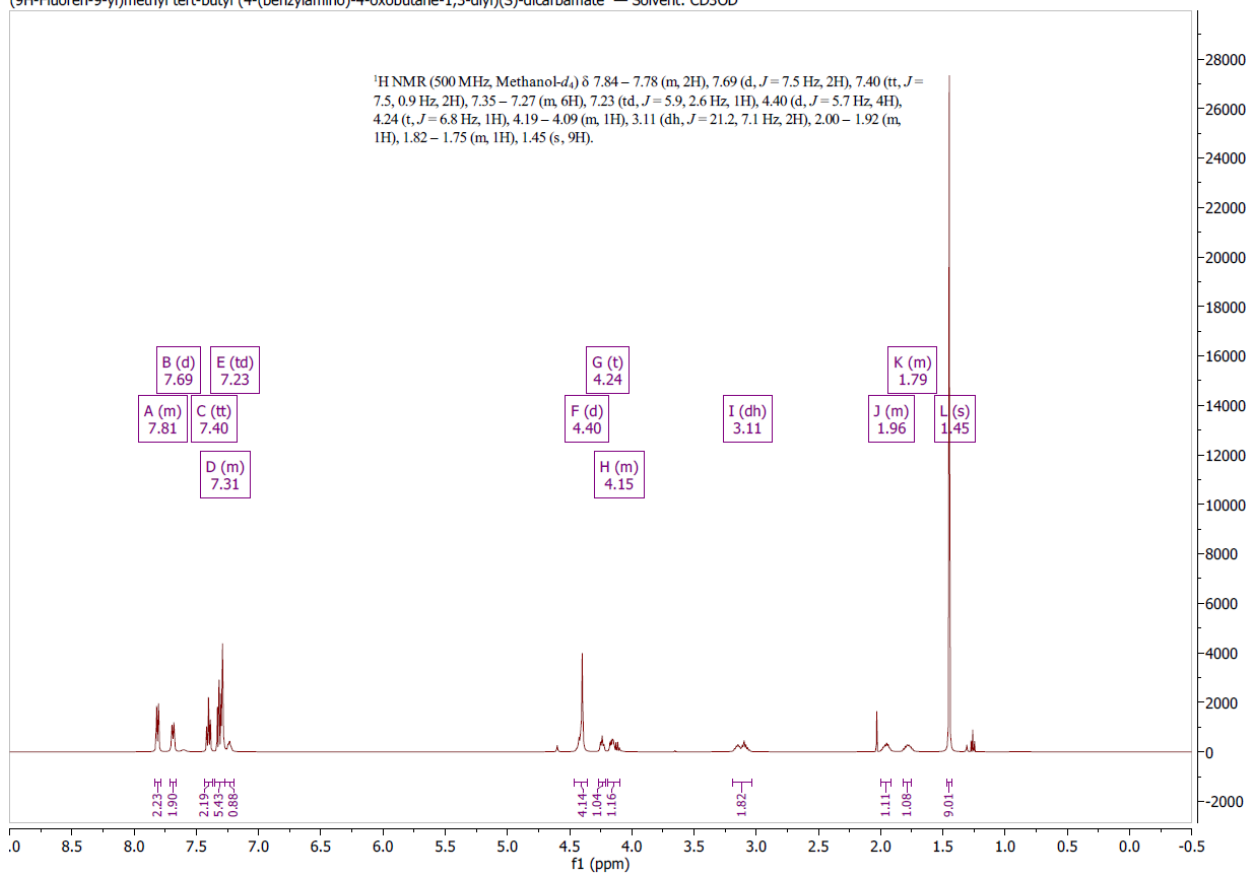
¹H NMR of benzyl (S)-(4-amino-1-(benzylamino)-1-oxobutan-2-yl)carbamate hydrochloride (**73**).



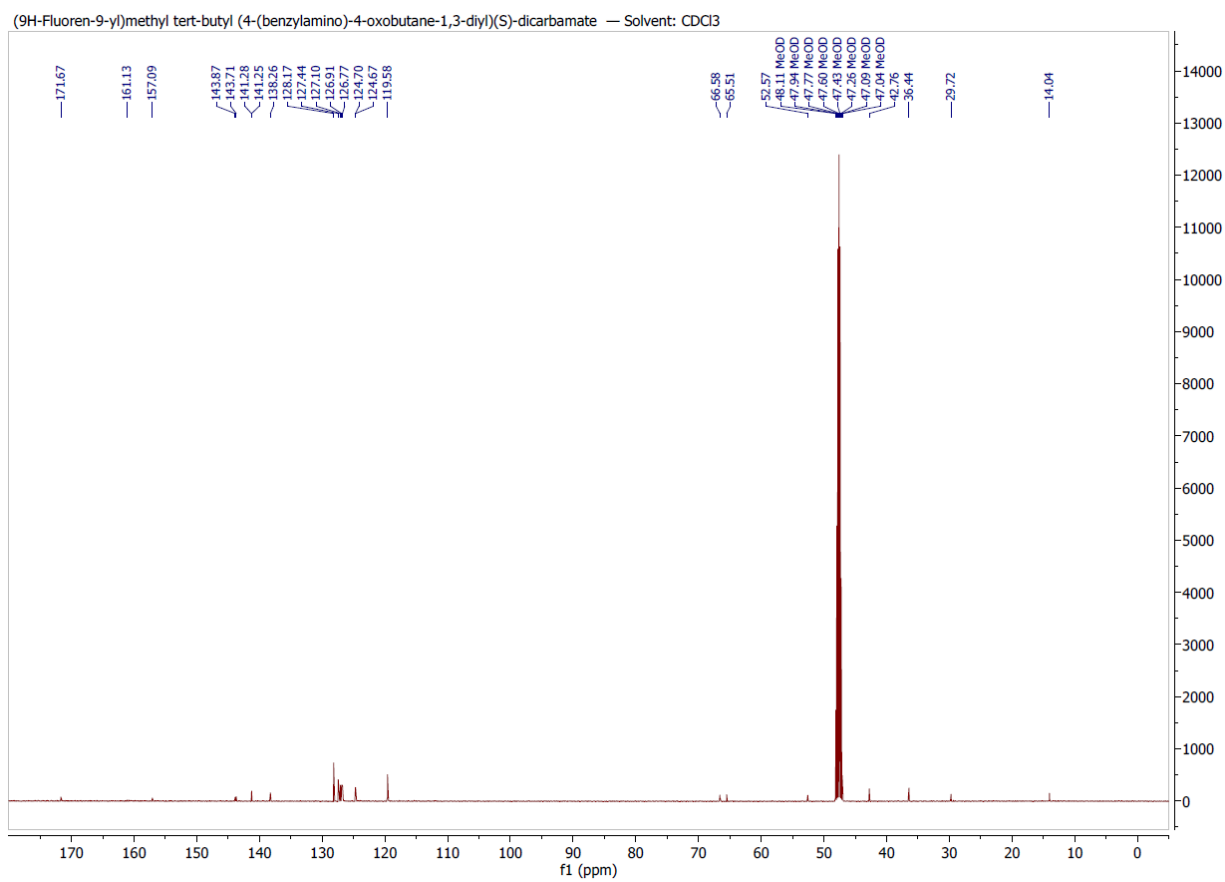
^{13}C NMR of benzyl (S)-(4-amino-1-(benzylamino)-1-oxobutan-2-yl)carbamate hydrochloride (**73**).



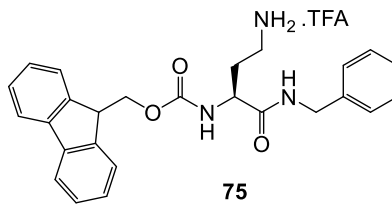
(9H-Fluoren-9-yl)methyl *tert*-butyl (4-(benzylamino)-4-oxobutane-1,3-diyl)(*S*)-dicarbamate — Solvent: CD₃OD



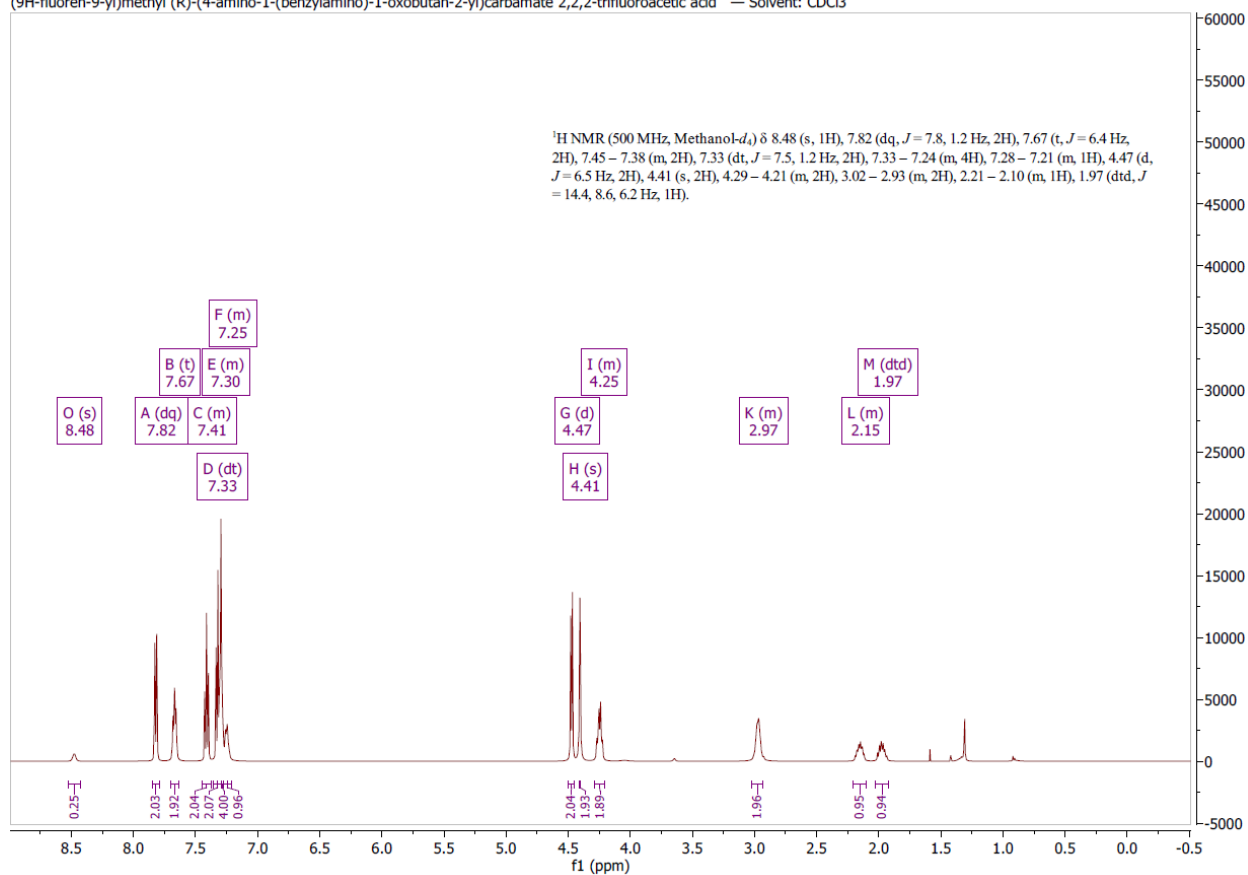
¹H NMR of (9H-fluoren-9-yl)methyl *tert*-butyl (4-(benzylamino)-4-oxobutane-1,3-diyl)-(*S*)-dicarbamate (**74**).



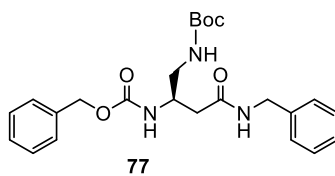
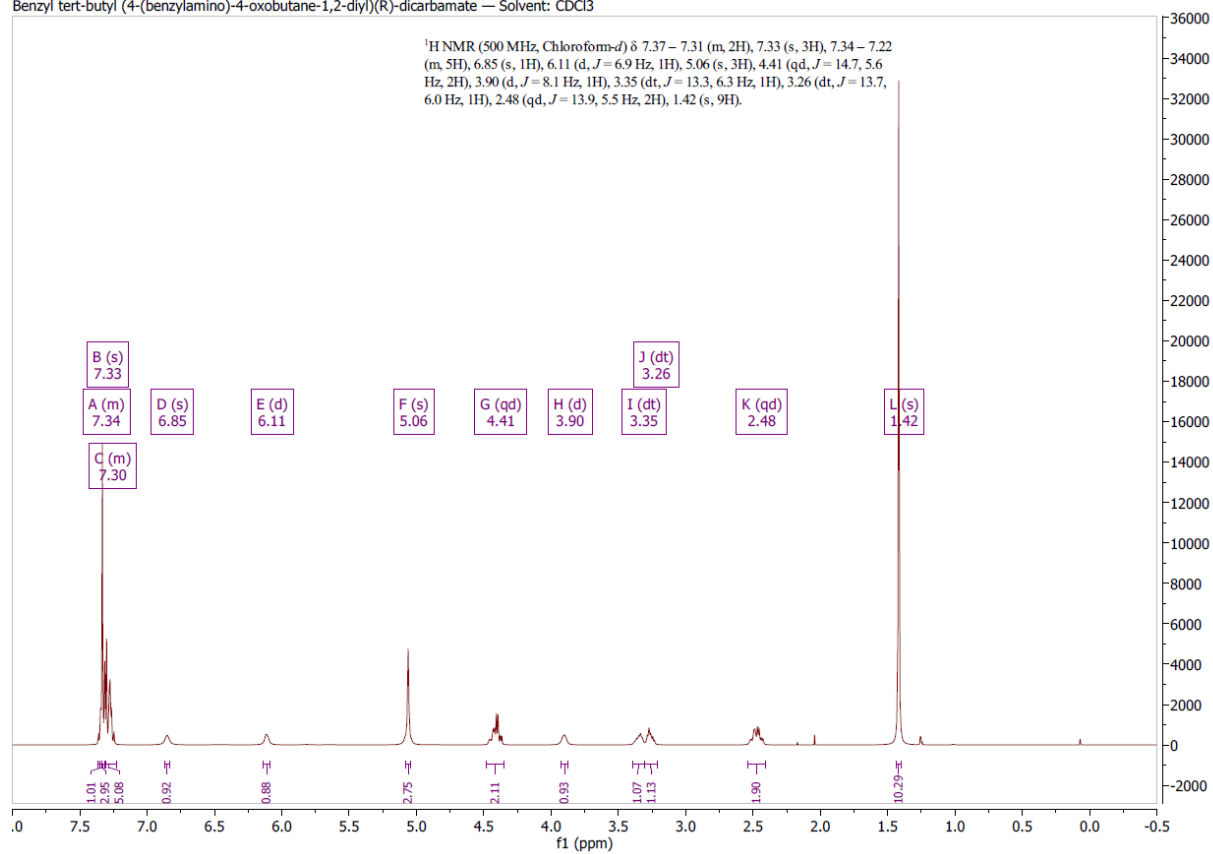
¹³C NMR of (9H-fluoren-9-yl)methyl *tert*-butyl (4-(benzylamino)-4-oxobutane-1,3-diyl)-(*S*)-dicarbamate (**74**).

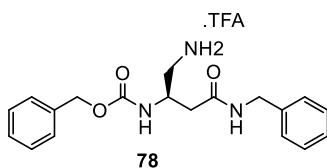


(9H-fluoren-9-yl)methyl (R)-(4-amino-1-(benzylamino)-1-oxobutan-2-yl)carbamate 2,2,2-trifluoroacetic acid — Solvent: CDCl₃

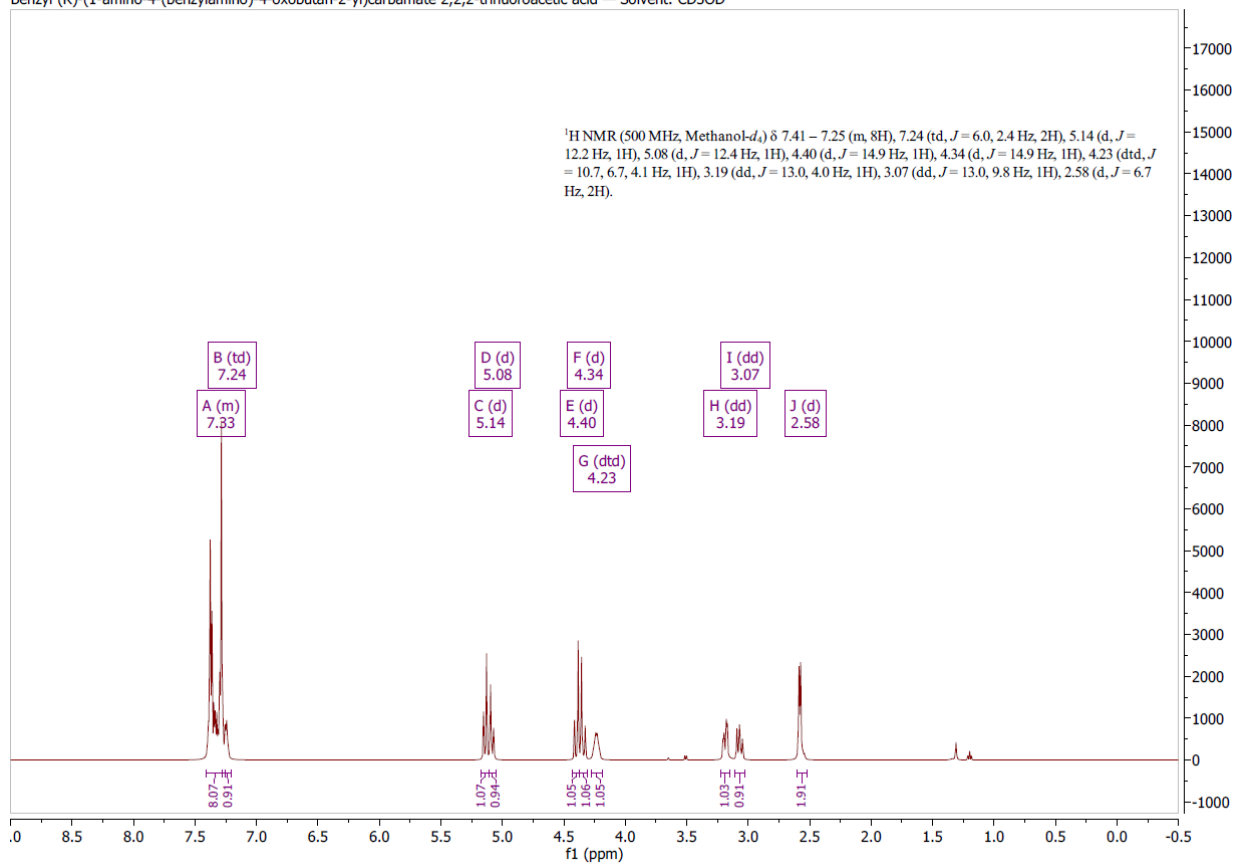


¹H NMR of (9H-fluoren-9-yl)methyl (*S*)-(4-amino-1-(benzylamino)-1-oxobutan-2-yl)carbamate 2,2,2-trifluoroacetic acid (**75**).

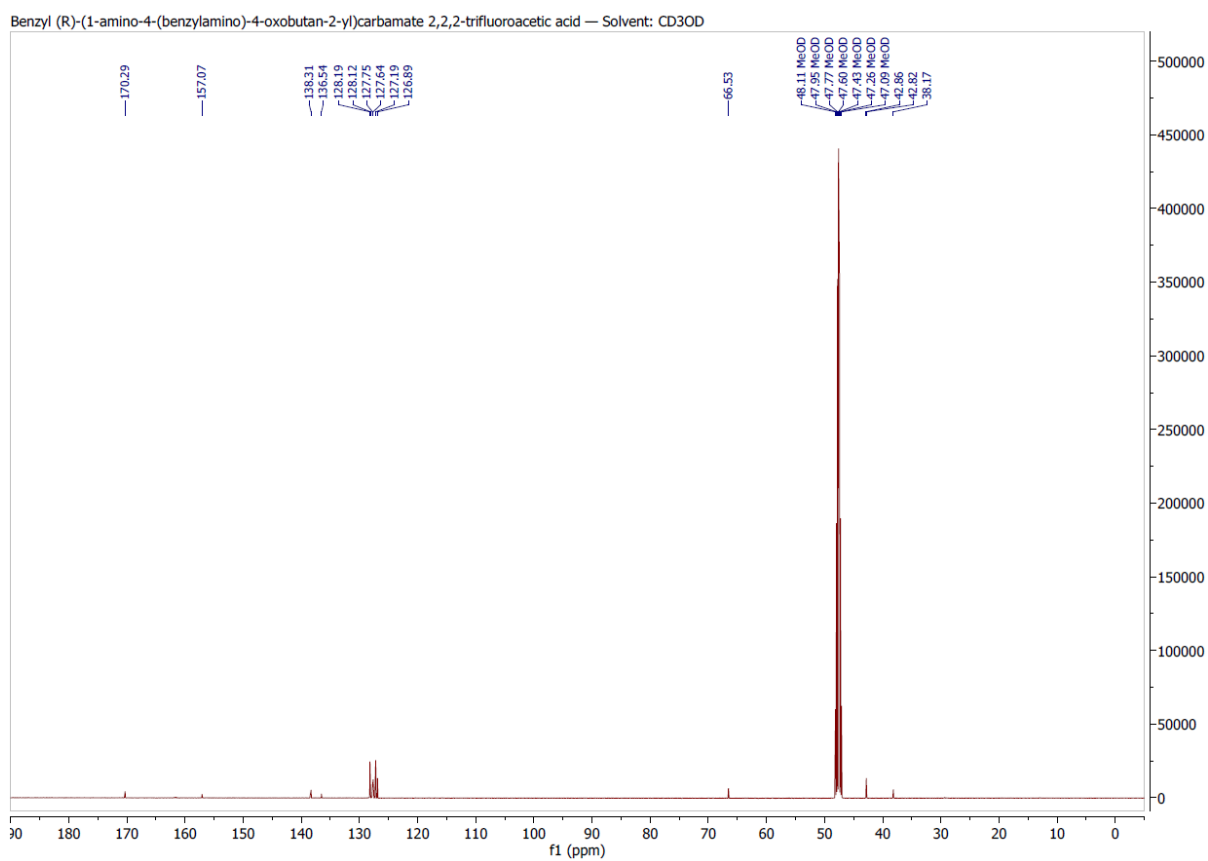
Benzyl *tert*-butyl (4-(benzylamino)-4-oxobutane-1,2-diyl)(*R*)-dicarbamate — Solvent: CDCl₃¹H NMR of benzyl *tert*-butyl (4-(benzylamino)-4-oxobutane-1,2-diyl)-(*R*)-dicarbamate (**77**).



Benzyl (R)-(1-amino-4-(benzylamino)-4-oxobutan-2-yl)carbamate 2,2,2-trifluoroacetic acid — Solvent: CD3OD



¹H NMR of benzyl (R)-(1-amino-4-(benzylamino)-4-oxobutan-2-yl)carbamate 2,2,2-trifluoroacetic acid (**78**).



^{13}C NMR of benzyl (*R*)-(1-amino-4-(benzylamino)-4-oxobutan-2-yl)carbamate 2,2,2-trifluoroacetic acid (**78**).

BIBLIOGRAPHY

1. Payne, D. J. Desperately Seeking New Antibiotics. *Science* **2008**, *321*, 1644-1645.
2. Queener, S.; Queener, S. *Beta-lactam antibiotics for clinical use*; Informa Health Care: 1986; Vol. 4.
3. Kong, K.; Schneper, L.; Mathee, K. Beta-lactam antibiotics: from antibiosis to resistance and bacteriology. *APMIS* **2010**, *118*, 1-36.
4. Gaude, G. S.; Hattiholli, J. Rising bacterial resistance to beta-lactam antibiotics: Can there be solutions? *Journal of Dr.NTR university of Health sciences* **2013**, *2*, 4-9.
5. Jacob, J. T.; Klein, E.; Laxminarayan, R.; Beldavs, Z.; Lynfield, R.; Kallen, A. J.; Ricks, R.; Edwards, J.; Srinivasan, A.; Fridkin, S.; Rasheed, J. K.; Lonsway, D.; Bulens, S.; Herrera, R.; McDonald, L. C.; Patel, J.; Limbago, B.; Bell, M.; Cardo, D. Vital Signs: Carbapenem-Resistant Enterobacteriaceae. *Morbidity and Mortality Weekly Report* **2013**, *62*, 165-170.
6. Courvalin, P. Transfer of antibiotic resistance genes between gram-positive and gram-negative bacteria. *Antimicrob. Agents Chemother.* **1994**, *38*, 1447.
7. Stamm, W. E.; Norrby, S. R. Urinary Tract Infections: Disease Panorama and Challenges. *J. Infect. Dis.* **2001**, *183*, S1-S4.
8. Kaitin, K. I. Deconstructing the Drug Development Process: The New Face of Innovation. *Clinical Pharmacology & Therapeutics* **2010**, *87*, 356-361.
9. DiMasi, J. A.; Grabowski, H. G.; Hansen, R. W. Innovation in the pharmaceutical industry: New estimates of R&D costs. *J. Health Econ.* **2016**, *47*, 20-33.
10. Anonymous 2019 Antibacterial agents in clinical development: an analysis of the antibacterial clinical development pipeline. *Geneva: World Health Organization* **2019**, CC BY-NC-SA 3.0 IGO.
11. Årdal, C.; Balasegaram, M.; Laxminarayan, R.; McAdams, D.; Outtersson, K.; Rex, J. H.; Sumpradit, N. Antibiotic development — economic, regulatory and societal challenges. *Nature Reviews Microbiology* **2020**, *18*, 267-274.

12. Lee-Ruff, E.; Mladenova, G. Enantiomerically Pure Cyclobutane Derivatives and Their Use in Organic Synthesis. *Chemical Reviews (Washington, DC, United States)* **2003**, *103*, 1449-1483.
13. Armoush, N.; Syal, P.; Becker, D. P. Synthesis of substituted 2-aminocyclobutanones. *Synth. Commun.; Synthetic Communications* **2008**, *38*, 1679-1687.
14. Belluš, D.; Ernst, B. Cyclobutanones and Cyclobutenones in Nature and in Synthesis [New Synthetic Methods (71)]. *Angew. Chem. Int. Ed Engl.* **1988**, *27*, 797-827.
15. Pankey, G. A.; Sabath, L. D. Clinical relevance of bacteriostatic versus bactericidal mechanisms of action in the treatment of gram-positive bacterial infections. *Clin. Infect. Dis.* **2004**, *38*, 864-870.
16. Zapun, A.; Contreras-Martel, C.; Vernet, T. Penicillin-binding proteins and β -lactam resistance. *FEMS Microbiol. Rev.* **2008**, *32*, 361-385.
17. Macheboeuf, P.; Contreras-Martel, C.; Job, V.; Dideberg, O.; Dessen, A. Penicillin Binding Proteins: key players in bacterial cell cycle and drug resistance processes. *FEMS Microbiol. Rev.* **2006**, *30*, 673-691.
18. Garau, J. Beta-lactamases: Current situation and clinical importance. *Intensive Care Med.* **1994**, *20*, S5-S9.
19. Queenan, A. M.; Bush, K. Carbapenemases: the versatile \hat{I}^2 -lactamases. *Clin. Microbiol. Rev.* **2007**, *20*, 440-458.
20. Walsh, T. R.; Toleman, M. A.; Poirel, L.; Nordmann, P. Metallo-beta-lactamases: the quiet before the storm? *Clin. Microbiol. Rev.* **2005**, *18*, 306-325.
21. Gehringer, M.; Laufer, S. A. Emerging and Re-Emerging Warheads for Targeted Covalent Inhibitors: Applications in Medicinal Chemistry and Chemical Biology. *J. Med. Chem.* **2019**, *62*, 5673-5724.
22. Jöst, C.; Nitsche, C.; Scholz, T.; Roux, L.; Klein, C. D. Promiscuity and Selectivity in Covalent Enzyme Inhibition: A Systematic Study of Electrophilic Fragments. *J. Med. Chem.* **2014**, *57*, 7590-7599.
23. Singh, J.; Petter, R. C.; Baillie, T. A.; Whitty, A. The resurgence of covalent drugs. *Nature Reviews Drug Discovery* **2011**, *10*, 307-317.

24. Robertson, J. G. Mechanistic Basis of Enzyme-Targeted Drugs. *Biochemistry (N. Y.)* **2005**, *44*, 5561-5571.
25. Jollow, D. J.; Mitchell, J. R.; Potter, W. Z.; Davis, D. C.; Gillette, J. R.; Brodie, B. B. Acetaminophen-induced hepatic necrosis. Role of covalent binding *in vivo*. *J. Pharmacol. Exp. Ther.* **1973**, *187*, 195-202.
26. Bandyopadhyay, A.; Gao, J. Targeting biomolecules with reversible covalent chemistry. *Curr. Opin. Chem. Biol.* **2016**, *34*, 110-116.
27. Sutanto, F.; Konstantinidou, M.; Dömling, A. Covalent inhibitors: a rational approach to drug discovery. *RSC Med. Chem.* **2020**, *11*, 876-884.
28. Bauer, R. A. Covalent inhibitors in drug discovery: from accidental discoveries to avoided liabilities and designed therapies. *Drug Discov. Today* **2015**, *20*, 1061-1073.
29. Krippendorff, B.; Neuhaus, R.; Lienau, P.; Reichel, A.; Huisinga, W. Mechanism-Based Inhibition: Deriving KI and kinact Directly from Time-Dependent IC50 Values. *J. Biomol. Screen.* **2009**, *14*, 913-923.
30. Leung, D.; Abbenante, G.; Fairlie, D. P. Protease inhibitors: Current status and future prospects. *J. Med. Chem.* **2000**, *43*, 305-341.
31. Johnson, J. W.; Gretes, M.; Goodfellow, V. J.; Marrone, L.; Heynen, M. L.; Strynadka, N. C. J.; Dmitrienko, G. I. Cyclobutanone analogues of β -lactams revisited: Insights into conformational requirements for inhibition of serine- and metallo- β -lactamases. *J. Am. Chem. Soc.* **2010**, *132*, 2558-2560.
32. Abboud, M. I.; Kosmopoulou, M.; Krismanich, A.; Johnson, J. W.; Hinchliffe, P.; Brem, J.; Claridge, T. D.; Spencer, J.; Schofield, C.; Dmitrienko, G. I. Cyclobutanone Mimics of Intermediates in Metallo- β -Lactamase Catalysis. *Chemistry-A European Journal* **2017**, *24*, 5734-5737.
33. Lowe, G.; Swain, S. Synthesis of a cyclobutanone analogue of a β -lactam antibiotic. *J. Chem. Soc., Perkin Trans. 1* **1985**, 391-398.
34. Lowe, G.; Swain, S. Synthesis of 7 β -phenylacetamido-6-oxo-2-oxabicyclo [3.2. 0] heptane-4 α -carboxylic acid, a cyclobutanone analogue of a β -lactam antibiotic. *Journal of the Chemical Society, Chemical Communications* **1983**, 1279-1281.
35. Palacios, A. R.; Rossi, M.; Mahler, G. S.; Vila, A. J. Metallo- β -Lactamase Inhibitors Inspired on Snapshots from the Catalytic Mechanism. *Biomolecules* **2020**, *10*.

36. Lowe, G.; Swain, S. Synthesis of a cyclobutanone analog of a β -lactam antibiotic. *Journal of the Chemical Society, Perkin Transactions 1: Organic and Bio-Organic Chemistry (1972-1999)* **1985**, 391-398.
37. Lange, G.; Savard, M. E.; Viswanatha, T.; Dmitrienko, G. I. Synthesis of 4-carboxy-2-thia-bicyclo [3.2. 0] heptan-6-ones via 3-carboxy-2, 3-dihydrothiophenes: Potential β -lactamase inhibitors. *Tetrahedron Lett.* **1985**, 26, 1791-1794.
38. Cocuzza, A.; Boswell, G. Cyclobutanone analogs of β -lactam antibiotics: synthesis of *N*-acetyldeazathienamycin. *Tetrahedron Lett.* **1985**, 26, 5363-5366.
39. Pauls, H. W.; Cheng, B.; Reid, L. S. 2-(Peptidamido)cyclobutanones: a novel strategy for the inhibition of serine elastases. *Bioorg. Chem.* **1992**, 20, 124-134.
40. Stewart, A. C.; Clifton, I. J.; Adlington, R. M.; Baldwin, J. E.; Rutledge, P. J. A cyclobutanone analogue mimics penicillin in binding to isopenicillin N synthase. *ChemBioChem* **2007**, 8, 2003-2007.
41. Filippova, E. V.; Weston, L. A.; Kuhn, M. L.; Geissler, B.; Gehring, A. M.; Armoush, N.; Adkins, C. T.; Minasov, G.; Dubrovskaya, I.; Shuvalova, L.; Winsor, J. R.; Lavis, L. D.; Satchell, K. J. F.; Becker, D. P.; Anderson, W. F.; Johnson, R. J. Large Scale Structural Rearrangement of a Serine Hydrolase from *Francisella tularensis* Facilitates Catalysis. *J. Biol. Chem.* **2013**, 288, 10522-10535.
42. Edwards, P. D.; Andisik, D. W.; Bryant, C. A.; Ewing, B.; Gomes, B.; Lewis, J. J.; Rakiewicz, D.; Steelman, G.; Strimpler, A.; Trainor, D. A.; Tuthill, P. A.; Mauger, R. C.; Veale, C. A.; Wildonger, R. A.; Williams, J. C.; Wolanin, D. J.; Zottola, M. Discovery and biological activity of orally active peptidyl trifluoromethyl ketone inhibitors of human neutrophil elastase. *J. Med. Chem.* **1997**, 40, 1876-1885.
43. Tavares, F. X.; Deaton, D. N.; Miller, L. R.; Wright, L. L. Ketoamide-Based Inhibitors of Cysteine Protease, Cathepsin K: P3 Modifications. *J. Med. Chem.* **2004**, 47, 5057-5068.
44. Devi, P.; Rutledge, P. J. Cyclobutanone Analogues of β -Lactam Antibiotics: β -Lactamase Inhibitors with Untapped Potential? *ChemBioChem* **2017**, 18, 338-351.
45. Yang, G.; Ghosez, L. Synthesis of Enantiopure α -Chlorocyclobutanones and Cyclobutanols as Scaffolds for the Diverted Synthesis of Serine Protease Inhibitors. *Eur. J. Org. Chem.* **2009**, 2009, 1738-1748.

46. Lall, M. S.; Ramtohol, Y. K.; James, M. N. G.; Vederas, J. C. Serine and Threonine β -Lactones: A New Class of Hepatitis A Virus 3C Cysteine Proteinase Inhibitors. *J. Org. Chem.* **2002**, *67*, 1536-1547.
47. Bisel, P.; Breitling, E.; Frahm, A. W. Diastereo- and enantioselective synthesis of (+)- and (-)-cis-2-aminocyclobutanols. *European Journal of Organic Chemistry* **1998**, 729-733.
48. Rebolledo, F.; González-Sabín, Javier; Gotor, V. Enzymatic Dynamic Kinetic Resolution in Stereoselective Synthesis. *Stereoselective Synthesis of Drugs and Natural Products* **2013**, 1-30.
49. Bhat, V.; Welin, E. R.; Guo, X.; Stoltz, B. M. Advances in Stereoconvergent Catalysis from 2005 to 2015: Transition-Metal-Mediated Stereoablative Reactions, Dynamic Kinetic Resolutions, and Dynamic Kinetic Asymmetric Transformations. *Chem. Rev.* **2017**, *117*, 4528-4561.
50. Buchholz, K. A breakthrough in enzyme technology to fight penicillin resistance—industrial application of penicillin amidase. *Applied microbiology and biotechnology.* **2016**, *100*, 3825-3839.
51. Arroyo, M.; de la Mata, I.; Acebal, C.; Pilar Castellón, M. Biotechnological applications of penicillin acylases: state-of-the-art. *Appl. Microbiol. Biotechnol.* **2003**, *60*, 507-514.
52. Sambale, C.; Kula, M. R. Studies on the Enzymatic Hydrolysis of Amino Acid Carbamates. *Biotechnol. Appl. Biochem.* **1987**, *9*, 251-257.
53. Ufarté, L.; Laville, E.; Duquesne, S.; Morgavi, D.; Robe, P.; Klopp, C.; Rizzo, A.; Pizzut-Serin, S.; Potocki-Veronese, G. Discovery of carbamate degrading enzymes by functional metagenomics. *PLOS ONE* **2017**, *12*, e0189201.
54. Roelofsen, D.; Wils, E.; van Bekkum, H. Synthesis of acetals using molecular sieves. *Recueil des Travaux Chimiques des Pays-Bas* **1971**, *90*, 1141-1152.
55. Habeeb Mohammad, T. S.; Reidl, C. T.; Zeller, M.; Becker, D. P. Synthesis of a protected 2-aminocyclobutanone as a modular transition state synthon for medicinal chemistry. *Tetrahedron Letters* **2020**, 151632.
56. Bell, R. P. The Reversible Hydration of Carbonyl Compounds. *Advances in Physical Organic Chemistry* **1966**, *4*, 1-29.
57. Wiberg, K. B.; Morgan, K. M.; Maltz, H. Thermochemistry of carbonyl reactions. 6. A study of hydration equilibria. *J. Am. Chem. Soc.* **1994**, *116*, 11067-11077.

58. Anonymous Apex2 v2013.4-1, v2014.11, v2014.1-1, SAINT V8.34A, SAINT V8.30C. Bruker AXS Inc.: Madison (WI), USA, 2013/2014.
59. Krause, L.; Herbst-Irmer, R.; Sheldrick, G. M.; Stalke, D. Comparison of silver and molybdenum microfocus X-ray sources for single-crystal structure determination. *Journal of Applied Crystallography* **2015**, *48*, 3-10.
60. Sheldrick, G. SHELXL, V6. 12., Bruker Analytical X-ray Systems. Inc., Madison, WI, USA **2003**.
61. Sheldrick, G. M. A short history of SHELX. *Acta Crystallographica Section A* **2008**, *64*, 112-122.
62. Sheldrick, G. M. Crystal structure solution with ShelXT. *Acta Crystallogr. A* **2015**, *71*, 3-8.
63. Hübschle, C. B.; Sheldrick, G. M.; Dittrich, B. ShelXle: a Qt graphical user interface for SHELXL. *Journal of applied crystallography* **2011**, *44*, 1281-1284.
64. Gygli, S. M.; Borrell, S.; Trauner, A.; Gagneux, S. Antimicrobial resistance in *Mycobacterium tuberculosis*: mechanistic and evolutionary perspectives. *FEMS Microbiology Reviews* **2017**, *41*, 354-373.
65. Fair, R. J.; Tor, Y. Antibiotics and bacterial resistance in the 21st century. *Perspect Medicin Chem* **2014**, *6*, 25-64.
66. Belete, T. M. Novel targets to develop new antibacterial agents and novel alternatives to antibacterial agents. *Human Microbiome Journal* **2019**, *11*, 100052.
67. Gillner, D. M.; Becker, D. P.; Holz, R. C. Lysine biosynthesis in bacteria: a metallodesuccinylase as a potential antimicrobial target. *JBIC, J. Biol. Inorg. Chem.* **2013**, *18*, 155-163.
68. Karita, M.; Etterbeek, M. L.; Forsyth, M. H.; Tummuru, M. K. R.; Blaser, M. J. Characterization of *Helicobacter pylori* dapE and construction of a conditionally lethal dapE mutant. *Infect. Immun.* **1997**, *65*, 4158-4164.
69. Pavelka, M. S., Jr.; Jacobs, W. R., Jr Biosynthesis of diaminopimelate, the precursor of lysine and a component of peptidoglycan, is an essential function of *Mycobacterium smegmatis*. *J. Bacteriol.* **1996**, *178*, 6496-6507.

70. Usha, V.; Lloyd, A. J.; Roper, D. I.; Dowson, C. G.; Kozlov, G.; Gehring, K.; Chauhan, S.; Imam, H. T.; Blindauer, C. A.; Besra, G. S. Reconstruction of diaminopimelic acid biosynthesis allows characterisation of *Mycobacterium tuberculosis* N-succinyl-L,L-diaminopimelic acid desuccinylase. *Sci. Rep.* **2016**, *6*, 23191.
71. Pendleton, J. N.; Gorman, S. P.; Gilmore, B. F. Clinical relevance of the ESKAPE pathogens. *Expert Review of Anti-infective Therapy* **2013**, *11*, 297-308.
72. Badger, J.; Sauder, J.; Adams, J.; Antonysamy, S.; Bain, K.; Bergseid, M.; Buchanan, S.; Buchanan, M.; Batiyenko, Y.; Christopher, J. Structural analysis of a set of proteins resulting from a bacterial genomics project. *Proteins: Structure, Function, and Bioinformatics* **2005**, *60*, 787-796.
73. Nocek, B. P.; Gillner, D. M.; Fan, Y.; Holz, R. C.; Joachimiak, A. Structural Basis for Catalysis by the Mono- and Dimetalated Forms of the dapE-Encoded N-succinyl-L,L-Diaminopimelic Acid Desuccinylase. *J. Mol. Biol.* **2010**, *397*, 617-626.
74. Starus, A.; Nocek, B.; Bennett, B.; Larrabee, J. A.; Shaw, D. L.; Sae-Lee, W.; Russo, M. T.; Gillner, D. M.; Makowska-Grzyska, M.; Joachimiak, A.; Holz, R. C. Inhibition of the dapE-Encoded N-Succinyl-L,L-diaminopimelic Acid Desuccinylase from *Neisseria meningitidis* by L-Captopril. *Biochemistry* **2015**, *54*, 4834-4844.
75. Kochert, M.; Nocek, B. P.; Habeeb Mohammad, T. S.; Gild, E.; Lovato, K.; Heath, T. K.; Holz, R. C.; Olsen, K. W.; Becker, D. P. Atomic-Resolution 1.3 Å Crystal Structure, Inhibition by Sulfate, and Molecular Dynamics of the Bacterial Enzyme DapE. *Biochemistry (N. Y.)* **2021**, *60*, 908-917.
76. Nocek, B.; Reidl, C.; Starus, A.; Heath, T.; Bienvenue, D.; Osipiuk, J.; Jedrzejczak, R. P.; Joachimiak, A.; Becker, D. P.; Holz, R. C. Structural Evidence for a Major Conformational Change Triggered by Substrate Binding in DapE Enzymes: Impact on the Catalytic Mechanism. *Biochemistry (N. Y.)* **2018**, *57*, 574.
77. Molecular Operating Environment (MOE), 2013.08; Chemical Computing Group ULC, 1010 Sherbooke St. West, Suite #910, Montreal, QC, Canada, H3A 2R7, 2018. **2017**.
78. Reidl, C. T.; Majorek, K. A.; Dang, J.; Law, M.; Tran, D.; Jew, K.; Chiarelli, P.; Minor, W.; Kuhn, M.; Becker, D. P. PA4794 Gcn5-related N-acetyltransferase bisubstrate inhibitors and mechanistic insights from co-crystal structures, site-directed mutants, and molecular dynamics. *The FASEB Journal* **2017**, *31*, 923.6-923.6.

79. Nocek, B.; Starus, A.; Makowska-Grzyska, M.; Gutierrez, B.; Sanchez, S.; Jedrzejczak, R.; Mack, J. C.; Olsen, K. W.; Joachimiak, A.; Holz, R. C. The dimerization domain in DapE enzymes is required for catalysis. *PLoS One* **2014**, *9*, e93593/1-e93593/11, 11.
80. Copley, R. R.; Barton, G. J. A Structural Analysis of Phosphate and Sulphate Binding Sites in Proteins: Estimation of Propensities for Binding and Conservation of Phosphate Binding Sites. *Journal of Molecular Biology* **1994**, *242*, 321-329.
81. Kanyo, Z. F.; Christianson, D. W. Biological recognition of phosphate and sulfate. *J. Biol. Chem.* **1991**, *266*, 4264-4268.
82. Moras, D.; Olsen, K. W.; Sabesan, M. N.; Buehner, M.; Ford, G. C.; Rossmann, M. G. Studies of asymmetry in the three-dimensional structure of lobster D-glyceraldehyde-3-phosphate dehydrogenase. *J. Biol. Chem.* **1975**, *250*, 9137-9162.
83. Heath, T. K.; Lutz Jr, M. R.; Reidl, C. T.; Guzman, E. R.; Herbert, C. A.; Nocek, B. P.; Holz, R. C.; Olsen, K. W.; Ballicora, M. A.; Becker, D. P. Practical spectrophotometric assay for the dapE-encoded N-succinyl-L, L-diaminopimelic acid desuccinylase, a potential antibiotic target. *PloS one* **2018**, *13*, e0196010.
84. Dutta, D.; Mishra, S. Structural and mechanistic insight into substrate binding from the conformational dynamics in apo and substrate-bound DapE enzyme. *Phys Chem Chem Phys* **2016**, *18*, 1671-1680.
85. Humphrey, W.; Dalke, A.; Schulten, K. VMD: visual molecular dynamics. *J Mol Graph* **1996**, *14*, 33-8, 27-8.
86. Phillips, J. C.; Braun, R.; Wang, W.; Gumbart, J.; Tajkhorshid, E.; Villa, E.; Chipot, C.; Skeel, R. D.; Kale, L.; Schulten, K. Scalable molecular dynamics with NAMD. *J. Comput. Chem.* **2005**, *26*, 1781-1802.
87. Weng, J.; Fan, K.; Wang, W. The conformational transition pathways of ATP-binding cassette transporter BtuCD revealed by targeted molecular dynamics simulation. *PLoS One* **2012**, *7*, e30465.
88. Cheng, X.; Wang, H.; Grant, B.; Sine, S. M.; McCammon, J. A. Targeted molecular dynamics study of C-loop closure and channel gating in nicotinic receptors. *PLoS Comput. Biol.* **2006**, *2*, e134.
89. Gillner, D.; Armoush, N.; Holz, R. C.; Becker, D. P. Inhibitors of bacterial N-succinyl-L,L-diaminopimelic acid desuccinylase (DapE) and demonstration of in vitro antimicrobial activity. *Bioorg. Med. Chem. Lett.* **2009**, *19*, 6350-6352.

90. Kindler, S. H.; Gilvarg, C. *N*-Succinyl-L,L-diaminopimelic acid deacylase. *J. Biol. Chem.* **1960**, *235*, 3532-3535.
91. Bienvenue, D. L.; Gilner, D. M.; Davis, R. S.; Bennett, B.; Holz, R. C. Substrate specificity, metal binding properties, and spectroscopic characterization of the DapE-encoded *N*-succinyl-L,L-diaminopimelic acid desuccinylase from *Haemophilus influenzae*. *Biochemistry* **2003**, *42*, 10756-10763.
92. Berman, H.; Henrick, K.; Nakamura, H. Announcing the worldwide Protein Data Bank. *Nature Structural & Molecular Biology* **2003**, *10*, 980-980.
93. Rolain, J. M.; Parola, P.; Cornaglia, G. New Delhi metallo-beta-lactamase (NDM-1): towards a new pandemic? *Clinical Microbiology and Infection* **2010**, *16*, 1699-1701.
94. Wu, W.; Feng, Y.; Tang, G.; Qiao, F.; McNally, A.; Zong, Z. NDM Metallo- β -Lactamases and Their Bacterial Producers in Health Care Settings. *Clin. Microbiol. Rev.* **2019**, *32*, e00115-18.
95. Mahanta, N.; Szantai-Kis, D.; Petersson, E. J.; Mitchell, D. A. Biosynthesis and Chemical Applications of Thioamides. *ACS Chem. Biol.* **2019**, *14*, 142-163.
96. Newberry, R. W.; VanVeller, B.; Raines, R. T. Thioamides in the collagen triple helix. *Chem. Commun.* **2015**, *51*, 9624-9627.
97. Jagodziński, T. S. Thioamides as Useful Synthons in the Synthesis of Heterocycles. *Chem. Rev.* **2003**, *103*, 197-228.
98. DeBarber, A. E.; Mdluli, K.; Bosman, M.; Bekker, L.; Barry, C. E. Ethionamide activation and sensitivity in multidrug-resistant *Mycobacterium tuberculosis*. *Proc. Natl. Acad. Sci. USA* **2000**, *97*, 9677-9682.
99. Rajabi, N.; Auth, M.; Troelsen, K. R.; Pannek, M.; Bhatt, D. P.; Fontenas, M.; Hirschey, M. D.; Steegborn, C.; Madsen, A. S.; Olsen, C. A. Mechanism-Based Inhibitors of the Human Sirtuin 5 Deacylase: Structure–Activity Relationship, Biostructural, and Kinetic Insight. *Angew. Chem. Int. Ed.* **2017**, *56*, 14836-14841.
100. Ozturk, T.; Ertas, E.; Mert, O. Use of Lawesson's Reagent in Organic Syntheses. *Chem. Rev.* **2007**, *107*, 5210-5278.

101. Rao, Y.; Li, X.; Nagorny, P.; Hayashida, J.; Danishefsky, S. J. A Simple Method for the Conversion of Carboxylic Acids into Thioacids with Lawesson's Reagent. *Tetrahedron Lett.* **2009**, *50*, 6684-6686.
102. Clausen, K.; El-Barbary, A. A.; Lawesson, S. -. Studies on organophosphorus compounds—XXXV11Part XXXIV: A.A. El-Barbary, S. Scheibye, S.-O. Lawesson and H. Fritz, Acta. Chem. Scand. B34, 597 (1980).: A new route to 4-methoxyphenylphosphonothioic diamides from 2,4-bis(4-methoxyphenyl)-1,3,2,4-dithiadiphosphetane-2,4-disulfide and amines. *Tetrahedron* **1981**, *37*, 1019-1025.
103. Curphey, T. J. Thionation with the Reagent Combination of Phosphorus Pentasulfide and Hexamethyldisiloxane. *J. Org. Chem.* **2002**, *67*, 6461-6473.
104. Bergman, J.; Pettersson, B.; Hasimbegovic, V.; Svensson, P. H. Thionations Using a P₄S₁₀-Pyridine Complex in Solvents Such as Acetonitrile and Dimethyl Sulfone. *J. Org. Chem.* **2011**, *76*, 1546-1553.
105. Gavras, H.; Gavras, I. Angiotensin converting enzyme inhibitors. Properties and side effects. *Hypertension* **1988**, *11*, II37-41.
106. Uda, N. R.; Creus, M. Selectivity of Inhibition of N-Succinyl-L,L-Diaminopimelic Acid Desuccinylase in Bacteria: The product of dapE-gene Is Not the Target of L-Captopril Antimicrobial Activity. *Bioinorg Chem Appl* **2011**, *2011*, 306465.
107. Lipinski, C. A.; Lombardo, F.; Dominy, B. W.; Feeney, P. J. Experimental and computational approaches to estimate solubility and permeability in drug discovery and development settings. *Adv. Drug Deliv. Rev.* **1997**, *23*, 3-25.
108. Veber, D. F.; Johnson, S. R.; Cheng, H.; Smith, B. R.; Ward, K. W.; Kopple, K. D. Molecular Properties That Influence the Oral Bioavailability of Drug Candidates. *J. Med. Chem.* **2002**, *45*, 2615-2623.
109. Baell, J. B.; Holloway, G. A. New substructure filters for removal of pan assay interference compounds (PAINS) from screening libraries and for their exclusion in bioassays. *J. Med. Chem.* **2010**, *53*, 2719-2740.
110. Baell, J.; Walters, M. A. Chemistry: Chemical con artists foil drug discovery. *Nature News* **2014**, *513*, 481.
111. Baell, J. B. Feeling nature's PAINS: natural products, natural product drugs, and pan assay interference compounds (PAINS). *J. Nat. Prod.* **2016**, *79*, 616-628.

112. Daina, A.; Michielin, O.; Zoete, V. SwissADME: a free web tool to evaluate pharmacokinetics, drug-likeness and medicinal chemistry friendliness of small molecules. *Scientific reports* **2017**, *7*, 42717.
113. Grosdidier, A.; Zoete, V.; Michielin, O. SwissDock, a protein-small molecule docking web service based on EADock DSS. *Nucleic Acids Res.* **2011**, *39*, W270-W277.
114. Liu, D.; Zhao, G.; Xiang, L. Diverse Strategies for the Synthesis of the Indoline Scaffold. *Eur. J. Org. Chem.* **2010**, 3975-3984.
115. Reidl, C. T.; Heath, T. K.; Darwish, I.; Torrez, R. M.; Moore, M.; Gild, E.; Nocek, B. P.; Starus, A.; Holz, R. C.; Becker, D. P. Indoline-6-Sulfonamide Inhibitors of the Bacterial Enzyme DapE. *Antibiotics* **2020**, *9*, 595.
116. Zafrani, Y.; Yeffet, D.; Sod-Moriah, G.; Berliner, A.; Amir, D.; Marciano, D.; Gershonov, E.; Saphier, S. Difluoromethyl Bioisostere: Examining the "Lipophilic Hydrogen Bond Donor" Concept. *J. Med. Chem.* **2017**, *60*, 797-804.
117. Santos, L.; Panossian, A.; Donnard, M.; Vors, J.; Pazenok, S.; Bernier, D.; Leroux, F. R. Deprotonative Functionalization of the Difluoromethyl Group. *Org. Lett.* **2020**, *22*, 8741-8745.
118. Thappali, S. R. S.; Varanasi, K. V. S.; Veeraraghavan, S.; Vakkalanka, S. K. V. S.; K, M. Simultaneous quantitation of IC87114, roflumilast and its active metabolite roflumilast N-oxide in plasma by LC-MS/MS: application for a pharmacokinetic study. *J. Mass Spectrom.* **2012**, *47*, 1612-1619.
119. Herr, R. J. 5-Substituted-1H-tetrazoles as carboxylic acid isosteres: medicinal chemistry and synthetic methods. *Bioorg. Med. Chem.* **2002**, *10*, 3379-3393.
120. Matta, C. F.; Arabi, A. A.; Weaver, D. F. The bioisosteric similarity of the tetrazole and carboxylate anions: Clues from the topologies of the electrostatic potential and of the electron density. *Eur. J. Med. Chem.* **2010**, *45*, 1868-1872.
121. Nachman, R. J.; Zabrocki, J.; Olczak, J.; Williams, H. J.; Moyna, G.; Ian Scott, A.; Coast, G. M. cis-peptide bond mimetic tetrazole analogs of the insect kinins identify the active conformation. *Peptides* **2002**, *23*, 709-716.
122. Neochoritis, C. G.; Zhao, T.; Dömling, A. Tetrazoles via Multicomponent Reactions. *Chem. Rev.* **2019**, *119*, 1970-2042.

123. Myznikov, L.; Hrabalek, A.; Koldobskii, G. Drugs in the Tetrazole Series. *Chemistry of Heterocyclic Compounds* **2007**, *43*, 1-9.
124. Wei, C.; Bian, M.; Gong, G. Tetrazolium compounds: synthesis and applications in medicine. *Molecules (Basel, Switzerland)* **2015**, *20*, 5528-5553.
125. Gavriilyuk, J. I.; Evindar, G.; Chen, J. Y.; Batey, R. A. Peptide-Heterocycle Hybrid Molecules: Solid-Phase-Supported Synthesis of Substituted *N*-Terminal 5-Aminotetrazole Peptides via Electrocyclization of Peptidic Imidoylazides. *J. Comb. Chem.* **2007**, *9*, 644-651.
126. Murthy Boddapati, S. N.; Emmanuel Kola, A.; Kesana, S. B.; Bollikolla, H. B. Temperature dependent regioselective synthesis of aryl tetrazole amines using copper source. *Journal of Organometallic Chemistry* **2018**, *866*, 177-183.
127. Tahlan, S.; Kumar, S.; Narasimhan, B. Pharmacological significance of heterocyclic 1H-benzimidazole scaffolds: a review. *BMC Chemistry* **2019**, *13*, 101.
128. Goutelle, S.; Maurin, M.; Rougier, F.; Barbaut, X.; Bourguignon, L.; Ducher, M.; Maire, P. The Hill equation: a review of its capabilities in pharmacological modelling. *Fundam. Clin. Pharmacol.* **2008**, *22*, 633-648.
129. Prinz, H. Hill coefficients, dose-response curves and allosteric mechanisms. *Journal of chemical biology* **2010**, *3*, 37-44.
130. Yang, L.; Evans, D.; Xu, B.; Li, W.; Li, M.; Zhu, S.; Houk, K. N.; Zhou, Q. Enantioselective Diarylcarbene Insertion into Si-H Bonds Induced by Electronic Properties of the Carbenes. *J. Am. Chem. Soc.* **2020**, *142*, 12394-12399.
131. Tian, H.; Xia, Q.; Wang, Q.; Dong, J.; Liu, Y.; Wang, Q. Direct α -Monofluoroalkenylation of Heteroatomic Alkanes via a Combination of Photoredox Catalysis and Hydrogen-Atom-Transfer Catalysis. *Org. Lett.* **2019**, *21*, 4585-4589.
132. Schmitt, E.; Landelle, G.; Vors, J.; Lui, N.; Pazenok, S.; Leroux, F. R. A General Approach towards NH-Pyrazoles That Bear Diverse Fluoroalkyl Groups by Means of Fluorinated Iminium Salts. *Eur. J. Org. Chem.* **2015**, *2015*, 6052-6060.
133. Huang, C.; Wang, Y.; Li, X.; Ren, L.; Zhao, J.; Hu, Y.; Zhang, L.; Fan, G.; Xu, J.; Gu, X.; Cheng, Z.; Yu, T.; Xia, J.; Wei, Y.; Wu, W.; Xie, X.; Yin, W.; Li, H.; Liu, M.; Xiao, Y.; Gao, H.; Guo, L.; Xie, J.; Wang, G.; Jiang, R.; Gao, Z.; Jin, Q.; Wang, J.; Cao, B. Clinical features of patients infected with 2019 novel coronavirus in Wuhan, China. *The Lancet* **2020**, *395*, 497-506.
134. Lu, R.; Zhao, X.; Li, J.; Niu, P.; Yang, B.; Wu, H.; Wang, W.; Song, H.; Huang, B.; Zhu, N.; Bi, Y.; Ma, X.; Zhan, F.; Wang, L.; Hu, T.; Zhou, H.; Hu, Z.; Zhou, W.; Zhao, L.; Chen, J.; Meng, Y.;

Wang, J.; Lin, Y.; Yuan, J.; Xie, Z.; Ma, J.; Liu, W. J.; Wang, D.; Xu, W.; Holmes, E. C.; Gao, G. F.; Wu, G.; Chen, W.; Shi, W.; Tan, W. Genomic characterisation and epidemiology of 2019 novel coronavirus: implications for virus origins and receptor binding. *The Lancet* **2020**, *395*, 565-574.

135. Anonymous WHO Coronavirus (COVID-19) Dashboard. <https://covid19.who.int/> (accessed April, 22nd, 2021).
136. Andersen, K. G.; Rambaut, A.; Lipkin, W. I.; Holmes, E. C.; Garry, R. F. The proximal origin of SARS-CoV-2. *Nat. Med.* **2020**, *26*, 450-452.
137. Seyran, M.; Pizzol, D.; Adadi, P.; El-Aziz, T.; Hassan, S. S.; Soares, A.; Kandimalla, R.; Lundstrom, K.; Tambuwala, M.; Aljabali, A. A. A.; Lal, A.; Azad, G. K.; Choudhury, P. P.; Uversky, V. N.; Sherchan, S. P.; Uhal, B. D.; Rezaei, N.; Brufsky, A. M. Questions concerning the proximal origin of SARS-CoV-2. *J. Med. Virol.* **2021**, *93*, 1204-1206.
138. Harvey Lodish, Arnold Berk, S Lawrence Zipursky, Paul Matsudaira, David Baltimore, and James Darnell. Viruses: Structure, Function, and Uses. In *Molecular Cell Biology*; New York: W. H. Freeman: 2000; pp Section 6.3.
139. Chan, J. F.; Yuan, S.; Kok, K.; To, K. K.; Chu, H.; Yang, J.; Xing, F.; Liu, J.; Yip, C. C.; Poon, R. W.; Tsoi, H.; Lo, S. K.; Chan, K.; Poon, V. K.; Chan, W.; Ip, J. D.; Cai, J.; Cheng, V. C.; Chen, H.; Hui, C. K.; Yuen, K. A familial cluster of pneumonia associated with the 2019 novel coronavirus indicating person-to-person transmission: a study of a family cluster. *The Lancet* **2020**, *395*, 514-523.
140. Weiss, S. R.; Leibowitz, J. L. Chapter 4 - Coronavirus Pathogenesis. *Adv. Virus Res.* **2011**, *81*, 85-164.
141. Masters, P. S. Coronavirus genomic RNA packaging. *Virology* **2019**, *537*, 198-207.
142. Yang, D.; Leibowitz, J. L. The structure and functions of coronavirus genomic 3' and 5' ends. *Virus Res.* **2015**, *206*, 120-133.
143. Zhong, N. S.; Zheng, B. J.; Li, Y. M.; Poon; Xie, Z. H.; Chan, K. H.; Li, P. H.; Tan, S. Y.; Chang, Q.; Xie, J. P.; Liu, X. Q.; Xu, J.; Li, D. X.; Yuen, K. Y.; Peiris; Guan, Y. Epidemiology and cause of severe acute respiratory syndrome (SARS) in Guangdong, People's Republic of China, in February, 2003. *Lancet (London, England)* **2003**, *362*, 1353-1358.
144. Zaki, A. M.; van Boheemen, S.; Bestebroer, T. M.; Osterhaus, A. D. M. E.; Fouchier, R. A. M. Isolation of a Novel Coronavirus from a Man with Pneumonia in Saudi Arabia. *N. Engl. J. Med.* **2012**, *367*, 1814-1820.

145. Zhu, Z.; Lian, X.; Su, X.; Wu, W.; Marraro, G. A.; Zeng, Y. From SARS and MERS to COVID-19: a brief summary and comparison of severe acute respiratory infections caused by three highly pathogenic human coronaviruses. *Respiratory Research* **2020**, *21*, 224.
146. Rossi, G. A.; Sacco, O.; Mancino, E.; Cristiani, L.; Midulla, F. Differences and similarities between SARS-CoV and SARS-CoV-2: spike receptor-binding domain recognition and host cell infection with support of cellular serine proteases. *Infection* **2020**, *48*, 665-669.
147. Van Boheemen, S.; de Graaf, M.; Lauber, C.; Bestebroer, T. M.; Raj, V. S.; Zaki, A. M.; Osterhaus, A. D. M. E.; Haagmans, B. L.; Gorbalenya, A. E.; Snijder, E. J.; Fouchier, R. A. M. Genomic characterization of a newly discovered coronavirus associated with acute respiratory distress syndrome in humans. *mBio* **2012**, *3*, e00473-12.
148. Anonymous Repurposed Antiviral Drugs for Covid-19 — Interim WHO Solidarity Trial Results. *N. Engl. J. Med.* **2021**, *384*, 497-511.
149. Gupta, Y.; Maciorowski, D.; Mathur, R.; Pearce, C. M.; Ilc, D. J.; Husein, H.; Bharti, A.; Becker, D.; Brijesh, R.; Bradfute, S. B.; Durvasula, R.; Kempaiah, P. Revealing SARS-CoV-2 Functional Druggability Through Multi-Target Cadd Screening of Repurposable Drugs. *Preprints* **2020**.
150. Gupta, Y.; Maciorowski, D.; Zak, S. E.; Jones, K. A.; Kathayat, R. S.; Azizi, S.; Mathur, R.; Pearce, C. M.; Ilc, D. J.; Husein, H.; Herbert, A. S.; Bharti, A.; Rathi, B.; Durvasula, R.; Becker, D. P.; Dickinson, B. C.; Dye, J. M.; Kempaiah, P. Bisindolylmaleimide IX: A novel anti-SARS-CoV2 agent targeting viral main protease 3CL^{pro} demonstrated by virtual screening pipeline and in-vitro validation assays. *Methods* **2021**, .
151. Anonymous About Variants of the Virus that Causes COVID-19. <https://www.cdc.gov/coronavirus/2019-ncov/transmission/variant.html> (accessed April/23, 2021).
152. Rosenke, K.; Hansen, F.; Schwarz, B.; Feldmann, F.; Haddock, E.; Rosenke, R.; Barbian, K.; Meade-White, K.; Okumura, A.; Leventhal, S.; Hawman, D. W.; Ricotta, E.; Bosio, C. M.; Martens, C.; Saturday, G.; Feldmann, H.; Jarvis, M. A. Orally delivered MK-4482 inhibits SARS-CoV-2 replication in the Syrian hamster model. *Nature Communications* **2021**, *12*, 2295.
153. Zhang, C.; Zheng, W.; Huang, X.; Bell, E. W.; Zhou, X.; Zhang, Y. Protein Structure and Sequence Reanalysis of 2019-nCoV Genome Refutes Snakes as Its Intermediate Host and the Unique Similarity between Its Spike Protein Insertions and HIV-1. *J. Proteome Res.* **2020**, *19*, 1351-1360.

154. L. Schrodinger Small-Molecule Drug Discovery Suite 2020-1. **2020**, 2020-1.
155. Davidson, A. D.; Williamson, M. K.; Lewis, S.; Shoemark, D.; Carroll, M. W.; Heesom, K. J.; Zambon, M.; Ellis, J.; Lewis, P. A.; Hiscox, J. A.; Matthews, D. A. Characterisation of the transcriptome and proteome of SARS-CoV-2 reveals a cell passage induced in-frame deletion of the furin-like cleavage site from the spike glycoprotein. *Genome Medicine* **2020**, *12*, 68.
156. Nutho, B.; Mahalapbutr, P.; Hengphasatporn, K.; Pattarangoon, N. C.; Simanon, N.; Shigeta, Y.; Hannongbua, S.; Rungrotmongkol, T. Why Are Lopinavir and Ritonavir Effective against the Newly Emerged Coronavirus 2019? Atomistic Insights into the Inhibitory Mechanisms. *Biochemistry (N. Y.)* **2020**, *59*, 1769-1779.
157. Zhang, L.; Lin, D.; Sun, X.; Curth, U.; Drosten, C.; Sauerhering, L.; Becker, S.; Rox, K.; Hilgenfeld, R. Crystal structure of SARS-CoV-2 main protease provides a basis for design of improved α -ketoamide inhibitors. *Science* **2020**, *368*, 409.
158. Ullrich, S.; Nitsche, C. The SARS-CoV-2 main protease as drug target. *Bioorg. Med. Chem. Lett.* **2020**, *30*, 127377.
159. Shin, D.; Mukherjee, R.; Grewe, D.; Bojkova, D.; Baek, K.; Bhattacharya, A.; Schulz, L.; Widera, M.; Mehdipour, A. R.; Tascher, G.; Geurink, P. P.; Wilhelm, A.; van der Heden van Noort, Gerbrand J.; Ovaa, H.; Müller, S.; Knobloch, K.; Rajalingam, K.; Schulman, B. A.; Cinatl, J.; Hummer, G.; Ciesek, S.; Dikic, I. Papain-like protease regulates SARS-CoV-2 viral spread and innate immunity. *Nature* **2020**, *587*, 657-662.
160. Menachery, V. D.; Yount, B. L.; Josset, L.; Gralinski, L. E.; Scobey, T.; Agnihothram, S.; Katze, M. G.; Baric, R. S. Attenuation and Restoration of Severe Acute Respiratory Syndrome Coronavirus Mutant Lacking 2'-O-Methyltransferase Activity. *J. Virol.* **2014**, *88*, 4251.
161. Hackbart, M.; Deng, X.; Baker, S. C. Coronavirus endoribonuclease targets viral polyuridine sequences to evade activating host sensors. *Proc. Natl. Acad. Sci. USA* **2020**, *117*, 8094.
162. Ju, J.; Li, X.; Kumar, S.; Jockusch, S.; Chien, M.; Tao, C.; Morozova, I.; Kalachikov, S.; Kirchdoerfer, R. N.; Russo, J. J. Nucleotide analogues as inhibitors of SARS-CoV Polymerase. *Pharmacology research & perspectives* **2020**, *8*, e00674-e00674.
163. Zhu, W.; Chen, C. Z.; Gorshkov, K.; Xu, M.; Lo, D. C.; Zheng, W. RNA-Dependent RNA Polymerase as a Target for COVID-19 Drug Discovery. *SLAS DISCOVERY: Advancing the Science of Drug Discovery* **2020**, *25*, 1141-1151.

164. Shu, T.; Huang, M.; Wu, D.; Ren, Y.; Zhang, X.; Han, Y.; Mu, J.; Wang, R.; Qiu, Y.; Zhang, D.; Zhou, X. SARS-Coronavirus-2 Nsp13 Possesses NTPase and RNA Helicase Activities That Can Be Inhibited by Bismuth Salts. *Viol. Sin.* **2020**, *35*, 321-329.
165. Spratt, A. N.; Gallazzi, F.; Quinn, T. P.; Lorson, C. L.; Sönnnerborg, A.; Singh, K. Coronavirus helicases: attractive and unique targets of antiviral drug-development and therapeutic patents. **2021**, 1-12.
166. Dryjanski, M.; Kosley, L. L.; Pietruszko, R. N-Tosyl-l-phenylalanine Chloromethyl Ketone, a Serine Protease Inhibitor, Identifies Glutamate 398 at the Coenzyme-Binding Site of Human Aldehyde Dehydrogenase. Evidence for a Second "Naked Anion" at the Active Site. *Biochemistry (N. Y.)* **1998**, *37*, 14151-14156.
167. Lipinski, C. A. Drug-like properties and the causes of poor solubility and poor permeability. *J. Pharmacol. Toxicol. Methods* **2000**, *44*, 235-249.
168. Dror, O.; Schneidman-Duhovny, D.; Inbar, Y.; Nussinov, R.; Wolfson, H. J. Novel Approach for Efficient Pharmacophore-Based Virtual Screening: Method and Applications. *J. Chem. Inf. Model.* **2009**, *49*, 2333-2343.
169. White, M. A.; Lin, W.; Cheng, X. Discovery of COVID-19 Inhibitors Targeting the SARS-CoV-2 Nsp13 Helicase. *J. Phys. Chem. Lett.* **2020**, *11*, 9144-9151.
170. Ugwu, D. I.; Okoro, U. C.; Mishra, N. K. Synthesis, characterization and in vitro antitrypanosomal activities of new carboxamides bearing quinoline moiety. *PLOS ONE* **2018**, *13*, e0191234.
171. Johnson, C. M.; Linsky, T. W.; Yoon, D.; Person, M. D.; Fast, W. Discovery of Halopyridines as Quiescent Affinity Labels: Inactivation of Dimethylarginine Dimethylaminohydrolase. *J. Am. Chem. Soc.* **2011**, *133*, 1553-1562.
172. Marques, S. M.; Nuti, E.; Rossello, A.; Supuran, C. T.; Tuccinardi, T.; Martinelli, A.; Santos, M. A. Dual Inhibitors of Matrix Metalloproteinases and Carbonic Anhydrases: Iminodiacyl-Based Hydroxamate–Benzenesulfonamide Conjugates. *J. Med. Chem.* **2008**, *51*, 7968-7979.
173. Favrot, L.; Blanchard, J. S.; Vergnolle, O. Bacterial GCN5-Related N-Acetyltransferases: From Resistance to Regulation. *Biochemistry (N. Y.)* **2016**, *55*, 989.
174. Hentchel, K. L.; Escalante-Semerena, J. Acylation of Biomolecules in Prokaryotes: a Widespread Strategy for the Control of Biological Function and Metabolic Stress. *Microbiol. Mol. Biol. Rev.* **2015**, *79*, 321.

175. Baumgartner, J. T.; Habeeb Mohammad, T. S.; Czub, M. P.; Majorek, K. A.; Arolli, X.; Variot, C.; ck, M.; Minor, W.; Ballicora, M. A.; Becker, D. P.; Kuhn, M. L. Gcn5-Related N-Acetyltransferases (GNATs) With a Catalytic Serine Residue Can Play Ping-Pong Too. *Frontiers in Molecular Biosciences* **2021**, *8*, 154.
176. Capra, J. A.; Laskowski, R. A.; Thornton, J. M.; Singh, M.; Funkhouser, T. A. Predicting Protein Ligand Binding Sites by Combining Evolutionary Sequence Conservation and 3D Structure. *PLOS Computational biology* **2009**, *5*.
177. Majorek, K. A.; Kuhn, M. L.; Chruszcz, M.; Anderson, W. F.; Minor, W. Structural, functional, and inhibition studies of a Gcn5-related N-acetyltransferase (GNAT) superfamily protein PA4794: a new C-terminal lysine protein acetyltransferase from pseudomonas aeruginosa. *J Biol Chem* **2013**, *288*, 30223-30235.
178. Reidl, C.; Majorek, K. A.; Dang, J.; Tran, D.; Jew, K.; Law, M.; Payne, Y.; Minor, W.; Becker, D. P.; Kuhn, M. L. Generating enzyme and radical-mediated bisubstrates as tools for investigating Gcn5-related N-acetyltransferases. *FEBS Lett.* **2017**, *591*, 2348-2361.
179. Kuhn, M. L.; Majorek, K. A.; Minor, W.; Anderson, W. F. Broad-substrate screen as a tool to identify substrates for bacterial Gcn5-related N-acetyltransferases with unknown substrate specificity. *Protein Science* **2013**, *22*, 222-230.
180. Keller, R. United States of America Patent US4709075A, 1987.
181. Falagas, M. E.; Kasiakou, S. K.; Saravolatz, L. D. Colistin: The Revival of Polymyxins for the Management of Multidrug-Resistant Gram-Negative Bacterial Infections. *Clin. Infect. Dis.* **2005**, *40*, 1333-1341.
182. Czub, M. P.; Zhang, B.; Chiarelli, M. P.; Majorek, K. A.; Joe, L.; Porebski, P. J.; Revilla, A.; Wu, W.; Becker, D. P.; Minor, W.; Kuhn, M. L. A Gcn5-Related N-Acetyltransferase (GNAT) Capable of Acetylating Polymyxin B and Colistin Antibiotics in Vitro. *Biochemistry (N. Y.)* **2018**, *57*, 7011-7020.
183. Nguyen, T. T.; Ding, D.; Wolter, W. R.; Pérez, R. L.; Champion, M. M.; Mahasenan, K. V.; Heseck, D.; Lee, M.; Schroeder, V. A.; Jones, J. I.; Lastochkin, E.; Rose, M. K.; Peterson, C. E.; Suckow, M. A.; Mobashery, S.; Chang, M. Validation of Matrix Metalloproteinase-9 (MMP-9) as a Novel Target for Treatment of Diabetic Foot Ulcers in Humans and Discovery of a Potent and Selective Small-Molecule MMP-9 Inhibitor That Accelerates Healing. *J. Med. Chem.* **2018**, *61*, 8825-8837.

184. Hickman, A. B.; Namboodiri, M. A. A.; Klein, D. C.; Dyda, F. The Structural Basis of Ordered Substrate Binding by Serotonin *N*-Acetyltransferase: Enzyme Complex at 1.8 Å Resolution with a Bisubstrate Analog. *Cell* **1999**, *97*, 361-369.
185. Oda, K.; Matoba, Y.; Noda, M.; Kumagai, T.; Sugiyama, M. Catalytic Mechanism of Bleomycin *N*-Acetyltransferase Proposed on the Basis of Its Crystal Structure. *J. Biol. Chem.* **2010**, *285*, 1446-1456.
186. Montemayor, E. J.; Hoffman, D. W. The Crystal Structure of Spermidine/Spermine N1-Acetyltransferase in Complex with Spermine Provides Insights into Substrate Binding and Catalysis, *Biochemistry (N. Y.)* **2008**, *47*, 9145-9153.
187. Draker, K.; Wright, G. D. Molecular Mechanism of the Enterococcal Aminoglycoside 6'-*N*-Acetyltransferase': Role of GNAT-Conserved Residues in the Chemistry of Antibiotic Inactivation. *Biochemistry (N. Y.)* **2004**, *43*, 446-454.
188. Majorek, K. A.; Kuhn, M. L.; Chruszcz, M.; Anderson, W. F.; Minor, W. Structural, Functional, and Inhibition Studies of a Gcn5-related *N*-Acetyltransferase (GNAT) Superfamily Protein PA4794. *J. Biol. Chem.* **2013**, *288*, 30223.
189. Vetting, M. W.; de Carvalho, Luiz Pedro S.; Roderick, S. L.; Blanchard, J. S. A Novel Dimeric Structure of the RimL *N*^α-acetyltransferase from *Salmonella typhimurium*. *J. Biol. Chem.* **2005**, *280*, 22108-22114.
190. Sakamoto, T.; Ichihara, N.; Takeda, M. Characterization of indolamine *N*-acetyltransferase activity from the head ganglia of the American cockroach, *Periplaneta americana*. *Appl. Entomol. Zool.* **1998**, *33*, 97-104.
191. Filippova, E. V.; Kuhn, M. L.; Osipiuk, J.; Kiryukhina, O.; Joachimiak, A.; Ballicora, M. A.; Anderson, W. F. A Novel Polyamine Allosteric Site of SpeG from *Vibrio cholerae* Is Revealed by Its Dodecameric Structure. *J. Mol. Biol.* **2015**, *427*, 1316-1334.
192. Wong, L. J. C.; Wong, S. S. Kinetic mechanism of the reaction catalyzed by nuclear histone acetyltransferase A from calf thymus. *Biochemistry (N. Y.)* **1983**, *22*, 4637-4641.
193. Vetting, M. W.; Hegde, S. S.; Javid-Majd, F.; Blanchard, J. S.; Roderick, S. L. Aminoglycoside 2prime]-*N*-acetyltransferase from *Mycobacterium tuberculosis* in complex with coenzyme A and aminoglycoside substrates. *Nat Struct Mol Biol* **2002**, *9*, 653-658.
194. Charlop-Powers, Z.; Jakoncic, J.; Gurnon, J. R.; Van Etten, J. L.; Zhou, M. *Paramecium bur-saria* Chlorella Virus 1 Encodes a Polyamine Acetyltransferase *J. Biol. Chem.* **2012**, *287*, 9547-9551.

195. Dempsey, D. R.; Jeffries, K. A.; Bond, J. D.; Carpenter, A.; Rodriguez-Ospina, S.; Breydo, L.; Caswell, K. K.; Merkle, D. J. Mechanistic and Structural Analysis of *Drosophila melanogaster* Arylalkylamine *N*-Acetyltransferases. *Biochemistry (N. Y.)* **2014**, *53*, 7777-7793.

VITA

Dr. Thahani S. Habeeb Mohammad earned her Bachelor of Science degree in Chemistry with honors from the University of Peradeniya, Sri Lanka, in 2014. Her interest in Chemistry and Biological sciences led her to pursue Molecular Biology and Biotechnology, and Biology as the secondary specialization. In 2013, Dr. Habeeb Mohammad began research on natural product isolation under the supervision of Dr. Veranja Karunaratne, where she worked on isolation of an antifungal kaurane diterpenoid from the root extract of *Austroeupeatorium inulifolium* (an invasive plant). In collaboration with Dr. Sumedha Madawala, Dr. Habeeb Mohammad also studied the antifungal properties of *Ageratina riparia*.

Dr. Habeeb Mohammad started her Ph.D. studies at Loyola University Chicago in 2016 and began her research in Medicinal Chemistry with Dr. Daniel P. Becker. Her graduate research focused on small molecular drug design enabled through computer-aided drug design. Her work at Loyola and her collaborative work with Dr. Misty Kuhn from San Francisco State University earned her four publications in 2020 and 2021. In 2020, Dr. Habeeb Mohammad joined the collaborative project with Dr. Prakash Kempaiah at Stritch Medical School/Mayo Clinic toward the discovery of novel antivirals against SARS-CoV-2 in treating COVID-19. Dr. Habeeb Mohammad is a co-inventor in two shared

patent applications in progress with Mayo Clinic highlighting her work on potential anti-SARS-CoV-2 therapeutic agents.

During her time at Loyola University Chicago, Dr. Habeeb Mohammad was committed to teaching Organic Chemistry as an Organic laboratory teaching assistant, and she also taught several sections of Organic I and II lectures. In Summer 2019, Dr. Habeeb Mohammad mentored an undergraduate researcher as part of the ACS seed project, and she contributed to Loyola's First-Year Research Experience (FYRE) program and mentored three first-year students in Summer 2017, 2018, and 2019.

Commencing her career path toward the pharmaceutical industry, Dr. Habeeb Mohammad will be joining Dr. Rick Silverman's research group at Northwestern University as a postdoctoral researcher in August 2021, where she will focus on the GABA aminotransferase inactivators in treating epilepsy and addiction.